An investigation of the behaviour of the ground in response to energy extraction.

Benjamin David Philip Hepburn

Geoenvironmental Research Centre

Cardiff School of Engineering

Cardiff University

Thesis submitted to candidate for the degree of Doctor of Philosophy at Cardiff University

November 2013

CARDIFF UNIVERSITY
PRIFYSGOL CAERDYDD

Acknowledgements

The research contained in this thesis would not have been remotely possible without the contribution of a number of people, so without further due they will be acknowledged! I would first like to extend my gratitude to Professor Hywel Thomas, Dr Majid Sedighi and Dr Philip Vardon, without whose experience, expertise and guidance this research would not have been possible. I would also like to thank the past and present members of the Geoenvironmental Research Centre at Cardiff University; in particular Jamie and Lee whose office antics and laughter have never failed to raise spirits and will never be forgotten.

The work undertaken would not have been possible without the financial support of the Seren Project, funded by the Welsh European Funding Office (WEFO). Further to this, the financial and technical support provided by the projects industrial partners WDS Environmental and in particular Dr Aled Davies have proven invaluable.

The greatest thanks however are reserved for my friends and family. The experience of my PhD would not have been the same without the support of my friends, in particular Alex and Paul who have been there on a day to day basis without fail. I would not be where I am today without the love and values given to me by my parents and sister. With regard to this work, particular thanks must be given to my father who has given me exceptional time and effort. Words cannot express my true thanks. Finally (but by no means least), thanks must be given to Alisha. The continual love, support and friendship she has provided me throughout this journey will never be forgotten. Thank you please.

Declaration

This work has not been submitted in substance for any other degree or award at this or any other university or place of learning, nor is being submitted concurrently in candidature for any degree or other award.

Signed …….. *Date* 7nd November 2013

Statement 1

This thesis is being submitted in partial fulfilment of the requirements for the degree of PhD.

Signed …….. *Date* 7nd November 2013

Statement 2

This thesis is the result of my own independent work/investigation, except where otherwise stated. Other sources are acknowledged by explicit references. The views expressed are my own.

Signed …….. *Date* 7nd November 2013

Statement 3

I hereby give consent for my thesis, if accepted, to be available for photocopying and for inter-library loan, and for the title and summary to be made available to outside organisations.

Signed …….. *Date* 7nd November 2013

Abstract

The performance and sustainability of ground source heat systems is dependent on the thermal behaviour of neighbouring ground. This thesis describes a comprehensive experimental and numerical investigation into the ground behaviour in response to horizontal ground source heat systems.

Experimental investigations comprised of a field-scale monitoring scheme, designed and implemented in a horizontal ground source heat system providing space heating to a domestic property located in Mid-Wales, UK. A high resolution ground temperature data-set has been compiled over a 13 month period via 112 thermistors buried in the ground. Further data-sets representing the climatic variables and heat pump behaviour were also compiled over the same period, facilitating a thorough investigation of the ground behaviour in response to heat extraction at the site. Soil properties were also measured at the site as part of a larger site investigation undertaken.

The numerical model applied is a coupled thermal-hydraulic (TH) model previously developed at the Geoenvironmental Research Centre (GRC). The GRC's current model was extended to include developed boundary conditions for the TH simulation of horizontal ground source heat systems, describing the soil's interaction with the ground-loop and atmosphere. Developments were subject to rigorous validation including comparisons with ground-data collected at the experimental site. The validated model was applied to investigate the long-term ground behaviour at the monitoring site and the effects of different surface materials on the ground behaviour including the recharge process. Finally, the model was applied to investigate the validity of an existing design code for ground source heat system design.

The resolution and duration of the collated data-set facilitated extensive analysis, including a thorough investigation of the ground thermal distributions resulting from heat extraction and recharge. Findings indicated unsymmetrical distributions, highlighting potential avenues for system optimisation. Further to this it can be said that the data-set, in its own right, is a significant contribution to the scientific community and is able to provide a means of validation for future models.

Results from the numerical investigation indicated that the ground thermal behaviour exhibits an annual cyclic pattern after approximately 3 years. From a holistic perspective, the results demonstrate that horizontal ground source heat systems can provide a sustainable means of providing space heating. Further long-term studies investigating the effects of surface materials show that more thermal energy can be sustainably extracted from systems with urban surface types (i.e. asphalt and brick). Investigations into an existing design code revealed that a ground-loop designed to meet the loads of the monitoring site resulted in unsustainable heat extraction, in doing so demonstrating the simplification of ground-loop burial depth within the current design process.

Knowledge regarding the ground response to horizontal ground source heat systems has been furthered through the collection and analysis of field-scale data within this study. Further to this, the boundary developments and validation undertaken have allowed for a more thorough investigation of the long-term ground behaviour than previous studies.

Nomenclature

A	Cross-sectional area
A_0	Annual amplitude of surface soil temperature
$\mathbf{A}$	Defined in equation (5.144)
AE	Actual evaporation, defined in equation (6.11)
C_{aa}	Defined in equation (5.71)
C_{al}	Defined in equation (5.69)
C_{at}	Defined in equation (5.70)
C_{Cloud}	Fractional cloud cover coefficient
C_{la}	Defined in equation (5.50)
C_{ll}	Defined in equation (5.48)
C_{lT}	Defined in equation (5.49)
C_p	Specific heat capacity
C_{pda}	Specific heat capacity of dry air
C_{pl}	Specific heat capacity of liquid
C_{ps}	Specific heat capacity of soil solids
C_{pv}	Specific heat capacity of vapour
C_{Ta}	Defined in equation (5.98)
C_{Tl}	Defined in equation (5.96)
C_{TT}	Defined in equation (5.97)
C_z	Drag coefficient
$\mathbf{C}$	Matrix identifier
$\mathbf{C_{aa}}$	Defined in equation (5.136)
$\mathbf{C_{al}}$	Defined in equation (5.134)
$\mathbf{C_{aT}}$	Defined in equation (5.135)
$\mathbf{C_{la}}$	Defined in equation (5.120)

$\mathbf{C_{ll}}$	Defined in equation (5.118)
$\mathbf{C_{lT}}$	Defined in equation (5.119)
$\mathbf{C_{Ta}}$	Defined in equation (5.128)
$\mathbf{C_{Tl}}$	Defined in equation (5.126)
$\mathbf{C_{TT}}$	Defined in equation (5.127)
d	Damping depth, defined in equation (6.23)
d_p	Ground-loop pipe diameter
D_{atms}	Molecular diffusivity of vapour in air
e	void ratio
e_{air}	Vapour pressure at ground surface
e_{ea}	Saturation vapour pressure at ground surface
e_0	Initial void ratio
E	Evaporative flux
E_{ss}	Sink or Source
f	Flow area factor in vapour flux
$f(u)$	Transition function, defined in equation (6.10)
$\mathbf{f_a}$	Defined in equation (5.139)
$\mathbf{f_l}$	Defined in equation (5.124)
$\mathbf{f_T}$	Defined in equation (5.132)
$\mathbf{F}$	Defined in equation (5.145)
g	Gravitational constant
g	g-function, defined in equation (2.8)
h	Relative humidity
h	Pressure head (suction)
h	Material coefficient
h_{air}	Relative humidity of air
H_c	Heat capacity of soil
H_{LE}	Latent heat flux

$H_{LW}^{Absorbed}$	Longwave radiation flux absorbed
$H_{LW}^{Emitted}$	Longwave radiation flux emitted
H_{LW}^{Net}	Net longwave radiation flux
H_s	Henry's volumetric coefficient of solubility
H_{SEN}	Sensible heat flux
H_{SOIL}	Total radiation exchange at the soil surface
H_{SW}	Short-wave radiation flux
H_{SW}^{Absor}	Absorbed short-wave radiation flux
i	Iteration level
J_a	Defined in equation (5.74)
J_l	Defined in equation (5.54)
J_T	Defined in equation (5.102)
J_0, J_1	Bessel functions
k	von Karman constant
k_a	Effective permeability of air
k_l	Intrinsic permeability
k_{sat}	Saturated hydraulic conductivity
K_a	Unsaturated conductivity of pore air
K_{aa}	Defined in equation (5.73)
K_{al}	Defined in equation (5.72)
K_l	Unsaturated hydraulic conductivity
K_{la}	Defined in equation (5.53)
K_{ll}	Defined in equation (5.51)
K_{lT}	Defined in equation (5.52)
K_{Ta}	Defined in equation (5.101)
K_{Tl}	Defined in equation (5.99)
K_{TT}	Defined in equation (5.100)
K_{va}	Defined in equation (5.115)

K_{vl}	Defined in equation (5.113)
K_{vT}	Defined in equation (5.114)
$\mathbf{K}$	Matrix identifier
$\mathbf{K_{aa}}$	Defined in equation (5.138)
$\mathbf{K_{al}}$	Defined in equation (5.137)
$\mathbf{K_{la}}$	Defined in equation (5.123)
$\mathbf{K_{ll}}$	Defined in equation (5.121)
$\mathbf{K_{lT}}$	Defined in equation (5.122)
$\mathbf{K_{Ta}}$	Defined in equation (5.131)
$\mathbf{K_{Tl}}$	Defined in equation (5.129)
$\mathbf{K_{TT}}$	Defined in equation (5.130)
l_p	Ground-loop pipe length
L	Latent heat of vaporisation
L	Unit length
m	Material coefficient
$\dot{m}$	Mass-flow rate
n	Porosity
n	Material coefficient
n_{node}	Element node number
$\underline{n}$	Direction cosine normal to the surface
N_r, N_s	Shape functions
$\mathbf{N}$	Shape function matrix
P	Precipitation mass flux
PE	Potential evaporation
q_{air}	Air specific humidity
q_{ea}	Soil specific humidity
Q	Heat flux
Q_A	Heat flux per unit area

Q_C	Conductive heat flux through a snow layer
Q_E	Heat flux due to evaporation
Q_H	Longwave radiation heat flux emitted from a soil surface
Q_L	Heat flux per unit length
Q_{LE}	Longwave radiation heat flux diffused at a soil surface
Q_{LI}	Incident longwave radiation heat flux
Q_m	Net mass flux
Q_P	Heat flux due to precipitation
Q_{SI}	Incident solar radiation heat flux
Q_t	Total heat flux at a soil surface
r	Ground-loop pipe radius
r_a	Aerodynamic resistance
r_b	Borehole radius
R	Surface water run-off
R	Universal gas constant
R_b	Conductive resistance of a borehole
R_{da}	Specific gas constant for dry air
R_q	Time dependant thermal resistance, defined in equation (2.6)
R_v	Specific gas constant for water vapour
R_Ω	Residual error introduced due to approximation
$\mathbf{R}$	Matrix identifier
s	Matric suction
s_r	Suction at reference temperature
S_a	Degree of saturation of pore air
S_l	Degree of saturation of pore water
t	Time
t_s	Steady-state time scale factor
t_0	Time-lag from reference point

t'	Operation start time
T	Temperature
T_a	Constant ground temperature
T_{air}	Air temperature
T_b	Borehole temperature
T_{ea}	Temperature at ground surface
T_f	Fluid temperature
T_g	Ground temperature
T_{inlet}	Fluid temperature at the heat pump inlet
T_{outlet}	Fluid temperature at the heat pump outlet
T_r	Reference temperature
T_s	Far-field ground temperature
T_0	Initial temperature
$\mathbf{T}_s$	Nodal value of temperature
$\dot{\mathbf{T}}_\mathbf{s}$	Time derivative of nodal temperature
u	Integration constant
u_a	Pore-air pressure
u_{da}	Partial pressure of dry air
u_l	Pore-water pressure
u_v	Partial pressure of water vapour in pore space
u_z	Wind speed at reference elevation
$\mathbf{u}$	Displacement vector
$\mathbf{u}_{\mathbf{a}s}$	Nodal value of pore-air pressure
$\mathbf{u}_{\mathbf{l}s}$	Nodal value of pore-water pressure
$\dot{\mathbf{u}}_\mathbf{as}$	Time derivative of nodal pore-air pressure
$\dot{\mathbf{u}}_\mathbf{ls}$	Time derivative of nodal pore-water pressure
v_v	Mass flow factor

$\mathbf{v_a}$	Velocity of air
$\mathbf{v_l}$	Velocity of liquid water
$\mathbf{v_v}$	Velocity of water vapour
$\underline{\hat{\mathbf{v}}}_{\mathrm{ln}}$	Approximate liquid velocity normal to the boundary surface
$\underline{\hat{\mathbf{v}}}_{\mathrm{va}}$	Approximate pressure vapour velocity normal to the boundary surface
$\underline{\hat{\mathbf{v}}}_{\mathrm{vd}}$	Approximate diffuse vapour velocity normal to the boundary surface
V	Specific volume
V_d	Domain volume
V_s	Volume of solids
W	System heat load
W_t	Thermal energy extraction at reference time
X	Defined in equation (2.3)
x, y, z	Global coordinates
Y_0, Y_1	Bessel functions
z	Elevation from the reference level
z_0	Surface roughness
α	Thermal diffusivity
α	Material coefficient
β	Defined in equation (2.2)
Δ	Soil clay content
γ	Soil bulk density
γ_l	Unit weight of liquid
χ	Crank-Nicholson integration scheme constant
χ_a	Volume fraction of air components
χ_s	Volume fraction of solid components
χ_w	Volume fraction of water components
∂	Differential

∂V	Incremental volume
ε_{LW}	Longwave radiation emissivity
ε_{SW}	Short-wave radiation reflection factor
ε_v	Volumetric strain
κ	Soil sand content
λ	Thermal conductivity
λ_a	Thermal conductivity of pore air
λ_s	Thermal conductivity of solids
λ_T	Overall thermal conductivity
λ_{Tl}	Thermal conductivity of pore liquid
λ_w	Thermal conductivity of water
μ_a	Absolute viscosity of air
μ_l	Absolute viscosity of liquid
θ	Temperature difference, as defined in equation (2.4)
θ	Volumetric water content
θ_a	Volumetric air content
θ_l	Volumetric liquid content
θ_{res}	Residual water content
θ_{sat}	Saturated water content
θ_v	Volumetric vapour content
ξ	Surface energy (tension)
ξ_r	Surface energy (tension) at reference temperature T_r
π	Numerical constant ≈ 3.1416
ρ_a	Air density
ρ_{da}	Density of dry air
ρ_l	Density of liquid water
ρ_s	Density of soil solids

ρ_v	Density of water vapour
ρ_0	Density of saturated water vapour
σ	Stefan-Boltzmann constant
τ	Relative tolerance
τ_v	Tortuosity factor in vapour flux
ω	Defined in equation (5.103)
$\hat{\omega}$	Defined in equation (5.103)
ψ	Capillary potential, defined in equation (5.34)
∇	Gradient operator
Γ^e	Element boundary surface
Ω	Heat content of soil per unit volume
Ω	Soil silt content
Ω^e	Element domain
ϕ	Global unknown, defined in equation (5.141)

Contents

See accompanying CD for Appendices.

Chapter 1

Introduction

1.1 Introduction

There is a general consensus within the global scientific community that climate change is occurring as a result of greenhouse gasses, such as carbon dioxide, being emitted into the atmosphere (United Nations, 1998; IPCC, 2013). The emission of greenhouse gasses can be largely attributed to energy generation through the burning of fossil fuels, such as; coal, natural gas and oil (United Nations, 1998). Global population growth in conjunction with the rising needs from both developed and developing countries has further increased the demand for energy, resulting in fossil fuels being consumed at a faster rate than ever before in human history. As a direct result of this, the security of energy commodities, such as fossil fuels, for most countries is now of the upmost importance (UNEP, 2009a; UNEP, 2009b). Beyond environmental issues, the security of natural resources plays an important role globally in social, economic and political developments.

In recent years the topics of sustainable development, energy security and low carbon technologies have been increasing in importance on both social and political agendas, primarily due to the preceding global pressures. The successful application of sustainable development and low carbon technologies in particular, can help to reduce the dependency on finite fossil fuel reserves. From an environmental perspective, climate change may still be avoided so long as society converts its hydrocarbon dominated energy consumption to low carbon alternatives, utilising more sustainable energy resources available (UNEP, 2013).

The concerns associated with the global growth of energy usage can be significantly reduced through the use of renewable energy sources. Renewable energy techniques utilise the natural resources which are continually replenished through natural resources, for example solar radiation, wind, waves and tidal movements. To highlight the degree to which fossil fuels are relied upon for energy generation, figures representing the UK's energy generation are presented. The UK's current total energy usage can be analysed by type, with notable contributors being: Oil 48%, Gas 29.5% and electricity 18.5% (DECC, 2012). In 2008, the total energy consumed for heating purposes accounted for 47% of the UK's final energy consumption, rising to 77% if the transport section is emitted from the statistics (DECC, 2010). In addition to the previous statistics, there are growing interests at governmental levels in the UK to decentralise energy generation in order to reduce the demand on conventional power stations fuelled by fossil fuels. This can not only reduce the load on the national grid but also improve the future national energy security (Department of Trade and Industry (DTI), 2007).

Geothermal energy is a renewable energy source which can be utilised to provide electricity and space heating/cooling. The potential of geothermal energy can be harnessed through a number of techniques, all of which attempt to utilise the thermal energy stored within the earth. The techniques employed can be split broadly into two categories; those which attempt to harness thermal energy from so called 'deep' and 'shallow' geothermal systems. Shallow geothermal techniques, attempt to exploit the thermal energy stored within the upper layers of the Earth's crust (i.e. typically down to a depth of approximately 200 meters) (Sanner, et al., 2003). The methods employed to harness shallow geothermal energy are commonly referred to as so called 'ground source heat' systems (Sanner, et al., 2003). The systems are ideally suited to utilise low entropy systems in order to provide space heating and/or cooling.

The preceding UK government statistics demonstrated the proportion of energy consumed in order to provide space heating. This highlight the potential impact of ground source heat systems as an alternative to conventional fossil fuels, currently used to provide space heating. The utilisation of ground source heat systems can not only reduce energy loads on the national grid, but they can also help with energy diversity.

The thesis presented is concerned with the application of shallow ground source heat systems as an alternative means to provide space heating. Section 1.2 of this chapter will provide an overview of this technology. Following this, the study objectives for the work presented in this thesis will then be discussed in section 1.3. An overview of the research background and study scope and limitations are contained in sections 1.4 and 1.5 respectively. Finally, a structural overview of the work contained in this thesis is presented in section 1.6.

1.2 Background to ground source heat systems

Within the scope of this work, and with respect to ground source heat systems, shallow geothermal energy refers to heat stored in the ground down to a depth of approximately 200 meters (Sanner, et al., 2003; Banks, 2009). In a region such as the UK, which is not subject to active tectonics, it is possible to consider this ground region as having a constant annual temperature which is unaffected by seasonal climatic variations (Busby, et al., 2011). The temperature is predominantly a function of the upper surface, i.e. climatic conditions such as solar radiation and ambient air temperature. At greater depths, the ground temperature increases with depth according to the geothermal gradient that is itself determined by vertical heat flow in the Earth and the thermal properties of local geology (Busby, et al., 2011).

The ground located in closest proximity to the ground surface is subject to the greatest changes due to climatic variations. Typically, it is known that annual temperature variations occur within the upper 10 meters of ground, the exact depth is dependent on local climate and ground conditions (Kusuda & Archenback, 1965; Kusuda, 1975; Busby, et al., 2011). Beyond this depth, there is limited ground temperature variation within the shallow geothermal region in question. Within the UK, the ground temperature in this region is typically 9 – 13 °C (Busby, et al., 2011).

The first known concept of a ground source heat system and application was a Swiss patent issued in 1912 to Heinrich Zoelly (Yang, et al., 2010a). Following on from this, there was global interest from both North America and Europe post World War II until the early 1950's (Mei, 1986). Interest subsequently subsided when oil and gas became more widely available for heating purposes, removing the driving forces behind technological development. The next period of notable interest began in the early 1980's, when interest form North America and Europe was reignited after the first oil crisis of the 1970's (Yang, et al., 2010a). Since this period, the realisation of global warming and the diminishing supply of fossil fuels has provided a platform for research and led to an increased interest in ground source heat systems. From a market perspective, the rising cost of fossil fuels and social responsibility with regard to global warming has resulted in the popularity of ground source

heat systems increasing over the past 20 years. The systems have proven most popular in North America and some European countries; in particular Austria, Germany, Sweden and Switzerland (Curtis, et al., 2005). Within the past decade, system installations have increased within countries which have not been historically affiliated with ground source heat systems such as the UK and China (Chong, et al., 2013; Yang, et al., 2010b).

Shallow ground source heat systems can be either categorised as so called 'closed-loop' or 'open-loop systems'. Closed-loop systems fundamentally compromise of a buried impermeable pipe (or ground-loop) which is connected to a heat pump. The heat pump is responsible for pumping and extracting thermal energy from a fluid which circulates within the ground-loop (more technical details will be provided in Chapter 2). The circulating fluid acts as a mechanism to transport heat from the ground to the point of use in a heating system (or vice-versa in a cooling system). Within a heating system, this is achieved by circulating a fluid cooler in temperature than the ground, thereby inducing a thermal gradient which allows the fluid to absorb heat from the surrounding ground.

Similar to 'closed-loop' design, 'open-loop' systems use fluid as a means to extract ground heat. Instead of absorbing heat by inducing a thermal gradient, closed-loop systems instead simply extract ground water directly from the ground. Typically ground water will be extracted via wells or sometimes from surface water sources such as ponds or lakes. The focus of the research presented in this thesis is with regards to 'closed-loop' systems therefore 'open-loop' systems will not be discussed any further.

Within the scope of closed-loop ground source heat systems, various ground-loop configurations exist which can be employed to exchange heat with the ground. The ground-loop types can be broadly split into two categories according to their orientation; namely vertical and horizontal ground-loops (see Figures 1.1 and 1.2). Vertical systems are conventionally installed within boreholes with depths typically ranging between 20 and 200 meters (Yang, et al., 2010a). The ground-loop pipe diameter typically ranges between 19-38 mm whereas the borehole diameter typically ranges between 100-200 mm (Yang, et al., 2010a). Horizontal systems on the other hand typically range in depth between 1 and 2 meters (Wu, et al., 2010). The installation of the systems is typically achieved via trenching to the required depth, laying the ground-loop pipe and then simply backfilling using the excavated material. Conventionally a plastic pipe (often polyethylene) is used for the ground-loop based upon material properties (i.e. durability and flexibility) and cost (Chong, et al., 2013). The nominal pipe diameters commonly used in North America are ½, ¾ and 1 ¼ inches, while the standard pipe diameters used in the UK and Europe are 25, 32 and 40 mm (Chong, et al., 2013). Further details regarding the workings, design and installation of closed-loop systems is discussed in Chapter 2.

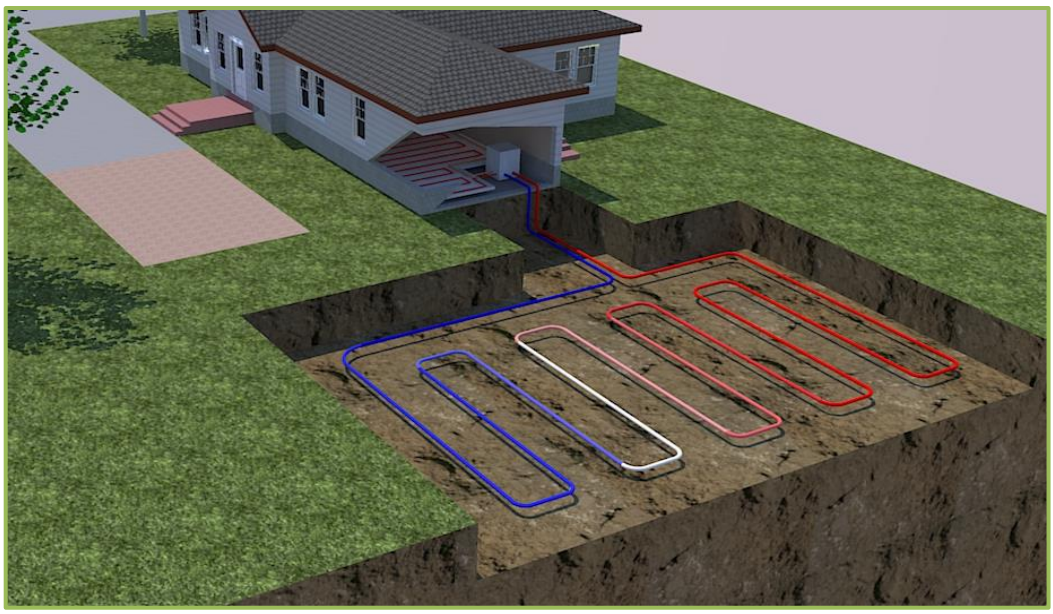

Figure 1.1 – Typical arrangement for a horizontal ground source heat system employing a parallel loop configuration.

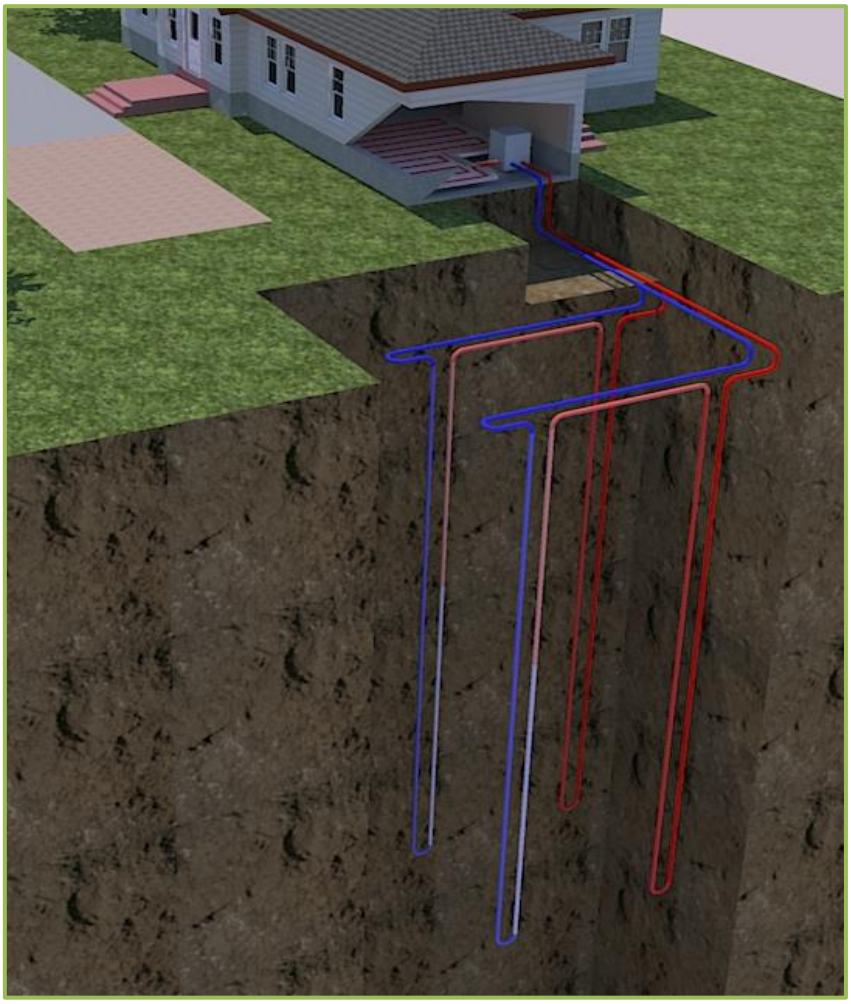

Figure 1.2 – Typical arrangement for a vertical ground source heat system.

1.3 Study objectives

The aim of the research presented is to advance knowledge regarding the ground thermal behaviour in response to heat extraction from horizontal ground source heat systems. This has been achieved through the field-scale monitoring of a newly installed system and the development of a numerical model capable of simulating the long-term ground behaviour of such a system.

The specific study objectives resulting from the above mentioned investigations are listed below:

i. To obtain a better understanding of horizontal ground source heat systems through the collection and analysis of field-scale ground, climatic and heat pump data.

ii. To extend modelling capabilities in the research area through the development of a numerical model including representation of the necessary boundary conditions.

iii. To undertake rigorous validation of the numerical model through comparisons between simulation results and data collected at the monitoring site.

iv. To investigate the long-term thermal and hydraulic ground behaviour in response to heat extraction via horizontal ground source heat systems through numerical modelling.

1.4 Research background

This work presented in this thesis has been undertaken at the Geoenvironmental Research Centre (GRC) at Cardiff University. Considerable previous research has been undertaken within the GRC both on experimental and computational aspects of geotechnical engineering. This section discusses relevant previous works undertaken, providing a context for the current work. It is not intended to replace more detailed reviews of literature in Chapter 2 or the theoretical formulations presented in Chapter 5.

A number of field-scale investigations have been previously undertaken within the research group. Thomas and Rees (1994) investigated ground movements and moisture content of Kimmeridge clay on a field-scale at a site in Swindon. Following this, Thomas and Rees (1997) presented a field-scale study investigating the seasonal heat losses through ground-floor slabs of a real

building located at Cardiff University. The study included a comprehensive in-situ monitoring of ground temperatures using thermo-couples, resulting in a data-set in excess of 4 million items.

Laboratory investigations into the coupled thermal-hydraulic behaviour of unsaturated sand were carried out by Ewen and Thomas (1987). A new method was developed to describe the thermal conductivity-moisture relationship using the thermal probe technique. More recently, experimental work has been undertaken at the GRC to investigate the properties of Bentonite which is a material commonly used as a geotechnical barrier in nuclear waste repositories. Singh (2007) presented an experimental and numerical study on the flow of vapour in highly compacted Kaolin and Bentonite while Bag (2011) investigated permeability and swelling properties of Bentonite.

Prior to this study, considerable previous work into the development of the numerical computer code COMPASS (**CO**de for **M**odelling **P**artially **S**aturated **S**oils) has been undertaken. The remainder of this section will describe the developments of the COMPASS code.

A two-dimensional solution for coupled transient heat and moisture transfer in unsaturated soil was presented by Thomas (1985). The principle of mass conservation was employed for moisture flow and the conservation of energy was used for heat transfer. In this solution moisture vapour flow was modelling according to the diffusive vapour flow proposed by Philip and de Vries (1957) and de Vries (1958), and the latent heat of vaporisation incorporated via the approach of Luikov (1966). Non-linearity of material parameters were then incorporated in the works presented by Thomas (1987), Thomas (1988a) and Thomas (1988b). Revised time-stepping schemes were investigated and implemented within the mentioned coupled heat and mass solution by Thomas and Rees (1988) and Thomas and Rees (1990).

Ewen and Thomas (1989) formulated numerical model in terms of moisture content and temperature to simulate the experimental work previously undertaken (Ewen & Thomas, 1987), including vapour transport via a diffusive mechanism. Thomas and King (1991) presented a theoretical heat and moisture formulation cast in terms of capillary potential and temperature and found good agreement with the Ewen and Thomas (1987) experiments. Thomas and Sansom (1995) extended this formulation to include elevated pore-air pressures and validated via comparison to experimental works on sand and clay. This formulation was presented in three-dimensions including work on pre and post-processing and visualisation by Sloper (1997) and Thomas et al. (1998).

Deformation was introduced by examining seasonal ground movements (Thomas and Rees, 1990, 1993), with an isothermal coupled moisture-mechanical numerical model presented by Thomas et al. (1992) utilising the non-linear elastic state-surface approach of Lloret and Alonso (1985). This model was applied to seasonal ground movements in Thomas and Zhou (1995). An elasto-plastic coupled thermo-hydro-mechanical (THM) model was presented by Thomas and He (1994) using the

elasto-plastic model of Alonso et al. (1990) and this was further developed to include some behaviour of expansive clays by Thomas and Cleall (1999). The developed model has been used extensively to investigate the thermal-hydraulic behaviour of large scale experiments, notably by Mitchell (2002), Thomas et al. (2003), Melhuish (2004), Cleall et al (2006) and Vardon (2009). It is also noted that further works have been carried out to extend the model to include non-reactive chemical processes within the THM model (Seetharam, 2003; Sedighi, 2011).

The mechanical and chemical model developments have been included in the preceding paragraphs for completeness, allowing the full capabilities of COMPASS to be presented. It is noted that neither the mechanical or chemical aspects of the model will be utilised within the current scope of work.

1.5 Scope and limitations

The scope of the work undertaken in this thesis and the limitations with regards to field-scale monitoring and numerical modelling developments are listed below:

Field-scale scope and limitations:

- The field-scale study investigates the ground behaviour in response to a horizontal ground source heat system.
- The investigated system is subject to domestic heating loads and only extracts heat from the ground (i.e. it is not used for space cooling purposes).
- The monitoring site measured the in-situ thermal behaviour of the soil while any hydraulic behaviour was measured periodically using ex-situ techniques.
- In-situ ground temperature, climatic variables and heat pump characteristics for a 13 month period between May 2012 and June 2013, spanning a single heating season, are presented and used for validation purposes. It is noted however that the data will be continuously collected until 2015.

Numerical modelling scope and limitations:

- Numerical approximation is used to find a solution to the system of coupled differential equations. The finite-element method is used to provide a spatial solution and the finite-difference method used to provide a temporal solution.

- Soil hysteresis behaviour such as found in the moisture retention behaviour in wetting/drying paths has not been included in the model. This is due in part to a lack of experimental evidence and a complex wetting/drying path.

- Vapour transport is assumed to be diffusive. At higher temperatures, elevated air pressure gradients may occur, leading to increased vapour movement. This has not been included in the theoretical formulation. Hence the valid temperature range, which can be modelled, is greater than 0°C in accordance with the moisture flow formulation.

- Radiation has been omitted from the theoretical formulations describing heat transfer based on the anticipated temperature range which the model will be subject to for the current scope of work.

- Mechanical/deformation changes caused by thermal and hydraulic variations have not been considered within the current scope of work.

1.6 Thesis overview

A brief overview of each chapter is presented below.

Chapter 2 contains a literature review salient to the work contained in this thesis. The literature review has been split broadly into four sections inspecting; *i) overview of ground source heat systems, ii) existing horizontal field-scale monitoring sites, iii) developed numerical approaches for the modelling ground source heat systems* and *iv) numerical investigations into horizontal ground source heat systems*.

The design and implementation of the field-scale monitoring site are presented in Chapter 3. The ground and climatic sensors selected for use are presented along with details regarding the spatial positioning of the ground temperature sensors. Following this, the logging and remote communication techniques used to download the recorded data are discussed. Details regarding the ground investigation undertaken during the sensor installation are also discussed along with the laboratory techniques used to characterise the soil.

Chapter 4 presents the data recorded at the monitoring site for the first 13 months of monitoring. The database developed to structure, interrogate and analyse the monitored data is presented and applied to investigate the ground thermal distributions in response to heat extraction.

The theoretical and numerical formulations for the coupled heat and mass model used in this thesis are presented in Chapter 5. Following this, methods capable of reducing computational times are explored and a parallel computational algorithm implemented within the current work is presented.

Chapters 6 presents the numerical developments implemented with the numerical model presented in Chapter 5, to simulate the field-scale monitoring site detailed in Chapter 3. Initial verification and validation of the developments is presented.

Chapter 7 presents the validation of the developed model with field-scale data. The validity of the model is tested against ground data collected at the monitoring site. Within this investigation, simulated ground behaviour both within and beyond the thermal influence of the ground-loop is tested against collected data.

Chapter 8 contains simulations investigating the long-term ground behaviour at the monitoring site, using the developed model. Following this, the performance of the parallel algorithm implemented within the code is investigated. The developed model is subsequently applied to investigate the ground behaviour under a range of different surface types/materials. Finally, the validity of the MIS 3005 (MCS, 2008) design standards, which are currently endorsed by the UK government, are investigated.

Concluding remarks and suggestions for further work are presented in Chapter 9.

References

Alonso, E., Gens, A. & Josa, A., 1990. A constitutive model for partially saturated soils. *Geotechnique*, 40(3), pp. 405-430.

Bag, R., 2011. *Coupled Thermo-Hydro-Mechanical-Chemical Behaviour of MX80 Bentonite In Geotechnical Applications.* Cardiff: PhD Thesis, Cardiff University.

Banks, D., 2009. Introduction to thermogeology and the exploitation of ground source heat. *Quarterly Journal of Engineering Geology and Hydrogeology*, 42(1), pp. 283-293.

Busby, J., Kingdon, A. & Williams, J., 2011. *The measured shallow temperature field in Britain.* Nottingham: British Geological Survey.

Chong, C. S. A. et al., 2013. Simulation of thermal performance of horizontal slinky-loop heat exchangers for ground source heat pumps. *Applied Energy,* 104(1), pp. 603-610.

Cleall, P. J., Melhuish, T. A. & THomas, H. R., 2006. Modelling the three-dimensional behaviour of a prototype nuclear waste repository. *Engineering Geology,* 85(2), pp. 212-220.

Curtis, R., Lund, J., Sanner, B. & Ryback, L., 2005. *Ground source heat pumps - Geothermal energy for anyone anywhere: Current worldwide activity.* Antalya, Turkey, Proceedings World Geothermal Congress.

De Vries, D. A., 1958. Simultaneous transfer of heat and moisture in porous media. *Transactions of the American Geophysical Union,* 39(5), pp. 909-916.

Department of Energy and Climate Change (DECC), 2010. *Estimates of heat use in the United Kingdom,* London: DECC.

Department of Energy and Climate Change (DECC), 2012. *Digest of United Kingdom Energy Statistics (DUKES Report), Chapter 1,* London: DECC.

Department of Trade and Industry (DTI), 2007. *Meeting the Energy Challenge: A White Paper on Energy,* London: DTI.

Ewen, J. & Thomas, H. R., 1987. The thermal probe - a new method and its use on an unsaturated sand. *Geotechnique,* 37(1), pp. 91-105.

Ewen, J. & Thomas, H. R., 1989. Heating unsaturated medium sand. *Geotechnique,* 39(3), pp. 455-470.

Intergovernmental Panel on Climate Change (IPCC), 2013. *Working Group I Contribution to the IPCC Fifth Assessment Report (AR5), Climate Change 2013: The Physical Science Basis,* Stockholm: IPCC.

Kusuda, T., 1975. *The effect of ground cover on earth temperature.* Fort Worth, Texas, USA, Conference proceedings of 'Alternatives in energy conservation: The use of earth-covered buildings'.

Kusuda, T. & Achenbach, P. R., 1965. Earth temperature and thermal diffusivity at selected stations in the United States. *ASHRAE Trans.,* 71(1), pp. 61-75.

Lloret, A. & Alonso, E. E., 1985. *State surfaces for partially saturated soils.* San Francisco, Proceedings of the 11th International Conference of Soil Mechanics and Foundation Engineering.

Luikov, A. V., 1966. *Heat and mass transfer in capillary porous bodies.* Oxford: Pergamon Press.

Mei, V. C., 1986. *Horizontal ground-coil heat exchanger theoretical and experimental analysis,* New York: Office of Buildings and Community Systems, U.S. Department of Energy.

Melhuish, T. A., 2004. *An investigation of the three-dimensional thermo/hydro/mechanical behaviour of large scale in-situ experiments.* Cardiff: PhD Thesis, University of Wales, Cardiff.

Microgeneration Certification Scheme (MCS), 2008. *Microgeneration Installation Standard: MIS 3005 Issue 3.0*. London: Department of Energy and Climate Change (DECC).

Mitchell, H. P., 2002. *An investigation into the thermo/hydro/mechanical interactions involved in high level nuclear waste disposal.* Cardiff: PhD Thesis, University of Wales, Cardiff.

Philip, J. A. & De Vries, D. A., 1957. Moisture movements in porous materials under temperature gradients. *Transactions of the American Geophysical Union,* 38(2), pp. 222-232.

Rees, S. W. & Thomas, H. R., 1997. Two-dimensional heat transfer beneath a modern commercial building: Comparison of numerical prediction with field measurement. *Building Services Engineering Research and Technology,* 18(1), pp. 169-174.

Sanner, B., Karytsas, C., Mendrinos, D. & Ryback, L., 2003. Current status of ground source heat pumps and underground thermal energy storage in Europe. *Geothermics,* 32(1), pp. 579-588.

Sedighi, M., 2011. *An investigation of hydro-geochemical processes in coupled thermal, hydraulic, chemical and mechanical behaviour of unsaturated soils.* Cardiff: PhD Thesis, Cardiff University.

Seetharam, S. C., 2003. *An investigation of the thermo/hydro/chemical/mechanical behaviour of unsaturated soils.* Cardiff: PhD Thesis, University of Wales, Cardiff.

Singh, R. M., 2007. *An experimental and numerical investigation of heat and mass movement in unsaturated clays.* Cardiff: PhD Thesis, Cariff University.

Sloper, N. J., 1997. *The development of a new three dimensional numerical model for fully coupled heat, moisture and air flow in unsaturated soil incorporating scientific visualisation and parallel computing techniques.* Cardiff: PhD Thesis, University of Wales.

Thomas, H. R., 1985. Modelling two-dimensional heat and moisture transfer in unsaturated soils, including gravity effects. *International Journal of Analytical Methods in Geomechanics,* 9(1), pp. 573-588.

Thomas, H. R., 1987. Non-linear analysis of heat and moisture transfer in partly saturated soil. *Journal of Engineering Mechanics, American Society of Civil Engineering,* 113(1), pp. 1163-1180.

Thomas, H. R., 1988a. A non-linear analysis of two-dimensional heat and moisture transfer in partly saturated soil. *International Journal of Analytical Methods in Geomechanics,* 12(1), pp. 31-44.

Thomas, H. R., 1988b. The influence of non-linear thermal parameters on moisture content distributions in unsaturated soils. *International Journal of Analytical Methods in Engineering,* 26(1), pp. 263-279.

Thomas, H. R. & Cleall, P. J., 1997. Chemico-osmotic effects on the behaviour of unsaturated expansive clays. In: R. N. Yong & H. R. Thomas, eds. *Geoenvironmental engineering, Contaminated ground; fate of pollutants and remediation.* London: Thomas Telford, pp. 272-277.

Thomas, H. R. & Cleall, P. J., 1999. Inclusion of expansive clay behaviour in coupled thermo hydraulic mechanical models. *International Journal of Engineering Geology,* 54(1), pp. 93-108.

Thomas, H. R. et al., 2003. Water infiltration into a large-scale in-situ experiment in an underground research laboratory. *Geotechnique,* 53(2), pp. 207-224.

Thomas, H. R. & King, S. D., 1991. Coupled temperature/capillary potential variations in unsaturated soil. *Journal of Engineering Mechanics, American Society of Civil Engineers,* 117(11), pp. 2475-2491.

Thomas, H. R. & Rees, S. W., 1988. *The use of Lee's algorithm in the analysis of some ground heat and mass transfer problems.* Innsbruck, Proceedings of the 6th International Conference on Numerical Methods in Geomechanics.

Thomas, H. R. & Rees, S. W., 1990. *An examination of the performance of a 3-level time stepping algorithm - Coupled heat and mass transfer computing.* Southampton, Proceedings of the 1st International Conference, Advances in Computer Methods in Heat Transfer.

Thomas, H. R. & Rees, S. W., 1993. The numerical simulation of seasonal soil drying in an unsaturated clay soil. *International Journal of Numerical and Analytical Methods in Geomechanics,* 17(1), pp. 119-132.

Thomas, H. R. & Rees, S. W., 1994. Seasonal ground movement in unsaturated clay: an examination of field behaviour. *Geotechnique,* 44(2), pp. 353-358.

Thomas, H. R., Rees, S. W. & Sloper, N. J., 1998. Three-dimensional heat, moisture and air transfer in unsaturated soils. *International Journal of Numerical and Analytical Methods in Geomechanics,* 22(2), pp. 75-95.

Thomas, H. R. & Sansom, M. R., 1995. Fully coupled analysis of heat, moisture and air transfer in unsaturated soil. *Journal of Engineering Mechanics, American Society of Civil Engineering,* 121(3), pp. 392-405.

Thomas, H. R. & Zhou, Z., 1995. A comparison of field measured and numerically simulated seasonal ground movement in unsaturated clay. *International Journal for Numerical and Analytical Methods in Geomechanics,* 19(1), pp. 249-265.

Thomas, H. R., Zhou, Z. & He, Y., 1992. *Analysis of consolidation of unsaturated soils.* Prague, Proceedings of the 2nd Czechoslovak Conference on Numerical Methods in Geomechanics.

United Nations Environment Programme (UNEP), 2013. *Climate Change.* [Online]
Available at: http://www.unep.org/climatechange/Introduction.aspx
[Accessed 20 3 2013].

United Nations Environmental Programme (UNEP), 2009a. *From conflict to peacebuilding. The role of natural resources and the environment,* Geneva: UNEP.

United Nations Evironment Programme (UNEP), 2009b. *Global trends in sustainable energy investment,* Geneva: UNEP.

United Nations, 1998. *Kyoto protocal to the United Nations framework convention on climate change,* New York: United Nations.

Vardon, P., 2009. *A three-dimensional numerical investigation of the thermo-hydro-mechanical behaviour of a large-scale prototype repository.* Cardiff: PhD Thesis, Cardiff University.

Wu, Y. et al., 2010. Experimental measurement and numerical simulation of horizontal coupled slinky ground source heat exchanger. *Applied Thermal Engineering,* 30(1), pp. 2574-2583.

Yang, H., Cui, P. & Fang, Z., 2010a. Vertical-borehole ground-coupled heat pumps: A review of models and systems. *Applied Energy,* 87(1), pp. 16-27.

Yang, W., Zhou, J., Xu, W. & Zhang, G., 2010b. Current status of ground-source heat pumps in China. *Energy Policy,* 38(1), pp. 323-332.

Chapter 2

Literature Review

2.1 Introduction

As previously discussed in Chapter 1, ground source heat has been the subject of research for a number of decades. The research programmes presented in literature cover a number of topics which can broadly be divided into three categories, namely; analytical, numerical or experimental investigations. This chapter will provide a literature review containing the notable research advances within the ground source heat field. The work presented will focus on research which has been conducted within the scope of the current thesis as specified in Chapter 1 (i.e. closed-loop horizontal systems).

The review has been sub-divided into four sections. The first of these, Section 2.2, contains an overview of ground source heat systems. Section 2.3 contains a review of horizontal field-scale

monitoring sites presented in literature. Following this, Section 2.4 presents a review of ground source heat models developed within the topic area. Finally, previous numerical studies investigating the ground behaviour in response horizontal ground source systems has been provided in Section 2.5. Concluding remarks regarding the current state of the research field will be provided in Section 2.6.

2.2 Overview of ground source heat systems

Chapter 1 previously presented a background to ground source heat systems. The following section will build on this, providing a more detailed overview of closed-loop ground source heat systems. Further technical details regarding the ground-loop configurations and mechanical workings will be provided here.

As previously discussed in Chapter 1, closed-loop configurations adopted within industry can be broadly split into two categories according to their orientations; namely vertical and horizontal systems. It is noted that the ground-loop is sometimes referred to as a heat exchanger within literature. In order to maintain consistency and avoid confusion, the term ground-loop will be used for the remainder of this thesis.

Within industry a number of horizontal ground-loop configurations have been adopted, the most common of which have been included in Figure 2.1. To date, the configuration of horizontal ground-loops in both North America and Europe has been non-standardised. Within the North America, the horizontal slinky arrangement is most common while in Europe both slinky and parallel arrangements are employed. The length of the ground-loop installed is a function of both the overall design heating load and configuration of the ground-loop. As previously stated in Chapter 1, the impermeable pipe employed for both horizontal and vertical systems is polyethylene or a plastic with similar properties (i.e. durability, flexibility and cost). The typical pipe dimensional for horizontal ground-loops has also been previously given in Chapter 1.

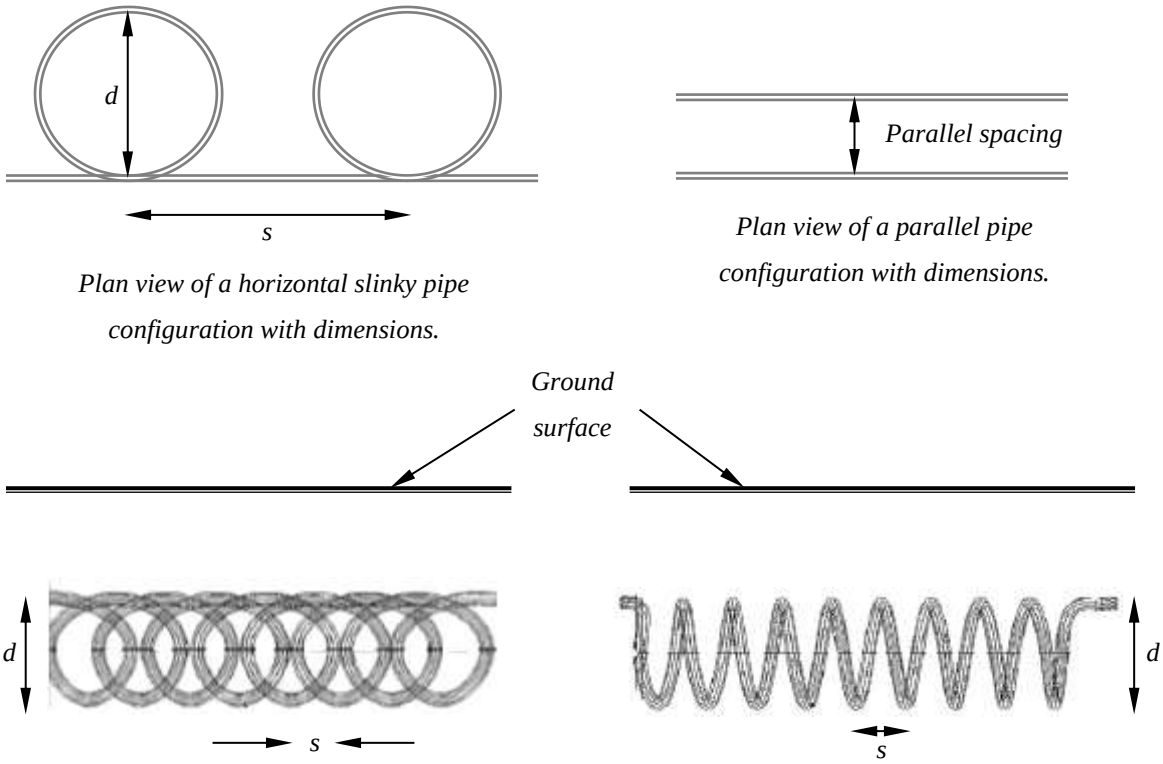

Plan view of a horizontal slinky pipe configuration with dimensions.

Plan view of a parallel pipe configuration with dimensions.

Side view of a vertical slinky configuration with dimensions (after Congedo et al. 2012).

Side view of a helical slinky configuration with dimensions (after Congedo et al. 2012).

s = slinky loop spacing

d = slinky loop diameter

Figure 2.1 – Schematic showing various horizontal ground loop configurations.

Vertical systems are conventionally installed within boreholes with depths typically ranging between 20 and 200 meters (Yang, et al., 2010). It is noted that in recent years the popularity of so called 'thermal foundations' has also grown. These systems typically house vertical ground-loops within vertical piles (Sanner, et al., 2003). Normally each borehole will contain a single ground-loop although systems may compromise of one, tens or even hundreds of boreholes. The vertical ground-loop contained within the borehole is often referred to as a 'U-tube' in literature, although for consistency and clarity it will be referred to as a ground-loop here. The typical borehole and ground-loop dimensions have been previously detailed in Chapter 1. The borehole annulus is generally backfilled with a material referred to a 'thermal grout' which is designed to prevent the potential contamination of ground water (in the case of leaking circulating fluid) and possess thermal properties which aid heat exchange between the fluid and ground. The fluid solution used within closed-loop systems is common to both horizontal and vertical systems. Typically an environmentally safe antifreeze solution approximately 75% water and 25% antifreeze (for example glycol or ethylene-glycol) by weight is used (Florides & Kalogirou, 2007).

The ground-loop type selected (i.e. horizontal or vertical) is primarily dependent on the overall system heating load and land constraints. Horizontal systems require access to a comparatively large plan footprint due to their orientation. Vertical systems on the other hand require a relatively small plan footprint but the installation process requires specialist equipment which inevitably increases installation costs. The deeper installation depths however do allow ground temperatures uninfluenced by surface conditions to be exploited. For this reason, multiple borehole systems are often used to meet the needs of larger commercial buildings.

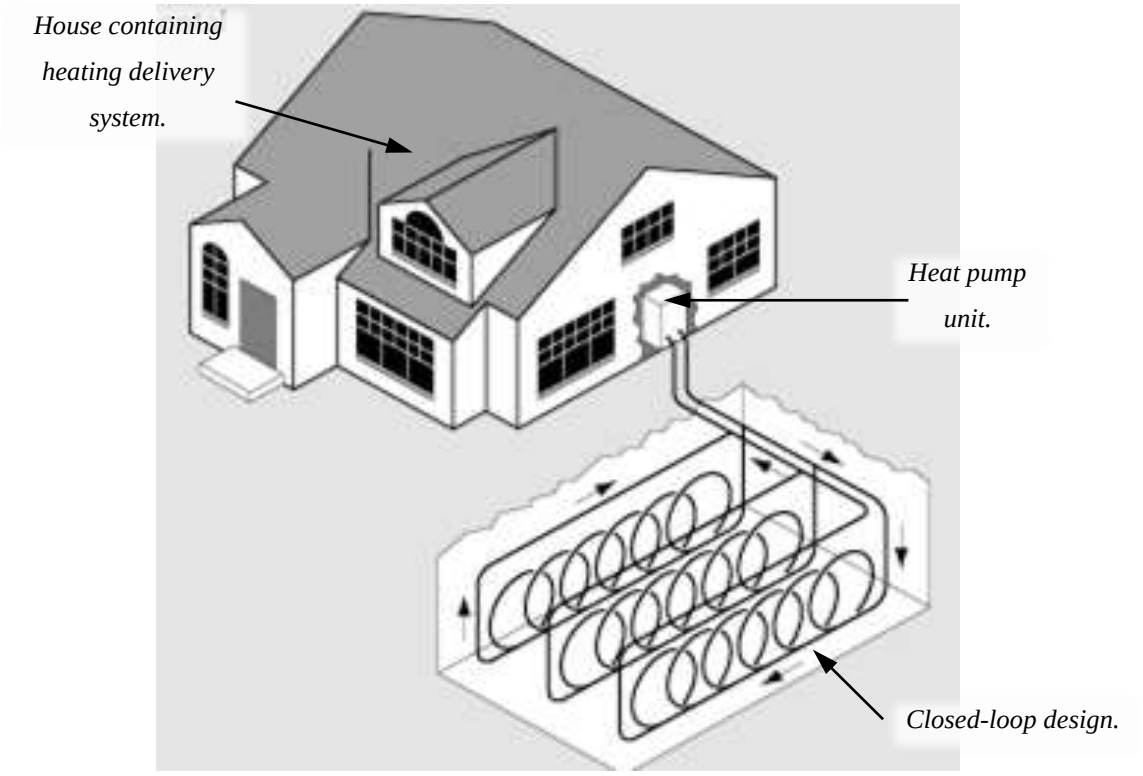

Figure 2.2 – Diagram showing an example 'closed-loop' ground source heat system, including the location of the heat pump (after U.S Department of Energy, 2008).

Both vertical and horizontal systems conventionally employ a heat pump to extract/inject thermal energy into the fluid circulating within the ground-loops (Sanner, et al., 2003). Figure 2.2 shows an arrangement including the location of the heat-pump. The heat pump is a mechanically driven device which transfers heat from the circulating fluid to a heat delivery system. Heat pumps comprise of four main components (in systematic order); evaporator, compressor, condenser and expansion valve. The components and thermal processes are much the same as those used within conventional refrigeration units, although in heating systems the processes are in the reverse order. The mechanical processes associated with the heat pump are well established and therefore shall not be discussed any further here.

The operational usage is ultimately dictated by the user heating/cooling requirements, often coupled to the climate of the local geographical area. Ground source heat systems have been successfully implemented to provide either space heating or cooling or both (dual operational systems). As stated in Chapter 1, the scope of the work presented in this thesis focusses on a ground source heat system serving a domestic house situated in the UK. The operational requirements of this system are heating only therefore ground source heat systems providing space heating will be the focus of this work.

2.3 Horizontal field-scale monitoring sites

Researchers from the 1930's to the 1950's began to consider horizontal ground source heat systems as a means for space heating, carrying out a range of preliminary field experiments (e.g. Coogan Jr, 1949; Vestal Jr & Fluker, 1957; Hooper, 1952). Initial experiments were small and conducted with copper ground-loops due to the materials available at the time (Mei, 1986). Beyond the 1950's there was no evidence of new monitoring sites until the 1980's. The apparent gap in research can be accredited to the low cost of energy during this period, removing research incentives (Mei, 1986). Since the 1980's there have been some examples of experimental horizontal ground source heat research. Much of the resulting data focused on the mechanical aspects of the systems and the so called Coefficient Of Performance (COP) which can be calculated without any ground temperature measurements. As a result, most experimental sites have not studied ground temperature behaviour. These sites will not be discussed any further within the current scope of work.

Globally, there are some examples of field-scale monitoring sites which include ground temperature monitoring. The experimental sites found in literature are presented and discussed in the following sections. For the purpose of this literature review the sites are presented and grouped according to geographical location. Information regarding the systems specifications (e.g. ground-loop length, ground-loop depth, system load etc.) and details regarding the measured system parameters will be presented where possible on a site by site basis. Following this, a more detailed overview of the monitoring sites located within the UK is presented.

2.3.1 Global field-scale monitoring sites

2.3.1.1 USA sites

Two field scale-site investigations within the United States are presented in this section. Metz (1980) reported a field-scale experimentation carried out by the U.S Department of Energy. The horizontal system served a small three bedroom house (total floor space 104 m^2) located in Upton, Long Island, New York (Metz, 1983). The experimental work was carried out to determine the cost feasibility for residential heating systems; identify any design, construction or operational problems; and to measure earth coil performance under realistic conditions. A dual system designed for both space heating and cooling was installed in October 1980 (the heating loads are not discussed). The ground-loop was 155 metres in total length, buried at a depth of 1.2 metres and installed with a parallel pipe arrangement (see Figure 2.3). A polyethylene pipe, 0.5 inches in diameter was installed to carry the circulating fluid which consisted of 25% ethylene-glycol and 75% water by weight. The system and ground responses were measured under realistic domestic use. In total four ground temperature sensors were installed, three of which positioned immediately adjacent to the ground-loop pipe at 45, 79 and 108 metres along the total 155 meter length. A fourth sensor was installed to measure the far-field earth temperature at a depth of 1.2 meters beyond the ground-loop's thermal influence. The transient thermal load of the system was determined from heat pump inlet/outlet fluid temperature and fluid mass-flow measurements. In addition, the ambient air temperature was monitored along with the electrical consumption of the heat and circulation pumps.

The work reported that the operation loads for the geographical location resulted in 50% more heat being removed from the ground in the winter month than was injected during the summer months. It was concluded that the performance of the site was significantly better than previous sites inspected.

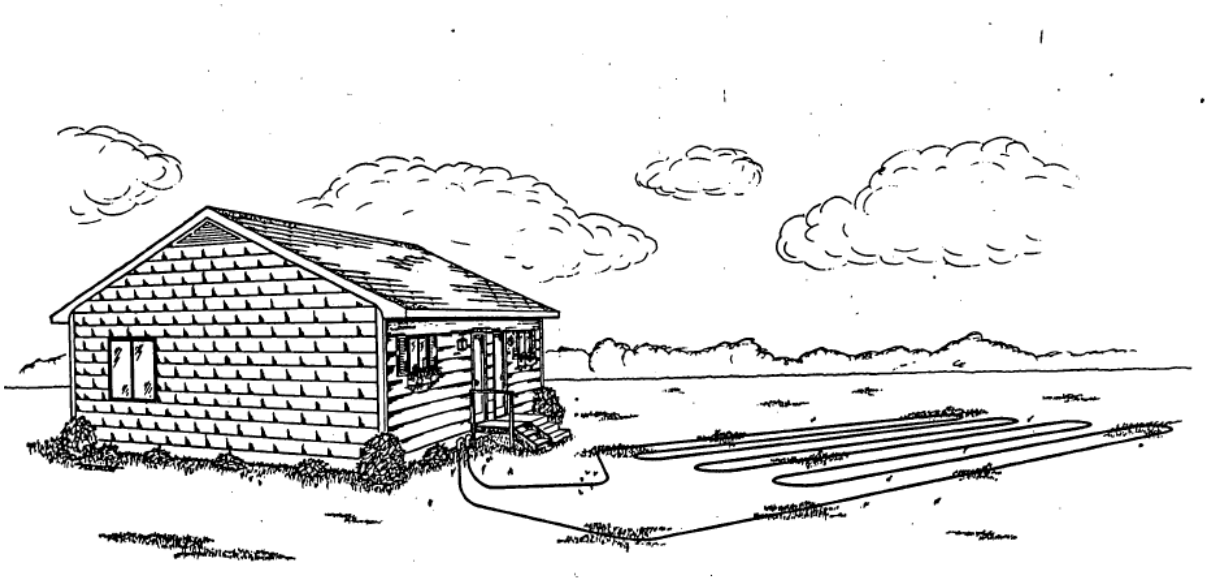

Figure 2.3 – Layout and parallel pipe configuration of the horizontal ground source heat system installed in Long Island, New York (Metz, 1983).

The second scheme presented from the USA consisted of two separate test sites in Virginia (Jones Jr, et al., 1996). The study aimed to evaluate the thermal performance of horizontal ground source heat systems when a so called 'flowable-ash' was used as backfill, replacing conventional soil backfill. 'Flowable-ash' is described as a cement-like mixture containing the waste produce fly-ash, which is produced as a by-product in coal-fired power plants (Jones Jr, et al., 1996). It was claimed the 'flowable-ash' has a greater structural stability, improving the pipe-ground thermal contact and therefore improving system performance.

The first field-scale test site under the above mentioned investigation was installed at a residential property, located in Charlottesville in 1994. A single trench 6 feet deep, 4 feet wide and 150 feet long contained six parallel pipes (3 parallel loops), equating to a ground-loop with a total length of 900 ft (approx. 274 meters). The lower 3 feet of the trench was backfilled using 'flowable-ash', with the remaining 3 feet backfilled using soil. Thermocouples were installed to monitor the backfill temperature although details regarding the exact spatial arrangement are not presented.

The second field-scale site was located at a residential property in Leesburg. Five trenches approximately 5 feet deep and 3 feet wide contained ground-loops with a slinky arrangement. Two of the trenches were monitored, one of which contained two feet of 'flowable-fill' and 3 feet of soil, whereas the remaining trench was completely backfilled with soil. The monitored trenches each contained eight thermocouples, four of which were positioned vertically at the centre of the trench and four of which were positioned vertically at a displacement of 3.5 feet from the centre of the trench. The sensor depths ranged between one and seven feet beneath the ground surface.

The system performance at both sites was evaluated through the analysis of energy consumption and peak electrical power. The monitoring of heat pump inlet/outlet fluid temperatures, fluid flow and climatic variables are not discussed within the report, nor are any ground investigations.

The research findings reported that the higher thermal conductivity of flowable-ash, when compared with the in-situ soil, allowed the thermal gradients induced by the ground-loop to be dissipated over a greater area. It was concluded that the flowable-ash backfill therefore improved the thermal performance of the ground source heat system.

2.3.1.2 Turkish sites

Four field-scale monitoring systems located within Turkey are presented, all of which were installed between 2002 and 2007. Two of the four monitoring systems were installed at Firat University, Elazig located in central Turkey. The first of these was installed in 2002 with the research aim of evaluating the effect of system parameters, namely the ground-loop depth and mass flow-rate, on performance (Inalli & Esen, 2004). A dual heating and cooling system with respective design loads of 2.5 kW and 3.1 kW was installed and connected to a test room at the university 16.24 m^2 in area. Two horizontal ground-loops, each 50 meters in length, were installed at depths of 1 and 2 meters with parallel pipe configurations. High density polyethylene pipe with a diameter of 16 mm was used to carry a 25% propylene-glycol solution (by weight). The ground temperature was measured at depth of 1 and 2 meters (no additional details are provided), using five T-type thermocouples. A number of sensors monitoring the mechanical and electrical performance of the system were aslo installed. These included sensors measuring the inlet/outlet heat pump temperatures along with the ground-loop fluid flow. The inlet/outlet temperatures of the condenser, compressor and evaporator were also measured along fluid pressure at various points in the heat exchange process. The research concluded that the installed ground-loop was oversized for the given heat loads, resulting in lower than expected COP values.

The second experimental system located in Elazig, Turkey was installed in 2007 (Benli, 2013). Unlike the first, this was an unconventional system, connecting both horizontal and vertical ground-loops to a single heat pump. The system provided heating for a glass greenhouse, 30 m^2 in area, which acted as a test environment. The horizontal ground-loop was 246 meters in total length and buried at a depth of 2 meters. The ground-loop consisted of polyethylene pipe, 16 mm in diameter which was used to carry a 25% ethylene-glycol solution (by weight). The ground temperature was measured at a single point, 2 meters below the ground surface using a thermocouple. The mechanical and electrical behaviour of the system were monitored with a greater number of

sensors. Again, the heat pump inlet/outlet fluid temperature was monitored along with the ground-loop fluid flow allowing the thermal energy extraction/rejection to the ground to be calculated. The electrical power consumption of the compressor, fans and circulation pumps were measured along with the condenser and evaporator pressures. Climatic measurements including ambient air temperature, air pressure and wind velocities were carried out at the site along with inside air temperature measurements at the greenhouse. Data regarding the solar radiation was taken from Elazig state meteorological records. With regards to the current scope of work, the research concluded that the performance of the experimental system was dependable on the ground temperature distribution around the ground-loop which is related to the ground thermal properties.

In 2004 an experimental study was also carried out at Uludag University, north-west Turkey (Coskun, et al., 2008; Pulat, et al., 2009). The system was originally designed to provide space cooling for a test room located within the university laboratories but was later modified to provide space heating. A 20 meter ground-loop was installed, buried at a depth of 2 meters and with a parallel pipe configuration. Polyethylene pipe with a diameter of 16 mm was used for the ground-loop. The ground temperature was measured at various points during the testing using a hand held digital thermometer. Installed sensors focussed on the mechanical and electrical behaviour of the system. The heat pump inlet/outlet fluid temperatures were measured but ground-loop fluid flow was not. The electrical power consumption of individual components was monitored as well as the condensing and evaporating pressures.

In 2005 an experimental system was installed at Yildiz Technical University, Istanbul, north-west Turkey (Demir, et al., 2009; Koyun, et al., 2009). The aim of the research was to investigate the system performance when an unconventional ground-loop consisting of an aluminium finned pipe was installed. The ground-loop consisted of three parallel pipes, each 40 meters in length to give a total approximate length of 130 meters. The ground-loop was buried at a depth of 1.8 meters on a site approximately 800 m^2 in plan area. The system was a designed to provide both space heating and cooling with design loads of 4 kW and 2.7 kW respectively. Details regarding the target heating/cooling space are omitted. The aluminium finned pipe was 0.5 inches in diameter (see Figure 2.4 for cross-section schematic). Seven T-type thermocouples were installed to monitor the ground temperature around a single pipe cross-section, measuring the vertical and horizontal temperature distribution (see Figure 2.4). The heat pump fluid inlet/outlet temperatures were also monitored. The reported work does not make any reference to fluid flow or climatic measurements at the experimental site. The presented work concluded that the finned pipe resulted in a better performing system after 150 hours of operation, due to the greater thermal conductive properties of the finned pipe over conventional plastics.

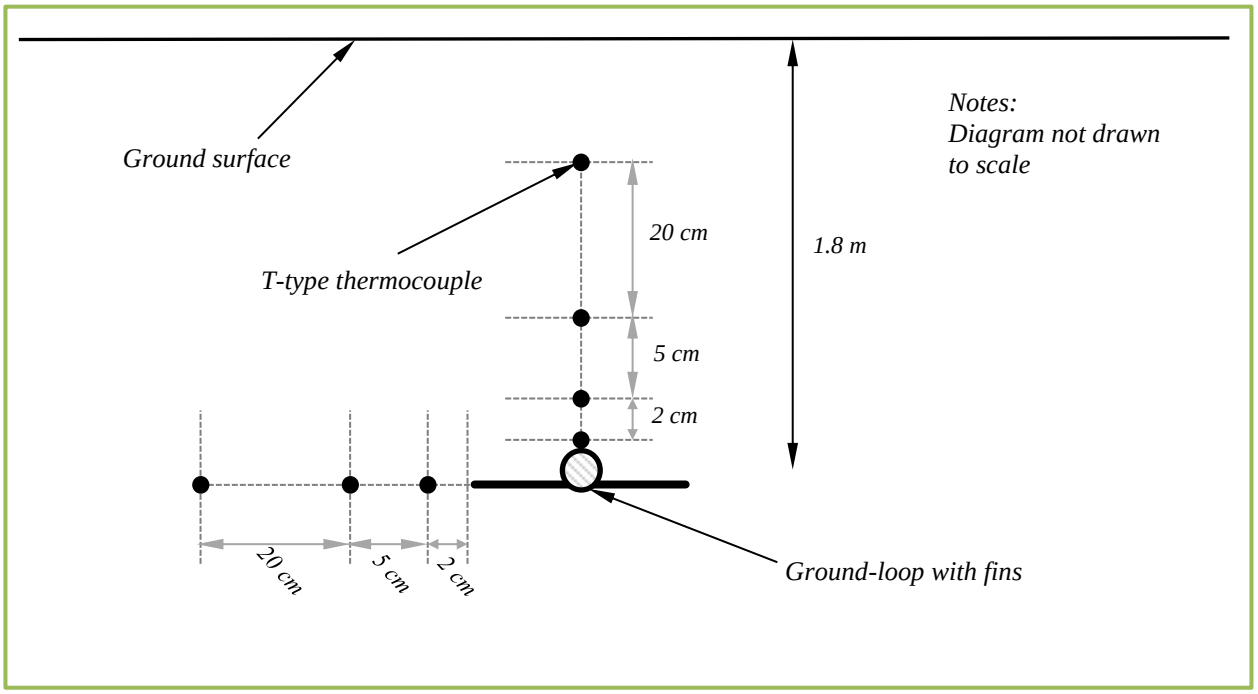

Figure 2.4 – Cross-section of the aluminium finned ground-loop installed in Yildiz Technical University, including the vertical and horizontal position of ground temperature monitoring thermocouples (adopted from Koyun, et al., 2009).

2.3.1.3 French sites

This literature review presents two field-scale monitoring schemes located in France. The first of these is an experimental site located in the Bureau de Recherches Geologiques et Mineral (BRGM), Orleans (Philippe, et al., 2010). The research work aimed to evaluate the influence of climatic variables on the performance of horizontal ground source heat systems, considering a range of soil properties and ground surface coverage. The system was combined heating and cooling with energy loads of 27 kW and 78 kW respectively. The plan area for the horizontal ground-loop installation was divided into four sectors, each measuring 100m^2. Each of the four sections had different types of surface coverage, namely; sunny grass, shaded grass, sunny car park and shaded car park. Each sector contained 400 meters of ground-loop pipe; buried at a depth of 1 meter (i.e. the ground-loop length totalled 1600 metres across the four sections). A fluid mixture of 40% monopropylene glycol and 60% water was used in the system. Optical fibres were used to take ground measurements at depths of 0.5, 1.0 and 1.5 metres. The extent to which these ground measurements are taken across the site in not discussed. The heat pump inlet/outlet fluid temperature was also monitored along the ground-loop fluid flow. Details regarding any climatic measurements are not reported. The study findings concluded that the surface type influenced the ground temperatures observed. Ground temperatures beneath the car park surfaces were found to be greater than the corresponding temperatures beneath the grass surfaces.

The second field-scale experimental system was installed in 2007 at a commercial property at EDF's research and development centre (Helpin, et al., 2011). A horizontal ground source heat system was installed in conjunction with solar collectors to investigate whether combined systems can reduce the total installation costs. A 9 kW system was selected and installed to mimic the cyclic heating operation of a residential property. The ground-loop consisted of 1300 meters of pipe; laid in four parallel lengths over an area of 3000 m^2 (installation depth of the ground-loop is not provided). Temperatures measurements along the ground-loop length were monitored however the variation of ground temperatures beyond the ground-loop were not studied. The heat pump inlet/outlet fluid temperatures were monitored along with the ground-loop fluid flow, allowing the thermal energy extraction/rejection to the ground to be monitored. The climatic variables of ambient air temperature and solar radiation were also measured. The study concluded that solar assisted ground source heat systems can reduce the capital cost of installations by 23% when compared to conventional ground source heat systems (depending upon the local economic conditions).

2.3.1.4 Remaining global sites

In 2008 field-scale tests were conducted on a horizontal ground source heat system located in Kyushu University, Fukuoka City, Japan (Fujii, et al., 2012). A dual heating and cooling system, with loads of 3-4 kW in both operation modes, was installed to serve a testing room with a floor area of 6.5 m^2. The ground-loop was installed over an 800 m^2 area at a depth of 1.5 meters with trench spacing of 4 meters. The length of the ground-loop is not provided. Polyethylene pipe with a diameter of 34 mm was used for the ground-loop and installed with a slinky pipe configuration. During the system installation, the local geology was found to consist of a non-uniform 10 meter thick surface soil underlay by thick granite. Soil samples were retrieved at a depth of 1.5 meters to test for water content and thermal conductivity. The groundwater level was also inspected using a 50 meter deep observation well located at the site, measuring 18 meters below the surface at the time of the installation. The ground temperature was monitored at two locations using thermistors. Each thermistor measured the ground temperature vertically above the ground coil, at a depth of 1 meter below the ground surface. Thermistors were also used to monitor the heat pump inlet/outlet fluid temperatures to the ground-loop. The fluid flow rate was actively controlled and monitored using a valve. Hourly climate measurements of ambient air temperature, precipitation, wind velocity and solar radiation were also taken (sensor specifications were not presented).

A horizontal ground source heat system, equipped with monitoring equipment was installed to serve a newly built residential property in Braslov County, Romania (Craciun, et al., 2010). A 10.5 kW heat pump was installed in 2008 to provide space heating to the residential property which had a

total floor area of 130 m^2. The ground-loop type adopted was a slinky pipe arrangement which was buried at a depth of approximately 1.4 meters. The ground temperature was monitored at depths of 0.01, 0.5, 0.1, 1.4 and 1.8 meters beneath the ground surface at a single plan location. The heat pump inlet/outlet fluid temperature was also monitored. Fluid flow and climatic measurements were not discussed.

A study has also been reported with the aim of evaluating the geothermal energy potential at an experimental site in Borj Cedria, northern Tunisia (Naili, et al., 2012). The experimental system was designed to provide space cooling to a 12 m^2 test room at the Research and Technology Centre of Energy, with a cooling capacity of 21.9 kW. A horizontal ground-loop 25 meters in length was buried at a depth of 1 meter. The loop consisted of a 20 mm polyethylene pipe positioned in a parallel arrangement. The ground temperature, heat pump inlet/outlet fluid temperatures and fluid mass flow rate were measured in order to evaluate system efficiency under the prescribed cooling load and climate in northern Tunisia. Ground temperatures were measured at depths of 0, 0.2, 0.4, 0.6, 0.8 and 1.0 meters beneath the ground surface at a single location using thermocouples. Two thermocouples were also used to measure the inlet/outlet fluid temperature and a rotameter was used to measure the fluid mass flow rate. Climatic variables for air temperature, relative humidity, wind velocity and solar radiation were measured elsewhere at the Research and Technology Centre of Energy. During the installation, soil samples were obtained and subsequent tests were conducted to determine selective thermal and physical properties of the soil. The research generally concluded that the ground thermal conditions found in northern Tunisia would be sufficient for the implementation of horizontal ground source heat systems.

2.3.2 UK field-scale monitoring sites

A number of studies into the performance of horizontal ground source heat systems have been undertaken by both universities and governmental organisations within the UK. A large number of commercial and residential properties have been fitted with monitoring equipment as part of these studies however; the focus of these sites has been predominantly on the heat pump output and performance (Rawlings, 1999; Singh, et al. 2010). In most monitoring sites only the mechanical and electrical characteristics have been studies and recorded (Wu, et al., 2010).

The largest UK study in the public domain was undertaken by the Department of Energy and Climate Change (DECC) (Energy Saving Trust, 2012). The scheme monitored in total 83 residential properties across the UK, installing a variety of heat, electrical and flow meters, however no ground measurements were taken at any of the ground source heat sites. Due to the large number and

geographical distribution of monitoring sites across the UK, the scheme implemented where possible, remote monitoring techniques using the mobile phone network to monitor and download recorded data.

A study was undertaken at Nottingham University to incorporate a ground source heat system consisting of both vertical and horizontal ground-loop configurations within an existing Eco-Experimental house (Doherty, et al., 2004). The system was designed to provide space heating and cooling to the existing four bedroom eco-house, located on the university campus. The eco-house was designed to be a full-scale laboratory for the field testing of innovative technologies in the area of sustainable energy systems. Prior to the ground source heat system, a range of other sustainable systems had been installed at the house, including; integrated photovoltaic slates, solar tube collectors, a solar chimney and a rainwater recovery system. A reversible 8 kW heat pump (providing space heating and cooling) was installed at the site. Two vertical ground-loops 36 meters in length were installed within two separate 18 meter deep boreholes, 8 inches in diameter. In addition to this, two horizontal slinkies 150 meters in length were installed in two separate trenches at a depth of two meters. High density polyethylene pipe was used for both ground-loop types. A range of mechanical measurements were taken, including the heat pump inlet/outlet fluid temperatures along with the ground-loop fluid flow which enabled the heat injection/rejection with the ground to be determined. Climatic variables including ambient air temperature and solar radiation were also measured; however no ground temperature monitoring was reported. The installed system was found to meet the heating and cooling demands of the eco-house. Further to this, the calculated energy extraction per unit length was found to agree with the rule thumb approach adopted for design purposes.

One existing UK field-scale monitoring site, which included the measurement of ground temperatures, was found in literature and is presented. The performance of a horizontal ground source heat system serving a domestic property in Drayton St Leonard, Oxfordshire was investigated by researchers from the Nottingham and Reading Universities (Wu, et al., 2010; Gonzalez, et al., 2012). In 2009, four ground-loops with a slinky configuration were installed in an 80 meter long by 20 meter wide paddock area at a depth of approximately 1.2 meters. Details regarding the heat pump type and load are not reported. Ground temperatures were measured at two separate locations, one directly above the slinky ground-loop at the centre of the trench and a second horizontally offset two meters from the trench centre. It was anticipated that the second location, 2 meters away from the slinky, was beyond the thermal influence of the ground-loop and would thus measure reference ground temperatures. The thermistors were located at depths of 0.02, 0.05, 0.1, 0.25, 0.5, 0.75, 1.0, 1.05, 1.1 and 1.4 meters below the ground surface at each location. T-type thermocouples were also installed at the heat pump inlet/outlet to monitor fluid temperature differential across the heat pump. Climatic variables including ambient air temperature, wind speed, solar radiation, relative humidity and rainfall were also measured using a weather station installed at the site. During the installation, three soil

samples were also retrieved at depths of 0.2, 0.8 and 1.0 meters and subsequently measured for thermal conductivity, thermal capacity, density and moisture content. The study findings concluded that the COP of the system decreased over a two month period of operation. It was stated that the COP of the system could have been increased provided that a longer ground-loop had been installed.

2.3.3 Overview of field-scale monitoring sites

Field-scale horizontal ground source heat monitoring sites from around the world have been presented in the previous sections. Research efforts into the performance of horizontal ground source heat systems has increased over the past two decades with a range of conventional and bespoke systems being monitored. The global spread of monitoring sites has inevitably led to systems being installed and monitored in an array of ground conditions and climates. Opportunities to monitor the system performance in conjunction with the local climates have often being overlooked as most monitoring sites either make no or very basic (i.e. ambient air temperature only) climatic measurements.

It can be concluded that the majority of the monitoring sites presented focus predominantly on the mechanical and electrical aspects of systems, a featured echoed in the UK sites presented. This leads to either no or minimal ground measurements being taken. In addition to this, the local geotechnical properties are also often simplified or overlooked completely. No conventional monitoring sites measuring both the vertical and horizontal temperature distribution around horizontal ground source heat systems were encountered. Through the mechanical monitoring of the heat pump inlet/outlet fluid temperature and ground-loop flow, most sites of the sites presented have collected sufficient data to allow the thermal energy extraction/rejection with the ground to be calculated.

Many of the monitoring schemes presented were in fact experimental sites, serving small testing facilities on university campuses. This not only influences the design specifications of systems, leading to smaller ground-loops being installed but can also affect the loading cycles of systems leading to unrealistic loading patterns. When inspecting the larger horizontal systems found in literature, it can be said that the majority adopted a slinky horizontal pipe configuration, including the single UK site found to be monitoring ground temperatures.

The anticipated duration of site monitoring was not discussed in any of the schemes presented. Ground temperature changes occur on an annual basis therefore it is necessary to observe ground thermal behaviour on a similar time-scale in order to fully understand the ground behaviour in response to ground source heat systems. No examples of long-term monitoring results (i.e. in the order of years) were found during the literature review.

Due to the nature of the work presented in this thesis, particular attention was paid to monitoring sites found within the UK. Significant research efforts have been made in the UK, particularly by the government organisation the 'Energy Saving Trust'. The research found primarily focussed on mechanical and electrical aspects of systems. A single UK site was however found to be monitoring some ground temperatures along with local climatic variables.

2.4 Ground source heat system modelling

A number of comprehensive modelling studies have been undertaken with regards to ground source heat systems (Yang, et al., 2010). Previous researchers have cited that a combination of the dynamic circulating fluid within the ground-loops and heat transfer within the soil gives rise to a complex system (Al-Khoury, et al., 2005). The major challenges when modelling horizontal ground source heat systems can be summarised as (Mei, 1986; Yang, et al., 2010):

i. heterogeneous nature of the ground leading to the uncertainty of soil parameters.
ii. influence of moisture on ground thermal behaviour.
iii. the effect of the ground surface boundary on season ground temperatures and properties at depth.
iv. the cyclic operation of ground source heat systems.
v. the ground loop-soil boundary conditions.

The problems highlighted in the previous items have led to a variety of modelling approaches to be developed in the field. The techniques employed to solve and/or simplify the highlighted problems have often been driven by the computational capabilities at the time of development (Al-Khoury, et al., 2005). A salient review of modelling approaches will be provided along with the more recent developments within the field. For the purpose of this study, the model developments have been split into three sections; namely *i) Analytical models*, *ii) Semi-Numerical models, iii) Numerical models* and *iv) Model developments for horizontal ground source heat systems,* all of which will be presented in the following sections.

Although many of the analytical solutions in the heat transfer field were developed in excess of 60 years ago, they still provide the basis for many semi-numerical models and design simulation tools developed and used in the field (Yang, et al., 2010; Al-Khoury, et al., 2005). As computational performance improved, many barriers preventing the application of numerical models were also removed. Although horizontal systems are the focus of this thesis, a salient review of semi-numerical and numerical vertical models has been undertaken as many of the modelling techniques employed

can be applied to both types of ground-loop configurations. Finally, an overview of bespoke horizontal ground source heat model developments has been undertaken.

2.4.1 Analytical models

The majority of analytical models found in literature are based on one of two models; either the so called 'Line source theory' or 'Cylindrical source solution' (He, 2012). The 'Line source theory' was originally proposed by Kelvin (1882). It is a generic one-dimensional theory which considers an infinitely long line source or sink of heat within an infinite uniform medium. The heat flux emitted at the source is assumed to be uniform and constant. The theory allows the variation temperature within the medium to be calculated with time. Ingersoll (1954) subsequently adopted the theory and applied it to ground source heat systems. The theory can be expressed as follows (Yavuzturk, 1999):

$$T - T_0 = \frac{Q}{2\pi\lambda}\int_X^\infty \frac{e^{-\beta^2}}{\beta}\,d\beta \tag{2.1}$$

where:

$$\beta = \frac{r}{2\sqrt{\alpha(t-t')}} \tag{2.2}$$

$$X = \frac{r}{2\sqrt{\alpha t}} \tag{2.3}$$

where T is temperature of the ground at radius r *(K)*, T_0 is the initial temperature of the uniform medium *(K)*, Q is the heat flux per unit length of the borehole *(W m^{-1})*, r is the radial displacement from the line source *(m)*, λ is the thermal conductivity of the medium *(W m^{-1}K^{-1})*, α is the thermal diffusivity of the medium *(m^2 s^{-1})* and t is the time since the start of operation, t' *(s)*.

Within the context of ground source heat, the 'line source theory' has often been adopted to model systems (Mei, 1986). The infinite line source or sink represents a simplified ground-loop and the medium takes on ground characteristics. Additional modifications have been made to the line source model, most notably Hart and Couvillion (1986) and the International Ground Source Heat Pump Association (IGSHPA) (1991).

The second of the two models commonly used as a basis for analytical solutions is the 'Cylindrical source theory' developed by Carslaw and Jaeger (1947). The theory considers a finite cylindrical heat source or sink of infinite length within an infinite uniform medium. Similar to the 'line source theory', the theory allows the temperature at any location within the medium to be calculated at any time provided the heat flux emitted is uniform and constant. The resulting one dimensional solution can be expressed as follows (Carslaw & Jaeger, 1947):

$$\theta(r,t) = \frac{2Q}{\pi\lambda}\int\left(1 - e^{-\alpha u^2 t}\right)\frac{J_0(u,r)Y_1(u\alpha) - Y_0(ur)J_1(u\alpha)}{u^2[J_1^2(u\alpha) + Y_1^2(u\alpha)]}\,du \qquad (2.4)$$

where J_0, J_1, Y_0 and Y_1 are the zero and first order Bessel functions, θ is the temperature difference between time t and initial time (K) and u is an integration constant.

The theory was further developed by Kavanaugh (1985) who applied the solution to model a vertical ground source heat system. The original theory simplified the internal components of a vertical system to a single cylinder of infinite length. Kavanaugh found that this simplification neglects thermal interactions between the ground-loop components, introducing some inaccuracies especially during short term analysis. In order to account for this, a number of coefficients taking into consideration the thermal properties and location of boreholes components were derived.

2.4.2 Semi-Numerical models

A variety of computational models and codes have been developed during the last four decades for the numerical simulation of ground source heat systems. The numerical approaches adopted by the models are influenced by three main factors, namely; computational capabilities, domain type and simulation duration. A complete three-dimensional field-scale simulation of a ground source heat system would require significant computational effort. To overcome this, a number of semi-numerical approaches have been developed by a range of authors.

For any given ground source heat model there are two modelling strategies which require attention. Firstly, the numerical schemes applied to model the spatial and temporal behaviour of the ground. Secondly, the boundary conditions prescribed to represent the transient behaviour of systems with particular attention being focussed on the ground-loop interaction with ground and the ground surface interaction with the atmosphere.

The earliest model developments were subjected to the greatest computational restrictions. To overcome this Eskilson (1987), Hellstrom (1991) and later Yavuzturk (1999) simplified the

ground-loop boundary by representing it with a so called 'response factor'. The approach allowed multiple borehole systems, often the focus of large commercial and community heating schemes, to be modelled (Yang, et al., 2010). The so called 'response factor' is in fact a function which describes the relationship between ground temperature and heat flux changes over a fixed period of time (He, 2012). Details of these models and the approaches taken to derive the response factor will be described in following sections.

2.4.2.1 Eskilson's Model

Eskilson developed a model to investigate possible thermal storage applications of vertical ground source heat systems. Response factors, which were referred to as 'g-functions' by Eskilson, describe the relationship between the average borehole temperature and the heat injected/rejected for a fixed time-step and for a defined borehole arrangement. The 'g-functions' are computed in a two-step process combining analytical and numerical methods. Firstly, a two-dimensional (radial-axial) finite difference model for a single vertical exchanger was created in order to determine the ground temperature response to heating load for a given time-step. Following this, the simulation results are subjected to spatial superposition techniques which are used to predict the ground temperature response for multiple borehole systems for the same time-step and heating load. The resulting superimposed temperature responses are characterised according to the borehole spacing and ratio of diameter to depth in order to derive the 'g-functions'. The 'g-function' can be expressed as follows, given a constant heat injection/extraction rate and a constant far-field ground temperature (He, 2012):

$$T_b(t) = T_s - Q \cdot R_q \tag{2.5}$$

where T_b is the borehole temperature at a time *t (K)*, T_s is the far-field ground temperature *(K)*, Q is the heat injection/extraction rate *(W m^{-1})* and R_q is a time-dependant thermal resistance given as (He, 2012):

$$R_q = \frac{1}{2\pi\lambda} \cdot g\left(\frac{t}{t_s}, \frac{r_b}{H}\right) \tag{2.6}$$

where *g(t s^{-1}, r_b H^{-1})* denotes the dimensionless 'g-function', t_s is a the steady state time-scale factor, r_b is the radius of the borehole *(m)*, H is the borehole depth *(m)* and λ is the ground thermal conductivity *(W mK^{-1})*.

The ‘g-function’ combines analytical and numerical techniques in order to investigate large borehole arrangements, which would otherwise overwhelm computational resources. The simplification of the ground thermal response inherently makes a number of assumptions and simplifications. Firstly, the ground-loop boundary is assumed to be constant, simplifying transient heating loads of ground source heat systems, and thereby neglecting any seasonal variation. The initial two-dimensional simulation also assumes that the system is axisymmetric and that the ground is homogeneous. Finally, there are also limitations when considering complex borehole configurations and borehole arrangements which do not conform to regular spacing or patterns.

2.4.2.2 Yavuzturk’s Model

Eskilson’s model was devised to investigate the long term response of thermal storage systems (up to 25 years) (Yavuzturk, 1999). The approach to calculate the ‘g-function’ is only valid for unit time-steps satisfying the criterion $t > \frac{5{r_b}^2}{\alpha}$ (Eskilson, 1987), which is equivalent to a few hours for conventional borehole configurations. Yavuzturk (1999) extended Eskilson’s model, allowing for the inclusion of smaller time-steps, less than the criterion previously stated. Yavuzturk modified the numerical aspect of Eskilson’s original model, adopting a finite volume method and two-dimensional model on a polar-grid to simulate a single vertical borehole (see Figure 2.5). From Figure 2.5 it can be seen that the domain and borehole components were assumed symmetrical. The model domain allowed for consideration of borehole components such circulating fluid, pipe and grout along with the associated thermal properties which were neglected in Eskilson’s original model. Consideration of these borehole components allowed the minimum permissible time-step of the model to be reduced (Yavuzturk, 1999).

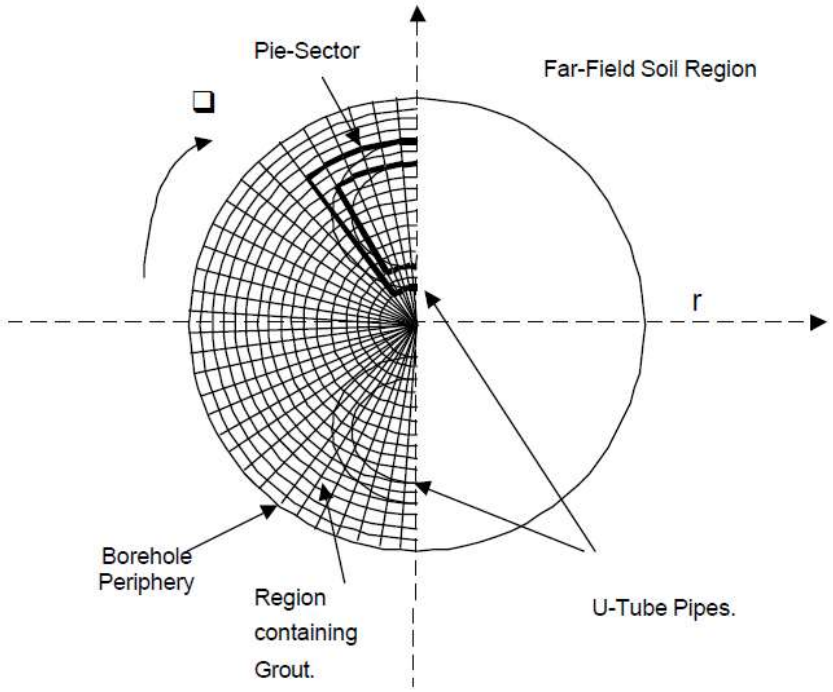

Figure 2.5 – Representation of the borehole region proposed by Yavuzturk including the so called 'pie-sector' region used to represent U-tubes (Yavuzturk, 1999).

From Figure 2.5 it can be seen that the borehole configuration was not explicitly modelled but instead approximated by a so called 'pie-sector method' (Yavuzturk, 1999). The temperature of the fluid is calculated for a known heating load by applying the finite volume method. The borehole temperature can be subsequently calculated using the following equation (Yavuzturk, 1999):

$$T_b(t) = T_f(t) - R_b \cdot Q \tag{2.7}$$

where R_b is the sum of the conductive resistance of the fluid, pipe and grout *(Km W^{-1})* and T_f is the fluid temperature *(K)*. Details regarding the calculation of these convective resistances can be found in (He, 2012) and (Paul, 1996).

Consequently, Yavuzturk modified the original 'g-function' (Equation 2.6) in order to account for the components of the borehole giving (Yavuzturk, 1999):

$$g\left(\frac{t}{t_s}, \frac{r_b}{H}\right) = \frac{2\pi\lambda \cdot \left(T_f(t) - R_b \cdot Q - T_s\right)}{Q} \tag{2.8}$$

For conventional borehole configurations, Yavuzturk states that this approach translates to a minimum time-step of approximately two and a half minutes (Yavuzturk, 1999). Yavuzturk's

approach still suffers from many of the limitations associated with Eskilson's original model as previously discussed. Yavuzturk's approach has been implemented in a number of popular design tools, most notably GLHEPro (Spitler, 2000), design software for vertical borehole ground-loop heat exchangers and EnergyPlus (Crawley, et al., 2001), a building energy simulation package. It is noted that further modifications were also made to Yavuzturk's approach by Fisher et al. (Fisher, et al., 2006).

2.4.2.3 Duct Storage (DST) Model

Hellstrom (1991) developed the DST model to simulate seasonal thermal energy storage using multiple borehole systems. The thermal energy storage systems in question typically compromise of multiple vertical boreholes which may or may not incorporate heat pump systems. The model sub-divides the ground domain into two distinct regions known as the 'local' and 'global' regions. The local regions each consist of an individual borehole along with a fixed volume of adjacent ground (see Figure 2.6). The global region consists of the ground beyond the local regions but within the model domain (see Figure 2.6). Figure 2.6 shows how the local and global regions interact in Hellstrom's DST model.

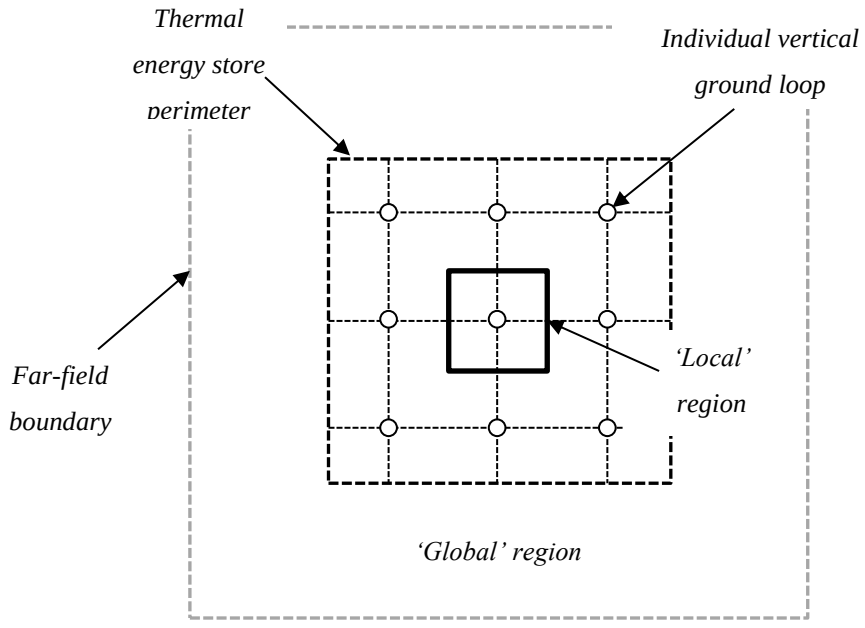

Figure 2.6 – Schematic showing the 'local' and 'global' regions as proposed by Hellstrom (after He, 2012).

The heat transfer within the local regions is represented as a one-dimensional heat transfer problem with individual borehole components represented by a single combined thermal resistance. A finite difference scheme is applied to simulate the transient temperature change, however over longer timescales the local region is assumed to reach steady-state at which point analytical solutions are deemed representative (He, 2012). The global region investigates the thermal interaction between the heat store (i.e. multiple boreholes represented as local regions) and the surrounding ground. Hellstrom (1991) stated that the thermal behaviour in the global region is a function of three components, namely: i) a transient thermal build-up component, ii) a steady-state heat loss component and iii) a periodic heat loss component (Hellstrom, 1991). The so called 'transient thermal build-up' is associated with the initial injection/extraction of thermal energy to the ground after which there will be a 'steady heat loss component' to the surrounding global region. The 'periodic heat loss component' is associated with the annual storage cycles in use. Using these three components, Hellstrom derived boundary conditions which were prescribed within a two-dimensional (radial-axial) finite difference scheme used to simulate heat transfer in the global region.

The DST model development assumes that vertical ground source heat exchangers are densely packed, similar to arrangements typically found in thermal heat stores. However, this assumption does not always hold true for conventional ground source heat systems which are often more widely spaced and irregular in nature (He, 2012). In order to implement the DST model, the heat injection/rejection is also required to be decomposed into a series of constant 'heat steps'. The numerical results of these heat steps are analytically superimposed in order to arrive at a final solution. However, this does lead to some problems when performing short term simulations or when prescribing irregular heating loads (He, 2012). It is noted that subsequent developments have been made to Hellstrom's model, most notably Thornton et al. (1997) and Sutton et al. (2002).

2.4.3 Numerical models

A variety of numerical models have been developed within the ground source heat field over the past three decades. The numerical approaches adopted and techniques within these models have been influenced by a number of factors, notably the computational hardware and techniques available at the time of conception.

The following subsections will present salient models within the ground source heat field. First, numerical models applicable to both vertical and horizontal systems will be presented. Following this, numerical models developed specifically to simulate horizontal ground source heat systems will be presented for discussion.

2.4.3.1 Al-Khoury et al. Model

A three-dimensional model has been developed by Al-Khoury et al. to simulate the transient thermal behaviour of vertical ground source heat systems (Al-Khoury, et al., 2005; Al-Khoury, et al., 2006). The finite element approach has been used to explicitly represent individual ground-loop components and geometries. It was estimated that a representative three-dimensional model of a 100 m borehole, containing a single U-tube in a 10 m by 10 m by 150 m domain would require in the order of 1,000,000 elements (Al-Khoury, et al., 2005). To reduce the mesh size, a model was devised which consisted of two element types; a one-dimensional element used to simulate the pseudo three-dimensional heat flow (and circulation) within the borehole and a three-dimensional element representing the surrounding ground. The borehole was therefore discretised into a series of one-dimensional elements along its length which applied energy conservation equations to calculate an overall heat flux at the ground-borehole interface. Each borehole component (i.e. circulating fluid, pipe and grout) and its spatial position was considered within a control volume in order to allow an overall heat flux for that one-dimensional element to be determined. Unlike previous models, the three-dimensional elements representing the ground considered the influence of groundwater flow and the associated convective thermal component. The ground was considered as a porous media, through which a fixed groundwater flow could be prescribed.

The two differing element types resulted in two global matrices which were linked together at the ground-borehole interface. The two systems are linked together via a calculated heat flux, representing the heat injection/extraction and calculated as a function of the borehole and soil temperatures. A sequential numerical algorithm was implemented to solve the two systems of non-linear equations, and then link the one-dimensional and three-dimensional finite elements together.

Although the assumptions are reasonable, the solution is not accurate for transient solutions where the ratio between the borehole diameter and depth is greater than 1:500 (He, 2012). Groundwater flow considerations are included but only below the water table level while the impact of moisture in the unsaturated zone is neglected.

Diersch et al. (2011a, 2011b) extended the Al-Khoury's model by modifying the thermal resistance approach used to model the borehole thermal behaviour. This modified approach enabled more complex borehole configurations to be represented, allowing the heat transfer within the borehole itself to be modelled more accurately.

2.4.3.2 He et al. Model

A three-dimensional finite volume model has been developed to simulate the transient behaviour of domestic ground source heat systems (He, et al., 2009). The development aim was to investigate the transient thermal response of heat extraction in and around a single vertical ground source heat exchanger. A finite volume solver known as GEMS3D (General Elliptical Multi-block Solver) was used as the basis of the model. GEMS3D applies the finite volume method to solve the general advection-diffusion equation of a three-dimensional boundary of a block structured mesh (He, et al., 2009) (see Figure 2.7).

As depicted in Figure 2.7, He et al. (2009) considered a single borehole with a line of symmetry dissecting its centre. The third dimension of the domain (depth) was represented as a series of layers. Finite volume cells representing the fluid and grout are included within the model, allowing the thermal interaction between borehole components to be explicitly modelled with depth (He, et al., 2009). The representation of the circulating fluid is based on the so called 'Compartments-In-Series' model (Wen & Fan, 1975), which has been successfully applied to a range of engineering problems (He, et al., 2009). This circulation model simplifies the fluid behaviour by assuming it to be fully turbulent and well mixed, thereby allowing circulation to be considered without any computational fluid dynamics. This approach represents fluid flow around the ground-loop as a one-dimensional convection term within a temperature differential equation, which according to (He, et al., 2009), allows fluid flow variation to be represented.

Using the developed model, a numerical investigation was undertaken into the circulating fluid temperature profile with varying fluid velocity (He, 2012). Over short timescales it was found that the fluid temperature profile was non-linear, regardless of the fluid velocity. Over longer timescales, the fluid temperature profile remained non-linear for low fluid velocities (< 0.2 ms^{-1}) however a linear profile was approached at greater fluid velocities. Consequently, the error incurred by two-dimensional models is, in part, influenced by the fluid flow characteristics of systems (He, 2012).

There are some notable differences and similarities between the Al-Khoury (2005 & 2006) and He (2009) models. Both models represent the energy load on ground source heat systems with fluid temperatures, not an energy flux value. Within the borehole, He's model explicitly accounts for the thermal interaction between borehole components, while this is analytically represented in Al-Khoury's model. Beyond the boundary of the ground-loop, He's model neglects any influence of moisture or groundwater flow on the ground thermal behaviour while Al-Khoury includes this consideration.

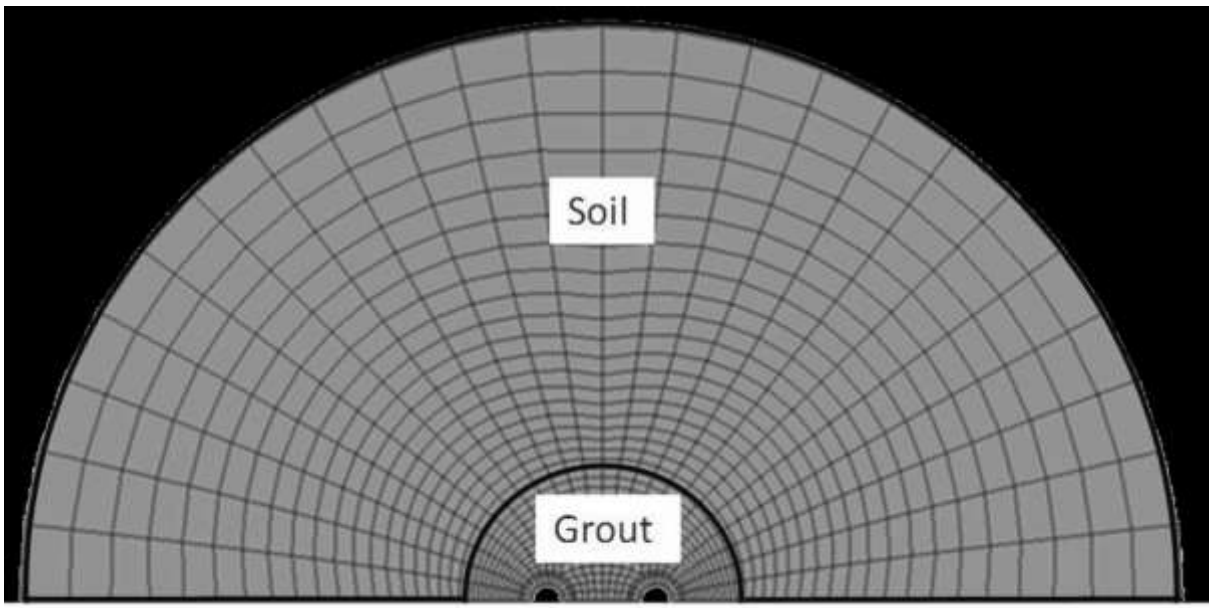

Figure 2.7 – Structured mesh used to model the vertical ground source heat system (He, et al., 2009).

2.4.3.3 Other notable numerical models

Lee and Lam (2008) applied a three-dimensional finite difference method to investigate the ground temperature behaviour surrounding a vertical ground source heat system. A rectangular mesh was adopted, with the borehole being represented by a single square column. Circulating fluid temperatures were considered using one-dimensional model which used the conservation of energy approach in conjunction with control volumes. The fluid temperature was considered to be in a quasi-steady state (i.e. fixed for a given time-step). The calculated fluid temperatures were subsequently used as a basis to calculate an overall borehole temperature which could be prescribed within the three-dimensional model. Within the numerical scheme, the ground was assumed to be homogenous and no groundwater or moisture considerations were made. The ground surface boundary was simplified to a uniform fixed temperature.

De Carli et al. (2010) developed the so called Capacity Resistance Model (CaRM) in order to model a single vertical ground source heat exchanger. The model divides the domain horizontally into a series of rings and vertically into layers. Each ring is represented with an assigned thermal capacity and resistance (He, 2012). Heat transfer in the ground is to be assumed one-dimensional, occurring radially only. Vertical heat transfer between layers is neglected. The model however, did allow complex borehole geometries to be investigated and accounted for fluid behaviour, modelling the fluid circulation in a one-dimensional approach similar to Al-Khoury (2006) and Ruan & Horton (2011).

Li & Zheng (2009) developed a three-dimensional unstructured finite volume model to investigate the performance of a vertical ground source heat system compromising of multiple boreholes. The model assumed a symmetrical borehole field, reducing the domain by half. To reduce computational effort the three-dimensional domain was discretised into a series of two-dimensional layers. The model domain did not extend beneath the borehole, thereby neglecting any ground thermal behaviour in this region. The behaviour of the circulating fluid is simplified, with fluid temperatures set equal to the fluid inlet temperature and influence of groundwater/moisture on the ground temperature behaviour was neglected.

Ruan & Horton (2011) developed a two-dimensional numerical model to investigate the long-term performance of a vertical ground source heat system compromising of multiple boreholes. The heat transfer within individual boreholes was simplified to a one-dimensional (vertical) quasi-steady state model in an approach similar to Al-Khoury (2005). A two-dimensional (vertical-radial) transient model was developed and linked to the one-dimensional borehole model to simulate the thermal behaviour of the ground. The model can account for varying ground properties with depth although groundwater and moisture effects on the thermal behaviour are neglected (Ruan & Horton, 2011). The circulating fluid temperature is calculated based upon the heating/cooling loads and efficiency of the heat exchanger, not on prescribed fluid temperatures.

2.4.4 Model Developments for horizontal ground source heat systems

As previously explained, the following section will present numerical schemes specifically developed to model horizontal ground source heat systems.

2.4.4.1 Mei Model

Mei (1986) developed a two-dimensional model to simulate the seasonal ground temperature variation in response to a horizontal ground source heat system. Prior to this, no comprehensive horizontal ground heat exchanger analysis had been undertaken due to the complex nature of the problem (Mei, 1986). The ground behaviour of a real system was investigated which comprised of a single horizontal ground-loop, installed with a parallel pipe arrangement. Further details of the site can be found in section 2.3.1.1. Within the model a single ground-loop was considered. A schematic of Mei's model is shown in Figure 2.8.

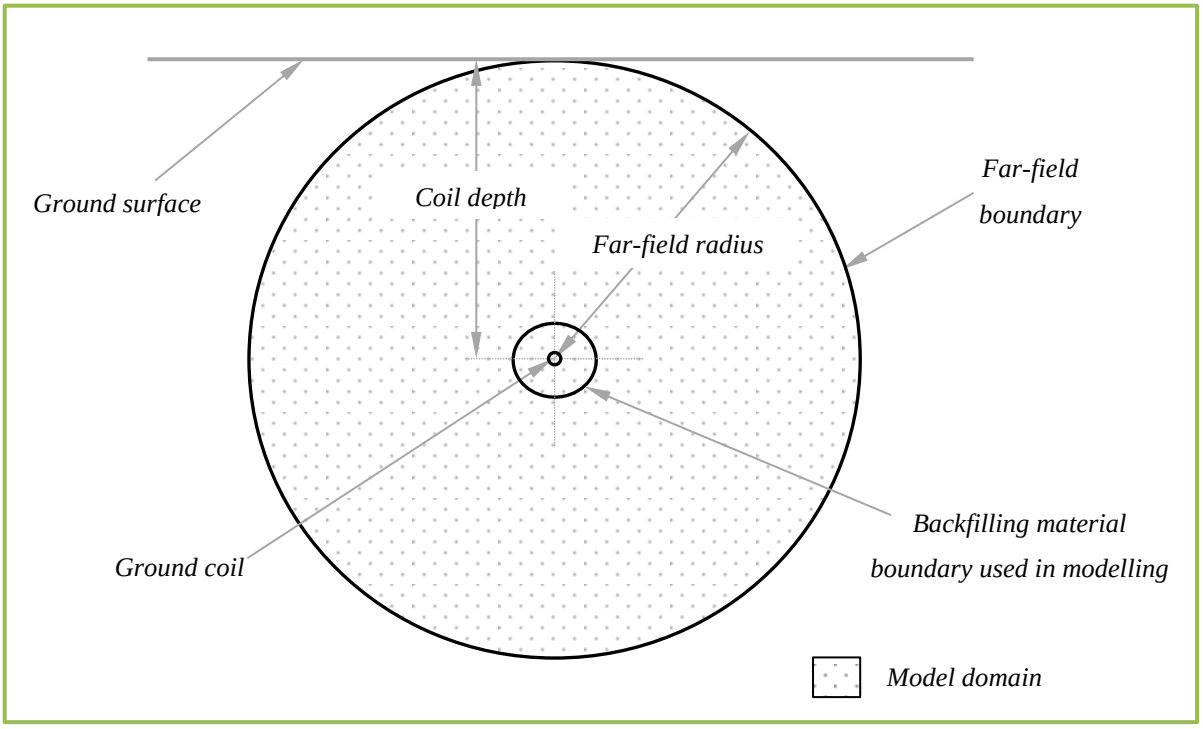

Figure 2.8 – Schematic showing the model setup and domain adopted by Mei (adopted from Mei, 1986).

An explicit finite difference scheme was applied to solve three partial differential equations describing the temperature distribution in the fluid, pipe and soil region. The fluid temperature was considered to vary linearly along the length of the ground-loop. By prescribing a ground-loop inlet and outlet fluid temperature in conjunction with a fluid velocity, a fluid temperature at any point along the ground-loop length was approximated. The appropriate fluid temperature was subsequently prescribed within the model at the ground-loop boundary. Monitoring of the fluid characteristics (i.e. temperature and velocity) allowed the transient thermal load of the system to be included in investigations (Mei, 1986).

Within the scope of the modelling work, a fixed temperature that is a function of time and depth is assigned to the far-field boundary (identified in Figure 2.8). The far-field temperature is calculated at a given point in time according to an analytical expression developed by Kusuda & Achenbach (1965). The model considers in-situ soil characteristics although the soil is assumed to be homogeneous. Groundwater and moisture transfer are neglected within the model. The ground surface behaviour is not explicitly modelled but is instead included by means of the varying far-field temperature profile. Simplifying the ground-loop configuration to a single pipe also neglects any thermal interactions which may occur between adjacent ground-loop pipes.

2.4.4.2 Piechowski Model

Piechowski (1999) developed a mathematical model based on Mei (1986). Piechowski's model aimed to predict the fluid temperature entering the heat exchanger unit. To achieve this, Mei's two-dimensional approach was applied along the length of the ground-loop to create a structured three-dimensional domain (see Figure 2.9).

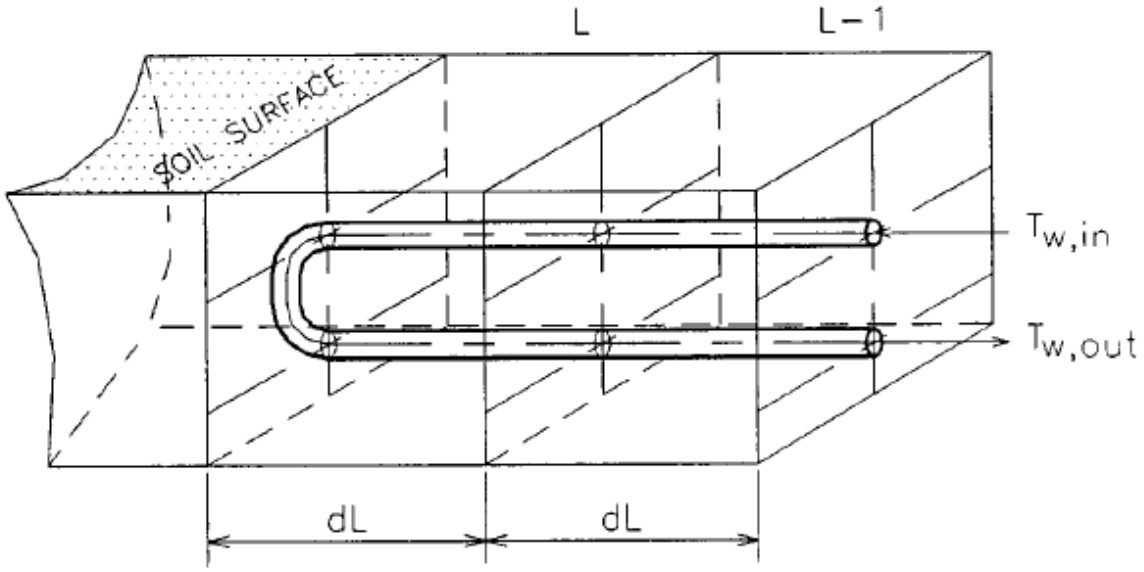

Figure 2.9 – Schematic showing the model domain adopted by Piechowski (Piechowski, 1999).

The circulating fluid is represented in a one-dimensional model, very similar to the approach applied by Al-Khoury et al. (2005) to model vertical ground source heat exchanges (see section 2.4.3.1 for details). The ground-loop length is discretised into a series of finite volumes to which an energy balance equation, similar to that implemented by Al-Khoury, is applied. The fluid temperature is calculated along the ground-loop length and for each time-step as a function of the fluid characteristics and surrounding ground temperature. The model applies a sequential algorithm, whereby a quasi-steady state is assumed at the ground-loop boundary for each time-step. The calculated fluid and ground temperatures enable a heat flux at the ground-loop-soil interface to be calculated.

With regards to the heat transfer in the soil, Piechowski (1999) extended the Mei (1986) model to include the coupled heat and mass interactions in regions surrounding the ground-loop. Although the entire pipe length is explicitly included within the fluid temperature calculations, only a single pipe is considered when modelling the ground, similar to Mei's original model (see Figure 2.8). A pre-defined region for coupled heat and mass transfer was set in order to reduce the computational effort (Piechowski, 1999). Beyond this region, only heat transfer calculations were performed. Both

the heat and mass transfer and heat only transfer were assumed to be axisymmetric; therefore gravity was not included in mass calculations. Mass effects from the ground surface boundary were also neglected within the model. Similar to Mei's original model, the ground surface is not explicitly represented within Piechowski's model. Instead, a varying fixed far-field temperature is prescribed within the model, representing the diurnal and seasonal ground temperature variations (see Figure 2.8).

2.4.4.3 Demir et al. Model

Demir et al. developed a three-dimensional model with the aim of simulating the ground temperature distributions about a horizontal ground source heat system, taking into consideration climatic affects (Demir, et al., 2009). An approach similar to Piechowski (1999) was adopted, whereby the three dimensional domain was divided into a series of two-dimensional cross-sections along the ground-loop length. The two-dimensional cross-sections were linked together by a one-dimensional circulating fluid model. The one-dimensional fluid model calculates the temperature profile along the ground-loop length at each time-step by means of conservation of energy, similar to the approaches of Al-Khoury et al. (2006) and Piechowski (1999) previously discussed.

A schematic of the two-dimensional domain used to model ground temperatures can be found in Figure 2.10. The model domain considers single pipe and an axis of symmetry dissecting its centre (see Figure 2.10). The thermal behaviour of the ground was modelled considering only heat conduction with mass transfer neglected. Heat conduction equations were solved numerically using a finite difference formulation, implemented in MATLAB.

The surface boundary condition is considered as a surface heat flux, calculated by means of a surface energy balance equation (Demir, et al., 2009). The surface heat flux equation and constitutive components can be found in the following equation:

$$Q_t = Q_C + Q_E + Q_H + Q_{LE} + Q_{LI} + Q_{SI} + Q_P \tag{2.10}$$

where Q_t is the total heat flux at soil surface, Q_C is the conductive heat flux through a snow layer, Q_E is the heat flux due to evaporation, Q_H is the emitted longwave radiation heat flux, Q_{LE} is the longwave radiation diffused at the surface, Q_{LI} is the incident longwave radiation heat flux, Q_{SI} is the surface solar incident radiation heat flux and Q_P is the heat flux due to precipitation. All fluxes have units $W\,m^{-2}$.

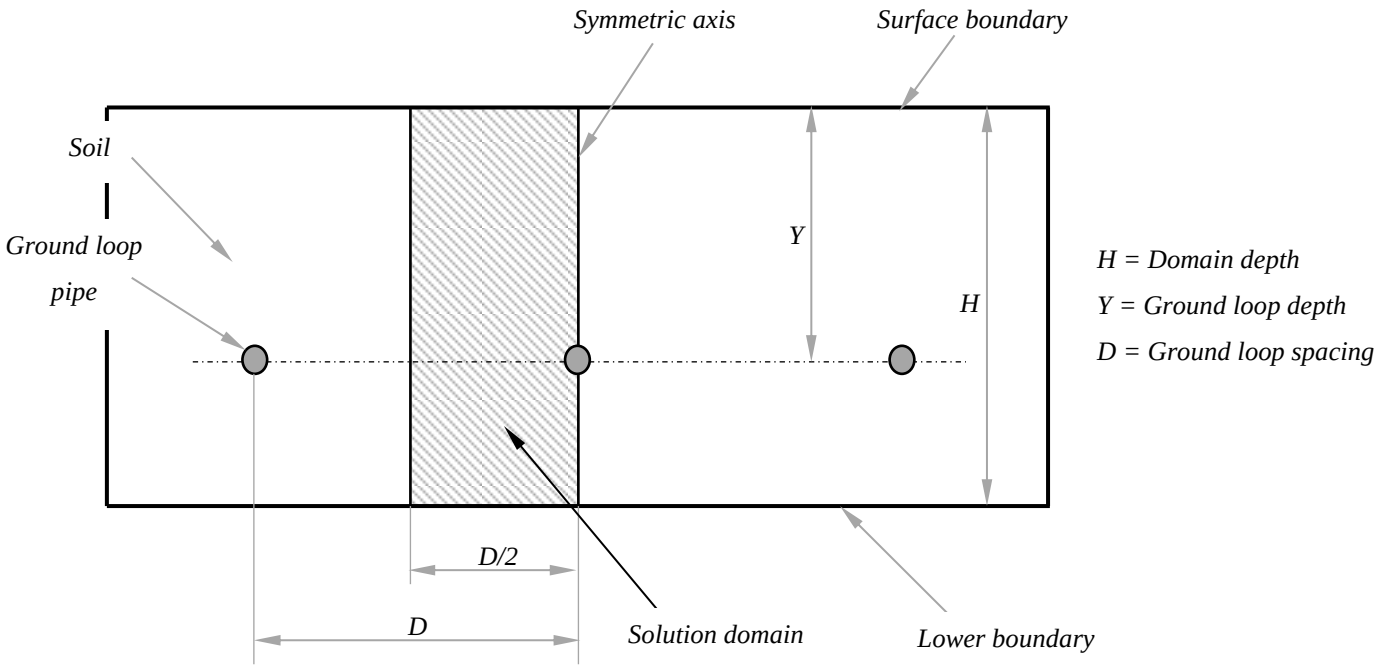

Figure 2.10 – Schematic showing the model domain adopted by Demir et al. (adopted from Demir, et al. 2009).

Demir et al. applied Equation (2.10) to investigate to ground thermal behaviour over a 30 day period with a snow covering. The expressions used to calculate the individual components of the energy balance equation were therefore geared for a snow covering. The inclusion of a snow covering allows the evaporative heat flux, Q_H, to be analytically included within the soil heat flux calculation without numerically modelling the soil as a coupled thermal-mass process. Representing the surface boundary in terms of the surface energy components does however allow the annual and temperature variations in the soil to be accounted for, bypassing the need to use analytical ground temperature expressions.

Although the model is three-dimensional, heat transfer within the ground is only considered in a series of two-dimensional cross-sections. The subsequent thermal interactions between the two-dimensional cross-sections are ignored. By reducing the model domain to include a single pipe, the model also neglects any thermal interactions between adjacent pipes.

2.4.4.4 Other model developments for horizontal ground source heat systems

Ozgener et al. (2007) developed an analytical steady-state model with the aim of simulating a solar assisted horizontal ground source heat system. The model focusses on the processes and efficiencies of the heat exchangers, only considering the inlet and outlet fluid temperature to the

ground-loop. The thermal behaviour of the ground is neglected in within the model. The model was validated using experimental data from a monitoring site previously presented in section 2.3.1.2

Esen et al. (2007) developed a two-dimensional finite difference approach to investigate temperature distributions in the vicinity of the ground-loop (Esen, et al., 2007). Two-dimensional temperature distributions were calculated considering heat conduction, while convective contributions were considered negligible. The two-dimensional domain adopted in the model considers a single ground-loop pipe, with a vertical line of symmetry dissecting the pipe centre. This approach is similar to that taken by Demir et al. (see Figure 2.10). The model assumes the soil to be homogeneous, with the influence of groundwater and moisture transfer on the soil temperature distributions assumed to be negligible. The ground source heat energy load is represented as an assumed fixed temperature assigned to the pipe perimeter. A fixed temperature has also been prescribed as the surface boundary condition, representing ambient air temperature. Model results were compared with experimental data and a modified analytical line-source theory. Details for the experimental setup can be found in section 2.3.1.2.

Wu et al. (2010) used the commercial computational fluid design (CFD) package FLUENT to model the thermal performance of a horizontal ground source heat system (Wu, et al., 2010). A fixed inlet fluid temperature of 1°C was used as a basis to prescribe a heat flux to the ground loop-ground boundary. Details regarding the exact numerical approach taken at the surface boundary condition are not discussed; however, the authors do state that both the ambient air temperature and wind speeds were included in the computation of the ground surface boundary. Unlike previously models, Wu et al. (2010) included multiple ground-loops within the two-dimensional domain, allowing thermal interactions between adjacent ground-loops to be accounted for. Simulation results from the model were validated with experimental data. Details for the experimental setup can be found in section 2.3.2.

2.4.5 Overview of model developments

A review of analytical, semi-numerical and numerical approaches developed to simulate ground source heat systems is provided in the following paragraphs. The developments of these models were discussed with regards to the mathematical approaches taken, representation of heat extraction (i.e. ground-loop boundary), representation of the ground surface boundary and the heat transfer within the ground. The analytical approaches reduce the ground-loop to a single infinite line or cylinder within a uniform media, along which a uniform heat flux is prescribed. The theories have been proven to give a good approximation for the temperature distribution around single vertical

ground source heat systems due to their slender profile and symmetrical geometry. The semi-numerical approaches were found to combine analytical solutions for a single ground-loop with the finite difference method. Superposition techniques are subsequently employed to simulate more complex systems compromising of multiple ground-loops. The main advantages of the analytical and semi-numerical techniques is the relatively low computational demand required, allowing the long term simulation of complex systems to be undertaken in practical timescales. The non-symmetric nature of horizontal ground source heat systems (i.e. their proximity to the ground surface) however restricts the applicability of such models.

A selective range of numerical models were presented. The majority of numerical models have been developed to simulate vertical systems. The thermal behaviour of overall systems was modelled using both two and three-dimensional domains, although many three dimensional schemes only model the ground thermal behaviour explicitly in two-dimensions. In terms of representing the circulating fluid, models took one of two approaches. Either the fluid was modelled using a one-dimensional model or a representative temperature value was assigned to the respective ground-loop boundaries. More often than not, the ground thermal behaviour was modelled using only conduction, with mass transfer being neglected.

The proximity of horizontal ground-loops to the ground surface increases the complexity of numerical models. Due to the ground-loop installation depths, the surrounding ground temperature is seasonally influenced placing a greater importance on both the initial ground temperature profile and ground surface boundary condition. Despite this, all but one of the horizontal models represented the surface boundary with a fixed or varying temperature. The proximity to the surface will also commonly position ground-loops above groundwater levels, within unsaturated soil. To the author's knowledge, there is only one example where the ground has been modelled under coupled heat and mass conditions.

It is worth noting that many models found, but not included in this selective literature review, focused of the mechanical aspects of system; either simplifying or completely neglecting any ground thermal behaviour. In general it can also be said that the majority of models found in literature focus on vertical systems. From a modelling perspective, vertical systems are more attractive due to the symmetrical geometry which can be exploited. The proximity of horizontal systems to the ground surface renders such approaches unsuitable.

2.5 Numerical investigations into the ground behaviour of horizontal ground source heat systems

Over the past three decades, a number of studies investigating the performance of horizontal ground source heat systems can be sourced in literature. Of the studies undertaken, the majority focus on the mechanical behaviour of systems (Wu, et al., 2010) although, some long-term studies investigating the optimisation of ground source heat systems with regards to ground thermal behaviour have been performed (Chong, et al., 2013). The following sections present the numerical investigations which have studied ground behaviour in response to horizontal ground source heat systems. It is understood that the performance of the systems greatly depends on the transient ground thermal behaviour (Leong, et al., 1998). This is in turn influenced by a range of factors including soil properties, moisture content and climatic conditions (Leong, et al., 1998; Florides & Kalogirou, 2007).

For the purpose of this review, numerical investigations found in literature are presented in three sections;

i. Ground properties and moisture content investigations
ii. Surface/climatic investigations
iii. Ground-loop investigations

The numerical procedures and model setups adopted within studies will be discussed along with any key findings.

2.5.1 Ground properties and moisture content investigations

Heat is transported in soil primarily by conduction (De Vries & Van Wijk, 1966), and in some cases to a certain degree by moisture migration (Leong, et al., 1998). By extracting/injecting thermal energy, ground source heat systems induce a heat flow and subsequently a moisture flow (Leong, et al., 1998). Thermal conduction is depends on the thermal properties of the soil, namely; the thermal conductivity and specific heat capacity. The thermal properties of a soil vary greatly with type, dependable on the mineral composition, texture, structure and constituents (De Vries & Van Wijk, 1966). Due to the coupled behaviour of heat and moisture, investigations relating to ground properties and moisture have been grouped together in this section.

Leong et al. (1998) investigated the performance of a horizontal ground source heat system when operating within three different soil types (sand, silty loam and silty clay) with five different

degrees of saturations (0, 12.5, 25, 50 and 100%). All simulations were carried out for a one year period using an in-house simulation package. The soil type and degree of saturation were assumed to be constant and uniform throughout the model domain during the simulation period. The prescribed surface boundary was based upon ambient air temperatures recorded in Ottawa (1987-88). The investigation found that soil moisture contents below 25%, drastically reduced the performance of systems in all three soil cases. Soil saturation levels above 25% lead to an increase in system performance, however, the effect of saturation above 50% resulted in relatively insignificant system performance improvements. Simulations predicted that sand facilitated the greatest heat conduction, allowing the greatest thermal energy to be extracted from the ground, followed by silty loam and silty clay which both exhibited similar results. As the saturation approached 100%, the simulated ground temperature distribution was approximately the same for all three soils.

Similar to Leong et al., Hailey et al. (1990) investigated the impact of varying thermal conductivity in soils adjacent to horizontal ground-loops. It was found that the soil moisture content was the dominant factor for seasonal conductivity variations and that high thermal energy injection rates (i.e. cooling mode operation) in general had a detrimental impact on soil conductivities and system performance (Hailey, et al., 1990).

A number of studies have simplified the previous approaches. Instead of considering the ground factors which influence thermal conductivity (e.g. moisture content), they have prescribed a range of thermal conductivity values. Chong et al. (2013), Congedo et al. (2012) and Wu et al. (2011) all conducted investigations whereby a range of constant soil thermal conductivities were prescribed uniformly within a model domain. All cited the importance of thermal conductivity and the impact it had on both the ground behaviour and system performance. In all three studies, the simulation with the greatest prescribed soil thermal conductivity coincided with the best performing systems. All three studies investigated additional system variables and will be described in greater detail in the following sections.

Jones Jr et al. (1996) evaluated the performance of a system using a non-conventional backfill called ‘flowable-ash’ at two experimental sites (details regarding the experimental monitoring site can be found in section 2.3.1.1). A transient two-dimensional conduction model was used to numerically investigate the impact of the fill on the system performance and ground thermal behaviour (Jones Jr, et al., 1996). The model represented the fill and surrounding soil as two uniform materials using representative thermal conductivity and capacity values. The surface was represented using empirical air temperature values for the geographical area and a fixed heat flux was prescribed to the ground-loop boundaries. Experimental and analytical results showed that the use of ‘flowable-ash’ resulted in more evenly distributed ground thermal gradients due to its greater thermal conductivity and heat storage capacity, improving the overall system performance. It was concluded that use of flowable-

fill as a backfill replacement could reduce the ground-loop length required to adequately heat and cool a domestic property by as much as 17% (Jones Jr, et al., 1996).

Mei (1986) conducted two numerical investigations within a larger parametric study regarding the effect of ground properties and ground conditions on the performance of horizontal ground source heat systems. The model used by Mei for the numerical investigations has been previously presented in section 2.4.4.1. Firstly, Mei investigated the impact on system performance when a finite region of ground, surrounding the ground-loop, was frozen. A ten hour simulation was conducted considering a system in cooling mode (i.e. rejecting heat to the ground). Mei deduced that the effect on system performance was likely to be very small provided that the fluid temperature entering the ground was no lower than -4°C. It was also noted that there would be an initial increase in the heat being absorbed by the ground due to the latent heat energy required to initially freeze soil moisture in the ground. Similar to (Jones Jr, et al., 1996), Mei also simulated the use of varying backfill material, namely; clay, sand and a fluidized mixture. It was found that the fluidized mixture, which had the greatest thermal conductivity, exchanged 47% more energy than the clay backfill and 23% more than sand over a 32 day period. Mei stressed, that the thermal contact between the ground-loop and soil is key, and that the selection of backfill material becomes of increasing importance if the system in question will be subject to high cooling loads (i.e. high ground thermal energy injection rates) (Mei, 1986).

2.5.2 Surface/climatic investigations

Seasonal ground temperature variations with depth have been studied by a range of authors, most notably Kusuda and Achenback (1965), Penrod et al. (1958) and Van Wijk and De Vries (1966). The proximity of horizontal ground-loops to the ground surface, positions them within a ground region subject to annual temperature variations, dependable on the climate, ground properties and surface conditions (Leong, et al., 1998). It can therefore be deduced, that the ground thermal behaviour is a function of both the thermal energy extracted/injected into the ground along with the climatic, ground properties and surface conditions. The following paragraphs present numerical horizontal ground source heat investigations which investigate the impact of the surface conditions.

Wu et al. (2011) presented a study which predicted the thermal performance of a horizontal system and ground temperature distributions considering three fixed ambient air temperatures (8, 5 and 1°C) and three fixed wind speeds (1, 3 and 5 ms^{-1}). The model used for numerical investigations is that previously presented within section 2.4.4.4. A two-dimensional domain, 10 meters by 10 meters was used in 600 hour simulations (25 days). Two system cycles were considered, the first of

which assumed a constant heating mode (i.e. constant thermal energy extraction) and the second considered a 24 hour periodic cycle with 8 hours of heat extraction and 16 hours of no energy exchange. The investigation reported that the ground temperatures at a horizontal distance of 1 meter from the ground-loop increased with ambient air temperature, leading to an improvement in system performance. After 600 hours, the ground temperature at a distance of 1 meter corresponding to an ambient air temperature of 8°C was 1°C and 2.2°C higher than the ground temperatures corresponding to ambient air temperatures of 5°C and 1°C respectively. When considering wind speed variations, the investigation reported no significant horizontal or vertical temperature variations in the soil. It is worth noting that details regarding how wind speed is considered within the surface boundary condition are omitted from the presented work. It was also found that an intermit cycle led to reduced system performance for all ambient air temperature and wind speed cases.

Esen et al. (2004) considered six fixed ambient air temperatures (0, 5, 10, 15, 20 and 25°C) when investigating the efficiency of a horizontal ground source heat system, 2 meters in depth operating in a cooling mode (i.e. rejecting heat to the ground) in Turkey (Esen, et al., 2007). A derived analytical model predicted that the efficiency of the system in cooling mode dropped from 56% to 46% when the ambient air temperature increased from 0°C to 25°C.

The properties of the ground surface and subsequent interactions with the atmosphere are influence by the ground surface coverage (Philippe, et al., 2010; Gonzalez, et al., 2012). Numerical investigations into both the performance and ground thermal behaviour of systems have been undertaken in a range of ground conditions, for example arid ground in Asia (Esen, et al., 2007), North America (Mei, 1986) and the UK (Wu, et al., 2011). However, to the knowledge of the author no numerical investigations have presented which study the effect of varying surface coverage/material types.

2.5.3 Ground-loop investigations

Besides the selection of mechanical components, the ground-loop length is the primary focus of ground source heat system design. Despite this, few investigations have considered the long-term influence of ground-loop characteristics on ground behaviour or with regard to system optimisation (Wu, et al., 2010; Chong, et al., 2013). To date, the design of ground-loops is non-standardised, leading to range of ground-loop configurations, installation depths, pipe diameters and materials being used. The following paragraphs present published numerical investigations which investigate one or a number of the ground-loop variables previously highlighted.

With regards to the ground-loop, Mei (1986) undertook two investigations as part of a larger parametric study. The model used in both investigations has been previously discussed in section 2.4.4.1. The first of these investigated the system performance when using two different pipe materials; namely polyethylene and copper. The performance of a single pipe was considered, buried at a depth of 2 meters. The polyethylene pipe was assumed to have an internal and external diameter of 35 and 42.2 mm respectively, whereas the copper pipe was assumed to be thin-walled with negligible thermal resistance. The parametric study reported that the use of copper tubing increased thermal energy extraction by 7.7% over a 15 day period when compared with the polyethylene tubing.

The second investigation undertook by Mei (1986) considered the use of so called 'layered' ground-loops, whereby more than one ground-loop is installed in a single trench. Two polybutylene pipes (internal and external diameters of 40.9 and 48.3 mm) were considered, buried vertically in line and at depths of 1.22 and 1.83 meters respectively. Three 28 day heat extraction simulations were performed; one considering both pipes while the remaining two simulated the performance of the individual pipes in isolations in order to allow comparisons to be drawn. The simulations predicted that individual pipe performance (i.e. the thermal energy extracted per unit length of pipe) decreased in the layered pipe arrangement. However, Mei (1986) also noted that the total energy extracted per unit length of soil increased by approximately 55% for the layered pipe arrangement.

Wu et al. (2010) investigated the system performance and ground thermal behaviour for parallel and an array of slinky pipe configurations. The study primarily focussed on investigating slinky pipe variations by examining a range of slinky diameters and spacings (see Figure 2.1 for reference). The numerical investigations were performed using the model previously discussed in section 2.4.4.4 considering a ground-loop at a depth of 1.2 meters and simulation duration of 140 hours. The investigation predicted that the parallel pipe arrangement extracted the greatest thermal energy per pipe length. For the set conditions, the parallel pipe extracted 3.5 Wm^{-1} more than the slinky pipe arrangement. The simulations also predicted that the slinky pipe arrangement would extract 12 Wm^{-1} more than the parallel arrangement per meter length of soil. The results presented by Wu et al. (2010) however, had not reached thermal equilibrium within the 140 hour simulation period therefore the reported values should be treated with caution.

Chong et al. (2013) conducted further investigations into the ground performance of five slinky pipe configurations within three different soils, namely; loamy sand, light dry soil and wet sand. Using the same numerical model as Wu et al. (2010), Chong et al. conducted a series of 60 day simulations investigating the ground behaviour under constant and intermittent heating cycles (i.e. thermal energy extraction). The ground-loop was modelled at a depth of 1.2 meters and the ground-loop temperature was assumed to be fixed. The ground surface boundary was simplified to a constant fixed temperature. The investigation findings reported that reducing the slinky loops spacings and

loop diameter (see Figure 2.1) would improve the performance of the ground source heat system in all three soil types and that intermittent system operation leads to higher ground heat transfer rates than continuous operation.

Similar to the investigations of Wu et al. (2010) and Chong et al. (2013), Congedo et al. (2012) investigated the performance of three ground-loop pipe configurations; parallel, vertical slinky and helical (see Figure 2.1 for reference). In addition to pipe configurations, the investigation also considered a range of pipe installation depths (1.5, 2.0 and 2.5 meters) and fluid flow flows (0.25, 0.5 and 1.0 kg s^{-1}) and the effect, if any, on ground heat transfer. All simulations were carried out using a 2 x 1.5 x 2 meter three-dimensional domain (length by width by depth) and for a simulation period of one year. The surface boundary was assumed to be a function of air-temperature only and assigned a periodic temperature based upon historical meteorological records for the area. The investigation findings reported that the helical ground-loop pipe configuration was the most efficient of the three configurations for heat transfer although the influence of ground thermal conductivity had a far greater impact of system performance than any loop configurations. The results indicated that the fluid velocity had relatively no impact on the system performance in a parallel system but that fluid velocities of 1ms^{-1} did lead to a slight increase in performance within helical and slinky systems. For the set conditions, it was reported that the ground-loop depths investigated had no observable impact on the system performance or ground behaviour.

2.5.4 Overview of numerical studies

A review of numerical investigations into the behaviour of horizontal ground source heat systems has been provided. The investigations presented span the last three decades and investigate a range of system variables. It can be said that the ground thermal behaviour is a function of the thermal energy injected/rejected along with the soil properties, moisture content and surface conditions of the system. Although the presented investigations have all simulated the ground thermal behaviour, the focus has been mainly on system performance and COP. Very few studies discuss or present simulated results explicitly with respect to the ground thermal behaviour changes.

The importance of the ground characteristics on the success of ground source heat systems has been recognised by the majority of investigations and some research efforts have been made to investigate the impact of soil properties and moisture content on ground thermal behaviour. The influence of soil moisture on thermal conductivity has been investigated however; the numerical models used only simulated heat transfer, neglecting any moisture transfer. Of the studies

investigating ground properties, all found that greater ground thermal conductivity resulted in better performing systems.

Most of the investigations presented considered the ground surface boundary to some extent; however the majority represented it as a fixed temperature based upon annual ambient air temperature variations. There are far fewer examples of investigations which consider the boundary as a function of inward and outward radiation components. Even though most investigations did represent the surface boundary in some shape or form, very few made it the subject of numerical investigations varying the factors such as the ambient air-temperature, radiation or surface coverage.

A range of studies have investigated the impact of various pipe configurations, with the majority focussing on so called slinky pipe configurations. In general, the investigations reported that a parallel pipe arrangement results in a greater energy exchange per unit length of pipe whereas the slinky arrangement results in a greater energy exchange per unit length of trench.

It is understood that the annual and diurnal variation of the surface boundary conditions leads to a cyclic ground temperature variation in the vicinity of horizontal ground source heat systems. Despite this annual cycle, none of the investigations presented simulated ground thermal behaviour beyond a period of one year, and most simulated ground thermal behaviour for less than one month. The results presented are therefore subject to the loading conditions and climate during the simulation period and do not allow an annual cyclic operation to be inspected. This is an oversight, when considering ground source heat systems are designed to have operational lifetimes beyond 20 years (MCS, 2008).

2.6 Conclusions

In this chapter a literature review on ground source heat under the current scope of research as defined in Chapter 1 has been presented. The review was broadly split into four sections investigating; an overview ground source heat systems, field-scale monitoring sites, model developments and numerical investigations undertaken.

Overall it can be said that the majority of work within the sector focusses on the mechanical aspects of systems, with much of the focus centring on the so called ‘coefficient of performance’. Field-scale monitoring site have been installed globally over the past few decades, although a very limited number of them have monitored ground behaviour. Data regarding climatic variables which are known to influence annual and diurnal ground temperature regimes are also often overlooked.

The majority of analytical and numerical models have been designed with vertical ground source heat systems in mind. From a modelling perspective, vertical systems are more attractive due to the cross-sectional symmetry within the domain, a feature not shared by horizontal systems due to the proximity of the ground surface. The proximity of horizontal ground-loops to the ground surface places an increased emphasis on the initial ground temperature profile and ground surface boundary condition.

A number of horizontal ground source heat models have been developed, although most simplify the ground surface boundary and do not consider mass movements of water within the soil. The published work included within the scope of this literature review generally concurred that the simulation of ground source heat systems is computationally expensive. Despite this, little work has been done to investigate the potential of computational optimisation and the techniques available to reduce computational times.

Finally, a series of numerical investigations into the ground behaviour surrounding ground source heat systems has been presented. Parametric studies were divided into three sections, namely; ground properties and moisture content investigations, surface/climatic investigations and ground-loop investigations. In general, the investigations related the ground behaviour to system performance and not explicit ground temperatures. Ground properties and the influence of moisture content have been previously looked at although the movement of water was not included in models. In general, greater thermal conductivities resulted in better performing systems, as expected. A limited number of surface boundary investigations are presented, all of which simplify the ground surface boundary to a function of temperature only. Investigations regarding the configuration of ground-loops have predominantly focussed on slinky pipe arrangements. In general it was found slinky pipe arrangements result in a greater heat extraction per unit length of soil whereas parallel pipe arrangements result in a greater heat extraction per unit pipe length.

Some of the knowledge gaps identified in the field ground source field through this state of the art review will be addressed within this thesis. The exact research objectives for this thesis have been previously outlined in Chapter 1.

References

Al-Khoury, R., Bonnier & G, P., 2006. Efficient finite element formulation for geothermal heating systems Part II: Transient. *Journal for Numerical Methods in Engineering,* 67(1), pp. 725-745.

Al-Khoury, R., Bonnier, R. & Brinkgreve, R. B., 2005. Efficient finite element formulation for geothermal heating systems Part I: Steady state. *International Journal for Numerical Methods in Engineering,* 63(1), pp. 988-1013.

Benli, H., 2013. A performance comparison between a horizontal source and a vertical source heat pump systems for a greenhouse heating in the mild climate, Elazig, Turkey. *Applied Thermal Engineering,* 50(1), pp. 197-206.

Carslaw, H. S. & Jaeger, J. C., 1947. *Conduction of Heat in Solids.* Oxford, UK: Claremore Press.

Chong, C. S. A. et al., 2013. Simulation of thermal performance of horizontal slinky-loop heat exchangers for ground source heat pumps. *Applied Energy,* 104(1), pp. 603-610.

Coogan Jr, C. H., 1949. Heat transfer rate. *Mechanical Engineering,* 71(1), p. 495.

Coskun, S., Pulat, E., Unlu, K. & Yamankaradeniz, R., 2008. Experimental performance investigation of a horizontal ground source compression refrigeration machine. *International Journal of Energy Research,* 32(1), pp. 44-56.

Craciun, A. V., Sandu, F. & Pana, G., 2010. *Monitoring of a ground source heat pump with horizontal collectors.* Brasov, 12th International Conference of Optimization of Electrical and Electronic Equipment.

Crawley, D. B. et al., 2001. EnergyPlus: Creating a new-generation building energy simulation program. *Energy and Buildings,* 33(1), pp. 319-331.

De Carli, M., Tonon, M., Zarrela, A. & Zecchin, R., 2010. A computational capacity resistance model (CaRM) for vertical ground-coupled heat exchangers. *Renewable Energy,* 35(1), pp. 1537-1550.

De Vries, D. A. & Van Wijk, W. R., 1966. Periodic temperature variations in a homogeneous soil. In: W. R. Van Wijk, ed. *Physics of the Plant Environment.* Amsterdam: North-Holland Publishing Company, p. 103.

Demir, H., Koyun, A. & Temir, G., 2009. Heat transfer of horizontal parallel pipe ground heat exchanger and experimental verification. *Applied Thermal Engineering,* 29(1), pp. 224-233.

Diersch, H.-J.G. et al., 2011. Finite element modelling of borehole heat exchanger systems Part 1. Fundamentals. *Computers & Geosciences,* 37(1), pp. 1122-1135.

Diersch, H.-J.G. et al., 2011. Finite element modelling of borehole heat exchanger systems Part 2. Numerical simulation. *Computers & Geosciences,* 37(1), pp. 1136-1147.

Doherty, P. S., Al-Huthaili, S., Riffat, S. B. & Abodahab, N., 2004. Ground source heat pump - description and preliminary results of the eco-house system. *Applied Thermal Engineering,* 24(1), pp. 2627-2641.

Energy Saving Trust, 2012. *Detailed analysis from the first phase of the Energy Saving Trust's heat pump field trial,* London: Department of Energy and Climate Change (DECC).

Esen, H., I. M. & Esen, M., 2007. Numerical and experimental analysis of a horizontal ground-coupled heat pump system. *Building and Environment,* 42(1), pp. 1126-1134.

Esen, H., Inalli, M., Esen, M. & Pihtili, K., 2007. Energy and exergy analysis of a ground-coupled heat pump system with two horizontal ground heat exchangers. *Building and Environment,* 42(1), pp. 3606-3615.

Eskilson, P., 1987. *Thermal analysis of heat extraction borehole.* Lund: PhD Thesis: University of Lund, Sweden.

Fisher, D. E., Padhmanabhan, S. K., Rees, S. J. & Murugapan, A., 2006. Implementation and validation of ground source heat pump system model in an integrated building and system simulation environment. *HVAC&R Research,* 12(3a), pp. 693-710.

Florides, G. & Kalogirou, S., 2007. Ground heat exchangers - a review of systems, models and applications. *Renewable Energy,* 32(1), pp. 2461-2478.

Fujii, H., Nishi, K., Komaniwa, Y. & Chou, N., 2012. Numerical modelling of slinky-coil horizontal ground heat exchangers. *Geothermics,* 41(1), pp. 55-62.

Gonzalez, R. G. et al., 2012. Interactions between the physical soil environment and a horizontal ground coupled heat pump, for a domestic site in the UK. *Renewable Energy,* 44(1), pp. 141-153.

Hailey, S. M., Kast, T. P. & Drown, D. C., 1990. *Thermal conductivity and soil conditions heat transfer effects on ground source heat pumps.* Halifax, Nova Scotia, Proceedings of the 16th Annual Conference of Solar Energy Socienty of Canada.

Hart, D. P. & Couvillion, R., 1986. Earth coupled heat transfer. *Publication of the national water well association.*

Hellstrom, G., 1991. *Ground heat storage: Thermal analysis of duct storage systems.* Lund: PhD Thesis: University of Lund, Sweden.

Helpin, V., Kummert, M. & Cauret, O., 2011. *Experimental and simulation study of hybrid ground-source heat pump systems with unglazed solar collectors for French office buildings.* Sydney, Australia, 12th Conference of International Building Performance Simulation Association.

He, M., 2012. *Numerical modelling of geothermal borehole heat exchanger systems.* Leicester: PhD Thesis: De Montfort University, UK.

He, M., Rees, S. & Shao, L., 2009. *Simulation of a domestic ground source heat pump system using a transient numerical borehole heat exchanger model.* Glasgow, Scotland, Building Simulation 2009.

Hooper, F. C., 1952. An experimental residential heat pump. *Canadian Journal of Technology,* 30(1), pp. 180-197.

IGSHPA (Bose, J.E., Editor), 1991. *Design and Installation Standards,* Oklahoma, USA: International Ground Source Heat Pump Association.

Inalli, M. & Esen, H., 2004. Experimental thermal performance evaluation of a horizontal ground-source heat pump system. *Applied Thermal Engineering,* 24(1), pp. 2219-2232.

Ingersoll, L. R., Zobel, O. J. & Ingersoll, A. C., 1954. *Heat conduction with engineering, geological and other applications.* New York: McGraw Hill.

Jones Jr, W. V., Beard, J. T., Ribando, R. J. & Wilhelm, B. K., 1996. *Thermal performance of horizontal closed-loop ground-coupled heat pump systems using flowable-fill,* Virginia, USA: University of Virginia.

Kavanaugh, S. P., 1985. *Simulation and experimental verification of vertical ground-coupled heat pump systems.* Oklahoma: PhD Thesis: Oklahoma State University, USA.

Kelvin, S. W. T., 1884. *Mathematical and Physical Papers, Vol. II.* London: Cambridge University Press.

Koyun, A., Demir, H. & Torun, Z., 2009. Experimental study of heat transfer of buried finned pipe for ground source heat pump applications. *International Communications in Heat and Mass Transfer,* 36(1), pp. 739-743.

Kusuda, T. & Achenbach, P. R., 1965. Earth temperature and thermal diffusivity at selected stations in the United States. *ASHRAE Trans,* 71(1), pp. 61-75.

Lee, C. K. & Lam, H. N., 2008. Computer simulation of borehole ground heat exchangers for geothermal heat pump systems. *Renewable Energy,* 33(1), pp. 1286-1296.

Leong, W. H., Tarnawski, V. R. & Aittomaki, A., 1998. Effect of soil type and moisture content on ground heat pump performance. *International Journal of Refrigeration,* 21(8), pp. 595-606.

Li, Z. & Zheng, M., 2009. Development of a numerical model for the simulation of vertical U-tube ground heat exchangers. *Applied Thermal Energy,* 29(1), pp. 920-924.

Mei, V. C., 1986. *Horizontal ground-coil heat exchanger theoretical and experimental analysis,* New York: Office of Buildings and Community Systems, U.S. Department of Energy.

Metz, P. D., 1983. *Ground-coupled heat-pump-system experimental results.* Washington D.C., ASHRAE.

Microgeneration Certification Scheme (MCS), 2008. *Microgeneration Installation Standard: MIS 3005 Issue 3.0.* London: Department of Energy and Climate Change (DECC).

Naili, N., Attar, I., Hazami, M. & Farhat, A., 2012. Experimental analysis of horizontal ground heat exchanger for northern Tunisia. *Journal of Electronics Cooling and Thermal Control,* 2(1), pp. 44-51.

Ozgener, O. & Hepbasli, A., 2007. Modelling and performance evaluation of ground source (geothermal) heat pump systems. *Energy and Buildings,* 39(1), pp. 66-75.

Paul, N. D., 1996. *The effect of grout thermal conductivity on vertical geothermal heat exchanger design and performance.* Brookings: Master of Science Thesis, South Dakota State University, USA.

Penrod, E. G., Walton, W. W. & Terrell, D. V., 1958. A method to describe soil temperature variation. *Journal of the Soil Mechanics, Proceedings of ASCE,* 1(1), pp. 1-21.

Philippe, M., Marchio, D., L. H. & Vrain, A., 2010. *An evaluation of ground thermal properties measurement accuracy by thermal response test of horizontal ground heat exchangers.* Bali, Indonesia, World Geothermal Congress.

Piechowski, M., 1999. Heat and mass transfer model of a ground heat exchanger: Theoretical development. *International Journal of Energy Research,* 23(1), pp. 571-588.

Pulat, E., Coskun, S., Unlu, K. & Yamankaradeniz, N., 2009. Experimental study of a horizontal ground source heat pump performance for mild climate in Turkey. *Energy,* 34(1), pp. 1284-1295.

Rawlings, R., 1999. Ground source heat pump: a technology review. *Building Services Engineering Research and Technology,* 20(3), pp. 119-129.

Ruan, W. & Horton, W. T., 2011. Long-term model-based performance of ground source heat exchanger. *HVAC&R Research,* 17(3), pp. 284-296.

Sanner, B., Karytsas, C., Mendrinos, D. & Rybach, L., 2003. Current statue of ground source heat pumps and underground thermal energy storage in Europe. *Geothermics,* 32(1), pp. 579-588.

Singh, H., Muetzeb, A. & Eamer, P. C., 2010. Factors influencing the uptake of heat pump technology by the UK domestic sector. *Renewable Energy,* 35(1), pp. 873-878.

Spitler, J. D., 2000. *GLHEPRO - A design tool for commercial building ground loop heat exchanger.* Aylmer, Quebec, Fourth International Heat Pumps in Cold Climates Conference.

Sutton, M. G., Couvillion, R. J., Nutter, D. W. & Davis, R. K., 2002. An algorithm for approximating the performace of vertical bore heat exchangers installed in a stratified geological regime. *ASHRAE Trans,* 108(2).

Thornton, J. W. et al., 1997. Residential vertical geothermal heat pump system models: calibration to data. *ASHRAE Trans,* 103(2), pp. 660-674.

U.S Department of Energy, 2008. *Geothermal Basics.* [Online]
Available at: http://www1.eere.energy.gov/geothermal/geothermal_basics.html
[Accessed 14 March 2011].

Van Wijk, W. A. & De Vries, D. A., 1966. Periodic Temperature Variations in a Homogeneous Soil. In: W. R. Van Wijk, ed. *Physics of the Plant Environment.* Amsterdam: North-Holland Publishing Company, p. 102.

Vestal Jr, D. M. & Fluker, B. J., 1957. Earth as a heat source and sink for heat pump. *ASHVE Trans,* 63(1), p. 41.

Wen, C. Y. & Fan, L. T., 1975. *Models for Flow Systems and Chemical Reactors.* 3rd ed. New York: Marcel Dekker Inc.

Wu, Y. et al., 2011. Prediction of the thermal performance of horizontal-coupled ground-source heat exchangers. *International Journal of Low-Carbon Technologies,* 6(1), pp. 261-269.

Wu, Y. et al., 2010. Experimental measurement and numerical simulation of horizontal-coupled slinky ground source heat exchangers. *Applied Thermal Engineering,* 30(1), pp. 2574-2583.

Yang, H., Cui, P. & Fang, Z., 2010. Vertical-borehole ground-coupled heat pumps: A review of models and systems. *Applied Energy,* 87(1), pp. 16-27.

Yavuzturk, C., 1999. *Modelling of vertical ground loop heat exchangers for ground source heat pumps.* Oklahoma: PhD Thesis: Oklahoma State Universuty, USA.

Young, T. R., 2004. *Development, verification, and design analysis of the borehole fluid thermal mass model for approximating short term borehole thermal responses.* Oklahoma: Master of Science Thesis: Oklahom State University, USA.

Chapter 3

Monitoring site design and site investigation

3.1 Introduction

The experimental design, installation and site investigation of a field-scale study carried out in this research are presented in this chapter. As described previously, the aim of the field-scale monitoring site is to analyse the ground thermal behaviour in response to heat extraction from a horizontal ground source heat system. The instrumentation of the monitoring site has been selected to facilitate the long-term data collection (minimum of 3 years) of the ground thermal response to a full-scale ground source heat system. The heat system was installed for an occupied domestic property, providing the dominant source for space heating. The ground temperatures, climatic and heat pump variables capable of influencing the ground thermal behaviour have been monitored. The study aims

to providing a comprehensive data-set which can be used for a detailed analysis of the ground thermal response, providing a more complete and detailed resolution data-set than existing sites.

The following sections will outline the procedures and methodologies implemented for the site selection and design of the field-scale monitoring study. A discussion of the technical problems encountered during installation is also provided. Following this, details regarding the site investigation and soil characterisation will be presented, including the methodologies and laboratory results.

3.2 Experimental design

As previously discussed in Chapter 2, there is a limited number of horizontal ground source heat monitoring schemes measuring ground thermal behaviour, especially at a field-scale. The scarcity of active sites results in very few examples or guidelines to follow when designing a suitable instrumentation set-up, capable of delivering a suitable resolution of data. The following sections present the systematic approach adopted during the design of the monitoring scheme.

3.2.1 Site selection and system design

A set of criteria was outlined in order to facilitate a successful site selection, provided as follows:

- *Accessibility* – the site should be accessible throughout the year.
- *Usage* – the ground source heat system should be connected to and used by a domestic property, occupied throughout the year.
- *Land availability* – a sufficient area of accessible land is required to install the horizontal ground-loops. The exact size is determined by the system load and ground characteristics.
- *Land use* – the use of the land should not limit the accessibility, adversely influence the thermal data or damage the installed sensors (e.g. heavy farming).
- *Solar obstruction* – the site should on the whole be un-obstructed from the Sun (i.e. recharge processes).
- *Communication* – if remote sensing is being employed, a mobile signal will be required (typically GSM level or better for data communication).

A suitable site fulfilling the above criteria was identified at Lower Pentre Farm located in Ffynnon Gynydd, Powys, Wales. A map showing the location can be found in Figure 3.1. A horizontal ground source heat system had been planned to be installed as the dominant space heating system for a large newly built farm house at the site. The design and installation of the ground source heat system, including the ground-loop arrangement was performed by the projects industrial partners WDS Environmental.

The ground source heat system compromises five horizontal ground-loops with a total pipe length of 750 meters. These five loops were evenly spread across a 40 meter wide by 80 meter long area within an adjacent south facing field. The five individual loops were connected via a manifold chamber. The loops were installed at an approximate depth of 1.8 meters, employing a parallel pipe arrangement (see Chapter 1 for further details regarding this configuration). A polyethylene pipe with an external diameter of 40 mm was used for all ground-loops. The mechanical components of the system compromise of a 16 kW Dimplex heat pump, which was installed within a plant room in the main building. The field containing the ground-loops was covered with short grass and used for animal grazing before the installation. Post installation, the field returned to the same condition and use. Figure 3.2 shows a schematic of the site, including the overall layout and arrangement of the horizontal ground-loops.

A trial trench was dug prior to the installation of the ground-loops in order to investigate the general ground conditions at the site and to retrieve preliminary soil samples. The trial trench was excavated in March 2011. The ground was found to compromise of reddish-brown gravelly-silt based on laboratory analysis performed on retrieved samples. The trench depth was approximately 3.1 metres beneath the ground surface. At this depth, no sign of a water table was observed. Information obtained from the trial trench was subsequently used for specifying the monitoring equipment, designing the sensor layout and outlining sampling procedures.

Figure 3.1 – Location of the monitoring site.

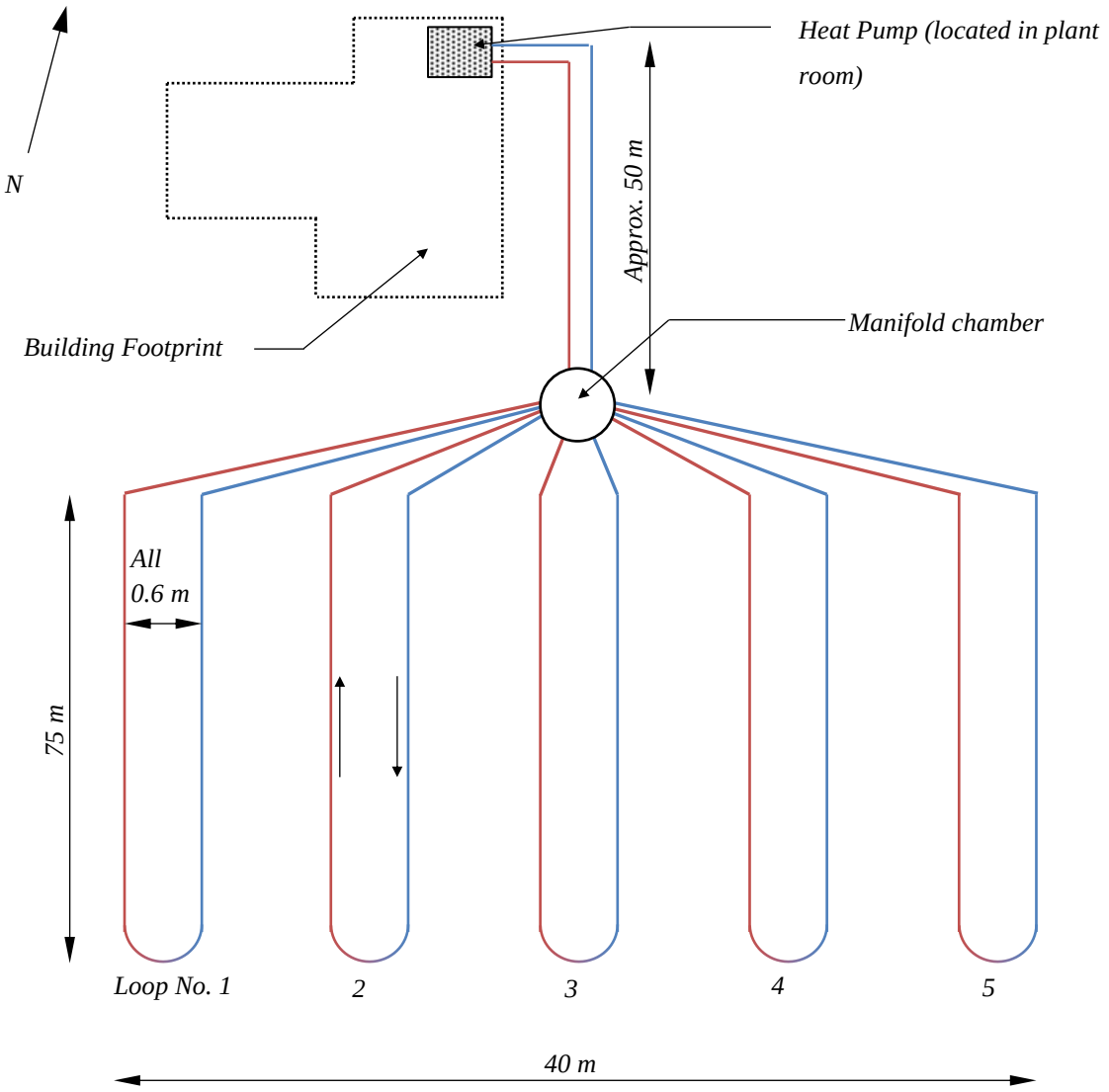

Figure 3.2 –Schematic of the horizontal ground source heat system installed at the monitoring site (plan view).

3.2.2 Ground temperature monitoring

The ground temperature sensors will be, for all intents and purposes, inaccessible for routine maintenance or reposition after the in-situ installation. The success of long-term monitoring is therefore greatly dependant on the sensor's ability to continually operate under the anticipated conditions which they may be subject to. Similar to the site selection, a set of criteria was outlined in order to help identify the most suited ground temperature sensor type; provided as follows:

- *Robustness* – the selected sensor should be capable of withstanding the in-situ ground conditions (for example the overburdening pressure, groundwater flow etc.).

- *Durability and Longevity* – the sensors are required to measure and transfer ground data for the lifetime of the project (a minimum of three years).
- *Operating range* – the sensors are required to operate and transfer ground data continually therefore it is necessary that they correctly function within the anticipated temperature range.
- *Resistance* – the sensors will be subject to moisture and potentially chemicals in the soil.
- *Precision and accuracy* – the precision and accuracy of the sensors should be sufficient enough to measure the temperature changes throughout the lifetime of the investigation.

By considering the above criteria, an RST Instruments Thermistor String was selected for use (RST Instruments, 2013). The technical operating specifications can be found in Appendix A.

The acquisition of an acceptable resolution of ground data is greatly dependent on the spatial positioning of the ground temperature sensors. It is recognised that installing excessive numbers of temperature sensors throughout the site would conflict with financial constraints therefore an appropriate spatial sensor arrangement is required. The adopted sensor arrangement reduced the number of required sensors by measuring the ground response around only one of the possible five horizontal loops shown in Figure 3.2. The horizontal ground-loop labelled 'No.1' in Figure 3.2 was selected for detailed monitoring. This loop was selected primarily because it is located on the edge of the horizontal loop plan footprint. This allowed temperature sensors measuring the undisturbed ground temperature (i.e. unaffected by the ground source heat system) to be included within a sensor layout without incurring excessive additional wiring costs.

Thermistors strings measuring the ground temperature were installed at eight cross-sections (see Figure 3.3). The cross-sections were evenly spaced at 10 meter intervals along the length of ground-loop. Two types of configurations were adopted when arranging thermistors at the cross-sections. The two arrangements are: i) the so called 'detailed' cross-section utilised at cross-sections AA and BB in Figure 3.3 and ii) the so called 'intermediate' cross-section utilised at cross-sections A, B, C, D, E and F in Figure 3.3. Figure 3.4 shows the sensor layout employed at each 'intermediate' cross-section and Figure 3.5 shows a photograph of an 'intermediate' cross-section taken during the installation process.

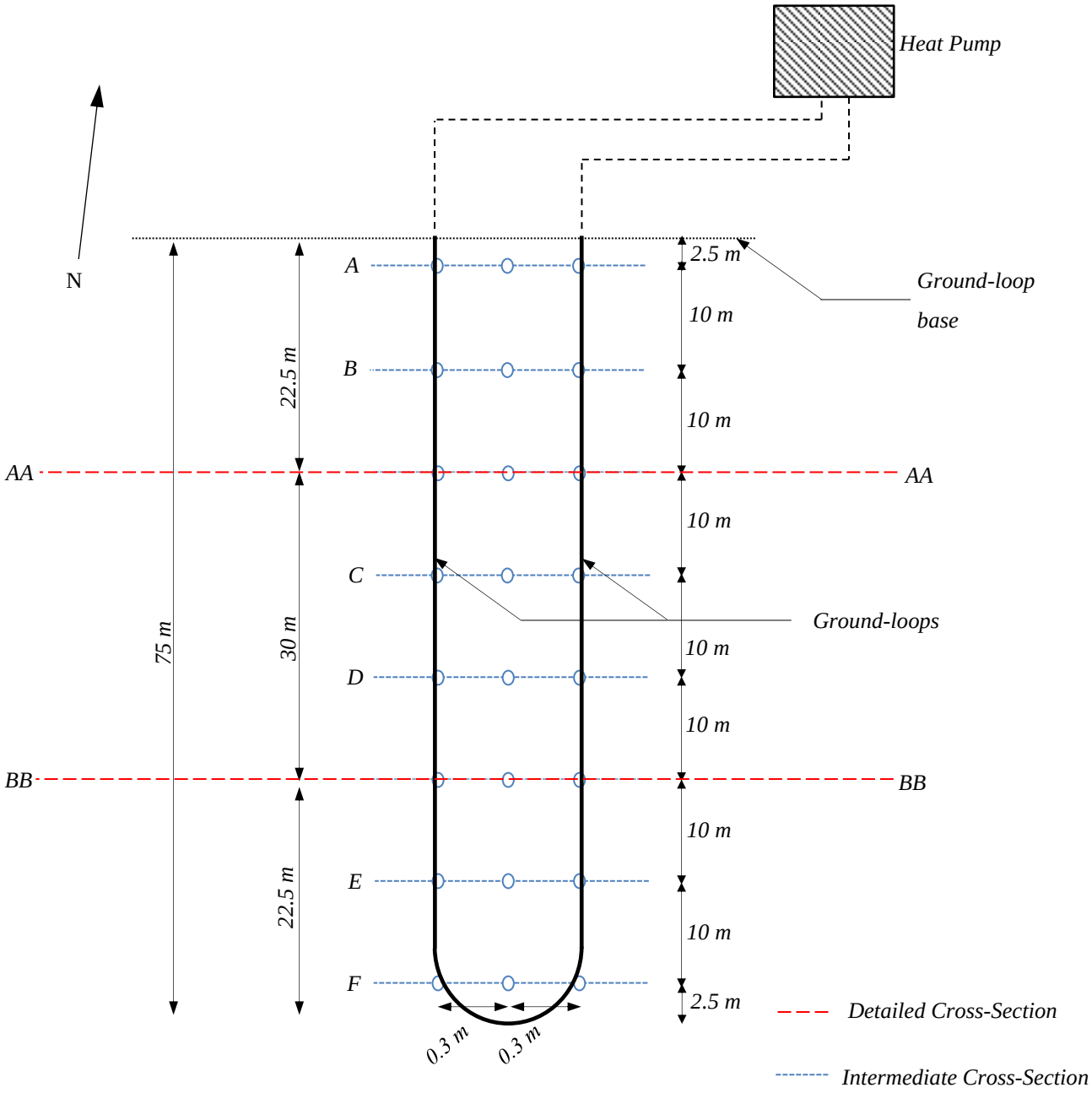

Notes

1. Not to scale
2. The above plan shows the eight thermistor cross-sections used to monitor the ground thermal behaviour of ground-loop No. 1

Figure 3.3 – Plan view of the thermistor layout showing the position of the 'intermediate' and 'detailed' cross-sections.

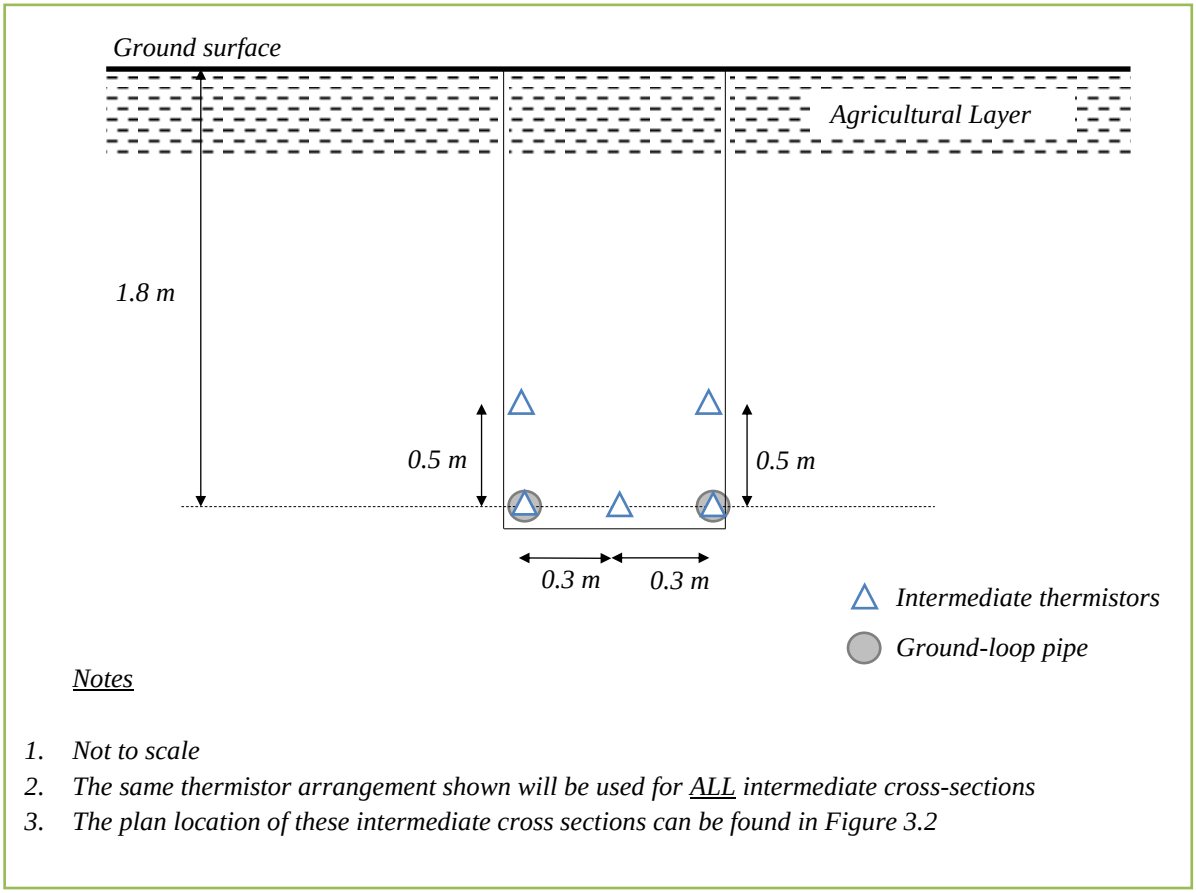

Notes

1. *Not to scale*
2. *The same thermistor arrangement shown will be used for ALL intermediate cross-sections*
3. *The plan location of these intermediate cross sections can be found in Figure 3.2*

Figure 3.4 – Thermistor layout employed at the intermediate cross-sections.

Figure 3.5– A photograph of an 'intermediate' cross-section at the monitoring site taken during installation.

Two ‘detailed’ cross-sections (denoted AA and BB in Figure 3.3) were located at 22.5 and 52.5 metres from the starting point of the ground-loop respectively. The location of the ‘detailed’ cross-sections was selected such that one provides data for the ground behaviour towards the top of the system, whereas the second provides information regarding the ground response towards the bottom. Such arrangements allow any difference in the ground thermal behaviour between the top and bottom of the system to be observed.

Similar to the ‘intermediate’ sections, a common template for the thermistor layout has been applied to both detailed cross-sections (see Figure 3.7). Each ‘detailed’ cross-section layout contained in total 41 thermistors, considerably greater than the 5 which make up each intermediate cross-section. The spatial arrangement of the 41 thermistors employed within the ‘detailed’ cross-sections is presented in Figure 3.7. The arrangement allows for a more detailed examination of the ground thermal behaviour in response to heat extraction. The ‘detailed’ cross-sections each contained four so called ‘far-field’ thermistors used to measure the undisturbed ground temperature beyond the thermal influence of the ground-loop (see Figure 3.7). The term ‘far-field’ is commonly used in the research area to describe undisturbed ground temperatures (i.e. unaffected by the ground-loop heat exchanges) and has therefore been adopted here. A photograph showing part of the ‘detailed’ cross-section BB during the site installation is presented in Figure 3.6.

Figure 3.6– Photograph showing part of the installed detailed cross-section BB.

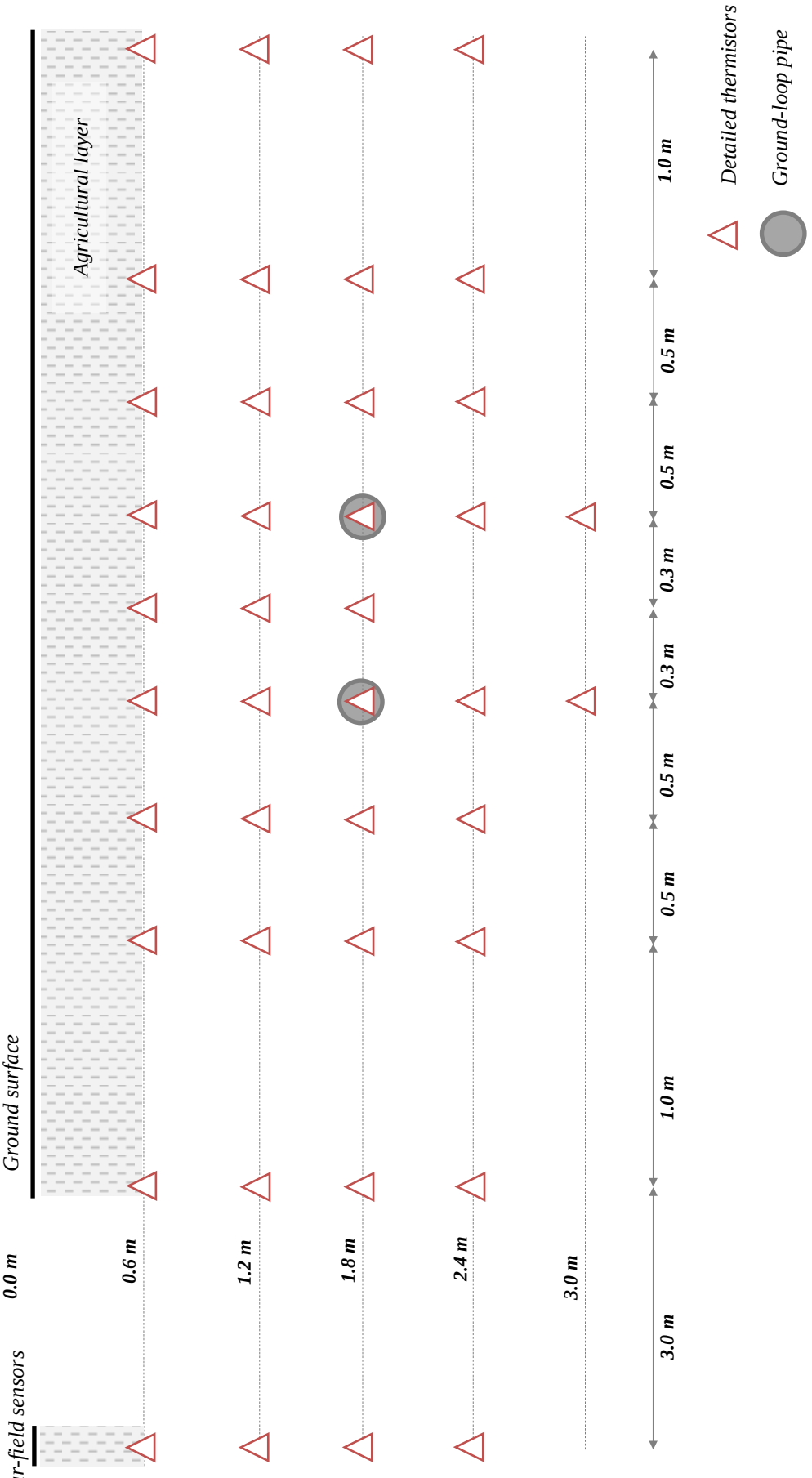

Figure 3.7 – Thermistor layout employed at the 'detailed' cross-sections.

The ground thermistors were installed in the winter of 2011/2012. Of the 112 thermistors installed into the ground, 7 were found to be faulty immediately after the installation. Due to the number of thermistors being installed and nature of the system, it was always anticipated that a certain number would fail. Efforts were made to identify and limit the number of faulty thermistors both before and during the installation process. The integrity of the thermistors was tested by the suppliers in order to identify any manufacturing faults prior to delivery. Due to the complexity and scale of the installation, it was not possible to re-test the thermistors on-site prior to the system installation. After the installation, conscious efforts were made to remove large rocks from the backfill as part of attempts to reduce the chances of thermistors being damaged. As previously discussed, the buried nature of system renders it practically unfeasible to access and repair any faulty thermistors therefore the failed devices have been left in-situ. Despite these failures, it can be said that over 93% of the installed thermistors worked as anticipated which has been viewed as an overall success.

The ground thermistor layout was based on data resolution requirements and to some extent the findings from the trail trench dug prior to the design process. As previously discussed, the trench was dug to ascertain the ground conditions on site, however, the full extent of in-situ cobbles and gravel found on site had not been revealed during this trial. The ground conditions resulted in problems when trying to install the 3 meters deep thermistors as the trenches could not be dug deep enough by the plant on site. The thermistors were therefore installed as deep as practically possible. The final position of the thermistors was recorded as part of a topographical study which will be discussed further in section 3.3.2.

3.2.3 Climatic monitoring

The ground surface is exposed to atmospheric conditions and solar radiation which play an important role within the surface energy balance (Deardorff, 1978). In order to fully investigate the ground thermal behaviour, climatic variables capable of influencing the surface energy balance need to be considered within the monitoring scheme. The climatic variables capable of influencing the surface energy balance are as follows (Deardorff, 1978; van Wijk, 1966):

- *Solar (or short-wave) radiation.*
- *Ambient air temperature.*
- *Relative humidity.*
- *Precipitation.*
- *Wind speed.*

The following subsections present the climatic sensors selected to measure the previously listed climatic variables. The sensors selection will be individually discussed and justified accordingly. The selected sensors were collectively installed as part of a weather station, the location of which can be found in Figure 3.8. A set of criteria was outlined prior to sensor selection in order to help identify the most suited monitoring equipment. These were as follows:

- *Robustness* – the equipment must be capable of withstanding the anticipated weather conditions which will be encountered at site (e.g. prolonged rain and wind).
- *Durability* – the equipment is required to record data over an extended period of time (minimum of 3 years) and be relatively maintenance free.
- *Operating range* - the sensors are required to function and record data over the anticipated data ranges that they will be monitoring.
- *Appearance* – the monitoring equipment will be above ground and located on private property therefore where possible unobtrusive devises should be selected.
- *Data logging* – the recorded data will be remotely logged therefore it must be compatible with the selected data logging equipment.
- *Precision and accuracy* – the equipment should be capable of measuring data sets to the required accuracy and precision over the duration of the monitoring scheme.

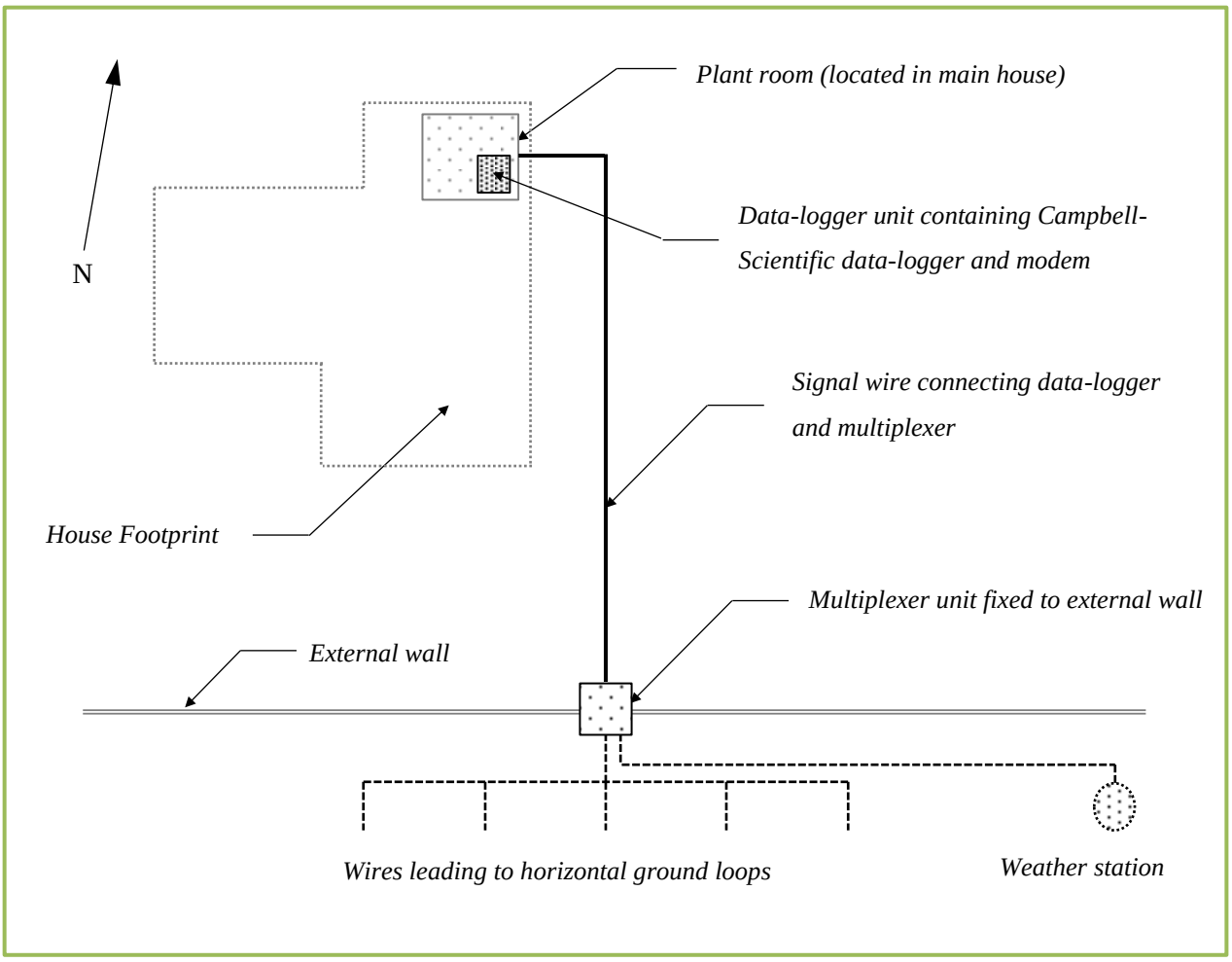

Figure 3.8 – Diagram showing the position of the data-logger and multiplexer within the monitoring site.

3.2.3.1 Solar radiation

The solar radiation sensor will be required to continually measure the short-wave radiation being received at the site within the anticipated radiation range. A silicon-cell pyranometer SP-110 (see Figure 3.9) was selected to perform this function. The selected sensor specifications state that it has an absolute accuracy to ±5% and sensitivity of 5 Wm^{-2} (Apogee Instruments, n.d.). This accuracy range has been found to satisfy the data resolution requirements of the short-wave radiation monitoring. The full specifications for the sensor can be found in Appendix A. The measured solar radiation is used in the computation of the surface boundary condition presented in Chapter 6, representing short-wave radiation striking the earth's surface.

Figure 3.9 – Photograph of the installed silicon-cell pyranometer used to measure the short-wave radiation.

3.2.3.2 Ambient air temperature and relative humidity sensor

Similar to the solar radiation, the air temperature and relative humidity sensors will be required to continually measure data over the anticipated data ranges. Using historical climate records for the area and recognising air temperature extremes, the expected temperature range was identified as approximately -16.0º to 34.0º (Met Office, 2013a; Tutiempo, 2013). A combined temperature and relative humidity probe (Campbell-scientific CS215) was selected to record the two variables based on the reported operational ranges and accuracy. The temperature component of the probe has an accuracy ±0.3ºC and the relative humidity component records data with an accuracy of ±2% (Campbell Scientific, 2013). These accuracies were deemed sufficient to differentiate between the expected annual and diurnal variations at the site. For optimum measurements, the temperature and relativity probes were housed in a solar shield which reflects solar radiation that would otherwise adversely affect recorded data. Figure 3.10 shows the installed solar shield housing the temperature and relative humidity probe. The full device specifications can be found in Appendix A.

Figure 3.10 – Photograph of the installed solar shield which houses the combined temperature and relative humidity probe.

3.2.3.3 Anemometer

In order to monitor the wind speed a Vortex cup anemometer (see Figure 3.11) was selected. The cup anemometer selected has a stated accuracy of ±4% from 10-50 mph and 0.25 mph from 4 to 10 mph (Audon electronics, 2013). Based on the anticipated wind speeds from regional data at the site and required measurement resolution, this was deemed acceptable. Appendix A contains the full technical specifications for the device. The installed anemometer can be found on the right hand side of Figure 3.11.

Figure 3.11 – Photograph of the installed anemometer along with the remaining climatic sensors.

3.2.3.4 Rain gauge

A rain gauge was installed to continually measure precipitation at the monitoring site throughout the duration of the monitoring period. Regional records obtained from the MET Office (Met Office, 2013b) showed that the monitoring site was subject to an approximate range of 540 – 1040 mm of rainfall per year. A device known as a 'tipping bucket' rain gauge (commonly used by meteorologists) has been selected for the precipitation monitoring based upon its accuracy and reputation for reliability. A 'Young' tipping bucket rain gauge (model 52202) was selected and installed at the site (see Appendix A for technical specifications). This gauge is capable of measuring rainfall to the nearest 1 mm (Young, 2013) which was deemed an acceptable data resolution based on the expected annual rainfall. Figure 3.12 shows the installed gauge at the monitoring site.

Figure 3.12 – Photograph of the installed tipping bucket rain gauge.

3.2.4 Heat pump monitoring

In order to understand the ground thermal behaviour, knowledge of the heat being extracted from the ground via the ground source heat system is required. This heat extraction is driven by the heating load on the system and is therefore dependent on the mechanical behaviour of the heat pump and circulating fluid. The energy being extracted from the ground can be determined if the temperature difference across the heat pump (i.e. difference in fluid temperature between the inlet and outlet to the ground-loop), mass-flow and fluid specific heat capacity are known. It is noted that the system installed at the site will only circulate fluid when the heat pump is active. Monitoring the mass-flow rate therefore indirectly records the system usage; thereby indicating active periods and non-active periods of heating. A set of criteria was outlined prior to equipment selection to help identify the most suited monitoring equipment. These criteria are as follows:

- *Robustness* – the sensors must be capable of withstanding the continual flow of the circulating fluid over the monitoring period (minimum of 3 years).

- *Operating range* – the sensors are required to function within the required temperature and flow ranges respectively.
- *Durability* – the sensors are required to operate and remain maintenance-free during the monitoring period.
- *Data logging* – the sensors should be able to remotely log data and be compatible with the selected data-logger.

In total, three sensors were identified and installed at the monitoring site. Two of them were installed to measure the circulating fluid temperature at the inlet and outlet of the heat pump (see Figure 3.13) with the third measuring the flow rate. RST Instruments Thermistors, the same as those used to monitor the ground temperatures, were employed to measure the fluid temperatures. The thermistors were encased within a pipe T-section and integrated within the system pipework at appropriate locations. The thermistors were subsequently integrated within the data-logger and data was recorded at the same time interval as the ground and climatic data sets. Details regarding the thermistor specification can be found in Appendix A while the data collection intervals of the data-logger will be discussed further in section 3.2.5.

The measurement of the fluid flow depends on the ground-loop flow characteristics, i.e. if the flow within the ground-loop is uniform or non-uniform. A conventional horizontal closed ground-loop was installed at the site. Such ground-loops keep air entrapment within the system to an absolute minimum as it adversely affects overall performance. Based on this setup and the compressibility of the circulating fluid, is can be assumed that there is a uniform fluid flow within the ground-loop; therefore a single flow meter has been installed to measure the fluid flow.

A range of flow meters are available on the market, not all of which were suitable to be installed at the monitoring site. An important feature to be considered when selecting a flow meter is the compatibility with the existing pipework and the practical installation within the overall system. Based upon this consideration, the design flow rate of the fluid pump and the outlined criteria, a Metron mechanical flow meter was selected (Metron FMC, 2013) (see Appendix A for details). The devise was positioned on the outward flowing leg of the ground-loop (see Figure 3.13) primarily due to space limitations at the site. The flow meter was configured to send a signal each time a specific volume of fluid had passed by. The data-logger was configured to receive and translate this signal allowing the flow meter to be integrated within the data-logger set up. Figure 3.14 presents a photograph of the mechanical flow meter used at the monitoring site, prior to its installation.

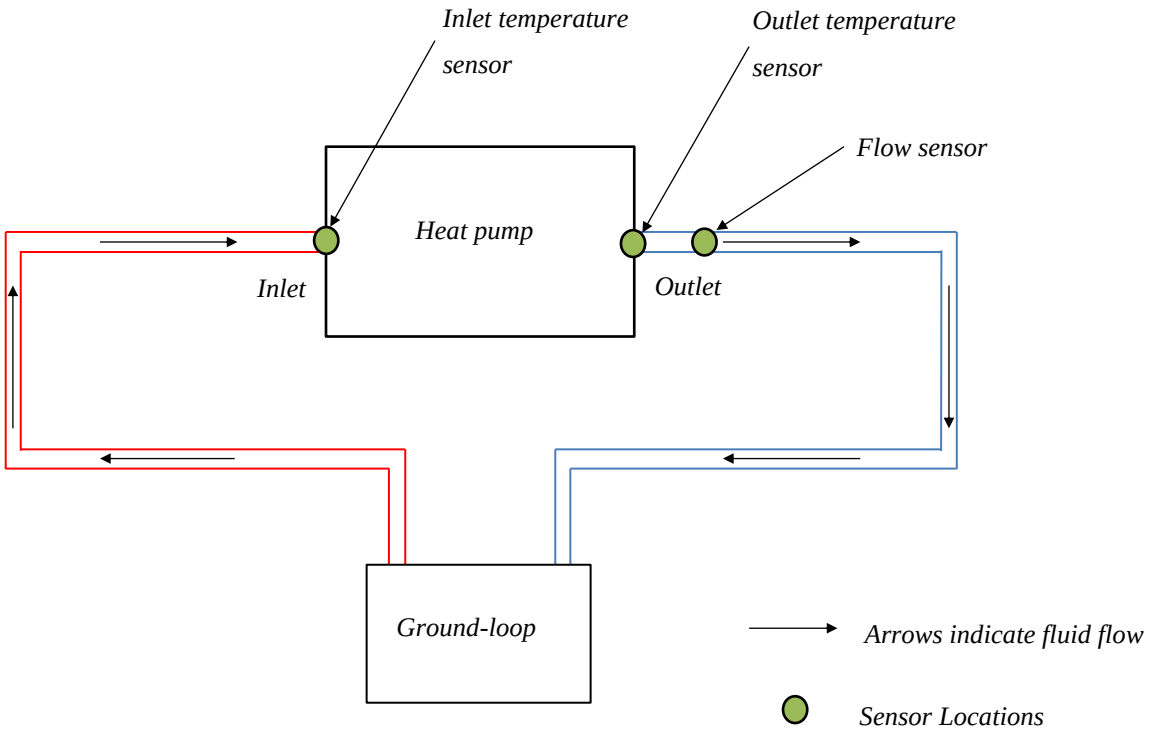

Figure 3.13 – Diagram showing the position of the temperature sensors and flow meter.

Figure 3.14 – Photograph of the Metron flow meter prior to installation.

3.2.5 Remote sensing and communication

The data being collected by ground, climatic and heat pump sensors are logged and stored by a data-logger located at the monitoring site. The total number of sensors (112 ground temperature sensors, 3 system sensors and 5 climatic sensors) is far in excess of the number of data channels typically found on commercial data-loggers. It was therefore necessary to use a multiplexer in conjunction with the data-logger so that signals from the individual sensors can be poled and simultaneously recorded. Figure 3.8 provides the location of the data-logger and multiplexer along with the remaining components which make up the remote communication aspect of the monitoring system.

The multiplexer device was positioned such that the ground sensors could be easily wired into it and maintained. In addition, positioning the device close to the base of the ground-loop would significantly reduce wiring costs. The multiplexer was housed within an IP 65 enclosure which was securely fixed to an external wall. This enclosure is capable of withstanding the ingress of dust and water typically encountered in external weather conditions. A signal wire subsequently connected the multiplexer and data-logger units allowing communication of the recorded data upon request.

The data-logger selected for use at the site was a Campbell Scientific CR 1000 (see Appendix A for details). A Visual Basic script was uploaded onto the programmable logger to control various aspects of the data collection regime, remote-communication and output data files. The logger was set to record and log data from all sensors at the monitoring site at 15 minute intervals. A 15 minute time interval between recordings was deemed as sufficient enough to meet the necessary data resolution requirements to suitably monitor the ground, climatic and heat pump variables. A 15 minute time interval also allowed data to be continually collected and stored for approximately 2 months on the data-logger's memory in case of remote communication failure. After this period, the incoming data would overwrite the oldest stored data. Figure 3.8 shows the data-logger's location within the site and Figure 3.15 shows the installed data-logger within the enclosure it is housed in.

The monitoring system was designed to incorporate remote communication techniques which allow for live communication and remote data downloading off-site. This communication capability is an important system specification due to the distance between the monitoring site and the Cardiff University campus. The logger was connected to a GPRS (General Packet Radio Service) modem, allowing the system to be contacted via the mobile phone network. The modem connected to the data-logger can be seen in Figure 3.15 (Silver/blue box half way up and to the left hand side.). An external areal was connected to the modem and affixed externally to the roof of the plant house in order to improve the mobile signal reception.

Figure 3.15 – Photograph of the installed data-logger and modem within the protective enclosure.

The remote sensing and communication components presented in the previous paragraphs were integrated and installed at the monitoring site during the winter of 2011/12. The scale and bespoke nature scheme inevitably resulted in a number of problems, most of which were encountered during the installation phase of the project. To facilitate future schemes, the problems encountered have been summarised in the following paragraphs.

Off the shelf multiplexers can be applied to an array of applications, the demands of which can vary significantly. The thermistors used to monitor the ground temperature use a single twisted wire pair which will occupy two channels on the multiplexer units (see Figure 3.16). The multiplexer can be set-up to receive either two or four channel wire inputs depending upon the input device. Initially, the multiplexer units were incorrectly set-up to receive four channel inputs as oppose to two. This resulted in the data-logger receiving only half of the in thermistor signals during initial tests. Identification of this hardware problem can prove difficult if the electronics of the multiplexer and data-logger units are not fully understood. Installers of future monitoring systems should be aware of this potential issue prior to any installation.

Post installation, there were an additional two faults encountered during the site monitoring. In July 2012 (approximately two months after the monitoring system had first being in use) whole data-sets for particular time intervals were being intermittently missed out on the data-files. Upon inspection, the missed data-sets appeared to correlate with greater ambient air temperatures but after a week the pattern became more sporadic. The problem was identified as an electrical dry join within the multiplex unit. The problem was solved by replacing the faulty wire section in question.

In January 2013, a second problem was encountered. This time, a specific section of ground temperature data was being intermittently omitted from the data-files as oppose to whole data sets. Again, the missed data seemed to coincide with periods of extreme ambient air temperature, this time cold. Initially it was believe to be another electrical dry join in the multiplexer wiring but it was later discovered, through a process of trial and error, to be a hardware failure in one of the multiplexer banks. The bank was subsequently replaced once the hardware fault had been proven.

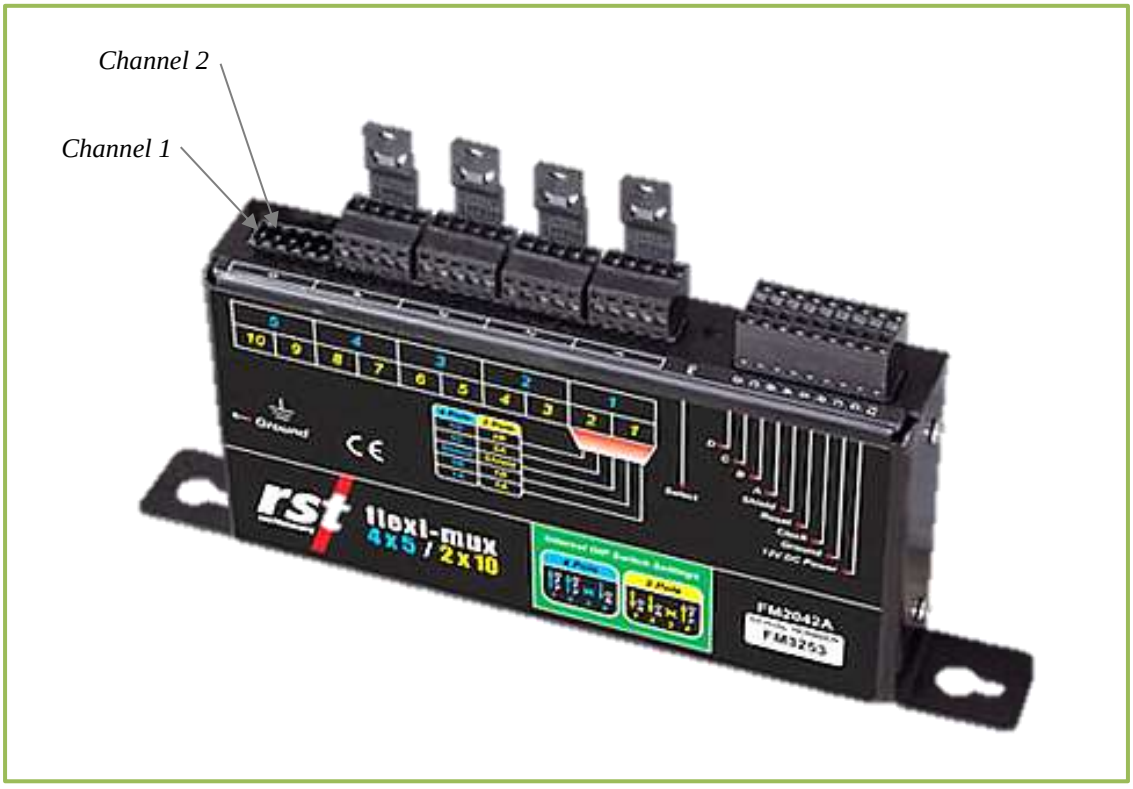

Figure 3.16 – Photograph of a single multiplexer bank used in the monitoring system. (after RST Instruments, 2013).

As previously discussed, remote communication was integrated within the system for practical reasons due to the distance between the monitoring site and Cardiff University. The initial site selection criteria specified the need for mobile signal coverage in order to allow wireless communication. Sufficient network coverage was obtained through a process of trial and error and

using an external areal fixed to the apex of the plant room roof. A second problem encountered with regards to the mobile communication, was the SIM (Subscriber Identity Module) type supplied. In order to transmit data remotely, a data SIM capable of at minimum GPRS (General Packet Radio Service) communication is required. Initially the mobile network provider issued a regular SIM, not capable of data transmission which resulted in communication failures. This SIM was subsequently changed and communication with the data-logger was made.

3.3 Site Investigation

During the installation of the monitoring system, a site investigation was carried out. The heat conduction in soil is controlled by thermal properties of soil, namely; thermal conductivity and specific heat capacity (De Vries & van Wijk, 1966). These properties vary greatly with soil type, composition, structure and constituents (De Vries & van Wijk, 1966). Based on these fundamentals, the following ground properties were identified to be investigated at the site:

- Soil mineral composition
- Particle Size Distribution (PSD)
- Bulk density
- Porosity
- Moisture content
- Saturated hydraulic conductivity
- Specific heat capacity
- Thermal conductivity

During the ground investigating a full topographical survey of the local terrain was also undertaken. The following sections will present the ground investigation procedures employed during the site investigation, the laboratory methods used to measure the ground characteristics and the soil properties obtained.

3.3.1 Ground investigation procedure

The adopted ground investigation procedure aimed to be as representative as possible for the site and encapsulate any significant ground property variations and heterogeneities. The listed ground properties were measured using; i) in-situ techniques, ii) undisturbed samples or iii) disturbed

samples. The following paragraphs will described the ground investigation procedures used in all three cases. In each instance, the problems encountered during the ground investigation procedure will be highlighted and discussed accordingly.

The in-situ ground properties measured were the thermal conductivity and specific heat capacity. The remaining ground properties were to be determined from either undisturbed or disturbed soil samples. A common template was developed to define the vertical location of in-situ measuring points. The testing points were located such that the ground measurements would be recorded at the ground-loop level (1.8 meter depth) and at a depth of 0.6 meters from both trench sides (see Figure 3.17). The plan location and number notation of the testing points can be found in Figure 3.18. The plan locations were selected to coincide with the 'intermediate' and 'detailed' cross-sections. Testing locations were also set in the additional trenching used to install the detailed cross-sections.

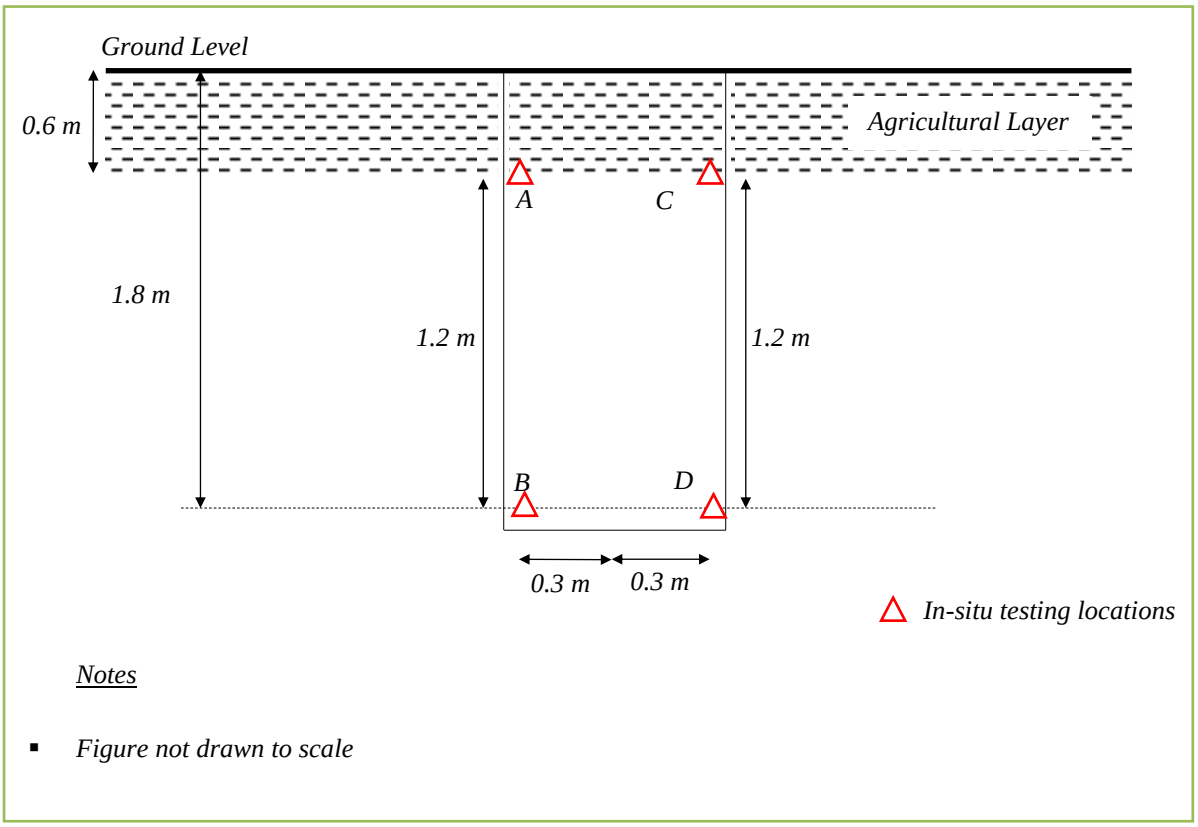

Figure 3.17 – Template used to define in-situ test points measuring thermal conductivity and specific heat capacity at various locations at the site.

The in-situ measurements of thermal conductivity and specific heat capacity were taken using a KD2 Pro thermal resistivity probe (see Appendix B for manufacturer's specifications). The manufacturer's device specifications quoted an associated error of ±2.5% for both the thermal conductivity and specific heat capacity measurements (Decagon Devices Inc., 2006). The in-situ

testing was performed in accordance with the relevant ASTM standard (American Society for Testing and Materials, 2008).

The main problem encountered with regard to the in-situ thermal conductivity and specific heat capacity testing was the probe penetration. The gravelly soils and cobbles encountered on site restricted the number of locations where the probe could be sufficiently inserted to take reliable readings. This resulted in some testing locations being moved from the planned locations. In such cases, measurements were taken as close to the specified points as possible but ultimately were taken wherever the probe could be sufficiently inserted into the trench wall. The exact location of all in-situ testing points was recorded as part of the topographical survey performed on site.

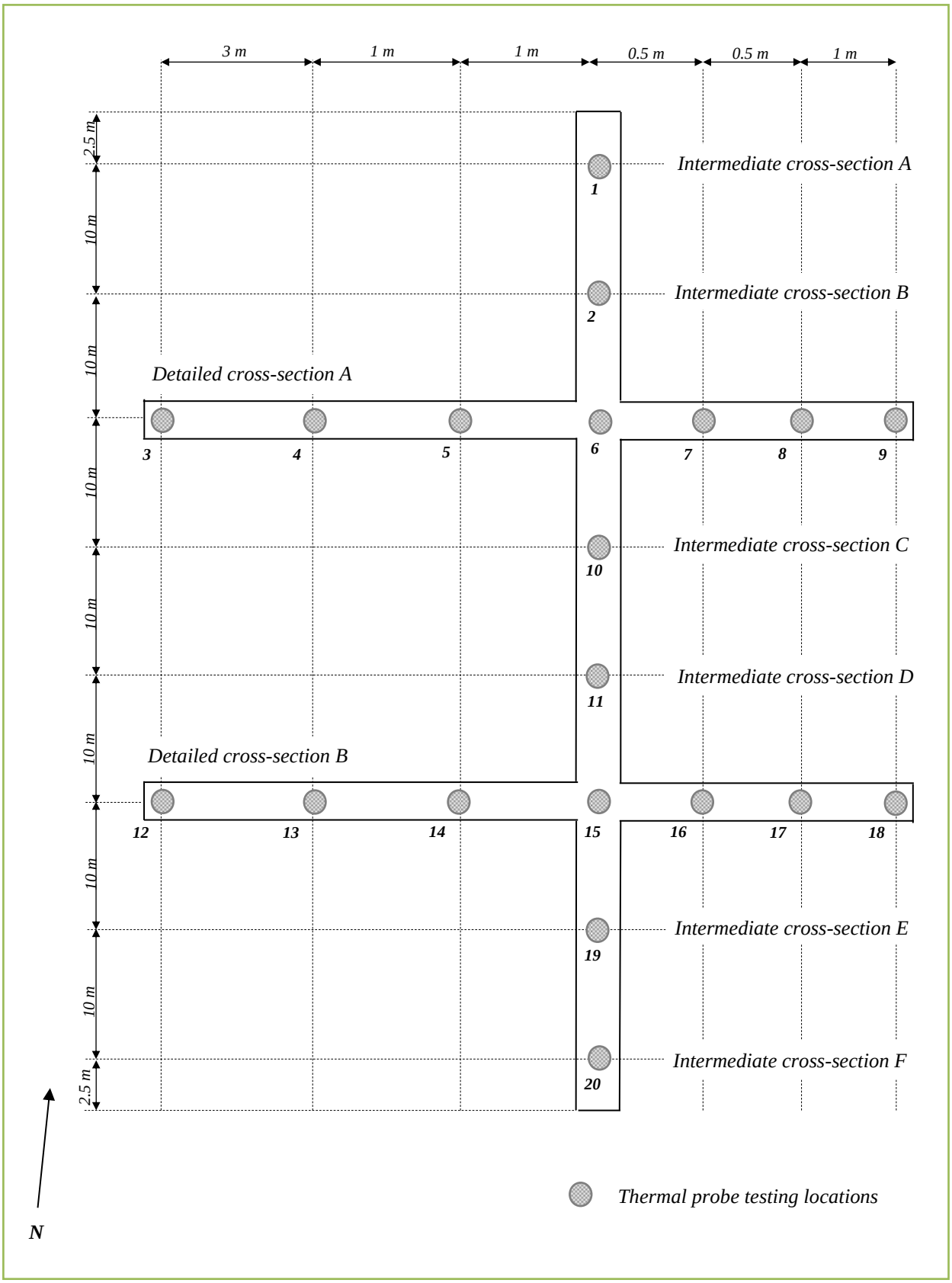

Figure 3.18 – Plan arrangement for the thermal probe testing locations.

As previously discussed, the remaining ground properties were determined by the analysis of disturbed and undisturbed soil samples collected from the site. The soil properties of bulk density and moisture content were analysed using undisturbed soil samples whereas the soil composition, particle size distribution (PSD) and saturated hydraulic conductivity were analysed using disturbed soil samples. The number and spatial arrangement of the sampling locations was selected to provide a sufficient granularity of the geotechnical parameters being investigated in accordance with the relevant British Standard (British Standards Institution, 2002a). Figure 3.19 and 3.20 show the plan and vertical arrangements for the undisturbed and disturbed soil samples.

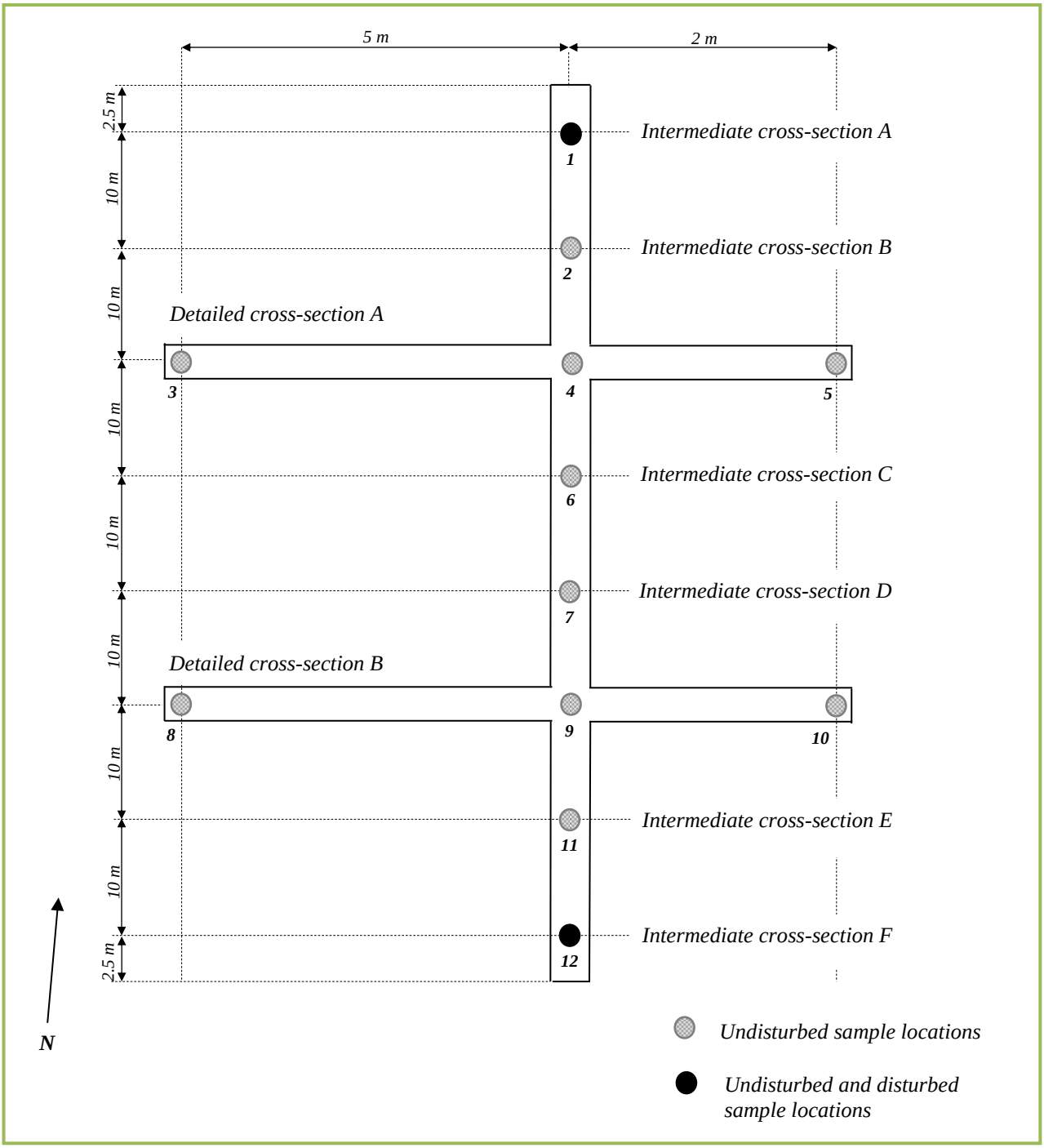

Figure 3.19 – Plan arrangement for the sample locations.

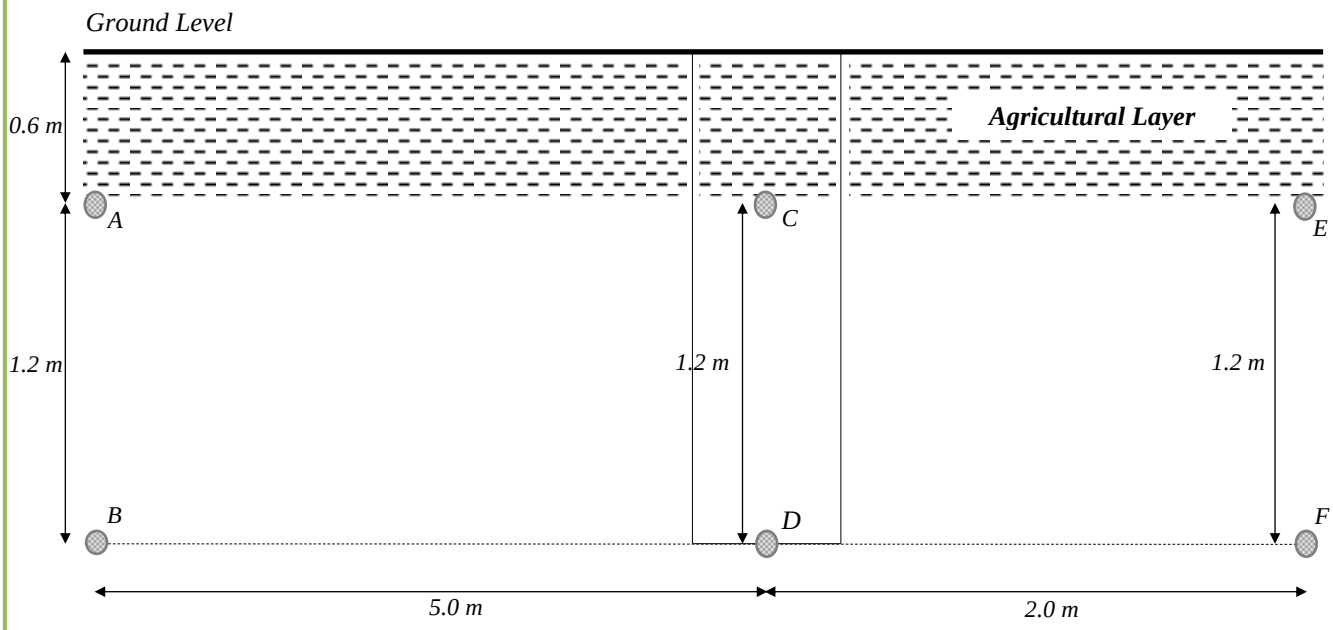

Figure 3.20 – Vertical cross-section of the undisturbed sample locations.

The undisturbed samples were extracted using 38mm diameter by 230mm long sample tubes affixed to a manual auger in accordance with British Standard BS 5390 (British Standards Institution, 1999). Figure 3.19 also shows the planned locations for the disturbed soil samples. The PSD sampling points were limited to two locations due to the large volume of earth required for testing in accordance with British Standard 1377-2:1990 (British Standards Institution, 1990b). This states that in order to perform a representative sieve analysis on the ground found during the trial excavation, a minimum sample of 15 kg was required (as specified for ground of which 10% of constituents have a diameter greater than 37.5 mm).

Once extracted, the samples were transported and stored at the soil laboratory located within Cardiff University's school of engineering. Suitable precautions were taken where possible to reduce any alteration of the in-situ properties in accordance with the British Standard BS ISO 18512 (British Standards Institution, 2007).

The main problem encountered during the sampling procedure was with regards to the undisturbed sample extraction on site. The gravely soils and cobbles encountered on site greatly restricted the number of locations where the hand-auger could extract suitable ground samples. The trial trench dug prior to the monitoring system's design had not revealed the full extent of the gravelly soils and cobbles which were to be encountered throughout the site investigation. The ground conditions encountered either partially or completely obstructed the sample extraction, limiting the obtainable sample depth. This significantly increased the difficulty of extracting representative in-situ samples. The sample locations proposed by the sample procedure (see Figure 3.19) were not always practically attainable. In such cases, the samples were extracted as close to the specified sampling point as possible. If it was suspected that the sample was of poor quality, it was either re-taken or an additional sample was extracted. The exact location of all samples was recorded as part of the topographical survey (see section 3.3.2).

Five out of the thirty samples taken from the site crumbled when extruded from sampling tubes in the laboratory. As a result of the crumbling, the bulk density could not be measured for these samples. These points have been identified within the experimental results accordingly.

3.3.2 Topographical survey

A topographical survey was undertaken in order to provide a detailed three-dimensional description of the monitoring site. A surveying device known as Topcon Hiper Pro RTK was employed for all site surveying. This device used Global Positioning System (GPS) to locate the three-dimensional position of data points across the site. The manufacturer's specifications of the device state that site measurements provide a horizontal accuracy and precision of 3mm and a vertical accuracy and precision of 5mm (Topcon, 2006). The topographical survey allowed the three-dimensional position of the ground-loop, ground sensors, sampling locations and surface to be recorded. When analysing the collected data, it is important that the three-dimensional position of the sensors and depth beneath the ground surface is known in order to investigate the ground thermal behaviour in response to heat extraction. Figure 3.21 shows a three-dimensional visualisation of some collected survey points.

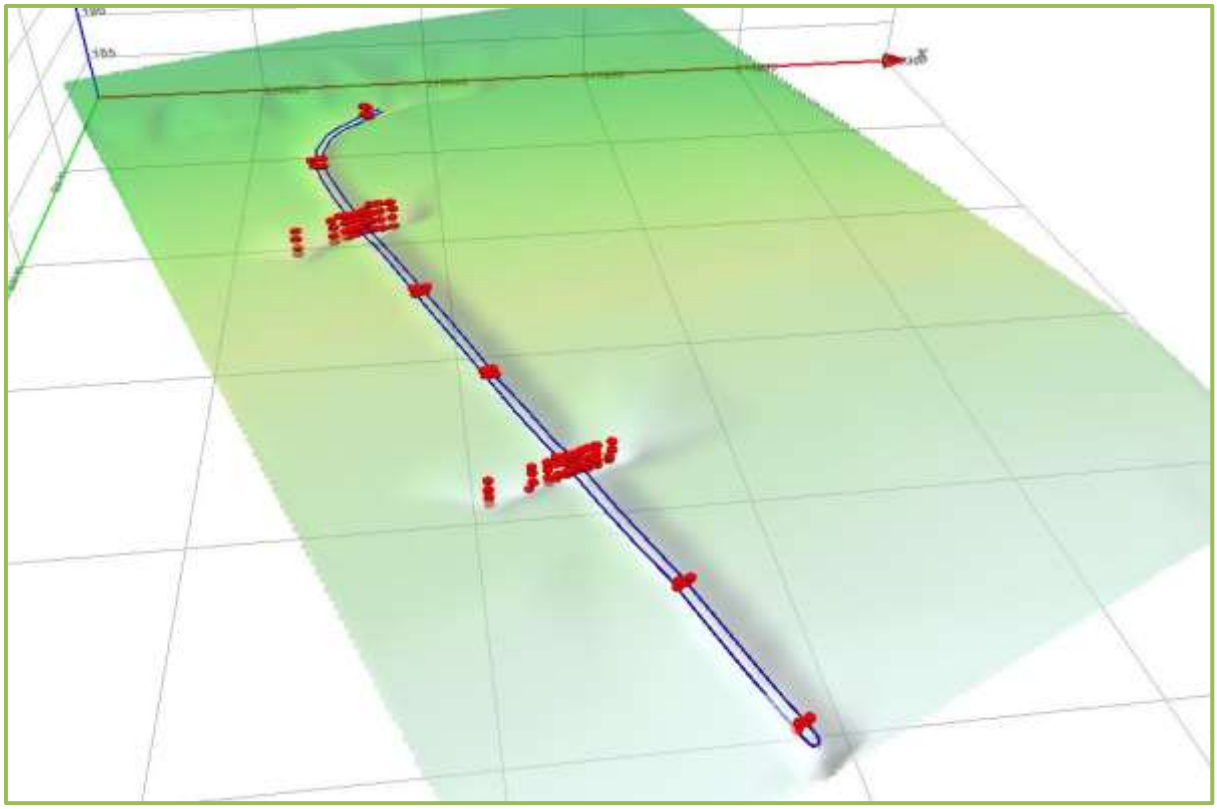

Figure 3.21 – Three-dimensional visualisation of the monitoring site showing the trench, ground-loop and thermistors locations.

3.3.3 Soil properties and characteristics

Investigations into the soil properties and characteristics at the monitoring site were primarily undertaken during the monitoring site installation. In addition to this, three smaller investigations were undertaken at selective dates post the monitoring site installation. The following sections will first discuss the soil investigations undertaken during the sensor installation. Following this, the post installation investigations will be discussed.

The soil classification, measured properties of bulk density, moisture content, thermal conductivity, specific heat capacity and saturated hydraulic conductivity; and the calculated property of porosity and presented in the following sections. In each instance the laboratory/calculation method will be discussed and the measured values will be discussed. Selected graphs showing the experimental results will be presented and discussed accordingly in order to provide an overview for the geotechnical properties measured on site. The raw geotechnical data can be found in full within Appendix C.

The in-situ soil characteristics and; undisturbed and disturbed soil samples used to measure the presented soil properties were measured/retrieved over the course of a three day period during

October 2011. The weather on all three days could be described a mild and dry while the ground conditions could be described as unsaturated. In general it can be said that better quality samples and thermal measurements were obtained from the southern half of the site.

3.3.3.1 Soil classification, sieve analysis and mineral composition

Soil classification at the monitoring site was undertaken for two locations, coinciding with the undisturbed soil sample locations positioned at the northern and southern most ends of the monitoring site. Based upon the measured ground properties and particle size distribution, the ground can be classified as coarse-gravel silt at the northern end of the site and a coarse-silt fine-gravel at the southern end of the site according to the British Standard classification (British Standards Institution, 2004a). The two differing classifications reflect observations made during the site investigation which indicated that the soil was generally coarser at the northern end of the site, and more gravelly towards the southern end.

The particle size distribution analysis was performed using the two disturbed soil samples as previously discussed in section 3.3.1. The particle size distribution analysis was performed using a standard sieve analysis in accordance with the British Standard BS 1377-2 (British Standards Institution, 1990b). The first sample, referred to as PSD 1, was taken from location 1 in Figure 3.19 (northern end of the sample plan) whereas the second sample, referred to as PSD 2, was taken from location 12 in Figure 3.19 (southern end of the sample plan). The particle size distribution curves obtained from both PSD analyses can be found in Figures 3.22. The experimental results for PSD 1 revealed that the sample was predominantly coarse gravel with silt whereas the results for PSD 2 revealed that the sample was predominantly coarse silt with fine gravel. PSD 1 results also describe the presence of the occasional cobble, greater than 63 mm in diameter. It can be said the characteristics highlighted by sieve analysis, reflected the general ground characteristics observed during the site investigation.

The soil mineral composition was again performed using the disturbed soil samples located at the northern and southern end of the site. The soil mineral composition was investigated using X-ray diffraction analysis undertaken within Cardiff University's soil laboratories in accordance with the relevant British Standard (British Standards Institution, 2005). The results of this analysis can again be found in Appendix C. Results from the analysis showed that the both samples contained minerals associated with silt and gravel based soils along with traces of silicon dioxide (sand). These findings concur both with the soil classifications and the traces of sand found during the sieve analysis.

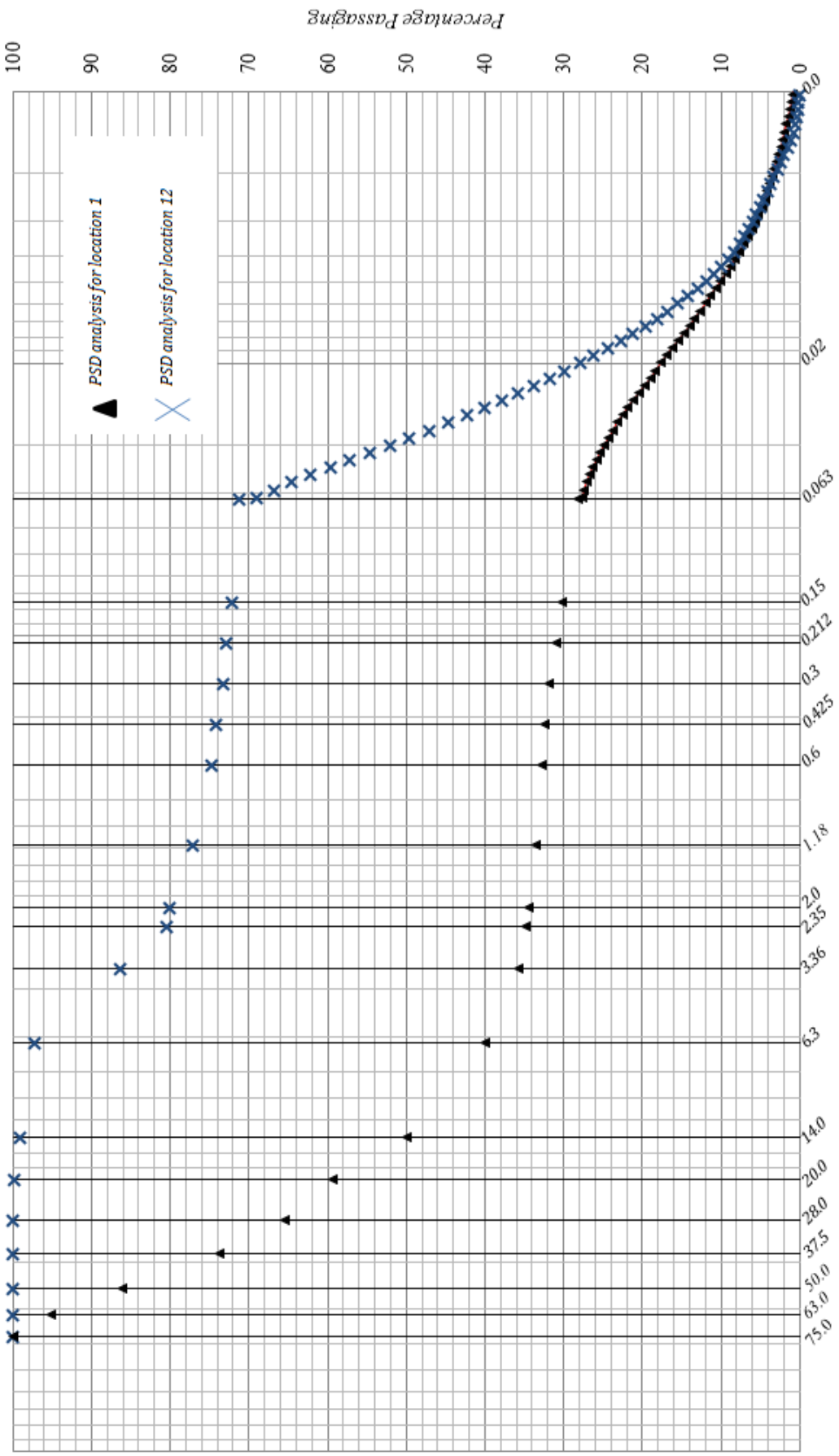

Figure 3.22 – Particle size distribution curve for the two disturbed samples extracted from the monitoring site.

3.3.3.2 Bulk density, moisture content and porosity

The bulk density, moisture content and porosity were measured/calculated using the undisturbed soil samples, the locations of which have been previously shown in Figure 3.19. The soil properties presented here has been broadly split into two groups, based on the plan location of the soil samples from which they were obtained. The first group represents samples from the northern half of the site (sample location 1-6 in Figure 3.19) whereas the second represents samples from the southern half of the site (sample location 7-12 in Figure 3.19). The division of the soil properties was to allow any differences between the northern and southern halves of the site to be identified based on general observations made during the site investigation which indicated that the soil characteristics found at the northern end of the site differed to those found at the southern end.

The bulk density was calculated from the undisturbed samples by measuring the mass and volume of a suitable sample section in accordance with the British Standard BS 1377-2 (British Standards Institution, 1990b). Figure 3.23 presents the measured bulk density, plotted against sample depth. The data indicates there was no apparent relationship between the measured bulk density and sample depth or between the measured bulk density and plan location throughout the site. The measured bulk density values ranged from 1373 to 2218 kg m^{-3}. The bulk density averaged 1830 kg m^{-3} across the site. The variation in measured bulk density can be attributed to a number of factors, most notably ground heterogeneities. It can be said that the measured values concur with the typical bulk densities reported in literature for the soil types encountered on site (Barnes, 2000).

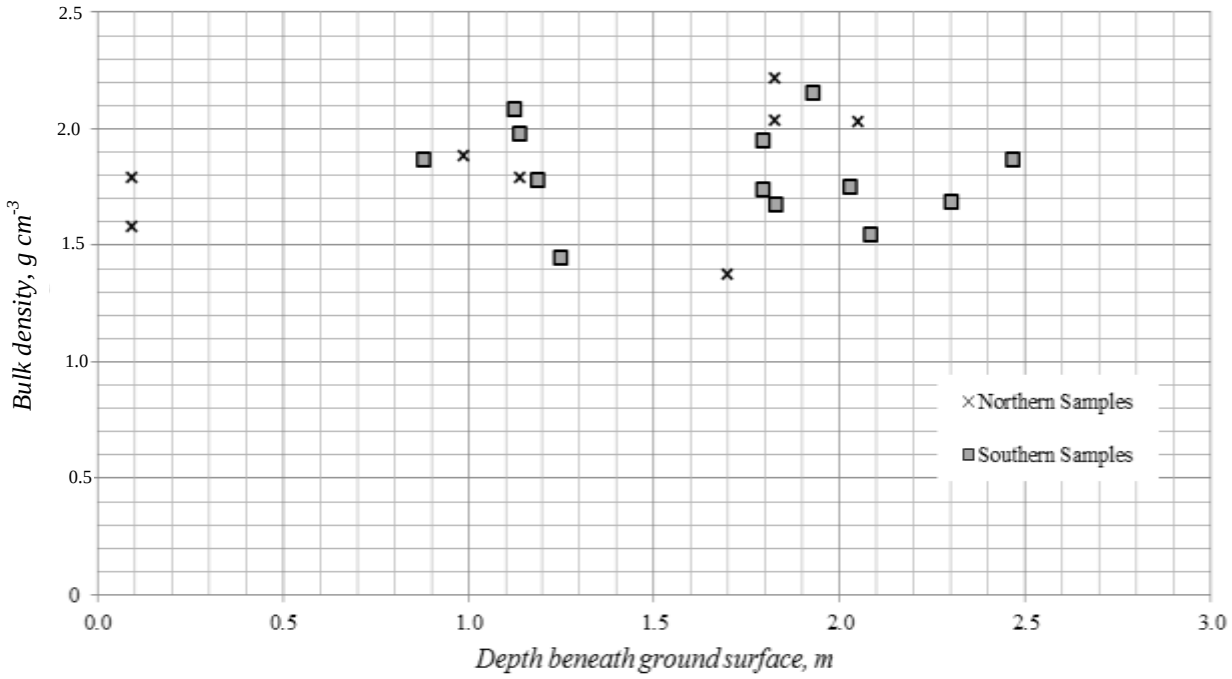

Figure 3.23 –Laboratory measured bulk density at different depths beneath the ground surface.

The moisture content was measured by comparing the mass between original and oven dried undisturbed samples in accordance with the British Standard BS 1377-2 (British Standards Institution, 1990b). Figure 3.24 presents the measured moisture content at different depths. No measurable relationship between the moisture content and plan location (i.e. north/south) was found from the results. However, it can be said that there is a weak correlation relating the measured moisture content and sample depth. The relationship indicates that moisture content generally increases with depth. The measured moisture contents ranged between 6.1% and 15.0%, with the exception of one data point which measured 29.1%. Negating this point, it can be said that the average moisture content was found to be 13.1%.

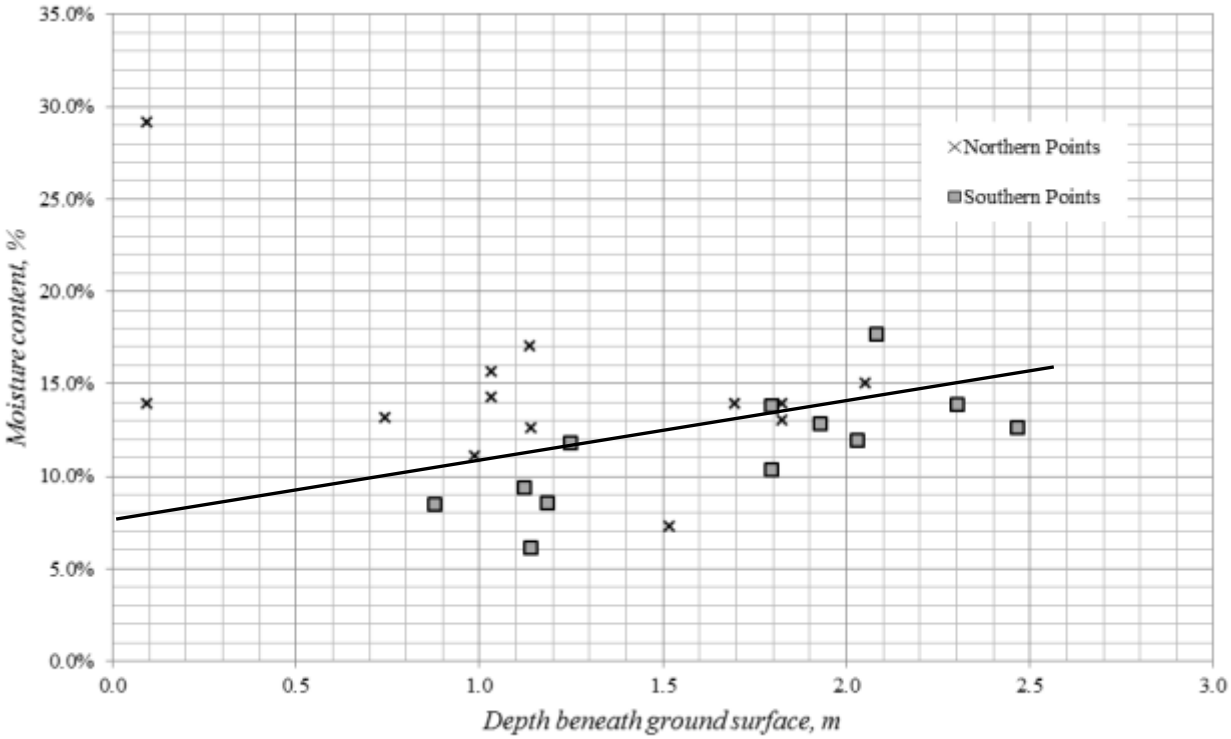

Figure 3.24– Laboratory measured moisture content at different depths beneath the ground surface.

The porosity was calculated using the bulk density and the density of the solid constituents of the soil, following the British Standard BS 1377-2 (British Standards Institution, 1990b), given as:

$$n = 1 - \frac{\rho_{Bulk}}{\rho_s} \tag{3.1}$$

where n is the porosity, ρ_{Bulk} is the bulk density of the soil sample *(kg m^{-3})* and ρ_s is the density of the soil constituent of the soil *(kg m^{-3})*. The value of ρ_s was assumed equal to 2.65 kg m^{-3} based on the soil classification and values reported in literature (Barnes, 2000).

Figure 3.25 presents the calculated porosity with sample depth. There was no apparent relationship between the calculated porosity and sample depth or plan location. The recorded porosity values ranged from 0.15 to 0.49 throughout the site, with similar characteristics being found in both the northern and southern half of the site. The heterogeneous nature of the ground found at site inevitably leads to variations in the measured porosity, therefore it can be said that the observed variation is not entirely unexpected. The measured porosity was compared to values reported in literature using the mean value for the entire site which is 0.31. When considering the soil type found on site, this value falls just below those reported in literature (Barnes, 2000).

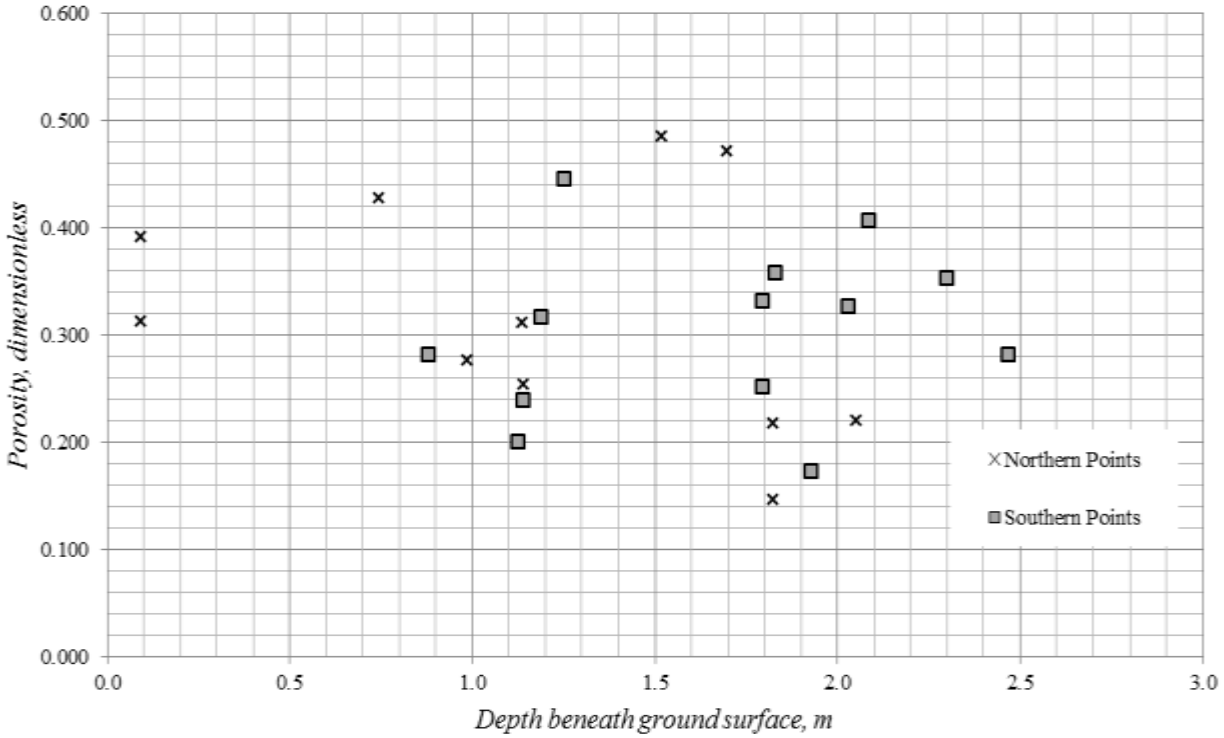

Figure 3.25 – Laboratory measured porosity at different depths beneath the ground surface.

3.3.3.3 Thermal conductivity and specific heat capacity

As previously discussed, the thermal conductivity and specific heat capacity were measured in-situ using a thermal probe. Similarly to the preceding soil properties, the measured thermal conductivity and specific heat capacity measurements have been divided in two (i.e. north and south groups) based on the plan location of the sampling points.

Figures 3.26 and 3.27 present the measured thermal conductivity and specific heat capacity at the monitoring site, relating these values to the sample depth. Figure 3.26 indicates that there was no apparent correlation between the thermal conductivity and spatial position within the site (i.e. either depth or plan location). Similarly, Figure 3.27 indicates that there is no apparent relationship between the specific heat capacity and spatial position within the site. The thermal conductivity and specific heat capacity values recorded for the site did however fall within the expected range reported by established literature when considering the calculated porosity and measured volumetric moisture contents (De Vries & van Wijk, 1966). The recorded thermal conductivity values ranged from 1.63 to 2.87 $Wm^{-1}K^{-1}$ (neglecting one apparent data anomaly which reported a value of 0.49 $Wm^{-1}K^{-1}$, which is significantly lower than any other reading). The recorded specific heat capacity values ranged from 932 to 1428 $Jkg^{-1}K^{-1}$. The observed thermal conductivity and specific heat capacity ranges again concurred with values reported by De Vries & van Wijk (1966).

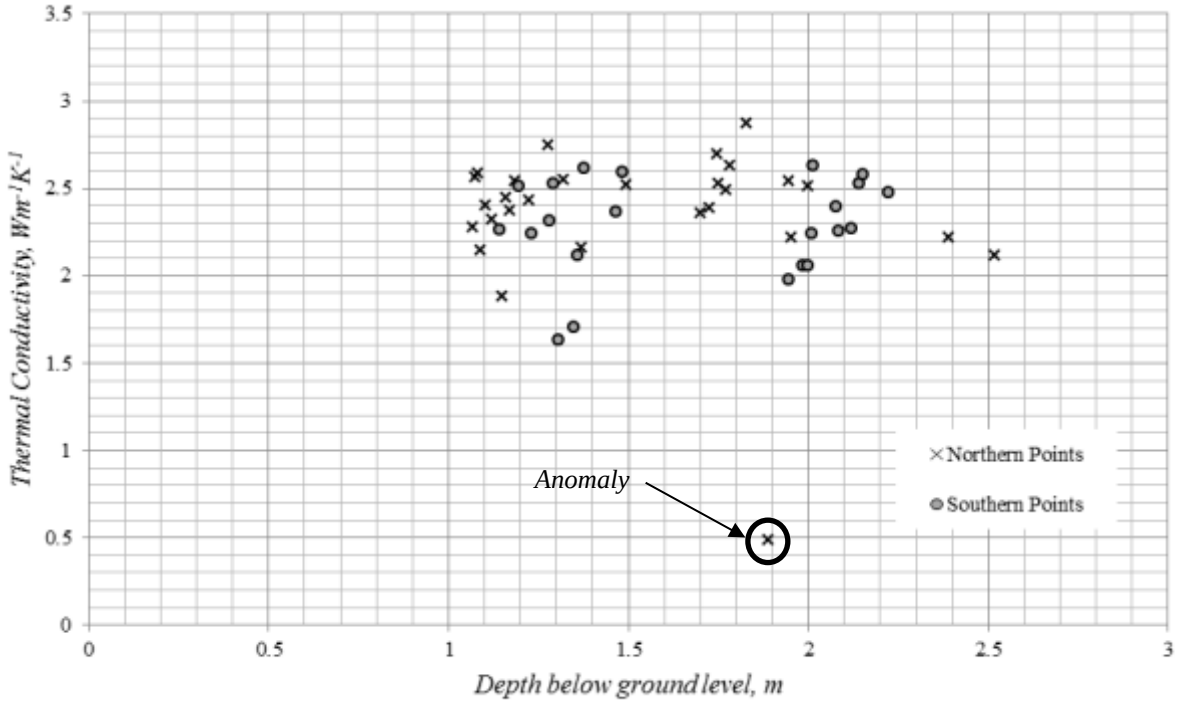

Figure 3.26 – Measured in-situ thermal conductivity at different depths below ground level.

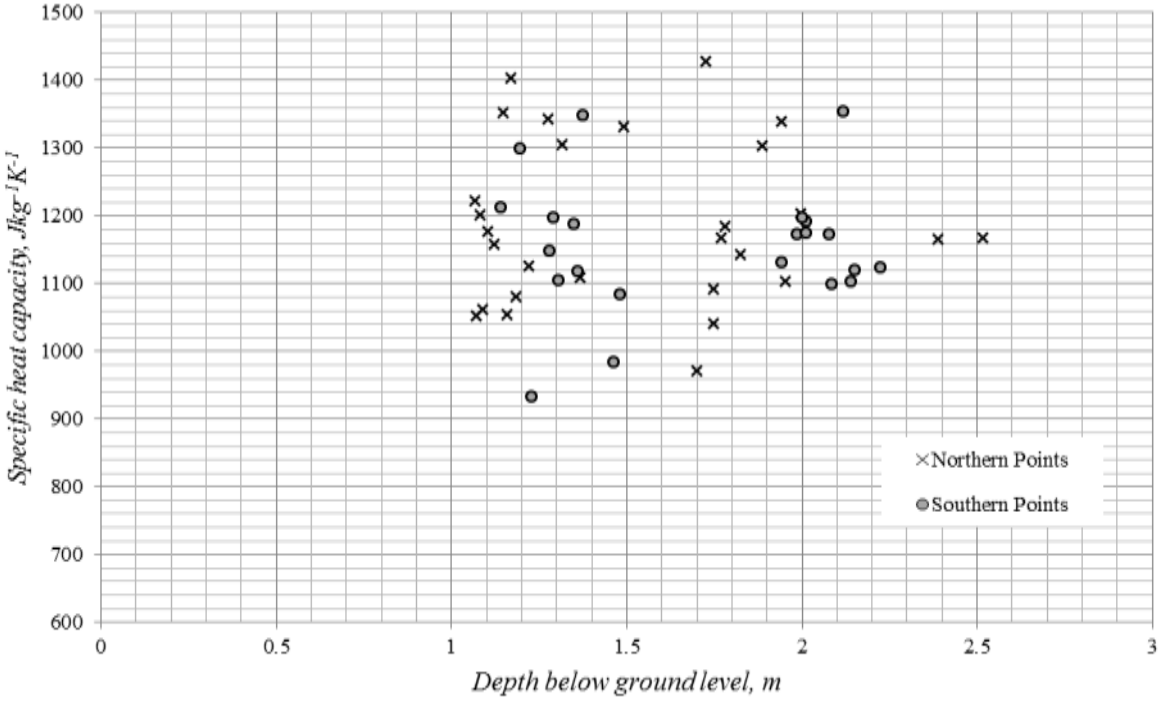

Figure 3.27 – Measured in-situ specific heat capacity at different depths below ground level.

3.3.3.4 Saturated hydraulic conductivity

Ideally in-situ hydraulic conductivity tests retaining the in-situ soil structure would have been carried out however, time restrictions associated with the work schedule on site ruled out this option. To address this shortfall in field data, laboratory tests were carried out using disturbed soil samples from the two locations previously highlighted in section 3.3.1. The saturated hydraulic conductivity was measured using a falling head permeability test in accordance with the British Standard BS ISO 17313 (British Standards Institution, 2004b). The samples were compacted to the in-situ density measured on site in accordance with the previous standards. The saturated hydraulic conductivity measured at the northern and southern ends of the site were 4.69×10^{-10} ms^{-1} and 9.65×10^{-11} ms^{-1} respectively. Both permeability results were lower than values sourced in literature which reported saturated hydraulic conductivity values for the soil type found at site to be in the region of 1×10^{-9} ms^{-1} (Gustafsson, 1946; Barnes, 2000).

3.3.3.5 Soil properties summary

In summary, the measured/calculated soil properties are presented in Table 3.1:

Table 3.1 – Average soil properties measured/calculated from the site investigation.

Soil property	***Average value***	***Standard deviation***
Bulk density, $kg\ m^{-3}$	1830	250
Moisture content, *%*	13.1	4.3
Porosity, *dimensionless*	0.31	0.1
Thermal conductivity, $W\ m^{-1}\ K^{-1}$	2.3	0.44
Specific heat capacity, $J\ kg^{-1}\ K^{-1}$	1172	108.7
Saturated hydraulic conductivity, $m\ s^{-1}$	2.83×10^{-10}	-

3.3.3.6 Post installation site investigations

Further to the soil characterisation study undertaken during the system installation, a series of three additional investigations were carried out. These additional investigations were on a smaller scale than the original characterisation study, compromising of a single trench measuring approximately 1 meter in depth. On each occasion, the trench was excavated in undisturbed ground located approximately half way down the monitored ground-loop. The purpose of the additional investigations was to inspect the hydraulic properties of the soil on site. The timing of the investigations was to set to coincide with the numerical validations, the details of which can be found in Chapter 7.

On each occasion, four samples were retrieved for laboratory analysis using a hand auger. Using the samples, tests for moisture contents and porosity were carried in accordance with the British Standard BS 1377-2 (British Standards Institution, 1990b). The results from the post installation investigations can be found in Tables 3.2, 3.3 and 3.4.

Table 3.2 – Moisture content and porosity measured from four samples retrieved from the monitoring site on 4th May 2012.

Depth of sample beneath ground surface, m	*Moisture content, %*	*Porosity*
0.28	40.4	0.47
0.38	23.6	0.40
0.62	21.7	0.35
0.78	30.8	0.41

Table 3.3 – Moisture content and porosity measured from four samples retrieved from the monitoring site on 7h September 2012.

Depth of sample beneath ground surface, m	*Moisture content, %*	*Porosity*
0.19	30.4	0.51
0.35	13.0	0.42
0.52	27.7	0.39
0.70	27.0	0.36

Table 3.4– Moisture content and porosity measured from four samples retrieved from the monitoring site on 23rd January 2013.

Depth of sample beneath ground surface, m	*Moisture content, %*	*Porosity*
0.21	46.0	0.46
0.41	38.6	0.42
0.63	27.7	0.35
0.84	19.9	0.28

3.4 Conclusions

This chapter has presented the design and implementation of a field-scale monitoring scheme installed to investigate the ground thermal behaviour in response to heat extraction via a horizontal ground source heat system. The site design and implementation is described, including; the site

selection, sensor selection, sensor arrangement and finally the installation. Consideration was given to the climatic conditions and heat load of the heat pump which are known to influence the ground thermal behaviour. The climatic variables of solar radiation, ambient air temperature, rainfall, relative humidity and wind speed were measured using a weather station installed at the site while the heat load of the heat pump is calculated by measuring the circulating fluid flow and fluid temperature difference across the heat pump. Remote monitoring and communication techniques employed at the site have also been presented. The considerations required to integrate the ground, climatic and heat pump sensors with the remote communication equipment have also been described. The design and implementation of the field-scale monitoring site demonstrates a template which could be used for the installation of future field-scale schemes, aiming to investigate the ground thermal behaviour in response horizontal ground source heat systems.

A site investigation undertaken during the ground sensor installation is also presented. The design and methodologies adopted during the site investigation have been described in full. The investigation included in-situ and laboratory testing, the latter of which was conducted on a mixture of undisturbed and disturbed samples. The results were used to characterise the physical and thermal properties of the soil throughout the site. A topographical survey was also conducted, recording the three-dimensional position of the ground-loop, ground thermistors and sample/survey locations, facilitating future data analysis. The site investigation results contained a sufficient resolution of ground data to allow both the thermal and hydraulic behaviour of the soil, in response to heat extraction from the horizontal ground source heat system, to be investigated.

References

American Society for Testing and Materials, 2008. *D5334 - Standard test method for determination of thermal conductivity of soil and soft rock by thermal needle probe procedure.* West Conshohocken, USA: ASTM International.

American Society for Testing Materials, 2009. *CI 699-09 - Standard Test Method for Moisture Retention Curves of Porous Building Materials Using Pressure Plates.* West Conshohocken, USA: ASTM International.

Apogee Instruments, 2013. *Pyranometer SP-110 user manual.* Utah, USA: Apogee Instruments.

Audon electronics, 2013. *Technical specifications for VORTEX wind speed sensor.* [Online]
Available at: http://www.audon.co.uk/weather_sensors/vortex.html
[Accessed 27 2 2013].

Barnes, G. E., 2000. In: *Soil Mechanics - Principles and Practice 2nd Edition.* New York: Palgrave.

British Standards Institution, 1990a. *BS 1377-1 Soils for Civil Engineering Purposes Part 1: General Requirements and Sample Preparation.* London: BSI Publications.

British Standards Institution, 1990b. *BS 1377-2 Soil for Civil Engineering Purposes - Part 2: Classification Tests.* London: BSI Publications.

British Standards Institution, 1999. *BS 5930 Code of Practive for Site Investigations.* London: BSI Publications.

British Standards Institution, 2002a. *BS ISO 10381-1 Soil Quality - Sampling.* London: BSI Publications.

British Standards Institution, 2002b. *BS ISO 14688-1 Geotechnical Investigation and Testing - Identification and Classification of Soil Part 1: Identification and Description.* London: BSI Publications.

British Standards Institution, 2004a. *BS ISO 14688-1 Geotechnical Investigation and Testing - Identification and Classification of Soil Part 2: Principles for a Classification.* London: BSI Publications.

British Standards Institution, 2004b. *BS ISO 17313 Soil Quality - Determination of hydraulic conductivity of saturated porous materials using a flexible wall permeameter.* London: BSI Publications.

British Standards Institution, 2005. *BS EN 13925-3 Non-destructive testing. X-ray diffraction from polycrystalline and amorphous materials.* London: BSI Publications.

British Standards Institution, 2007. *BS 18512 Soil Quality - Guidance on Long and Short Term Storage of Soil Samples.* London: BSI Publications.

Campbell Scientific, 2013. *CS215-L Specifications and Technical Data.* [Online]
Available at: http://www.campbellsci.com/cs215-specifications
[Accessed 27 2 2013].

De Vries, D. A., 1966. Thermal properties of soils. In: W. R. van Wijk, ed. *Physics of the Plant Environment.* Amsterdam: North Holland Publishing Co.

De Vries, D. A. & van Wijk, W. R., 1966. Periodic temperature variations in a homogeneous soil. In: W. R. van Wijk, ed. *Physics of the Plant Environment.* Amsterdam: North Holland Publishing Co.

Deardorff, J. W., 1978. Efficient prediction of ground surface temperature and moisture, with inclusion of a layer of vegetation. *American Geophysical Union,* 83(4), pp. 1889-1903.

Decagon Devices Inc., 2006. *KD2 Pro user manual.* s.l.:Decagon Devices Inc..

Gustafsson, Y., 1946. *Die Stromungsverhaltnisse in gedrahntem Boden.* Stockholm: Acta Agricult, Suecana.

Met Office, 2013a. *Met Office: Regional Climates.* [Online]
Available at: http://www.metoffice.gov.uk/climate/uk/wl/
[Accessed 27 2 2013a].

Met Office, 2013b. *Met Office: Midland Rainfall 1910 - Present.* [Online]
Available at: http://www.metoffice.gov.uk/climate/uk/datasets/Rainfall/ranked/Midlands.txt
[Accessed 25 2 2013b].

Metron FMC, 2013. *Flow meter specifications.* [Online]
Available at: http://www.metronfmc.com/watermeter.html
[Accessed 27 2 2013].

RST Instruments, 2013. *RST Instruments.* [Online]
Available at: http://www.rstinstruments.com/Flexi-Mux%20Multiplexer.htm
[Accessed 25 2 2013].

Topcon, 2006. *Topcon HiPer Pro Operator's Manual.* s.l.:Topcon Positioning Systems Inc..

Tutiempo, 2013. *Hereford - Credenhill Weather Station Data.* [Online]
Available at: http://www.tutiempo.net/en/Climate/HEREFORD_CREDENHILL/07-2006/35220.htm
[Accessed 25 2 2013].

van Wijk, W. R., 1966. Introduction, The Physical Method. In: W. R. van Wijk, ed. *Physics of the Plant Environment.* Amsterdam: North Holland Publishing Co..

Young, 2013. *Young tipping bucket rain gauge - Model 52202/52203 technical specification.* [Online]
Available at: http://www.youngusa.com/products/3/18.html
[Accessed 27 2 2013].

Chapter 4

Site monitoring results and discussion

4.1 Introduction

In Chapter 3, the design and installation of a horizontal ground source heat monitoring site has been presented. As previously described, the monitoring scheme has been developed to remotely record ground temperatures, relevant climatic conditions and various heat pump parameters in order to gain knowledge on ground thermal behaviour at the site in response to the application of a horizontal ground source heat system.

This chapter firstly discusses the management techniques adopted to handle the incoming data from the monitoring site and secondly present the results obtained from the full scale monitoring. As part of the data management approach adopted, a so called 'data management tool' was developed to store, structure, check and interrogate the recorded data. Section 4.2 discusses the details of data management which include the design and development of the data management tool. Data recorded

at the monitoring site during the first 13 months of operation between May 2012 and July 2013 is presented in Sections 4.3, 4.4 and 4.5. Section 4.3 presents climatic data recorded during this period and provides an analysis from the findings. Section 4.4 presents the heat pump data collected; namely the fluid flow rate and fluid temperature at the heat pump inlet/outlet. This data is subsequently interpreted in order to calculate the transient system heat loads for the monitoring period in question. Finally, ground temperatures recorded at the site for the first 13 months of monitoring are presented in Section 4.5. The ground thermal behaviour in response to seasonal climatic variations and heat extraction via the ground source heat system is presented and analysed in this section. Concluding remarks regarding the above mentioned will be provided in section 4.6.

4.2 Data management

Measurements from all sensors (i.e. ground, climatic and heat pump sensors) are taken at regular 15 minute intervals at the monitoring site in accordance with the data collection regime previously outlined in Chapter 3. At each 15 minute interval data recorded by 119 sensors is received and recorded by the data-logger on-site along with various other items of data including time-stamps, data-logger battery information and record numbers. The so called 'record number' previously mentioned is a unique number identifying each 15 minute time interval, used primarily for database purposes. Projecting forwards for a monitoring period of three years, and considering the current data collection regime, it can be said that a minimum of 105,120 collection intervals yielding 13,245,120 individual measurements are expected to be recorded at the site. The checking, organisation and interpretation of such a data-set requires a data management solution capable of effectively managing the incoming data. Therefore, a so called 'data management tool' was developed for this purpose. The following sections present an overview of the data management tool's design, implementation and finally the problems encountered during the development process.

4.2.1 Overview of design

The primary objective of the data-management tool developed was to provide a solution which can effectively structure, store and allow interrogation of the data collected from the monitoring site as outlined in Chapter 3. At each 15 minute interval of data recording, the installed data-logger simultaneously poles and saves the measurements from all sensors, storing the results in on-board memory. Based on the number of sensors, and the size and type of the data measurements, it is approximated that this on-board memory can store data for a two month period. Beyond this time

period, the oldest stored data is over-written with the newest read data. In order to maintain a complete data-set, remote downloads via the mobile phone network are conducted on a weekly basis. Further details regarding the remote communication systems can be found in Chapter 3. The data is downloaded in the form of a 'comma-separated values' (CSV) data file. In its raw form, it can therefore be said that the data-set compromises of a series of weekly data files. The following design specifications for the developed data management tool were defined and adopted:

- *Data storage* – the database must be capable of storing the anticipated volume of data incoming from the monitoring system.
- *Data management* – the incoming data must be suitably structured such that no master data is lost and data corruption and repetition is avoided.
- *Continual updating* – data is being continually recorded therefore the database will need to be continually updated as data is received.
- *Analysis* – features to allow an easy analysis of the recorded data are required (e.g. facilities to extract data between two time intervals).
- *User friendly* – The final tool will require a GUI (Graphic User Interface), designed to be simple, robust and user friendly.

4.2.2 Development of the data management tool

The developed data management tool consists of two components, namely*; i) the database* and *ii) a front-end GUI,* which is used to update and interrogate the database. Visual C# was used to build the database and code the GUI in accordance with the requirements set out by the design specifications. This programming language was used in conjunction with Microsoft SQL Server 2012 to create a database. Microsoft SQL Server 2012 provides a means for storing and structuring data in a relational database format. In its simplest terms the database format can be essentially thought of as a 'set' of data-tables which store and structure the raw data. Importantly, both Visual C# and Microsoft SQL Server 2012 incorporate the .NET framework introduced by Microsoft. This enables the most up-to-date programming features to be utilised (e.g. LINQ) and also allows the final software to be forward compatible, facilitating any future modifications.

The first task of the database is to convert the raw data files, remotely downloaded from the data-logger, into a structured SQL table format without incurring any data losses or corruption. As part of this process a series of checks are made to ensure that data has not been corrupted, duplicated or is missed within the database. Corrupted data is identified by comparing the new incoming data with historical values already stored within the database. If any 'out of the ordinary' values are identified, the database has being designed to flag-up the location of the suspected corrupt data for a

manual investigation. Similarly, if missing data is identified, the user is informed of the location of the missing data within the database. Appropriate procedures have also been implemented within the code to ensure that any multiple copies of data were removed from, and not duplicated within the database. The implementation of the previously discussed features can be greatly simplified providing that a suitably designed table structure is adopted within the database. Figure 4.1 shows an extract from a data-table taken from the database.

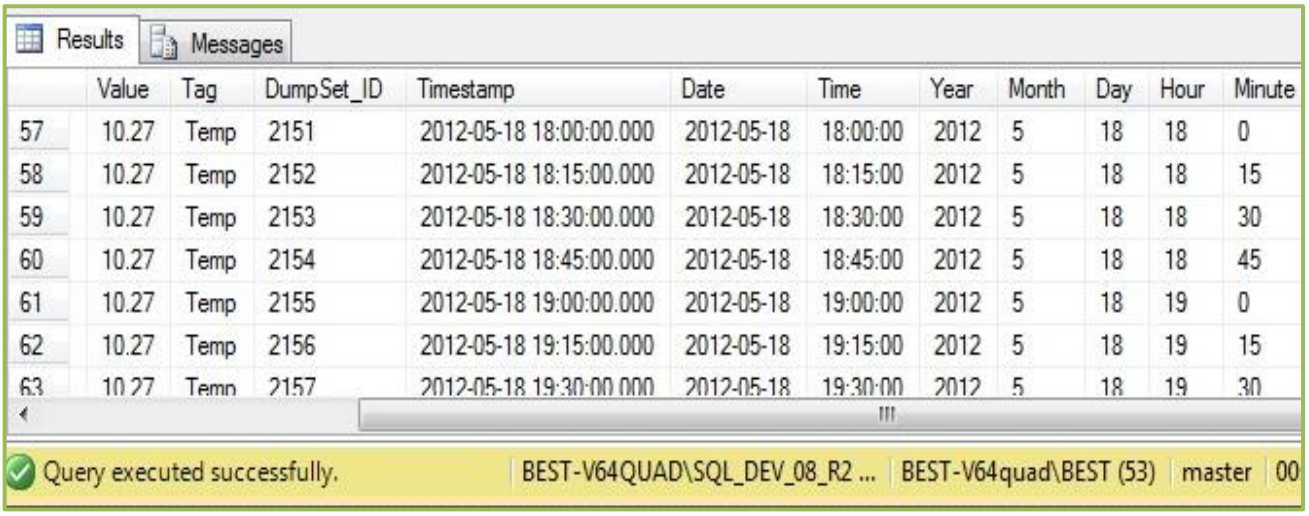

Results | Messages

	Value	Tag	DumpSet_ID	Timestamp	Date	Time	Year	Month	Day	Hour	Minute
57	10.27	Temp	2151	2012-05-18 18:00:00.000	2012-05-18	18:00:00	2012	5	18	18	0
58	10.27	Temp	2152	2012-05-18 18:15:00.000	2012-05-18	18:15:00	2012	5	18	18	15
59	10.27	Temp	2153	2012-05-18 18:30:00.000	2012-05-18	18:30:00	2012	5	18	18	30
60	10.27	Temp	2154	2012-05-18 18:45:00.000	2012-05-18	18:45:00	2012	5	18	18	45
61	10.27	Temp	2155	2012-05-18 19:00:00.000	2012-05-18	19:00:00	2012	5	18	19	0
62	10.27	Temp	2156	2012-05-18 19:15:00.000	2012-05-18	19:15:00	2012	5	18	19	15
63	10.27	Temp	2157	2012-05-18 19:30:00.000	2012-05-18	19:30:00	2012	5	18	19	30

Query executed successfully. | BEST-V64QUAD\SQL_DEV_08_R2 ... | BEST-V64quad\BEST (53) | master | 00

Figure 4.1 – Screenshot of a table within the produced SQL database.

The GUI has been developed using WPF (Windows Presentation Foundation), which is currently Microsoft's standard GUI platform for Visual C# and desktop systems. The purpose of the GUI was to provide a user friendly platform for updating (with the latest data downloads) and querying the database. The term 'query' is often used within the context of databases and describes a piece of code which is sent to the database in order to extract a specific set of data from it. Within the current context of work, this could include retrieving data for a specific sensor and/or for a specific time frame. Figure 4.2 shows a screenshot of the GUI developed for data analysis and extraction. Data can be identified and extracted based on a series of options including one or a combination of time ranges, temperature ranges and specific sensors groups (related to the three-dimensional position of the sensor). Once selected, the user defined inputs are used to generate SQL queries which extract the necessary data from the database. The data can then be exported as a CSV file (which is compatible with all common spread-sheet software) or in a Microsoft Excel format directly.

Figure 4.2 – Screenshot of the GUI main screen providing access to the upload and interrogation facilities of the data management tool.

4.2.3 Testing

Testing was continually carried out throughout the software developments, undertaken using a step-by-step process which isolated individual developments for testing where possible. The testing undertaken falls into one of the following categories:

- *Database structure.*
- *Data integrity.*
- *Developed analysis tools.*
- *File output.*

The primary focus of the 'database structure' tests was to ensure that the download data files were correctly read and converted into representative data-tables. This was achieved by manually comparing selected values from the raw data files and the generated data-tables. In general terms, the

data structure can be conveniently thought of in tabular format consisting of a series of sensors identifications (columns) and so called 'time-stamps' (rows) which identify exactly when data was recorded. By cross-referencing values held in the raw data files with the data-tables it is possible to verify that the data structure in the data-tables is representative of the raw data files.

The 'data integrity' tests concentrated on the database functions which removed duplicated data from the database and highlighted any 'data holes'. In the context of this work, duplicated data can be identified by the previously mentioned time-stamp. As measurements are taken simultaneously at regular 15 minute intervals there should only be one set of complete readings for a given time-stamp. Duplicated data can therefore be identified if more than one piece of data exists for a single sensor for a given time-stamp. Tests were conducted by inputting manufactured data files with known duplicated data. When performing correctly, the database would remove the duplicated data leaving only one copy. Missing data (or data holes) can be identified within the database by checking that data exists for each 15 minute time interval corresponding with the data collection regime. If data for a particular time interval is missing, an error message is generated warming the user that some data appears to be missing. The regular collection regimes and time-stamp make this procedure relatively straight forward. Similar to the duplicated data test, a manufactured data file with missing data was created to test the performance of this function.

As previously discussed, the data management tool contains a series of analysis tools which essentially generate SQL queries enabling specific data to be extracted from the overall database. The tools have been previously listed in section 4.2.1. Each tool was tested on an individual basis throughout the development process. The data extracted was manually inspected to ensure that it corresponded with the user constrains input at the GUI interface. The data extracted was also cross-referenced with the master data-table to ensure that correct values, representative of the sensor(s) in question were being extracted.

Finally, a series of tests were conducted whereby a specific section of data was identified and exported as either a CSV or excel file to examine the 'file output' component. The values contained in the exported files were cross-referenced with those contained within the master data-table to ensure that the values concurred with one another.

The previously discussed tests were diligently applied throughout the database development process to ensure that the features met the requirements as set out in section 4.2.1. Through the application of the previously highlighted tests, it can be said that the data contained in the data management tool is correctly structured and that the developed features work as anticipated.

4.2.4 Problems in Development

The main problems associated with the development of the data management tool can be attributed to hardware problems encountered on site (see Chapter 3 for further details). The first notable problem was caused by an electrical dry joint which subsequently resulted in error values equal to -104.99 Celsius being reported by selected ground sensors. It is important that these values are saved and maintained in the database for completion, however for analysis purposes, it proves convenient to omit such readings as they are not representative of true ground conditions. To overcome this, additional program features were created in order to omit error values from certain analysis. This was included within the GUI via a checkbox, which allows the user to interrogate the database while omitting the error values (see Figure 4.3).

A second problem was caused by the failing of one of the mux-flux units contained within the larger multiplexer unit (see Chapter 3 for further details). The failing of this unit caused the structure of the data file to temporarily change for a 6 week period, during which time the faulty unit was being bypassed. A code modification was made to account for this change in file structure, ensuring that the database remained correct and true to the raw data for this period. After this modification extensive tests were undertaken, cross-referencing the data-file with the database values.

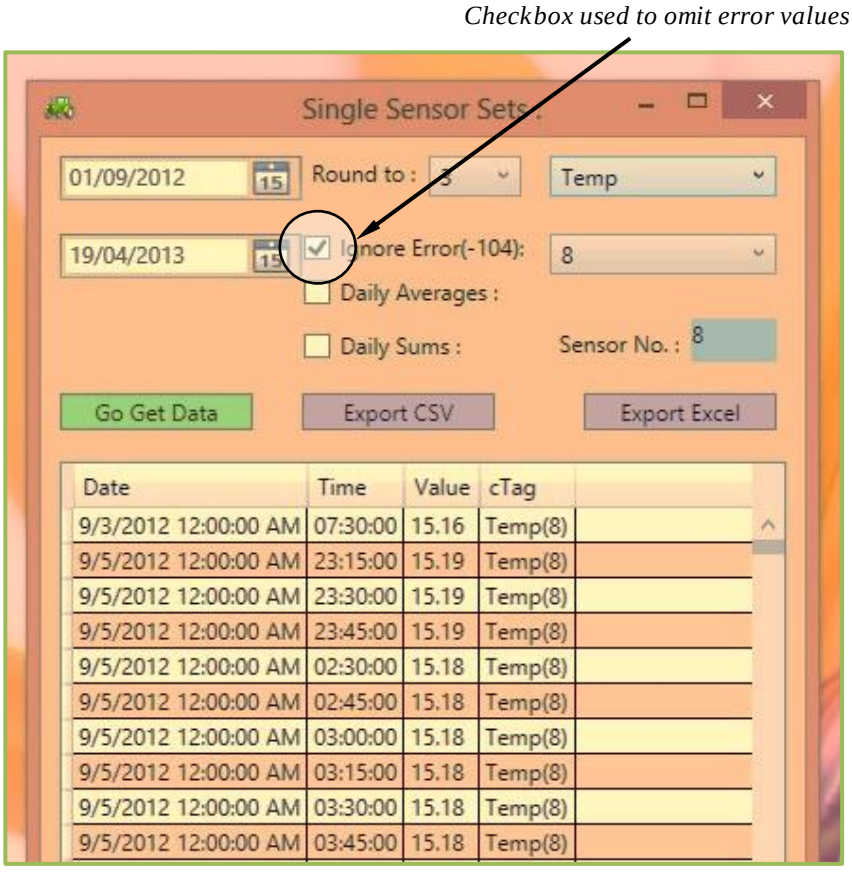

Figure 4.3 – Screenshot of the GUI used to interrogate data, including the checkbox used to omit error values.

4.3 Results: Climatic data

This section presents the climatic data recorded at the monitoring site for a 13 month period between May 2012 and June 2013. The climatic variables of solar radiation, ambient air temperature, rainfall, relative humidity and wind speed are presented in Figures 4.4, 4.5, 4.6, 4.7 and 4.8. For comparison purposes, historic climatic data has also been plotted on Figures 4.4 to 4.8. Due to availability, the source of the historic climatic data varied. Historic climate data for ambient air temperatures and rainfall are based on measurements recorded between 1981 and 2010 from a weather station located at Lyonshall, just outside Hay-on-Wye (MET Office, 2013a). On the other hand, historic climate data for wind speed and relative humidity are based on measurements recorded over a 10 year period between 2003 and 2013 from a Royal Air Force weather station located in Credenhill (Tutiempo, 2013), again just outside Hay-on-Wye. The two weather stations are located at distances of 12 and 14 km from the monitoring site respectively. Based on the proximity between the monitoring site and the weather stations, the data sets have been deemed representative of the local area.

Unlike the previously mentioned climatic data, the measurement of solar radiation is not typically included within meteorological weather stations. As a result, solar radiation is monitored at far fewer locations reducing the number of suitable data sets. An appropriate data set was eventually sourced from a monitoring station located at Queen's University, Belfast (Queen's University, Belfast, 2013). As part of research undertaken at Queen's University, solar radiation has been continually monitored since 2009. Average annual solar radiation values were calculated based on data from this period. Although it is recognised that Belfast is approximately 300 km from the monitoring site, it is worth noting that on a global scale, Belfast is on a similar latitude to the monitoring site. Latitude dictates the day length for a given location on the Earth surface and therefore plays a dominant role in dictating the amount of solar radiation being received at ground level for a given site (Revfeim, 1978).

Figure 4.4 presents the average daily radiation recorded at the monitoring site. The average daily radiation recorded at Queen's University Belfast has also being plotted. For clarity, the four years of data available from Queen's University has been plotted via a single line of best fit to represent the average daily variation.

It can be said that the average daily radiation recorded at the monitoring site is largest in the summer months and smallest in the winter months. The greatest daily average value recorded at the monitoring site was 325.9 Wm^{-2} on the May 26th 2012 whereas the smallest daily average was recorded at 3.4 Wm^{-2} on December 19th 2012. The observed variation in average daily solar radiation can be attributed to the variation in day lengths and solar declination associated with the time of year. The greatest fluctuation in the solar radiation data occurred during the summer and spring months.

These fluctuations are expectable and can be primarily attributed to changes in cloud coverage (Revfeim, 1978). In general, it can be said that the trends exhibited by the solar radiation data recorded at the monitoring site concurred with the measured data from Queen's University, Belfast.

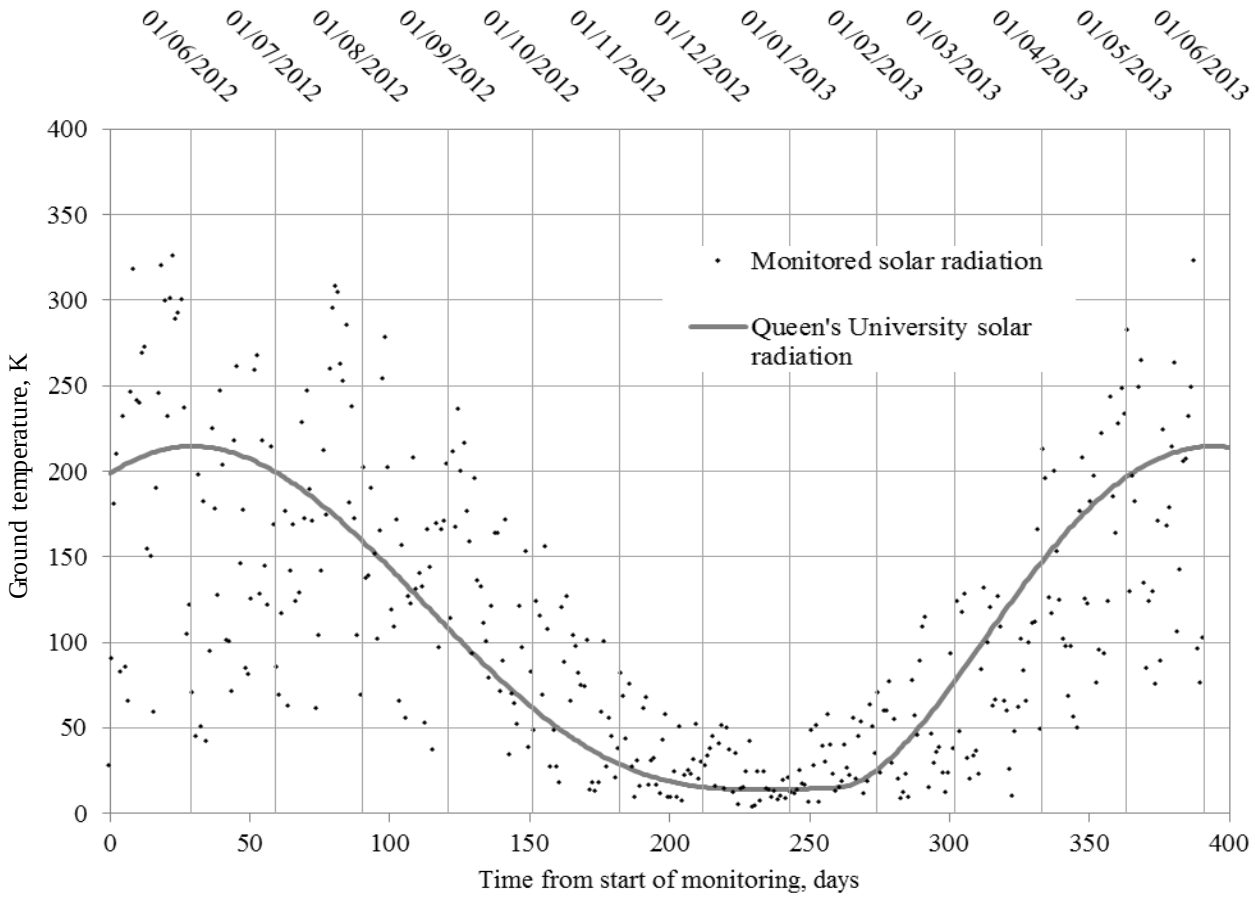

Figure 4.4 – Average daily solar radiation measured at the monitoring site between May 2012 and June 2013 and the average annual radiation recorded at Queen's University Belfast.

The mean daily ambient air temperatures measured at the monitoring site are presented in Figure 4.5 along with mean monthly ambient air temperatures according to 29 years of data recorded at the Lyonshall weather station (MET Office, 2013a). It can be said that the recorded ambient air temperatures were highest in the summer months and smallest in the winter months. The greatest mean daily ambient air temperature recorded at the monitoring site was 293.9 K on July 25th 2012, while the coolest mean temperature was recorded at 270.0 K on December 12th 2012. The temperature extremes observed at the monitoring site fall within the expected temperature range for the geographical location of the monitoring site (MET Office, 2013b).

When comparing the collected ambient air temperature data with historical records, it is possible to identify a number of differences. Firstly, there were a number of abnormally cold days between December 2012 and April 2013, 16 of which had average daily temperatures below zero Celsius. However, within this time frame there was also a 3.5 week period between December 13th and January 6th where prolonged above average air temperatures were recorded at the site. It can be said that the ambient air temperatures in the second half of February and month of March were cooler than historical records by approximately 5 K (on average). This difference can be accredited to the abnormally cold temperatures observed nationally across the UK in March 2013, representing the second coldest March since records began over 100 years ago according to the MET Office (BBC, 2013). Despite these abnormal temperature observations, it can still be said that the general trends exhibited by the recorded data concurred with the presented historical data for the area.

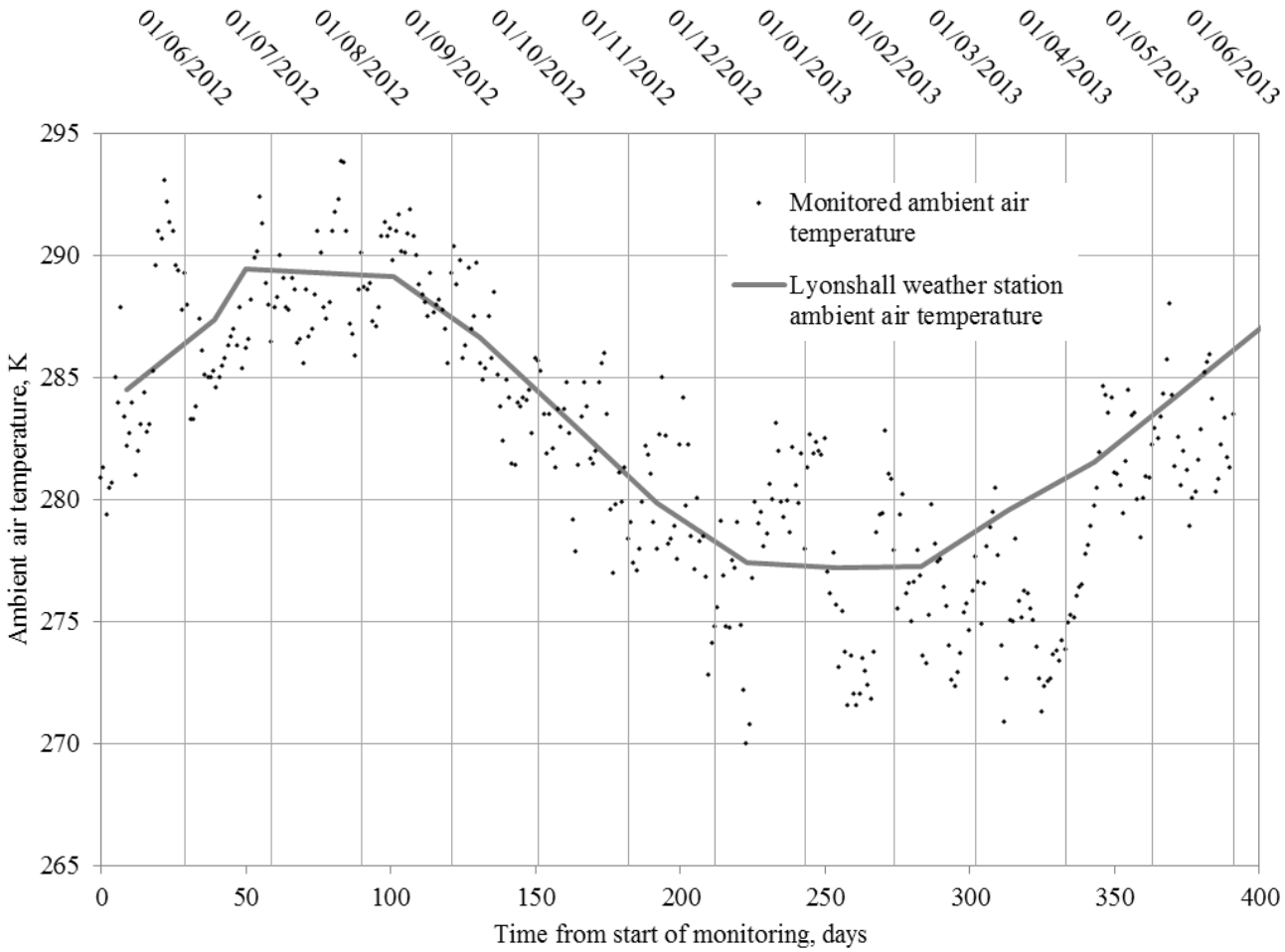

Figure 4.5 – Average daily ambient air temperature measured at the monitoring site between May 2012 and June 2013 and the average monthly ambient air temperatures recorded at Lyonshall weather station.

Figure 4.6 shows the total monthly rainfall recorded at the monitoring site throughout the inspection period. The average total monthly rainfall according to 29 years of data recorded at

Lyonshall is also plotted for comparison (MET Office, 2013a). Overall, it can be deduced from Figure 4.6 that higher precipitation levels were observed during the inspection period compared with those of previous years. In particular the months of June, August and December 2012 received higher monthly rainfalls than corresponding historical monthly averages. Although the measured rainfall was greater during these months, the values are within the recorded rainfall extremes for the region (MET Office, 2013b). On the whole, it can be said that rainfall observations generally concurred with trends exhibited by the historical data presented.

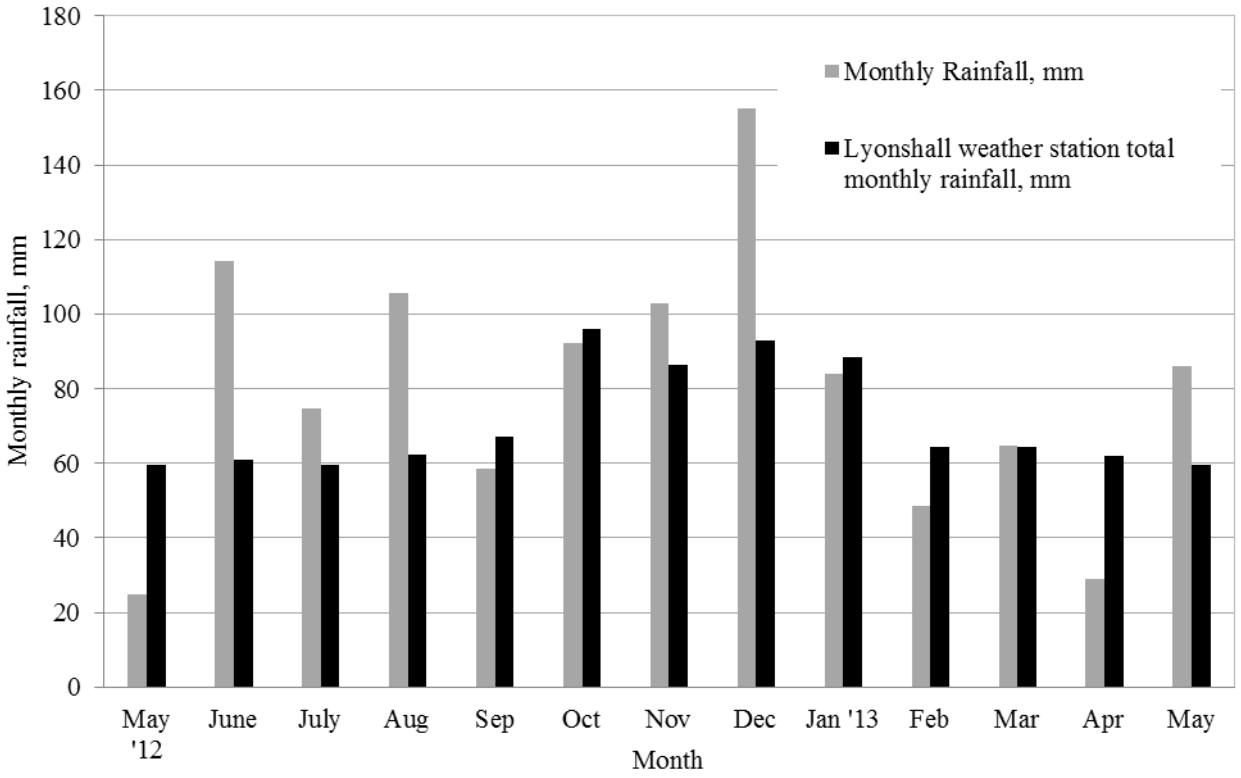

Figure 4.6 – Total monthly rainfall measured at the monitoring site between May 2012 and June 2013 and the average total monthly rainfall recorded at Credenhill weather station.

Relative humidity, by definition, is a function of the water vapour content of air relative to its content at saturation at some temperature. The saturated water content of air is a function of two factors, namely pressure and temperature therefore it can be said that relative humidity reflects a combination of environmental factors. In many cases, this can result in the relative humidity fluctuating over the course of days and even hours which is also reflected in the results presented. The relative humidity fluctuation is greatest for approximately the first 150 and last 100 days, corresponding with spring and summer months at the monitoring site. The fluctuation of the relative humidity in the winter months, between October 2012 and March 2013, was lower primarily due to the above average measurements and the upper limit of 100 per cent.

Despite humidity fluctuations, there is a general annual trend for mean daily relative humidity in the northern hemisphere and more specifically in the UK (DEFRA, 2009). In the United Kingdom, the mean daily relative humidity has been historically greatest in the winter months reaching approximately 90%, reducing to approximately 74% in mid-summer. This trend is reflected by the 10 year mean daily relative humidity measurements recorded at the Credenhill weather station. In general it can be deduced that the relative humidity measured at the monitoring site was greatest in the winter months between October 2012 and April 2013 and lowest during the spring and summer months. This general trend concurs with the historical relative humidity behaviour previously observed within the UK and at the Credenhill weather station. Despite this, there are discrepancies between the measured data from the monitoring site and historic data. It can be clearly seen from Figure 4.7 that the relative humidity between November 2012 and February 2013 is consistently above the previous ten year average by approximately 10%. The elevated relative humidity for this period can be attributed to a number of factors. The rainfall in November and December 2012 was greater than expected for this time of year by 17 and 63 mm respectively (see Figure 4.6). Increased rainfall increases the moisture in both the ground and air resulting in higher relative humidity at ground level (Thornton, et al., 2000). For the months of January and February the higher than expected relative humidity values coincided with lower than average ambient air temperatures.

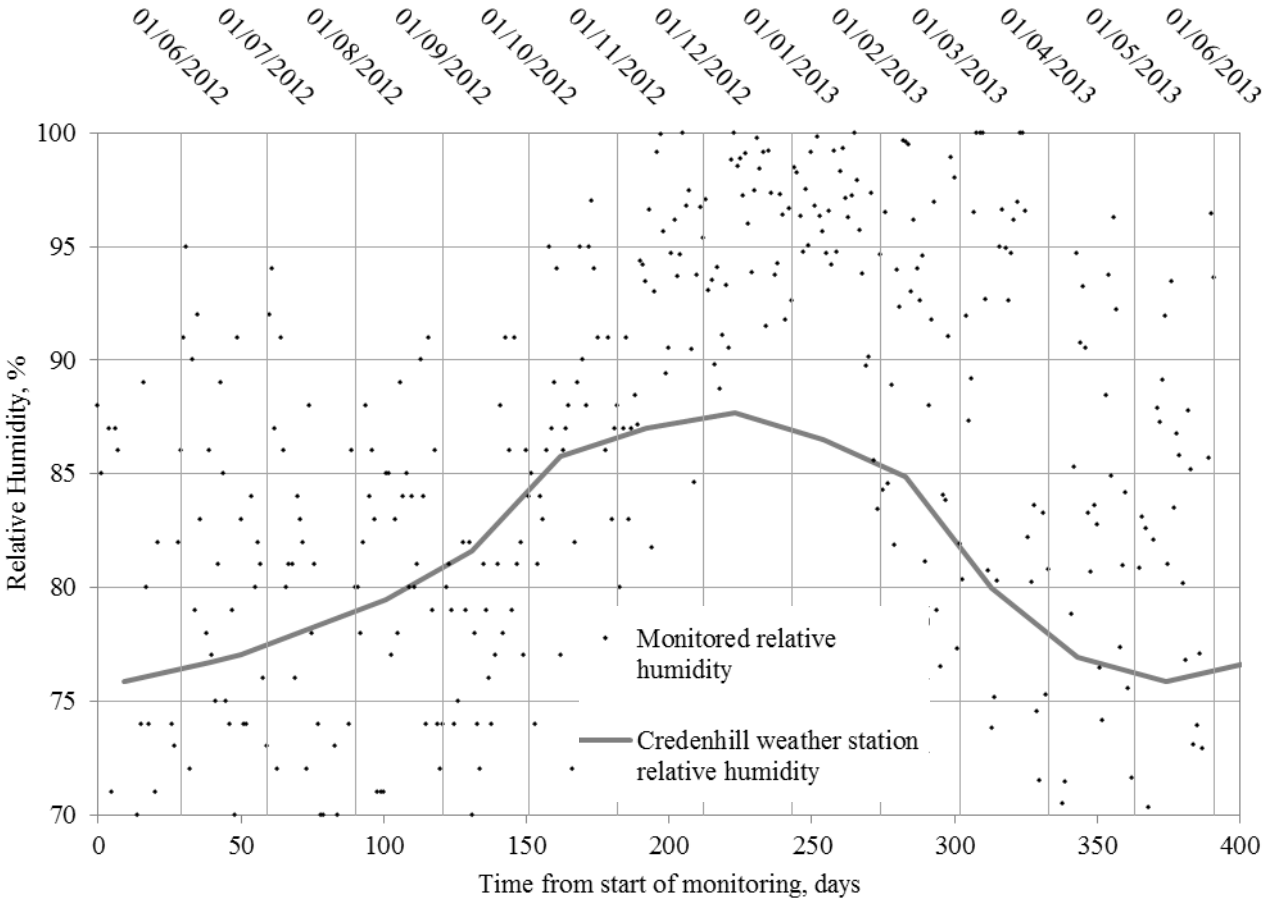

Figure 4.7 – Average daily relative humidity measured at the monitoring site between May 2012 and June 2013 and the average monthly relative humidity recorded at Credenhill weather station.

Figure 4.8 shows average daily wind speed recorded at the monitoring site throughout the inspection period. Average monthly wind speeds according to 10 years of data recorded at the Credenhill weather station (Tutiempo, 2013) have also been plotted for comparison. In general it can be said that the average daily wind speeds recorded at the monitoring site concurred with historical records for approximately the first 150 days. Beyond this initial period, the average wind speeds drop off, falling below the historical wind speeds recorded at Credenhill. Unlike the previous climatic variables presented, wind is particularly sensitive to local conditions, varying with a range of factors such as local topography and the position and size of local structures. Efforts were made during the site installation to position the anemometer away from local structures, in an open and exposed area. There is no evidence to suggest abnormal wind behaviour during the inspection period therefore the differences between the monitored and historical wind speeds can be attributed to the local topography. The monitoring site is located on a low hill and protected from the North and West which can cause a deviation in local wind speed data as depicted by the results.

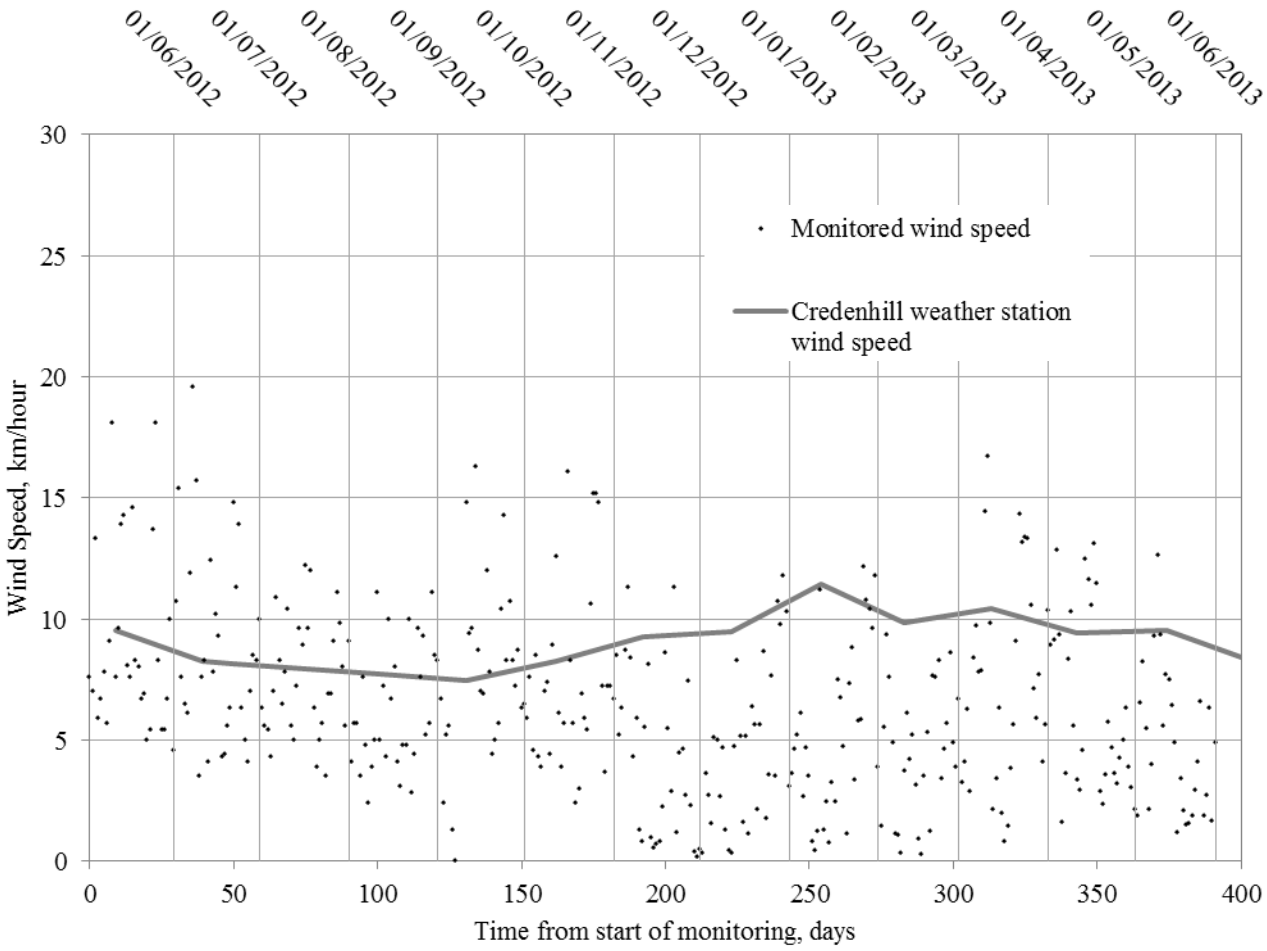

Figure 4.8 – Average daily wind speeds measured at the monitoring site between May 2012 and June 2013 and the average monthly wind speeds recorded at Credenhill weather station.

4.4 Results: Heat pump data

This section presents data collected from sensors measuring the heat pump performance at the monitoring site. For coherency with the climatic and ground data-sets, the following heat pump data is presented for a period between May 2012 and June 2013 although the heat pump was only active after September 7th 2012. As previously explained in Chapter 3, three sensors were installed to monitor the heat pump performance, measuring the fluid flow rate (within the ground-loop) and the inlet/outlet fluid temperatures to the heat pump. First, the data collected by the individual sensors at the monitoring site will be presented and discussed. Following this, the data will be collectively inspected and analysed in order to calculate the heat pump load for the inspection period.

4.4.1 Ground-loop fluid flow

Heat pumps generally adopt one of two flow regimes; either fluid is circulated regardless of whether or not heat is being extracted or fluid is only circulated as and when heat is being extracted. It can therefore be said that the ground-loop fluid flow is a function of the flow regime adopted by the heat pump (i.e. intermittent or continual flow) and the user demands on the system (i.e. heating requirements of the occupants). The heat pump installed at the monitoring site has been designed to operate an intermittent flow regime, which means fluid is only circulated through the ground-loop when the heat pump is in operation. It can therefore be said that the fluid flow, unlike the ground and climatic conditions, is subject to high rates of change varying between zero and maximum flow almost instantaneously. In order to capture this behaviour, the fluid flow is cumulatively measured over the 15 minute data intervals. Details regarding the mechanical flow meter device installed at the monitoring site have been discussed in Chapter 3. Based on the flow meter characteristics and data collection regime, the measured cumulative flow is recorded in units of litres per 15 minutes. The recorded values can be subsequently converted into a more meaningful unit for analysis purposes (i.e. litres per second). Figure 4.9 presents the average daily ground-loop flow rate measured between May 2012 and June 2013.

As fluid only flows when the heat pump is in operation, the fluid flow measurements directly correspond to system usage by the occupants (i.e. the greater the measured fluid flow, the greater the system usage). This allows the fluid data to be used as a means to inspect the operational patterns of the system.

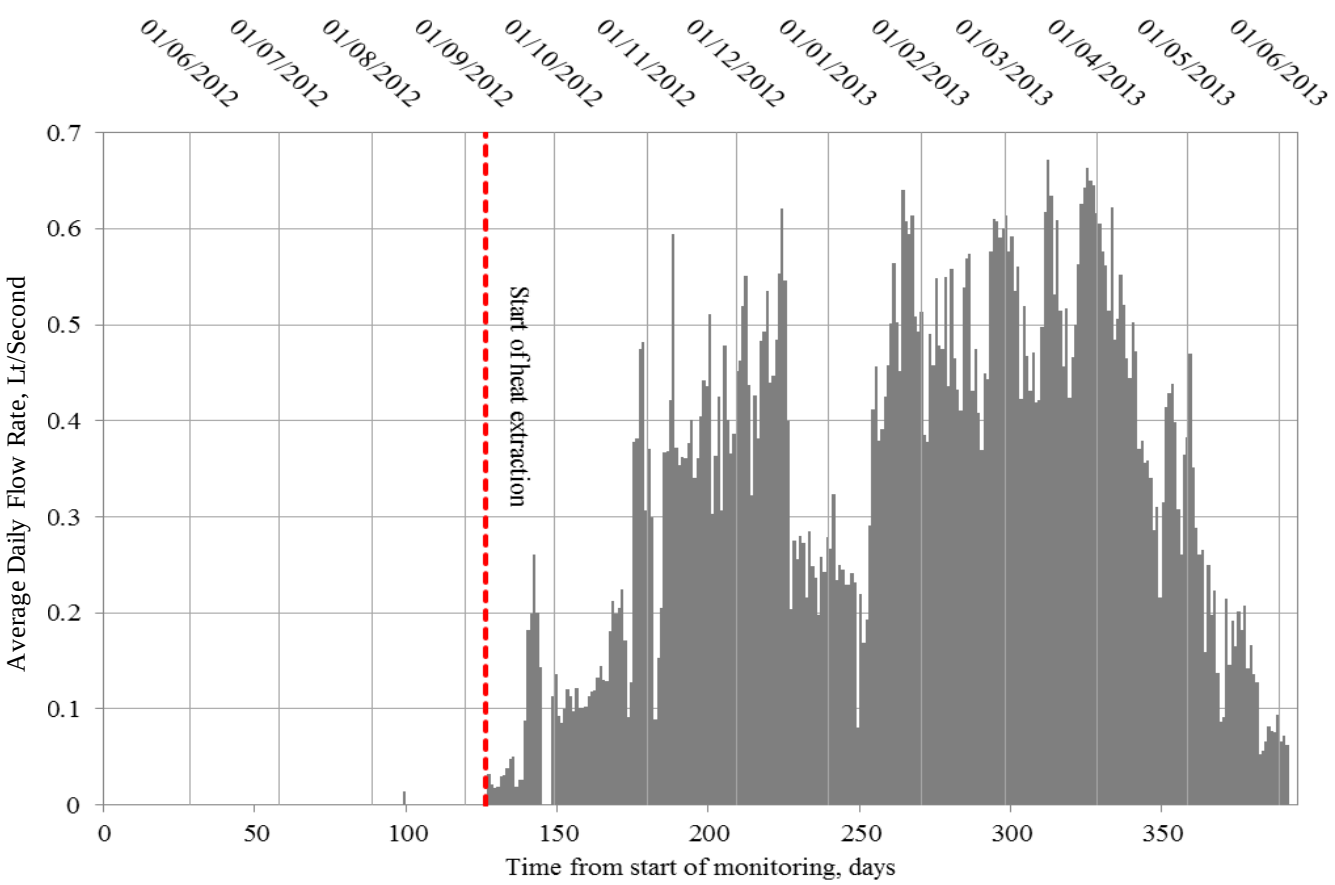

Figure 4.9 – Average daily fluid flow rate measured at the monitoring site.

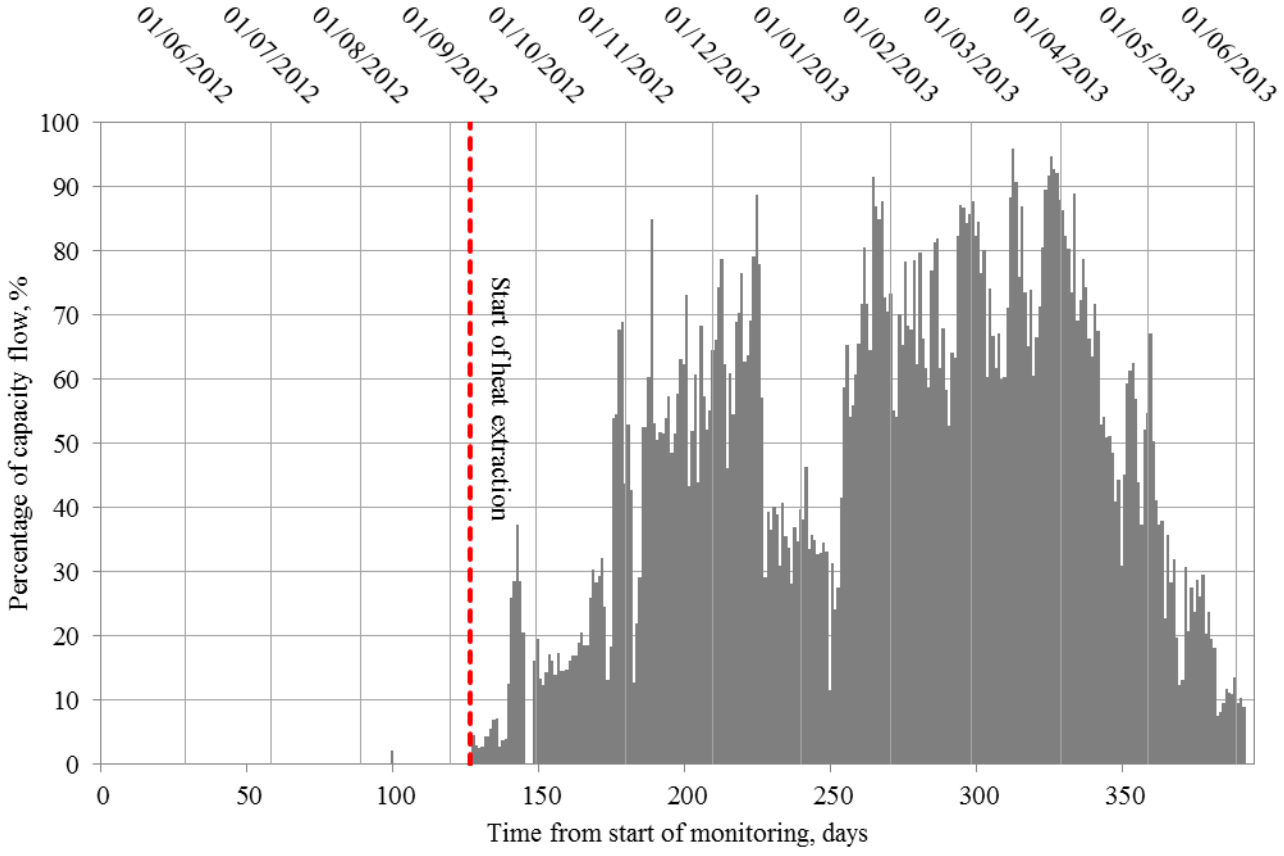

Figure 4.10 – Average daily fluid flow rate measured at the monitoring site as a percentage of the heat pump capacity

When the heat pump is active, the flow rate in the system (in accordance with the heat pump flow capacity) is equal to 2520 litres per hour or 0.7 litres per second. It can therefore be said, that if the heat pump was running continuously for an entire day the average fluid flow would also equal 0.7 litres per second. An alternative way to view the data contained in Figure 4.9, is to present the system flow as a percentage in terms of the maximum potential fluid flow for a given day. This essentially allows the system usage for a given day to be viewed in terms of the system capacity. Figure 4.10 presents the average daily flow rate measured between May 2012 and June 2013 in terms of the system capacity.

Prior to September 7th 2012, the heat pump system was not in use. Figures 4.9 and 4.10 show only one isolated period of system flow prior to September 7th on August 10th 2012. This isolated case can be attributed to a system test which was conducted by WDS Environmental, during the heat pump installation. As previously stated, the system was used for heating purposes for the first time on September 7th 2012. This is clearly reflected by the data presented in Figures 4.9 and 4.10. The mean daily fluid flow generally increased from September 7th 2012 to 13th December 2012, with one notable three day exception between 25th and 27th September where the flow was zero. This was due to a system fault, leading to the system being inactive for this three day period. The general increase in system usage directly corresponds to a decrease in external ambient air temperatures recorded for the same period (see Figure 4.5). This is the expected trend as, logically, a decrease in external air temperatures would lead to an increase of internal heating. Interestingly, beyond December 13th 2012 until 11th January 2013 there is a clear drop of in system usage with mean daily system flows dropping from a peak of 89% of system capacity on December 13th to 12% of system capacity January 7th (see Figure 4.10). The decrease in system usage directly corresponds with a prolonged period of mild weather observed at the site between mid-December and early January (see Figure 4.5). The occupants did not leave the property for an extended period of time; therefore this decrease in system usage has been directly attributed to the mild external temperatures.

Section 4.3 has already presented climatic data showing the abnormally cold weather conditions in late February and March 2013. This period of cold weather has been reflected in the Figure 4.10, with the system daily usage remaining constantly above 63% for the period between late January and early April. Beyond mid-April, the heat extraction steadily decreases, corresponding with an increase in ambient air temperatures. From the 23rd May 2013 onwards, the heat pump usage remains consistently below 10%, reflecting the rising air temperatures.

The previous fluid flow data has clearly demonstrated the close link between system usage and external air temperatures. This is compatible with the fact that a heating only system will only be in use when heating is required, reflecting the needs of the occupants which is closely dictated by external air temperature.

4.4.2 Inlet/outlet fluid temperatures

Within the current context of work, the inlet temperature corresponds to the fluid temperatures entering the heat pump from the ground-loop whereas; the outlet fluid temperature corresponds to the fluid temperature leaving the heat pump and entering the ground-loop. The heat pump inlet and outlet fluid temperatures provide important information regarding the overall system performance and allow the temperature differential across the heat pump unit to be calculated. The fluid temperature is a function of a number of system variables, notably the heating load of the heat pump, fluid flow and ground temperature. The fluid temperature data recorded for the heat pump inlet and outlet are presented in Figures 4.11 and 4.12 respectively.

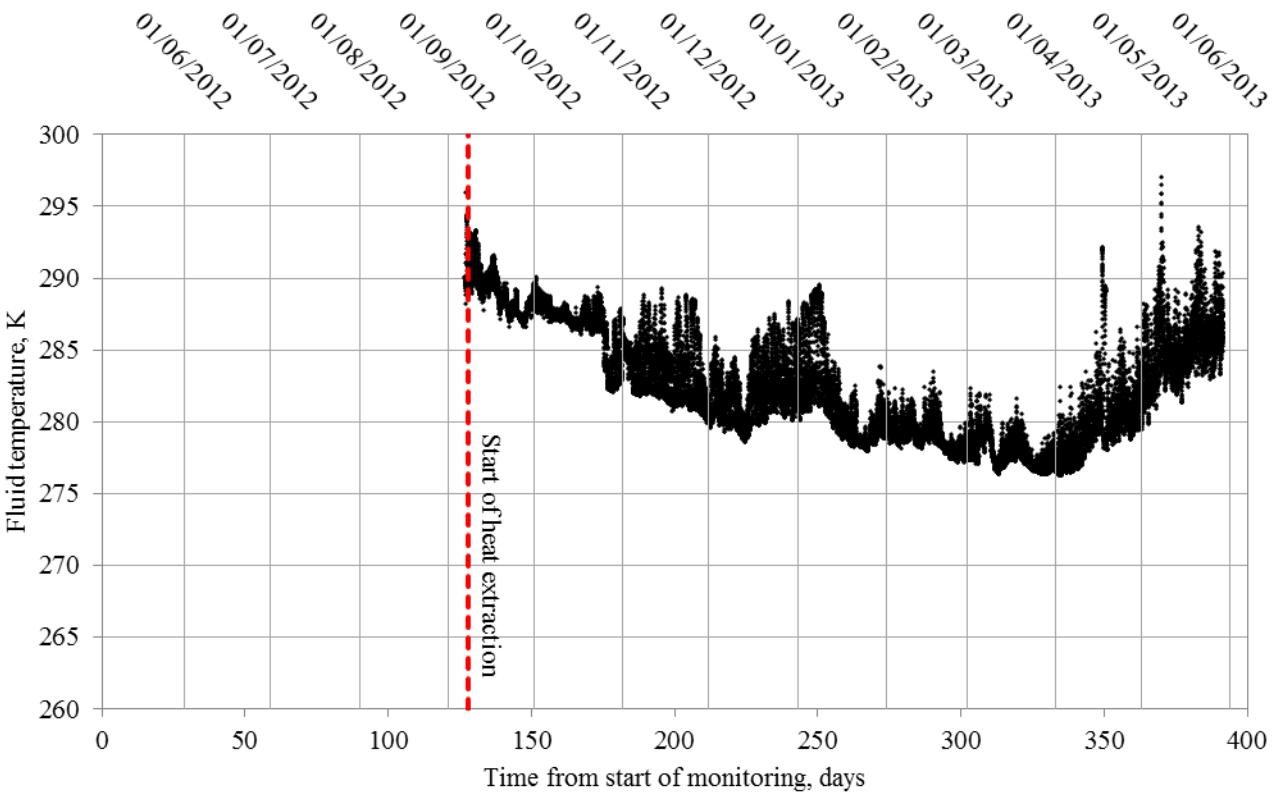

Figure 4.11 – Inlet fluid temperature measured at the monitoring site.

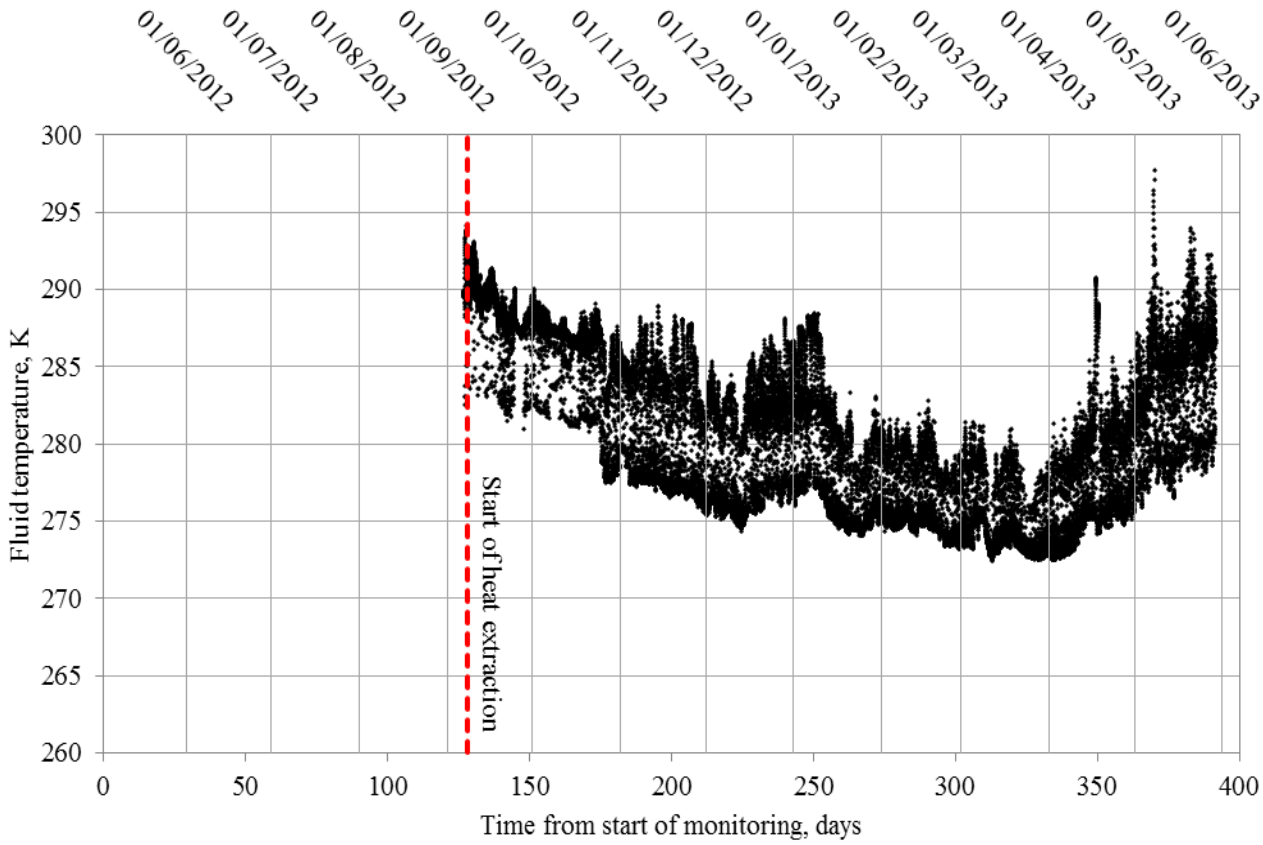

Figure 4.12 – Outlet fluid temperature measured at the monitoring site.

In general, from Figures 4.11 and 4.12 it can be said that the both the inlet and outlet fluid temperature decrease from the initiation of the system to early April 2013. The fluid temperatures appear to correlate with the system usage, previously illustrated in Figure 4.10. In general, both the inlet and outlet fluid temperatures decrease from September 7th until mid-December when there is a brief recovery period. This directly correlates to a period of reduced operational usage previously discussed in section 4.4.1 (depicted in Figure 4.10). As the operational usage increases from early January, the fluid temperatures once again continue to decrease until April 2013, beyond which the fluid temperatures increase. The behaviour exhibited demonstrates that the fluid temperatures are closely coupled with the operation loads of the system.

As previously discussed in section 4.4.1, the heat pump system installed at the monitoring site operates on an intermittent basis, only circulating fluid and extracting heat as and when required. The main limitation, with regards to the current data collection regime, is that the fluid inlet and outlet temperatures are recorded only once per 15 minutes. The fluid temperatures recorded at this single instance may either correspond to a period of heat extraction or not. Immediately after a period of heat extraction, the fluid temperatures at both the inlet and outlet of the heat pump have been subject to high rates of change. The resolution of the current data collection regime is unable to capture all of

this behaviour however; over the course of the inspection period it is possible to identify the general trends needed to examine the system. These will be discussed in more detail within the following paragraphs.

Upon inspection of Figures 4.11 and 4.12, it can be seen that the outlet fluid temperature is subject to the greatest fluctuation. The data points presented in Figure 4.12 are broadly divided into two collections. The lower of these collections, contains data points associated with periods of operational use (i.e. heat extraction). The upper collection, on the other hand, contains data points associated with periods of inactivity. The difference between the two collections of data points demonstrates the change in the outlet fluid temperature between periods of operational use. Despite the variation of measured outlet fluid temperatures, it is still possible to identify the outlet fluid temperature during periods of operation and the general trends.

In contrast, Figure 4.11 predominantly shows only a single collection of data points representing the inlet fluid temperature. This demonstrates that there is minimal change in the inlet fluid temperature between periods of operational use. Both the inlet and outlet fluid temperatures recorded during the investigatory period are below that of the plant room within which the heat pump is situated (during the winter and spring months the plant room air temperature is just below the air temperature of the main house). It can therefore be said that the cooler outlet fluid temperature has a greater temperature differential from the surroundings and therefore was subject to the greatest thermal gradient/change. The insulation used to cover the pipes is insufficient to prevent the observed fluid temperature change within the outlet pipe.

In order to investigate the fluid temperature differential across heat pump unit, Figure 4.13 has been produced. Similar to Figure 4.12, the data points can be predominantly divided into two collections. For clarity, Figure 4.13 has been annotated, showing the so-called upper and lower data collections. The upper data collection contains data points which represent the greatest temperature differential across the heat pump. It can therefore be deduced that these data points represent the fluid temperature differential at times of operation. In contrast to this, it can be deduced that the so called lower collection of data points represent the fluid temperature differential at times of inactivity. The data points located in between the upper and lower collections of data points are believed to represent fluid temperature differentials recorded in the instances just after heat pump operation has ceased.

Considering only the upper data collection in Figure 4.13, it can be said the fluid temperature difference during periods of operation reduced from approximately 5.5 K in early September 2012 to approximately 4 Kelvin in February 2013. The temperature difference begins to plateau out at this stage, settling at a temperature differential of approximately 4 K before once again increasing to approximately 5 K beyond April 2013. The variation in the fluid temperature difference can be attributed to varying ground temperatures and operational usage. Considering the current data-set,

this would logically make sense as an increase ground temperature would increase the inlet fluid temperatures while a reduction in operational usage would prevent the system from reaching a steady state.

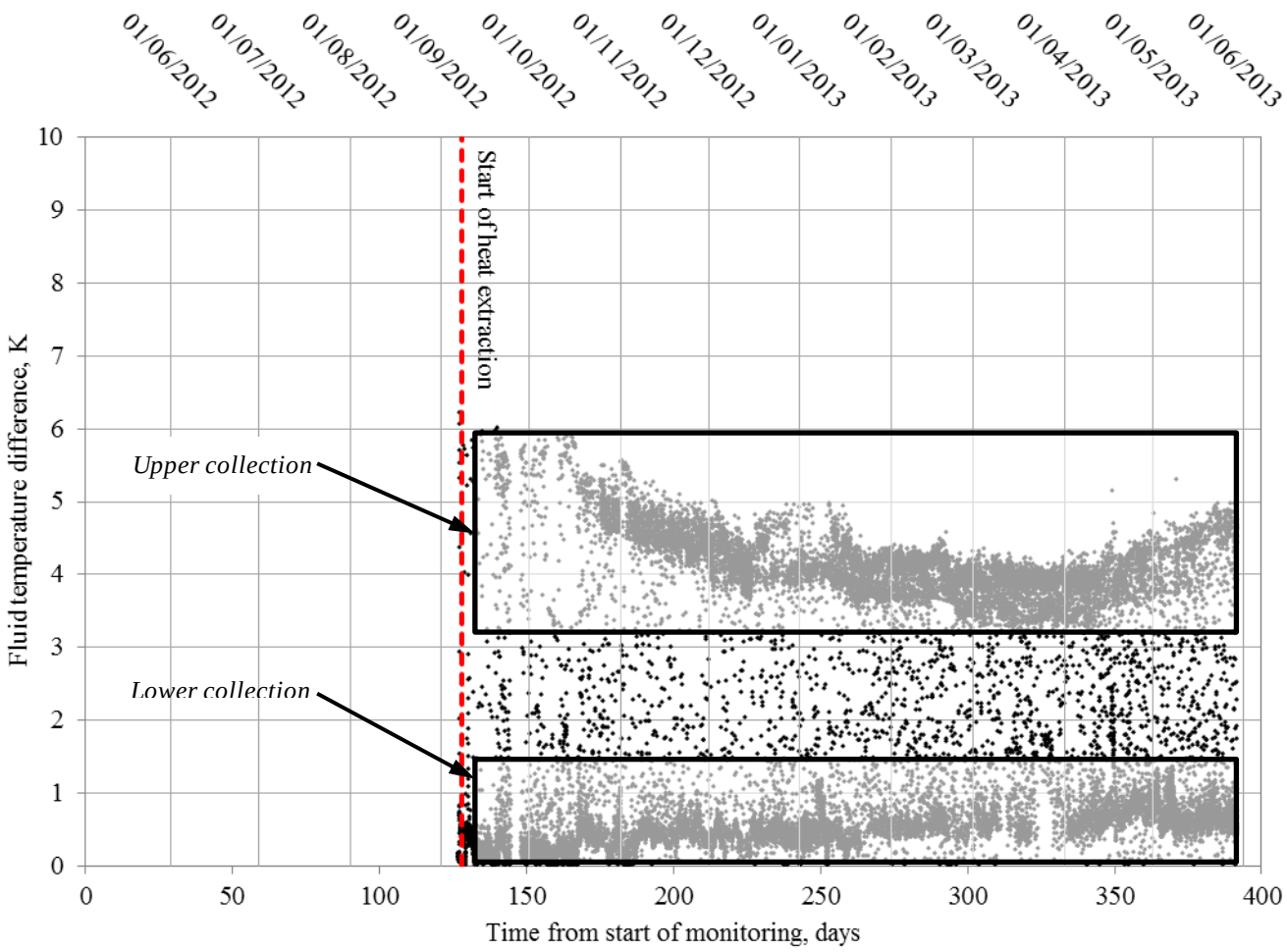

Figure 4.13 – Fluid temperature difference measured across the heat pump at the monitoring site.

4.4.3 Heat load

In order to analyse the behaviour of the overall ground source heat system, it is essential that the total heat exchanged via the ground-loop is obtained. The total heat being exchanged at a particular time (referred to as the heat load) can be calculated using knowledge of the circulating fluid's specific heat capacity, flow rate and temperature difference across the heat pump. Upon inspection of the previously presented flow and fluid temperature data for the inspection period, it can be seen that the heat load is a transient system parameter which varies with time. The mathematical procedure used to calculate the system heat loads is presented in Equations 4.1 and 4.2.

$$W = \Delta T . C_p . \dot{m} \quad (4.1)$$

where:

$$\Delta T = T_{inlet} - T_{oulett} \quad (4.2)$$

where W is the system thermal energy load (or heat load) $(J\ s^{-1})$, C_p is the specific heat capacity of the circulating fluid $(J\ kg^{-1}\ K^{-1})$, $\dot{m}$ is the mass flow rate of the circulating fluid $(kg\ s^{-1})$, T_{inlet} is the fluid temperature entering the heat pump *(K)* and T_{outlet} is the fluid temperature leaving the heat pump *(K)*.

By applying Equations 4.1 and 4.2 it is possible to calculate the system heat load for the inspection period between May 2012 and June 2013. Figure 4.14 presents the average daily heat load of the ground source heat system at the monitoring site according to the recorded fluid flow and inlet/outlet temperatures.

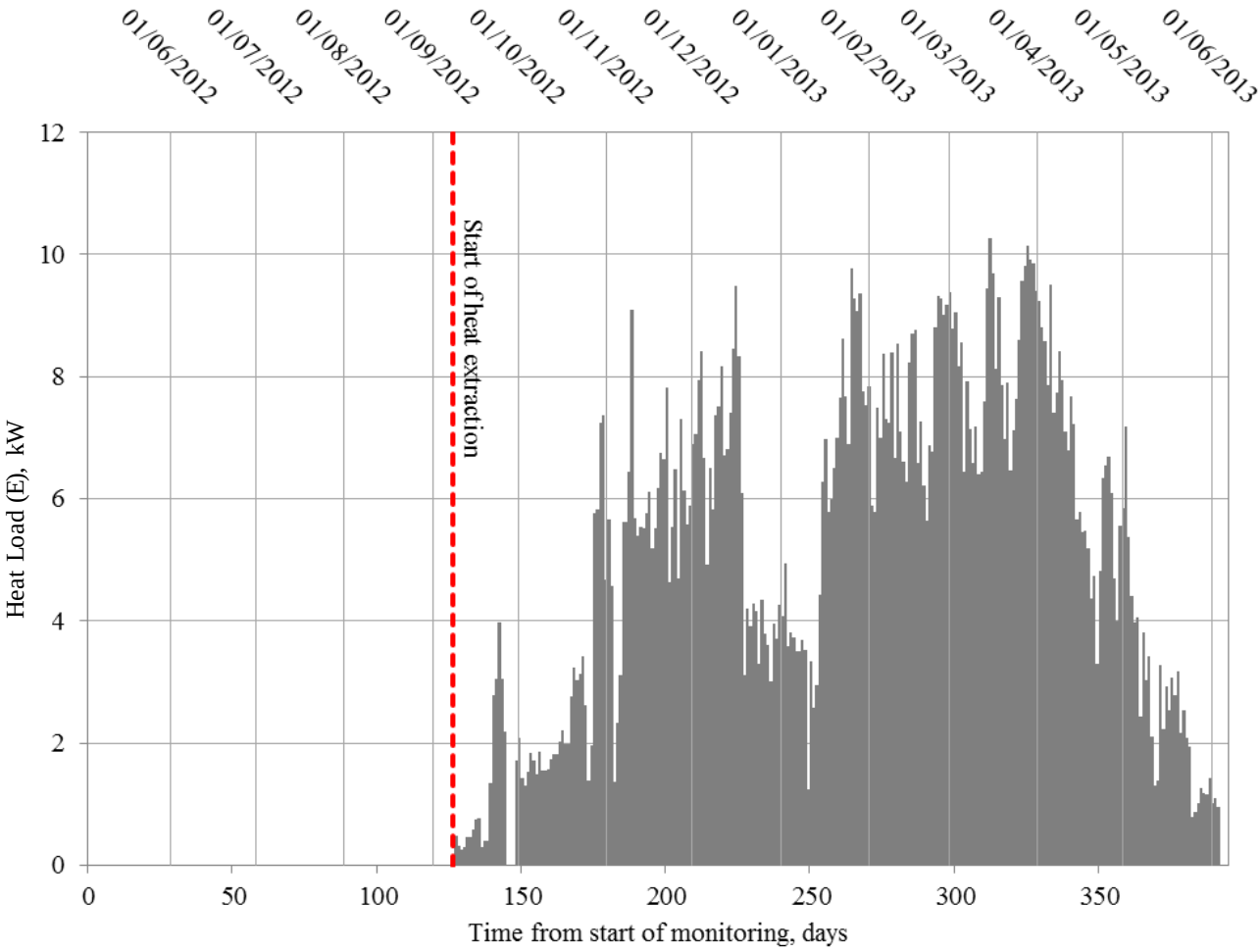

Figure 4.14 – Calculated daily heating load based upon the recorded fluid flow and fluid temperatures at the monitoring site.

Comparisons between Figure 4.14 and 4.10 reveal that the shape of the heat load profile is closely coupled with the flow characteristics measured at the monitoring site. Mathematically, both the system fluid flow and fluid temperature differential will have an impact on the calculated heating load. In this particular instance, the fluid flow has a far greater impact on the heat load profile due to the fact that the fluid flow varies considerably more than the measured temperature differential over the monitoring period.

Similar to the fluid flow, there is no heating load prior to September 7th 2012 when the system was turned on for the first time. After this day, the heating loads exerted by the ground source heat system increased, corresponding with the decreasing external air temperatures presented in Figure 4.5. On the whole, the average daily heating load of the system remained predominantly above 6 kW from November through to the end of April, with the exception of one 3.5 week period from mid-December onwards. This period coincides with measured mid-air temperatures, previously discussed within section 4.4.1. The greatest average daily heat load was recorded to be 10.27 kW on March 11th 2013. As expected, beyond April, the heating load of the system significantly reduced, in response to the increasing ambient air temperatures. In summary, the heating load profile is closely coupled with the operational usage of the system and therefore also the external ambient air temperature.

4.5 Results: Ground temperature data

This section presents ground temperature data collected from the 112 thermistors installed at the monitoring site. As described in Chapter 3, a small proportion of the thermistors (9 of the 112) were found to have failed post installation. The data-set resulting from the working ground thermistors is far greater in size than the climatic and heat pump data previously presented. In order to facilitate a precise discussion only salient ground temperature data will be presented here for analysis purposes and discussion, although a complete set of temperature evolution graphs for the working thermistors can be found within Appendix D. The following section presents the ground temperature data using two graphical methods: *i) temperature evolution plots (i.e. temperature data plotted with time)* and *ii) contour plots showing two-dimensional ground temperature distributions*.

4.5.1 Ground temperature evolution plots with time

The following pages contain a series of plots which present ground temperature data recorded at the monitoring site between May 2012 and June 2013. As previously discussed, it proves impractical to present data from all 103 working ground thermistors; therefore only selected graphs

will be presented here for discussion purposes. The following plots can be broadly divided into four sections. First, a plot comparing raw ground temperature data and average daily ground temperature data will be presented in section 4.5.1.1. Following this, plots showing undisturbed ground temperature data will be examined in section 4.5.1.2. Thirdly, section 4.5.1.3 presents the ground temperature changes immediately adjacent to the ground-loop. Finally, the temperature evolution plots for selected thermistors in conjunction with the calculated heat loads are presented and discussed in section 4.5.1.4.

4.5.1.1 Ground temperature and average daily ground temperature data

Figures 4.15 and 4.16 present raw and average daily ground temperature data for two thermistors located in detailed cross-section AA (labelled AB4 and AB8 in Appendix D). One of the thermistors (AB4) is located immediately adjacent to the ground-loop while the second (AB8) is located at a vertical displacement of approximately 0.5 meters above the ground-loop.

Upon general inspection of Figure 4.15 and 4.16, it can be deduced that the raw and average daily ground data concur with one another, particularly in the period prior to heat extraction. Beyond the initial heat extraction, the raw temperature data presented in Figure 4.15 begins to exhibit fluctuations. This is due to two factors, namely; the cyclic operation of the heat pump and the resolution of the data collection. The 15 minute time intervals adopted for the data collection recorded a mixture of ground temperatures associated with period or heat extraction and inactivity (i.e. cyclic operational usage). The fluctuations observed in the raw temperature data represent the fluctuating ground temperatures associated with the cyclic loading. The average daily ground data was unable to capture these fluctuations due to the coarser (daily) resolution; however, the general trends are still reflected. In contrast to Figure 4.15, the raw temperature data presented in Figure 4.16 contains no fluctuations due to the greater displacement from the ground-loop. In this case, the raw and average daily data sets closely resemble one-another throughout the entire inspection period. It is worth noting that only thermistors located immediately adjacent to the ground-loop exhibited fluctuations while the majority of thermistors included within the monitoring scheme exhibited no such behaviour.

Upon further inspection of Figures 4.15 and 4.16, it can be said there are two groupings of apparent anomalies in the raw data. The first of these periods spans between June 2012 and September 2012 with the second period occurring in January 2013. Between June 2012 and September 2012, there was an electrical dry joint located in the multi-plexer unit which led to anomalies being recorded. Similarly, in January 2013 there was a fault with a mux-flux unit which caused similar anomalies and three day data gap in some on the ground thermistors. Further details

regarding the nature of these two hardware faults and how they were resolved can be found in Chapter 3. Despite the rogue data, it is still possible to interpolate a realistic ground temperature based on the overall trends exhibited by the surrounding data points. It is worth noting that the two thermistors (i.e. AB4 and AB8) were selected because the data they recorded clearly exhibited the data anomalies. In many of the remaining thermistors, the extent of the anomalies was significantly reduced.

In summary it can be concluded that the average daily ground temperatures are capable of representing the long-term ground behaviour and trends. Hardware faults caused a number of data anomalies over the 13 month monitoring period, although it is still possible to identify the a representative ground temperature based on the good data for these periods. Further discussions regarding the nature of the temperature changes with time can be found in section 4.5.1.4.

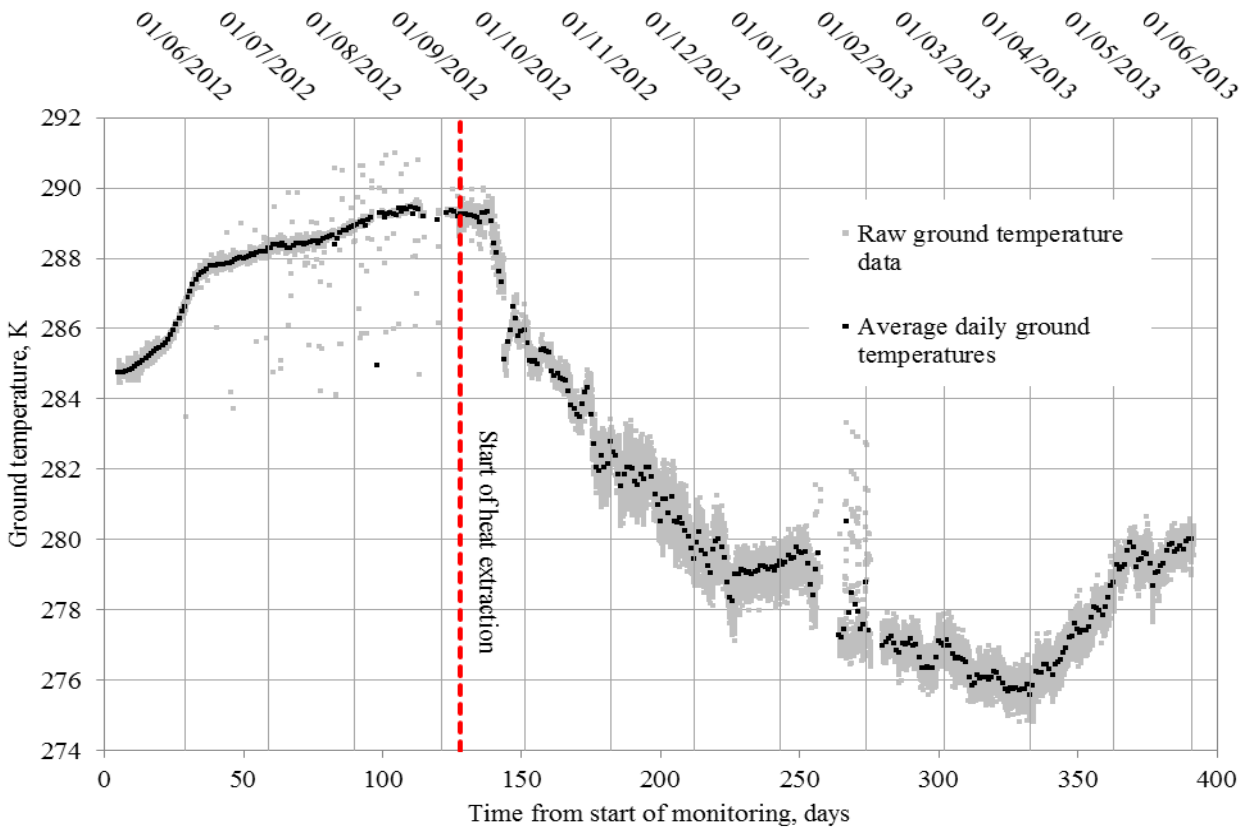

Figure 4.15 – Raw and average daily ground temperature data for thermistor AB4 located immediately adjacent to the ground-loop in detailed cross-section AA.

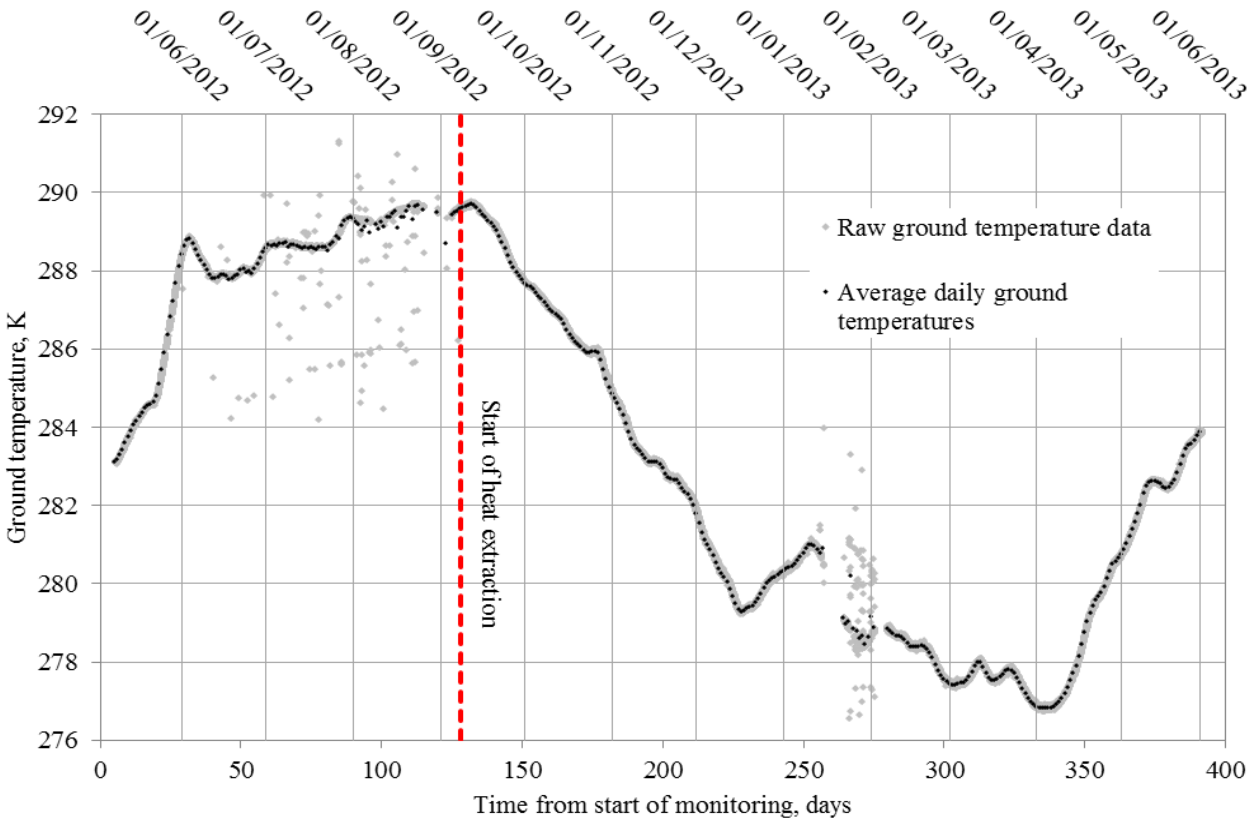

Figure 4.16 – Raw and average daily ground temperature data for thermistor (AB8) located approximately 0.5 meters above the ground-loop in detailed cross-section AA.

4.5.1.2 Undisturbed ground temperature

In the context of this discussion, the term 'undisturbed' refers to ground beyond the thermal influence of the ground-loop. It is possible to consider ground thermal behaviour in the undisturbed region as a function of seasonal climatic variations and ground properties (Kusuda & Achenbach, 1965). As part of the monitoring scheme, a collection of four thermistors were positioned within each of the detailed cross-sections (denoted AA and BB) in order to measure the undisturbed ground temperatures. Further details regarding exact spatial position of these thermistors and the detailed cross-sections AA and BB can be found in Chapter 3. The thermistors measuring undisturbed temperatures varied in depth between 0.75 and 2.6 meters beneath the ground surface. Figures 4.17 and 4.18 show the undisturbed ground temperatures measured at detailed cross-section AA and BB for the current inspection period.

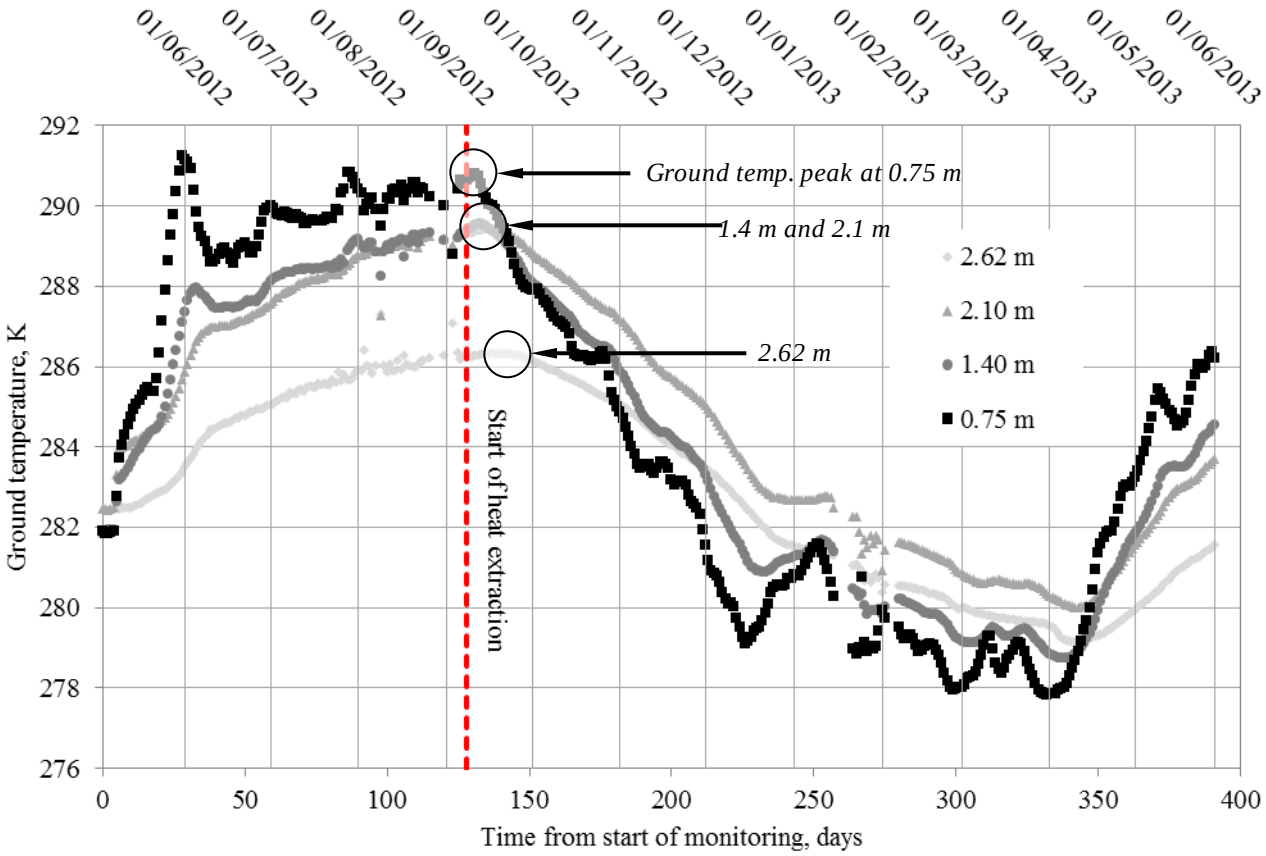

Figure 4.17 – Far-field ground temperatures measured at detailed cross-section AA.

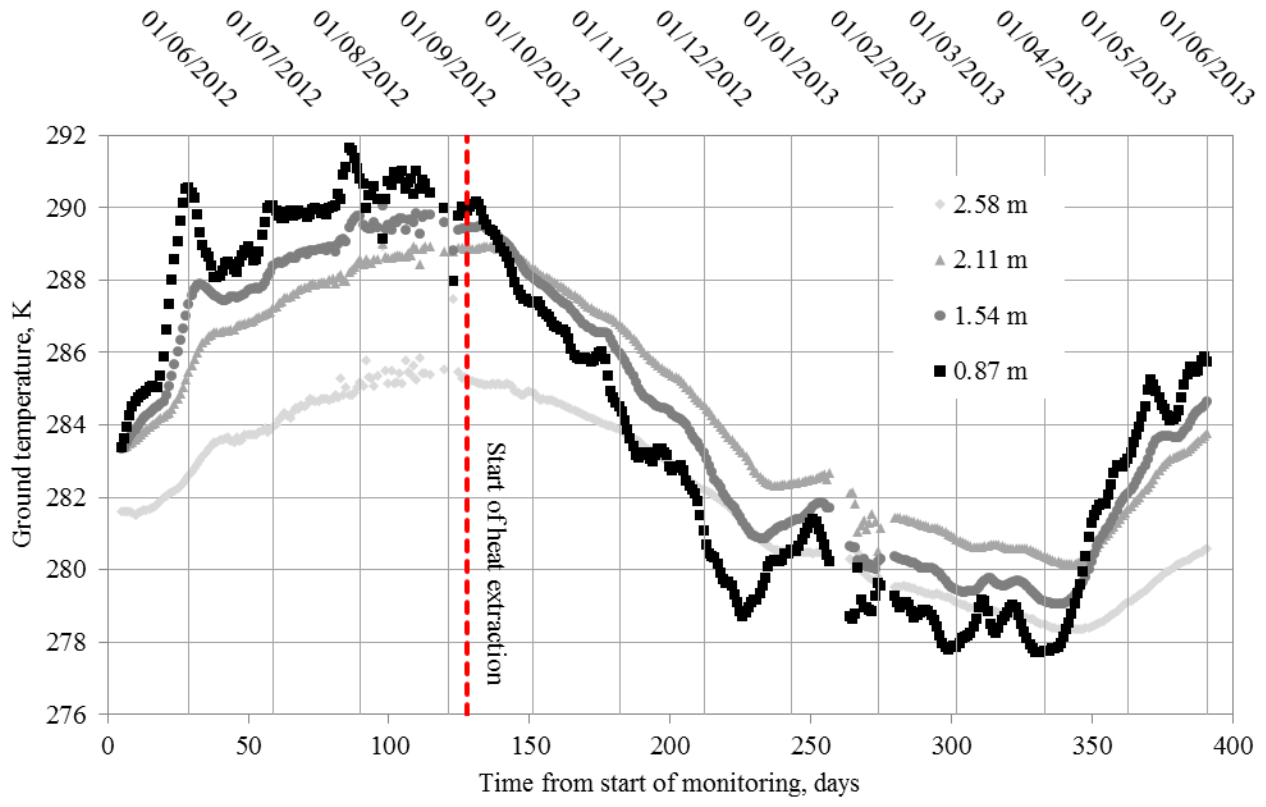

Figure 4.18 – Far-field ground temperatures measured at detailed cross-section BB.

The efficiency of ground source heat extraction depends on a number of factors, one being the seasonal undisturbed ground temperatures. The temperature of the ground surrounding the ground-loop, will in part, dictate how much thermal energy can be efficiently extracted by systems.

The thirteen month inspection period presented in Figures 4.17 and 4.18 is long enough to capture a single annual ground temperature cycle. Upon the collective inspection of the figures, it is possible to identify a number of seasonal ground temperature trends common to both detailed cross-sections AA and BB. In both cases, the ground temperature range across the four thermistors is largest in late summer (approximately mid-August) and smallest mid-spring (approximately April). For example, in Figure 4.17 the range across the four thermistors corresponding to mid-August is 4.5 K whereas, in early April the temperature range is 2.5 K. The ground temperature fluctuations are most evident in data collected from thermistors located closest to the ground surface. As the depth increases the fluctuations appear to decrease. At depths of 2.62 and 2.58 meters, only the general annual trends are evident and there are minimal signs of the local fluctuations which are visible at the shallower depths.

When inspecting the individual thermistor temperature evolutions it can be deduced that the thermistor located closest to the ground surface exhibited the greatest temperature range, recording both the highest and lowest ground temperatures over the inspection period. Figure 4.17 shows that at a depth of 0.75 meters the ground temperature variation throughout the inspection period is 13.4 K, whereas in Figure 4.18 the variation at a depth of 0.87 meters is 13.8 K. It can be said that as the thermistor depth increases, the corresponding temperature range over the inspection period decreased. This trend is most evident when considering the deepest thermistors located at depths of 2.62 and 2.58 meters where the temperature range was 7.5 K and 7.2 K respectively.

It has been shown that the undisturbed ground temperature within the shallow geological depths (i.e. less than 15 meters in depth) is a function of climatic conditions and ground properties (Kusuda & Achenbach, 1965). For further analysis, the ground data presented in Figures 4.17 and 4.18 can be compared with ambient air temperatures recorded at the monitoring site. Comparisons between the ground data and ambient air temperatures presented in Figure 4.5 reveal that the annual ground temperature trends exhibited directly correspond to the annual ambient air temperature changes. As expected, this is most evident in the data recorded by the shallowest thermistors located at depths of 0.75 and 0.87 meters. At deeper locations, the ambient air temperatures are reflected in the ground temperature trends although the effects are dampened and subject to an apparent lag period. For convenience, this lagging effect has been highlighted in Figure 4.17 by identifying the summer ground temperature peaks (i.e. the point at which ground temperatures begins generally decrease due to the onset of winter) for each of the four thermistors. By inspecting the position of the curve peaks it is possible to highlight the lagging effect at various depths in the soil. It can be said

that the lag time between the seasonal temperature change and ground temperature increases with depth.

The preceding points have demonstrated the theory previously presented by Kusuda & Achenbach (1965) and Nofziger (2003); namely, that ground temperature variation is a function of climatic conditions and the influence of seasonal variations diminish with ground depth. From a ground source heat perspective, an understanding of the undisturbed ground temperature behaviour can be applied to optimise system performance, making use of the most favourable ground-loop depths with respect to temperature. The current design standards endorsed by the UK government greatly simplify the impact of undisturbed ground temperatures on system design. Within the current design process, the undisturbed ground temperature is only considered via design tables which specify the maximum permissible ground-loop flux for a given region between the depths of 0.8 and 1.2 meters (MIS, 3005). Not only does this fail to recognise local geological changes but it also fails to consider ground-loops laid at a depth greater than 1.2 meters. The undisturbed data presented in Figures 4.17 and 4.18 suggest that in the current case a ground-loop laid at a 2 meter depth would benefit from winter ground temperatures approximately 1 – 2 K greater than a ground-loop laid at a depth of 1.2 meters.

4.5.1.3 Ground temperature changes adjacent to the ground-loop

The circulatory fluid is the sole mechanism used to transfer the heat from the ground to the point of extraction. This process results in a variation in fluid temperature along the length of the ground-loop. Previous research within the ground source heat topic area has referred to this variation in fluid temperature as the so called 'fluid temperature profile' (He, 2012). The following analysis aims to identify whether the fluid temperature variation has any observable impact on the thermal behaviour of ground located in close proximity to the ground-loop.

By comparing the ground temperature data collected by thermistors located immediately adjacent to the ground-loop it is possible to deduce whether the varying fluid temperature within the ground-loop has had any impact on ground temperature behaviour. Figure 4.19 is a plan schematic showing the location of the thermistors positioned immediately adjacent to the ground-loop. Figure 4.20 shows the ground temperature data recorded by these thermistors over the monitoring period. Temperature plots have been coloured such that the graded blue lines correspond to thermistors on the cool leg of the ground-loop while the graded red lines correspond to thermistors on the warm-leg of the ground-loop (see Figure 4.19).

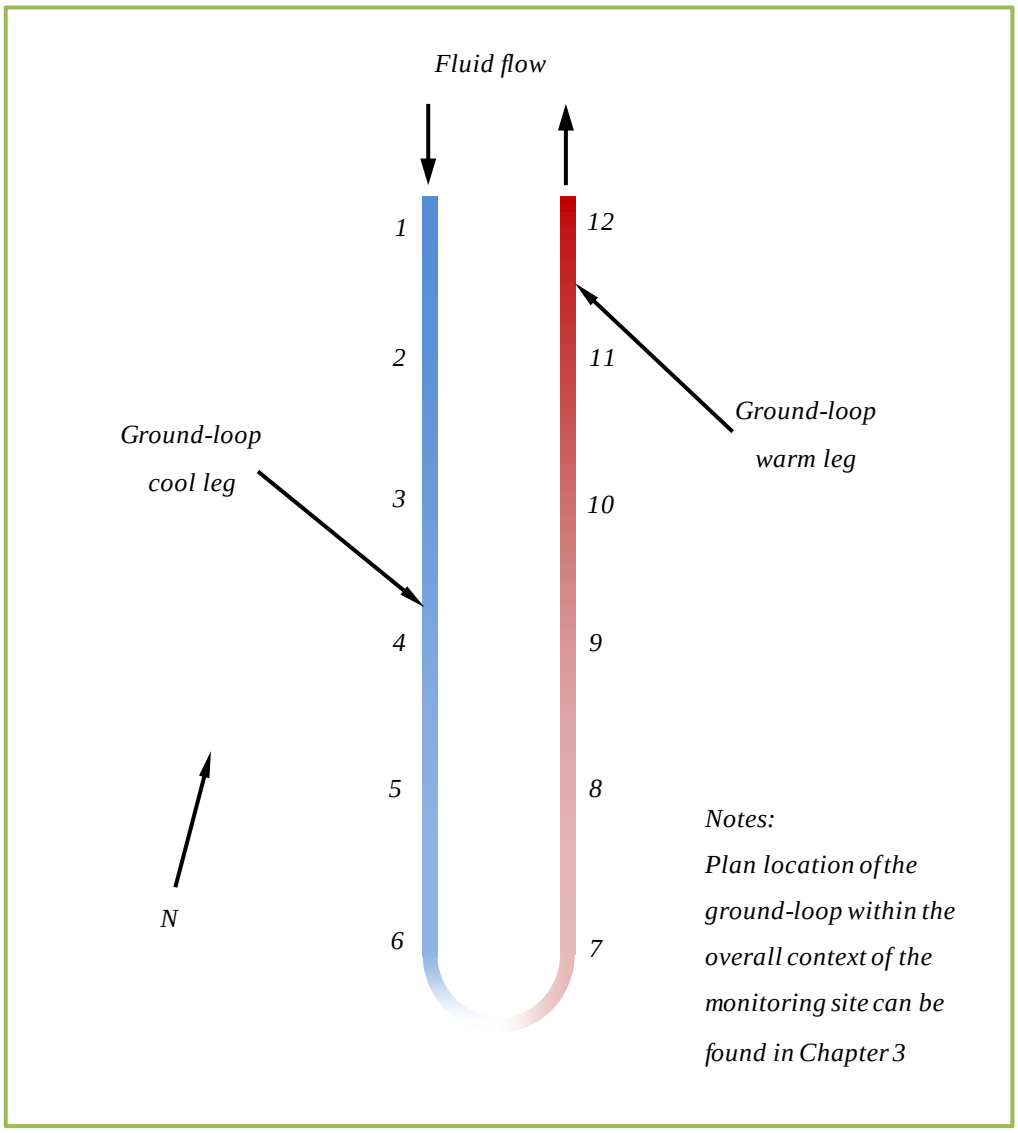

Figure 4.19 – Schematic diagram providing the locations of the thermistors presented in Figure 4.20 and used to investigate the ground temperatures immediately adjacent to the ground-loop.

From Figure 4.20 it can be said that the ground temperature trends, exhibited at all twelve locations, are on the whole very similar. Ground temperatures generally increased until September 7th, beyond which the ground temperature at all locations started to decrease. This change in behaviour directly coincided with the initiation of heat extraction (highlighted in Figure 4.20 with a dashed line). All twelve thermistors were positioned such that they were in direct contact with the ground-loop, thereby measuring the ground temperature immediately surrounding the ground-loop surface. The sudden change in ground behaviour, coinciding with the system initiation was therefore expected. It is noted that the general decrease in ground temperatures beyond September 7th can be attributed to both heat extraction and seasonal variations. It is possible to evaluate the ground temperature difference due to heat extraction alone by comparing the presented data with undisturbed ground measurements. This comparison will be the focus of future analysis in section 4.5.1.4.

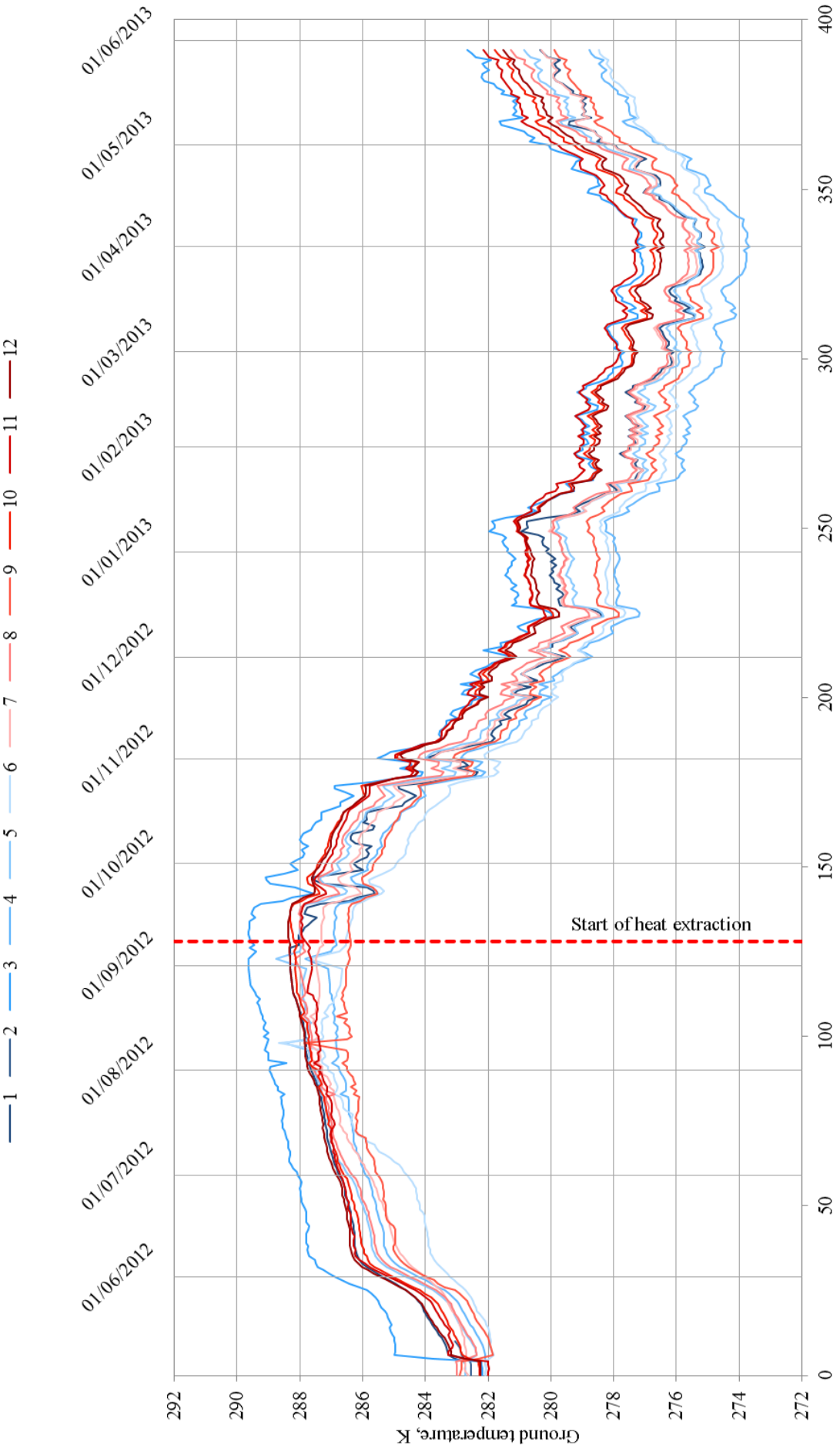

Figure 4.20– Temperature evolution plots for the thermistors located immediately adjacent to the ground-loop.

In general, the trend lines presented in Figure 4.20 exhibited similar temperature fluctuations, especially beyond September 7th. In order to investigate the potential source of fluctuations, the data contained in Figure 4.20 was cross-referenced with the recorded ambient air temperature (Figure 4.5) and calculated heat load profile (Figure 4.14) for the inspection period. From these comparisons, it was possible to deduce that fluctuations directly corresponded to heat load profile and not the ambient air temperature. This would be the expected outcome due to the proximity of the thermistors to the ground-loop surface.

Prior to September 7th no obvious relationship can be observed between the ground-loop position and ground temperatures. After September 7th, a weak relationship between measured ground temperatures and ground-loop position can be deduced. Figure 4.20 shows that the measured ground temperatures in close proximity to the warm leg of the ground-loop (red lines on Figure 4.20) are in general greater than those measured in close proximity to the cool leg (blue lines on Figure 4.20). For a heating system, the fluid entering the so called cool leg of the ground-loop (depicted in Figure 4.19) is theoretically cooler than the fluid leaving the so called warm leg. In a heat conduction dominated system, this would logically result in lower ground temperatures around the cool leg of the ground-loop and visa-versa due to the induced thermal gradients. It can therefore be said that the weak correlation observed concurs with the theory.

All twelve thermistors were buried at similar depths, therefore prior to heat extraction it is expected that the temperature recorded by the thermistors would be similar. On the other hand, after heat extraction, ground temperature adjacent to the ground-loop would no longer be a function of depth alone but also the corresponding ground-loop temperature. By inspecting the ground temperature range both before and after heat extraction, it is possible to identify the impact (if any) of heat extraction on the observed ground temperature range. On April 1st, the temperature range across the twelve trend lines is approximately 3.5 K, with eight of the trend lines separated by less than 2.0 K. Prior to heat extraction, on September 6th 2012, the temperature range across the twelve trend lines was 3.0 K, with elven of the twelve thermistors separated by 1.9 K. The variation in ground temperature prior to heat extraction can be attributed to a number of factors, although ground heterogeneities have been identified as the most likely cause. By comparing the two ground temperature ranges it can be deduced that the change induced by heat extraction is relatively small.

Although the ground temperature observations loosely concur with the fluid temperature theory previously discussed, it has been deemed that the data does not show sufficient evidence of an explicit relationship between the ground temperature and spatial position on the ground-loop. There are a number of potential explanations as to why this is the case. From fluid temperature data, it is known that the temperature difference across the heat pump is approximately 4 K during prolonged periods of heat extraction. This is a relatively small temperature difference within the context of

annual ground temperature variations, especially when it is considered that this is the greatest fluid temperature difference at any point in the ground-loop. A low fluid temperature difference subsequently results in small changes in the thermal gradient between the circulating fluid and adjacent ground around the ground-loop. This factor, in conjunction with the heterogeneity of the ground properties at the site could be cited as potential reasons to explain the weak relationship between the varying fluid temperature and observed ground temperatures.

Overall, the findings suggest that ground temperatures do not significantly vary with fluid temperature along the length of horizontal ground-loops. This suggests that the detailed thermal monitoring of horizontal ground source heat systems could be performed using a single cross-section, provided that the system does not contain any abnormal features and that significant ground heterogeneity does not exist. The findings provide evidence that suggest the modelling of horizontal ground source heat systems can be reduced from three-dimensions to two-dimensions, without incurring any significant errors which would otherwise be associated with the varying fluid temperatures.

4.5.1.4 Ground temperature changes due to heat extraction

Two final temperature evolution plots have been produced as part of the current section in order to further investigate the ground temperature changes occurring at the monitoring site due to heat extraction. Clearly, it is not feasibly possible to present all of the data recorded at the monitoring site here, therefore only salient graphs are presented with the aim of highlighting the overall data trends. The following graphs have been based on ground temperature data collected from intermediate cross-section A and undisturbed ground temperatures recorded within detailed cross-section AA. Figure 4.21 shows vertical position of the thermistors being investigated within the following paragraphs. Further details regarding the plan location of the thermistors can be sourced in Chapter 3.

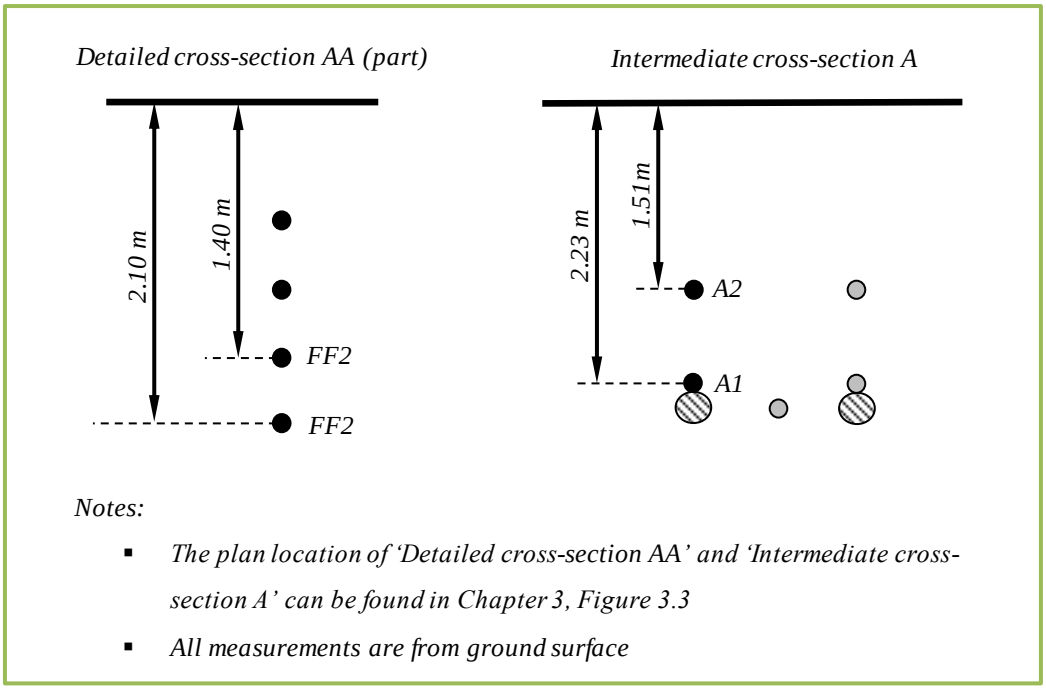

Figure 4.21 – The vertical position of the thermistors within 'Intermediate cross-section A' and vertical position of the thermistors used to measure the undisturbed ground temperature contained in 'Detailed cross-section AA'.

The first temperature evolution plot, shown in Figure 4.22, aims to compare average daily ground temperature data collected by thermistors A1 (as denoted in Figure 4.21) with undisturbed ground temperatures recorded at a depth of 2.1 meters over the inspection period. The depth of thermistor A1 is 2.23 meters, therefore is can be said that the undisturbed ground temperature data recorded at a depth of 2.1 meters represents a good benchmark for comparison. By comparing the ground temperature data collected by thermistor A1 with the undisturbed ground temperature data it is possible to investigate the extent of the impact of heat extraction (via the ground-loop) on ground temperature. In addition to the ground temperatures previously mentioned, the heat pump load for the inspection period has also been plotted for analysis purposes.

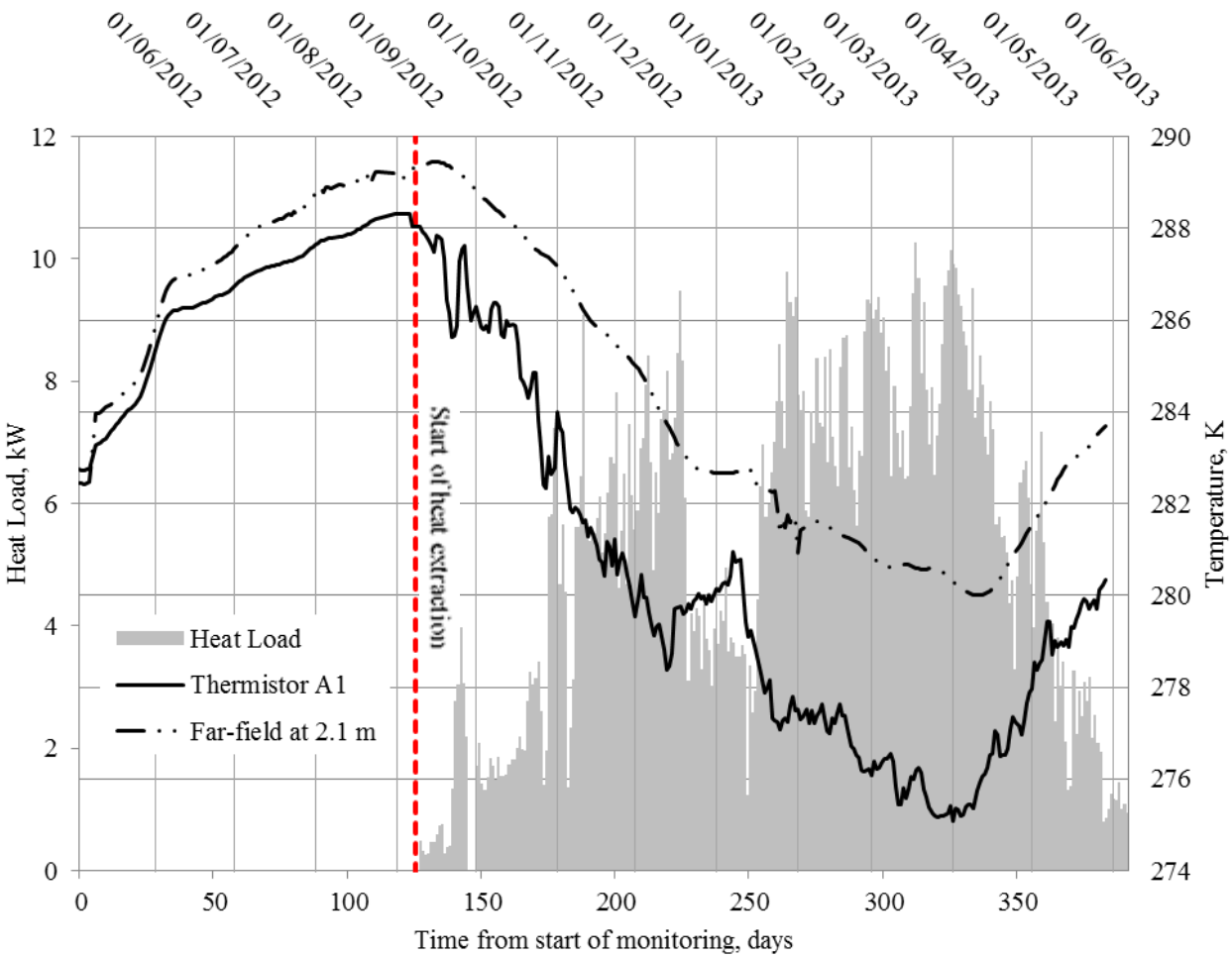

Figure 4.22 – Ground temperatures measured by thermistor A1, far-field thermistor FF1 (as denoted in Figure 4.21) and the average daily system heating load.

Since no heat extraction had taken place prior to September 7th, it can be said that the ground temperatures recorded by thermistor A1 prior to this point represents undisturbed conditions. Comparison between the data collected by thermistor A1 and the undisturbed ground temperature during this period allows the validity of undisturbed benchmark to be inspected. Prior to September 7th the characteristics exhibited by both trend lines are quantitatively similar, although on the 7th September the difference between the two thermistor readings was 0.8 K. The difference between the two values can be attributed to a number of potential factors, predominantly associated with the heterogeneity of the ground properties. Although there is a slight difference between the ground temperature readings as recorded on September 7th, the undisturbed ground temperature has been deemed a representative benchmark for analysis purposes.

Similar to the findings in section 4.5.1.3, the initiation of heat extraction resulted in an immediate drop in the ground temperature recorded at thermistor A1. This response is expected in a conduction dominant system based on the proximity of the thermistor to the ground-loop surface and

the associated thermal resistance. This behaviour is in contrast to the ground temperatures recorded at the far-field which continued to rise for a short period prior to mid-September.

The influence of the heat load is again visible when studying the ground temperature decrease between September 2012 and April 2013. It can be said that the ground temperature recorded by thermistor A1 decreases at a greater rate than the undisturbed ground temperature, which itself decreases due to the onset of winter. Upon further inspection of the data beyond September 7th it can be deduced that the ground temperature fluctuations recorded by thermistor A1 increase in frequency and amplitude, a feature not reflected in the far-field data. By comparing the exhibited peaks and troughs with the remaining climatic and system data recorded at the site it is possible to accredit these fluctuations to changes in the heat load (see Figure 4.14). This becomes particularly evident for a period between mid-December and early January where the ground temperatures notably increase, coinciding with a period of reduced heating load. From perspective of ground source heat performance, the sensitivity of adjacent ground has a number of implications. Firstly, it suggests that the immediate ground is subject to noticeable short term fluctuations which could adversely influence the performance of heating systems. Secondly, it suggests that ground temperatures are noticeably affected by the operational behaviour of ground source heat systems (i.e. cyclic or continual operation). The later feature has also been previously noted by Wu et al. (2011).

During the period between September 2012 and mid-April 2013, the far-field ground temperature drops by 9.3 K, whereas the temperature decrease recorded by thermistor A1 for the same period was 13.3 K. Although the temperature decrease for thermistor A1 was 4 K greater, it can be deduced that the majority of the ground temperature decrease at the location of thermistor A1 is actually due to surface conditions and not heat extraction. The observed temperature range demonstrates the influence of the surface boundary condition, even on the ground temperature immediately adjacent to the ground-loop. Despite the influence of the surface boundary, there was still a noticeable difference between the two trend lines, with the greatest temperature difference occurring on March 28th and measuring 5.3 K.

Beyond April 1st, both thermistor A1 and the far-field report an increase in ground temperatures. This increase can be accredited to the on-set of summer and the combination of increased solar radiation and ambient air temperatures. In the case of thermistor A1, the ground temperature increased despite continual heating loads of above 6 kW for the first 12 days of April. This again demonstrates the influence of the surface climate on the ground temperature immediately adjacent to the ground-loop.

On June 1st 2013, the far-field ground temperature was 2.0 K lower than the previous year whereas thermistor A1 recorded a value 5.1 K lower than the previous year. These values represent an annual change in the thermal behaviour of the ground. The lower far-field temperature has been

accredited to the abnormally cold March of 2013. The greater annual difference observed at thermistor A1, on the other hand, can be attributed to a combination of the cold March and prescribed heating loads which will inevitably slow down the thermal recovery of ground temperatures.

In summary, it can be said that the ground temperature in the vicinity of the ground-loop are closely linked to the heat load profile of the heat pump. As expected, heat extraction resulted in ground temperature decreases in the vicinity of the ground-loop although the majority of the observed temperature decrease can be attributed to surface climate changes and not heat extraction. A greater level of ground temperature fluctuations were observed in the ground adjacent to the ground-loop, all of which coincided with varying heat loads exerted by the heat pump system.

The final temperature evolution plot, shown in Figure 4.23, aims to compare the average daily ground temperatures collected by thermistors A1 and A2 (as denoted in Figure 4.21) in conjunction with heat pump load for the inspection period. Thermistor A2 is located at a depth of 1.51 meters, 0.72 meters vertically above thermistor A1. Comparison of the two data-sets therefore allows the ground-temperature behaviour at two varying displacements from the ground-loop surface to be investigated. In addition to the previous data-sets, the undisturbed ground temperature recorded at a depth of 1.40 meters over the inspection period has also been plotted. The depth of thermistor A2 is 1.51 meters, therefore it can be said that the undisturbed ground temperature data at 1.40 meters represents a reasonable benchmark for comparison purposes. Inclusion of this data-set also allows the impact of heat extraction at the location of thermistor A2 to be investigated.

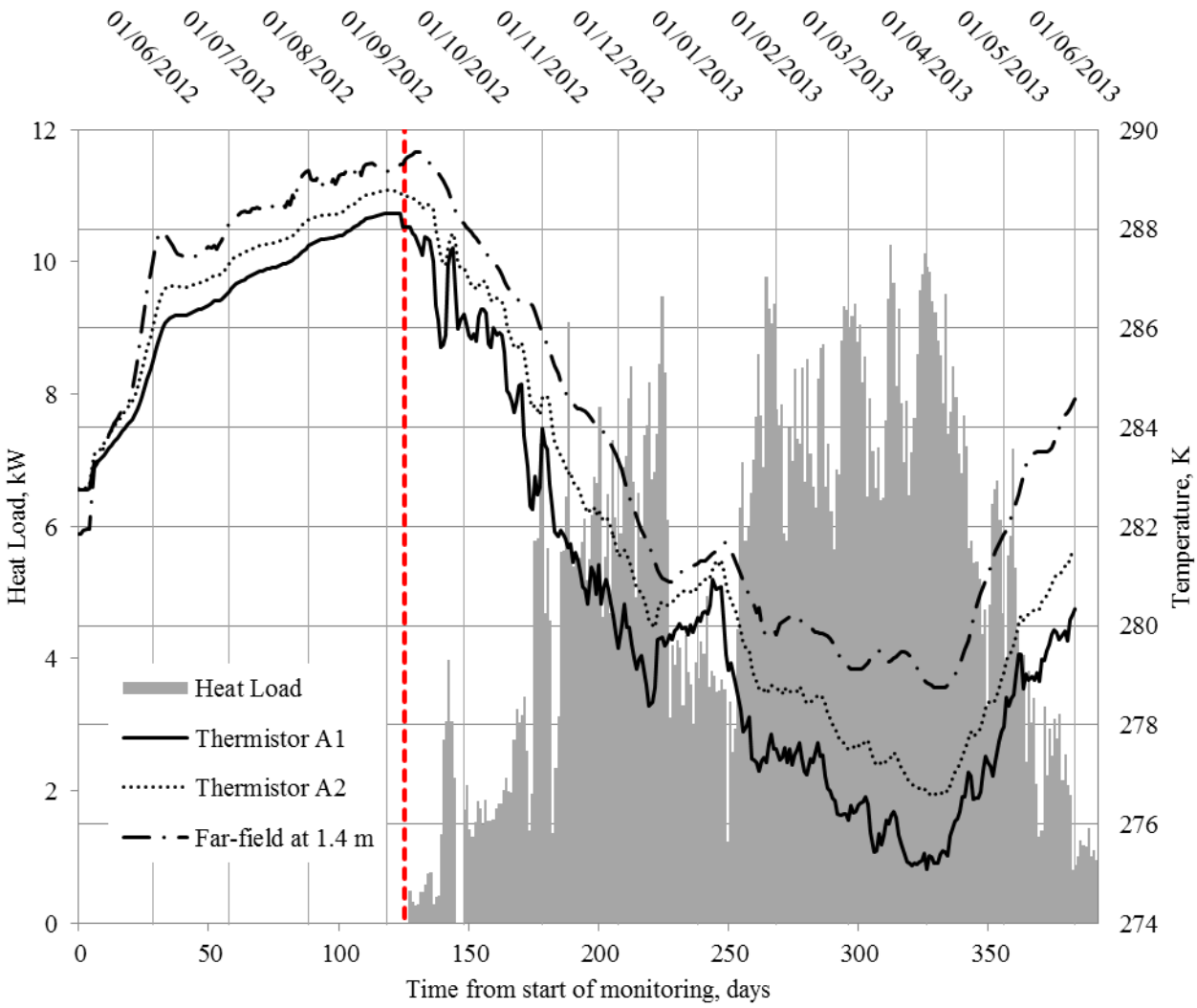

Figure 4.23 – Evolution plots for the ground temperatures measured by thermistors A1, A2 and far-field thermistor FF2 (as denoted in Figure 4.21) along with the average daily system heating load.

Prior to any heat extraction, the trends exhibited by the evolution plots for thermistors A1 and A2 are very similar. On September 7th, the ground temperatures recorded at thermistor A2 is 0.4 K greater than that recorded at thermistor A1. The elevated ground temperature at thermistor A2 is expected based upon the respective depths of the thermistors and the time of year (i.e. end of summer). As previously discussed, the ground temperature prior to September 7th represents undisturbed ground temperatures for all thermistors. This period therefore provides an opportunity to investigate the validity of the undisturbed ground temperature data at 1.4 meters which is to be used as a benchmark for comparison. Prior to September 7th it can be seen that the undisturbed ground temperatures at a depth of 1.4 m are consistently higher than those recorded at the location of thermistor location A2 by approximately 0.5 K. These differences can be attributed to a number of variables, although ground heterogeneities are likely to be the most possible cause for such behaviour.

Despite the observed difference, the undisturbed ground data can still be used as a guide for analysis purposes.

In general, the trends exhibited by thermistors A1 and A2 are similar throughout the inspection period. Beyond September 7th, the ground temperatures recorded by both thermistors A1 and A2 decrease. In general it can be said that the ground temperatures recorded by thermistor A2 are approximately 1 K greater than those recorded at A1 for the period between mid-October 2012 and April 2013. Considering the heat extraction in isolation, this would be the expected outcome as the thermal gradient is induced at the ground-loop surface and thermistor A2 is at a greater displacement than thermistor A1. Upon further inspection of the data beyond September 7th it can be seen that the ground temperature fluctuations exhibited by thermistor A2 are less prominent than those exhibited by thermistor A1. This is the expected outcome based on the displacements of the two thermistors from the ground-loop surface and the conduction nature of the system. Beyond the ground-loop surface, fluctuations will reduce according to the increased thermal resistance and increased thermal mass from the surrounding ground. From the perspective of ground source heat performance, temperature fluctuations at various displacements are an important behavioural trait to consider as they indicate the ground region affected by cyclic operation. Chapter 2 previously presented research which has aimed to increase this region by replacing the ground with a greater conducting backfill; thereby increasing the ground region subject to cyclic operation and improving the short term response of systems.

From early September to February, the difference between the undisturbed ground temperatures and those recorded by thermistor A2 does not exceed 1.8 K and often measures less than 1.2 K. After a period of reduced heating load during mid-December to early January, the temperature difference at one point reduces to less than 0.1 K on January 5th. Beyond early January the difference once again grows coinciding with a period high heat extraction, reaching at most, 2.2 K on March 28th 2013. The temperature trends exhibited in Figure 4.23 suggest that the ground behaviour at the location of thermistor A2 is influenced by a combination of the climate and heat extraction. At this location, the effects of heat extraction via ground-loop are observable but only result in significant deviation from the undisturbed ground temperature after prolonged periods of heating, with loads greater than approximately 5 kW.

In summary, the ground temperature 0.72 m vertically above the ground-loop has been investigated. It can be said that at this location some fluctuations resulting from varying heating loads can be still be observed although the effects are dampened due to the thermal mass of the soil surrounding the ground-loop. As expected a noticeable temperature decrease is observed although it is not as great as the decline observed at the location of thermistor A1. Although the ground

temperature at thermistor A2 was shown to decrease due to heat extraction, it can be said that the climatic conditions have much more influence on the ground temperatures at this location.

4.5.2 Spatial variation of ground temperature

Contour plots have been employed to present the two-dimensional temperature distributions for detailed cross-sections AA and BB at the monitoring site. Further details regarding the spatial arrangement of the thermistors can be found in Chapter 3. Detailed cross-sections AA and BB each contained a total of 41 thermistors, a far greater number than the remaining intermediate cross-sections which contained a total of only 5. The greater number and spatial position of the thermistors provided a resolution of data sufficient enough to generate two-dimensional contour plots of the ground temperature distribution. The following plots have been created using GNUPLOT software, which is an open source command line driven graphic utility (Williams & Kelley, 2012). The contour plots were created via a script which derives a series of cubic polynomials, the coefficients of which are found be weighting the data points. Using the derived functions it is subsequently possible to generate a three-dimensional function, and contour plot, representing the spatial position and values of the data points.

A series of monthly contour plots have been generated between September 2012 and June 2013. Contour plots representing months prior to September 2012 have been omitted from the contour plot analysis as the ground source heat system was inactive during this period. The presented plots have been generated using ground data corresponding to the first day of the month in question, i.e. September 2012 corresponds to the ground data as recorded on September 1st 2012. Although the measured ground properties at detailed cross-sections AA and BB varied slightly, the trends exhibited by the generated contour plots are very similar. To avoid repetition, only monthly contour plots from detailed cross-section AA will be presented here for discussion. For completeness the contour plots generated for detailed cross-section BB can be found in Appendix E.

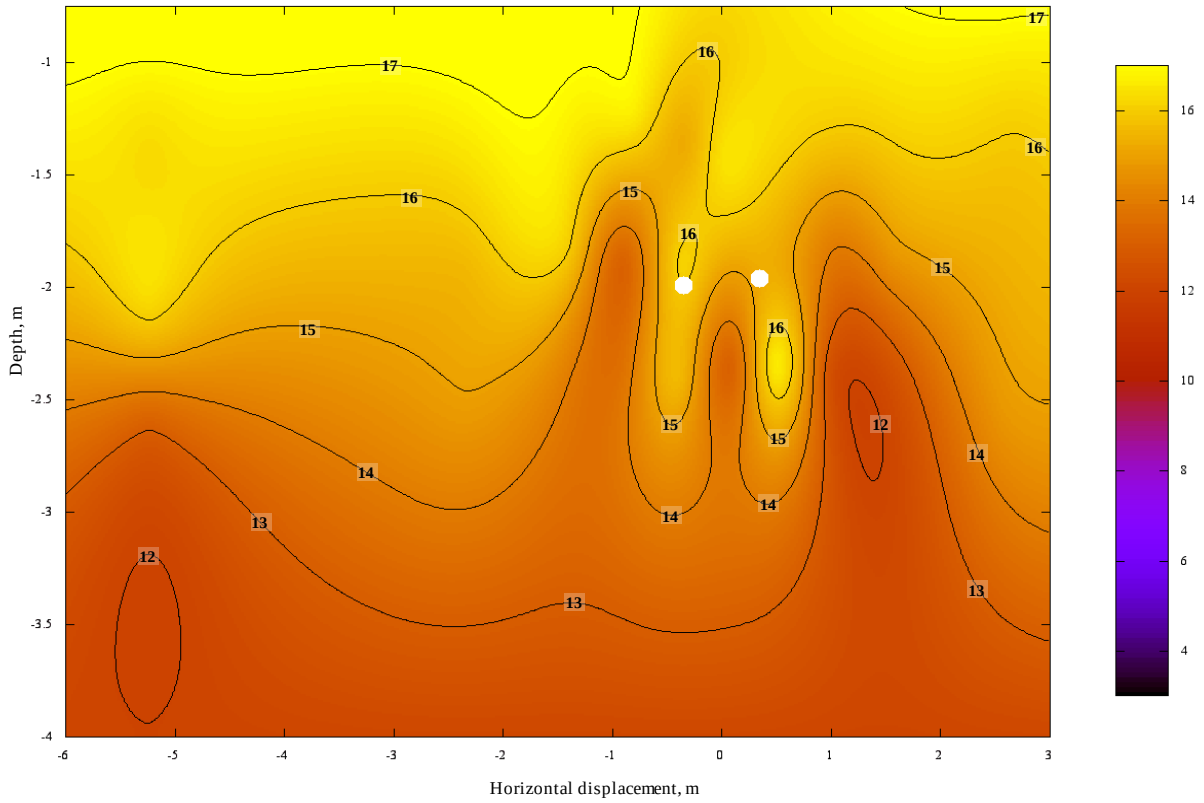

Figure 4.24- Two-dimensional ground temperature distribution at detailed cross-section AA on September 1st 2012.

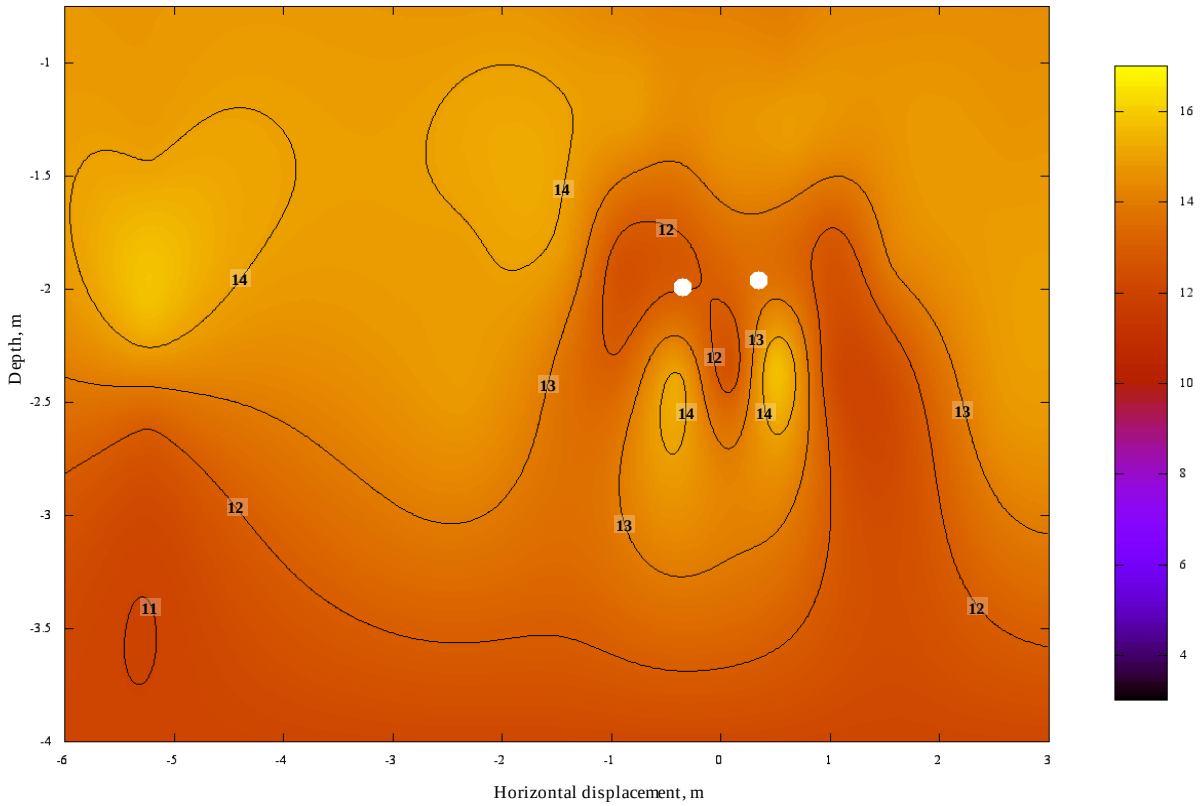

Figure 4.25- Two-dimensional ground temperature distribution at detailed cross-section AA on October 1st 2012.

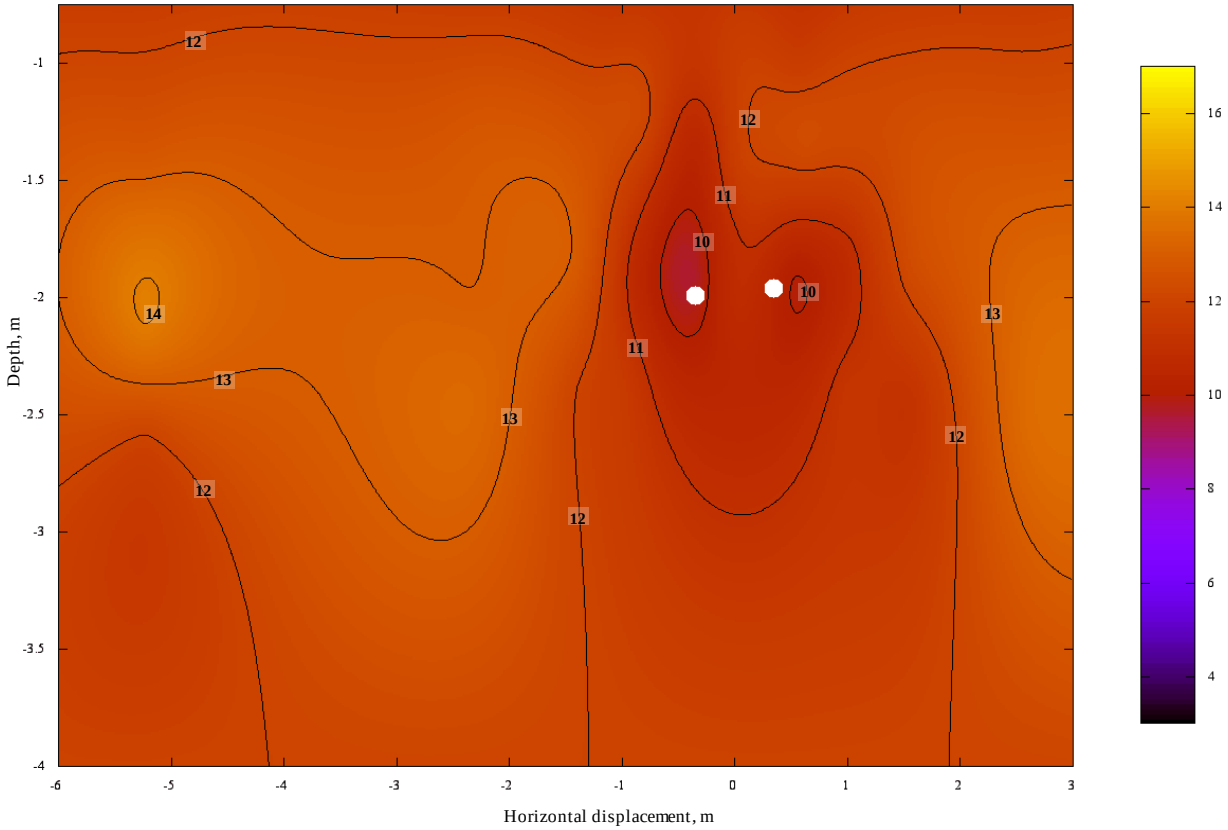

Figure 4.26 - Two-dimensional ground temperature distribution at detailed cross-section AA on November 1st 2012.

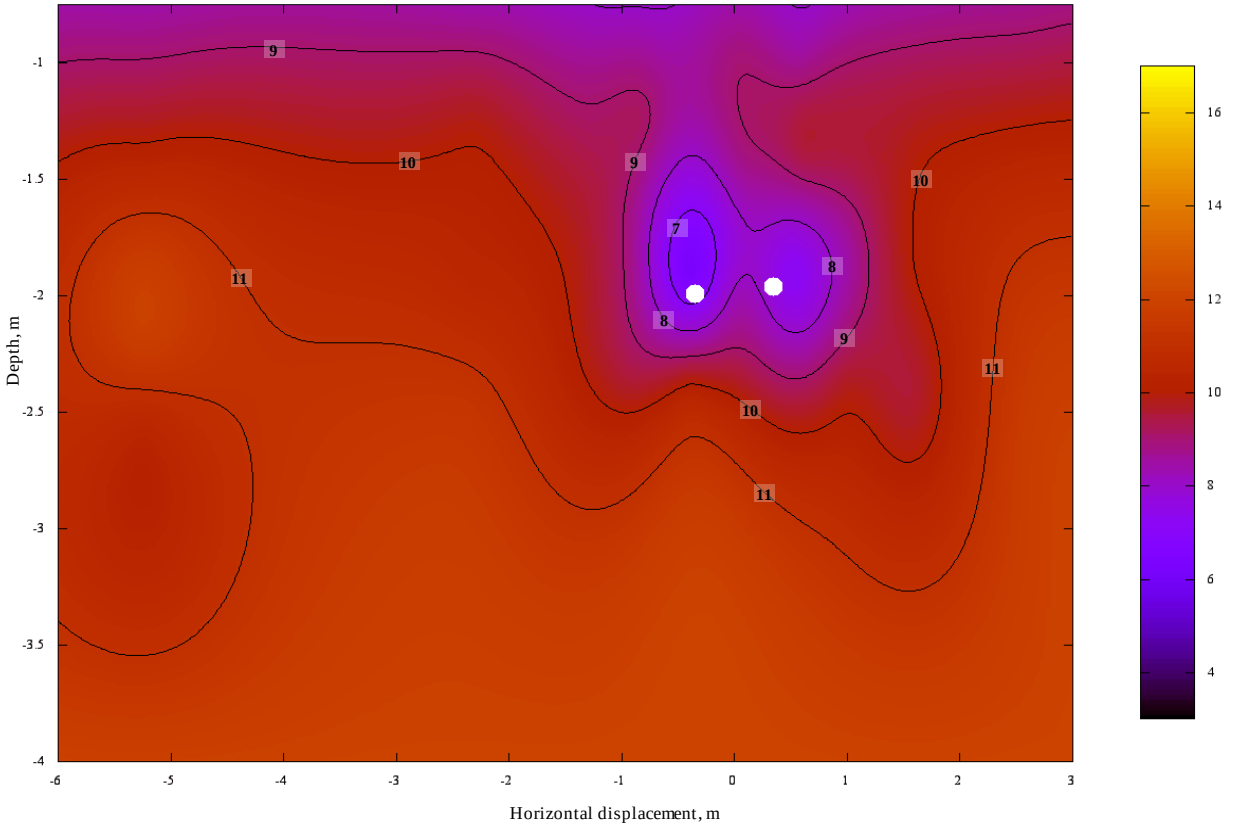

Figure 4.27 - Two-dimensional ground temperature distribution at detailed cross-section AA on December 1st 2012.

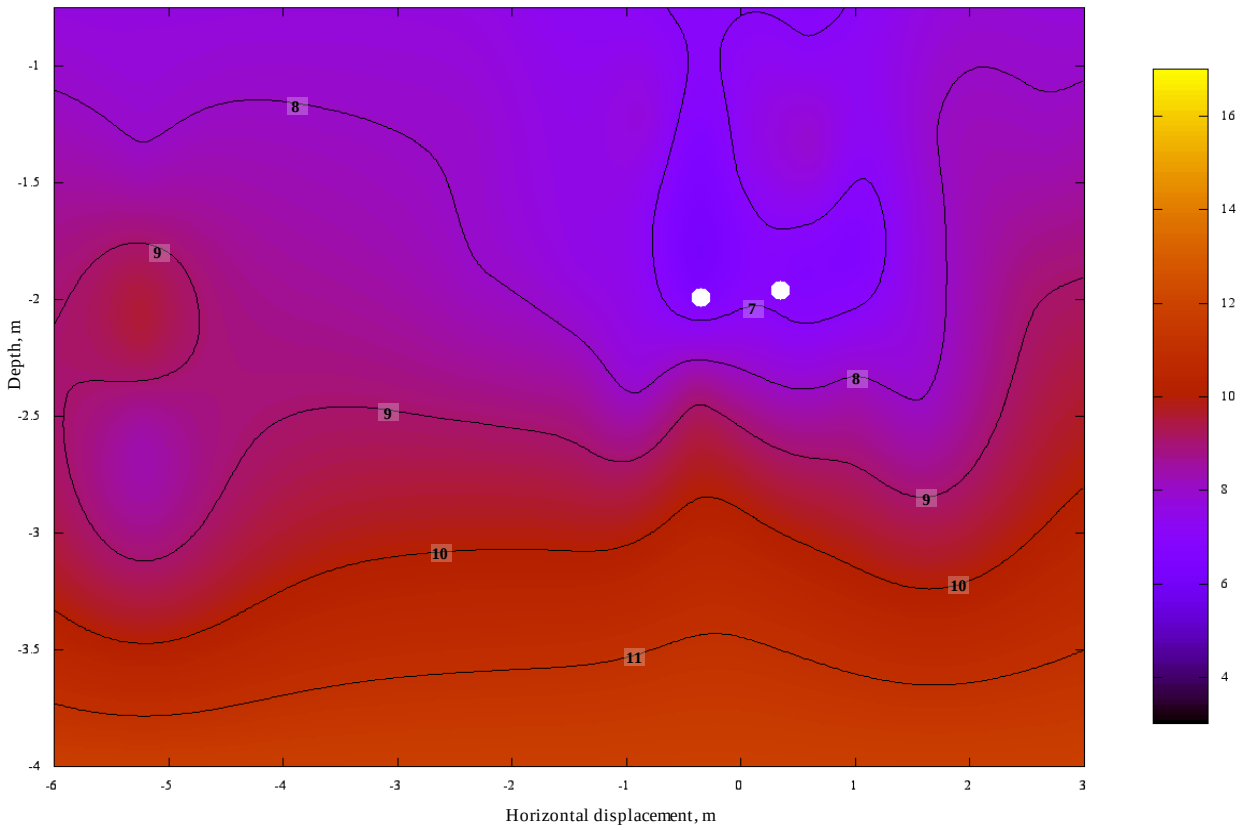

Figure 4.28 - Two-dimensional ground temperature distribution at detailed cross-section AA on January 1st 2013.

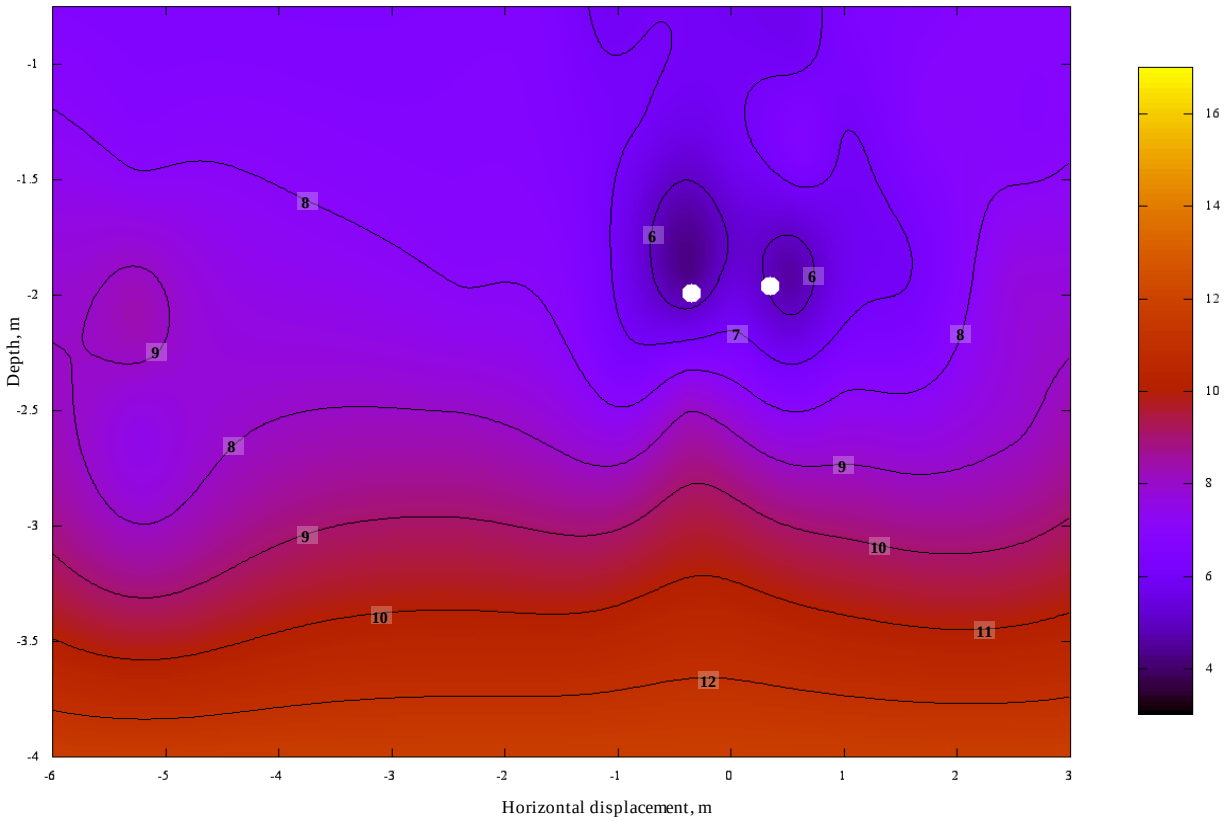

Figure 4.29 - Two-dimensional ground temperature distribution at detailed cross-section AA on February 1st 2013.

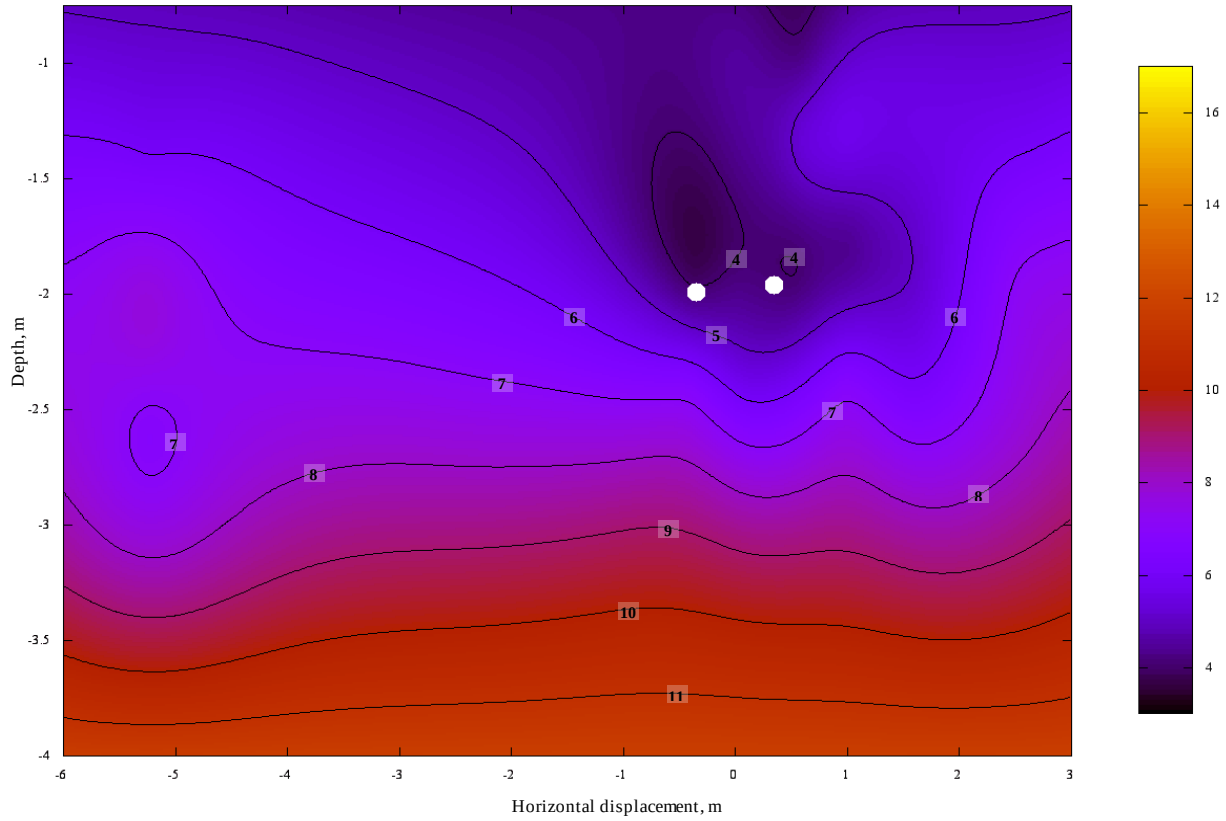

Figure 4.30 - Two-dimensional ground temperature distribution at detailed cross-section AA on March 1st 2013.

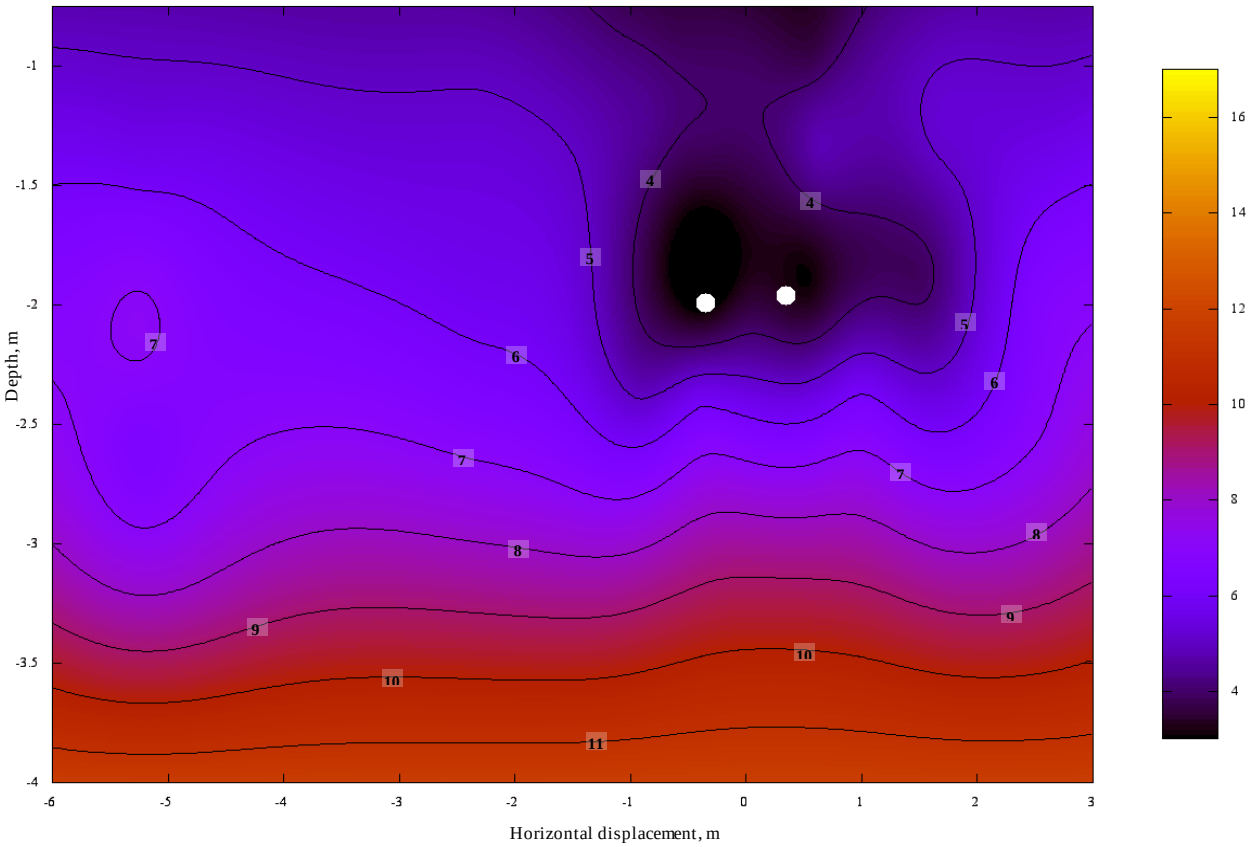

Figure 4.31 - Two-dimensional ground temperature distribution at detailed cross-section AA on April 1st 2013.

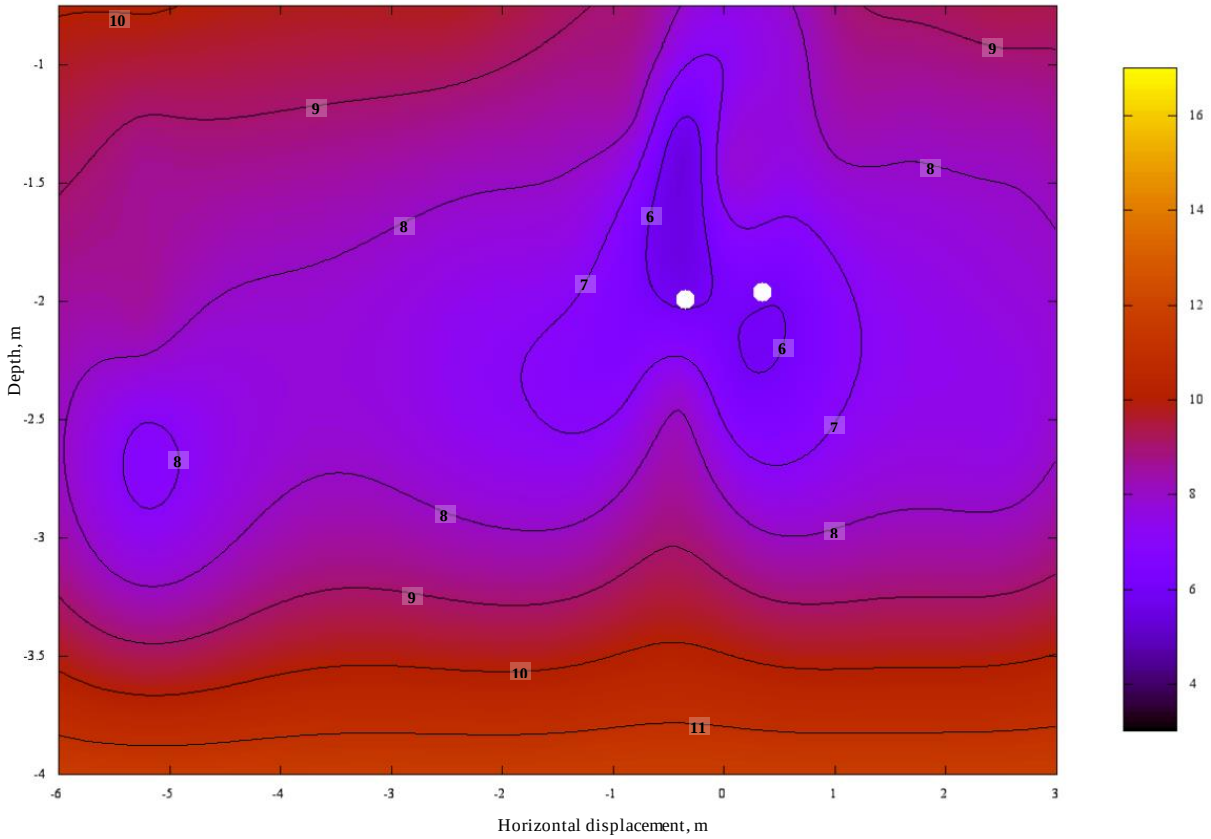

Figure 4.32 - Two-dimensional ground temperature distribution at detailed cross-section AA on May 1st 2013.

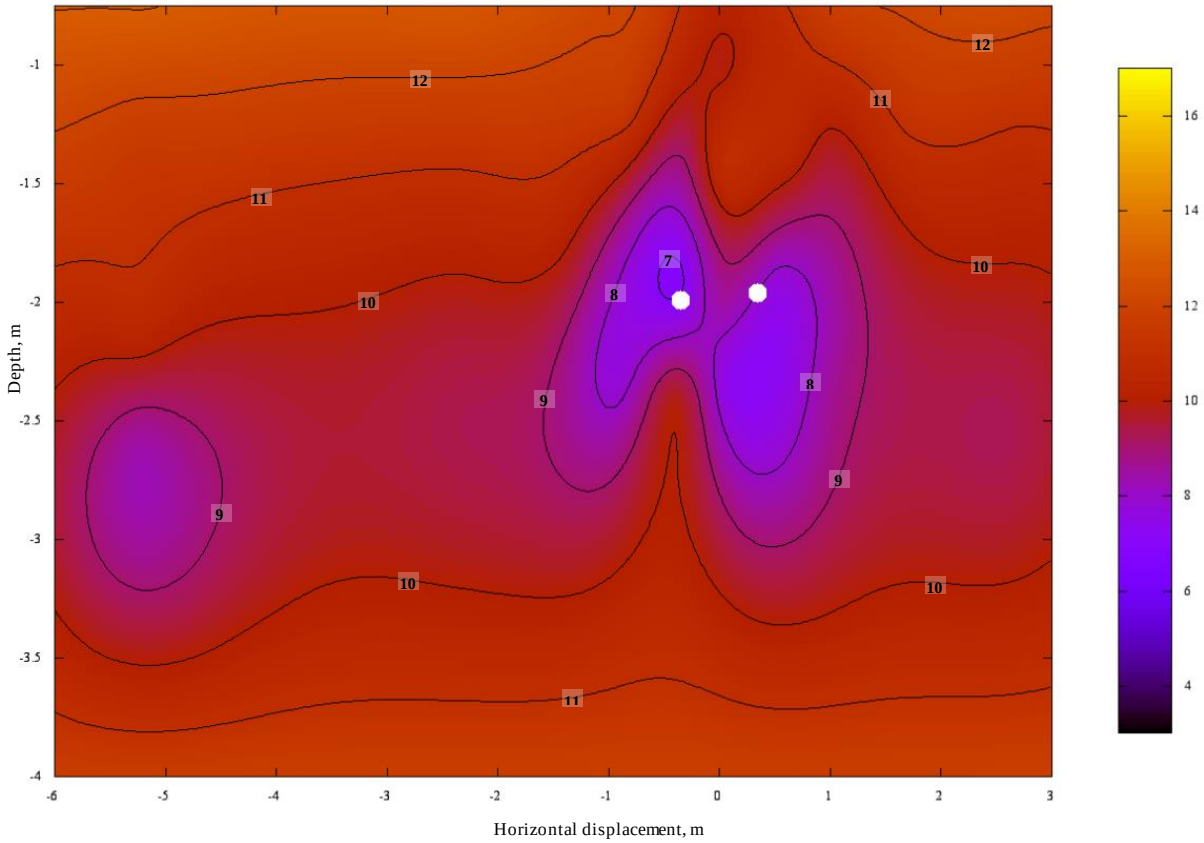

Figure 4.33 - Two-dimensional ground temperature distribution at detailed cross-section AA on June 1st 2013.

The fundamental aim when producing the contour plots was to provide a means of collectively inspecting the temperature data collected at the detailed cross-sections. In order to achieve this, a plotting domain was required which covered the position of all 41 thermistors located in detailed cross-section AA and BB respectively. This was achieved using a domain 9 meters wide by 3.25 meters in depth. The ground region from the surface to a depth of 0.75 meters has been omitted from the contour plots as no ground data was collected from this region. An upper plotting domain boundary of 0.75 meters was therefore set with a lower boundary of 4 meters. In order to generate the plots, a constant ground temperature of 285.15 K (12 °C) was set at a depth of 10 meters in accordance with experimental data presented by Busby (2011) and Kusuda and Achenbach (1965), although the final presentation of the plots only extended downwards to a depth of 4 meters.

Two white circles have been shown which represent the ground-loop intersections within the plotted domain in Figures 4.24 to 4.33. The ground-loop has been positioned according to measurements taken during the topographical survey undertaken during the site installation (see Chapter 3). The resulting 'slant' of the ground-loop corresponded with the observations made at detailed cross-section AA during the system installation.

As previously stated, heat extraction began at the monitoring site on September 7th 2012; therefore Figure 4.24 represents the ground temperature distribution prior to heat extraction. From Figure 4.24, it can be seen that prior to heat extraction the ground temperature varies predominantly with depth, although it is noted that there are two local regions of elevated ground temperatures. This initial undisturbed temperature distribution demonstrates that the ground does not vary uniformly with depth across the plotting domain. These findings concur with the previously discussed plots, which found that undisturbed ground temperatures at similar depths varied slightly across the site. The observed differences can be attributed to a number of factors; however for the current case it is more than likely due to the ground heterogeneities. Although Figure 4.24 is the only plot which shows undisturbed ground temperatures throughout the entire domain, the left hand side of the remaining plots (Figures 4.25 to 4.32) are beyond the thermal influence of the ground-loop and therefore also represent the undisturbed ground temperature.

Upon collective inspection of the contour plots it can be seen that the ground immediately surrounding the ground-loop generally decreases in temperature from October 2012 through to April 2013, coinciding with the heating loads of the system (see Figure 4.14). Previous monitoring efforts highlighted in Chapter 2 have lacked a data resolution capable of capturing the size and shape of the resulting temperature distributions. From a ground source heat perspective, the induced thermal distributions allow thermal gradients and so called 'thermal influence' of the ground-loop to be inspected. The term 'thermal influence' within the current context, relates to the ground region which is subject to temperature changes as a direct result of heat extraction. The following paragraphs will

first discuss the varying thermal influence of the ground-loop, as depicted in the figures, followed by the thermal gradients.

The temperature distributions arising around the ground-loop pipes are initially weak for the months of October and November (Figures 4.25 and 4.26). This can be attributed to a combination of factors, namely; the relatively warm ground temperatures observed in the vicinity of the ground-loop and the low heating loads. During this period, Figure 4.25 and 4.26 indicate that the thermal influence of the ground-loop does not horizontally exceed 1 meter, although the weak distributions can increase the uncertainty associated with this figure.

The temperature distributions for December through to April (Figures 4.27 to 4.31) depict stronger thermal distributions around the ground-loop. The stronger thermal distributions can be attributed to the noticeable increase in heating load measured during this period (see Figure 4.14). Upon further inspection, it is possible to identify a number of characteristics associated with the ground temperature distributions. Firstly, the horizontal thermal influence of the ground-loop grows from approximately 1.5 meters on December 1st to approximately 2.5 meters on April 1st. During this time, some of the horizontal gradients depicted on the right hand side of the contour plots appear steeper than those on the left. This unsymmetrical distribution could be attributed to a number of in-situ characteristics although it is recognised that the reduced data resolution on the right hand side could be a contributing factor. Following on from this, the vertical distributions were inspected for the Figures 4.27 to 4.31. Upon collective inspection, the one common characteristic which becomes apparent is the unsymmetrical shape of the vertical thermal distributions. In all five contour plots, the thermal distribution around the ground-loop appears to extend to greater distances above then below. For example, Figure 4.31 shows a thermal distribution which extends to a distance greater than 1 meter above the ground-loop but only approximately 0.5 meters below. This variation in vertical distributions can be attributed to a combination of factors, namely; the influence of the surface climate and constant ground temperatures found at depth.

Inspection of the contour lines depicted in Figures 4.27 to 4.31 reveal that as the thermal influence of the ground-loop grows, the thermal gradients induced in the immediate ground region also increase. Within a conduction dominated system, this thermal behaviour would be the expected outcome as predicted by Fourier's law of conduction. Further inspection of Figures 4.27 to 4.31 reveals that the thermal gradient formed beneath ground-loop is steeper than that above it. From a ground source heat perspective, the steeper induced thermal gradient suggests that the more heat is being absorbed from the ground region below the ground-loop than above it during the winter months. This is an important behaviour trend, especially with regards to the optimisation of system performance.

The thermal distributions depicted for May and June (Figures 4.32 and 4.33) are noticeably different to those for the preceding months. Figure 4.32 shows that the thermal distributions formed in Figure 4.31 have somewhat dissipated and the ground temperatures have generally increased. These trends further continue through to Figure 4.33. The change in behaviour can be attributed to a combination of reduced heating load for the periods and increasing ambient air temperatures and solar radiation. The dissipation of the thermal distributions presented in Figure 4.32 and 4.33 represents the so called thermal recharge of the system where ground temperatures are being replenished following the cool winter months and prolonged periods of heat extraction.

When inspecting the temperature distributions around the ground-loop pipe, it can be seen that in general the coldest ground temperature can be found in two distinct areas. The first of these corresponds to a ground region immediately above the left hand side ground-loop pipe, while the second can be found slightly to the right of the right hand side ground-loop pipe. In reality, the coldest regions would be expected to coincide with the surface of the ground-loop and not be offset as depicted in the figures. The slight off-set depicted in the distributions can be attributed to one of two factors, namely; the spatial positions of the thermistors and the plotting algorithms used to generate contours. Chapter 3 previously presented the spatial arrangement of the thermistors which, where possible, positioned the thermistors in a structured pattern around the ground-loop. The arrangement however, was unable to completely capture the steeper thermal gradient arising in close proximity to the ground-loop. Within the context of the plotting algorithm, this presents a slight problem when trying to fit cubic functions, resulting in minima being slightly off-set from the true location.

In summary, the previous contour plots and discussion have quantitatively presented the thermal distributions and gradients arising from heat extraction. The thermal influence of the ground-loop grew with heat extraction, exceeding 2.5 meters in the horizontal and exceeding 1 meter vertically above the ground-loop. Vertical distributions were noticeably unsymmetrical resulting in steeper thermal gradients forming beneath the ground-loop. Beyond April, the formed thermal distributions began to dissipate indicating that ground temperatures had begun to replenish.

4.6 Conclusions

This chapter presented investigations into 13 months of ground and climatic data collected at the monitoring site between May 2012 and June 2013. The resulting data-set contains a greater spatial resolution of ground temperature data in response to heat extraction than any previous works. The developed data management tool was used to store, structure and interrogate the compiled data-

set. Applying the developed interrogation features, a series of investigations into the data were conducted.

Firstly, climatic data recorded at the site was compared with historical data for the region. In general, it was found that the trends exhibited by monitored climatic data concurred with historical trends for the area and fell within the expected weather extremes. During this period, the heating load for the system was also calculated using fluid flow and fluid temperature data collected. The calculated heat load was found to be closely linked to the external ambient air temperature recorded at the site. This was due to the system type, which provided space heating only.

Undisturbed ground temperatures ranging in depth between 0.75 and 2.6 meters were then presented and discussed. The general trends exhibited by the data concurred with the expected outcomes as predicted by theory, namely, that the observable impact from the climatic conditions on the ground temperature diminished with depth. Applying the findings from the previous investigation highlights the performance benefit which would be gained by installing a ground-loop deeper than the 1.2 meter limit currently defined in design MIS 3005 standards (MCS, 2008).

The resolution and spatial position of the ground sensors allowed the ground temperature behaviour immediately adjacent to the ground-loop to be investigated at a series of locations. It was found that there was no clear relationship linking the fluid temperature profile within the ground-loop to the monitored ground temperatures. From a modelling perspective, this suggests that horizontal ground source heat systems could be simulated with a two-dimensional model without incurring any noticeable errors associated with the varying fluid temperature profile. Further to this, the findings suggest that for the current monitoring site, a single detailed cross-section would have been sufficient to capture the required ground temperature behaviour.

Ground temperature changes associated with heat extraction were then investigated by comparing ground temperature data immediately adjacent to the ground-loop with corresponding far-field values. Although the results confirmed the basic principle of heat conduction (i.e. the ground around the ground-loop got cooler with continued heat extraction), observations revealed that the majority of the ground temperature decrease adjacent to the ground-loop was due to seasonal influences and not heat extraction. To the author's knowledge, this is the first time this system characteristic has been identified and quantified.

The spatial resolution of ground temperature data collected at the monitoring site was sufficient enough to generate a series of contour plots over the 13 month period. Unlike previous research efforts, the contour plots allowed the thermal distributions induced by a horizontal ground source heat system to be fully investigated. As expected it was found that the thermal influence grew with increasing heat load, however; it was also found that the thermal distributions were none

symmetrical, particularly in the vertical. It was found that the thermal gradients formed beneath the ground-loop were significantly steeper than those above. The differing thermal gradients indicate that the absorption of heat from the ground is non-symmetrical. Application of this knowledge can be used in the design process to optimise system performance, a feature which will be discussed further in Chapter 9.

The results obtained from this experimental programme provide a greater insight into the behaviour of horizontal ground source heat systems than previous studies. In addition, the high resolution of data obtained provides a unique large-scale benchmark to validate numerical models in this field. Confidence in the design and development of horizontal ground source heat systems has been achieved through the analysis of the field-scale investigations.

References

BBC, 2013. *March weather was second coldest on record*. London: BBC News.

Busby, J., Kingdon, A. & Williams, J., 2011. *The measured shallow temperature field in Britain*. Nottingham: British Geological Survey.

Department for Environment, Food and Rural Affairs (DEFRA), 2009. *The climate of the United Kingdom and recent trends*, London: DEFRA.

He, M., 2012. *Numerical modelling of geothermal borehole heat exchanger systems, PhD Thesis*. Leicester: De Montfort University.

Kusuda, T., 1975. *The effect of ground cover on earth temperature*. Fort Worth, Texas, USA, Conference proceedings of 'Alternatives in energy conservation: The use of earth-covered buildings'.

Kusuda, T. & Achenbach, P. R., 1965. Earth temperature and thermal diffusivity at selected stations in the United States. *ASHRAE Trans*, 71(1), pp. 61-75.

MET Office, 2013a. *Lyonshall 1981-2010 averages*. [Online]
Available at: http://www.metoffice.gov.uk/climate/uk/averages/19812010/sites/lyonshall.html
[Accessed 10 4 2013].

MET Office, 2013b. *Regional Climates*. [Online]
Available at: http://www.metoffice.gov.uk/climate/uk/regional/
[Accessed 10 4 2013].

Microgeneration Certification Scheme (MCS), 2008. *Microgeneration Installation Standard: MIS 3005 Issue 3.0*. London: Department of Energy and Climate Change (DECC).

Nofziger, D. L., 2003. *Soil Temperature Changes with Time and Depth*. Stillwater, Oklahoma: Department of Plant and Soil Sciences, Oklahoma State University.

Queen's University, Belfast, 2013. *GAP Weather Station*. [Online]
Available at: http://www.qub.ac.uk/schools/gap/AboutUs/GAPWeatherStation/
[Accessed 10 4 2013].

Revfeim, K. J. A., 1978. A simple procedure for estimating global daily radiation on any surface. *Journal of Applied Meteorology*, 17(1), pp. 1126-1131.

Thornton, P. E., Hasenauer, H. & White, M. A., 2000. Simultaneous estimation of daily solar radiation and humidity from observed temperature and precipitation: an application over complex terrain in Austria. *Agriculture and Forest Meteorology*, 104(4), pp. 255-271.

Tutiempo, 2013. *Hereford/Credenhill historical weather*. [Online]
Available at: http://www.tutiempo.net/en/Climate/HEREFORD_CREDENHILL/2012/35220.htm
[Accessed 10 4 2013].

Williams, T. & Kelley, C., 2012. *gnuplot 4.6 - An interactive plotting program*. [Online]
Available at: http://www.gnuplot.info/docs_4.6/gnuplot.pdf
[Accessed 12 4 2013].

Wu, Y. et al., 2011. Prediction of the thermal performance of horizontal-coupled ground-source heat exchangers. *International Journal of Low-Carbon Technologies*, 6(1), pp. 261-69.

Chapter 5

Theoretical/numerical formulations and computational aspects

5.1 Introduction

The theoretical and numerical formulations of the model are presented in this chapter. Following this, computational aspects employed within the current scope are presented. The main objective is to present the developments with regard to the current scope of work, namely; the thermo-hydro behaviour of ground subject to conditions imposed by ground source heat extraction. The theoretical and numerical formulations presented are based on the coupled Thermo/Hydro/Chemical/Mechanical *(THCM)* model previously detailed within work by Cleall (1998), Mitchell (2002), Vardon (2009) and Sedighi (2011). The formulation presented here is for the coupled Thermo-Hydro *(TH)* behaviour of an unsaturated rigid porous soil. The mechanical and chemical aspects of the previous work fall beyond the scope of the current thesis and have therefore

being omitted. The heat transport formulation is based on the conservation of energy, whereas the flow variables for liquid and air are considered via mass conservation.

In the following sections the theoretical formulation will be addressed first. The general aspects of the theoretical formulations are presented in section 5.2 which include the basic assumptions and primary variables. The governing equation describing moisture transfer is developed in section 5.3 based upon the principle of conservation of mass and treating water as a two phase flow process. The governing equation for air transfer is presented in section 5.4 considering the air to be a binary mixture of dry air and water vapour. Air is considered to be found both as air dissolved within the water phase of the ground matrix and bulk air. Finally, the governing equation for heat transfer is presented in section 5.5 based upon the conservation of energy; identifying conduction, convection and radiation as the main modes of transfer. The numerical formulations are presented within section 5.7; with the spatial discretisation described in section 5.8 and the temporal discretisation presented in section 5.9.

The final section of this chapter presents the computational formulation which has been implemented in conjunction with the numerical formulation. The various options available to optimise the computational performance will be discussed within the context of the current work in sections 5.11, 5.12.

5.2 Theoretical formulations - General

Soil is considered to be a three-phase system, consisting of a solid skeleton, pore-water and pore-air, which consists of dry air and water vapour. The architecture of the solid component, the soil skeleton, forms what is commonly referred to as the soil matrix. In the following formulation the flow of heat, moisture and air in a rigid soil are considered. Governing differential equations are developed for heat energy, moisture and air components respectively. These governing equations are expressed in terms of three primary variables, namely:

i. Pore-water pressure, u_l
ii. Pore-air pressure, u_a
iii. Temperature, T

As previously described in the introduction to this chapter, theoretical formulations have been previously extended to include the mechanical and chemical coupled behaviour of unsaturated porous materials however; these components were deemed beyond the scope of the current investigation and

therefore excluded from the current discussion. Details for these additional system components can be found in Seetharam (2003), Vardon (2009), Sedighi (2011) and Al-Masum (2012).

The behaviour of the three variables listed is included within the coupled thermo-hydro *(TH)* formulation. Liquid and water vapour transfer are considered utilising the principle of conservation of mass, as is the transfer of pore-air. The pore air is considered as a binary mixture of dry air and water vapour. The heat transfer is governed by the conservation of energy, taking into account conduction, convection and the phase change via latent heat of vaporisation. Radiation is assumed to be negligible within the current context due to the expected temperature ranges (Mitchell, 1993). All of the governing equations are then developed in a three-dimensional form.

5.3 Moisture transfer

Moisture transfer within unsaturated soils can be described as a two phase process, compromising of both liquid and vapour flows. The total volumetric water content, θ, is defined as the sum of these phases:

$$\theta = \theta_l + \theta_v \tag{5.1}$$

where θ_l is the volumetric liquid content and θ_v is the volumetric vapour content.

The conservation of mass for each phase may be considered separately in order to formulate the governing equation of moisture transfer.

The principle of local thermodynamic equilibrium dictates that at any point the volumetric liquid water and water vapour are in equilibrium (De Vries, 1958). This principle is used to define the following relationship:

$$\theta_v = \frac{(n - \theta_l)\rho_v}{\rho_l} \tag{5.2}$$

where, n is the porosity, ρ_v is the density of water vapour and ρ_l is the density of the liquid water.

The principle of conservation of mass is considered separately in liquid and vapour phases in order to derive the general mass conservation for moisture transfer. Considering the liquid water phase, the principle of conservation of mass dictates that the time derivative of the liquid content is equal to the spatial gradient of the liquid flux. This can be expressed mathematically with the

inclusion of a sink/source term which allows the change (i.e. vaporisation and condensation) to be expressed as follows:

$$\rho_l \frac{\partial(\theta_l \partial V)}{\partial t} = -\rho_l \partial V \, \nabla \cdot \mathbf{v_l} - \rho_l \partial V E_{ss} \tag{5.3}$$

where ∂V is the incremental volume, t is the time, ∇ is the gradient operator, $\mathbf{v_l}$ is the velocity of the liquid and E_{ss} is a sink/source term for water/vapour exchange.

Applying the principle of mass conservation similarly for the vapour phase, the time derivative of the vapour content is equal to the spatial gradient of the vapour flux with an equal and opposite sink/source term accounting for the change of phase. This is expressed as:

$$\rho_l \frac{\partial(\theta_v \partial V)}{\partial t} = -\rho_l \partial V \, \nabla \cdot \mathbf{v_v} - \partial V \, \nabla \cdot (\rho_v \mathbf{v_a}) + \rho_l \partial V E_{ss} \tag{5.4}$$

where, $\mathbf{v_v}$ is the equivalent velocity of vapour and $\mathbf{v_a}$ is the velocity of pore air.

The volumetric air content, θ_a, (including dry air and vapour) can be expressed as:

$$\theta_a = (n - \theta_l) \tag{5.5}$$

Substituting equations (5.2) and (5.5) into equation (5.4), the law of conservation of mass for water vapour flow may now be written in terms of porosity and volumetric air content:

$$\frac{\partial(\rho_v \theta_a \partial V)}{\partial t} = -\rho_l \partial V \nabla \cdot \mathbf{v_v} - \partial V \, \nabla \cdot (\rho_v \mathbf{v_a}) + \rho_l \partial V E_{ss} \tag{5.6}$$

Summing the respective mass conservation equations for liquid and vapour, i.e. equations (5.3) and (5.6), the general equation for the moisture flow can be described as:

$$\rho_l \frac{\partial(\theta_l \partial V)}{\partial t} + \frac{\partial(\rho_v \theta_a \partial V)}{\partial t} = -\rho_l \partial V \nabla \cdot \mathbf{v_l} - \rho_l \partial V \nabla \cdot (\mathbf{v_v}) - \partial V \nabla \cdot (\rho_v \mathbf{v_a}) \tag{5.7}$$

The volumetric liquid and air contents may be expressed in terms of porosity and degree of saturation:

$$\theta_l = n S_l \tag{5.8}$$

$$\theta_a = nS_a \tag{5.9}$$

where S_l and S_a are the degrees of saturation of pore water and pore air respectively. The incremental volume, ∂V, is defined as the summation of the solid volume and void volume, hence:

$$\partial V = (1+e)\partial V_s \tag{5.10}$$

where e is the void ratio and V_s is the volume of the solids. Substitution of equations (5.8), (5.9) and (5.10) into equation (5.7) gives:

$$\rho_l \frac{\partial(nS_l(1+e)\partial V_s)}{\partial t} + \frac{\partial(\rho_v nS_a(1+e)\partial V_s)}{\partial t} + \rho_l(1+e)\partial V_s \nabla\cdot\mathbf{v_l} + \rho_l(1+e)\partial V_s\nabla\cdot\mathbf{v_v} + (1+e)\partial V_s\nabla\cdot(\rho_v\mathbf{v_a}) = 0 \tag{5.11}$$

It is assumed that the volume of solids is a control volume and therefore remains constant, hence ∂V_s can be eliminated from equation (5.11). Moreover, the porosity can be related to the void ratio by $n = e/(1+e)$. Dividing equation (5.11) by $(1+e)$ therefore gives:

$$\frac{\rho_l}{(1+e)}\frac{\partial(eS_l)}{\partial t} + \frac{1}{(1+e)}\frac{\partial(\rho_v eS_a)}{\partial t} + \rho_l\nabla\cdot\mathbf{v_l} + \rho_l\nabla\cdot\mathbf{v_v} + \nabla\cdot(\rho_v\mathbf{v_a}) = 0 \tag{5.12}$$

The spatial derivative terms of equation (5.12) (i.e. the right hand side of the equation), show that the moisture flux includes:

i. A liquid flux
ii. A component of vapour flux due to vapour pressure gradients
iii. A component of vapour flux due to the bulk flow of vapour arising from the movement of pore air

Also from the left hand side of equation (5.12) it can be seen that the mechanisms of water flow are described by the velocities of the liquid, vapour and air phases. The flow rates and laws that govern them are discussed in the following sections.

5.3.1 Mechanisms of liquid water flow

The various mechanisms that have found to contribute to liquid water flow are as follows (Mitchell, 1993) (Fredlund & Rahardjo, 1993):

i. water flow due to pressure head
ii. water flow due to elevation head
iii. water flow due to osmosis phenomena (e.g. chemical and thermal osmosis)
iv. water flow due to electrical gradients

The first two of the listed mechanisms have been considered within the scope of this work.

The hydraulic head is described by combining the first two listed components, namely the pressure and elevation heads. Darcy's law (1856) can be used to present this potential for unsaturated soils (Childs, 1969) (Nielson, et al., 1986). For multiphase flow in unsaturated media Darcy's law can be expressed as:

$$\mathbf{v_l} = -\frac{k_l}{\mu_l}\left[\nabla\frac{u_l}{\gamma_l} + \nabla z\right] = -K_l\left[\nabla\frac{u_l}{\gamma_l} + \nabla z\right] \tag{5.13}$$

where $\mathbf{v_l}$ is the liquid velocity due to the pressure and elevation heads, k_l; is the intrinsic permeability, μ_l is the absolute viscosity, γ_l is the unit weight of the liquid, z is the elevation and K_l is the unsaturated hydraulic conductivity. The absolute viscosity is strongly influenced by the absolute temperature. Kaye and Laby (1973) presented a relationship between the absolute viscosity of liquid water and the absolute temperature valid within the range 273 K < T < 373 K:

$$\mu_l(T) = 661.2\,(T - 229)^{-1.562} \times 10^{-3} \pm 0.5\% \qquad (N\,s/m^2) \tag{5.14}$$

Unsaturated hydraulic conductivity of a soil is influenced by a number of factors, namely; the fabric of the soil, degree of saturation and turbulence of the flow (Leong & Rahardjo, 1997). The dominating characteristic with regards to the soil fabric is the amount of pore volume that can be used for flow (Leong & Rahardjo, 1997). Turbulence may be neglected if the resulting flow is slow. It can be said that the exact value of the unsaturated hydraulic conductivity is therefore dependent on the material characteristics and in-situ conditions. Various theoretical and empirical theories have been proposed, although the latter clearly requires that either laboratory testing or an existing solution is attainable for the soil in question. Mualam (1976) proposed a theoretical approach based on the water retention properties of soil as follows:

$$K_l(h) = \frac{\{1 - (\alpha h)^{n-1}[1 + (\alpha h)^n]^{-m}\}^2}{[1 + (\alpha h)^n]^{m/2}} \qquad \left(m = 1 - {}^1/_n\right) \tag{5.15}$$

where K_l is the unsaturated hydraulic conductivity at a specific hydraulic head, *h*. *α, m, and n* are material coefficients which are obtained from the related laboratory tests.

Matyas and Radhakrishna (1968) proposed that the degree of liquid saturation is a function of the initial void ratio, the initial liquid saturation, and the stress parameters: net stress, deviatoric stress and suction. Alonso et al (1988) found that the effect of stress upon the degree of saturation to be relatively insignificant. Based on this observation, if the initial void ratio of a soil sample is maintained and the sample is confined, the degree of saturation can be expressed in terms of suction, *s*, as follows:

$$S_l = S_l(s) \tag{5.16}$$

Phillip and de Vries (1957) stated that the change in soil-water potential is attributed to the temperature effect on interfacial tension of pure water. Thus, for unsaturated soils, suction is therefore dependant on the surface energy which is in turn dependant on the absolute temperature. The surface energy, ξ, was expressed by Edlefsen and Anderson (1943) as a function of temperature as follows:

$$\xi = 0.1171 - 0.0001516T \qquad (J/m^2) \tag{5.17}$$

Therefore, if the relationship between suction and degree of saturation at a reference temperature, T_r, is known, the suction at any temperature and degree of saturation can theoretically be found:

$$s = \frac{\xi}{\xi_r} s_r \tag{5.18}$$

where ξ_r and s_r are the surface energy and suction at reference temperature and; ξ and s are the surface energy and suction at the temperature, *T*.

If the dependency of soil suction on temperature is incorporated in the temporal derivative of equation (5.16), the variation of the degree of saturation with respect to time can be expressed as:

$$\frac{\partial S_l}{\partial t} = \frac{\partial S_l}{\partial s}\frac{\partial s}{\partial t} + \frac{\partial S_l}{\partial T}\frac{\partial T}{\partial t} \tag{5.19}$$

The matric suction is defined as the difference between the pore air pressure and the pore liquid pressure, expressed as (Fredlund & Rahardjo, 1993):

$$s = u_a - u_l \tag{5.20}$$

Other forms of suction, such as osmotic, are neglected as changes in these variables due to changes in the other primary variables will not be significant within the current scope of investigation due to the expected temperature range and omission of chemical analysis.

The degree of saturation can then be expressed in terms of the primary variables by substituting equation (5.20) into equation (5.19):

$$\frac{\partial S_l}{\partial t} = \frac{\partial S_l}{\partial s}\frac{\partial u_a}{\partial t} + \frac{\partial S_l}{\partial T}\frac{\partial T}{\partial t} - \frac{\partial S_l}{\partial s}\frac{\partial u_l}{\partial t} \tag{5.21}$$

The application of the above expression with regards to the dependency of suction, i.e. matric soil water potential, on temperature is theoretically limited to the capillary component of matric soil water potential or capillary suction. Within the current scope of work, the so called Soil Water Characteristic Curve (SWCC) relating suction to the degree of saturation has been applied.

A number of relationships have been suggested to describe the SWCC of soil, e.g. Brooks and Corey (1964), Fredlund and Xing (1994) and van Genuchten (1980). The relationship proposed by van Genuchten (1980) has been successfully applied to an extensive range of unsaturated soils. This relationship is given as (van Genuchten, 1980):

$$\theta_l = \theta_{res} + \frac{(\theta_{sat} - \theta_{res})}{[1 + (\alpha h)^n]^m} \tag{5.22}$$

where θ_l is the water content θ_{res} is the residual water content, θ_{sat} is the saturated water content, h is the pressure head (suction). α, m and n are material coefficients.

The material coefficients α, m and n can be experimentally measured through the determination of the SWCC. Vereecken et al. (1989) proposed a series of empirical equations in order to estimate the SWCC based on basic soil properties. The empirical equations were developed from a catalogue of 182 soil samples from which SWCC were developed. The soil types found within this catalogue, closely match the soil type found at the monitoring site (see Chapter 3) therefore the empirical relationships proposed by Vereecken (1989) were deemed representative within the scope of this investigation.

$$\theta_{sat} = 0.81 - 0.283\gamma + 0.001\Delta \tag{5.23}$$

$$\theta_{res} = 0.015 + 0.005\Delta + 0.014\Omega \tag{5.24}$$

$$\log(\alpha) = -2.486 + 0.025\kappa - 0.351\Omega - 2.617\gamma - 0.023\Delta \tag{5.25}$$

$$\log(n) = 0.053 - 0.009\kappa - 0.013\Delta + 0.00015\kappa^2 \tag{5.26}$$

where γ is the soil bulk density, Δ is the clay content, Ω is the silt content and κ is the sand content of the soil.

5.3.2 Mechanisms of water vapour flow

As previously explained, vapour transfer occurs as a result of two main mechanisms, namely; diffusive and vapour flows. The bulk air is considered to be a binary mixture of water vapour and dry air (Pollock, 1986) and is dealt with using a generalised form of Darcy's law, following the approach of a number of researchers (Carman, 1956) (Alonso, et al., 1988). Diffusive flow behaviour is represented by diffusive vapour flow theory for unsaturated soil, proposed by Philip and de Vries (1957).

Considering the transport of bulk air phase, the primary driving mechanism is the pore air pressure gradient, with elevation providing only a negligible contribution (Fredlund & Rahardjo, 1993). Therefore, a generalised Darcy's law for air flow in unsaturated soil is used, described as:

$$\mathbf{v_a} = -\frac{k_a}{\mu_a}\nabla u_a = -K_a \nabla u_a \tag{5.27}$$

where $\mathbf{v_a}$ is the velocity of pore air, k_a is the effective permeability of pore air, μ_a is the absolute viscosity of pore air and K_a is the unsaturated conductivity of pore air. The unsaturated conductivity of gases in soil is a function of the pore air properties and volume/mass of a soil (Clifford & Webb, 2006). As the properties of the air are generally assumed to be constant during the flow process, the volume/mass properties control the air conductivity (Olsen, 1963). For consistency, K_a is therefore considered to be a function of the void ratio (i.e. e) and degree of pore air saturation (i.e. S_a) (Fredlund & Rahardjo, 1993), therefore:

$$k_a = k_a(e, S_a) \tag{5.28}$$

Philip and de Vries (1957) proposed a vapour flow law in unsaturated soil, where the velocity of vapours is described by:

$$\mathbf{v_v} = -\frac{D_{atms} v_v \tau_v \theta_a}{\rho_l} \nabla \rho_l \tag{5.29}$$

where D_{atms} is the molecular diffusivity of vapour through air, v_v is a mass flow factor, τ_v is a tortuosity factor and $\nabla\rho_v$ is the spatial vapour density gradient.

Philip and de Vries (1957) adopted the following expression proposed by Krischer and Rohnalter (1940) for the molecular diffusivity of vapour through air:

$$D_{atms} = 5.893 \times 10^{-6} \frac{T^{2.3}}{u_a} \tag{5.30}$$

Philip and de Vries (1957) also introduced an expression for the mass flow vector, v_v. It was incorporated to allow for the mass flow of vapour arising from the difference in boundary conditions governing the air and vapour components of the diffusion system. They adopted an expression proposed by Partington (1949), who showed that steady state diffusion in a closed system between an evaporating source and a condensing sink could be described as:

$$v_v = \frac{u_a}{u_a - u_v} \tag{5.31}$$

where u_v is the partial pressure of vapour and which be calculated using the following thermodynamic relationship under assuming 'ideal gas' behaviour:

$$u_v = \rho_v R_v T \tag{5.32}$$

where R_v is the specific gas constant for water vapour (Kaye and Laby, 1973).

Philip and de Vries (1957) recognised that the values of the mass flow factor, v_v, predicted by equation (5.31) may not be valid under non-stationary conditions, however, the expression was able to predict the correct order of magnitude. They also commented that the factor is close to 1 under normal soil temperatures.

A thermodynamic relationship was proposed by Edlefsen and Anderson (1943), known as the psychrometric law, showing the density of water vapour can be given as:

$$\rho_v = \rho_0 h = \rho_0 \exp\left(\frac{\varphi g}{R_v T}\right) \qquad (kg/m^3) \tag{5.33}$$

where ρ_0 is the density of saturated water vapour, h is the relative humidity and g is the gravitational constant. φ is the capillary potential and can defined as:

$$\varphi = \frac{u_l - u_a}{\gamma_l} = \frac{s}{\gamma_l} \qquad (m) \tag{5.34}$$

Ewen and Thomas (1989) presented a relationship fitted to standard data (Mayhew and Rogers, 1976) for the density of saturated water vapour:

$$\rho_0 = \frac{1}{194.4 \exp(-0.06374(T - 273) + 0.1634 \times 10^{-3}(T - 273)^2)} \tag{5.35}$$

From equation (5.33) and with substitution from equation (5.20) for suction, the gradient of vapour density is expressed as:

$$\nabla\rho_v = \left(h\frac{\partial\rho_0}{\partial T} + \rho_0\frac{\partial h}{\partial T}\right)\nabla T + \left(\rho_0\frac{\partial h}{\partial s}\right)\nabla u_a - \left(\rho_0\frac{\partial h}{\partial s}\right)\nabla u_l \tag{5.36}$$

The above expression has been obtained assuming that the density of saturated water vapour is dependent on temperature whilst the relative humidity is dependent on both suction and temperature. The time derivative of vapour density considering the same assumptions, is obtained as:

$$\frac{\partial\rho_v}{\partial t} = \left(h\frac{\partial\rho_0}{\partial T} + \rho_0\frac{\partial h}{\partial T}\right)\frac{\partial T}{\partial t} + \left(\rho_0\frac{\partial h}{\partial s}\right)\frac{\partial u_a}{\partial t} - \left(\rho_0\frac{\partial h}{\partial s}\right)\frac{\partial u_l}{\partial t} \tag{5.37}$$

Substituting equation (5.36) into equation (5.29) gives:

$$\begin{aligned}\mathbf{v_v} = {} & \frac{D_{atms} v_v \tau_v \theta_a}{\rho_l}\left(\rho_0\frac{\partial h}{\partial s}\right)\nabla u_l - \frac{D_{atms} v_v \tau_v \theta_a}{\rho_l}\left(h\frac{\partial\rho_0}{\partial T} + \rho_0\frac{\partial h}{\partial T}\right)\nabla T \\ & - \frac{D_{atms} v_v \tau_v \theta_a}{\rho_l}\left(\rho_0\frac{\partial h}{\partial s}\right)\nabla u_a\end{aligned} \tag{5.38}$$

In experimental tests undertaken by Philip and de Vries (1957) the theory shown in equation (5.38) did not fully capture the behaviour of vapour flows at increased temperature gradients. To address this, two refinements were made to the temperature gradient term. A flow factor, *f*, was included to allow for a reduction of the vapour flow when higher moisture contents reduce the available flow area. A microscopic pore temperature gradient factor,$(\nabla T)_a/(\nabla T)$, was also proposed. This is the ratio of the average temperature gradient in the air filled pores to overall temperature gradient. The factor allows for the inclusions of microscopic temperature gradients in the air filled pores, which may be much higher than the macroscopic temperature gradients across the whole sample. Heat flow paths shared between sections of solid and fluid paths give rise to this effect. Equation (5.38) is modified to include the aforementioned factors gives:

$$\mathbf{v_v} = \frac{D_{atms} v_v \tau_v \theta_a}{\rho_l}\left(\rho_0 \frac{\partial h}{\partial s}\right)\nabla u_l - \frac{D_{atms} v_v \tau_v \theta_a}{\rho_l} f \frac{(\nabla T)_a}{\nabla T}\left(h\frac{\partial \rho_0}{\partial T} + \rho_0 \frac{\partial h}{\partial T}\right)\nabla T - \frac{D_{atms} v_v \tau_v \theta_a}{\rho_l}\left(\rho_0 \frac{\partial h}{\partial s}\right)\nabla u_a \tag{5.39}$$

Two alterations to the flow area factor of Philip and de Vries (1957) equation were proposed by Ewen and Thomas (1989). Firstly, the flow area factor had not been applied to the moisture term, but assuming vapour velocity is proportional to vapour density the factor should appear in both temperature and moisture terms. The second alteration made is that the reduction in velocity due to a reduction in flow area, predicted by the equation, was not shown experimentally by Philip and de Vries. Ewen and Thomas suggested the form of the flow area factor is modified to be in terms of the porosity so that this phenomenon is not predicted by the equation. It is noted however, that at saturation no vapour movement would occur. Adopting these alterations, the vapour velocity equation shown in equation (5.39) can be expressed as:

$$\mathbf{v_v} = \frac{D_{atms} v_v n}{\rho_l}\left(\rho_0 \frac{\partial h}{\partial s}\right)\nabla u_l - \frac{D_{atms} v_v n}{\rho_l} f \frac{(\nabla T)_a}{\nabla T}\left(h\frac{\partial \rho_0}{\partial T} + \rho_0 \frac{\partial h}{\partial T}\right)\nabla T - \frac{D_{atms} v_v n}{\rho_l}\left(\rho_0 \frac{\partial h}{\partial s}\right)\nabla u_a \tag{5.40}$$

where $(\nabla T)_a/(\nabla T)$ is derived from the work of Preece (1975) for Washington Sand (de Vries, 1966).

It is recognised that the experimental work above was conducted on a dense cohesion-less material, medium sand. It is therefore acknowledged that the application of an approach validated for

sand requires further research and development prior to its application to calculate the movement of vapour within a cohesive medium, such as clay.

5.3.3 Governing differential equations for moisture flow

The components of flow for the liquid and vapour were defined in the previous sections. In this section, the governing equations for flow are incorporated into the equation of mass conservation for moisture flow, detailed in equation (5.12). The resulting equation is then restructured in terms of the primary variables to produce the governing equation.

With the expansion of the first two terms of equation (5.12), again recognising $n = e/(1+e)$ and with the substitution of $S_a = 1 - S_l$ equation (5.12) can be expressed as:

$$\rho_l n\frac{\partial S_l}{\partial t} + \frac{\rho_l S_l}{(1+e)}\frac{\partial e}{\partial t} + \frac{\rho_v(1-S_l)}{(1+e)}\frac{\partial e}{dt} + (1-S_l)n\frac{\partial \rho_v}{\partial t} - \rho_v n\frac{\partial S_l}{\partial t} + \rho_l \nabla\cdot\mathbf{v_l} + \rho_l\nabla\cdot\mathbf{v_v} + \nabla\cdot(\rho_v\mathbf{v_a}) = 0 \quad (5.41)$$

Grouping all similar terms gives:

$$n(\rho_l - \rho_v)\frac{\partial S_l}{\partial t} + n(1-S_l)\frac{\partial \rho_v}{\partial t} + \left[\frac{\rho_l S_l + \rho_v(1-S_l)}{(1+e)}\right]\frac{\partial e}{\partial t} + \rho_l\nabla\cdot\mathbf{v_l} + \rho_l\nabla\cdot\mathbf{v_v} + \nabla\cdot(\rho_v\mathbf{v_a}) = 0 \quad (5.42)$$

Considering the third term in equation (5.42) it can be seen that:

$$\frac{\partial e}{(1+e)\partial t} = \frac{\partial \varepsilon_v}{\partial t} \quad (5.43)$$

where ε_v is the volumetric strain which by definition is the rate of change of void ratio with respect to the initial volume.

With the above substitution, equation (5.42) yields:

$$n(\rho_l - \rho_v)\frac{\partial S_l}{\partial t} + n(1-S_l)\frac{\partial \rho_v}{\partial t} + [\rho_l S_l + \rho_v(1-S_l)]\frac{\partial \varepsilon_v}{\partial t} + \rho_l\nabla\cdot\mathbf{v_l} + \rho_l\nabla\cdot\mathbf{v_v} + \nabla\cdot(\rho_v\mathbf{v_a}) = 0 \quad (5.44)$$

As outlined within section 5.2 of this Chapter, only the formulation of heat and moisture transfer is considered within the scope of this investigation. The deformation of soil is not considered

here, hence the change in volumetric strain, ε_v, will also equal zero and the third term in equation (5.44) can be removed.

Considering the first term in equation (5.44) and including substitution from equation (5.21), the following expression can be derived whereby the temporal derivative of the degree of saturation, S_l, is expressed in terms of partial derivatives with respect to the primary variables:

$$n(\rho_l - \rho_v)\frac{\partial S_l}{\partial t} = -n(\rho_l - \rho_v)\frac{\partial S_l}{\partial s}\frac{\partial u_l}{\partial t} + n(\rho_l - \rho_v)\frac{\partial S_l}{\partial T}\frac{\partial T}{\partial t} + n(\rho_l - \rho_v)\frac{\partial S_l}{\partial s}\frac{\partial u_a}{\partial t} \tag{5.45}$$

Considering the second term in equation (5.44) and including substitution from equation (5.37), it can be said that:

$$n(1 - S_l)\frac{\partial \rho_v}{\partial t} = n(1 - S_l)\left[\left(h\frac{\partial \rho_0}{\partial T} + \rho_0\frac{\partial h}{\partial T}\right)\frac{\partial T}{\partial t} + \left(\rho_0\frac{\partial h}{\partial s}\right)\frac{\partial u_a}{\partial t} - \left(\rho_0\frac{\partial h}{\partial s}\right)\frac{\partial u_l}{\partial t}\right] \tag{5.46}$$

Substituting equations (5.45) and (5.46) for the first and second terms of (5.44) respectively while removing the third, and equations (5.13), (5.27) and (5.40) for $\mathbf{v_l}$, $\mathbf{v_a}$ and $\mathbf{v_v}$ respectively into equation (5.44) yields the governing equation for moisture transfer in terms of primary variables:

$$C_{ll}\frac{\partial u_l}{\partial t} + C_{lT}\frac{\partial T}{\partial t} + C_{la}\frac{\partial u_a}{\partial t} = \nabla \cdot [K_{ll}\nabla u_l] + \nabla \cdot [K_{lT}\nabla T] + \nabla \cdot [K_{la}\nabla u_a] + J_l \tag{5.47}$$

where:

$$C_{ll} = -n(\rho_l - \rho_v)\frac{\partial S_l}{\partial s} - n(1 - S_l)\rho_0\frac{\partial h}{\partial s} \tag{5.48}$$

$$C_{lT} = n(\rho_l - \rho_v)\frac{\partial S_l}{\partial T} + n(1 - S_l)\left(h\frac{\partial \rho_0}{\partial T} + \rho_0\frac{\partial h}{\partial T}\right) \tag{5.49}$$

$$C_{la} = n(\rho_l - \rho_v)\frac{\partial S_l}{\partial s} + n(1 - S_l)\rho_0\frac{\partial h}{\partial s} \tag{5.50}$$

$$K_{ll} = \rho_l\left[\frac{K_l}{\gamma_l} - \frac{D_{atms}v_v n}{\rho_l}\left(\rho_0\frac{\partial h}{\partial s}\right)\right] \tag{5.51}$$

$$K_{lT} = \rho_l\frac{D_{atms}v_v n}{\rho_l}\frac{(\nabla T)_a}{\nabla T}\left(h\frac{\partial \rho_0}{\partial T} + \rho_0\frac{\partial h}{\partial T}\right) \tag{5.52}$$

$$K_{la} = \rho_v K_a + \rho_l \left[\frac{D_{atms} v_v n}{\rho_l} \left(\rho_o \frac{\partial h}{\partial s} \right) \right] \tag{5.53}$$

$$J_l = \rho_l \nabla \cdot (K_l \nabla z) \tag{5.54}$$

5.4 Air transfer

Dry air is considered to exist in two forms in unsaturated soils, i.e. bulk air and dissolved air (Fredlund & Rahardjo, 1993). The air pressure gradient is the driving mechanism for the transfer of bulk air, the flow of which can be determined by the application of Darcy's law. The flow of the dissolved air is considered as an advective flow within the pore liquid. Henry's law governs the proportion of air dissolved in the pore liquid. The dissolved air flow is therefore coupled with the pore-liquid flow whereas the bulk air flow is driven by the air pressure gradient.

Conservation of mass dictates that the temporal derivative of the dry air content and the spatial derivative of the dry air flux must be equal, yielding:

$$\frac{\partial([\theta_a + H_s \theta_l] \rho_{da} \partial V)}{\partial t} = -\partial V \nabla \cdot [\rho_{da} (\mathbf{v_a} + H_s \mathbf{v_l})] \tag{5.55}$$

where H_s is Henry's volumetric coefficient of solubility and ρ_{da} is the density of dry air. Substituting equation (5.8), (5.9) and (5.10) into equation (5.55) yields the mass conservation equation in terms of degree of saturation, porosity and void ratio:

$$\frac{\partial([S_a + H_s S_l] \rho_{da} n(1+e) \partial V_s)}{\partial t} = -(1+e) \partial V_s \nabla \cdot [\rho_{da} (\mathbf{v_a} + H_s \mathbf{v_l})] \tag{5.56}$$

As previously stated, since ∂V_s is constant, this term can be eliminated from equation (5.56). Substituting $n(1+e) = e$ and $S_a = 1 - S_l$ yields:

$$\frac{\partial([1 - S_l + H_s S_l] \rho_{da} e)}{\partial t} + (1+e) \nabla \cdot [\rho_{da} (\mathbf{v_a} + H_s \mathbf{v_l})] = 0 \tag{5.57}$$

Expanding the first term of equation (5.57) gives:

$$\frac{\partial([1-\ S_l+\ H_sS_l]\rho_{da}e)}{\partial t} = \rho_{da}(1-\ S_l+\ H_sS_l)\frac{\partial e}{\partial t}+e(1-\ S_l+\ H_sS_l)\frac{\partial \rho_{da}}{\partial t}-e\rho_{da}\frac{\partial S_l}{\partial t} + e\rho_{da}H_s\frac{\partial S_l}{\partial t} \tag{5.58}$$

Grouping similar terms gives:

$$\frac{\partial([1-\ S_l+\ H_sS_l]\rho_{da}e)}{\partial t} = \rho_{da}(1-\ S_l+\ H_sS_l)\frac{\partial e}{\partial t}+e(1-\ S_l+\ H_sS_l)\frac{\partial \rho_{da}}{\partial t}-e\rho_{da}(H_s-1)\frac{\partial S_l}{\partial t} \tag{5.59}$$

Substituting equation (5.59) into equation (5.57), dividing the resultant by $(1+e)$ and recognising $e/(1+e)=n$, yields:

$$\rho_{da}\frac{(1-\ S_l+\ H_sS_l)}{(1+e)}\frac{\partial e}{\partial t}+n(1-\ S_l+\ H_sS_l)\frac{\partial \rho_{da}}{\partial t}+n\rho_{da}(H_s-1)\frac{\partial S_l}{\partial t}+\ \nabla \cdot[\rho_{da}(\mathbf{v_a}+\ H_s\mathbf{v_l})]=0 \tag{5.60}$$

Substituting equation (5.43) into equation (5.60) yields:

$$\rho_{da}(1-\ S_l+\ H_sS_l)\frac{\partial \varepsilon_v}{\partial t}+n(1-\ S_l+\ H_sS_l)\frac{\partial \rho_{da}}{\partial t}+n\rho_{da}(H_s-1)\frac{\partial S_l}{\partial t}+\ \nabla \cdot[\rho_{da}(\mathbf{v_a}+\ H_s\mathbf{v_l})]=0 \tag{5.61}$$

As outlined within section 5.2 of this Chapter, the scope of the current investigation assumes a rigid soil system, therefore the change in volumetric strain, ε_v, is considered to be equal to zero. The first term in equation (5.61) can therefore be removed, giving:

$$n(1-\ S_l+\ H_sS_l)\frac{\partial \rho_{da}}{\partial t}+n\rho_{da}(H_s-1)\frac{\partial S_l}{\partial t}+\ \nabla \cdot[\rho_{da}(\mathbf{v_a}+\ H_s\mathbf{v_l})]=0 \tag{5.62}$$

The bulk gas phase has been found, within a sufficient degree of accuracy, to obey the laws of ideal gases (Geraminegad & Saxena, 1986). The partial pressures of dry air and vapour can therefore be expressed as:

$$u_{da}=\ \rho_{da}R_{da}T \tag{5.63}$$

and:

$$u_v = \rho_v R_v T \tag{5.64}$$

where R_{da} and R_v are the specific gas constants of dry air and water vapour respectively. The air pressure can be calculated by the application of Dalton's law of partial pressures:

$$u_a = u_{da} + u_v \tag{5.65}$$

The dry air density can then be found by the substitution of equations (5.63) and (5.64) into equations (5.65), yielding:

$$\rho_{da} = \frac{u_a}{R_{da} T} - \frac{\rho_v R_v}{R_{da}} \tag{5.66}$$

The partial derivative, with respect to time, can be expressed as:

$$\frac{\partial \rho_{da}}{\partial t} = \frac{1}{R_{da} T}\frac{\partial u_a}{\partial t} - \frac{\rho_a}{T}\frac{\partial T}{\partial t} - \frac{R_v}{R_{da}}\frac{\partial \rho_v}{\partial t} \tag{5.67}$$

It is noted that the last differential term in equation (5.67) can be obtained from equation (5.37).

Substituting for the time derivative terms of degree of saturation from equations (5.21) and density of dry air from equation (5.66), velocity of pore liquid and pore air from equations (5.13) and (5.27) respectively into equation (5.62) leads to the governing equation for air transfer in terms of primary variables:

$$C_{al}\frac{\partial u_l}{\partial t} + C_{aT}\frac{\partial T}{\partial t} + C_{aa}\frac{\partial u_a}{\partial t} = \nabla \cdot [K_{al} \nabla u_l] + \nabla \cdot [K_{aa} \nabla u_a] + J_a \tag{5.68}$$

where:

$$C_{al} = -n\rho_{da}(H_s - 1)\frac{\partial S_l}{\partial s} + n(S_a + H_s S_l)\frac{\partial R_v}{\partial R_{da}}\left(\rho_0 \frac{\partial h}{\partial s}\right) \tag{5.69}$$

$$C_{at} = n\rho_{da}(H_s - 1)\frac{\partial S_l}{\partial T} - n(S_a + H_s S_l)\left(\frac{\rho_a}{T} - \frac{R_v}{R_{da}}\left(h\frac{\partial \rho_0}{\partial T} + \rho_o \frac{\partial h}{\partial T}\right)\right) \tag{5.70}$$

$$C_{aa} = n\rho_{da}(H_s - 1)\frac{\partial S_l}{\partial s} + n(S_a + H_s S_l)\left(\frac{1}{R_{da} T} - \frac{R_v}{R_{da}}\rho_0 \frac{\partial h}{\partial s}\right) \tag{5.71}$$

$$K_{al} = \frac{\rho_{da} H_s}{\gamma_l} K_l \tag{5.72}$$

$$K_{aa} = \rho_{da} K_a \tag{5.73}$$

$$J_a = \rho_{da} H_s \nabla \cdot (K_l \nabla z) \tag{5.74}$$

5.5 Heat transfer

Heat transfer is the energy transport between two material bodies due to a temperature difference (Lewis, et al., 2004). The primary mechanisms of heat transfer, namely conduction, convection and radiation were identified by Jakob (1949). The formulation presented here ignores radiation effects as its influence is assumed to be negligible within the current scope of work based on the anticipated temperature range (Mitchell, 1993).

Conservation of energy dictates that the temporal derivative of the heat content, Ω, is equal to the spatial derivative of the heat flux, Q, expressed as:

$$\frac{\partial(\Omega \partial V)}{\partial t} = -\nabla . Q(\partial V) \tag{5.75}$$

The heat content for a partially saturated soil, per unit volume (i.e. Ω) is the sum of the product of the heat storage capacity with temperature change and the contribution of enthalpy characterised by the latent heat of vaporisation (Ewen & Thomas, 1989). This gives:

$$\Omega = H_c(T - T_r) + LnS_a\rho_v \tag{5.76}$$

where L is the latent heat of vaporisation. The following approach was presented by Ewen and Thomas (1989) to calculate the heat capacity of an unsaturated soil at a reference temperature T_r.

$$H_c = (1-n)C_{ps}\rho_s + n\left(C_{pl}S_l\rho_l + C_{pv}S_a\rho_v + C_{pda}S_a\rho_{da}\right) \tag{5.77}$$

where C_{ps}, C_{pl}, C_{pv} and C_{pda} are the specific heat capacities of the solid, vapour and dry air respectively and ρ_s is the density of the solid.

Following Thomas and He (1995), the heat flux, Q, can be defined by considering three components of heat transportation. The first term in equation (5.78) describes the thermal conduction in accordance with Fourier's law and the second term describes the latent heat flow associated with vapour movement. The third term describes the heat convection in terms of the liquid phase movements, vapour phase associated with a vapour pressure gradient, vapour phase associated with bulk air flow and the air phase.

$$Q = -\lambda_T \nabla T + L(\mathbf{v_v}\rho_l + \mathbf{v_a}\rho_v) + \left(C_{pl}\mathbf{v_l}\rho_l + C_{pv}\mathbf{v_v}\rho_l + C_{pv}\mathbf{v_a}\rho_v + C_{pda}\mathbf{v_a}\rho_{da}\right)(T - T_r) \tag{5.78}$$

where λ_T is the coefficient of thermal conductivity.

Following the approach of Thomas and Rees (2009) the coefficient of thermal conductivity for an unsaturated soil can be defined in terms of the soil constituents (i.e. the solid, liquid and air phases), the known volume fraction of each phase and the associated thermal conductivities.

$$\lambda = \prod_{i=1}^{3} \lambda_i^{\chi_i} = \lambda_s^{\chi_s} \cdot \lambda_w^{\chi_w} \cdot \lambda_a^{\chi_a} \tag{5.79}$$

where λ_i is the coefficient of thermal conductivity corresponding to the solid, water and air components of the soil and χ_i is the volume fractions of the soil components which can be found by application of the following expressions:

$$\chi_s = 1 - n \tag{5.80}$$

$$\chi_w = n\, S_l \tag{5.81}$$

$$\chi_a = n(1 - S_l) \tag{5.82}$$

The law of conservation of energy as defined in equation (5.75), with the substitution of equations (5.76) and (5.78) can be expressed as:

$$\frac{\partial}{\partial t}\left[(H_c(T - T_r) + LnS_a\rho_v)\,\partial V\right] = -\nabla.\left\{\begin{bmatrix} -\lambda_T \nabla T + L(\mathbf{v_v}\rho_l + \mathbf{v_a}\rho_v) + \\ \left(C_{pl}\mathbf{v_l}\rho_l + C_{pv}\mathbf{v_v}\rho_l + C_{pv}\mathbf{v_a}\rho_v + C_{pda}\mathbf{v_a}\rho_{da}\right)(T - T_r) \end{bmatrix}\partial V\right\} \tag{5.83}$$

Substituting equation 5.10 into equation 5.83, and cancelling the term ∂V_s yields;

$$\frac{\partial}{\partial t}[(H_c(T - T_r) + LnS_a\rho_v)(1+e)] = -\nabla.\left\{\left[\begin{matrix}-\lambda_T \nabla T + L(\mathbf{v_v}\rho_l + \mathbf{v_a}\rho_v) + \\ (C_{pl}\mathbf{v_l}\rho_l + C_{pv}\mathbf{v_v}\rho_l + C_{pv}\mathbf{v_a}\rho_v + C_{pda}\mathbf{v_a}\rho_{da})(T - T_r)\end{matrix}\right](1+e)\right\} \quad (5.84)$$

The first term on the left hand side of equation (5.84) can be expanded, yielding:

$$\frac{\partial}{\partial t}[H_c(T - T_r)(1+e)] = (T - T_r)\frac{\partial}{\partial t}[H_c(1+e)] + H_c(1+e)\frac{\partial T}{\partial t} \quad (5.85)$$

Substituting equation (5.77) into the first term on the right hand side of equation (5.85) and rearranging yields:

$$(T - T_r)\frac{\partial}{\partial t}[H_c(1+e)] = (T - T_r)\frac{\partial}{\partial t}\left[\left(C_{ps}\rho_s + n\left(-C_{ps}\rho_s + C_{pl}S_l\rho_l + C_{pv}S_a\rho_v + C_{pda}S_a\rho_{da}\right)\right)(1+e)\right] \quad (5.86)$$

Expanding further and recognising $n(1+e) = e$ yields:

$$(T - T_r)\frac{\partial}{\partial t}[H_c(1+e)] = (T - T_r)\left[\begin{matrix}C_{ps}\rho_s\frac{\partial e}{\partial t} + \left(-C_{ps}\rho_s + C_{pl}S_l\rho_l + C_{pv}S_a\rho_v + C_{pda}S_a\rho_{da}\right)\frac{\partial e}{\partial t} \\ + e\left(\begin{matrix}C_{pl}\rho_l\frac{\partial S_l}{\partial t} - C_{pv}\rho_v\frac{\partial S_l}{\partial t} + C_{pv}(1 - S_l)\frac{\partial \rho_v}{\partial t} \\ + C_{pda}(1 - S_l)\frac{\partial \rho_{da}}{\partial t} - C_{pda}\rho_{da}\frac{\partial S_l}{\partial t}\end{matrix}\right)\end{matrix}\right] \quad (5.87)$$

Noting that $\frac{\partial e}{\partial t} = (1+e)^2\ \frac{\partial n}{\partial t}$ and rearranging, grouping like terms gives:

$$(T - T_r)\frac{\partial}{\partial t}[H_c(1+e)] = (T - T_r)\left[\begin{matrix}\left(C_{pl}S_l\rho_l + C_{pv}S_a\rho_v + C_{pda}S_a\rho_{da}\right)(1+e)^2\frac{\partial n}{\partial t} \\ + e\left(C_{pl}\rho_l - C_{pv}\rho_v - C_{pda}\rho_{da}\right)\frac{\partial S_l}{\partial t} + eC_{pv}(1 - S_l)\frac{\partial \rho_v}{\partial t} + eC_{pda}(1 - S_l)\frac{\partial \rho_{da}}{\partial t}\end{matrix}\right] \quad (5.88)$$

Considering the second term on the left hand side of equation (5.84) and substituting $n(1+e)=e$ yields:

$$\frac{\partial}{\partial t}[LnS_a\rho_v(1+e)] = \frac{\partial}{\partial t}[LeS_a\rho_v] \tag{5.89}$$

Expanding equation (5.89) yields:

$$\frac{\partial}{\partial t}[LeS_a\rho_v] = L(1-S_l)e\frac{\partial \rho_v}{\partial t} - Le\rho_v\frac{\partial S_l}{\partial t} + L(1-S_l)\rho_v\frac{\partial e}{\partial t} \tag{5.90}$$

Again, recognising that $\frac{\partial e}{\partial t} = (1+e)^2\frac{\partial n}{\partial t}$ and rearranging gives:

$$\frac{\partial}{\partial t}[LeS_a\rho_v] = L(1-S_l)e\frac{\partial \rho_v}{\partial t} - Le\rho_v\frac{\partial S_l}{\partial t} + L(1-S_l)\rho_v(1+e)^2\frac{\partial n}{\partial t} \tag{5.91}$$

Substituting equations (5.85), (5.88) and (5.91) into equation (5.84) yields the governing equation for heat flow:

$$\begin{aligned}(T-T_r)&\begin{bmatrix}\left((C_{pl}S_l\rho_l + C_{pv}S_a\rho_v + C_{pda}S_a\rho_{da})(1+e)^2\right)\frac{\partial n}{\partial t}\\ + e\left(C_{pl}\rho_l - C_{pv}\rho_v - C_{pda}\rho_{da}\right)\frac{\partial S_l}{\partial t} + eC_{pv}(1-S_l)\frac{\partial p_v}{\partial t} + eC_{pda}(1-S_l)\frac{\partial \rho_{da}}{\partial t}\end{bmatrix}\\ &+ H_c(1+e)\frac{\partial T}{\partial t} + L(1-S_l)e\frac{\partial \rho_v}{\partial t} - Le\rho_v\frac{\partial S_l}{\partial t} + L(1-S_l)\rho_v(1+e)^2\frac{\partial n}{\partial t}\\ &= -\nabla\begin{bmatrix}-\lambda\nabla T + L(\mathbf{v_v}\rho_l + \mathbf{v_a}\rho_v)\\ + \left(C_{pl}\mathbf{v_l}\rho_l + C_{pv}\mathbf{v_v}\rho_l + C_{pv}\mathbf{v_a}\rho_v + C_{pda}\mathbf{v_a}\rho_{da}\right)(T-T_r)\end{bmatrix}(1+e)\end{aligned} \tag{5.92}$$

Dividing equation (5.92) by (1 + e) and substituting $e/(1+e) = n$ yields:

$$\begin{aligned}(T-T_r)&\begin{bmatrix}\left(C_{pl}S_l\rho_l + C_{pv}S_a\rho_v + C_{pda}S_a\rho_{da}\right)(1+e)\frac{\partial n}{\partial t}\\ + n\left(C_{pl}\rho_l - C_{pv}\rho_v - C_{pda}\rho_{da}\right)\frac{\partial S_l}{\partial t} + nC_{pv}(1-S_l)\frac{\partial \rho_v}{\partial t} + nC_{pda}(1-S_l)\frac{\partial \rho_{da}}{\partial t}\end{bmatrix}\\ &+ H_c\frac{\partial T}{\partial t} + L(1-S_l)n\frac{\partial \rho_v}{\partial t} - Ln\rho_v\frac{\partial S_l}{\partial t} + L(1-S_l)\rho_v(1+e)\frac{\partial n}{\partial t}\\ &= -\nabla\Big[\lambda\nabla T + L(\mathbf{v_v}\rho_l + \mathbf{v_a}\rho_v)\\ &+ \left(\left(C_{pl}\mathbf{v_l}\rho_l + C_{pv}\mathbf{v_v}\rho_l + C_{pv}\mathbf{v_a}\rho_v + C_{pda}\mathbf{v_a}\rho_{da}\right)(T-T_r)\right)\Big]\end{aligned} \tag{5.93}$$

Substituting the derivatives with respect to time for the degree of saturation from equation (5.21); vapour density, equation (5.37); dry air density, equation (5.67) and porosity into the left hand side of the governing equation (5.93); and equations (5.13), (5.27) and (5.40) for the velocity terms of liquid, air and vapour respectively, yields:

$$C_{T1}\frac{\partial u_l}{\partial T} + C_{TT}\frac{\partial T}{\partial t} + C_{Ta}\frac{\partial u_a}{\partial T} + C_{Tu}\frac{\partial \mathbf{u}}{\partial T} = \nabla.[K_{Tl}\nabla u_l] + \nabla.[K_{TT}\nabla T] + \nabla.[K_{Ta}\nabla u_a] + J_T \tag{5.94}$$

Again, as outlined within section 5.2 of this Chapter, the scope of the current investigation assumes a ridged soil therefore volumetric strain and vector displacement, **u**, has been considered to be equal to zero. Removing the fourth term in equation (5.94) gives:

$$C_{Tl}\frac{\partial u_l}{\partial T} + C_{TT}\frac{\partial T}{\partial t} + C_{Ta}\frac{\partial u_a}{\partial T} = \nabla.[K_{Tl}\nabla u_l] + \nabla.[K_{TT}\nabla T] + \nabla.[K_{Ta}\nabla u_a] + J_T \tag{5.95}$$

where:

$$C_{Tl} = \left[\begin{array}{c} -\left(C_{pl}\rho_l n - C_{pv}\rho_v n - C_{pda}\rho_{da} n\right)\frac{\partial S_l}{\partial s} - C_{pv}S_a n\left(\rho_0\frac{\partial h}{\partial s}\right) \\ + C_{pda}S_a n\frac{R_v}{R_{da}}\left(\rho_0\frac{\partial h}{\partial s}\right) \end{array}\right](T - T_r) + Ln\rho_v\frac{\partial S_l}{\partial s} - LnS_a\left(\rho_0\frac{\partial h}{\partial s}\right) \tag{5.96}$$

$$C_{TT} = H_c + \left[\begin{array}{c} \left(C_{pl}\rho_l n - C_{pv}\rho_v n - C_{pda}\rho_{da} n\right)\frac{\partial S_l}{\partial T} + C_{pv}S_a n\left(h\frac{\partial \rho_0}{\partial T} + \rho_0\frac{\partial h}{\partial T}\right) \\ + C_{pda}S_a n\left(-\frac{\rho_a}{T} - \frac{R_v}{R_{da}}\left(h\frac{\partial \rho_0}{\partial T} + \rho_0\frac{\partial h}{\partial T}\right)\right) \end{array}\right](T - T_r) - Ln\rho_v\frac{\partial S_l}{\partial T} + LnS_a\left(h\frac{\partial \rho_0}{\partial T} + \rho_0\frac{\partial h}{\partial T}\right) \tag{5.97}$$

$$C_{Ta} = \left[\begin{array}{c} \left(C_{pl}\rho_l n - C_{pv}\rho_v n - C_{pda}\rho_{da} n\right)\frac{\partial S_l}{\partial s} + C_{pv}S_a n\left(\rho_0\frac{\partial h}{\partial s}\right) \\ + C_{pda}S_a n\left(\frac{1}{R_{da}T} - \frac{R_v}{R_{da}}\left(\rho_0\frac{\partial h}{\partial s}\right)\right) \end{array}\right](T - T_r) - Ln\rho_v\frac{\partial S_l}{\partial s} - LnS_a\left(\rho_0\frac{\partial h}{\partial s}\right) \tag{5.98}$$

$$K_{Tl} = -L\rho_l \frac{D_{atms} v_v n}{\rho_l}\left(\rho_0 \frac{\partial h}{\partial s}\right) + (T - T_r)\rho_l \left(\frac{C_{pl} K_l}{\gamma_l} - C_{pv} \frac{D_{atms} v_v n}{\rho_l}\left(\rho_0 \frac{\partial h}{\partial s}\right)\right) \tag{5.99}$$

$$K_{TT} = \lambda_T + L\rho_l \frac{D_{atms} v_v n (\nabla T)_a}{\rho_l \nabla T}\left(h \frac{\partial \rho_0}{\partial T} \rho_0 \frac{\partial h}{\partial T}\right) + (T - T_r)\rho_l C_{pl}\left(h \frac{\partial \rho_0}{\partial T} \rho_0 \frac{\partial h}{\partial T}\right) \tag{5.100}$$

$$\begin{aligned} K_{Ta} = {} & L\rho_l \frac{D_{atms} v_v n}{\rho_l}\left(\rho_0 \frac{\partial h}{\partial s}\right) + L\rho_v K_a \\ & + (T - T_r)\left(\rho_l C_{pv} \frac{D_{atms} v_v n}{\rho_l}\left(\rho_0 \frac{\partial h}{\partial s}\right) + \rho_v C_{pv} K_a + \rho_{da} C_{pda} K_a\right) \end{aligned} \tag{5.101}$$

$$J_T = (T - T_r)\, C_{pl} \rho_l \nabla (k_1 \nabla z) \tag{5.102}$$

5.6 Theoretical summary

The governing equations for moisture, dry air and heat transfer have been presented in terms of three primary variables, namely; pore-water pressure (u_l), pore-air pressure (u_a) and temperature, T. The theoretical governing equations of these processes as follows:

Moisture transfer:

$$C_{ll} \frac{\partial u_l}{\partial t} + C_{lT} \frac{\partial T}{\partial t} + C_{la} \frac{\partial u_a}{\partial t} = \nabla \cdot [K_{ll} \nabla u_l] + \nabla \cdot [K_{lT} \nabla T] + \nabla \cdot [K_{la} \nabla u_a] + J_l$$

Dry air transfer:

$$C_{al} \frac{\partial u_l}{\partial t} + C_{aT} \frac{\partial T}{\partial t} + C_{aa} \frac{\partial u_a}{\partial t} = \nabla \cdot [K_{al} \nabla u_l] + \nabla \cdot [K_{aa} \nabla u_a] + J_a$$

Heat transfer:

$$C_{T1} \frac{\partial u_l}{\partial T} + C_{TT} \frac{\partial T}{\partial t} + C_{Ta} \frac{\partial u_a}{\partial T} = \nabla . [K_{Tl} \nabla u_l] + \nabla . [K_{TT} \nabla T] + \nabla . [K_{Ta} \nabla u_a] + J_T$$

5.7 Numerical formulation - General

The governing equations for the flow of moisture, air and heat have been presented in the previous sections. The finite-element method (FEM) is employed to spatially discretise the system of

equations, whereas a finite difference (FD) scheme is used to achieve temporal discretisation. The following sections describe the FEM and FD techniques and their application within the current scope of work in greater detail.

5.8 Spatial discretisation

Within the presented work the *Galerkin weighted residual finite-element* approach has been employed for the spatial discretisation. The approach is widely recognised as a general technique for the solution of partial differential equation systems subject to boundary and initial conditions (Hinton & Owen, 1977). The features of this approach are also well documented (Cleall, 1998) (Thomas & He, 1995) (Thomas, et al., 1998) and it has been shown to be both effective and robust for the type of coupled equations described in the previous sections. Since a detailed description of this method has been broadly presented elsewhere (Thomas & He, 1995) (Thomas, et al., 1998), the spatial discretisation of the governing equations is presented here in an abbreviated form. Within the work presented in this thesis, linear three-noded isoparametric triangular elements have been used in two dimensional analysis and linear isoparametric four-noded tetrahedral elements have been used for three-dimensional analysis. A *Galerkin weighted residual method* has been used to minimise the spatial residual error, resulting from nodal estimations by the use of shape functions.

5.8.1 Spatial discretisation of the governing equations for flow

The processes employed for the spatial discretisation of the three flow variables (i.e. moisture, dry air and temperature) are similar, therefore only a single case, moisture flow, is presented. The numerical processes presented can subsequently be applied to all three flow variables.

Based on the Galerkin weighted residual method, the primary variables and their spatial derivatives can be approximated using shape functions. For an element with n_{node} nodes, this yields (Lewis, et al., 2004);

$$\omega \approx \hat{\omega} = \sum_{s=1}^{n_{node}} N_s \, \omega_s \tag{5.103}$$

$$\nabla\hat{\omega} = \sum_{s=1}^{n_{node}} (\nabla N_s) \, \omega_s \tag{5.104}$$

where ω represents any of the primary variables $\{u_l, u_a, T\}$, N_s is the shape function, the subscript, $_s$, characterises the nodal points and the accent,$\hat{}$, denotes the approximate form.

The governing equation for moisture flow, with substitution for the primary variables from equations (5.103) and (5.104) may be written as:

$$\begin{bmatrix} -C_{ll}\dfrac{\partial \hat{u}_l}{\partial t} - C_{lT}\dfrac{\partial \hat{T}}{\partial t} - C_{la}\dfrac{\partial \hat{u}_a}{\partial t} \\ +\nabla[K_{ll}\nabla \hat{u}_l] + \nabla\left[K_{lT}\nabla \hat{T}\right] + \nabla[K_{la}\nabla \hat{u}_a] + J_l \end{bmatrix} = R_\Omega \tag{5.105}$$

where R_Ω is the residual error which is introduced by substitution of the approximate values of the variables and can be defined as:

$$R_\Omega = \omega - \hat{\omega} \tag{5.106}$$

The Galerkin weighted residual approach is used to minimise the residual error over the elemental volume, Ω^e, by using the shape functions, N_r, as weighted coefficients. Equation (5.105) can therefore be given as:

$$\int_{\Omega^e} N_r \begin{bmatrix} -C_{ll}\dfrac{\partial \hat{u}_l}{\partial t} - C_{lT}\dfrac{\partial \hat{T}}{\partial t} - C_{la}\dfrac{\partial \hat{u}_a}{\partial t} \\ +\nabla[K_{ll}\nabla \hat{u}_l] + \nabla\left[K_{lT}\nabla \hat{T}\right] + \nabla[K_{la}\nabla \hat{u}_a] + J_l \end{bmatrix} d\Omega^e = 0 \tag{5.107}$$

Employing integration by parts, the weak form of equation (5.107) may be obtained. The 4th and 7th terms, for example, including substitution from section 5.2 can be expressed as:

$$\int_{\Omega^e} N_r[\nabla (K_{ll}\nabla \hat{u}_l)]\, d\Omega^e = \int_{\Omega^e} \nabla (N_r K_{ll}\nabla \hat{u}_l)\, d\Omega^e - \int_{\Omega^e} K_{ll}\nabla \hat{u}_l \nabla N_r\, d\Omega^e \tag{5.108}$$

and:

$$\begin{aligned} \int_{\Omega^e} N_r[J_1]\, d\Omega^e &= \int_{\Omega^e} N_r \rho_l \nabla [K_l \nabla z]\, d\Omega^e \\ &= \int_{\Omega^e} \nabla (N_r \rho_l K_l \nabla z)\, d\Omega^e - \int_{\Omega^e} K_l \rho_l \nabla z \nabla N_r\, d\Omega^e \end{aligned} \tag{5.109}$$

Repeating the above process for the remaining flux terms and substituting the reduced form into equation (5.107) yields:

$$\int_{\Omega^e} \begin{bmatrix} \nabla(N_r K_{ll} \nabla \hat{u}_l) - K_{ll} \nabla \hat{u}_l \nabla N_r + \nabla\left(N_r K_{lT} \nabla \hat{T}\right) - K_{lT} \nabla \hat{T} \nabla N_r \\ + \nabla(N_r K_{la} \nabla \hat{u}_a) - K_{la} \nabla \hat{u}_a \nabla N_r + \nabla(N_r \rho_l K_l \nabla z) - K_l \rho_l \nabla z \nabla N_r \\ + N_r \left[-C_{ll} \frac{\partial \hat{u}_l}{\partial t} - C_{lT} \frac{\partial \hat{T}}{\partial t} - C_{la} \frac{\partial \hat{u}_a}{\partial t} \right] \end{bmatrix} d\Omega^e = 0 \tag{5.110}$$

The *Gauss-Green Divergence* theorem (e.g. Zienkiewicz and Morgan, 1982) is employed to relate surface integrals to boundary integrals. The implementation of this theorem reduces the second order differential terms to first order and surface integrals are introduced. These surface integrals cancel each other out on adjacent elements, leaving only a contribution at the limits of the domain. Application of the divergence theorem on (5.110) yields:

$$\int_{\Omega^e} \begin{bmatrix} -K_{ll} \nabla \hat{u}_l \nabla N_r - K_{lT} \nabla \hat{T} \nabla N_r \\ -K_{la} \nabla \hat{u}_a \nabla N_r - K_l \rho_l \nabla z \nabla N_r \\ -N_r \left[C_{ll} \frac{\partial \hat{u}_l}{\partial t} + C_{lT} \frac{\partial \hat{T}}{\partial t} + C_{la} \frac{\partial \hat{u}_a}{\partial t} \right] \end{bmatrix} d\Omega^e + \int_{\Gamma^e} N_r \begin{bmatrix} K_{ll} \nabla \hat{u}_l + K_{lT} \nabla \hat{T} \\ + K_{la} \nabla \hat{u}_a + K_l \rho_l \nabla z \end{bmatrix} \underline{n} d\Gamma^e = 0 \tag{5.111}$$

where Γ^e is the element boundary surface and $\underline{n}$ is the direction cosine normal to the surface. The surface integral in equation (5.111) in physical terms is the sum of the liquid and vapour fluxes normal to the boundary surface. This surface integral may be expressed with respect to moisture transfer and with appropriate substitution from section 5.3, by:

$$\begin{aligned} &\int_{\Gamma^e} N_r \left[K_{ll} \nabla \hat{u}_l + K_{lT} \nabla \hat{T} + K_{la} \nabla \hat{u}_a + K_l \rho_l \nabla z \right] \underline{n} d\Gamma^e \\ &= \int_{\Gamma^e} N_r \left[\rho_l K_l \left(\frac{1}{\gamma_l} \right) + \rho_l \left(K_{vl} \nabla \hat{u}_l + K_{vT} \nabla \hat{T} + K_{va} \nabla \hat{u}_a \right) + \rho_v (K_a \nabla \hat{u}_a) \right] \underline{n} d\Gamma^e \\ &= \int_{\Gamma^e} \mathrm{N}^T \left[\rho_l \underline{\hat{\mathbf{v}}}_{ln} + \rho_l \underline{\hat{\mathbf{v}}}_{vd} + \rho_v \underline{\hat{\mathbf{v}}}_{va} \right] d\Gamma^e \end{aligned} \tag{5.112}$$

where $\underline{\hat{\mathbf{v}}}_{ln}$ is the approximate liquid velocity normal to the boundary surface, $\underline{\hat{\mathbf{v}}}_{vd}$ is the approximate diffuse vapour velocity normal to the boundary surface, $\underline{\hat{\mathbf{v}}}_{va}$ is the approximate pressure vapour velocity normal to the boundary surface and:

$$K_{vl} = \frac{D_{atms} v_v n}{\rho_l} \left(\rho_0 \frac{\partial h}{\partial s} \right) \tag{5.113}$$

$$K_{vT} = -\frac{D_{atms} v_v n}{\rho_l} \frac{(\nabla T)_a}{\nabla T} \left(h \frac{\partial \rho_0}{\partial T} + \rho_0 \frac{\partial h}{\partial T} \right) \tag{5.114}$$

$$K_{va} = -\frac{D_{atms} v_v n}{\rho_l}\left(\rho_0 \frac{\partial h}{\partial s}\right) \tag{5.115}$$

Introducing the expressions for the derivatives of the primary variables and expressing in vector form, equation (5.112) becomes:

$$\begin{aligned}\int_{\Omega^e} [K_{ll}\,\nabla \mathrm{N}^T\,\nabla \mathrm{N}] d\Omega^e \mathbf{u_{ls}} + \int_{\Omega^e} [K_{lt}\,\nabla \mathrm{N}^T\,\nabla \mathrm{N}]\, d\Omega^e \mathbf{T_s} + \int_{\Omega^e} [K_{la}\,\nabla \mathrm{N}^T\,\nabla \mathrm{N}] d\Omega^e \mathbf{u_{as}} \\ + \int_{\Omega^e} [C_{ll}\mathrm{N}^T\mathrm{N}] d\Omega^e \frac{\partial \mathbf{u_{ls}}}{\partial t} + \int [C_{lT}\mathrm{N}^T\mathrm{N}] d\Omega^e \frac{\partial \mathbf{T_s}}{\partial t} \\ + \int [C_{la}\mathrm{N}^T\mathrm{N}] d\Omega^e \frac{\partial \mathbf{u_{as}}}{\partial t} + \int_{\Omega^e} [K_l \rho_l \mathrm{N}^T\,\nabla z]\, d\Omega^e \\ - \int_{\Gamma^e} \mathrm{N}^T \left[\rho_l \hat{\underline{\mathbf{v}}}_{ln} + \rho_l \hat{\underline{\mathbf{v}}}_{vd} + \rho_v \hat{\underline{\mathbf{v}}}_{va}\right] d\Gamma^e = 0\end{aligned} \tag{5.116}$$

where *N* is the matrix of the shape functions, $\mathbf{u_{ls}}$ is the vector of pore-water pressure values at nodes, $\mathbf{T_s}$ is the vector of temperature values at nodes and $\mathbf{u_{as}}$ is the vector of pore-air pressure values at nodes.

This can be expressed in concise form as:

$$\mathbf{C_{ll}} \frac{\partial \mathbf{u}_{ls}}{\partial t} + \mathbf{C_{lT}} \frac{\partial \mathbf{T}_s}{\partial t} + \mathbf{C_{la}} \frac{\partial \mathbf{u}_{as}}{\partial t} + \mathbf{K_{ll}} \mathbf{u}_{ls} + \mathbf{K_{lT}} \mathbf{T}_s + \mathbf{K_{la}} \mathbf{u}_{as} = \mathbf{f_l} \tag{5.117}$$

where:

$$\mathbf{C_{ll}} = \sum_{e=1}^{m} \int_{\Omega^e} [C_{ll}\mathrm{N}^T\mathrm{N}] d\Omega^e \tag{5.118}$$

$$\mathbf{C_{lT}} = \sum_{e=1}^{m} \int_{\Omega^e} [C_{lT}\mathrm{N}^T\mathrm{N}] d\Omega^e \tag{5.119}$$

$$\mathbf{C_{la}} = \sum_{e=1}^{m} \int_{\Omega^e} [C_{la}\mathrm{N}^T\mathrm{N}] d\Omega^e \tag{5.120}$$

$$\mathbf{K_{ll}} = \sum_{e=1}^{m} \int_{\Omega^e} [K_{ll} \nabla \mathrm{N}^T \nabla \mathrm{N}] \, d\Omega^e \tag{5.121}$$

$$\mathbf{K_{lT}} = \sum_{e=1}^{m} \int_{\Omega^e} [K_{lT} \nabla \mathrm{N}^T \nabla \mathrm{N}] \, d\Omega^e \tag{5.122}$$

$$\mathbf{K_{la}} = \sum_{e=1}^{m} \int_{\Omega^e} [K_{la} \nabla \mathrm{N}^T \nabla \mathrm{N}] \, d\Omega^e \tag{5.123}$$

$$\mathbf{f_l} = \sum_{e=1}^{m} \int_{\Omega^e} [K_l \rho_l \nabla \mathrm{N}^T \nabla z] d\Omega^e - \sum_{e=1}^{m} \int_{\Gamma^e} \mathrm{N}^T m \left[\rho_l \underline{\hat{\mathbf{v}}}_{ln} + \rho_l \underline{\hat{\mathbf{v}}}_{vd} + \rho_v \underline{\hat{\mathbf{v}}}_{va}\right] d\Gamma^e \tag{5.124}$$

Similarly, this process can be replicated for the other flow variables, T and u_a, producing for:

i. Heat transfer:

$$\mathbf{C_{Tl}} \frac{\partial \mathbf{u}_{ls}}{\partial t} + \mathbf{C_{TT}} \frac{\partial \mathbf{T}_s}{\partial t} + \mathbf{C_{Ta}} \frac{\partial \mathbf{u}_{as}}{\partial t} + \mathbf{K_{Tl}} \mathbf{u}_{ls} + \mathbf{K_{TT}} \mathbf{T}_s + \mathbf{K_{Ta}} \mathbf{u}_{as} = \mathbf{f_T} \tag{5.125}$$

where:

$$\mathbf{C_{Tl}} = \sum_{e=1}^{m} \int_{\Omega^e} [C_{Tl} \mathrm{N}^T \mathrm{N}] d\Omega^e \tag{5.126}$$

$$\mathbf{C_{TT}} = \sum_{e=1}^{m} \int_{\Omega^e} [C_{TT} \mathrm{N}^T \mathrm{N}] d\Omega^e \tag{5.127}$$

$$\mathbf{C_{Ta}} = \sum_{e=1}^{m} \int_{\Omega^e} [C_{Ta} \mathrm{N}^T \mathrm{N}] d\Omega^e \tag{5.128}$$

$$\mathbf{K_{Tl}} = \sum_{e=1}^{m} \int_{\Omega^e} [K_{Tl} \nabla \mathrm{N}^T \nabla \mathrm{N}] \, d\Omega^e \tag{5.129}$$

$$\mathbf{K_{TT}} = \sum_{e=1}^{m} \int_{\Omega^e} [K_{TT} \nabla \mathrm{N}^T \nabla \mathrm{N}] \, d\Omega^e \tag{5.130}$$

$$\mathbf{K_{Ta}} = \sum_{e=1}^{m} \int_{\Omega^e} [K_{Ta} \nabla \mathrm{N}^T \nabla \mathrm{N}] \, d\Omega^e \tag{5.131}$$

$$\mathbf{f_T} = \sum_{e=1}^{m} \int_{\Omega^e} \left[C_{pl} \rho_l k_l \nabla \mathrm{N}^T \nabla z\right] d\Omega^e - \sum_{e=1}^{m} \int_{\Gamma^e} \mathrm{N}^T [\mathbf{F}_h] d\Gamma^e \tag{5.132}$$

where $\mathbf{F}_h$ is the approximate heat flux normal to the boundary surface.

ii. Air transfer:

$$\mathbf{C_{al}} \frac{\partial \mathbf{u_{l}}_s}{\partial t} + \mathbf{C_{aT}} \frac{\partial \mathbf{T}_s}{\partial t} + \mathbf{C_{aa}} \frac{\partial \mathbf{u_{a}}_s}{\partial t} + \mathbf{K_{al}} \mathbf{u_{l}}_s + \mathbf{K_{aa}} \mathbf{u_{a}}_s = \mathbf{f_a} \tag{5.133}$$

where:

$$\mathbf{C_{al}} = \sum_{e=1}^{m} \int_{\Omega^e} [C_{al} \mathrm{N}^T \mathrm{N}] d\Omega^e \tag{5.134}$$

$$\mathbf{C_{aT}} = \sum_{e=1}^{m} \int_{\Omega^e} [C_{aT} \mathrm{N}^T \mathrm{N}] d\Omega^e \tag{5.135}$$

$$\mathbf{C_{aa}} = \sum_{e=1}^{m} \int_{\Omega^e} [C_{aa} \mathrm{N}^T \mathrm{N}] d\Omega^e \tag{5.136}$$

$$\mathbf{K_{al}} = \sum_{e=1}^{m} \int_{\Omega^e} [K_{al} \nabla \mathrm{N}^T \nabla \mathrm{N}] \, d\Omega^e \tag{5.137}$$

$$\mathbf{K_{aa}} = \sum_{e=1}^{m} \int_{\Omega^e} [K_{aa} \nabla \mathrm{N}^T \nabla \mathrm{N}] \, d\Omega^e \tag{5.138}$$

$$\mathbf{f_a} = \sum_{e=1}^{m} \int_{\Omega^e} [k_l \rho_{da} \nabla \mathrm{N}^T \nabla z] d\Omega^e - \sum_{e=1}^{m} \int_{\Gamma^e} \mathrm{N}^T \rho_{da} \left[\hat{\underline{\mathbf{v}}}_{fn} + \hat{\underline{\mathbf{v}}}_{an}\right] d\Gamma^e \tag{5.139}$$

The approximate velocities of free and dissolved air flux normal to the boundary surface are included as $\hat{\underline{\mathbf{v}}}_{fn}$ and $\hat{\underline{\mathbf{v}}}_{an}$ respectively.

5.9 Temporal discretisation

To determine the value of the primary variables over time, a temporally discrete formulation is used. Within the scope of this study, a fully implicit mid-interval backward difference time-stepping algorithm was employed. This algorithm has been found to be a suitable for solving highly non-linear classes of equations, such as those which will be encountered within the scope of this work (Cook, 1981) (Thomas, et al., 1998).

Expressing the spatially discretised governing equations for heat, moisture and air (previously presented within section 5.8) in matrix form gives:

$$\begin{bmatrix} \mathbf{K_{ll}} & \mathbf{K_{lT}} & \mathbf{K_{la}} \\ \mathbf{K_{Tl}} & \mathbf{K_{TT}} & \mathbf{K_{Ta}} \\ \mathbf{K_{al}} & \mathbf{0} & \mathbf{K_{aa}} \end{bmatrix} \begin{bmatrix} \mathbf{u}_{ls} \\ \mathbf{T}_s \\ \mathbf{u}_{as} \end{bmatrix} + \begin{bmatrix} \mathbf{C_{ll}} & \mathbf{C_{lT}} & \mathbf{C_{la}} \\ \mathbf{C_{Tl}} & \mathbf{C_{TT}} & \mathbf{C_{Ta}} \\ \mathbf{C_{al}} & \mathbf{C_{aT}} & \mathbf{C_{aa}} \end{bmatrix} \begin{bmatrix} \dot{\mathbf{u}}_{ls} \\ \dot{\mathbf{T}}_s \\ \dot{\mathbf{u}}_{as} \end{bmatrix} = \begin{bmatrix} \mathbf{f_l} \\ \mathbf{f_T} \\ \mathbf{f_a} \end{bmatrix} \tag{5.140}$$

where $\left[\dot{\mathbf{u}}_{ls}, \dot{\mathbf{T}}_s, \dot{\mathbf{u}}_{as}\right]$ are time derivatives of the primary variable vectors. The matrix equation (5.140) can be expressed as:

$$\mathbf{K}\{\emptyset\} + \mathbf{C}\frac{\partial \phi}{\partial t} = \{f\} \tag{5.141}$$

where $\emptyset$ refers to the global unknown, that is $\{u_{ls}\ T_s\ u_{as}\}^T$.

As previously stated, the spatially discretised equations are temporally discretised by the application of a fully implicit mid-interval backward difference time-stepping algorithm. The general form of this algorithm can be expressed as (Thomas, et al., 1998):

$$\chi\mathbf{K}\{\emptyset^{n+1}\} + \frac{\mathbf{C}\{\emptyset^{n+1}\}}{\Delta t} = (1-\chi)\{\mathbf{R}^n\} + \chi\{\mathbf{R}^{n+1}\} - (1-\chi)\mathbf{K}^n\{\emptyset^n\} + \frac{\mathbf{C}\{\emptyset^n\}}{\Delta t} \tag{5.142}$$

where χ represents a constant controlling the integration scheme, varying from 1, *for implicit*, 0.5 for *Crank-Nicholson* and 0 for *explicit* time integration schemes.

To solve the highly non-linear problem considered here, χ is recommended to be set to be equal to 1 (Thomas, et al., 1998), and **K**, **C** and **R** are evaluated at the mid-interval value of the primary variables. The scheme thus becomes the fully implicit mid-interval backward difference algorithm as previously stated.

Re-writing equation (5.142) in alternate notation yields:

$$\mathbf{A}\{\phi^{n+1}\} = \{\mathbf{F}\} \tag{5.143}$$

where

$$\mathbf{A} = \chi\mathbf{K} + \frac{\mathbf{C}}{\Delta t} \tag{5.144}$$

and

$$\{\mathbf{F}\} = (1-\chi)\{\mathbf{R}^n\} + \chi\{\mathbf{R}^{n+1}\} - (1-\chi)\mathbf{K}^n\{\phi^n\} + \frac{\mathbf{C}\{\phi^n\}}{\Delta t} \tag{5.145}$$

Therefore a solution of ϕ^{n+1} is achievable, providing the matrix **A** and vector **F** can be obtained. This is actually achieved by the used of an iterative solution procedure. At the beginning of each time interval, the first estimate of ϕ^{n+1} is assumed to be chosen as the value at the last time interval, i.e. ϕ^n. Thus the value of ϕ^{n+1} for the first iteration can be obtained by:

$$\{\phi_1^{n+1}\} = \mathbf{A}_1^{-1}\{\mathbf{F}_1\} \tag{5.146}$$

where $\mathbf{A_1}$ and $\mathbf{F_1}$ are calculated at the value of ϕ^n.

After the first iteration, it is possible to correct the mid-interval value of ϕ^{n+1} and evaluate the matrix **A** and the vector **F** at time level n + ½. The iteration will continue until the values of ϕ^{n+1} converge.

Convergence is monitored between every successive solution and deemed to have been achieved when the following criterion is satisfied:

$$\left|\frac{\phi_{i+1}^{n+1} - \phi_i^{n+1}}{\phi_i^{n+1}}\right| \leq \tau \tag{5.147}$$

where i is the iteration level and τ is the relative tolerance.

The time-step increment is controlled by two factors, maximum iterations and minimum iterations. Should the actual number of iterations for convergence exceed the maximum specified, the time-step size is reduced. Likewise, should the iteration number be less than the minimum, the time-step size will be increased. The procedure enables a variable time-step size to be employed, which will benefit the analysis of heat and moisture transfer taking place over a long period of time but with more rapid variations taking place during the initial stages of the problem.

This model has been incorporated into the computer code COMPASS, *the **Co**de for **M**odelling **Pa**rtially **S**aturated **S**oils*, which has been incrementally developed at the Geoenvironmental Research Centre (GRC), Cardiff University.

5.10 Computational formulation - General

In this section the computational techniques adopted to implement the previously presented theoretical and numerical formulations will be discussed. In computationally expensive simulations, such as the coupled large-scale/long-term problems presented in this thesis, it is essential that appropriate approaches are explored in order to identify the most efficient computational methods available. In Chapter 2, model developments and previous numerical investigations were studied as part of the literature review. Published works recognise that large-scale/long-term simulations are computationally expensive; however no work was found investigating computational optimisation and the techniques available to improve computational performance with regards to ground source heat simulation. The following sections will explore the computational methods that can be used in conjunction with the TH modelling of ground source heat systems. Finally, a parallel computational formulation implemented within the current scope of work is presented and full explained.

5.11 Computational components

When solving a problem, the computational operations of the numerical tool COMPASS can be divided into four sections, namely (in chronological order):

i. Performing pre-processing

ii. Forming the matrices

iii. Solving the system of equations

iii. Performing post-process analysis

Within the current study, a third party program called GiD (GiD, 2006) has been used for both the pre and post-processing. The compatibility issues associated with combining GiD with COMPASS have been previously addressed by Vardon (2009).

The system matrix formation is a relatively simple operation with well-established numerical operations. The size of the system matrix is dependent on the size, geometry, connectivity of the nodes and the processes being considered (e.g. thermal or coupled TH). The maximum size of the resulting matrix can be described as the square of the total number of freedoms that exist within the domain. The typical nature of model domains results in sparse system matrices, with real terms typically appearing along the diagonal. In terms of physical memory, the system matrix sparsity is utilised by using Compressed Row Storage (CRS), a method whereby only non-zeros are stored in memory with accompanying vector pointers which describe the location of the value within the complete system matrix.

Various options exist for the matrix solver component of the algorithm. There are two main types of solvers compatible with the highly coupled problem considered within the scope of this study. They can be broadly categorised as direct and iterative solvers (Duff & van der Vorst, 1999). It is noted that some direct solvers apply iterative techniques to improve performance and likewise some iterative solvers use direct preconditioners.

In this work a Krylov subspace iterative method known as a Bi-Conjugate Gradient (BiCG) solver has been employed. This approach has shown to be appropriate and numerically robust for the non-symmetric coupled TH equations found within the scope of this work (Owen, 2000). Owen showed how this solver could be implemented, reducing the computational time over direct solvers, and used in conjunction with parallelisation techniques.

Vardon (2009) identified that the selected BiCG solver can be further improved by the selection of an appropriate preconditioner. The preconditioner plays a key role in providing numerical stability to the analysis. A Jacobi preconditioner, which is effectively a vector-vector multiplication, has been employed for its simplicity, performance and parallelisation applicability (Owen, 2000).

5.12 Computational algorithms

The computational algorithms applied within the scope of this work can be divided into two categories, namely; serial and parallel algorithms. Each of the algorithm types are presented along with the various optimisation approaches employed to improve computational efficiency. Prior to exploring computational and algorithm optimisation techniques it is worth highlighting that computational time and effort can be reduced through the appropriate selection of model domains and hardware. It is often possible to reduce the size and complexity of models without compromising performance by reducing dimensions (i.e. two-dimensions to three-dimensions), recognising lines of symmetry and selecting appropriate mesh coarseness. Similarly, the selected computational hardware (i.e. processor type, number and speed; and the Random Access Memory) will have a ceiling performance level which will restrict the computational performance. Although the previous options may appear simple, they are often overlooked during optimisation efforts.

5.12.1 Serial algorithm

The serial algorithm implemented in COMPASS is shown in Figure 5.1. The major aspects are described as the *Initialisation*, the *System Matrix Build*, the *Iterative Solver* and the *End*. Of these, the Initialisation and End sections are only ever undertaken once per analysis, whereas the System Build Matrix and the Iterative Solver sections are performed at each iteration, of each time-step. The latter two sections make up the majority of the run-time, although time spent in the initialisation phase can be significant for large models.

The System Matrix Build loops through all elements in the domain and populates matrices *[K]* and *[C]* from equation (5.141). The Iterative Solver section solves the system of linear equations by undertaking a number of vector-vector multiplications and two matrix-vector multiplications per iteration. The amount of computational work required for the System Matrix Build and the Iterative Solver at each iteration is proportional to the number of freedoms in the model. A previously stated, a preconditioned Bi-Conjugate Gradient (BiCG) solver is employed. This solver method has serial speed advantages of direct solvers as well as maintaining sparsity in the system matrix and vastly reducing the storage required (Barret, et al., 1995). .

Significant efforts have been previously made to optimise the performance of the serial code by Cleall (1998) and Vardon (2009). Vardon (2009) preformed a series of optimisation analyses, identifying the time spent within each section of the code depicted in Figure 5.1. Based on the results of these analyses, areas were identified for improvement with respect to computational times. A typical example of the improvements made by Vardon (2009) was to identify and remove repetitive

calculations that were being performed unnecessarily at each iteration, instead performing them once and storing the results in memory. By progressively inspecting the code and the associated run times of each code section, Vardon was able to reduce serial computational times of COMPASS by 30%, while maintaining the codes accuracy and future ability to be parallelised. The following sections will take a more detailed look at the solver used within the current scope of work and a more detailed look at some additional compiler and style techniques which can be employed to optimise serial code.

Factors commonly overlooked during the optimisation procedure include the effective use of programming style and compilers. Clarity of the code and avoiding unnecessary computations, not only help to improve performance but can also provide code with structure. Effective use of compiler specific options can help to improve computational efficiency. In order to implement these options, it is important to understand what the compiler will do automatically and what it is necessary for the programmer to do explicitly. The following methods were initially established by Vardon and have been implemented within the current COMPASS code:

i. ***Compiler options*** – compilers typically offer a range of options with relation to how the visible code is transferred into an executable file. The level of optimisation can vary significantly with some being processor specific and other methods being more general. Some compilers offer processor specific optimisations which allow code to be specifically complied for a given processor, thereby maximising the properties of that processor. Alternatively, pipelining is a general technique that takes full advantage of the amount of instructions that a single processor can perform simultaneously.

ii. ***Reduce cache misses*** – data during simulations will be either stored in RAM or cache. The location and access of certain items of data are controlled to maximise the performance of code. Some compilers do this automatically, whereas some may require specific instructions.

iii. ***Eliminating repetition*** – repeated calculations performed unnecessarily are removed from loops and instead only undertaken a single time. This is a compromise between processor use and memory storage.

iv. ***In-lining loops*** – Some loops may be in-lined which overall can aid the performance in terms of complementary instructions and reducing cache misses.

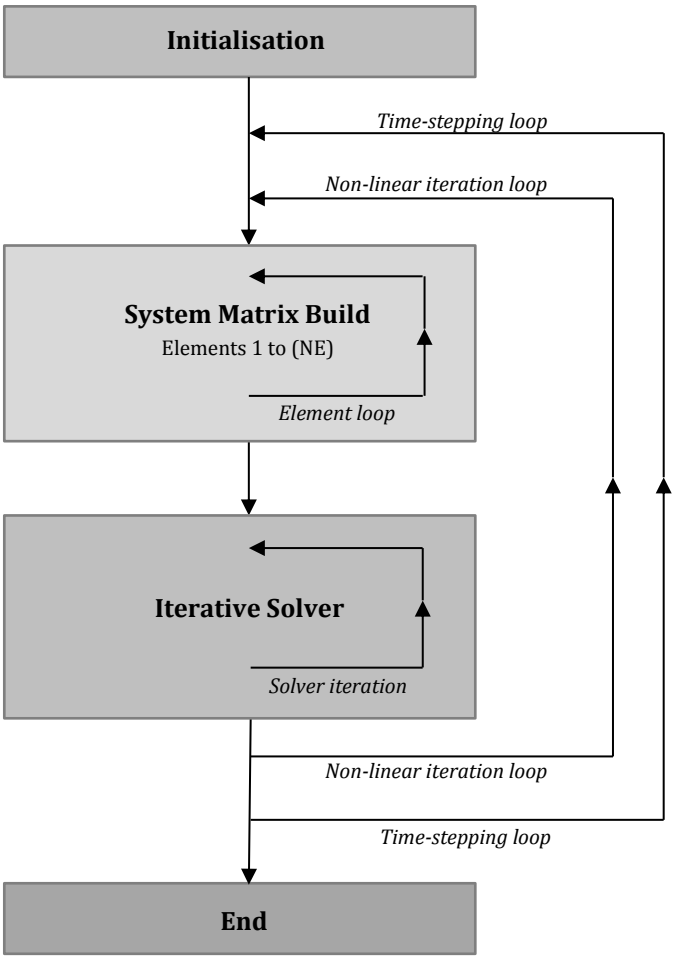

Figure 5.1 – Serial COMPASS algorithm. (after Vardon, 2009).

5.12.2 Parallel algorithms

High Performance Computing (HPC) is a generic term and can take a number of forms. For the purpose of this work, the HPC options have been broadly categorised into two subsections, namely; supercomputing/distributed computing; and parallel computing. To some extent, the former of these can be thought of as a type of parallel computing with the only major difference being the configuration of the hardware. In recent years, the development of multiple processor cores has enabled high performance computing, and more specifically parallel computing, to be undertaken on desktop machines. Within the current scope of work, the HPC developments aimed to utilise this improvement in hardware, concentrating on parallel computing for modern desktop machines. First, suitable programing paradigms for the current problem are presented and discussed, namely; multi-

threaded and message-passing. Following this, the implemented paradigm along with the devised algorithm in COMPASS is discussed.

5.12.2.1 Multi-threaded paradigm

Multi-threading is a programming technique that allows a single program to use multiple processors. The multiple processors access a single block of shared memory, using a shared system memory architecture (see Figure 5.2 a). Share memory architectures allow multiple processors to access a single block of memory via a shared bus. The advantage of this architecture is that there are no explicit messages or processes passed between processors; therefore little time is wasted. The main limitation with regard to this technique is the size of the bus band width. It can be seen from Figure 5.2 a, that all data being passed between the memory block and individual processors is transferred along a single shared bus. Once the bus bandwidth is reached, the capacity of the system is also reached, essentially limiting the number of processors which can effectively be used in this architecture. An alternative to overcome this limitation is to increase the amount of cache on processors however care must be taken to ensure cache coherency.

As the name suggest, the paradigm uses multiple threads, which can be defined as a series of instructions executed in parallel. The number of threads created is user defined, although typically a single thread will be assigned per processor. A single master thread is normally created at the initiation of the program, from which additional threads can be created and killed at the programmer's discretion from within the code. Figure 5.3 graphically shows this process. OpenMP is a common implementation of this paradigm, which allows the programmer to easily control the behaviour of the threads via compiler directives (OpenMP, 2009). The overriding difficulty associated with OpenMP is the so called race condition (Netzer & Miller, 1992). This is when a particular value or values are dependable on the timing of processes being executed by different threads. If the processes are executed in an incorrect order, the resulting value, and therefore overall results, will often be adversely affected. When implementing OpenMP, programmers must therefore be careful to control the threads in such a way as to avoid race condition.

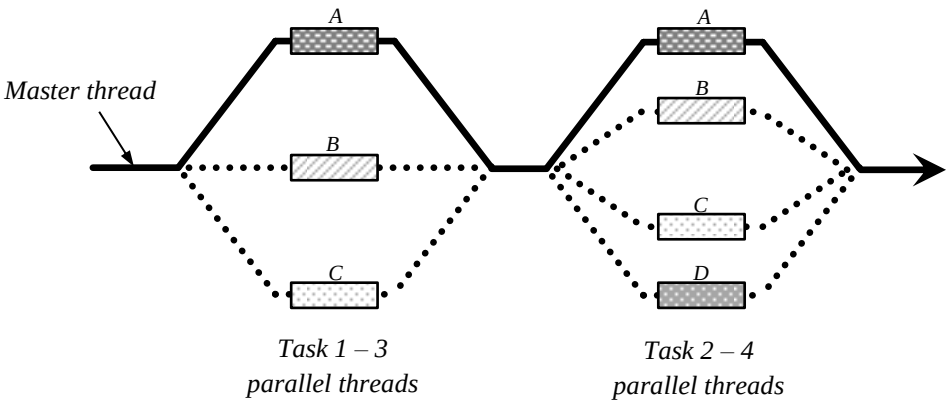

Figure 5.3 – Illustration of the creation and killing of parallel threads during a process.

5.12.2.2 Message passing paradigm

The message passing paradigm uses a distributed memory architecture (see Figure 5.2 b). Distributed memory architectures compromise of multiple processors; each of which has a private memory allocation. The processors are connected to memory via buses and are connected to one another via interconnects which allows data to be passed explicitly to one another. This allows a single program to be executed. The main advantage of this architecture, in contrast to the shared memory architecture, is that there is no shared bus between the processor and the memory. This means a single processor can use the full bus bandwidth, maximising the amount of data which can be exchanged. With no bus bandwidth limitation, there is no limit to how many processors can be connected to one another; therefore the architecture can be scaled upward easily. No processor can overwrite data being processed by other processors therefore there are no cache coherency problems. The main disadvantage associated with distributed memory architecture occurs when data is required by one processing unit which belongs to another. The process of sending and receiving these messages between processors has an associated time overhead. For completeness, it is worth recognising that there is also a hybrid memory architecture which is a combination of the shared and distributed memory types (see Figure 5.2 c). It compromises of a series of shared memory nodes, with a number of multi-core processors accessing shared memory, enabling HPC machines to take advantage of small-scale shared memory architecture speeds due to the reduction in message passing.

Message Passing Interface (MPI) is a common implementation of the message passing paradigm, which allows one-sided communications whereby a processor can read data from or place data in another processor memory (Message Passing Interface, 2009). In MPI, each processor runs a program which contains all the necessary commands that need to be executed. This paradigm is designed with HPC machines in mind, although it can be applied to shared memory machines by

effectively splitting the memory into private allocations. The message-passing does have a time overhead associated with it, as previously discussed; therefore such split-memory programs are likely to have a limit on how scalable they are.

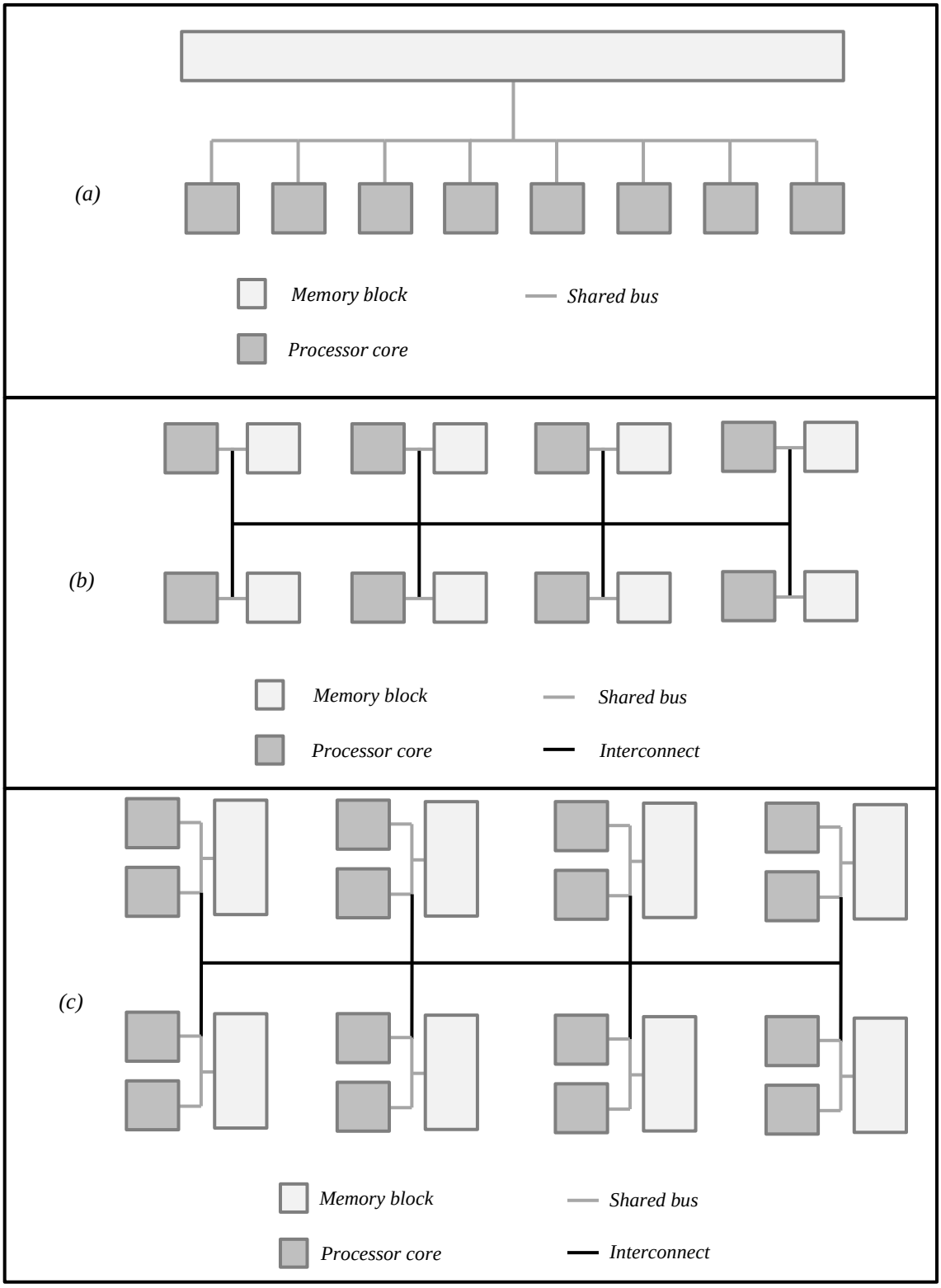

Figure 5.2 – Schematic of a shared (a), distributed (b) and hybrid (c) memory architectures containing 8 processor cores.

5.12.2.3 Implemented COMPASS algorithm

As the previous section would suggest, there are two paradigm implementations which have been identified for application, namely; OpenMP and MPI. The multi-threaded OpenMP approach can be incorporated within the numerical algorithm by identifying code sections where multiple threads can be created and used to carry out calculations. Provided that race conditions are avoided, the numerical algorithm proposed in sections 5.9 and 5.10 can be modified to use multiple processors while performing simulations. The implementation of MPI can be achieved through a number of methods, all of which split the domain (i.e. and the resulting system matrix) into smaller sections which can be subsequently solved. These methods are considered in terms of granularity. In a coarse grained parallelisation, sections of the computation can be undertaken with little or no communication between processors (i.e. embarrassingly parallel) whereas in fine grained parallelisation the impact of a specific calculation has a large effect on other areas, therefore computations cannot be carried out in isolation. Within the current scope of work, sections of the systems matrix cannot be solved independently of one another and an interaction between matrix sections would be required.

The current scope of work aims to provide a parallel computational approach for modern desktop machines, capable of simulating the large-scale/long-term TH soil behaviour in response to ground source heat. Considering this specification and assuming that the numbers of processors range between 2 and 8, it was decided that OpenMP would be the most suited of the two options. At this scale, it is anticipated that the band width to the shared memory would not be exceeded, while the removal of message passing between processors would also result in greater computational speeds. The parallel COMPASS algorithm employed with OpenMP paradigm can be found in Figure 5.4. The OpenMP code developed by Vardon (2009) was further developed within the scope of this work and tested with coupled TH problems. All new developed code was parallelised where possible and improvements were made to the existing code.

In order to formulate an efficient parallel algorithm it is first necessary to identify the sections of analysis where most computational effort is expelled. It is known that within the current scope of work, that the system matrix build and iterative solver will consume the majority of the computational effort primarily because they are performed at each iteration for every time-step whereas the remaining code, broadly speaking, is only performed once per analysis. It can be seen from Figure 5.4 that these two sections of the algorithm have been predominantly parallelised. The performance of the OpenMP parallel algorithm within the current scope of work will be investigated as part of Chapter 8.

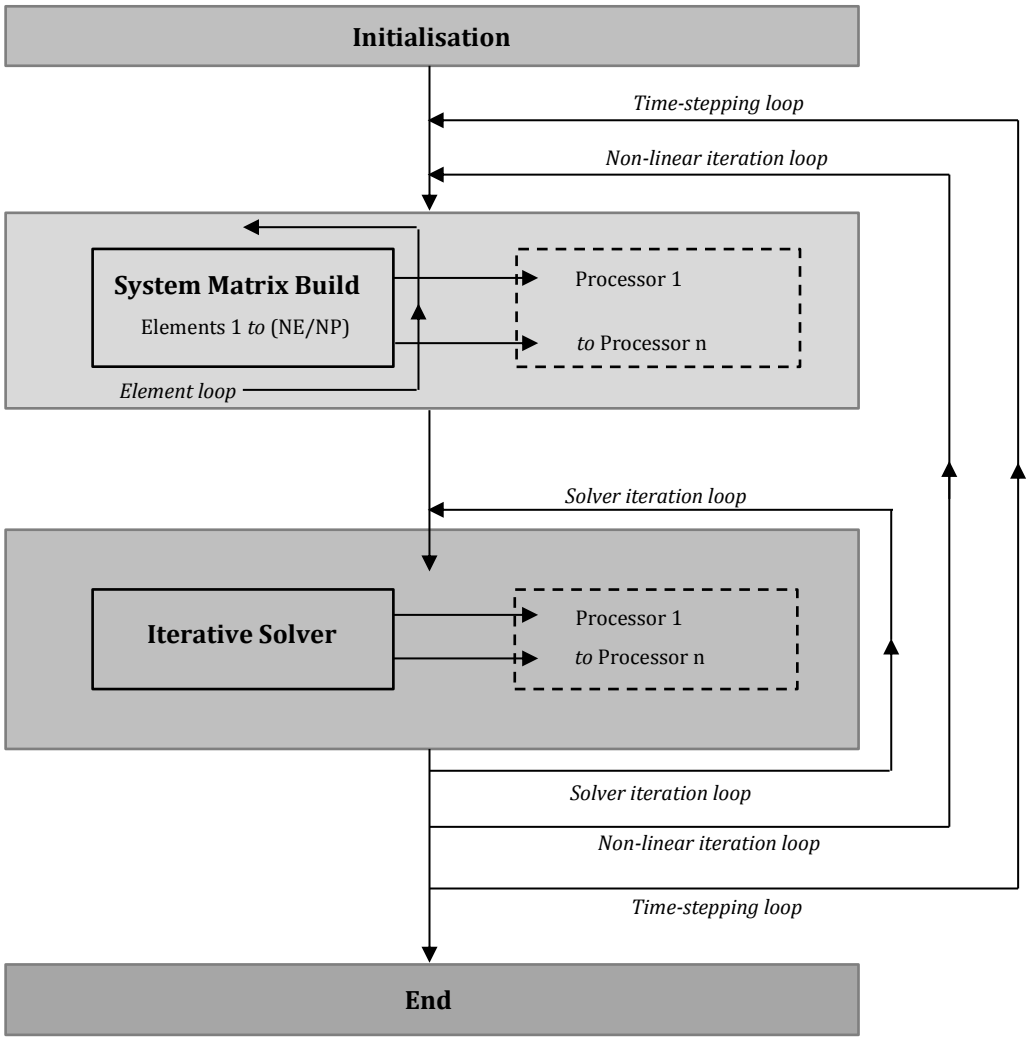

Figure 5.4 – Multi-threaded parallel COMPASS algorithm.

5.13 Conclusions

The theoretical and numerical approximations for the transient solution of coupled thermo-hydro behaviour have been presented. The governing equations for moisture transfer, dry air transfer and heat transfer have been presented in the form of three primary variables. The spatial and temporal discretisation of these governing equations have been achieved using the finite-element method and fully implicit mid-interval backward-difference algorithm respectively.

The final section of this chapter presented the computational formulation and algorithms adopted within the current scope of work. The available computational algorithms were presented in two sections, relating to serial and parallel approaches. The mitigating approaches taken to optimise

each of the individual factors were then presented, followed by a brief discussion of HPC paradigms available. It was decided that a multi-threading parallel programing technique would be implemented for use in the current work. Existing OpenMP code was modified and further developed to incorporate new developments.

The modelling aspects required for the simulation of coupled thermal-hydraulic ground behaviour in response to ground source heat exchange have been developed and presented. The developed model will be applied in the following chapters.

References

Alonso, E. E., Battle, F., Gens, A. & Lloret, A., 1988. *Consolidation analysis of partially saturated soils – Application to earthdam construction.* Innsbruck, Numerical Methods in Geomechanics, pp. 1303-1308.

Barret, R. et al., 1995. *Templates for the solution of linear systems: building blocks for iterative methods.* New York: John Wiley Press.

Brooks, R. H. & Corey, A. T., 1964. *Hydraulic properties of porous media. Hydro. Paper No. 3.* Fort Collins, Colorado: Colorado State University .

Carman, P. C., 1956. *Flow of gases through porous media.* London: Butterworths Scientific Publications.

Childs, E. C., 1969. *An introduction to the physical basis of soil water phenomena.* New York: John Wiley & Sons.

Cleall, P. J., 1998. *An investigation of the hydro/hydraulic/mechanical behaviour of unsaturated soils, including expansive clays.* Cardiff: PhD Thesis, Cardiff University.

Clifford, K. H. & Webb, S. W., 2006. *Gas transport in porous media.* 1st ed. Dordrecht: Springer.

Cook, R. D., 1981. *Concepts and applications of finite element analysis.* New York: John Wiley & Sons.

Darcy, H., 1856. *Les Fontaines Publiques da la Ville de Dijon.* Paris: Dalmont.

De Vries, D. A., 1958. Simultaneous transfer of heat and moisture in porous media. *Transactions of the American Geophysical Union,* 39(5), pp. 909-916.

De Vries, D. A., 1966. *Thermal properties of soils.* 2nd ed. Amsterdam: North Halland Publishing Co.

Duff, I. S. & van der Vorst, H. A., 1999. *Developments and trends in the parallel solution of linear systems,* s.l.: CERFACS, Technical Report, TR/PA/99/10.

Edlefsen, N. E. & Anderson, A. B. C., 1943. Thermodynamics of soil moisture. *Hilgardia,* 15(2), pp. 31-298.

Ewen, J. & Thomas, H. R., 1989. Heating unsaturated medium sand. *Geotechnique,* 39(3), pp. 455-470.

Fox, G. C., 1992. *Lessons from massively parallel applications on message passing computers.* San Francisco, Compcon Spring 1992. Thirty-Seventh IEEE Computer Society International Conference.

Fredlund, D. G. & Rahardjo, H., 1993. *Soil mechanics for unsaturated soils.* New York: John Wiley & Sons.

Fredlund, D. G. & Xing, A., 1994. Equations for the soil-water characteristic curve. *Candian Geotechnical Journal,* 31(1), pp. 521-532.

Geraminegad, M. & Saxena, S., 1986. *Finite elements in plasticity: Theory and practice.* Swansea: Pineridge Press.

GiD, 2006. *The personal pre and post processor.* [Online]
Available at: http://www.gid.cimne. upc.es
[Accessed 4 12 2012].

Hinton, E. & Owen, D. R. J., 1977. *Finite element programming, Computational Mathematics and Applications.* London: Academic Press.

Jakob, M., 1949. *Heat transfer Vol. 1.* New York: John Wiley & Sons.

Kaye, G. W. C., Laby & M, T., 1973. *Tables of physical and chemical constants.* 14th ed. London: Longmans.

Krischer, D. & Rohnalter, H., 1940. Warmeleitung und Dampfdiffusion in feutchen Gutern. *Verein Duetscher Ingenieure Forschungsheft,* 402(11), pp. 1-18.

Leong, E. C. & Rahardjo, H., 1997. Permeability functions for unsaturated soils. *Journal of geotechnical and geoenvironmental engineering,* 123(1), pp. 1118-1126.

Lewis, R. W., Nithiarasu, P. & Seetharamu, K. N., 2004. *Fundamentals of the Finite Element Method for Heat and Fluid Flow.* 1st ed. Chichester: John Wiley & Sons.

Matyas, E. L. & Radhakrishna, H. S., 1968. Volume change characteristics of partially saturated soils. *Geotechnique,* 18(4), pp. 432-448.

Mayhew, Y. R. & Rogers, G. F. C., 1976. *Thermodynamic and transport properties of fluids.* 2nd Edition ed. Oxford: Blackwell.

Message Passing Interface, 2009. [Online]
Available at: http://www.mcs.anl.gov/mpi
[Accessed 4 12 2012].

Mitchell, H. P., 2002. *An investigation into thermo/hydro/mechanical interactions involved in high level nuclear waste disposal.* Cardiff: PhD Thesis, Cardiff University.

Mitchell, J. K., 1993. *Fundamentals of soil behaviour.* New York: John Wiley & Sons.

Mualem, Y., 1976. A new model for predicting the hydraulic conductivity of unsaturated porous media. *Water Resources Research,* 12(3), pp. 513-522.

Netzer, R. H. B. & Miller, P. B., 1992. What are race conditions? Some issues and formalisation. *In ACM letters on programming languages and systems,* 1(1).

Nielson, D. R., van Genuchten, M. & Biggar, J. W., 1986. Water flow and solute transport processes in the unsaturated zone. *Water Resources Research,* 22(9), pp. 89-108.

Olsen, R. E., 1963. Effective stress theory of compaction. *Proceedings of the American Society of Civil Engineering,* 81(1), pp. 27-44.

OpenMP, 2009. *The OpenMP API Specification for Parallel Programming.* [Online]
Available at: http://www.openmp.org/wp
[Accessed 4 12 2012].

Owen, D. H., 2000. *Preconditioned parallel iterative solution methods for coupled finite element analysis.* Cardiff: PhD Thesis, University of Wales, Cardiff.

Partington, J. R., 1949. *Advanced Treatise on Physical Chemistry.* Volume One ed. London: Longmans.

Philip, J. A. & De Vries, D. A., 1957. Moisture movements in porous materials under temperature gradients. *Transactions of the American Geophysical Union,* 38(2), pp. 222-232.

Pollock, D. W., 1986. Simulation of fluid flow and energy transport processes associated with high-level radioactive waste disposal in unsaturated alluvium. *Water Resources Research,* 22(5), pp. 765-775.

Preece, R. J., 1975. *The measurement and calculation of physical properties of cable bedding sands. Part 2; specific thermal capacity, thermal conductivity and temperature ratio across 'air' filled pores,* London: Central Electricity General Board, Laboratory Note No. RD/L/N 231/74.

Romero, E., Gens, A. & Lloret, A., 2001. Temperature effects on the hydraulic behaviour of an unsaturated clay. *Geotechnical and Geological Engineering,* 19(1), pp. 311-332.

Sedighi, M., 2011. *An investigation of hydro-geochemical processes in coupled thermal, hydraulic, chemical and mechanical behaviour of unsaturated soils.* Cardiff: PhD Thesis, Cardiff University.

Singh, R. M., 2007. *An experimental and numerical investigation of heat and mass movement in unsaturated clays.* Cardiff: PhD Thesis, Cardiff University.

Thomas, H. R. & He, Y., 1995. Analysis of coupled heat, moisture and air transfer in a deformable soil. *Geotechnique,* 45(4), pp. 677-689.

Thomas, H. R., He, Y. & Onofrei, C., 1998. An examination of the validation of a model of the hydro/thermo/mechanical behaviour of engineered clay barriers. *International Journal of Numerical and Analytical Methods in Geomechanics,* 22(1), pp. 49-71.

Thomas, H. R. & Rees, S. W., 2009. Measured and simulated heat transfer to foundation soils. *Geotechnique,* 59(4), pp. 365-375.

Thomas, H. R. & Samson, M. R., 1995. A fully coupled analysis of heat, moisture and air transfer in unsaturated soil. *Journal of Engineering Mechanics, American Society of Civil Engineering,* 13(3), pp. 392-404.

van Genuchten, M. T., 1980. A closed-form equation for predicting hydraulic conductivity of unsaturated soils. *Journal of Soil Society of America,* 44(1), pp. 892-898.

Vardon, P., 2009. *A three-dimensional numerical investigation of the thermo-hydro-mechanical behaviour of a large-scale prototype repository.* Cardiff: PhD Thesis, Cardiff University.

Vardon, P. J. et al., 2009. *Coupled thermo-hydro-mechanical modelling: A new parallel approach.* Rome, PDSEC-09 workshop of the IPDPS.

Vereecken, H., Maes, J., Feven, J. & Darius, P., 1989. Estimating the soil moisture retention characteristic from texture, bulk density, and carbon content. *Soil Science,* 148(6), pp. 389-403.

Zienkiewicz, O. C. & Morgan, K., 1982. *Finite Elements and Applications.* New York: John Wiley & Sons.

Chapter 6

Heat extraction/surface boundaries - development and initial validation/verification

6.1 Introduction

In Chapter 5, the theoretical and numerical formulations of the model have been presented to describe the coupled thermal and hydraulic (TH) behaviour of soil. Within the context of this study, the formulated model has been applied to the investigate ground behaviour in response to thermal energy extraction via horizontal ground source heat systems. Based on the literature review presented in Chapter 2, it was shown that such modelling requires consideration of two boundary conditions, namely; i) the ground surface boundary and ii) ground-loop boundary (e.g. Mei, 1986 and Leong, et al., 1998). The ground surface boundary represents the ground interaction with atmosphere whereas the ground-loop boundary represents the ground interaction with the buried ground-loop pipe surface. It is at this boundary that any heat being extracted from the ground via the heat pump is represented.

Figure 6.1 and 6.2 show the mentioned boundary conditions in relation to a horizontal ground-source heat system. Figure 6.1 provides an illustration of a typical horizontal ground source heat system whilst Figure 6.2 shows a two-dimensional schematic of a horizontal ground source heat system.

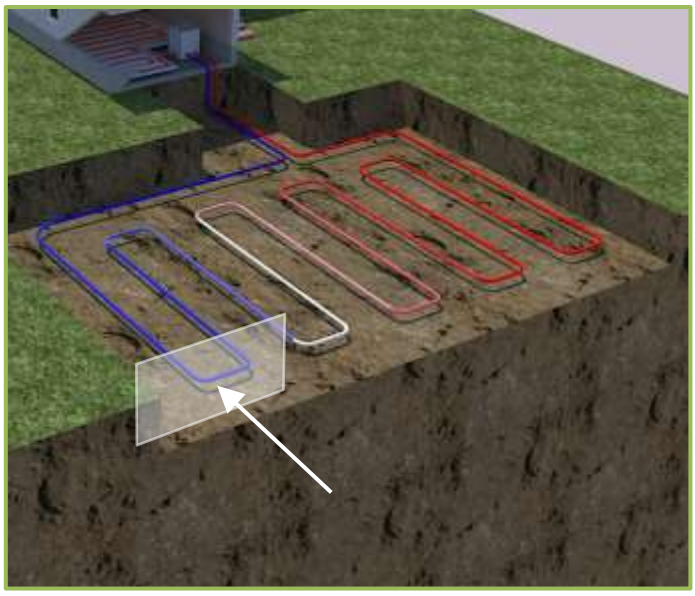

Figure 6.1 – Typical horizontal ground source heat system. The cross-section shown is presented in Figure 6.2.

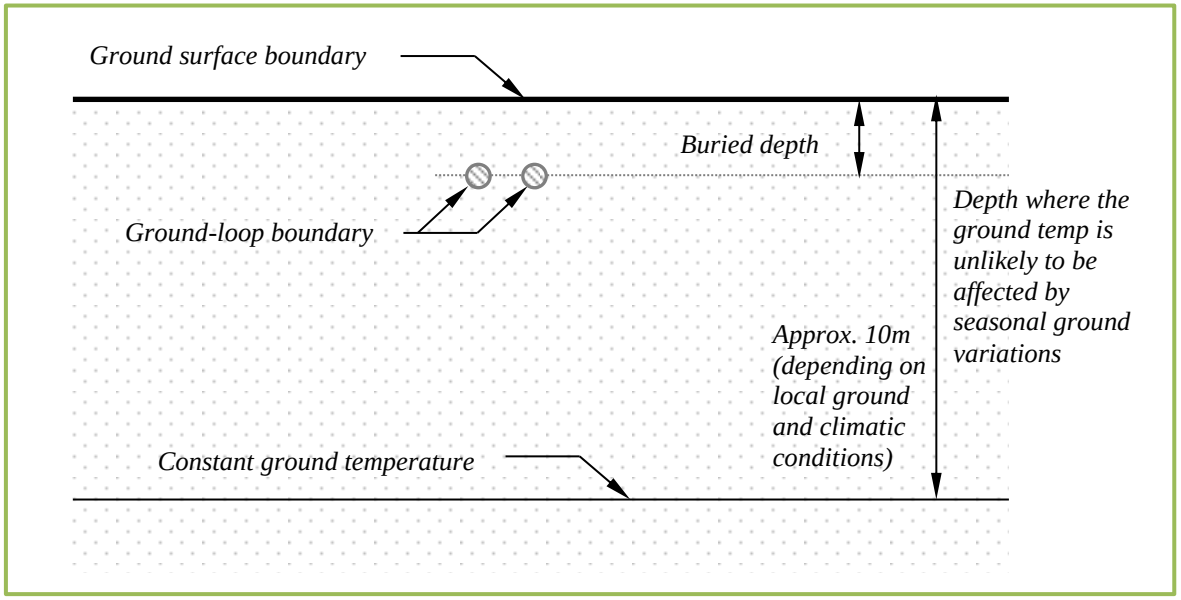

Figure 6.2 – Schematic of a horizontal ground source heat system presented in Figure 6.1 showing the boundary conditions described.

The concluding remarks in Chapter 2 highlighted that the majority of models developed for horizontal ground source heat systems simplify the ground-loop and surface boundary conditions. It was found that the majority of models consider the two boundary conditions as either fixed temperatures or fixed fluxes. In particular, the surface boundary condition has been simplified with little consideration to include climatic variables such as solar radiation, varying ambient air temperature or rainfall.

This Chapter first presents the theoretical development of a coupled TH ground surface boundary. Following this, the theoretical developments of two considered ground-loop boundaries are presented. Section 6.4 presents an initial validation into the hydraulic aspect of the surface boundary condition using data sourced from literature. Further validations regarding the thermal components will be presented in Chapter 7. Section 6.5 presents verification for the developed ground-loop boundary conditions. All of the boundary conditions have been implemented in the coupled TH code COMPASS. Finally, concluding remarks are given in section 6.6.

6.2 Surface boundary development

The ground surface is exposed to atmospheric conditions which play an important role within the surface energy balance, a process responsible for maintaining seasonal ground temperature variations (Deardorff, 1978). The proximity of horizontal ground-loops to the ground surface, positions them with a ground region subject to annual temperature variations (Leong, et al., 1998). It can therefore be deduced that to model the ground thermal behaviour, appropriate considerations of the ground surface boundary are required (Deardorff, 1978). The formulated boundary condition considers the surface in terms of a heat and moisture flux. The following sections will first describe the heat aspect of the formulated surface boundary. Following this, section 6.2.5 describes the surface moisture flux and the nature with which it is coupled to the surface heat flux.

Various researchers within the fields of meteorology and agriculture have investigated the atmospheric influence on the diurnal and annual ground temperature regimes. Findings show that temperature variations predominantly occur as a function of depth in conjunction with the thermal characteristics of the ground (Penrod, et al., 1960; Carson, 1963; Kusuda, 1975). The so called ‘energy balance equation’ has been reported to provide the most accurate annual and diurnal predication of ground temperatures (Deardorff, 1978; Bhumralkar, 1975). The energy balance equation essentially calculates the overall radiant energy being absorbed or emitted by a thin upper layer of the ground surface. The form of the energy balance equation can be presented as (van Wijk, 1966):

$$H_{SOIL} = H_{SW} - (H_{LW}^{Net} + H_{SEN} + H_{LE}) \tag{6.1}$$

where H_{SOIL} is the total radiation absorbed or emitted at the soil surface, H_{SW} is the short-wave radiation flux, H_{LW}^{Net} is the net long-wave radiation flux, H_{SEN} is the sensible heat flux and H_{LE} is the latent heat flux. All components have units of Wm^{-2} and are the values associated with the ground surface. Figure 6.3 provides a schematic showing the components of the energy balance equation presented in Equation 6.1.

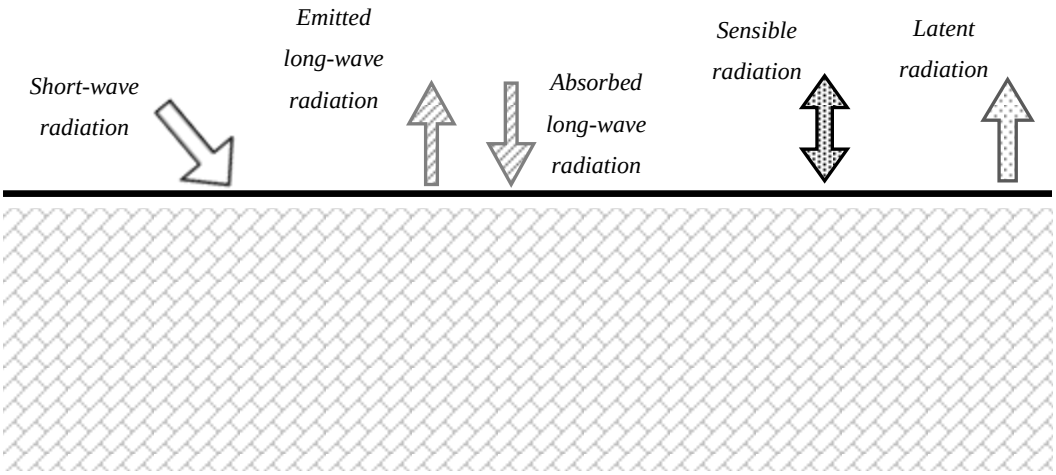

Figure 6.3 – Schematic showing the various components of the energy balance equation.

The following sections will inspect each of the individual components of the surface energy balance equation described in Equation 6.1. The components will be mathematically expressed in a form that allows them to be implemented and computed within the existing numerical model. Details regarding the implementation of the theory within the model are presented in section 6.2.6.

6.2.1 Short-wave radiation

Short-wave radiation is a combination of direct and diffused solar radiation striking the Earth's surface. The diffused radiation is primarily caused by clouds, dust and molecular scattering in the atmosphere (van Wijk & Scholte Ubing, 1966). It is commonly referred to as *short-wave radiation* as the majority of the associated radiation has wavelengths within the infra-red and visible bands of the electromagnetic spectrum, with a relatively small fraction falling within the ultra-violate band (van Wijk & Scholte Ubing, 1966). In fact, approximately 98% of the heat radiation reaching the Earth's surface is contained within the wavelength interval between 0.25μ and 4μ with

approximately 1% falling either side of the upper and lower limits previously stated (van Wijk & Scholte Ubing, 1966). The remaining fractions of the electromagnetic spectrum emitted by the Sun are reflected by the Earth's upper atmosphere.

Short-wave flux is the total short-wave solar radiation that strikes a unit area of ground surface. The total short-wave flux striking the Earth's surface varies on a diurnal and annual basis, depending on the solar inclination and climatic conditions. In addition to this, not all of the short-wave flux that physically strikes the ground surface will be absorbed. A considerable fraction of the short-wave flux that reaches the Earth's surface is reflected. The exact proportion of the radiation reflected depends on the ground surface coverage and reflection properties. Equation 6.2 presents a relationship adopted within the formulation to account for this phenomenon, given as (Deardorff, 1978);

$$H_{sw}^{Absor} = \varepsilon_{sw} H_{sw} \tag{6.2}$$

where H_{sw}^{Absor} is the absorbed short-wave radiation flux *(Wm^{-2})*, H_{SW} is the short-wave radiation flux striking the ground surface *(Wm^{-2})* and ε_{SW} is the short-wave reflection factor associated with the ground surface type. For reference, Table 6.1 presents some common material reflection factors.

Table 6.1 – Reflection factors of natural surfaces for short-wave radiation (after. van Wijk, W.R. & Scholte Ubing, D.W, 1966).

Surface type	**Reflection factor (% reflected)**
Fresh snow	80-85
Compressed snow	70
Lime	45
Quartz sand	35
Granite	15
Dark clay, wet	2-8
Dark clay, dry	16
Sand, wet	9
Sand, dry	18
Bare fields	12-25
Grass, green	16-27
Grass, dried	16-19
Grain crops	10-25
Pine, spruce wood	10-14
Yellow leaves	33-36
Desert, midday	15
Water (0º)	2
Water (60º)	6
Water (85º)	58

In order to compute the short-wave radiation component within Equation 6.1, a representative value of short-wave radiation is required. Values can either be obtained via monitoring, using appropriate historical records or approximated using irradiance models. A number of theoretical and empirical irradiance models have been proposed, most notably work by Angstrom (1925), van Wijk and Scholte Ubing (1963a), Revfeim (1978), Johnson et al. (1995) and Woodward et al. (2001). Within the context of this work, the short-wave radiation prescribed in models will be based on data collected at the monitoring site presented in Chapter 3.

6.2.2 Net long-wave radiation

The source of this type of thermal radiation is the incessant molecular motion, caused by energised particles on an atomic level. Collisions between the atomic particles convert kinetic energy into thermal energy, thereby raising the temperature of the body (van Wijk & Scholte Ubing, 1966). The atmosphere (i.e. the vapour and gas constituents) and ground both emit long-wave radiation as a function of their temperatures. The net long-wave radiation at the ground surface can be described as a combination of long-wave radiation being emitted from the ground and long-wave radiation being absorbed from the atmosphere. Within the context of this formulation, the absorbed radiation will be referred to as the long-wave radiation passing from the atmosphere towards the Earth's surface, with the emitted radiation travelling in the opposite direction. This can be mathematically expressed as follows:

$$H_{LW}^{net} = H_{LW}^{Absorbed} - H_{LW}^{Emitted} \tag{6.3}$$

where H_{LW}^{net} is the net radiation at the ground surface *(Wm^{-2})*, $H_{LW}^{Absorbed}$ is the radiation absorbed at the ground surface *(Wm^{-2})* and $H_{LW}^{Emitted}$ is the radiation emitted from the ground surface *(Wm^{-2})*.

The long-wave radiation being emitted by a body can be calculated using Stefan-Boltzmann's law (Woodward, et al., 2001; van Wijk & Scholte Ubing, 1966). The Stefan-Boltzmann law states that the power emitted by a body is directly proportional to the forth power of its absolute temperature, given as (Lewis, et al., 2004);

$$H_{LW}^{Emitted} = \varepsilon_{LW}\, \sigma\, (T)^4 \tag{6.4}$$

where ε_{LW} is the long-wave emissivity of the body *(non-dimensional)*, σ is the Stefan-Boltzmann constant which is equal to $5.67\times10^{-8}\ Wm^{-2}\ K^{-4}$ and T is the absolute temperature of the body *(K)*.

The long-wave radiation absorbed from the atmosphere is dependent on cloud formation. Several empirical approaches have been proposed to calculate the cloud cover effect, most notably Angstrom (1915), De Vries (1955) and Penman (1956). All of these approaches incorporate coefficients which are specific to local regions. A more general approach was formulated by Imberger and Patterson (1981) to calculate the long-wave radiation being absorbed at the ground surface from the atmosphere, given as;

$$H_{LW}^{Absorbed} = \varepsilon_{LW}^{A}\, \sigma\, (1 + 0.17\, {C_{Cloud}}^{2})\, (T_{air})^{4} \tag{6.5}$$

where ε_{LW}^{A} is the long-wave emissivity of the air at ground level *(non-dimensional)*, C_{Cloud} is the fractional cloud cover coefficient (0 = clear sky, 1 = total overcast) and T_{air} is the absolute temperature of the air adjacent to the ground surface *(K)*.

Equations 6.4 and 6.5 have been used to calculate the $H_{LW}^{Emitted}$ and $H_{LW}^{Absorbed}$ long-wave components of Equation 6.3 within the developed surface boundary condition.

6.2.3 Sensible heat radiation

Sensible heat radiation can be defined as the heat exchange within a thermo-dynamic system that has a sole effect of temperature change on the constituent bodies (i.e. not energy associated with a phase change) (Adkins, 1975). Sensible heat radiation is a function of both thermal conduction and convection. With respect to the ground surface boundary, the sensible heat flux has been modelled using the following equation (Deardorff, 1978; Choudhury & Moneith, 1988):

$$H_{SEN} = \rho_a C_p r_a (T_{ea} - T_{air}) \tag{6.6}$$

where ρ_a is the air density *(kg m^{-3})*, C_p is the ground specific heat capacity *(J kg^{-1} K^{-1})*, r_a is the aerodynamic resistance, (as defined in Equation 6.10) and T_{ea} is the absolute temperature of the ground surface *(T)*.

The formula presented in Equation 6.6 is essentially a form of Fourier's law of conduction which forms the foundation of one-dimensional heat conduction (Deardorff, 1978). The components ρ_a, C_p and r_a combine to calculate a modified thermal conductivity value which considers the surface aerodynamic influences; thereby incorporating a convective component within the equation (Deardorff, 1978). The so called aerodynamic resistance will be discussed at greater length within section 6.2.4 of this chapter.

6.2.4 Latent heat radiation

Latent heat radiation can be defined as the absorption or release of energy within a thermodynamic system that occurs without a change in temperature (i.e. energy related to molecule changes of state) (Perrot, 1998). Within the context of the surface boundary condition, this is primarily linked to the evaporation of water from the upper regions of the ground surface. The latent heat flux due to evaporation is calculated as follows:

$$H_{LE} = L\,E \tag{6.7}$$

where L is the latent heat of vaporisation *(J kg^{-1})* and E is the water vapour flux *(kg m^{-2} s^{-1})*.

The water vapour flux presented in Equation 6.7 is a moisture flux at the ground surface which represents the evaporation from the soil surface. The following paragraphs will present the theoretical development of the approach used to calculate the evaporation within the developed surface boundary condition.

The evaporation process is affected/controlled by atmospheric, surface and ground factors which directly influence it (Deardorff, 1978; Fuchs & Tanner, 1967). The rate of evaporation is greatly influenced by the moisture content of soil at the ground surface, linking the boundary to the moisture transfer in the soil. A formulation for the coupled TH behaviour of the soil has already being presented in Chapter 5. The focus of this section will therefore be the evaporation from the ground surface. A number of approaches have been developed within theoretical and numerical models with the aim of predicting evaporation from a ground surface e.g. Penman (1948), Hillel (1980), Barton (1979) and Wilson et al. (1997). Based on the calculations of Dalton's mass transfer formula (Dalton, 1802), the evaporation rate can be given as:

$$E = f(u)(e_{ea} - e_{air}) \tag{6.8}$$

where E is the rate of evaporation *(mm s^{-1})*, e_{ea} is the saturation vapour pressure at ground surface temperature *(kPa)*, e_{air} is the air vapour pressure at the ground surface *(kPa)* and *f(u)* is the so called 'transition function'.

Similarly, Equation 6.8 can be presented in terms of the specific humidity (Deardorff, 1978):

$$E = \rho_a\, f(u)\,(q_{ea} - q_{air}) \tag{6.9}$$

where E is the evaporation mass flux *(kg m^{-3} s^{-1})*, ρ_a is air density *(kg m^{-3})*, q_{ea} is soil specific humidity at the ground surface *(kg kg^{-1})* and q_{air} is air specific humidity *(kg kg^{-1})*.

The transition function, *f(u)* (also referred to as aerodynamic resistance in Equation 6.6), accounts for the mixing and turbulence of the air above the evaporating surface (Fuchs & Tanner, 1967). A range of solutions have been presented to calculate the transition function, e.g. Gray (1970), Conaway & van Bavel (1967), Sellers (1965) and Sverdrup (1946). For the formulation of the surface boundary condition presented here, the following transition function proposed by Sverdrup (1946) has been applied:

$$f(u) = \frac{k^2 u_z}{[\ln z/z_0]^2} = C_z u_z = r_a \tag{6.10}$$

where k is the von Karman constant equal to 0.41, u_z is the wind speed at an elevation z *(m s^{-1})*, z is a reference elevation *(m)*, z_0 is surface roughness *(m)*, C_z is a drag coefficient and r_a is aerodynamic resistance.

The parameter z_0, presented in Equation 6.10, allows the surface texture (e.g. grass, concrete etc.) to be considered when calculating the mixing characteristics of the air immediately above the ground surface, thereby including the surface type in the latent heat calculation. When considering the effect of the surface boundary, this feature can be important in the recharge of the ground.

The value of the rate of evaporation (E), calculated by Dalton's formula is equal to the so called Potential Evaporation (*PE*). The term Potential Evaporation can be described as the upper limit or maximum rate of evaporation from a surface (Barton, 1979). For this reason, Dalton's formula in its original form is often applied to calculate the rate of evaporation from open and therefore free water surfaces, for example lakes (van Wijk & Borghorst, 1966). With respect to the evaporation from soil, PE remains a valid approximation of the overall evaporation provided there is a constant supply of water available at the ground surface, i.e. when the ground surface is saturated (Wilson, et al., 1997). As the upper surface of soil enters the unsaturated state, the availability of water will be dependable on the water retention characteristics of the soil. It has been shown that Equation 6.9 over estimates the evaporation rate when applied to unsaturated soils without modification (Wilson, et al., 1997; Gray, 1970). Therefore, Dalton's mass transfer approach without modification will incur errors if the supply of water to the surface is inhibited (i.e. when the ground surface is unsaturated). To address this limitation modifications have been suggested to Equation 6.9 (Penman, 1948; Hillel, 1980; Barton, 1979 and Wilson, et al., 1994).

Wilson et al. (1997) presented a modified Dalton's mass transfer equation to predict the evaporative rates from unsaturated soil surfaces. A theoretical relationship between the actual

evaporation and soil suction was derived and is presented in Equations 6.11. This development of the Dalton mass transfer equation has been implemented within the presented surface boundary condition to determine the evaporation from the ground surface in the unsaturated case.

$$AE = PE\left(\frac{h - h_{air}}{1 - h_{air}}\right) \tag{6.11}$$

where *AE* is actual evaporation *(kg m^{-3} s^{-1})*, *PE* is potential evaporation *(kg m^{-3} s^{-1})*, *h* is relative humidity of the ground surface *(non-dimensional)*, h_{air} is the air relative humidity at ground surface *(non-dimensional)* (see section 5.3.2).

In summary, when the ground surface is saturated the value of the rate of evaporation (*E*) is equal to the potential evaporation (PE) as calculated in Equation 6.9. In the unsaturated case, the value of the rate of evaporation is equal the modified potential evaporation, the actual evaporation (AE), as calculated in Equation 6.11.

6.2.5 Surface moisture flux

In order to model the coupled TH ground boundary, a representative mass boundary describing hydrological processes at the ground surface is presented. Assuming that the net moisture flux at the surface boundary is a function of hydrological process only, the following equation can be applied to calculate the ground surface moisture flux (Fredlund, et al., 2011):

$$Q_m = P - E - R \tag{6.12}$$

where Q_m is the net mass flux at the ground surface *(kg m-^{2} s^{-1})*, *P* is the precipitation mass flux *(kg m^{-2} s^{-1})*, *E* is the evaporation mass flux according to Equation 6.9 with modification from Equation 6.11 if the ground surface is unsaturated *(kg m^{-2} s^{-1})*. *R* is the run-off *(kg m^{-2} s^{-1})*.

Equation 6.12 considers the surface moisture exchange in terms of liquid and vapour phases. A vapour component representing evaporation has already been formulated and considered within section 6.2.4, as part of the latent heat formulation. From Equation 6.12 it can be seen that a term representing the climatic variable precipitation is required. Precipitation data is available for most geographical regions; therefore representative values can be obtained and prescribed in most cases. Within the current scope of work, precipitation data is obtained within the monitoring scheme presented in Chapter 3. Data collected at the monitoring site will therefore be applied within the modelling work. The final term in Equation 6.12 accounts for excess water run-off due to saturation

within the upper soil layers (Liang, et al., 2003). At degrees of saturation below 1, the run-off is assumed to be zero. It can be said that the calculated run-off is therefore intrinsically linked to the hydraulic material characteristics and conditions of the upper ground layers (Fredlund, et al., 2011).

6.2.6 Numerical implementation

Implementation of the developed surface boundary formulations, presented in sections 6.2.1 to 6.2.5, within the numerical model presented in Chapter 5 is described here. The numerical implementation presented here has been split into two sections, the first part discusses the climatic data required by the surface boundary formulations (in order to compute surface fluxes) and the second part discusses numerical model developments.

Figure 6.4 shows a schematic of the ground surface boundary and a model domain discretised into a number of elements. The climatic variables needed to model the surface are listed below:

i. Ambient air temperature, K
ii. Solar radiation flux, Wm^{-2}
iii. Air relative humidity, $\%$
iv. Wind speed, ms^{-1}
v. Rainfall, $kg\ m^{-2}\ s^{-1}$

The climatic variables listed above are commonly monitored in the field and representative values can be obtained for most regions globally from metrological data. For the simulation of the monitoring site presented in Chapter 3, the required climatic variables have been prescribed using recorded climatic data (see Chapter 4 for details). The climatic variables were prescribed as time-dependent variables for the computation of the surface boundary condition. Linear interpolation is subsequently used to calculate representative climatic variables between the time-dependant values. The resolution of the prescribed data is dependent on the nature of the variables (i.e. fluctuating on hourly or diurnal basis), maximum simulation time-step and the resolution of the original data.

The ground surface boundary is prescribed by two fluxes, one representing hydraulic surface interactions (i.e. moisture, see section 6.2.5) and the other representing thermal interactions. As previously discussed, the two fluxes are connected i) by the coupled thermo-hydraulic behaviour of the soil and ii) by the latent heat component of the energy balance equation (see Equation 6.1). In order to calculate these fluxes in the model, a sequential algorithm was developed and implemented

within the existing numerical code. A flow diagram showing the developed algorithm can be found in Figure 6.5.

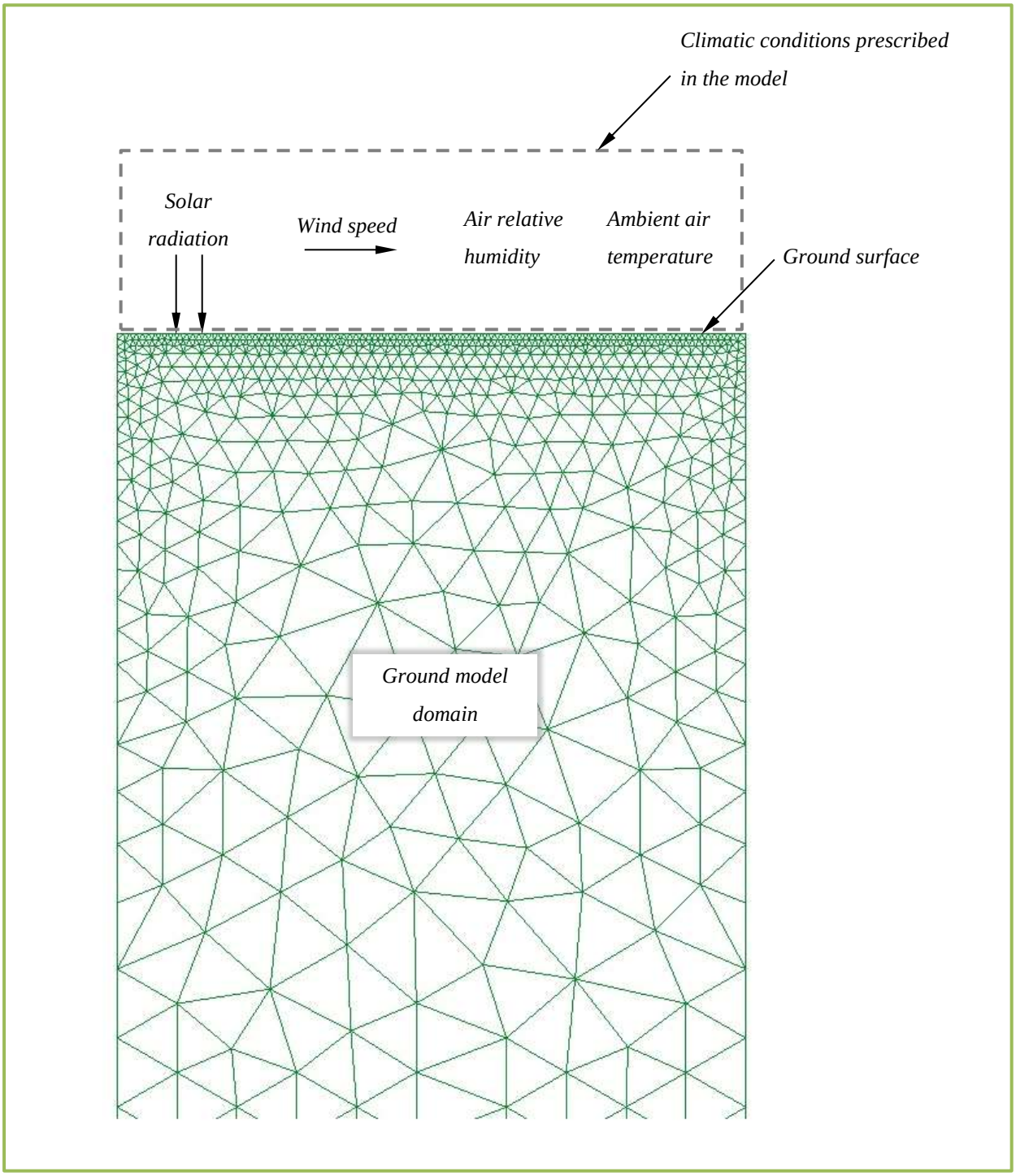

Figure 6.4 – Schematic of a ground domain showing the ground surface boundary condition and the climatic variables required in order to calculate the ground surface boundary components.

As shown in Figure 6.5, the heat and moisture fluxes representing the ground surface boundary are calculated prior to each time-step. According to the surface boundary formulation, calculation of the fluxes requires ground surface information regarding temperature, relative humidity and degree of saturation. The ground properties previously listed are extracted prior to each time-step for each node located at the ground surface within the model domain. This allows the surface fluxes to be locally calculated on a node by node basis.

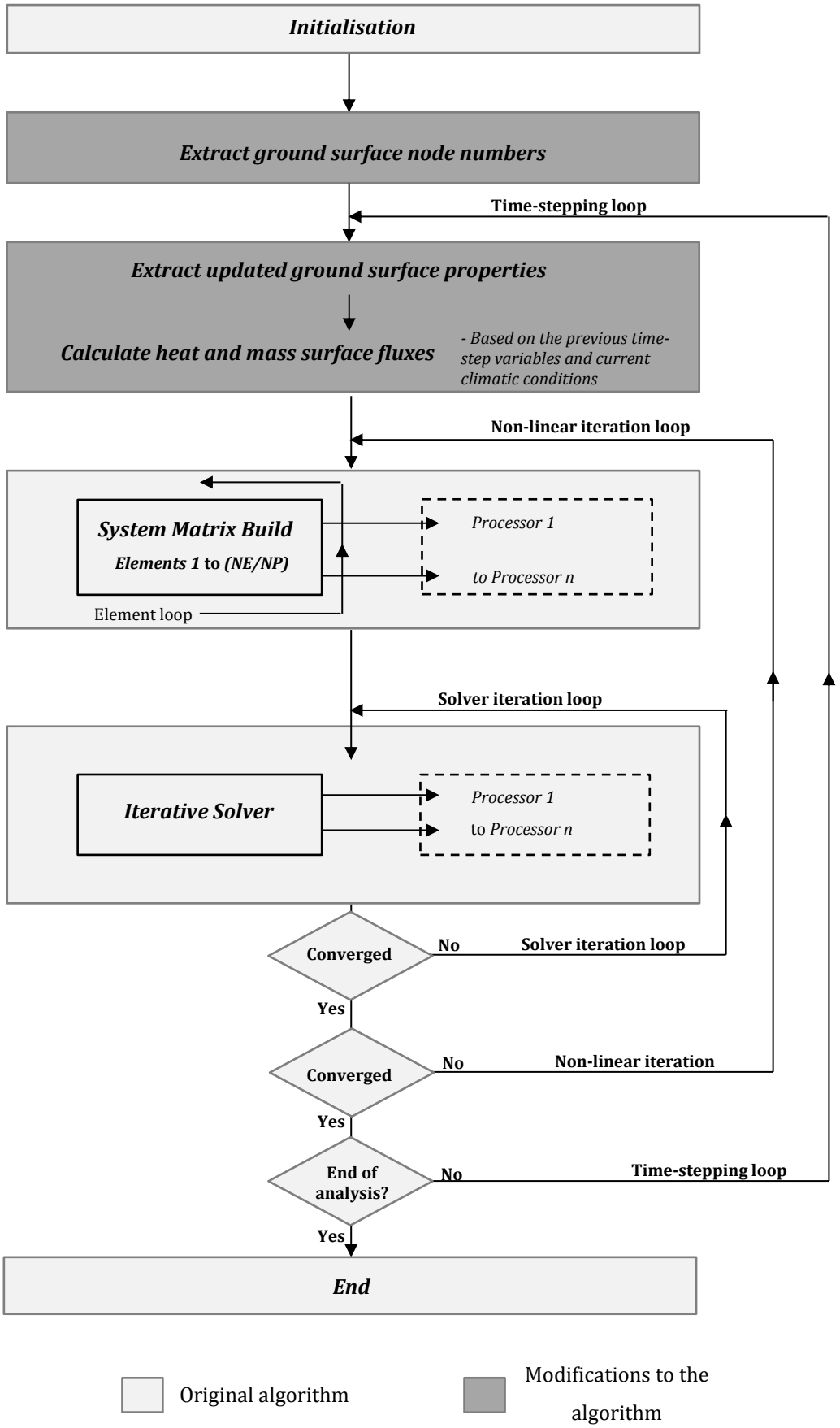

Figure 6.5 – Multi-threaded parallel algorithm including modifications to implement the ground surface boundary formulations.

6.3 Ground-loop boundary development

As described in Chapter 2, the fluid which circulates around ground-loop systems transfers and exchanges the heat from the ground to the heat pump. The term 'ground-loop boundary' is commonly used within ground source heat literature to describe the heat exchange between the circulating fluid and surrounding ground in the modelling context (Yang, et al., 2010). The literature review contained in Chapter 2 presented a range of analytical and numerical approaches, developed to model the ground-loop boundary with varying degrees of complexity.

The scope of this study focusses on closed-loop ground source heat systems, therefore the following boundary developments are tailored towards such systems. When considering closed-loop systems, the prescribed ground-loop boundary can be considered as a function of heat only due to the impermeable properties of the ground-loops installed. Further details regarding the pipe properties and closed ground-loop configurations can be found in Chapter 1.

The following sections present the development of two ground-loop boundaries, namely; i) a uniform and ii) a non-uniform ground-loop boundary. The uniform boundary condition provides a calculation of a single heat flux for the whole ground-loop based on the total heat extracted by the heat pump. The non-uniform boundary condition provides a calculation of a heat flux which varies across the ground-loop surface, depending on the local ground and circulating fluid temperatures. The formulations of these two boundary conditions are presented in sections 6.3.1 and 6.3.2 followed by verifications analysis in section 6.3, carried out to test developments.

6.3.1 Ground-loop boundary – uniform heat flux

The ground-loop heat boundary at any point of the ground-loop can be described as a function of the ground and fluid temperatures corresponding to that specific location. The difference in temperature between the fluid and ground is a function of the overall heat being extracted by the system. Consequently it can be said that the ground-loop heat boundary can be described as a function of the overall heating load for the system. Within the current scope, the term 'system heating load' refers to the thermal energy being exchanged by the heat pump.

Rather than explicitly simulating fluid circulation, one alternative is to calculate a ground-loop flux based upon the overall system heat load at a point in time. The system heat load is dependent on two factors namely; operational settings and the heat pump capacity. The system heat load can be measured and subsequently calculated at any time of analysis using values of the circulating fluid's specific heat capacity, flow rate and temperature difference across the heat pump.

Mathematical equations which can be applied to calculate the heat load based on the previous factors have been presented in Chapter 3, however for convenience the equations are also presented here. Equation 6.13 gives the heat load at a particular point in time:

$$W = \Delta T . C_p . \dot{m} \tag{6.13}$$

where:

$$\Delta T = T_{inlet} - T_{oulett} \tag{6.14}$$

where W is the system heating load $(J\ s^{-1})$, C_p is the specific heat capacity of the circulating fluid $(J\ kg^{-1}\ K^{-1})$, $\dot{m}$ is the flow rate of the circulating fluid $(kg\ s^{-1})$, T_{inlet} is the fluid temperature entering the heat pump (K) (see Figure 6.6) and T_{outlet} is the fluid temperature leaving the heat pump (K) (see Figure 6.6).

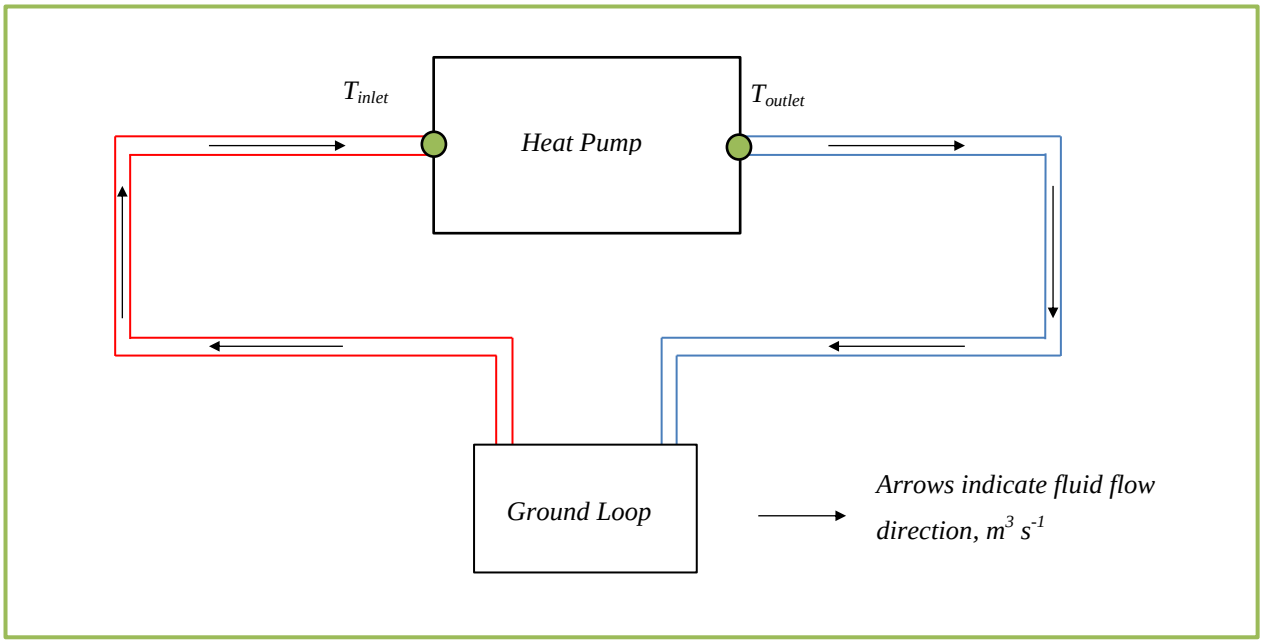

Figure 6.6 – Schematic showing the fluid flow and fluid inlet/outlet of the heat pump.

Provided that the basic loop dimensions (i.e. the ground-loop diameter and length) are known, the average heat flux per unit length and per unit area for the ground-loop can be calculated. Equations 6.15 and 6.16 give the heat flux per unit length and per unit area of the ground-loop respectively.

$$Q_L = {}^{W}/_{l_p} \tag{6.15}$$

$$Q_A = {}^{Q_L}/_{\pi\, d_p} \tag{6.16}$$

where Q_L is the heat flux per unit length of ground-loop *(Wm^{-1})*, Q_A is the heat flux per unit area of ground-loop *(Wm^{-2})*, l_p is the total ground-loop length and d_p is the ground-loop diameter *(m)*.

The temporal variations in the system behaviour resulting from cyclic operation or seasonal changes in the system heating load can be represented in models through an updated calculation of the parameter *W*.

In summary, the formulations can be described as a 3 step process as follows:

i. The heat load of the system is calculated using Equations 6.13 and 6.14
ii. The average heat flux per unit length of the ground-loop is calculated using Equation 6.15
iii. The average heat flux per unit area of the ground-loop is calculated using Equation 6.16
iv. The calculated heat flux per unit area is prescribed to the ground-loop boundary within the numerical model

6.3.2 Ground-loop boundary - non-uniform heat flux

When developing the following non-uniform boundary condition, the aim was to allow local ground and fluid temperatures to be included within the computation of the boundary heat flux. The term 'non-uniform' has been used in the current context because the heat flux resulting from the application of local ground and fluid temperatures varies spatially and temporally across the ground-loop. The following section first presents the theoretical development of this boundary condition. An algorithm used to implement the non-uniform ground-loop boundary condition within the numerical model previously presented in Chapter 5 will then be discussed.

When considering the capabilities of the numerical model presented in Chapter 5, it becomes apparent that the main obstacle preventing the implementation of a non-uniform boundary condition is the determination of the local fluid temperature. In order to determine the local fluid temperature, it is necessary to have an understanding of the so called 'fluid temperature profile' along the ground-loop length. The fluid temperature profile has been the focus of some previous experimental and

theoretical research within the ground source heat subject area. Chapter 2 presented a range of analytical and numerical approaches used to calculate the fluid temperature profile and resulting ground-loop boundary. Al-Khoury et. al. (2006), Piechowski (1999) and Demir et al. (2009) calculated the ground-loop boundary as a function of fluid temperature. In all three cases, the fluid temperature profile was modelled using a one-dimensional fluid model based on the conservation of energy principle (see Chapter 2 for more detail). Following the previously highlighted works, a one-dimensional model based on the conservation of energy principle has been developed to predict the fluid temperature profile. The developed model has been linked to the three-dimensional thermo-hydraulic model, presented in Chapter 5, at the ground-loop boundary surface.

The theoretical formulation of the non-uniform boundary condition is described in two parts. The first part provides the formulation of the one-dimensional fluid temperature model, as previously discussed, while the second is the actual calculation of the heat flux boundary considering the local fluid and ground temperatures. In order to simulate the heat carried by fluid flow, it is necessary to discretise the circulating fluid into a series of elements. Figure 6.7 shows the system considered within the current formulation and the discretisation of the circulating fluid into a series of uniform control volumes.

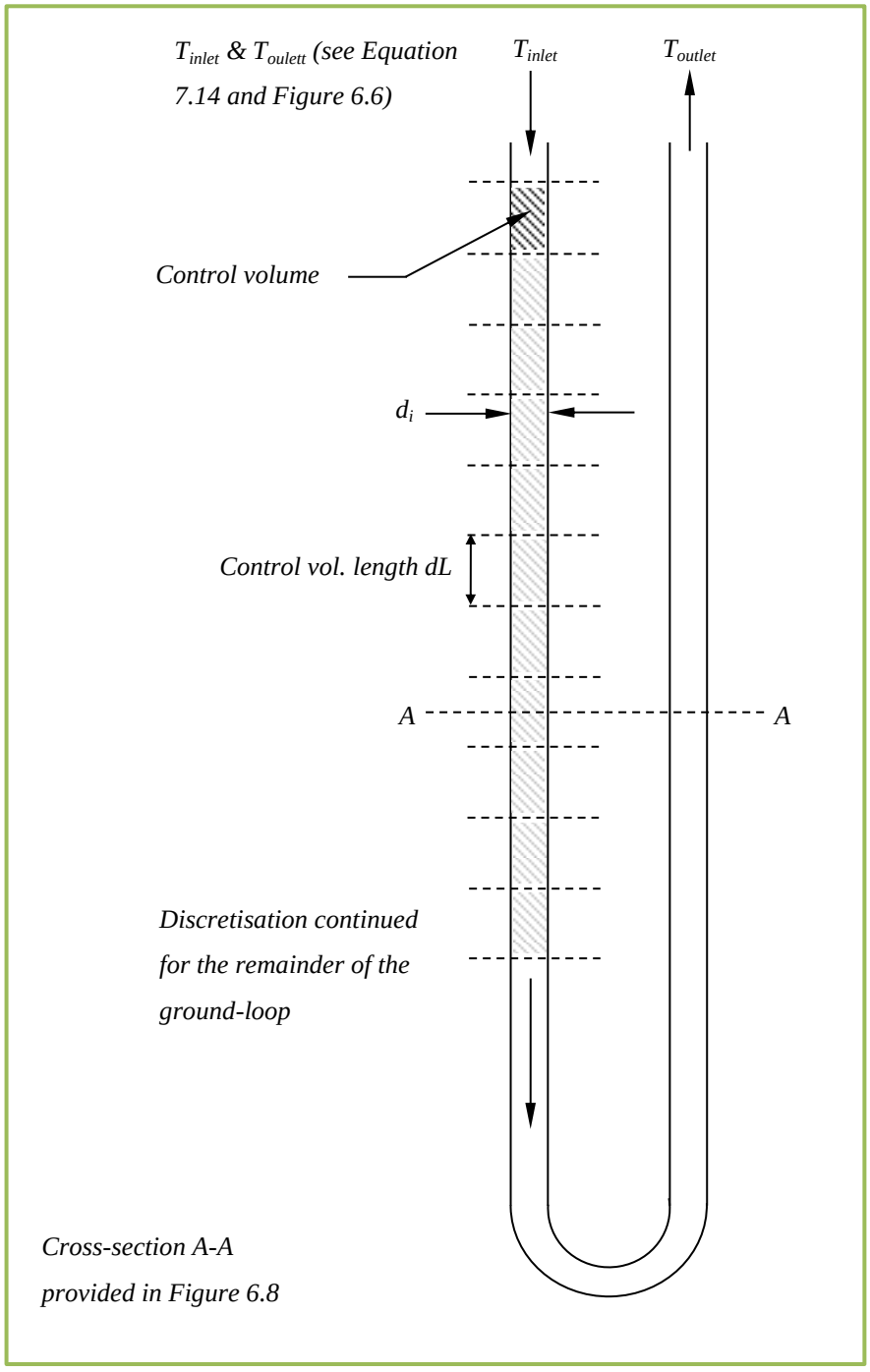

Figure 6.7 – Schematic of the ground-loop including discretisation of control volumes used in one-dimensional fluid formulations.

Figure 6.8 shows a vertical cross-section at the point AA (see Figure 6.7) of the discretisation used to calculate the fluid temperature profile. It is assumed that each control volume has uniform flow characteristics (i.e. flow rate, velocity and viscosity), thereby simplifying dynamic fluid behaviour to one-dimension. The validity of this simplification is dependent on mixing characteristics and properties of the fluid (i.e. Reynold's number) which is a function of the system flow rates and ground-loop diameter. The flow and ground-loop properties found at the monitoring site presented in Chapter 3, result in a turbulent flow based on the measured fluid flow rate and ground-loop diameter. This thereby renders the previous simplification as valid within the current scope of work.

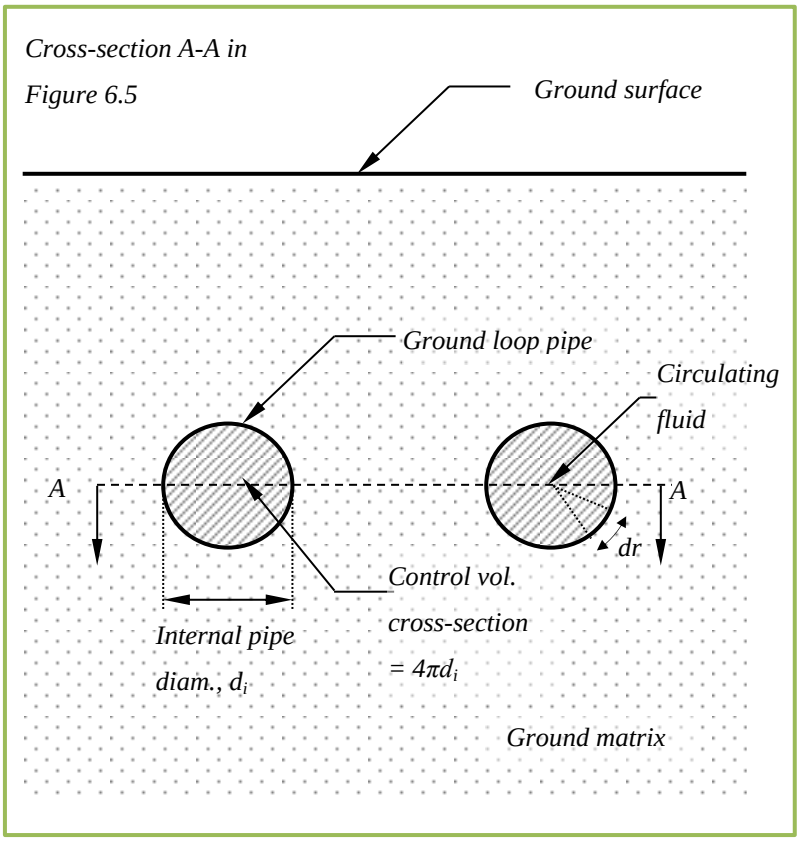

Figure 6.8 – Cross-section of a horizontal ground-loop showing the horizontal section A-A (Figure 6.7).

A theoretical formulation was developed and applied to each element for a given time-step, in order to allow representative changes in the fluid temperature for that period to be determined.

The presented ground-loop boundary formulations calculate the conductive heat flux at each control volume according to Fourier's Law. This is achieved by radially discretising the control volume circumference into incremental lengths of *dr* (see Figure 6.8) and applying Fourier's Law of

Conduction accordingly. The total heat flux across the circumference of a control volume can therefore be given as:

$$Q_L = \int_0^{(2\pi r)} -\lambda \left(T_f - T_g\right) \frac{1}{r}\, dr \tag{6.17}$$

where Q_L is the total heat flux per meter *(Wm^{-1})*, r is the ground-loop pipe radius *(m)*, λ is thermal conductivity of the fluid *(W m^{-1} K^{-1})*,T_f is the fluid temperature at the control volume under inspection *(K)*, T_g is the ground temperature adjacent to the ground-loop control volume under inspection *(K)*.

The heat flux per unit area, based upon the control volume dimensions outlined in Figure 6.7 and 6.8 is:

$$Q_A = \frac{Q_L}{dL} \tag{6.18}$$

where Q_A is the total heat flux per unit area, *(W m^{-2})* and dL is the length of control volume *(m)*.

The fluid temperature, T_f, contained in Equation 6.17 is assumed to be uniform across each control volume based on the turbulent flow nature described. The ground adjacent to the ground-loop, on the other hand, is not assumed to have a uniform temperature. This allows local ground temperature variations around the ground-loop pipe to be considered. The heterogeneous nature of the ground matrix and thermal interactions between adjacent ground-loop legs are just two possible reasons why the surrounding ground may vary locally in temperature. The three-dimensional modelling of the ground allows any differences in ground temperature around the circumference of the ground-loop pipe to be considered.

By multiplying the heat flux, Q, in Equation 6.18 by the control volume surface area it is possible to calculate the total energy leaving/entering a control volume for a given time period. Provided that the total specific heat capacity of the fluid is known, it is possible to calculate the theoretical temperature change of the fluid for a given time period as follows:

$$\frac{dT_f}{dt} = \frac{Q_A . dL . 2\pi r}{C_p \rho_l \, dA \, dL} \tag{6.19}$$

where dT_f is the change in fluid temperature within a control volume *(K)*, C_p is the specific heat capacity of the fluid *(J kg^{-1} K^{-1})*, ρ_l is the fluid density *(kg m^{-3})* and A is segment the cross-section area *(m^2)*.

Substituting Equations 6.17 and 6.18 into Equation 6.19 and rearranging gives the general equation used to calculate the fluid temperature change in each control volume:

$$\frac{dT_f}{dt} = \frac{2}{C_p\,\rho_l\,dL\,r}\int_0^{(\pi\times 2r)} -\lambda\left(T_f - T_g\right)\frac{1}{r}\,dr \tag{6.20}$$

Application of Equation 6.20 allows the updated fluid temperature in each control volume (i.e. along the length of the ground-loop) to be calculated. It is subsequently possible to calculate the local ground-loop boundary flux using the calculated local fluid temperatures and the local ground temperatures (i.e. adjacent to the ground-loop) using Fourier's Law of Conduction.

In order to calculate the dynamic fluid temperature profile with time an additional formulation is required to account for the temperature change as fluid passes through the heat pump (as illustrated in Figure 6.9). Within a time increment, *dt*, the heat pump removes thermal energy from a portion of circulating fluid which passes through the heat pump. The resulting change in fluid temperature can be calculated as follows:

$$dT_f = \frac{W_t}{C_p\rho_l\,dA\,dL} \tag{6.21}$$

where W_t is the total energy extraction for the time *dt* (i.e. the system heating load, *W* multiplied by *dt*) *(J).*

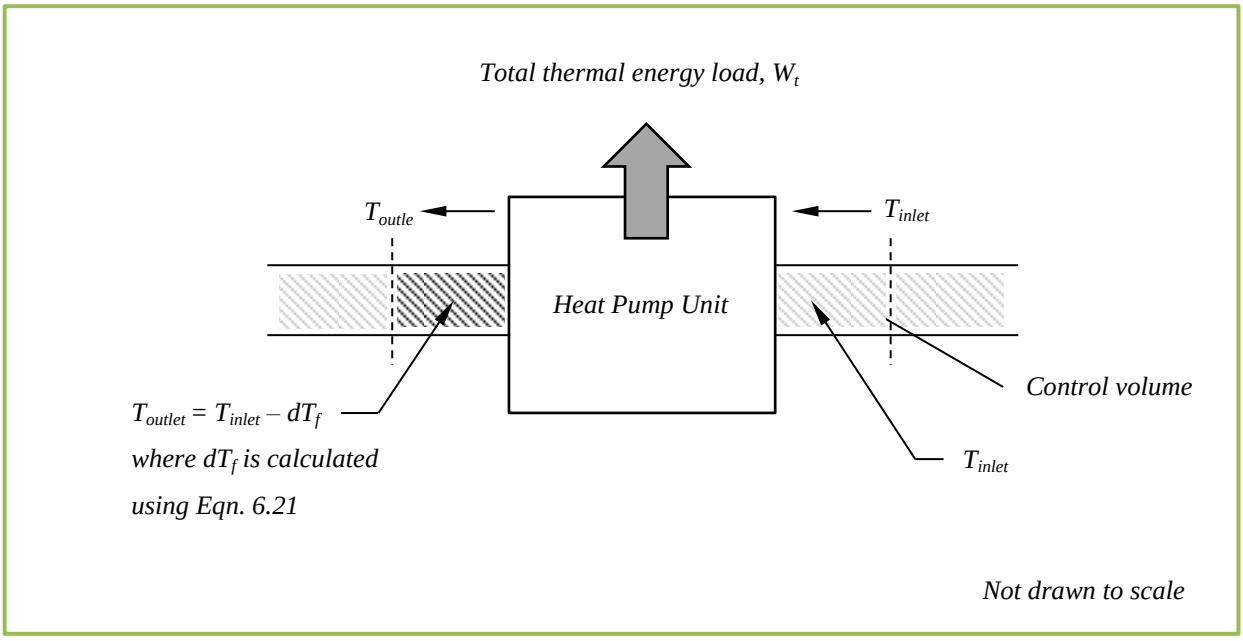

Figure 6.9 – Schematic showing the thermal energy extraction at the heat pump.

The preceding formulations can be summarised as a pseudo algorithm as follows:

i. Heat flux per unit area of each fluid control volume calculated using the local ground and fluid temperatures (Equations 6.17 and 6.18).
ii. Updated fluid temperature profile calculated using the heat flux from step (i) and Equation 6.20.
iii. Modify the fluid temperature profile, accounting for the heat removed by the heat pump by applying Equation 6.21 to the appropriate control volumes.
iv. Calculate the non-uniform heat flux between the fluid and the ground using the updated fluid temperatures from step (iii) and Fourier's one-dimensional law of heat conduction
v. Model the ground behaviour based on the heat flux calculated in step (iv)
vi. Return to step (i)

6.3.2.1 Multiple time-step algorithm to implement the non-uniform ground-loop flux

Provided that the measurable system characteristics (i.e. ground-loop length, diameter and heating load), time-step and control volume dimensions are defined, the non-uniform heat flux boundary can be incorporated within a numerical model according to the previous section. As previously discussed, the heat extraction by the fluid is linked to the three-dimensional TH ground model by means of a non-uniform heat flux prescribed at the ground-loop boundary. In order to implement this boundary condition within the numerical code presented in Chapter 5, modifications to the existing algorithm were required. The algorithm modifications have been implemented in the model for two reasons; i) to accommodate the calculation of the fluid temperature profile, and ii) the accommodate the calculation and application of the non-uniform ground-loop flux.

In order to calculate the updated fluid temperature profile it is necessary to adopt a time-step which retains flow characteristics of the circulating fluid. As the flow rate has been assumed uniform, it can be said that the representation of the fluid flow is dependent on the fluid velocity, which varies from system to system depending on pump and ground-loop characteristics. For the monitored system presented in Chapter 3, the anticipated fluid velocity based on the system characteristics is approximately 0.15 ms^{-1}. In order to calculate the fluid temperature profile in such a system, a maximum time-step of only a few seconds would be required. This requires much smaller time increments than the TH modelling of the ground behaviour which typically employs time-steps in excess of one day. Modelling the ground behaviour with time-steps suitable for the calculation of the fluid temperature profile would vastly increase the number of time-steps required for simulation, subsequently increasing the computation time and effort. This option was therefore rendered

unsuitable for the current case. An alternative option available to overcome the conflicting time-step requirements is to apply a multiple time-step algorithm. This will allow the efficient computation of both the fluid temperature profile and ground behaviour within the current numerical model, without compromising computational times. The algorithm implemented to model the fluid flow and its implementation within the numerical model is discussed below.

The developed multi-time step algorithm compromises of two time-steps, namely the so called 'fluid time-step' and 'global time-step'. The 'fluid time-step' has been used to calculate the updated fluid temperature profile, whereas the 'global time-step' has been used within the overall TH model. The selection, and subsequent validity, of the fluid time-step is dependent on the fluid velocity within the system. If the fluid velocity is known, it is possible to calculate the fluid displacement, and circulation, for a given fluid time-step. By repeating this procedure for multiple fluid time-steps it is essentially possible to mimic fluid circulation within the ground-loop, allowing consideration of the local ground temperatures within the fluid temperature profile calculations. Figure 6.10 shows a schematic of this procedure. At each fluid time-step, steps (i), (ii) and (iii) from the pseudo algorithm previously described in section 6.3.2 are undertaken. By repeating the procedure it is possible to calculate a fluid temperature profile for a given set ground temperatures and heating loads.

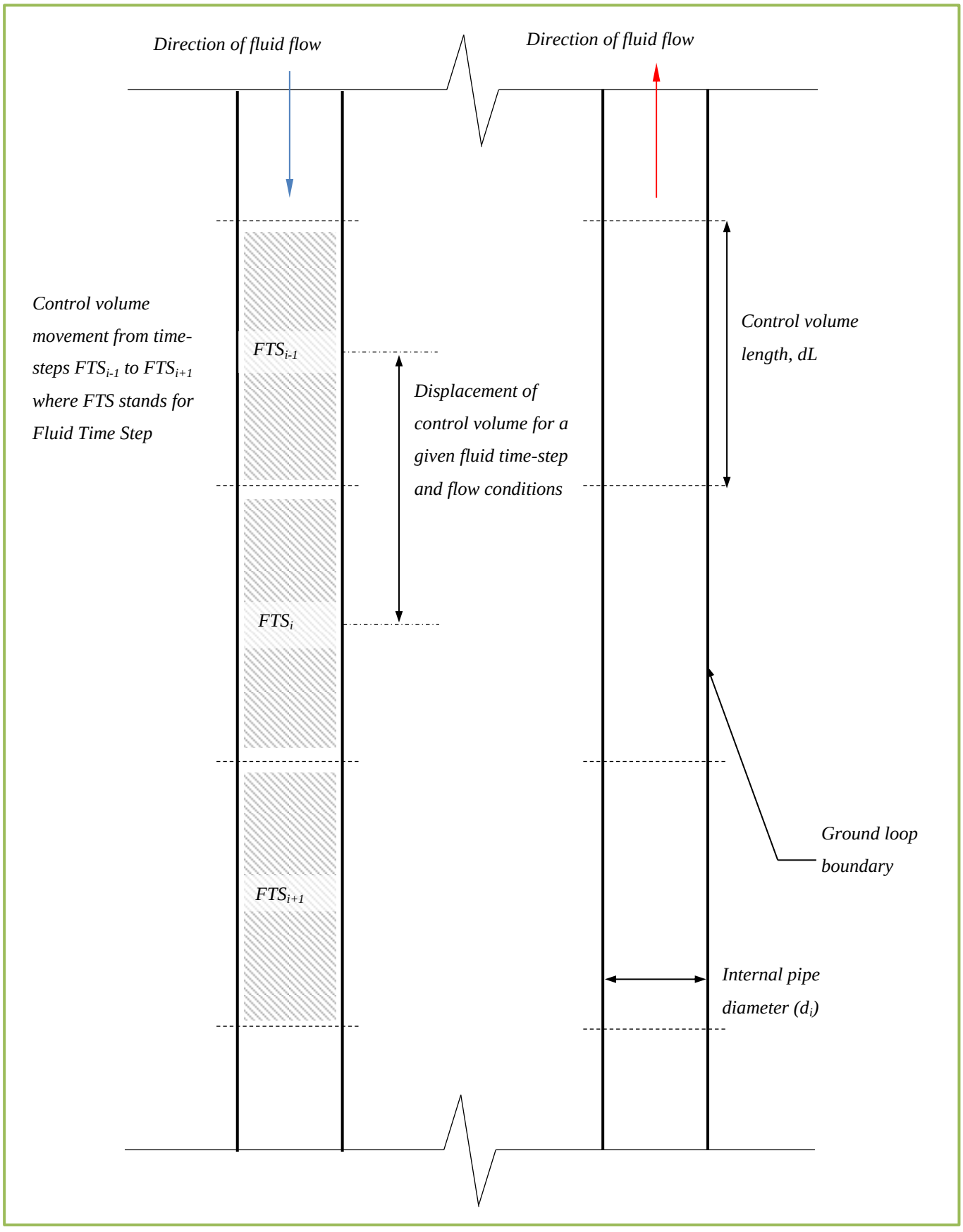

Figure 6.10 – Ground-loop section showing some of the proposed algorithm components used to calculate the fluid temperature profile.

In order to implement both the fluid time-step and global time-step within the model, a sequential algorithm was developed which allowed the calculation of the fluid temperature profile and TH ground model to be run. Figure 6.11 contains a flow chart showing how the devised multi-step algorithm has been implemented within the numerical formulations presented in Chapter 5.

As shown in Figure 6.11, the fluid temperature profile is calculated between the previous and current global time-steps (denoted *i-1* and *i* in Figure 6.11) using the smaller fluid time-steps. This operation is performed for each global time-step prior to the matrix build and solve. Within this procedure the updated fluid temperature profile is calculated using the most up to date ground temperatures (i.e. from the global time-step *i-1* in Figure 6.11). This essentially assumes that a quasi-steady-state system exists between the fluid and ground. This approach was originally proposed in work presented by Hellstrom (1991).

Once an updated fluid temperature profile has been calculated between the previous and current global time-step, the non-uniform heat flux boundary is calculated using the updated fluid temperature profile and current ground temperatures (i.e. step iv in the pseudo algorithm presented in section 6.3.2). The calculation of the non-uniform heat flux is performed prior to the system matrix build (see Figure 6.11), thereby allowing the calculated ground-loop boundary flux to be incorporated within the current time-step matrix solver. The coupled TH ground behaviour is then modelled for the time period between the current *(i)* and next *(i+1)* global time-steps. The ground-loop boundary flux is assumed constant for this period, thereby again assuming that a quasi-steady state has formed between the fluid and ground.

It is worth noting that the greatest temperature change in both the fluid and ground will occur when the ground source heat system has initially been turned on. In order to model the resulting ground behaviour and non-uniform ground-loop boundary, care must be taken to ensure that the global time-step is restricted within this initial period otherwise errors are incurred based on the quasi-steady-state assumptions (Hellstrom, 1991). Over longer time periods of heat extraction, the rate of temperature change in the ground reduces, increasing the validity of the quasi-steady–state assumption (Hellstrom, 1991).

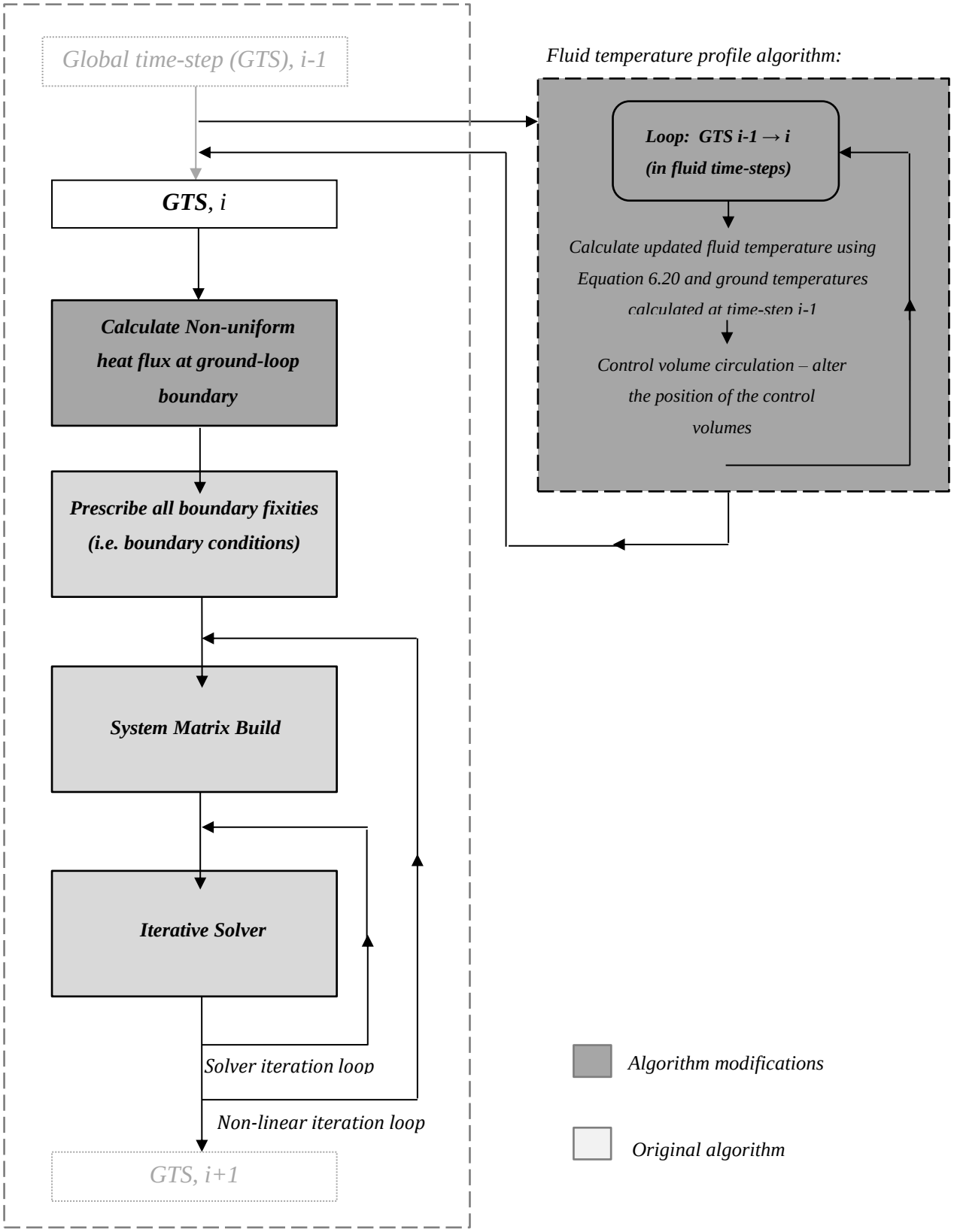

Figure 6.11 – Diagram showing how the multi time-step algorithm used to calculate the non-uniform heat flux ground-loop boundary condition.

6.4 Initial surface boundary validations

In order to validate the hydraulic component of the surface boundary condition, a representative evaporative flux is required. Evaporation rates are typically inferred from the soil heat flux, the measurement of which requires a buried plate or sensor just beneath the ground surface (Gonzalez-sosa et al., 1999a; Deardorff, 1978). Ideally, sensors capable of measuring the soil heat flux would have been installed at the monitoring site however this was not possible due to the site constraints previously outlined in Chapter 3. This shortfall in data means that the validation of the hydraulic component of the surface boundary condition cannot be performed using data solely collected from the monitoring site detailed in Chapter 3. A viable alternative to overcome this was found to be the use of data sourced from literature. A subsequent literature review found there was limited suitable data sets which contained the evaporation, ground temperature and soil property data necessary to undertake a boundary validation. Based on the literature review and sourced data, the validation of the surface boundary was split into two parts; one validating hydraulic component of the surface boundary using data obtained from literature and a second part, validating the thermal component using temperature data collected from the monitoring site detailed in Chapter 3. The thermal validation of the surface boundary condition is presented as part of Chapter 7. The following section will present the validation of the hydraulic component of the surface boundary condition.

Gozalez-sosa et al. (1999a) investigated the long-term exchange of energy and water at the surface of agricultural land in southern France. As part of this investigation, sensors were installed to measure the surface water exchanges and a soil investigation was conducted to measure the soil properties at the site. Adopting the results of this research, a validation model representing the TH ground behaviour at the site between January 1st and March 7th 1995 was developed. The model included the climatic data, surface hydraulic components (i.e. evaporation, precipitation and run-off) and soil properties published. The simulated hydraulic components (i.e. surface run-off and evaporation) predicted by the model are compared with experimental data presented by Gonzalez-sosa et al. (1999a) in order to assess the validity of the ground surface boundary.

The climatic variables of ambient air temperature, solar radiation, specific air humidity, wind speed and rainfall presented by Gonzalez-sosa et al. (1999a) and prescribed in the model are shown in Figures 6.12, 6.13 and 6.14.

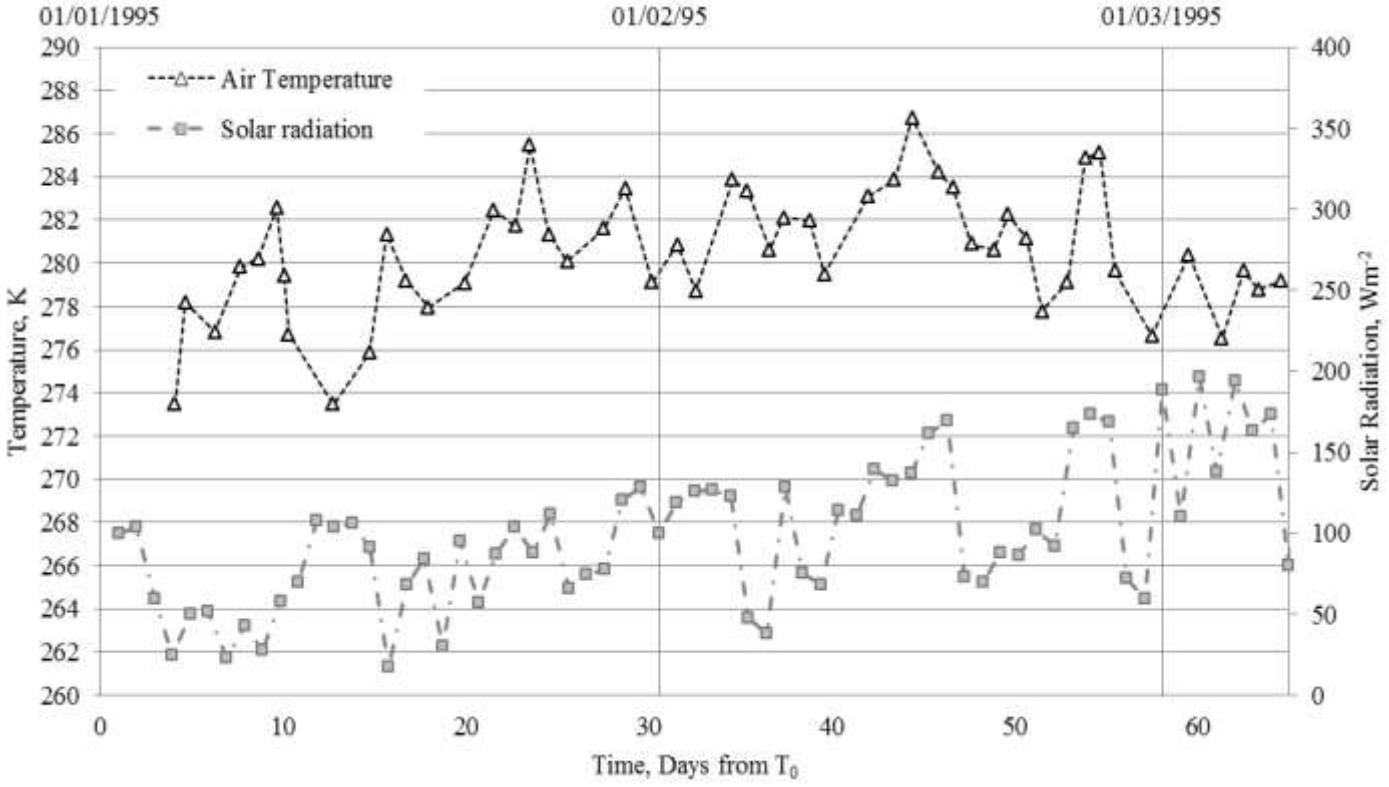

Figure 6.12 - Daily evolution of air temperature and solar radiation recorded at an agricultural site in southern France (after Gonzalez-sosa et al., 1999a).

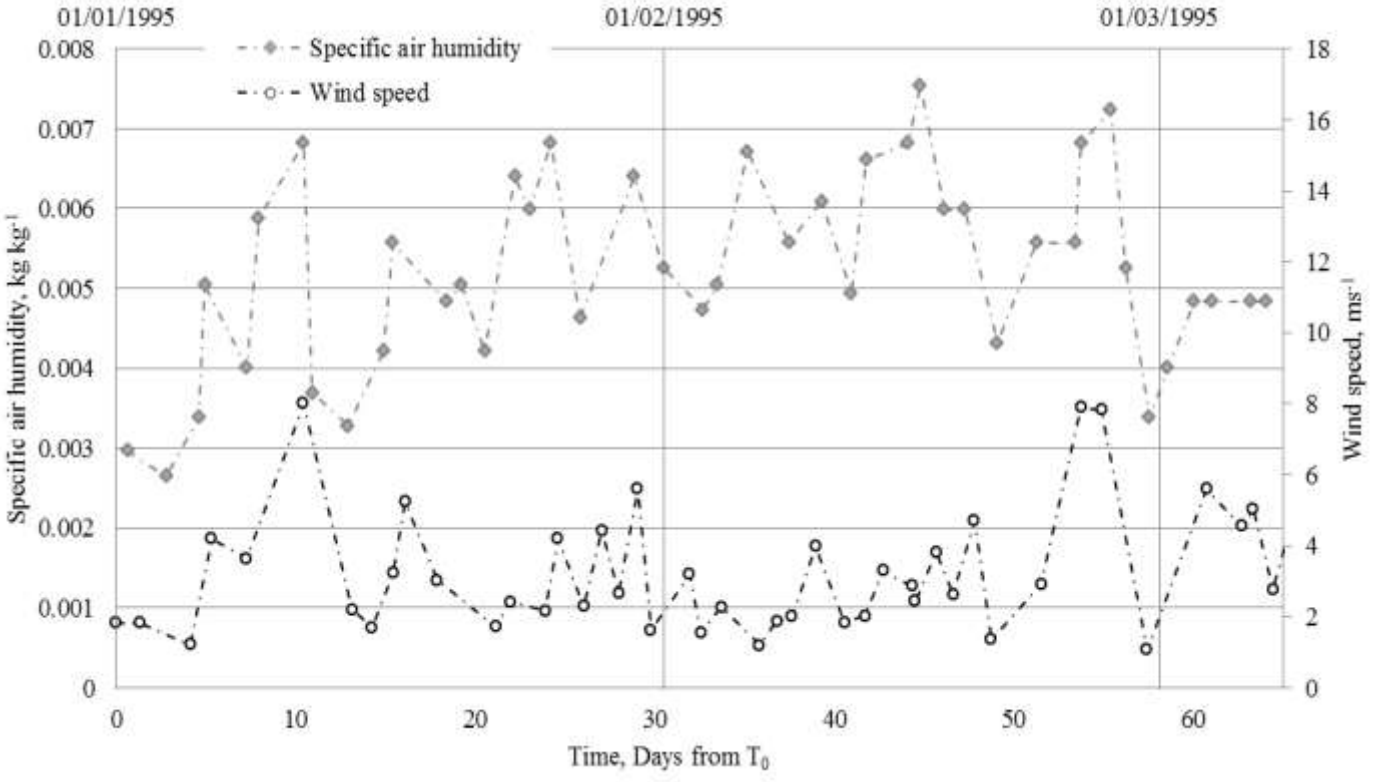

Figure 6.13 - Daily evolution of specific air humidity and wind velocity recorded at an agricultural site in southern France (after Gonzalez-sosa et al., 1999a).

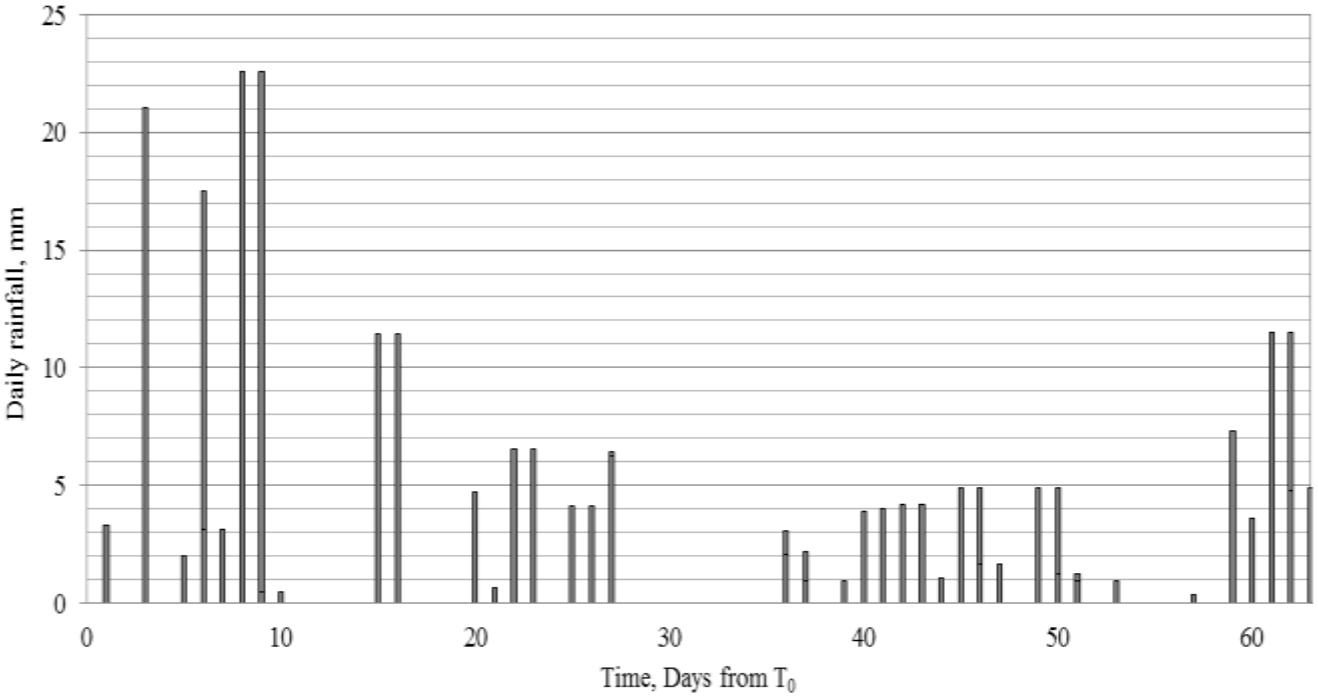

Figure 6.14 - Daily evolution of rainfall recorded at an agricultural site in southern France (after Gonzalez-sosa et al., 1999a)

A two-dimensional simulation was carried out to replicate the site experiment based on the following assumptions and considerations:

- *The soil was assumed to be anisotropic in the vertical according to the soil data provided.*
- *Climatic variables were assumed uniform across the whole site.*
- *The ground properties were assumed representative across the whole site.*

Based on the preceding information, and to reduce computational effort; a two-dimensional model has been adopted (see Figure 6.15). The selected domain extends downwards to a depth of 10 meters and across to a width of 0.1 metres. For the given ground properties, previous research has shown that at a depth of 10 meters beneath the ground surface there should be no annual ground temperature variation due to seasonal climate changes (Kusuda & Achenbach, 1965; Kusuda, 1975). This domain depth was therefore deemed sufficient for the validation model.

An empirical relationship describing the soil thermal conductivity with pore water pressures was presented by Gonzalez-sosa et al. (1999a) for the specific soil type found at the experimental site. This relationship was deemed to be more representative than the general approach presented in Chapter 5 (Equation 5.79) and was therefore employed for the current validation model. The

remaining constitutive relationships employed have been previously presented in Chapter 5. For convenience they have been summarised in Table 6.2.

The model was discretised into a mesh consisting of non-structured and non-uniform linear triangular elements. A varying time-stepping algorithm was employed within the simulation with the initial time-step being set to 1 second. The simulation length was 5,702,400 seconds, coinciding with the 66 day period between January 1st and March 7th 1995.

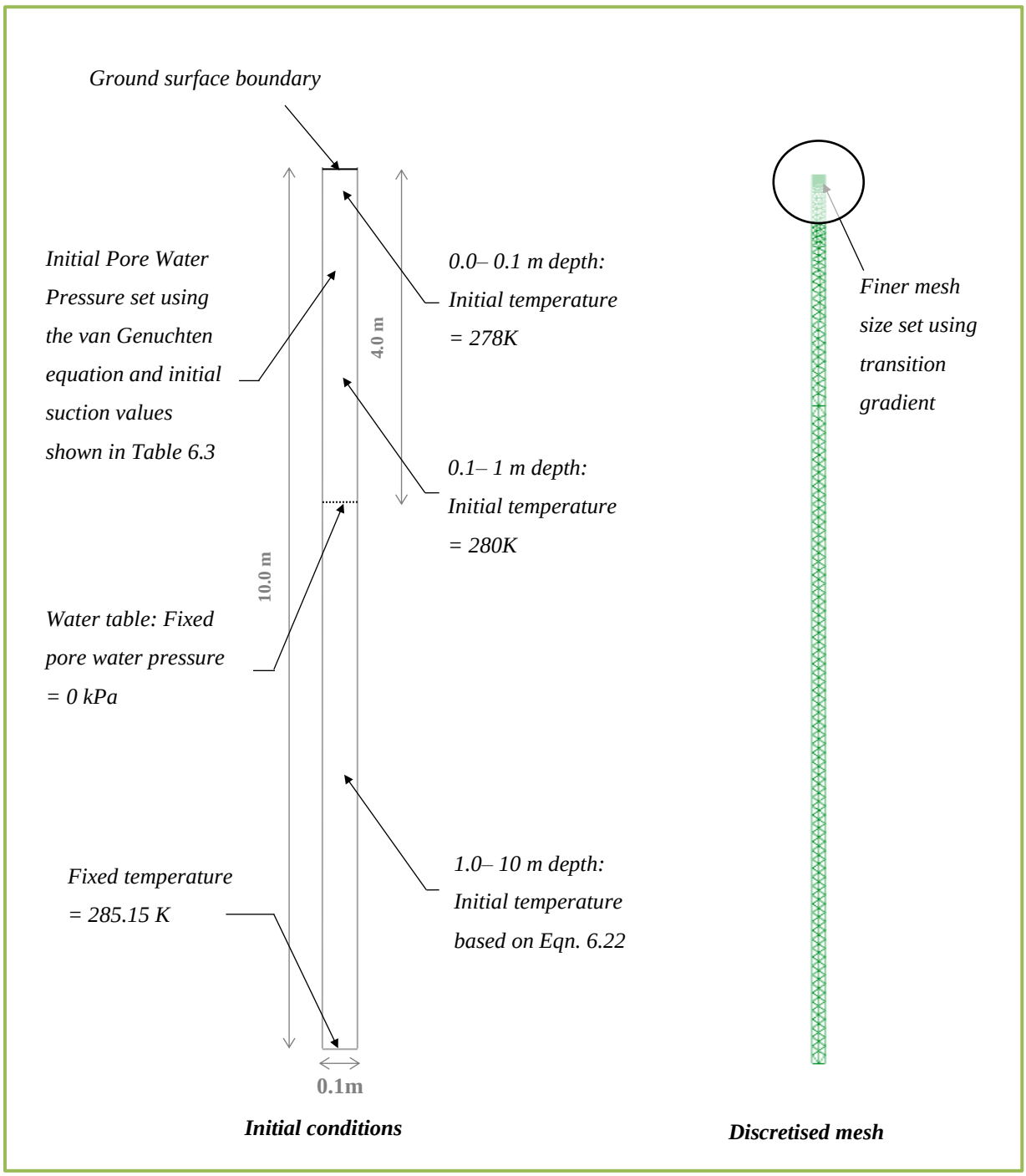

Figure 6.15 – Schematic showing the initial boundary conditions and discretised mesh the validation exercise.

Table 6.2 – Table of constitutive relationships used in the validation model.

Material parameter	*Relation*
Thermal conductivity	$\lambda = 0.729 + 0.135\ \frac{\theta}{\theta_{sat}} + 1.26\ \left\{1 - exp\left(-10.3\left(\frac{\theta}{\theta_{sat}}\right)^{1.84}\right)\right\}$
Heat capacity	$H_c = (1-n)C_{ps}\rho_s + n\left(C_{pl}S_l\rho_l + C_{pv}S_a\rho_v + C_{pda}S_a\rho_{da}\right)$
Hydraulic conductivity	$K_l(h) = \frac{\{1 - (\alpha h)^{n-1}\,[1 + (\alpha h)^n]^{-m}\}^2}{[1 + (\alpha h)^n]^{m/2}} \qquad \left(m = 1 - {}^1/_n\right)$
SWCC	$\theta = \theta_{res} + \frac{(\theta_{sat} - \theta_{res})}{[1 + (\alpha h)^n]^m}$

6.4.1 Initial and boundary conditions

The initial pore-water pressures were defined by Gonzalez-sosa et al. (1999a) as a function of pressure head, measured at a series of strata (see Table 6.3). The pressure heads reported can be subsequently converted to pore-water pressures by applying van Genuchten's Soil Water Characteristic Curve (SWCC) (van Genuchten, 1980), given in Table 6.2. Initial pore-water pressures were therefore prescribed in the model according to the calculated pore-water pressures and reported strata depths. During the inspection period, the water-table was reported to be at a depth of 4 meters below the ground surface (Gonzalez-sosa, et al., 1999a). To replicate this feature, a pore water pressure equal to zero was prescribed at a depth of 4 meters within the model (see Figure 6.15). Below that depth, pore water pressures were prescribed according to a gravitational hydraulic head, calculated as a function of depth beneath the water table.

Initial ground temperatures were provided at depths of 0.01, 0.05 and 0.5 meters. The initial ground temperature beyond a depth of 0.5 meters was approximated using an analytical expression proposed by Hillel (1980) which approximates the ground temperature profile based on soil parameters and climatic conditions, given as:

$$T(z,t) = T_a + A_0 e^{-z/d} \sin\left[\frac{2\pi\,(t - t_0)}{365} - \frac{z}{d} - \frac{\pi}{2}\right] \tag{6.22}$$

where

$$d = \left({}^{2\alpha}/_{\omega}\right)^{0.5} \tag{6.23}$$

where $T(z, t)$ is the soil temperature at time t *(days)* and depth z beneath the ground surface *(m)*. T_a is the constant ground temperature which is not subject to seasonal surface variations *(^oC)*, A_0 is the annual amplitude of the surface soil temperature *(^oC)*, t_0 is the lag time from arbitrary start date to the occurrence of the minimum soil temperature in a year *(days)*, α is the thermal diffusivity *(m^2s^{-1})*, ω is $2\pi/365$ *($days^{-1}$)* and d is the damping depth *(m)* which is equal to $(2\alpha/\omega)^{0.5}$.

The values of A_0 and t_0 as stated in Equation 6.22 are provided in Gonzalez-sosa et al. (1999b). The only remaining unknown is the value of T_a which is equivalent to the constant ground temperature found beyond the ground region affected by seasonal fluctuations. In the northern hemisphere, a reasonable value to assume for this is 285.15 K (12 °C) (Busby, et al., 2011).

The developed surface boundary condition has been assigned to ground surface (see Figure 6.15). The climatic variables required to compute the TH surface fluxes have been previously presented in Figures 6.12, 6.13 and 6.14.

6.4.2 Material parameters

The soil type has been described as a 'typical hydromorphic boulbene with silt loam texture' throughout the site (Gonzalez-sosa, 1999a). Soil properties presented Gonzalez-sosa et al. (1999a) have been summarised in Table 6.3. The properties were presented in the form of discrete strata, the upper and lower levels of which are included within Table 6.3. Materials were prescribed within the validation model such that they coincided with the defined strata. Beyond the depth of 1.3 meters, no material data was provided within the literature therefore the material parameters for deepest reported strata (0.62-1.3 meters) have been adopted within the remainder of the model (i.e. ground ranging from 1.3 to 10.0 meters in depth). In order to compute the heat capacity according to the constitutive relationship summarised in Table 6.2, a representative value for the specific heat capacity of the solid phase of the soil found on site is required. This was not presented within the published work by Gonzalez-sosa (1999a) therefore values for the specific heat capacity and density were alternatively obtained from literature using the basic soil information provided. The values used for soil density and specific heat capacity have been prescribed uniformly throughout the model domain and are presented in Table 6.4.

Table 6.3 – Soil parameters at various depths beneath the ground surface. θ_{sat} and n are van Genuchten's parameters, s is the suction, k_s is the saturated hydraulic conductivity and λ is the thermal conductivity (after Gonzalez-sosa et al., 1999a and Gonzalez-sosa et al., 1999b).

Strata range (cm)	*Porosity, n*	*θ_{sat}, m^3m^{-3}*	*n*	*s, m*	*K_s, ms^{-1}*	*λ, $Wm^{-1}K^{-1}$*
0-0.05	0.6	0.48	2.30	-1.62	4.8×10^{-6}	0.1
0.05-2	0.55	0.46	2.30	-1.62	9.8×10^{-6}	*See Table 6.2*
2-10	0.5	0.40	2.30	-1.62	5.0×10^{-6}	*See Table 6.2*
10-62	0.45	0.35	2.27	-1.70	7.5×10^{-6}	*See Table 6.2*
62-130	0.39	0.30	2.13	-2.00	1.0×10^{-6}	*See Table 6.2*

Table 6.4 – Prescribed density and specific heat capacity for the solid component of the soil.

Material parameter	*Value*
Density, k*g m^{-3}*	2700 (De Vries, 1966)
Silt-loam specific heat capacity, *$J\ kg^{-1}K^{-1}$*	736.9 (De Vries, 1966)

6.4.3 Results

As previously discussed, the primary aim of this model was to validate the hydraulic component of the developed surface boundary condition. The hydraulic exchange at the ground surface can be analysed knowing the controlling parameters, namely; precipitation, evaporation and run-off (Deardorff, 1978). In this case, the precipitation is a measured value prescribed within the model and therefore is known to be correct. Run-off only occurs once the upper ground surface is saturated. The experimental data reported no run-off during the period investigated. At no point during the simulation did the upper ground regions reach saturation, leading to a zero run-off. It can therefore be said that the experimental run-off data and simulations results concurred with one another.

The remaining surface hydraulic component is evaporation. The simulated evaporation and the measured evaporation based on data collected at the French monitoring site can be found in Figure 6.16. For the purpose of this comparison, the total daily evaporation (mm) for the simulated and measured data has been presented. From Figure 6.16, it can be seen that the simulated daily evaporation trends were generally in close agreement with those exhibited by the real data. It is noted

that the simulated evaporation rates did differ from the experimental results between days 5 and 15. Based on the proximity of the deviations to the beginning of the simulation, it is believed that this period of deviation is due to the initial conditions assumed within the model. Over the 65 day simulation period, the average absolute error between the simulated and experimental data was 0.09 mm per day.

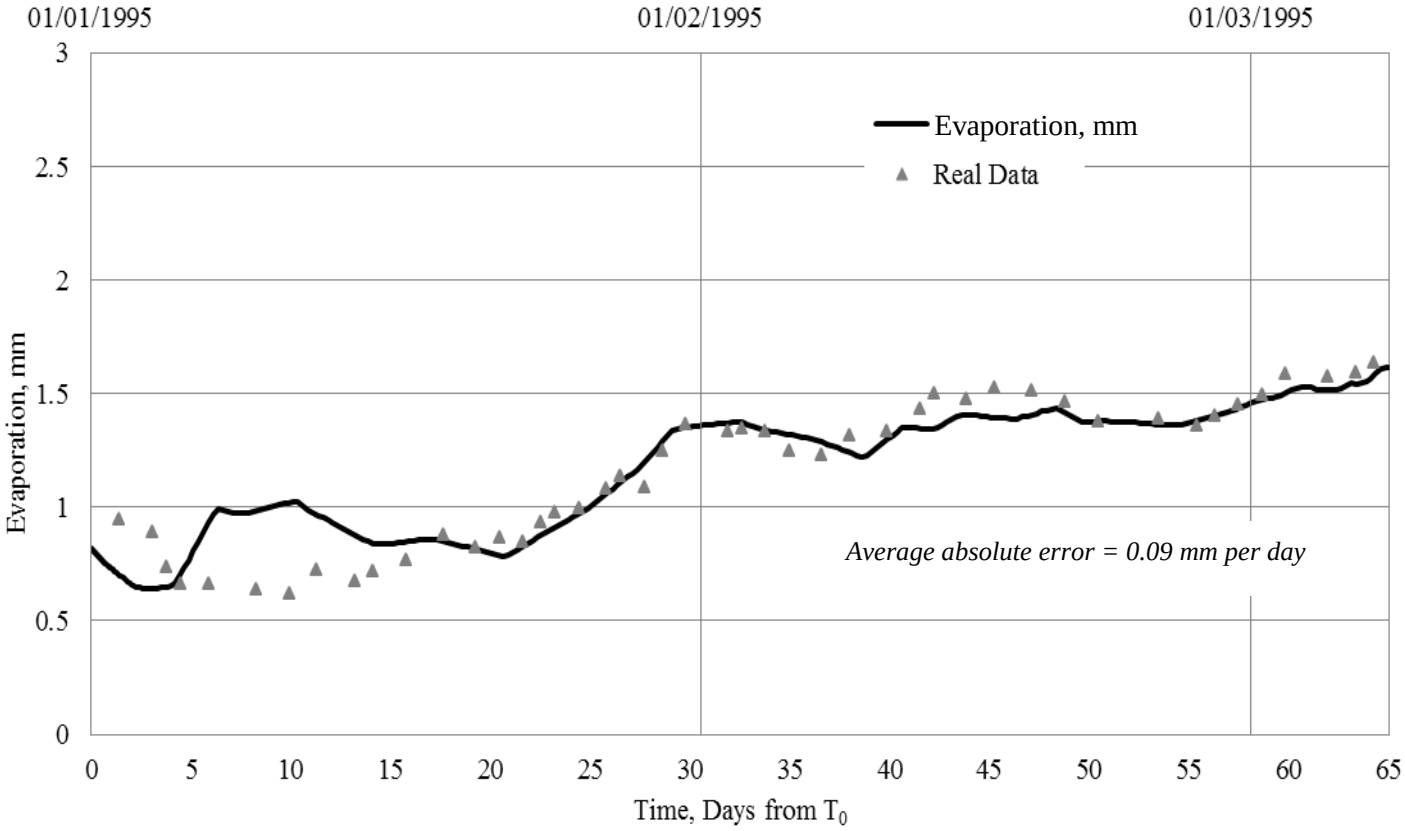

Figure 6.16 – Simulated and observed total daily evaporation rates.

6.4.4 Conclusions

The hydraulic component of the developed surface boundary condition was analysed in terms of the predicted run-off and evaporation. At no point during the simulation did the surface reach saturation, leading to no surface run-off, concurring with the reported experimental data. The simulated evaporation showed close agreement with the measured values over the 65 day simulation period with the exception of one ten day period.

6.5 Ground-loop boundary verifications

This section presents the verification exercises carried out on the developed uniform and non-uniform ground-loop boundary conditions. Verification is an important aspect of the boundary development and provides a means to explore if the developed solution and implemented algorithm is correct. Only verifications are discussed here, whilst model validations examining the whole system are presented separately in Chapter 7.

The coupled TH mathematical and numerical formulations presented as part of Chapter 5 have been extensively examined and verified within previous works, most notably by Thomas (1987), Thomas & He (1995) and Thomas & Sansom (1995). To avoid unnecessary repetitions, the verification of the TH behaviour in the ground is not re-examined here and the verification instead focusses on the ground-loop boundary conditions developed here.

The verification procedure presented has been divided into two sections, inspecting the uniform and non-uniform ground-loop boundary conditions. In both cases, the boundary conditions will be implemented within the numerical model presented in Chapter 5 and compared with a corresponding analytical solution using Kelvin's line source theory. Kelvin's line source theory is an established heat transfer theory which has been extensively applied to predict the ground thermal behaviour in response to ground source heat systems (Ingersoll, et al., 1954). Further details regarding Kelvin's theory including the theory, equation, limitations and assumptions has been provided in Chapter 2 of this thesis. Details regarding the verification models including the domain size/type, material parameters prescribed and constitutive relationships are discussed accordingly. The results of the verification exercises will also be presented and discussed accordingly.

6.5.1 Verification I: Uniform ground-loop boundary

The verification of the uniform ground-loop boundary developed considers a two-dimensional circular domain with a radius of 20 meters. At the centre of this domain there is a separate circle, 0.04 meters in diameter which represents the cross-section of a ground-loop (see Figure 6.17). The ground-loop dimensions were selected to coincide with the ground-loop installed at the monitoring site detailed in Chapter 3 while the overall domain size was selected such that the ground temperature at far distance remains unchanged during the analysis period. The uniform ground-loop boundary condition was prescribed to the inner circle.

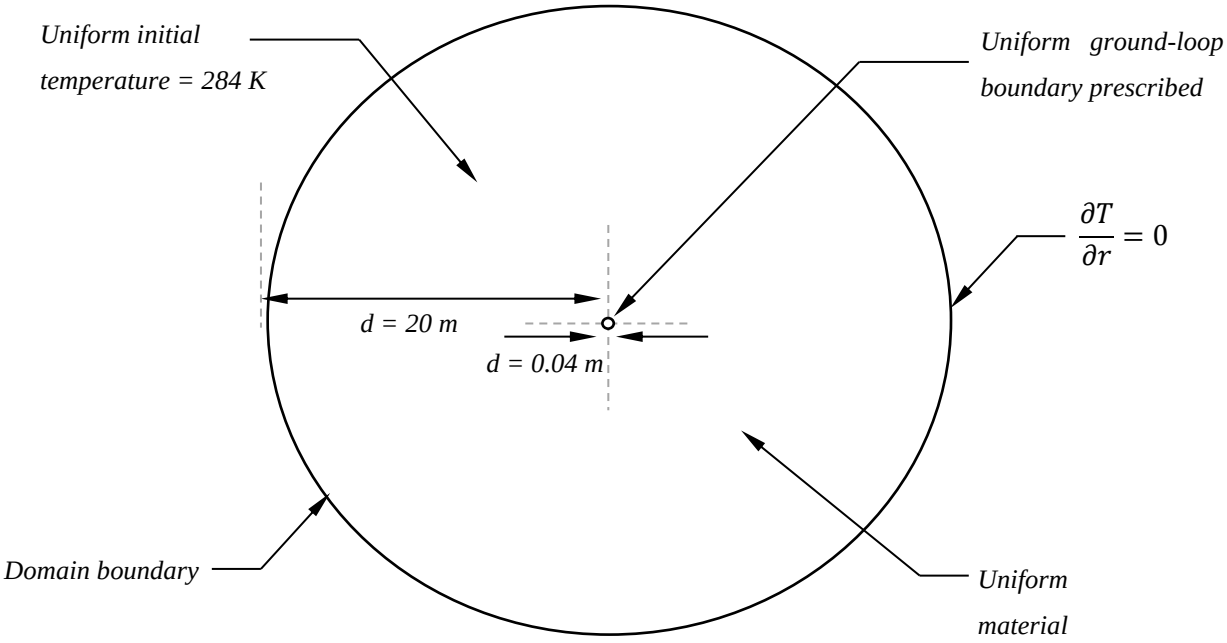

Figure 6.17 – Schematic showing the domain, material, initial and boundary conditions used in the verification of the uniform ground-loop boundary.

Analysis was carried out for a period of 1 year. This time period is great enough in order to allow thermal gradients, large enough to draw comparisons, to be formed. A constant heat load of 5 kW, which corresponds to the heat load of a small sized house (DECC, 2012), was assigned and used to compute the uniform ground-loop boundary. As a result, a constant heat flux of -53.05 Wm^{-2} was applied at the ground-loop boundary. A uniform initial temperature of 284 K was prescribed within the whole model domain. The soil was assumed to be fully saturated and therefore only the thermal component of the TH model was utilised for analysis. A schematic containing the initial and boundary conditions of the domain can be found in Figure 6.17.

One of the assumptions of the Kelvin line source theory is that the ground surrounding the heat source (i.e. the ground-loop) in homogeneous. Therefore, in order to replicate the analytical solution conditions a single material type was prescribed within the model domain. The material properties applied within the numerical model can be found in Table 6.5. The constitutive relationships employed by the numerical model have been previously discussed in Chapter 5. For convenience, they have been summarised in Table 6.6.

Table 6.5 – Material parameters and circulating fluid properties.

Parameter	***Value***
Porosity, n	0.33
Density (solid particles), ρ_s	2650 kg m^{-3}
Specific heat capacity (solids), C_{ps}	820 J kg^{-1} K^{-1}
Thermal conductivity (solids), λ_s	2.93 W $m^{-1}K^{-1}$
Degree of saturation, S_l	1
Fluid density, ρ_l	1000 kg m^{-3}
Fluid specific heat capacity, C_{pl}	4181 kg m^{-3}
Fluid thermal conductivity, λ_l	0.6 W m^{-1} K^{-1}

Table 6.6 – Constitutive relationships applied within the verification models.

Material parameter	***Relation***
Thermal conductivity	$\lambda = \prod_{i=1}^{3} \lambda_i^{\chi_i}$
Heat capacity	$H_c = (1-n)C_{ps}\rho_s + nC_{pl}\rho_l$

Figure 6.18 presents the results of the simulation and analytically calculated ground temperatures after a period of one year. The analytical calculations have been computed using the same conditions and parameters used for the numerical modelling. The graph presents the radial temperature variation from the heat sink (ground-loop surface) to domain boundary. It can be seen from the results that there is a good correlation between the numerically simulated and analytically calculated results. As anticipated, the greatest temperature decrease occurs in the ground region immediately adjacent to the heat sink. As the radial displacement from the heat sink increases the temperature change decreases. Both the numerical and analytical solutions reported a temperature change less than 0.01 K at a radial displacement of 20 meters (i.e. the domain boundary). Based on the results obtained, the boundary condition development and implementation was deemed verified according to the Kelvin line source theory under the applied conditions.

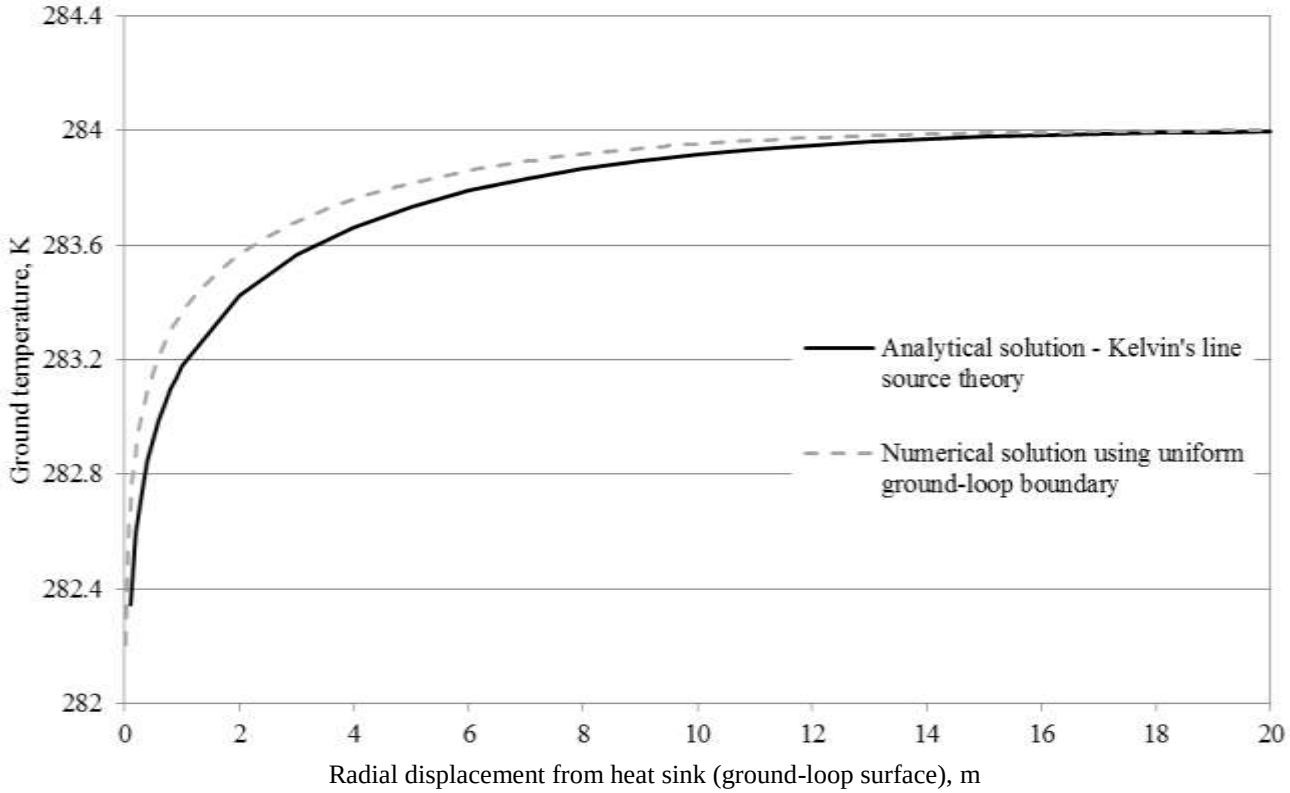

Figure 6.18 – Radial ground temperature profiles for the numerical and analytical solutions.

6.5.2 Verification II: Non-uniform ground-loop boundary

The verification of the non-uniform boundary condition presents a greater challenge due to the increased complexity of the boundary condition. The non-uniform nature of the prescribed heat flux and quasi-steady state algorithm assumptions present a number of challenges when trying to identify the total heat being exchanged at the ground-loop surface for a given time. To overcome this complexity, the non-uniform verification procedure has been split into stages. Similar to the uniform boundary verification, Stage I provides a comparison between numerical simulation results and analytical solutions results using Kelvin's line source theory. Following this, Stage II will provide a numerical verification to ascertain whether the heat being exchanged over the total ground-loop surface is in fact equal to the theoretical heating extraction load being applied. The following paragraphs will describe the domain characteristics common to both stage I and II of the non-uniform ground-loop boundary verifications.

The verification simulations for stages I and II have been conducted using a three-dimensional domain. The boundary formulation of the non-uniform ground-loop requires that a three-

dimensional domain is created. A three-dimensional cylindrical domain was created with a radius of 20 meters and measuring 105 meters in length (see Figure 6.19). Within this domain, a ground-loop 0.04 meters in diameter and 75 meters in length was defined. The ground-loop dimensions were defined to coincide with the ground-loop characteristics found at the monitoring site previously discussed in Chapter 3. The overall domain radius was selected such that the ground temperature at the far reaches remained unchanged during the verification simulation. In addition to this, the created domain extended 15 meters beyond both ends of the ground-loop to ensure that the temperature at far extremities of the domain remained unchanged for the verification period.

6.5.2.1 Stage I

The numerical conditions prescribed to Stage I of the non-uniform verification model are very similar to those previously outlined in section 6.5.1. Analysis was carried out for a period of one year. A constant heat load corresponding to a heat load of 5 kW was prescribed in order to compute the non-uniform ground-loop boundary. A uniform initial temperature of 284 K was applied to the ground domain. A homogeneous material has been prescribed within the model domain, the properties of which have been previously summarised in Table 6.5. The soil was assumed to be fully saturated and therefore only the thermal component of the TH model was utilised for analysis. The constitutive relationships employed by the numerical model have been previously discussed in Chapter 5. For convenience, they have been previously summarised in Table 6.6.

In order to compute the non-uniform ground-loop boundary an additional parameter, the fluid flow rate, is required. This was set equal to 2.5 m^3 per hour, which is similar to the flow rate observed at the monitoring site outlined in Chapter 3. A ground-loop length of 750m (in-line with the monitoring site in Chapter 4) was used to compute the ground-loop flux.

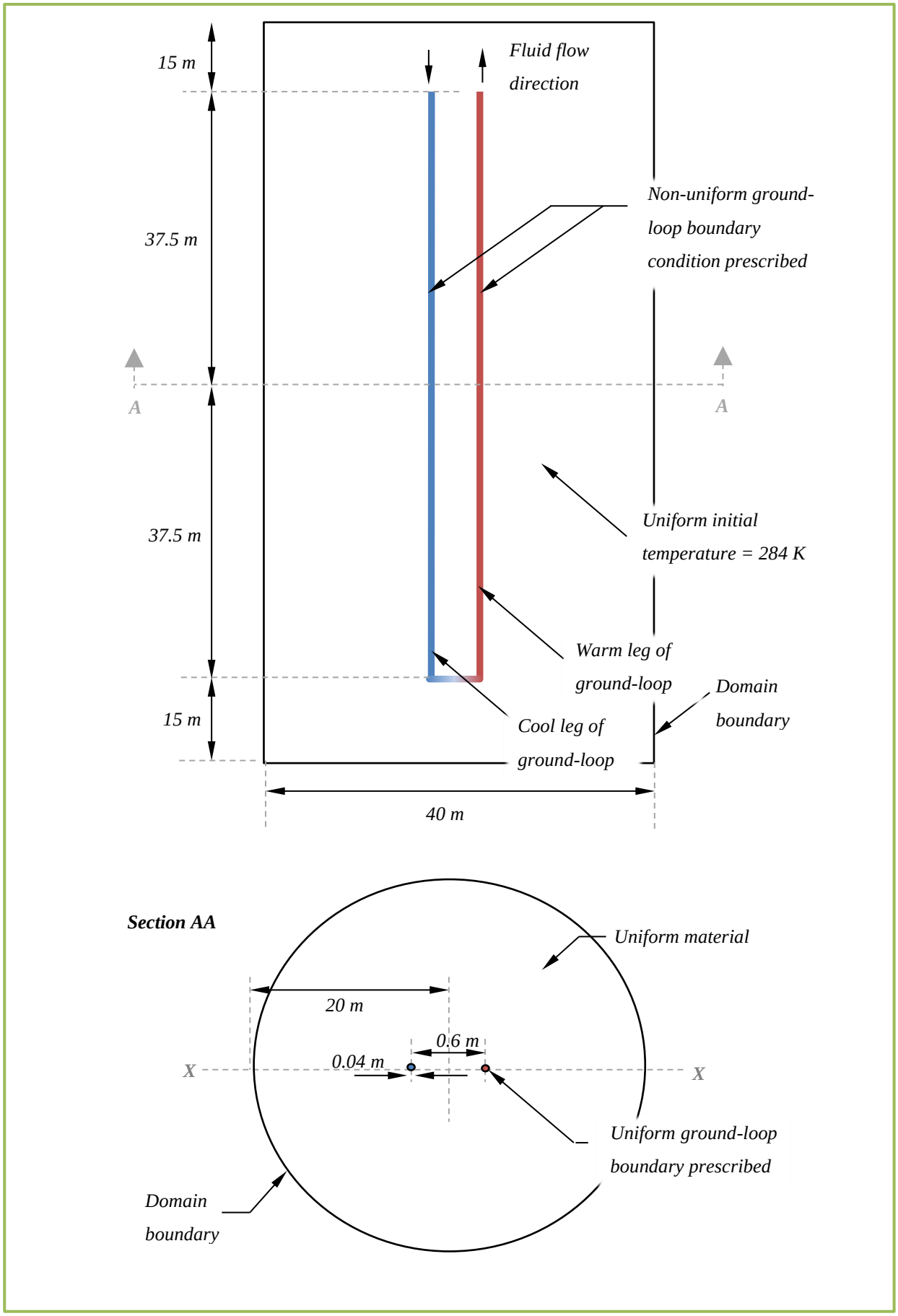

Figure 6.19 – Schematics showing the initial and boundary conditions along with the prescribed material in the three-dimensional non-uniform ground-loop boundary verification exercises.

Figure 6.19 presents the simulated and analytically calculated ground temperature profiles obtained after a period of one year. The analytical solution has been computed by applying the same conditions, where necessary, as the previously discussed numerical model. When drawing comparisons, it is important to recognise that the simulated results were obtained using a three-dimensional model while the Kelvin line source theory is a one-dimensional analytical solution. Figure 6.20 presents three temperature profiles representing the numerical and analytical solution. The so called 'cool leg' (lefts hand side of Figure 6.19) represents the ground-loop leg which the circulatory fluid enters immediately after leaving the heat pump. Within a heating system, this is often referred to as the cool leg as the fluid will be theoretically coldest in this ground-loop section. The remaining leg denoted the 'warm leg' is called so for the opposite reasons. The temperature profiles presented in Figure 6.20 represent the ground temperature variation with radial displacement between the heat sink and domain boundary along the line XX shown in Figure 6.19.

It can be seen from the results that there is a good correlation between the numerically simulated and analytical results. The greatest temperature decrease occurs in the ground region immediately adjacent to the heat sink. As the radial displacement from the heat sink increases the temperature change decreases. Both the numerical and analytical solutions reported a temperature change less than 0.01 K at a radial displacement of 20 meters (i.e. the domain boundary). The difference between the temperature values at the opposing warm and cool sides of the ground domain is very small. At the end of the one year simulation period, the temperature difference at a displacement of 0.5 meters was 0.2 K, which decreased to a temperature difference of less than 0.05 K at a displacement of 2 meters. Based on this evidence, it can be said that for the given ground and system characteristics the variation in ground temperature predicted by the non-uniform ground-loop boundary condition is minimal. Based on the results obtained, the boundary condition development and implementation was deemed verified according to the Kelvin line source theory under the applied conditions.

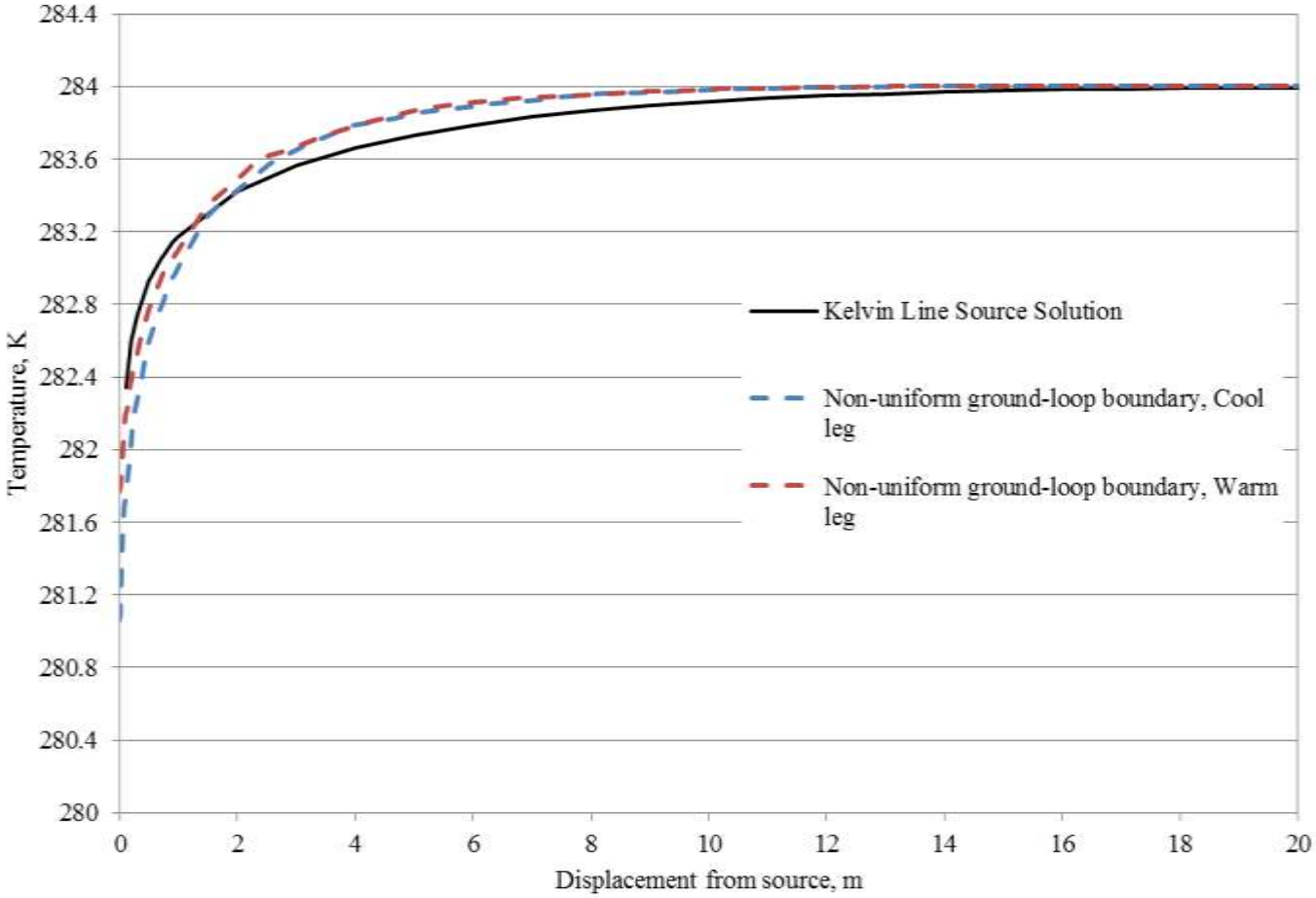

Figure 6.20 – Radial ground temperature profiles calculated using the non-uniform ground-loop boundary condition and analytical solutions.

6.5.2.2 Stage II

The complexity of the non-uniform formulations and multi-step algorithm present a number of challenges which increase the difficulty of ascertaining whether the boundary condition is performing as expected throughout the three-dimensional model domain. In order to overcome this, a second verification test was devised to further examine whether the overall heat exchange at the ground-loop surface is equal to the prescribed heating load used in its formulation.

Based on the principle of energy conservation, the temperature change in a material can be calculated provided that the heat capacity and energy exchange in the system are known. Applying this knowledge, a modelling scenario was designed whereby a heat load was applied for a certain time. Beyond this period of time, the domain temperature was allowed to thermally equilibrate. This allowed the theoretical energy change in the model to be compared with the simulated temperature change. Applying this approach, a 15 year analysis was carried out in which a heat load was only

prescribed for the first year. Beyond this time the heat load was removed as previously discussed. For clarity, the heat load profile is graphically presented in Figure 6.21.

The domain used is very similar to that previously discussed in section 6.5.2.1 and presented in Figure 6.19. The only alterations are that the domain radius is 30 meters as oppose to the 20 meter value used in the previous example and the heating load is 10 kW. The soil was assumed to be saturated throughout the analysis, therefore only the thermal component of the TH model is utilised.

A homogeneous material was assigned to the model domain, the properties of which have been previously summarised in Table 6.5. The constitutive relationships employed by the numerical model have been discussed in Chapter 5. For convenience, they have been summarised in Table 6.6. The fluid flow rate was set equal to 2.5 m^3 per hour which is similar to the flow rate observed at the monitoring site outlined in Chapter 3. A uniform initial ground temperature of 280 K was prescribed throughout the model domain.

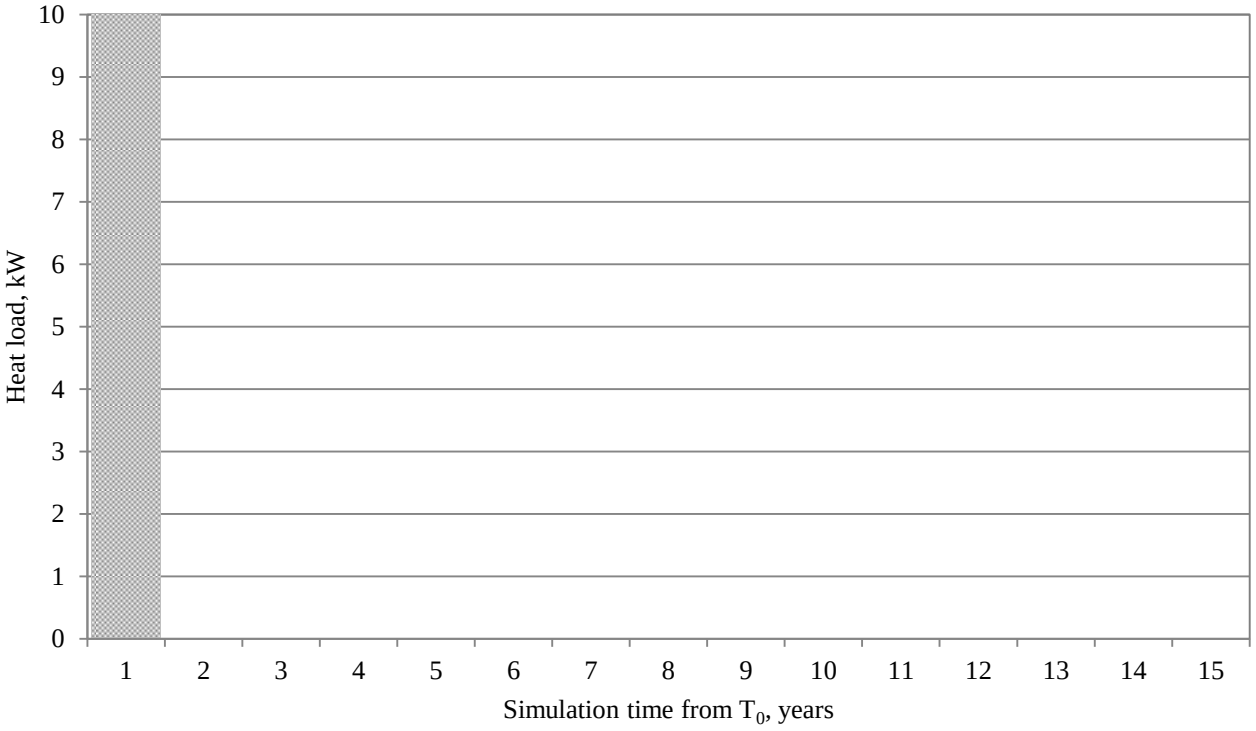

Figure 6.21 – Graphical representation of the heat load applied over the simulation period.

Figures 6.22 and 6.23 show the simulated thermal distribution at the cross-section A-A (see Figure 6.19) for various times of the analysis. It can be seen that during the first year of the simulation, when heat is has been extracted, temperatures radially varied around the ground-loop. After this time period, at which point the heat load is removed, the thermal variations around the ground-loop decreases rapidly. The subsequent thermal equilibration can be clearly seen within Figure 6.23 where after a period of 15 years, the domain can be described as having a uniform temperature. The identification of a uniform domain temperature greatly simplifies the following error calculations.

From Figure 6.23, it can be seen that the final uniform domain temperature, i.e. 279.49 K, was below the initial temperature, i.e. 280.0 K, a temperature decrease of 0.51 K. The theoretical temperature decrease within the domain can be described as a function of the total heat extracted via the ground-loop, domain specific heat capacity and domain density using:

$$\frac{dT}{dt} = \frac{W_t}{C_p \rho \, V_d} \tag{6.24}$$

where W_t is the total heat extracted via the ground-loop for a period of one year at a rate of 10 kW, equal to 3.1535 x 10^8 kJ, C_p is the specific heat capacity of the domain *(J kg^{-1} K^{-1})*, ρ is the domain density *(kg m^{-3})* and V_d is the domain volume.

Using Equation 6.24, the theoretical temperature decrease was calculated to be 0.53 K, 0.02 K greater than the simulated final domain temperature. It can therefore be said that the numerical model incurred errors of 3.7% when compared with the theoretical outcome.

The results obtained show that the simulated and theoretical temperature changes as a result of heat extraction agree with one another, giving confidence to the implementation of the boundary condition. Based on these findings, the boundary condition development and implementation was deemed verified under the applied conditions.

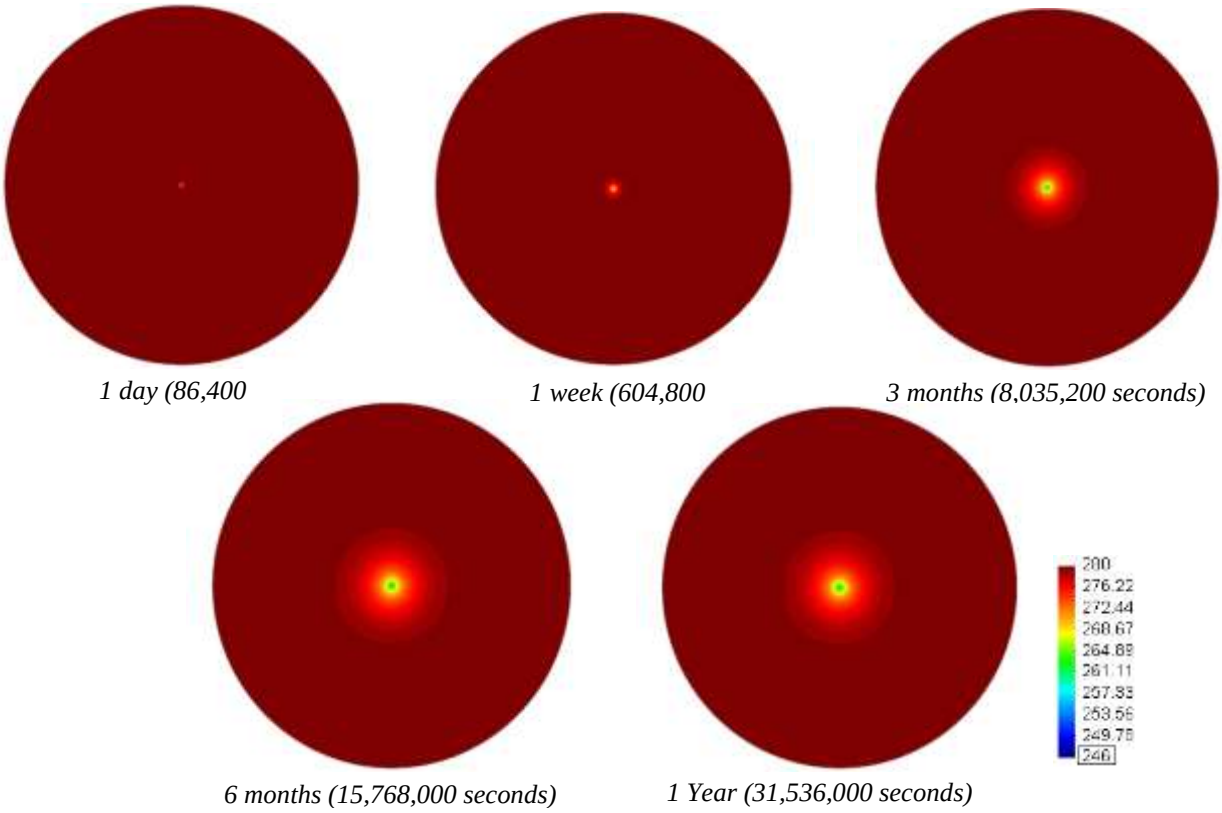

Figure 6.22- Temperature contour plots at the cross-section A-A (see Figure 6.19) during heat extraction period (time = 0 to 1 year).

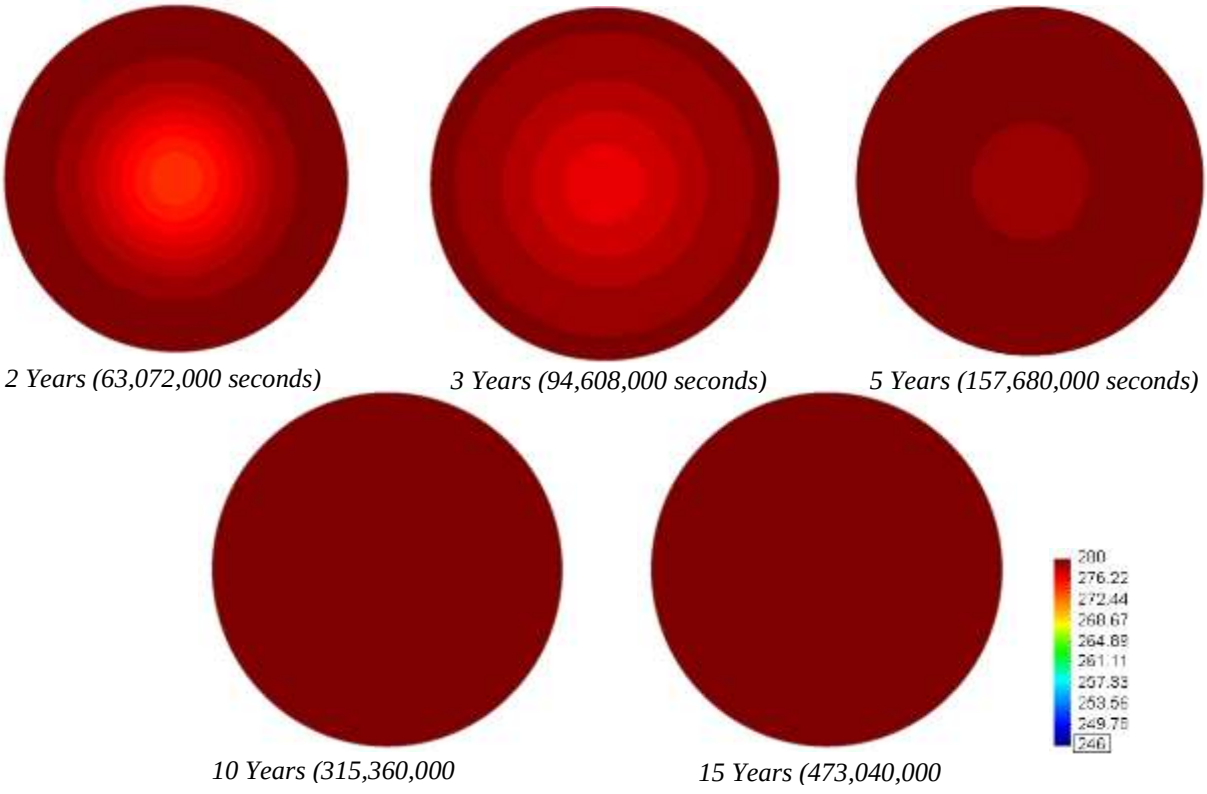

Figure 6.23 - Temperature contour plots at the cross-section A-A (see Figure 6.19) during heat extraction period (time = 1 to 15 years).

6.6 Conclusions

This chapter has presented the theoretical developments of two boundary conditions, namely; the ground surface and ground-loop boundaries. The developed surface boundary condition represents coupled thermo-hydraulic behaviour between the ground surface and atmosphere, considering a range of climatic variables and mechanisms. These include solar radiation, ambient air temperature, relative humidity, wind speed, rainfall and evaporation. The developed boundary condition was subsequently implemented within the numerical model previously described in Chapter 5 using a developed algorithm. The performance of the hydraulic aspect of the surface boundary condition was compared with data sourced from literature. The simulated results were found to compare favourably with the reported values. The development and implementation of the boundary allows climatic variables, which previously could not be considered, to be included within future models. This will enable a more detailed inspection of the climate's role in the coupled thermo-hydraulic ground behaviour in response to heat extraction via horizontal ground source heat systems.

Two separate ground-loop boundary conditions were developed; namely the uniform and non-uniform ground-loop boundary conditions. The first of these calculated a heat flux based upon the overall system heating load whereas the second calculated a boundary heat flux according to local fluid temperatures within the ground-loop. Both developed boundary conditions included the heating load of ground source heat systems within their formulations, a feature which previously could not be included within the model. The developed boundary conditions were subsequently implemented within the existing numerical model. The inclusion of the non-uniform boundary condition within the existing numerical model required the development of a sequential algorithm. The resulting models were verified in a series of exercises against the Kelvin line source analytical solution. The results from the numerical models were found to agree with those predicted by the analytical solutions, verifying the models under the applied conditions.

The developed boundary conditions, and there implementation within the existing numerical model, improves the representation of the surface and ground-loop boundaries within the model. The new boundary conditions include factors which could previously not be included within models, increasing the scope of potential applications. The boundary developments presented have been incorporated within the model and utilised for applications presented in the remained of this thesis.

References

Adkins, C. J., 1975. *Equilibrium Thermodynamics.* 2nd ed. London: McGraw-Hill.

Al-Khoury, R., Bonnier & G, P., 2006. Efficient finite element formulation for geothermal heating systems Part II: Transient. *Journal for Numerical Methods in Engineering,* 67(1), pp. 725-745.

Angstrom, A., 1915. *A study of the radiation of the atmosphere.* Chicago: Chicago Press.

Angstrom, A., 1925. Solar and terrestrial radiation. *Q. Journal of the Royal Meteorology Society,* 50(1), p. 121.

Barton, I. J., 1979. A parameterisation of the evaporation from non-saturated surfaces. *Journal of Applied Meteorology,* 18(1), pp. 43-47.

Bhumralkar, C. M., 1975. Numerical experiments on the computation of ground surface temperature in an atmospheric general circulation model. *Journal of Applied Meteorology,* 14(1), pp. 1246-1258.

Busby, J., Kingdon, A. & Williams, J., 2011. *The measured shallow temperature field in Britain.* Nottingham: British Geological Survey.

Carson, J. E., 1963. Analysis of soil and air temperature by Fourier techniques. *Journal of Geophysical Research,* 68(1), pp. 2217-2232.

Choudhury, B. J. & Moneith, J. L., 1988. A four-layer model for the heat budget of homogeneous land surfaces. *Q. Journal of the Royal Meteorology Society,* 114(1), pp. 373-389.

Conaway, J. & van Bavel, C. H. M., 1967. Radiometric surface temperature measurements and fluctuations in sky radiant emittance in the 600-1300 cm-1 waveband. *Argon Journal,* 59(5), pp. 389-390.

Dalton, J., 1802. On the expansion of elastic fluids by heat. *Memoirs of the Literary and Philisophical society of Manchester,* 5(2), pp. 595-602.

De Vries, D. A., 1955. Solar radiation at Wageningen. *Landbouwhogeschool, Wageningen,* 55(6), pp. 277-304.

De Vries, D. A., 1966. Thermal properties of soils. In: W. R. van Wijk, ed. *Physics of the Plant Environment.* Amsterdam: North Holland Publishing Co, p. 210.

Deardorff, J. W., 1978. Efficient prediction of ground surface temperature and moisture, with inclusion of a layer of vegetation. *American Geophysical Union,* 83(4), pp. 1889-1903.

Deardorff, J. W., 1978. Efficient prediction of ground surface temperature and moisture, with inclusion of a layer of vegetation. *American Geophysical Union.*

Demir, H., Koyun, A. & Temir, G., 2009. Heat transfer of horizontal parallel pipe ground heat exchanger and experimental verification. *Applied Thermal Engineering,* 29(1), pp. 224-233.

Department of Energy and Climate Change (DECC), 2012. *Detailed analysis from the first phase of the Energy Saving Trust's heat pump field trial,* London: Department of Energy and Climate Change.

Edlefsen, N. & Anderson, A., 1943. Thermodynamics of soil moisture. *Hilgardia,* 15(3), pp. 31-299.

Fredlund, D. G. & Rahardjo, H., 1993. *Soil mechanics for unsaturated soils.* New York: John Wiley & Sons.

Fredlund, M. D., Zhang, J. M., Tran, D. & Fredlund, D. G., 2011. *Coupling heat and moisture flow for the computation of actual evaporation.* Toronto, Pan-Am CGS Geotechnical Conference.

Fuchs, M. & Tanner, C. B., 1967. Evaporation from a drying soil. *Journal of Applied Meteorology,* 6(1), pp. 852-857.

Gonzalez-sosa, E., 1999a. Modelling heat and water exchanges of fallow land covered with plant-residue mulch. *Argiculture and Forest Meteorology,* 97(1), pp. 151-169.

Gonzalez-sosa, E., 1999b. MUREX: a land-surface field experiment to study the annual cycle of the energy and water bugets. *Geophysicae,* 17(1), pp. 838-854.

Gray, D. M., 1970. *Handbook on the principles of hydrology,* Ottawa, Canada: Canadian National Research Committee for the International Hydrological Decade, National Research Council.

GRC, 2010. *COMPASS User Manual.* Cardiff: Geoenvironmental Research Centre (GRC).

Hellstrom, G., 1991. *Doctoral Theses - Ground heat storage: Thermal analysis of duct storage systems.* Lund: Department of Mathematical Physics, University of Lund.

Hillel, D., 1980. *Applications of soil physics.* New York: Academic Press.

Imberger, J. & Patterson, J. C., 1981. A dynamic reservoir simulation model – DYRESM:5. In: H. B. Fischer, ed. *Transport modes for inland and coastal waters.* California, USA: Academic Press, pp. 310-361.

Ingersoll, L. R., Zobel, O. J. & Ingersoll, A. C., 1954. *Heat conduction with engineering, geological and other applications.* New York: McGraw Hill.

Johnson, I. R., Riha, S. J. & Wilks, D. S., 1995. Modelling daily net canopy photosynthesis and its adaption to irradiance and atmospheric CO2 concentration. *Agricultural Systems,* 50(1), pp. 1-35.

Kusuda, T., 1975. *The effect of ground cover on earth temperature.* Fort Worth, Texas, USA, Conference proceedings of 'Alternatives in energy conservation: The use of earth-covered buildings'.

Kusuda, T. & Achenbach, P. R., 1965. Earth temperature and thermal diffusivity at selected stations in the United States. *ASHRAE Trans,* 71(1), pp. 61-75.

Leong, W. H., Tarnawski, V. R. & Aittomaki, A., 1998. Effect of soil type and moisture content on ground heat pump performance. *International Journal of Refrigeration,* 21(8), pp. 595-606.

Lewis, R. W., Nithiarasu, P. & Seetharamu, K. N., 2004. *Fundamentals of the Finite Element Method for Heat and Fluid Flow.* 1st ed. Chichester: John Wiley & Sons.

Liang, X., Xie, Z. & Huang, M., 2003. A new parameterization for surface and groundwater interactions and its impact on water budgets with the variable infiltration capacity (VIC) land surface model. *Journal of Geophysical Research,* 108(16), pp. 1984-2012.

Mei, V. C., 1986. *Horizontal ground-coil heat exchanger theoretical and experimental analysis,* Oak Ridge: Office of Buildings and Community Systems, U.S. Department of Energy.

Mihalakakou, G., 2002. On estimating soil surface temperature profiles. *Energy and buildings,* 34(1), pp. 251-259.

Penman, H. L., 1948. Natural evapotranspiration from open water, bare soils and grass. *Proceedings of the Royal Society of London,* 193(Series A), pp. 120-145.

Penman, H. L., 1956. Estimating evaporation. *Tran. American Geophysical Union,* 37(1), pp. 43-46.

Penrod, E., Elliot, J. M. & Brown, W. K., 1960. Soil temperature variation at Lexington, Kentucky. *Journal of Soil Science,* 90(1), pp. 275-283.

Perrot, P., 1998. *A to Z of Thermodynamics.* Oxford: Oxford University Press.

Piechowski, M., 1999. Heat and mass transfermodel of a ground heat exchanger: Theoretical development. *International Journal of Energy Research,* 23(1), pp. 571-88.

Revfeim, K. J. A., 1978. A simple procedure for estimating global daily radiation on any surface. *Journal of Applied Meteorology,* 17(1), pp. 1126-1131.

Sellers, D. W., 1965. *Physical climatology.* Chicago: Chicago University Press.

Sverdrup, H. U., 1946. The humidity gradient over the sea surface. *Journal of Meteorology,* 3(1), pp. 1-3.

Thomas, H. R., 1987. Non-linear analysis of heat and moisture transfer in partly saturated soil. *Journal of Engineering Mechanics, American Society of Civil Engineering,* 113(1), pp. 1163-1180.

Thomas, H. R. & He, Y., 1995. Analysis of coupled heat, moisture and air transfer in a deformable unsaturated soil. *Geotechnique,* 45(4), pp. 677-689.

Thomas, H. R. & Rees, S. W., 1988. *The use of Lee's algorithm in the analysis of some ground heat and mass transfer problems.* Innsbruck, Proceedings of the 6th International Conference on Numerical Methods in Geomechanics.

Thomas, H. R. & Sansom, M. R., 1995. Fully coupled analysis of heat, moisture and air transfer in unsaturated soil. *Journal of Engineering Mechanics, American Society of Civil Engineering,* 121(3), pp. 392-405.

van Genuchten, M. T., 1980. A closed-from equation for predicting hydraulic conductivity of unsaturated soils. *Journal of Soil Society of America,* 44(1), pp. 892-898.

van Wijk, W. R., 1966. Introduction, The Physical Method. In: W. R. van Wijk, ed. *Physics of the Plant Environment.* Amsterdam: North Holland Publishing Co.

van Wijk, W. R. & Borghorst, A. J. W., 1966. Turbulent transfer in air. In: W. R. van Wijk, ed. *Physics of the Plant Environment.* Amsterdam: North Holland Publishing Co.

van Wijk, W. R. & Scholte Ubing, D. W., 1966. Radiation. In: W. R. van Wijk, ed. *Physics of the Plant Environment.* Amsterdam: North Holland Publishing Co.

Vardon, P., 2009. *A three-dimensional numerical investigation of the thermo-hydro-mechanical behaviour of a large-scale prototype repository.* Cardiff: PhD Thesis, Cardiff University.

Wilson, G. W., Fredlund, D. G. & Barbour, S. L., 1994. Coupled soil atmospheric modelling for soil evaporation. *Canadian Geotechnical Journal,* 31(1), pp. 151-161.

Wilson, G. W., Fredlund, D. G. & Barbour, S. L., 1997. The effect of soil suction on evaporative fluxes from soil surfaces. *Canadian Geotechnical Journal,* 34(1), pp. 145-155.

Woodward, S. J. R., Baker, D. J. & Zyskowski, A., 2001. Practical model for predicting soil water deficit in New Zealand pastures. *New Zealand Journal of Agricultural Research,* 44(1), pp. 91-109.

Yang, H., Cui, P. & Fang, Z., 2010. Vertical-borehole ground-coupled heat pumps: A review of models and systems. *Applied Energy,* 87(1), pp. 16-27.

Chapter 7

Model validation against experimental data

7.1 Introduction

In Chapter 5, the developed theoretical and numerical formulations for a model to simulate the coupled TH behaviour of soil have been presented. Chapter 6 presented the theoretical developments and implementation of boundary conditions representing the ground surface and ground-loop interactions. Here, the validity of the developed numerical model and boundary conditions will be tested against data collected at the monitoring site, previously detailed in Chapter 3. This Chapter presents the development and results from the validation exercises carried out.

The theoretical and numerical formulations presented in Chapter 5, describing the coupled TH behaviour of soil, have been extensively validated as part of a previous study undertaken by Thomas

(1987). The formulation used in the mentioned work has been implemented here therefore no further examination was undertaken. However, the boundary developments presented in Chapter 6 have not been the subject of previous validations. The validation procedure presented in the following sections focusses on testing the TH model which also includes the developed ground surface and ground-loop boundaries.

The validations tests are broadly sub-divided into two stages. Stage I aims to investigate the model performance during periods of no heat extraction (i.e. only the ground surface boundary will be tested). For the current data-set, this corresponds to the so called 'pre-heat extraction' phase which is the ground data collected prior to any heat extraction via the ground source heat system (May to September 2012). The second stage, i.e. Stage II, aims to investigate the model accuracy during periods of heat extraction (i.e. the effects of both the ground surface and ground-loop boundaries will be considered). For the current data-set, this corresponds to a period between September 2012 and June 2013. The two stage procedure adopted allows the complexity of the model to be gradually increased during the validation process.

Sections 7.2 and 7.3 describe the validation exercises and present detailed comparisons between the monitored data and simulation results for Stages I and II respectively. Finally, section 7.4 will discuss the conclusions from the work.

7.2 Stage I – Pre-heat extraction

Ground and climatic data has been continually logged at the monitoring site from 7th May 2012. Heat extraction via the ground source heat system began at the site from early September 2012; therefore ground data collated prior to this date can be regarded as completely uninfluenced by the ground source heat system. From a validation perspective, the data collected during this period can be used to investigate the model's performance during periods of no heat extraction. In particular, the thermal performance of the developed surface boundary condition can be investigated in isolation (i.e. the ground-loop boundary is not required for this period).

As previously discussed in Chapter 6, the measurement of evaporation was omitted from the monitoring site due to local constraints. Chapter 6 presented a validation exercise which compared the surface hydraulic exchanges with data reported in literature. The following exercises will focus on the thermal performance of the surface boundary condition using data collected from the monitoring site. Although comparisons will concentrate on the thermal performance of the model, the simulations will be conducted using coupled TH formulations as previously discussed in Chapters 5 and 6.

Chapter 3 previously detailed the spatial arrangement of thermistors throughout the monitoring site. Within this arrangement, eight thermistors were positioned to monitor the undisturbed ground temperature. Four of the eight thermistors were located at far-field location A, while the remaining four were located at far-field location B (see Figure 7.1). At each far-field location, the four thermistors varied in depth between 0.8 and 2.6 meters. Additional information regarding the spatial position of these thermistors can be found in Chapter 3. It is the temperature data recorded at these far-field positions which will be used as a basis to validate the model's performance during periods of no heat extraction.

As part of a ground investigation undertaken during the thermistor installation, soil samples were retrieved from both far-field locations A and B (see Chapter 3 for details). As described in Chapter 3, the soil properties measured at far-filed locations A and B were found to vary. To address this difference, two validation exercises were undertaken, referred to as 'Far-field A validation' and 'Far-field B validation' in the following sections. Both simulations were carried out on the ground thermal behaviour prior to heat extraction between the 9th May and 29th August 2012. The simulation details including the domain; initial and boundary conditions; and materials properties are similar for both models. To avoid repetition, the simulation details are collectively discussed in the following sub-sections.

As explained in Chapter 3, the monitored climatic variables, namely; ambient-air temperature, solar radiation, wind-speed, relative humidity and rainfall are all measured at a single location at the monitoring site. The measured variables are assumed to be representative and uniform across the monitoring site. The climatic data has been previously presented in Chapter 4 however for clarity, Figures 7.2, 7.3 and 7.4 show the measured climatic variables between 7th May and 29th August. The climatic data presented has been used for the computation of the surface boundary condition applied within both far-field A and B simulations.

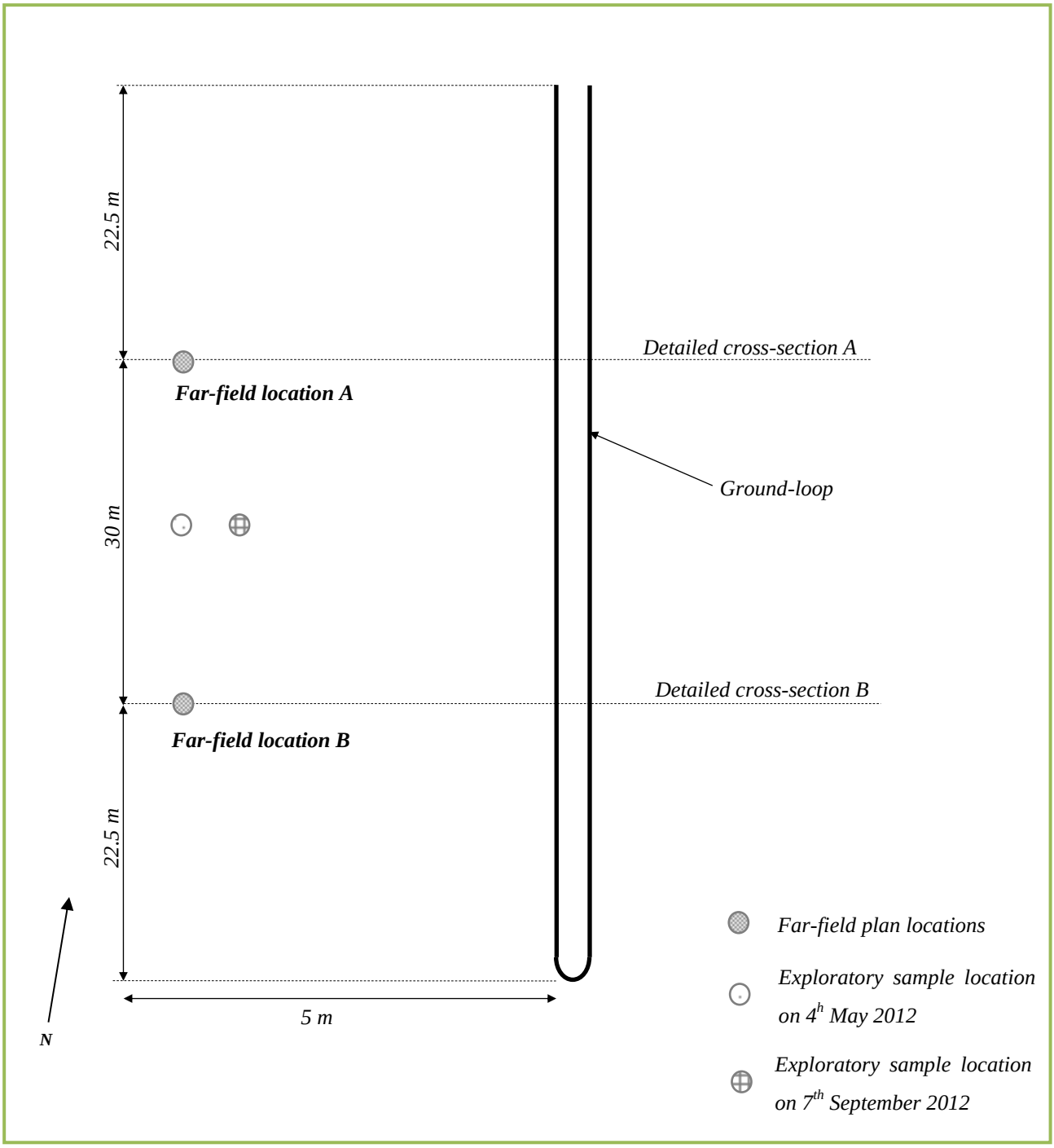

Figure 7.1 – The locations of far-field inspection points A and B at the monitoring site. More information regarding the spatial position of the thermistors is provided in Chapter 3.

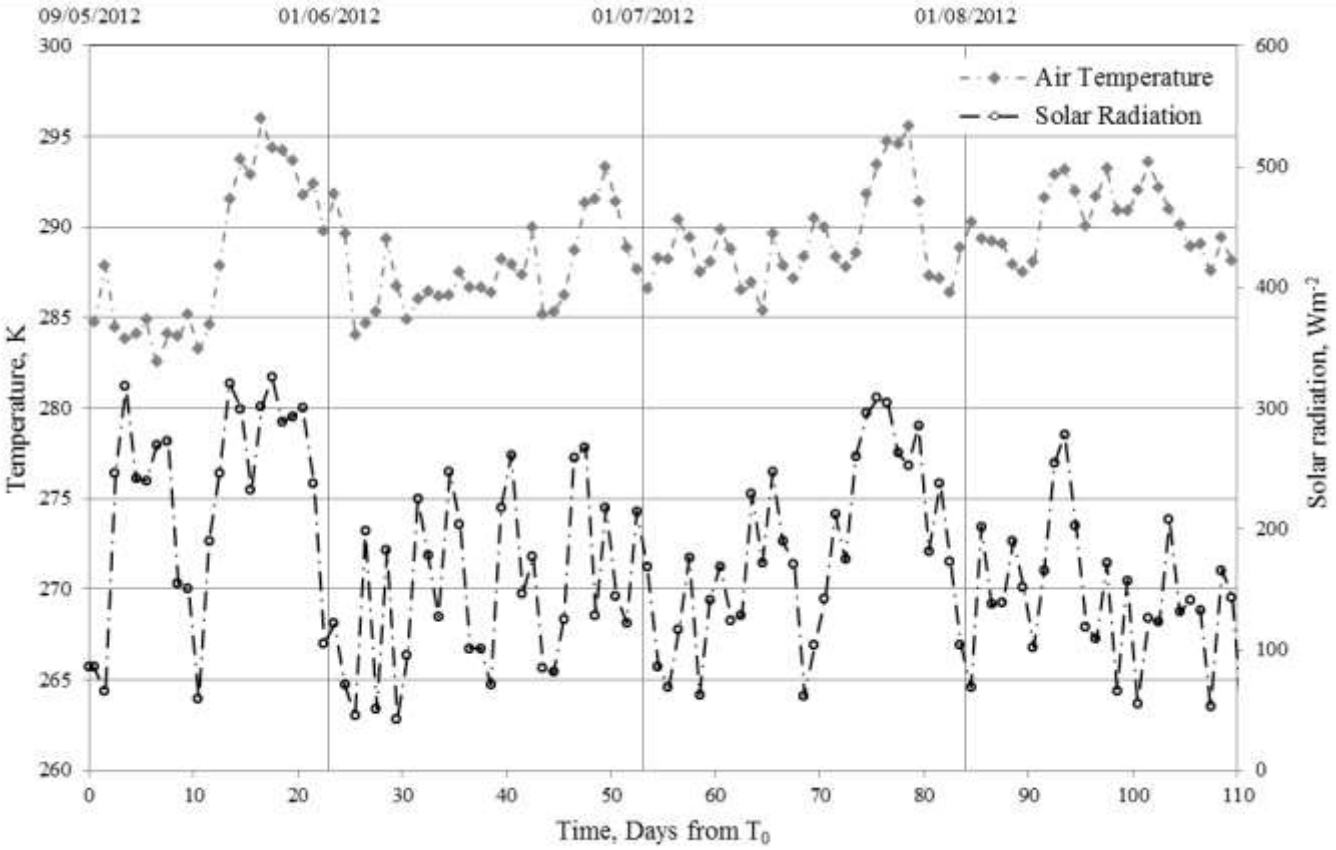

Figure 7.2 – Average daily ambient air temperature and solar radiation observed at the monitoring site between May 9th and August 29th 2012.

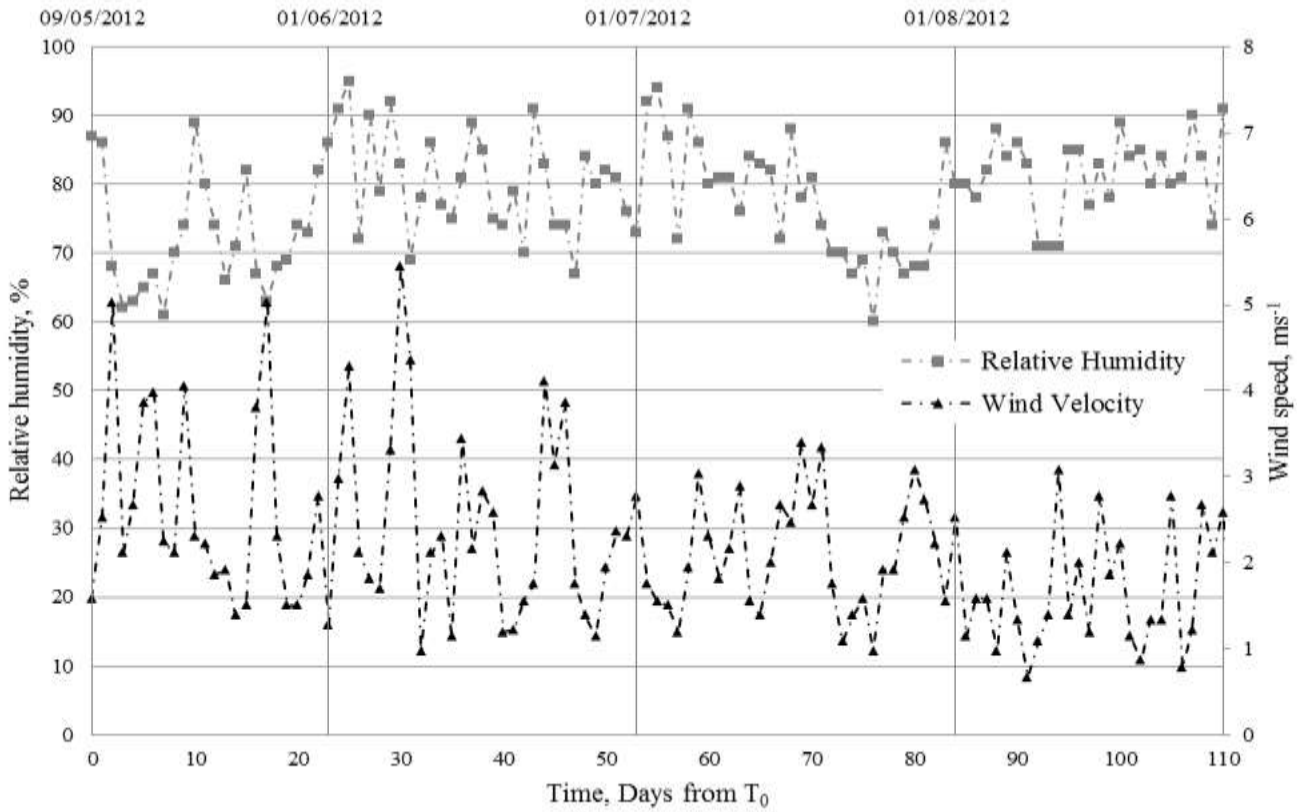

Figure 7.3 – Average daily relative humidity and wind-speed observed at the monitoring site between May 9th and August 29th 2012.

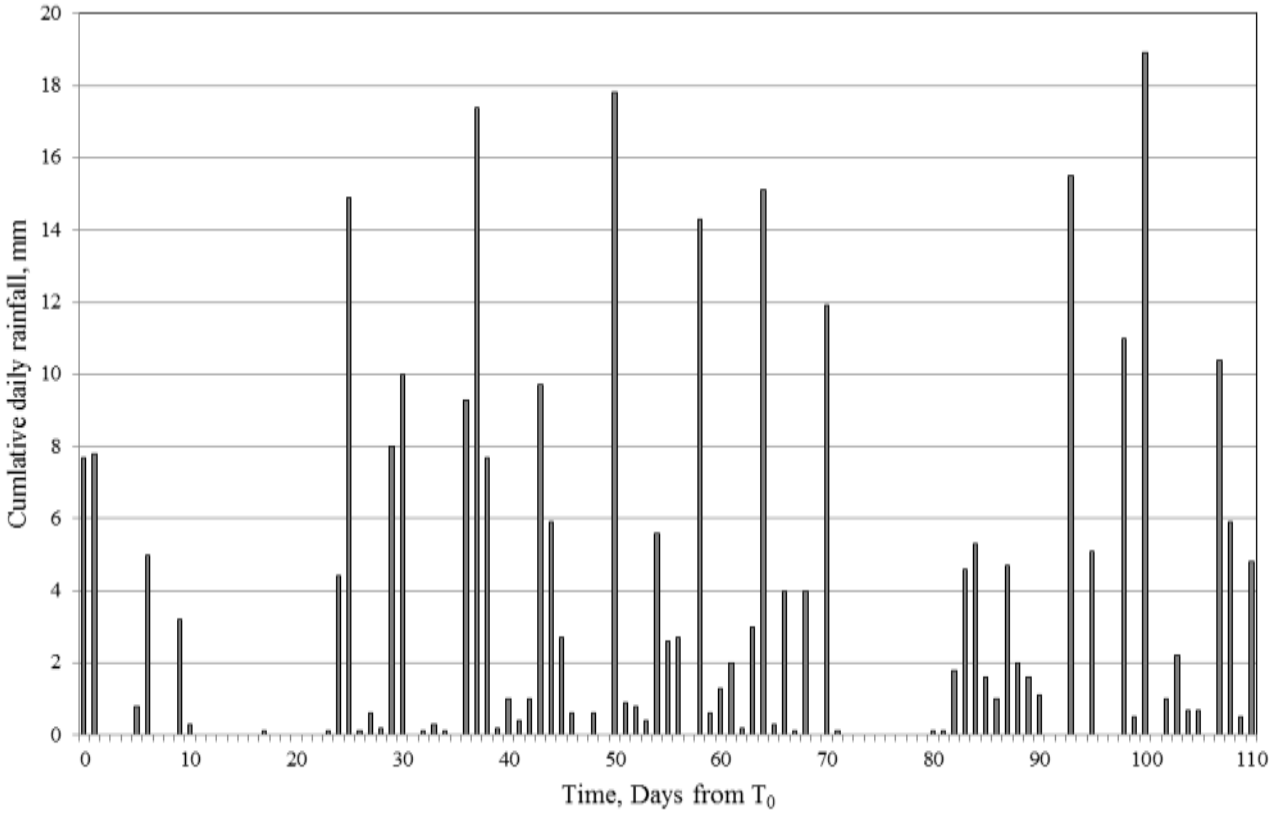

Figure 7.4 – Cumulative daily rainfall observed at the monitoring site between May 9th and August 29th 2012.

7.2.1 Domain

Figure 7.5 shows the two-dimensional domain which has been adopted for far-field validation models A and B. A two-dimensional domain has been selected based on the following considerations:

- *Climatic variables have been assumed constant across the whole site.*
- *Ground properties are assumed to only vary with depth at the far-field locations.*

The selected domain extends to a depth of 10 meters and to a width of 0.1 metres. For the given ground properties, previous research works have shown that at a depth of 10 meters beneath the ground surface the annual ground temperature variations due to seasonal climate changes are negligible (Kusuda & Achenback, 1965; Kusuda, 1975). For the current case, the heat transfer induced from the ground surface is predominantly one-dimensional (in the vertical direction) therefore the domain width can be kept to a small size, i.e. 0.1 meters.

The domain has been discretised using 2877 unstructured non-uniform linear triangular elements. As depicted in Figure7.5, the elements are smaller at the top of the domain where the greatest thermal and hydraulic exchanges are expected, thus providing a finer mesh. A varying time-stepping algorithm was applied with an initial time-step of 1 second and the simulation period was 9,936,000 seconds, coinciding with the 115 days between May 7th and August 29th.

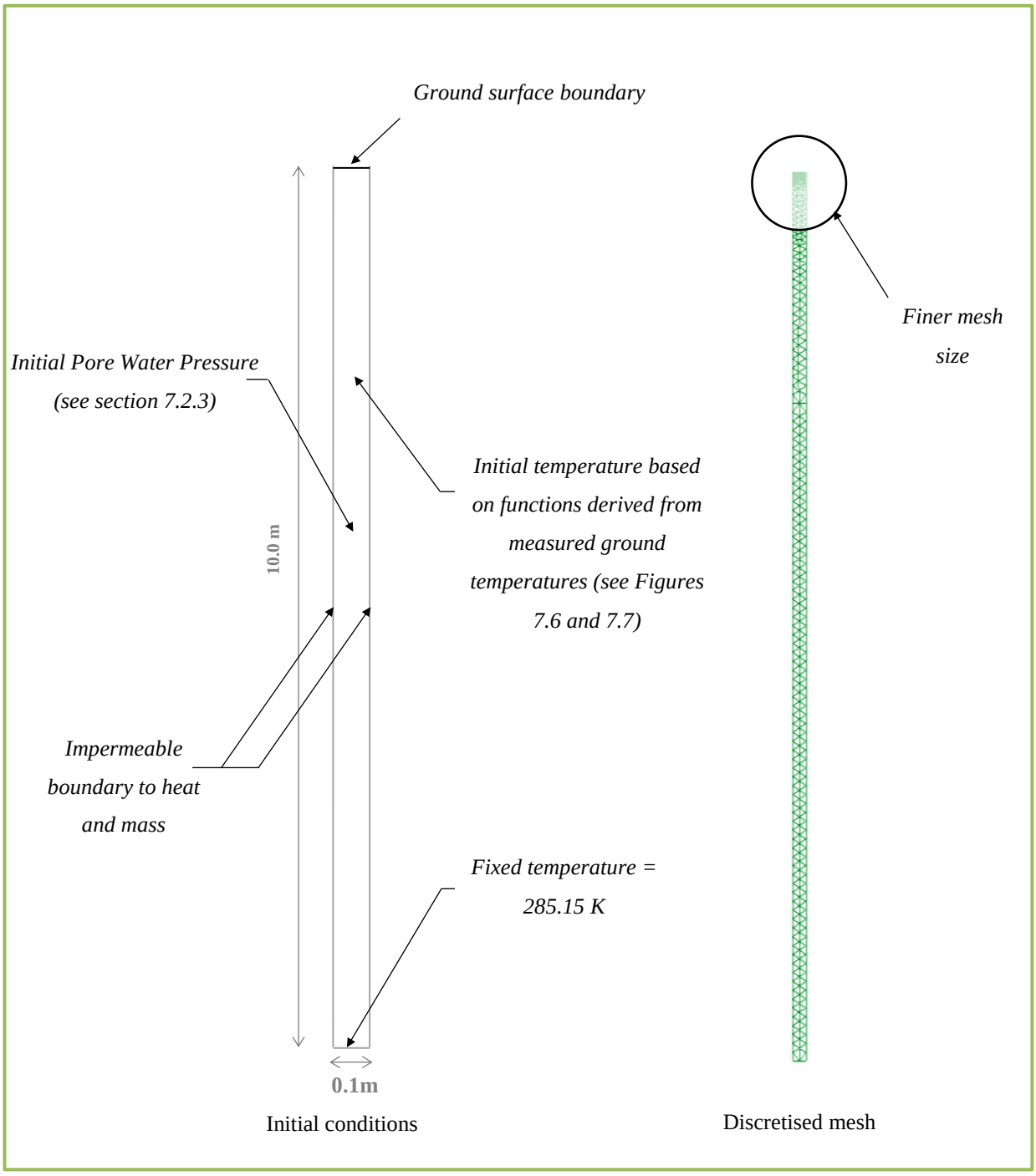

Figure 7.5 – Schematic showing the domain, initial conditions, boundary conditions and discretised mesh for far-field validation models A and B.

The constitutive relationships used to calculate the thermal conductivity, heat capacity, hydraulic conductivity and degree of saturation (based on suction) are the same as those previously highlighted in Chapter 5. For convenience, they have been summarised in Table 7.1.

Table 7.1 – Constitutive relationships used in the validation exercises.

Material parameter	***Relation***
Thermal conductivity	$\lambda = \prod_{i=1}^{3} \lambda_i^{\chi_i}$
Heat capacity	$H_c = (1-n)C_{ps}\rho_s + n\left(C_{pl}S_l\rho_l + C_{pv}S_a\rho_v + C_{pda}S_a\rho_{da}\right)$
Hydraulic conductivity	$K_l(h) = \frac{\{1 - (\alpha h)^{n-1}[1 + (\alpha h)^n]^{-m}\}^2}{[1 + (\alpha h)^n]^{m/2}} \qquad \left(m = 1 - 1/n\right)$
Soil Water Characteristic Curve (SWCC)	$\theta = \theta_{res} + \frac{(\theta_{sat} - \theta_{res})}{[1 + (\alpha h)^n]^m}$

7.2.2 Initial and boundary conditions

The initial ground temperature adopted within the far-field models A and B has been based on the ground temperature data recorded at the respective locations on May 7th 2012 (i.e. the starting point of the simulations) and theory. Figures 7.6 and 7.7 show the ground temperature data recorded on 7th May 2012, along with the initial ground temperature profile prescribed within the models. As shown in Figures 7.6 and 7.7, ground data was only gathered to a depth of approximately 2.5 meters. Beyond this depth the initial ground temperature was approximated using research presented by Kusuda (1975) and an analytical solution presented by Hillel (1980) (see Equation 6.22). These works indicated that the annual ground temperature variation would be less than 0.2 K at a depth of 6 meters for the conditions found at the monitoring site. Applying this theory and a fixed ground temperature of 285.15 K (12 ºC) to the lower boundary, an initial ground temperature was approximated using a combination of measured data and theory (see Figures 7.6 and 7.7). The fixed ground temperature was prescribed according to a geothermal report of the area presented by the British Geological Society (Busby, et al., 2011). As previously discussed, the ground temperature at this depth should remain constant all year round, remaining independent of seasonal climatic variations.

The initial pore water pressure profile was based on the degree of saturation obtained from four samples retrieved from the monitoring site on May 4th 2012 (see Chapter 3 for details and Figure 7.1 for the plan location). The pore water pressure was subsequently calculated according to van Genuchten's Soil Water Characteristic Curve (SWCC) (van Genuchten, 1980).

The four samples were retrieved from the location shown in Figure 7.1 at depths of 0.28, 0.38, 0.62 and 0.78 meters. The degree of saturation was found to vary 0.27 across the four samples and the average was obtained to be 0.72. The results from the laboratory experiments can be found in Appendix F. The retrieved samples indicated that there was no clear relationship between the degree of saturation and sample depth at the time of sampling. From a visual inspection undertaken during the exploratory sampling it can be said that there was no clear signs of saturation or a water table in the local or surrounding fields. Based on these observations, and the average degree of saturation, a uniform initial pore water pressure of -1700 kPa was prescribed throughout the model domain. This corresponded to a degree of saturation of 0.73. It is recognised that this is an approximation based upon the available site data.

The developed surface boundary condition has been assigned to the ground surface within the model (see Figure 7.5). The climatic variables required to compute the TH surface boundary fluxes have been previously presented in Figures 7.2, 7.3 and 7.4.

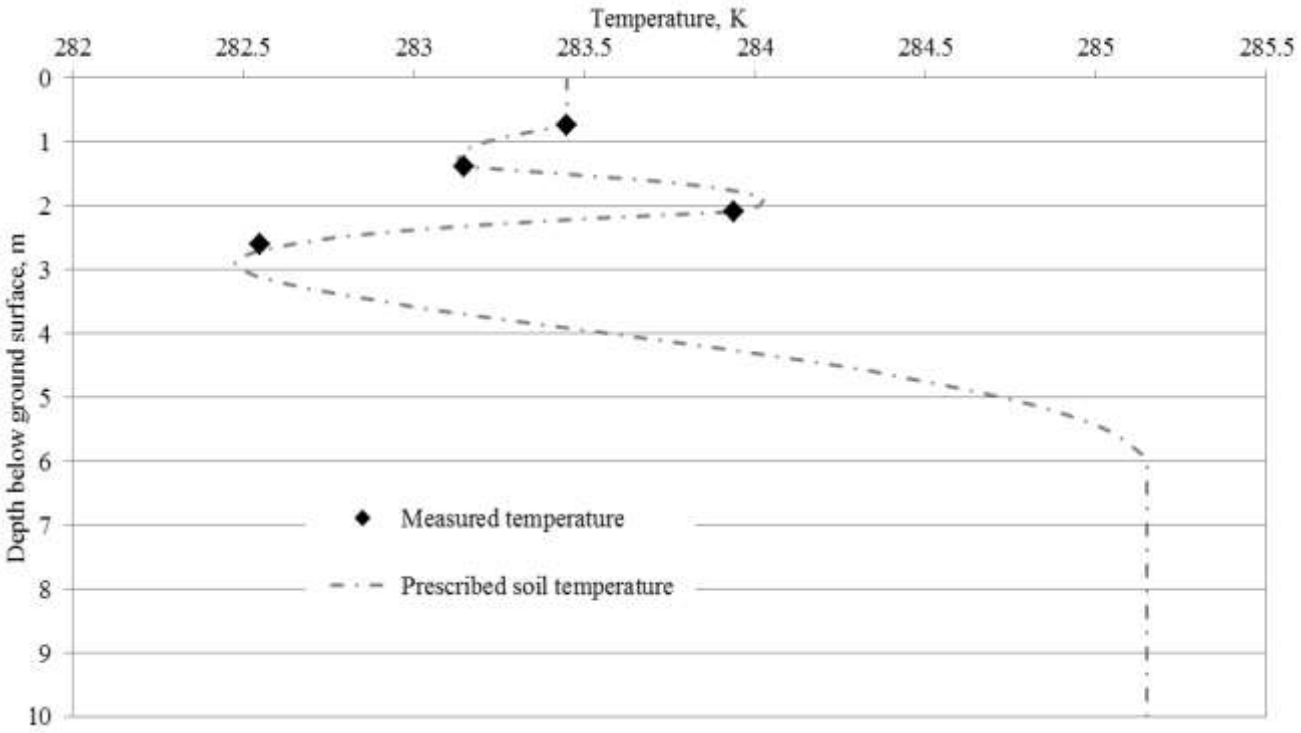

Figure 7.6 – Measured initial ground temperature on 7th May 2012 along with the initial ground temperature profile prescribed within the far-field validation model A.

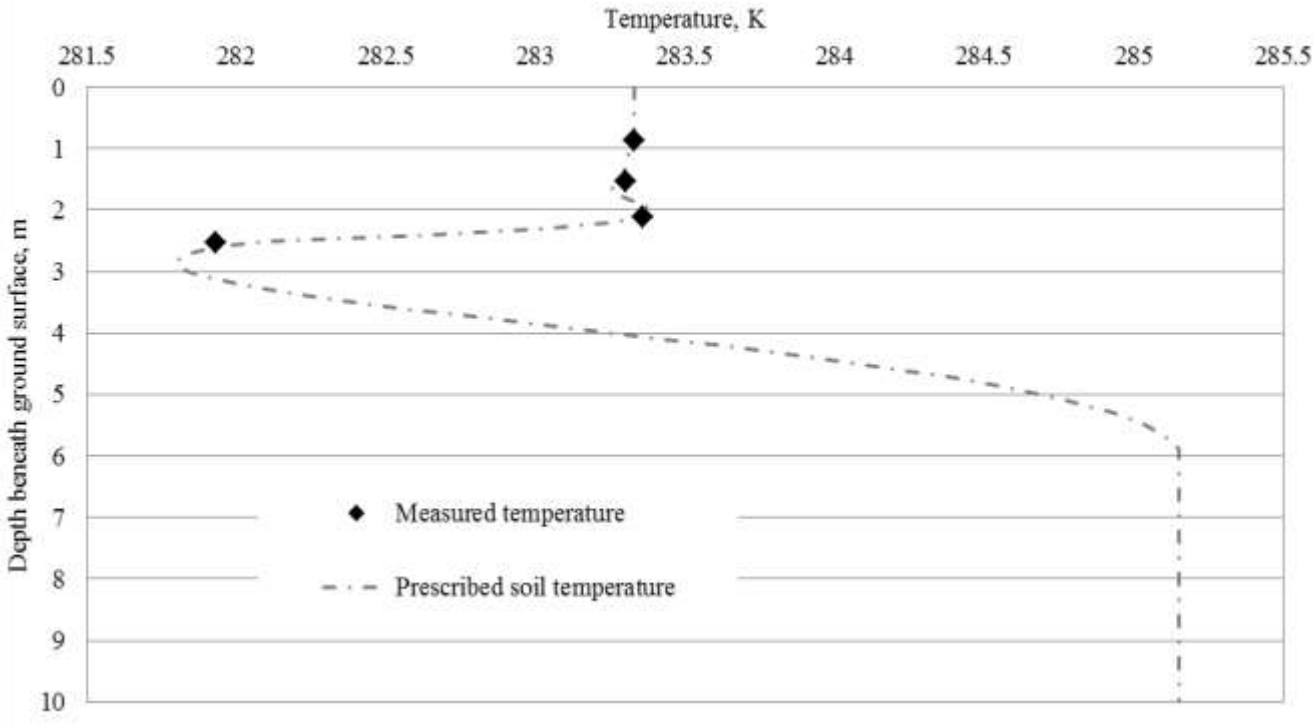

Figure 7.7 – Measured initial ground temperature on 7th May 2012 along with the initial ground temperature profile adopted within the far-field model B.

7.2.3 Material parameters

Two soil samples were retrieved from each far-field location as part of the ground investigations previously detailed in Chapter 3. In general, it can be said that the site investigation found the measured soil parameters to be independent of spatial position and depth, both in the local and field-scale. A single material was prescribed within each of the far-field simulations based on the two samples retrieved at the respective locations.

The sample data from the individual samples can be found in Appendix C and the average material properties used in the simulations can be found in Tables 7.2 and 7.3. The computation of the surface boundary condition required further material parameters related to the reflectivity, emissivity and aerodynamic drag of the ground surface (see Chapter 6 for further details regarding these parameters). For the current inspection period, the surface at the monitoring site consisted of short green grass. The corresponding surface parameters prescribed in the model have been included within Tables 7.2 and 7.3.

Table 7.2 – Table of material parameters adopted within far-field validation model A.

Parameter	***Value***
Porosity	0.4
Density (solids)	2650 kg m^{-3}
Specific heat capacity (solids)	820 J kg K^{-1}
Thermal conductivity (solids)	2.93 W $m^{-1}K^{-1}$ (De Vries, 1966)
Saturated hydraulic conductivity	1 x 10^{-9} ms^{-1} (Gustafsson, 1946)
Shortwave reflection factor	0.25 (van Wijk & Scholte Ubing, 1966)
Longwave emissivity factor	0.97 (van Wijk & Scholte Ubing, 1966)
Aerodynamic drag at 2 meter height	0.023 m (Sheppard, 1947)

Table 7.3 – Table of material parameters prescribed within far-field validation model B.

Parameter	***Value***
Porosity	0.23
Density (solids)	2650 kg m^{-3}
Specific heat capacity (solids)	820 J kg K^{-1}
Thermal conductivity (solids)	2.93 W $m^{-1}K^{-1}$ (De Vries, 1966)
Saturated hydraulic conductivity	1 x 10^{-9} ms^{-1} (Gustafsson, 1946)
Shortwave reflection factor	0.25 (van Wijk & Scholte Ubing, 1966)
Longwave emissivity factor	0.97 (van Wijk & Scholte Ubing, 1966)
Aerodynamic drag at 2 meter height	0.023 m (Sheppard, 1947)

7.2.4 Results

The following section presents the simulation results from the far-field validation models A and B. In this section, the simulated results are compared with ground temperature data collected between May 7th and August 29th 2012 at the monitoring site. As previously discussed, far-field validation point A and B each contained four thermistors at various depths. The thermistors' exact position was recorded as part of a topographical survey presented in Chapter 3. This allowed points within the simulation domains, corresponding to the measured thermistor depths, to be identified for inspection. The results presented on the following pages directly compare the monitored data with the

corresponding simulation results from far-field validation models A and B. Figures 7.8, 7.9, 7.10 and 7.11 show the monitored and simulated ground temperatures for far-field location A, whereas Figures 7.12, 7.13, 7.14 and 7.15 show the monitored and simulated ground temperatures for far-field location B at various depths. The exact depth of the individual thermistors is contained within the figure titles. The absolute error between the monitored and simulation results is also presented on each graph.

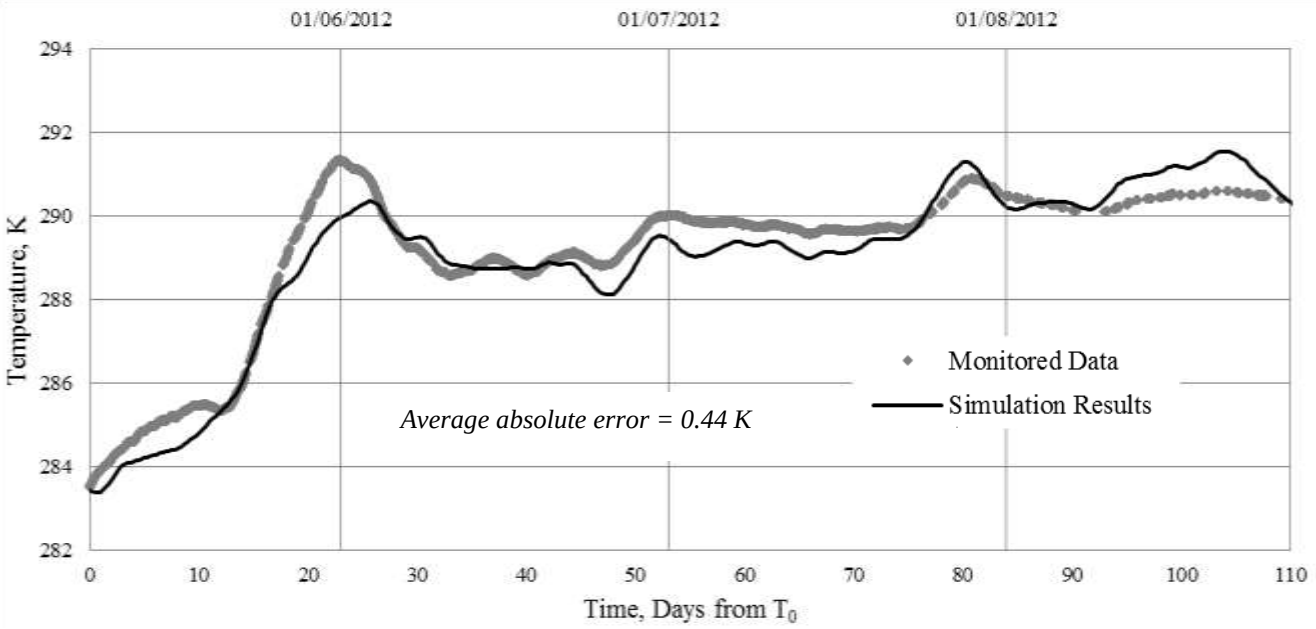

Figure 7.8 –Monitored and simulated ground temperatures at a depth of 0.75m at location A.

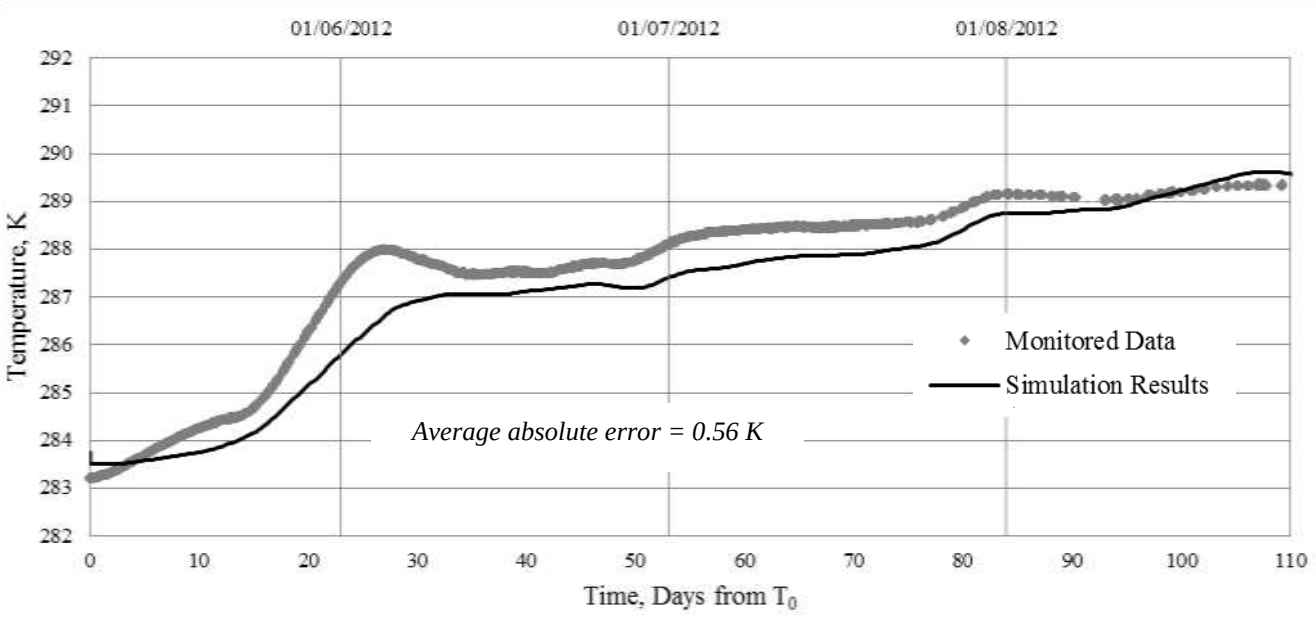

Figure 7.9 – Monitored and simulated ground temperatures at a depth of 1.40 m at location A.

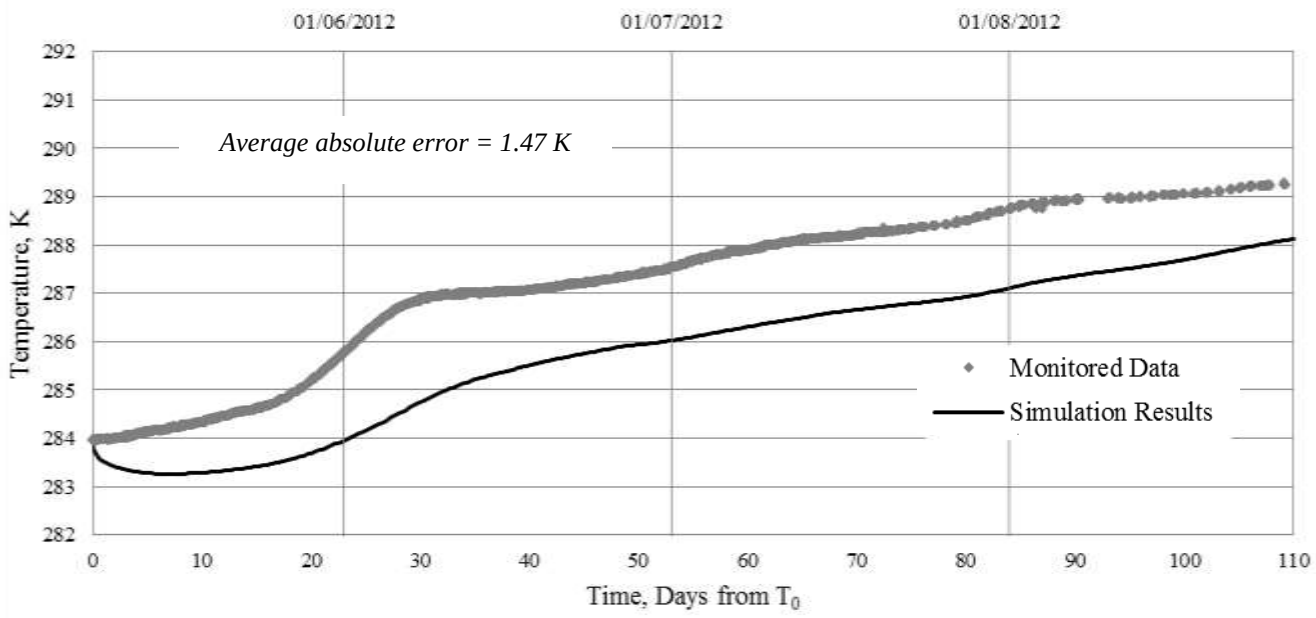

Figure 7.10 – Monitored and simulated ground temperatures at a depth of 2.10 m at location A.

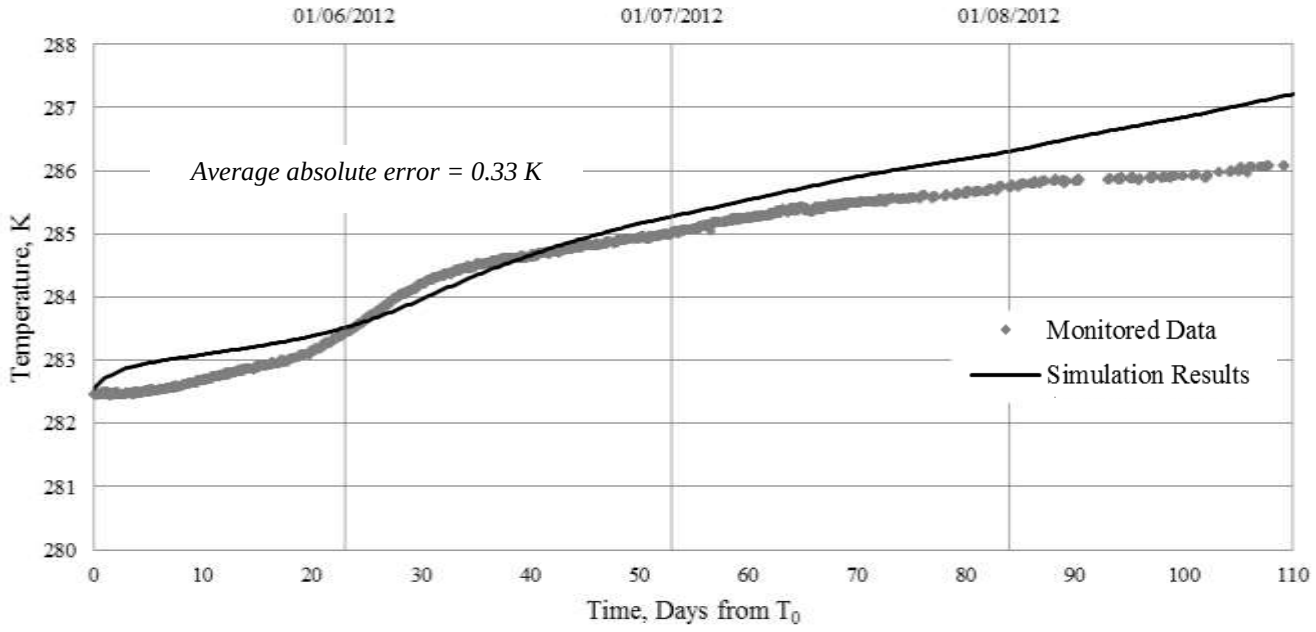

Figure 7.11 – Monitored and simulated ground temperatures at a depth of 2.62 m at location A.

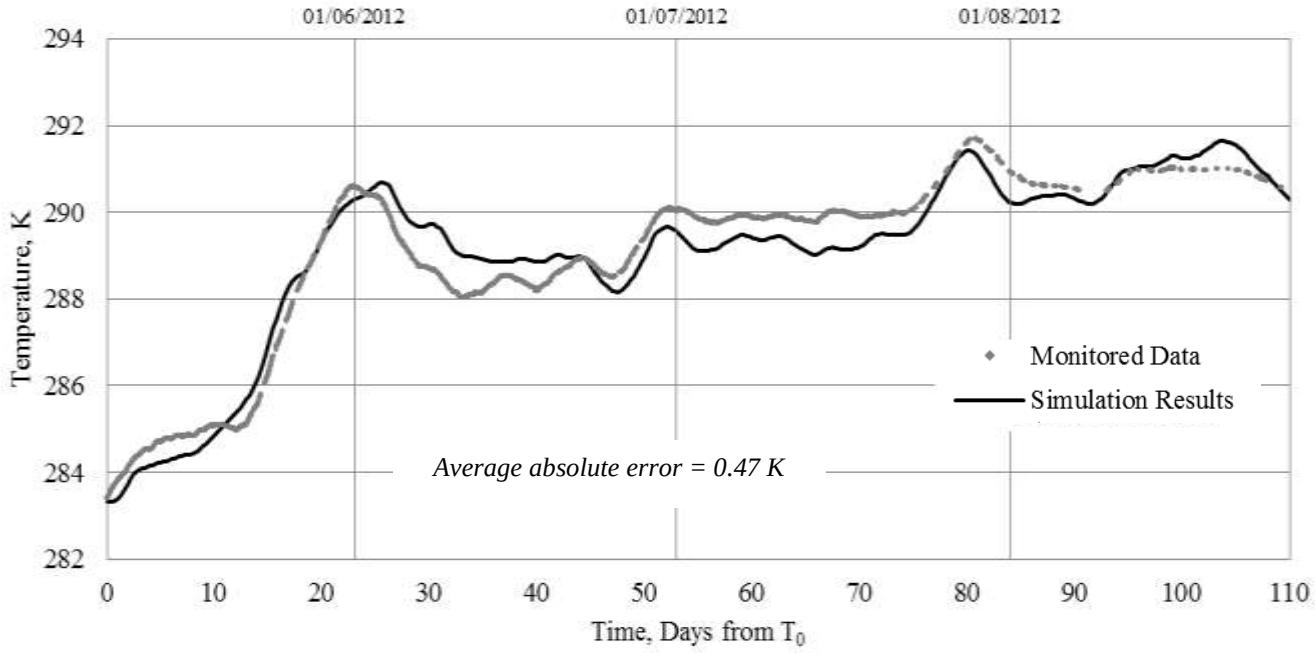

Figure 7.12 – Monitored and simulated ground temperatures at a depth of 0.87 m at location B.

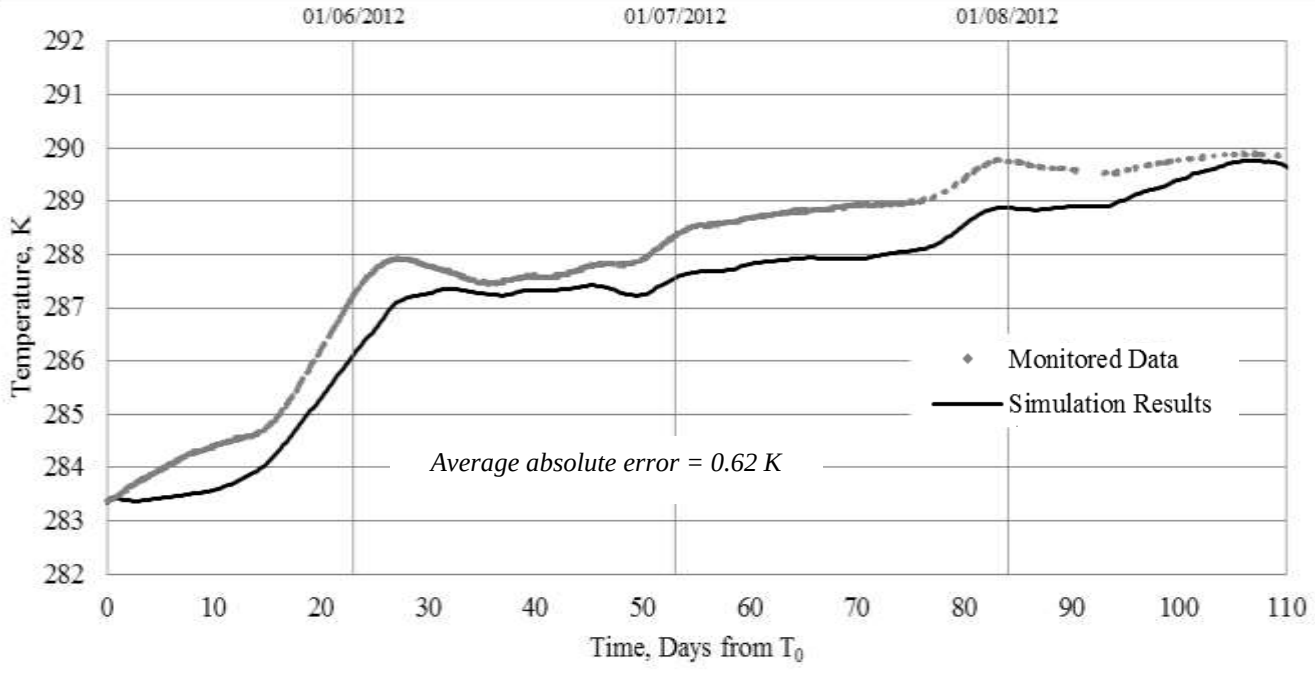

Figure 7.13 – Monitored and simulated ground temperatures at a depth of 1.54 m at location B.

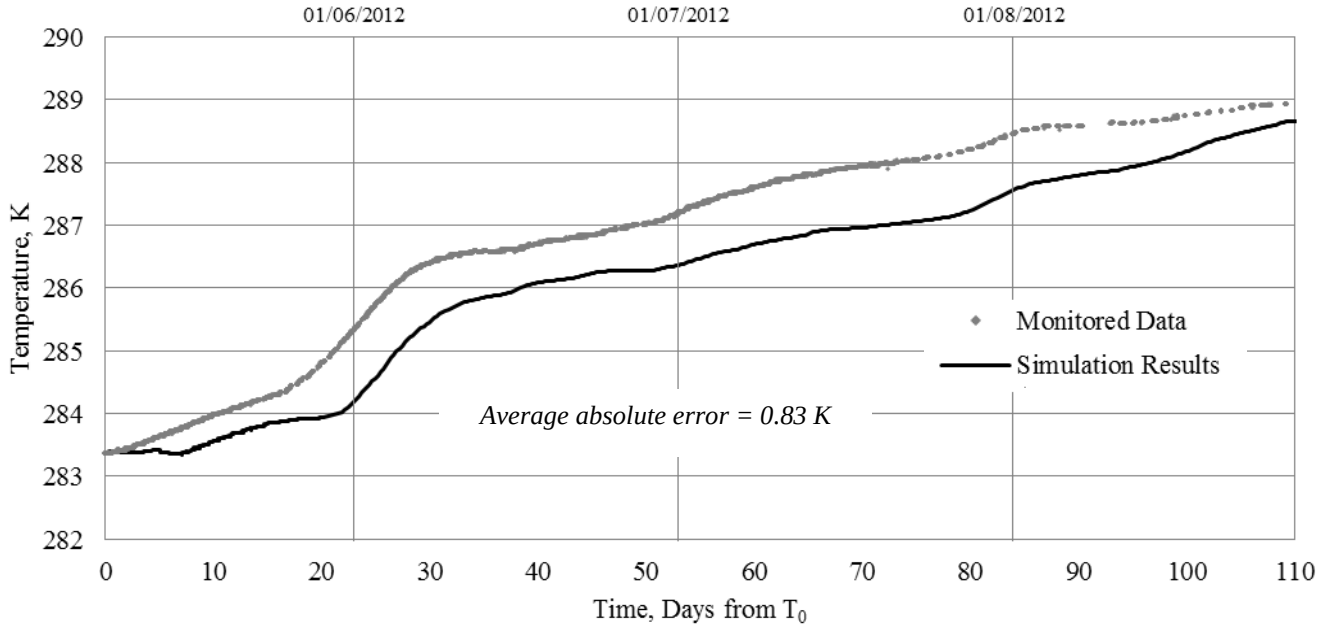

Figure 7.14 – Monitored and simulated ground temperatures at a depth of 2.11 m at location B.

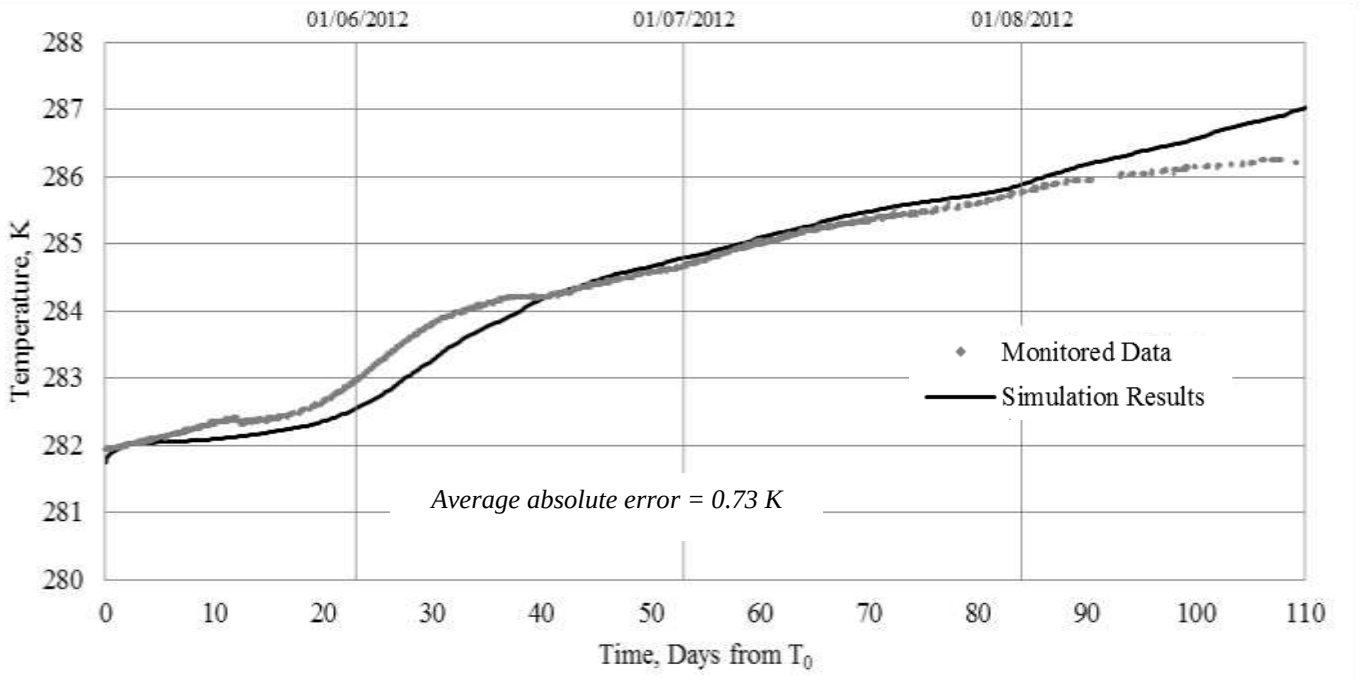

Figure 7.15 – Monitored and simulated ground temperatures at a depth of 2.52 m at location B.

In general it can be said that the simulated ground temperatures at far-field location A are in close agreement with the ground data collected during the inspection period. Similar behavioural trends observed in the monitored data can be observed in the simulated data, particularly at a depth of 0.75 meters. The one noticeable exception to these statements is the simulated ground temperature at a depth of 2.10 meters (see Figure 7.10). At this depth the simulated ground temperature was consistently lower than the monitored ground temperature, resulting in an average absolute error of 1.47 K over the simulation period. Despite this, the general increase in ground temperature and gradient of the temperature curve exhibited by the monitored data was replicated in the simulation, all be it at a lower temperature. The remaining errors between the simulated and monitored data were 0.44 K, 0.56 K and 0.33 K for the depths 0.75, 1.40 and 2.62 metres respectively.

In general it can be said that the simulated ground temperatures at far-field location B are also in close agreement with the monitored data recorded during the inspection period. The simulated results, presented in Figures 7.12 to 7.15, showed close agreement with the monitored data at all four of the inspection depths. The general ground temperature trends exhibited by the monitored data were reflected in the simulated ground temperatures, particularly at a depth of 0.88 which had an average absolute error with the monitored data of 0.47 K.

After reviewing all eight monitored and simulated ground temperatures over far-field validation points A and B, it can be seen that in only one case did the simulated ground temperature significantly differ from the monitored values. The general ground temperature behaviour exhibited by monitored ground data was replicated by the simulations. The absolute error between monitored and simulated data was less than 0.63 K at five of the eight inspection points and furthermore less than 0.5 K at three of these points. The close agreement between the simulation and monitored data over the 110 day inspection period has been deemed sufficient to validate the developed model subject to no heat extraction and in particular the thermal component of formulated theoretical surface boundary condition presented in Chapter 6.

The preceding sections have presented the validation for the developed TH model subject to no heat extraction. In particular, these conditions allowed the validity of the thermal aspect of the developed surface boundary condition to be investigated. It has be deduced from the findings presented in this section that the formulated TH model and developed surface boundary condition is capable of representing the thermal behaviour in the ground and thermal exchange at the ground surface during periods of zero heat extraction.

7.3 Stage II – Heat extraction phase

Stage II of the validation process aims to validate the developed model during periods of heat extraction by the ground source system. The uniform ground-loop boundary condition, as oppose to the non-uniform boundary condition, has been selected for the validation tests here based upon findings from Chapters 4 and 6. The findings in these chapters indicated that heat extraction from a horizontal ground-loop can be represented with a uniform flux based on the total system load. Validation exercise Stage II builds upon Stage I by incorporating the uniform ground-loop boundary condition in conjunction with the previously validated surface boundary condition.

Chapter 3 previously detailed the spatial arrangement of thermistors throughout the monitoring site. Within this arrangement, two detailed cross-sections (denoted AA and BB) contain a greater number of thermistors than the remaining cross-sections (41 in total). The greater number of thermistors located within these detailed cross-sections provides a greater resolution of ground temperature data for validation purposes. The location of detailed cross-sections AA and BB can be found in Figure 7.1 and additional details can be found in Chapter 3. In total, two validation models based on detailed cross-sections AA and BB are presented in the following sections. Figures 7.16 and 7.17 show the exact position of the ground thermistors within the detailed cross-sections according to the topographic survey carried out during the thermistor installation.

Ground temperature data collected at the monitoring site between September 1st and December 28th 2012 has been used as the benchmark for validation. As previously stated in section 7.2, the ground source heat system was first turned on for domestic use on 7th September 2012, therefore this period represents the initial ground thermal behaviour resulting from heat extraction. The following sections present details of two exercises developed for the validation of the numerical model simulating heat extraction. The results from the exercises are compared with the ground data collected from the monitoring site and discussed accordingly.

First, factors common to both validation models such as the climatic conditions and the total thermal energy extracted from the ground by the ground source heat system are presented and discussed. Following this simulation details including domain; initial and boundary conditions; and prescribed materials properties are described. Many of the simulation details are common to the detailed cross-section AA and BB models. To avoid repetition the simulation details are therefore collectively discussed.

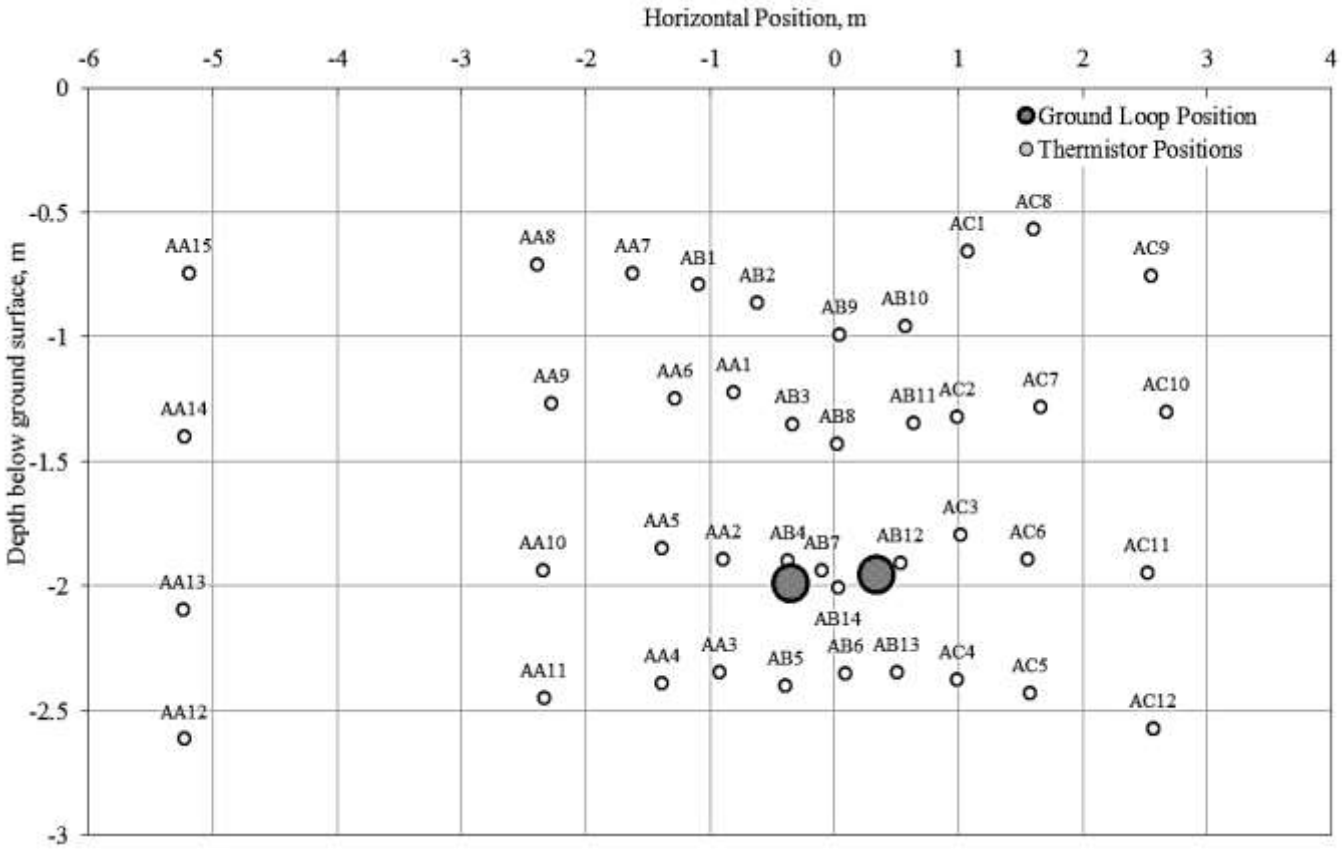

Figure 7.16 – Spatial position of the ground thermistors within detailed cross-section AA.

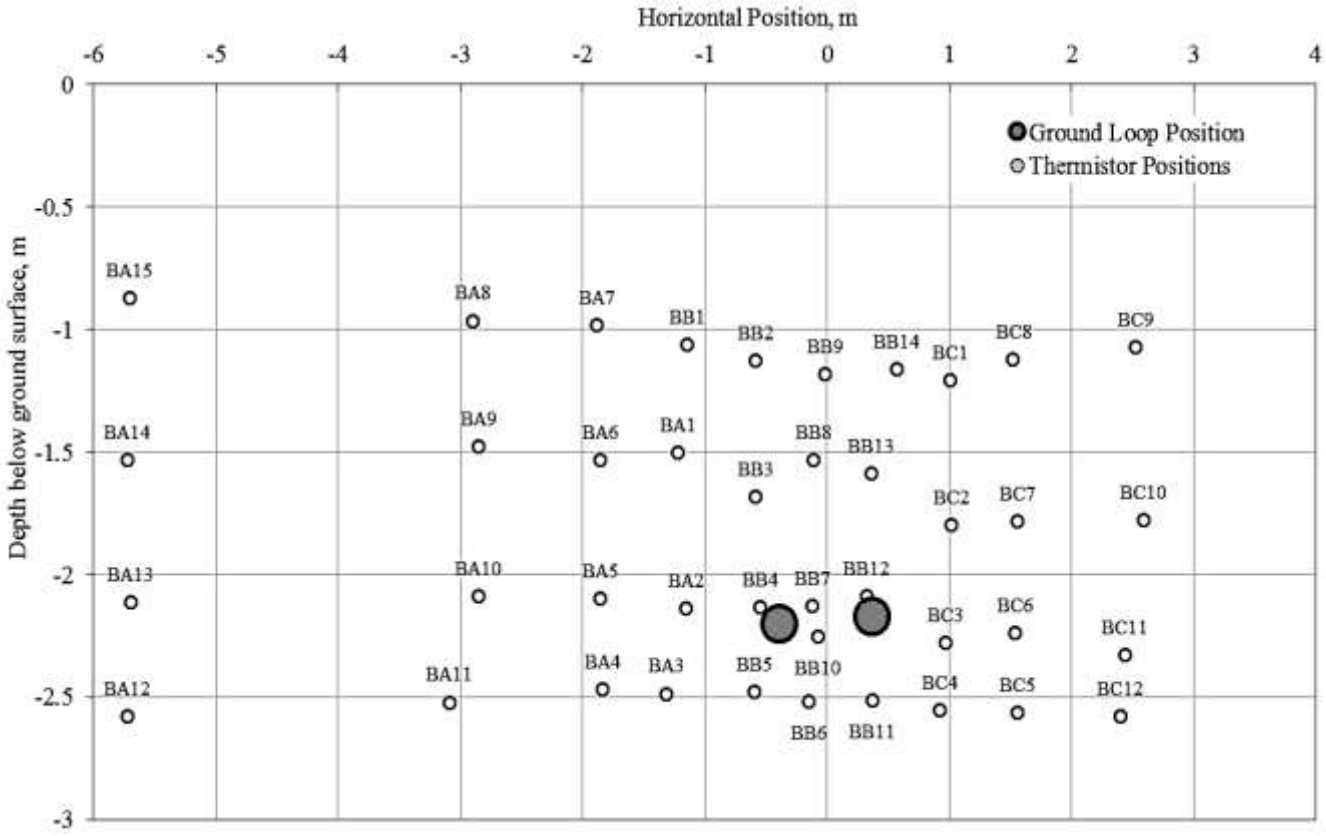

Figure 7.17 – Spatial position of the ground thermistors within detailed cross-section BB.

7.3.1 Climatic variables

Similarly to Stage I, the climatic variables recorded at the monitoring site will be used in the computation of the surface boundary condition for both validation exercises. The climatic variables ambient-air temperature, solar radiation, wind-speed, relative humidity and rainfall measured at the monitoring site between September 1st and December 28th 2012 are presented in Figures 7.18, 7.19 and 7.20. The measured variables are assumed to be uniform and representative of the whole monitoring site.

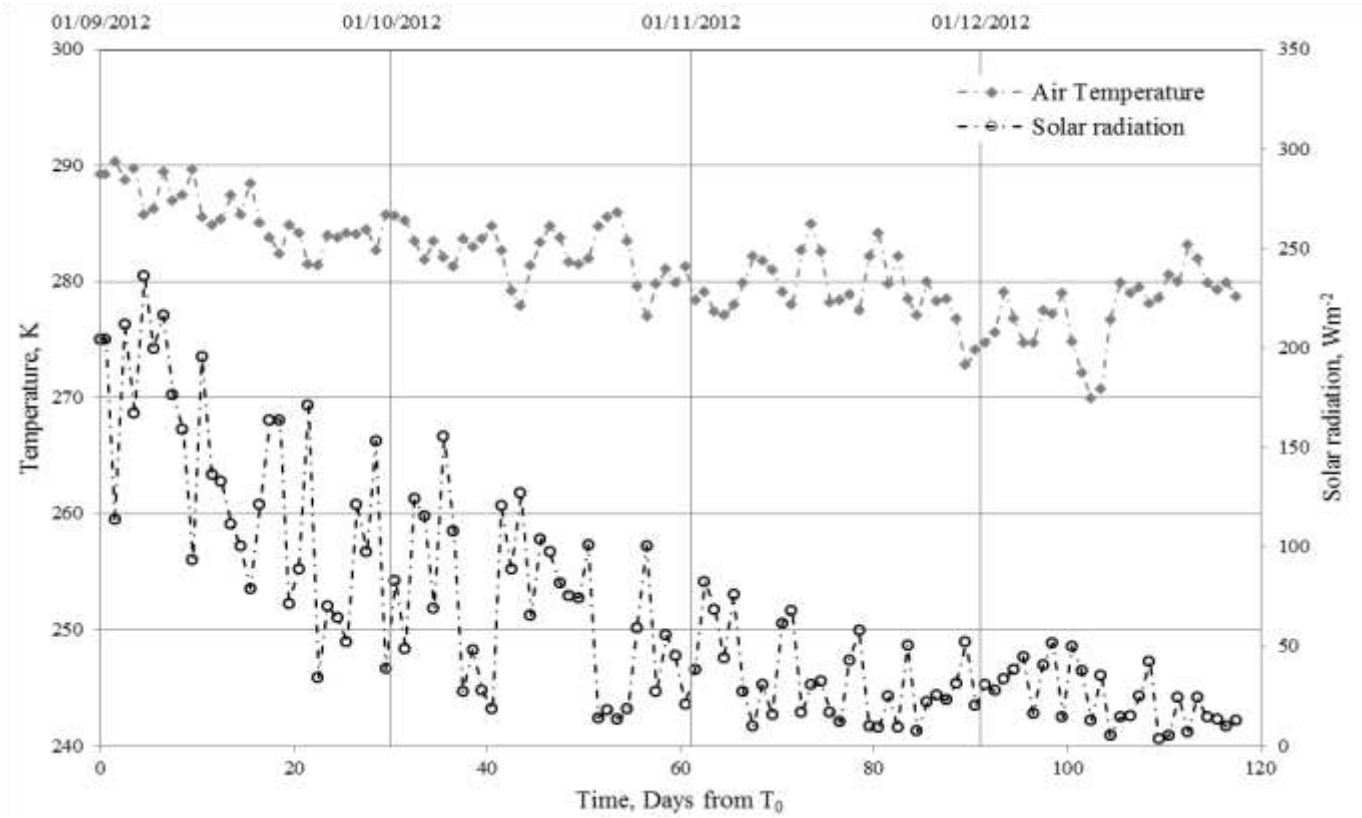

Figure 7.18 – Average daily air temperatures and solar radiation observed at the monitoring site between September 1st and December 28th 2012.

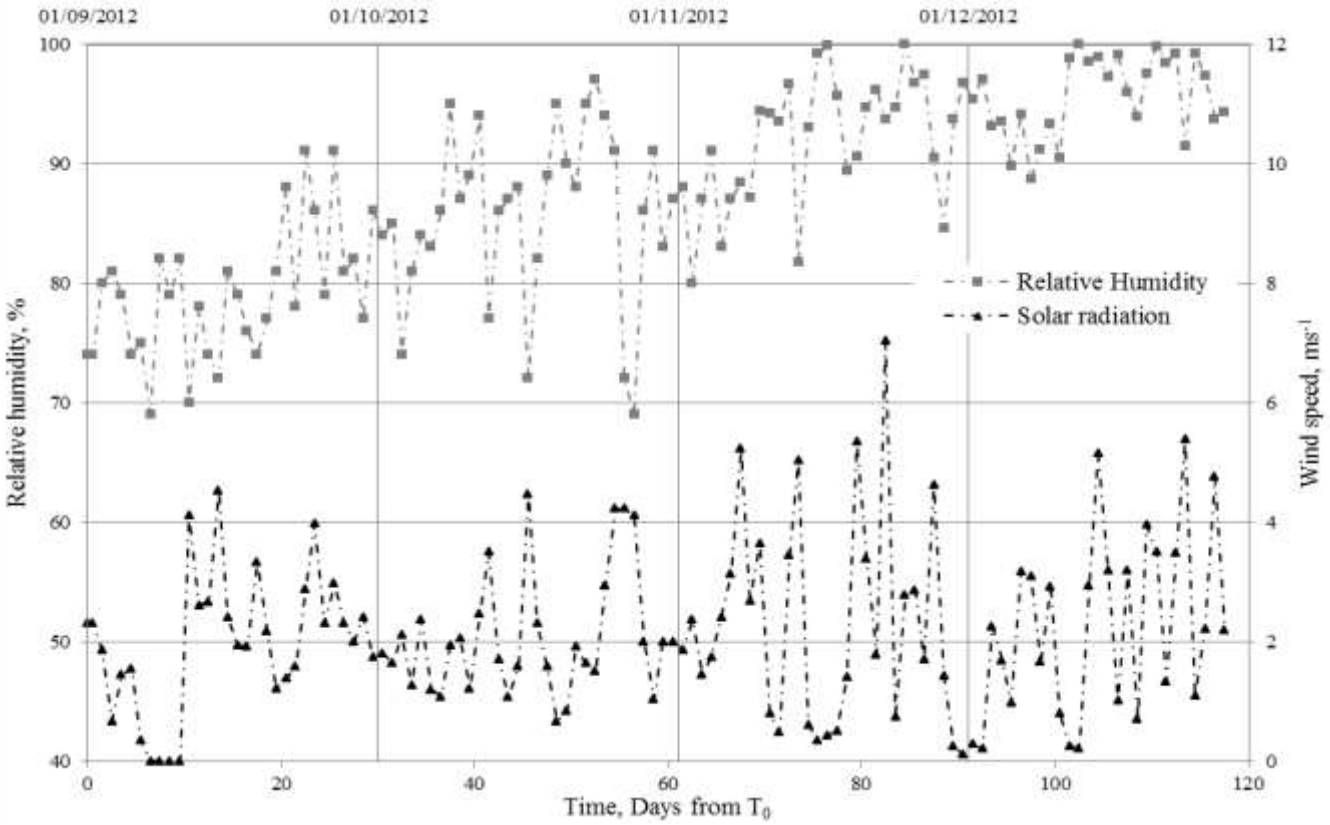

Figure 7.19 – Average daily relative humidity and wind speed observed at the monitoring site between September 1st and December 28th 2012.

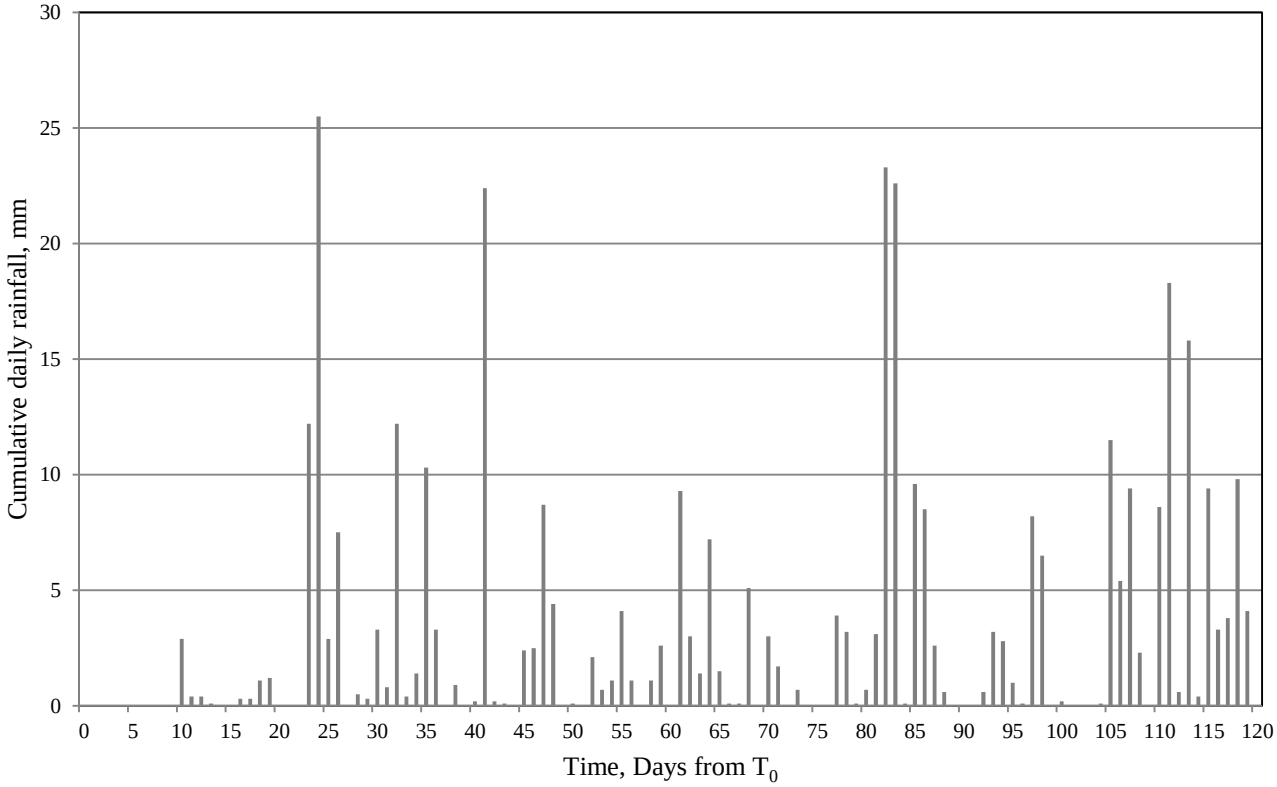

Figure 7.20 – Cumulative daily rainfall observed at the monitoring site between September 1st and December 28th 2012.

7.3.2 Total heat extraction

In order to compute the uniform ground-loop boundary at any time, the heat extracted from the ground via the ground source heat system (otherwise referred to as the heat load) is required. The heat extraction for any given time can be calculated using the fluid mass flow rate, fluid temperature differential across the heat pump and fluid specific heat capacity. Equations 6.15 and 6.16 presented in Chapter 6 describe how these variables can be used to compute the system heat load at given time.

The monitoring scheme detailed in Chapter 3, describes the equipment and collection regimes used to measure flow rate and fluid temperature differential across the heat pump. The remaining unknowns required to compute the system heat load are the fluid density and specific heat capacity. The circulating fluid used in the system at the monitoring site consists of a 75% water and 25% ethylene-glycol solution. The density and specific heat capacity of the water, ethylene-glycol and overall solution are presented in Table 7.4. The fluid properties have been assumed constant based on the expected operational conditions. Figure 7.21 shows the calculated heat load (in kilo-Watts) for the simulation period (i.e. September 1st to December 28th 2012) based upon the previously discussed factors.

Table 7.4 – Circulating fluid's specific heat capacity and density.

Constituent/Solution	***Specific heat capacity (J kg^{-1} K^{1})***	***Density (kg m^{-3})***
Water	4217.4 (at 10 °C) (Kaye, et al., 1973)	999.05 (at 10 °C) (Kaye, et al., 1973)
Ethylene-glycol	2330.17 (at 10 °C) (ME Global, 2008)	1100 (at 10 °C) (Siegfried, 2005)
Water / Ethylene-glycol solution (3 : 1 ratio)	3745.3	1024.3

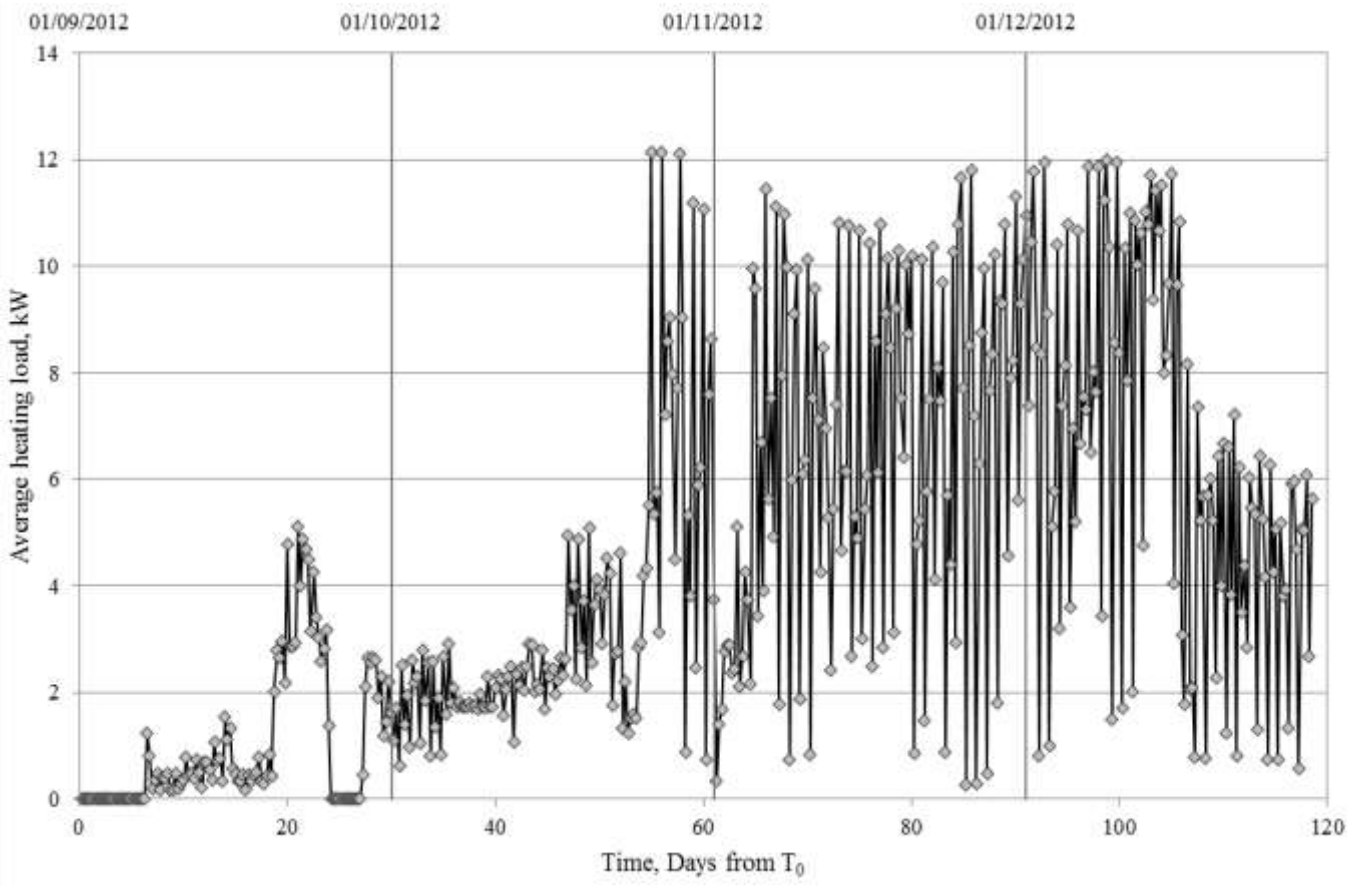

Figure 7.21 – Average heat load of the ground source heat system at 6 hour time intervals between September 1st and December 28th 2012.

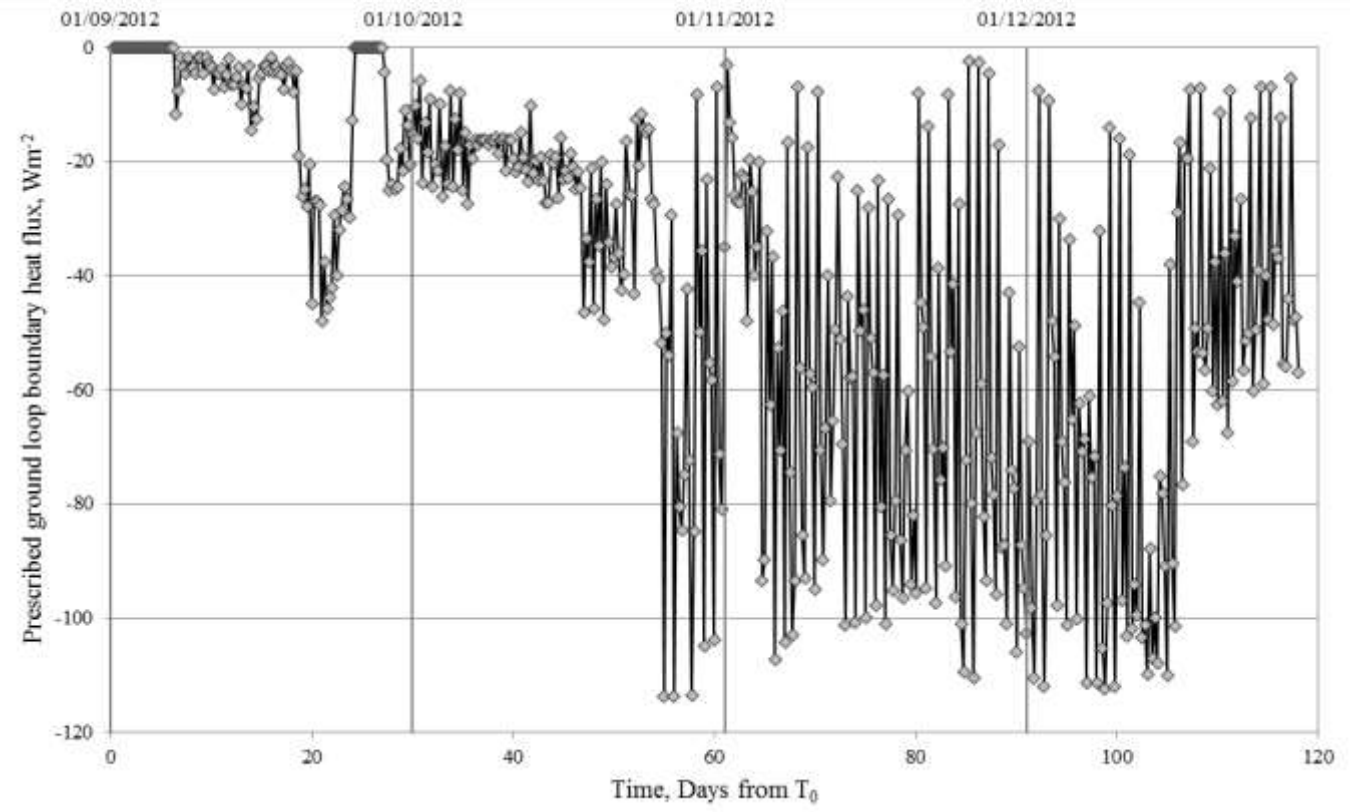

Figure 7.22 – Calculated heat flux applied by the uniform ground-loop boundary condition prescribed within validation models between September 1st and December 28th 2012.

Provided that the ground-loop total length and diameter are known, it is possible to calculate the uniform ground-loop boundary condition for the validation period between September 1st and December 28th 2012 using Equations 6.15 and 6.16 (see Chapter 6); and the calculated heat loads presented in Figure 7.21. Figure 7.22 shows the calculated uniform ground-loop boundary heat flux for the simulation period (in Wm^{-2}) based on the ground-loop length of 750 meters and external diameter of 0.04 meters. The heat flux is negative because the system removes heat from the ground. As described in Chapter 6, the boundary condition is assumed to be a uniform heat flux across the ground-loop surface therefore it has been prescribed to both ground-loop surfaces within the validation exercises for detailed cross-sections AA and BB.

7.3.3 Domain

A two-dimensional domain has been employed to model the TH ground behaviour at the detailed cross-sections based on the following considerations:

- *The ground temperatures used as a basis for validation have been measured across a single two-dimensional cross-section at each of the detailed cross-sections.*
- *Climatic conditions have been assumed uniform across the whole site.*
- *The uniform ground-loop boundary condition assumes a single uniform ground-loop heat flux boundary throughout the site.*

Figure 7.23 shows the two-dimensional model domain; initial and boundary conditions; and the discretised mesh used in the detailed cross-section models AA and BB. The domain extends to a depth and width of 10 meters. At a depth of 10 meters there should no annual ground temperature change resulting from seasonal climatic variations (Kusuda & Achenbach, 1965; Kusuda, 1975). A 10 meter domain width allows the spatial location of all 41 thermistors located in the detailed cross-sections to be included within the model domain. The ground-loop has been represented within the model domains via two circular holes which measure 0.04 meters in diameter, corresponding to the external diameter of the ground-loop. The coordinates relating to the centre of these holes can be found in Table 7.5. The uniform ground-loop boundary condition is prescribed to the circumference of these holes. The ground-loop itself has not being explicitly represented in the model and therefore the associated thermal capacity and resistance have been assumed negligible. This assumption has been made according to the relatively thin pipe thickness (2.4 mm) of the poly-ethylene ground-loop pipes.

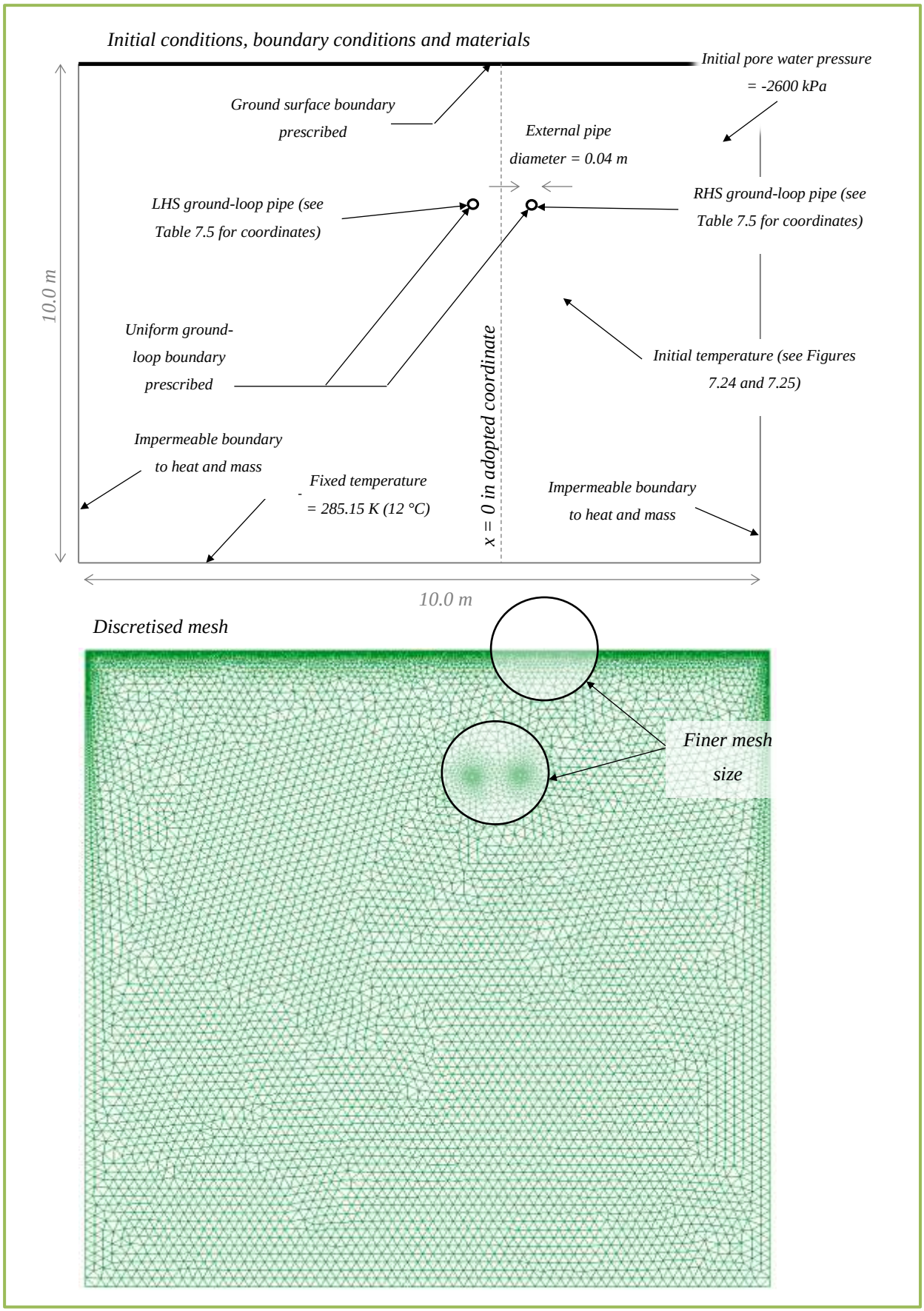

Figure 7.23 – The domain, initial conditions, boundary conditions and discretised mesh for the detailed cross-section AA and BB validation exercises.

The domain has been discretised using unstructured non-uniform linear triangular elements. As depicted in Figure 7.23, the elements are smaller at the top of the domain and in the regions around the ground-loops where the greatest thermal and hydraulic exchanges are expected, thus providing a finer mesh. A varying time-stepping algorithm was applied with an initial time-step of 1 second and the simulation period was 10,368,000 seconds, coinciding with the 120 days between September 1st and December 28th.

The constitutive relationships used to calculate the thermal conductivity, heat capacity, hydraulic conductivity and degree of saturation (based on suction) are the same as those previously highlighted in Chapter 5 and summarised in Table 7.1.

Table 7.5 – Central coordinates of the ground-loop pipes used in the detailed cross-section AA and BB models.

Model	***LHS ground-loop coordinates (center of pipe)***	***RHS ground-loop coordinates (center of pipe)***
Detailed cross-section AA	(-0.35, -1.99)	(0.35, -1.96)
Detailed cross-section BB	(-0.38, -2.21)	(0.38, -2.17)

7.3.4 Initial and boundary conditions

The initial ground temperature adopted within the detailed cross-section AA and BB exercises has been based on ground temperature data recorded on 1st September 2012 (i.e. the starting point of the simulations) and previous research presented by Kusuda (1975) and Hillel (1980). Figures 7.24 and 7.25 show the ground temperature data recorded on 1st September 2012 along with the initial ground temperature profile prescribed within the respective models. As previously discussed in section 7.2.2, the ground temperature beyond the depth of the thermistors has been approximated according to the highlighted research which suggests that the annual ground temperature at 6 meters will be approximately equal to the constant ground temperature found at depths beyond 10 meters. A fixed ground temperature of 285.15 K (12 ºC) was prescribed to the lower boundary (see Figures 7.24 and 7.25) based upon a geothermal report of the area presented by the British Geological Society (Busby, et al., 2011). The ground temperature at this depth should remain constant all year round, independent of seasonal climatic variations.

The initial pore water pressure in both detailed models was calculated based on the degree of saturation obtained from four samples retrieved on September 7th 2012 (see Chapter 3 for sampling details). The pore water pressure was subsequently calculated according to van Genuchten's SWCC (van Genuchten, 1980).

The four samples were retrieved from the location shown in Figure 7.1 at depths of 0.19, 0.35, 0.52 and 0.70 meters. The degree of saturation varied 0.44 across the four samples and averaged 0.61. The laboratory result obtained can be found in Appendix F. The retrieved samples indicated that there was no clear relationship between the degree of saturation and sample depth at the time of sampling. From a visual inspection undertaken during the exploratory sampling it can be said that there was no clear signs of saturation or a water table in the local or surrounding fields. Based on these observations, and the average degree of saturation, a uniform initial pore water pressure of -2600 kPa was prescribed to the model domains within the detailed cross-section AA and BB exercises respectively. This corresponded to a degree of saturation of approximately 0.6. It is recognised that this is an approximation based upon the available site data.

The developed surface boundary condition has applied in the model (see Figure 7.23). The climatic variables required to compute the TH surface boundary fluxes have been previously presented in Figures 7.18, 7.19 and 7.20. The uniform ground-loop boundary condition was prescribed to the ground-loop circumferences as shown in Figure 7.23.

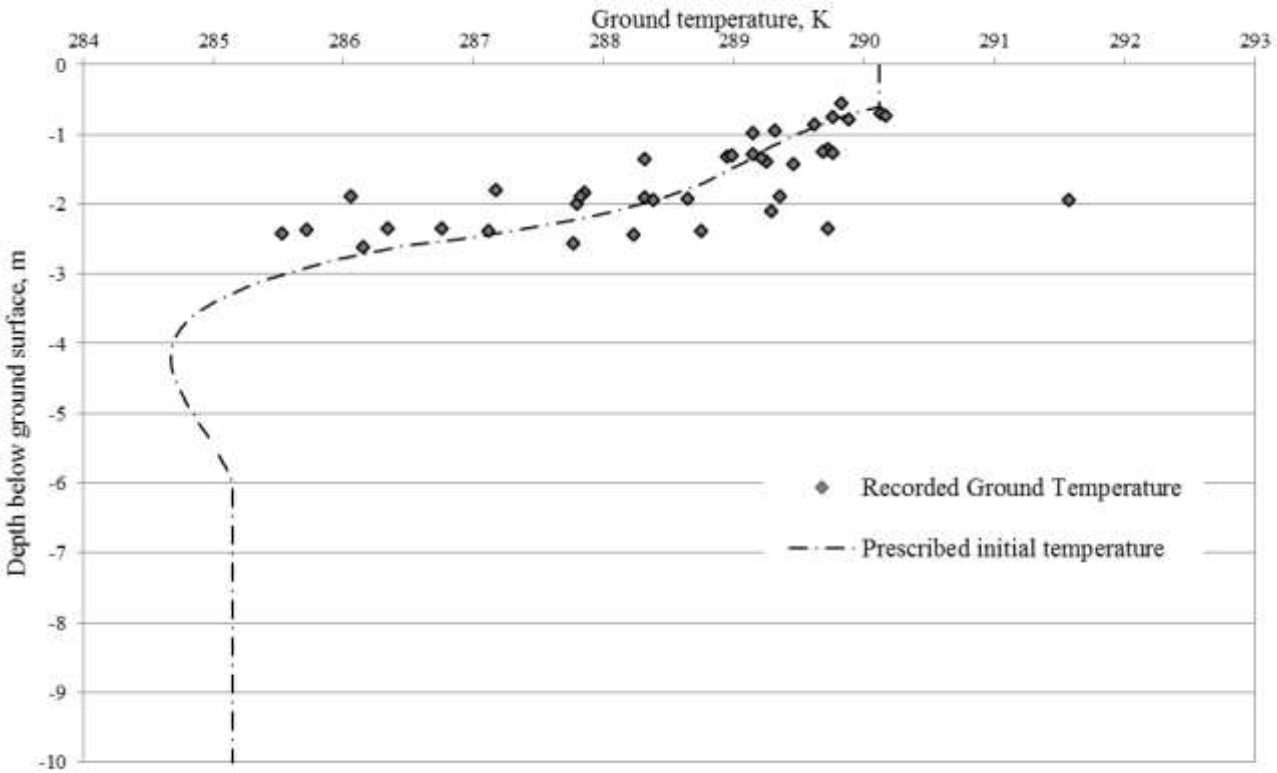

Figure 7.24 – Measured ground temperatures on 1st September 2012 along with the initial ground temperature profile prescribed within the detailed cross-section AA validation exercise.

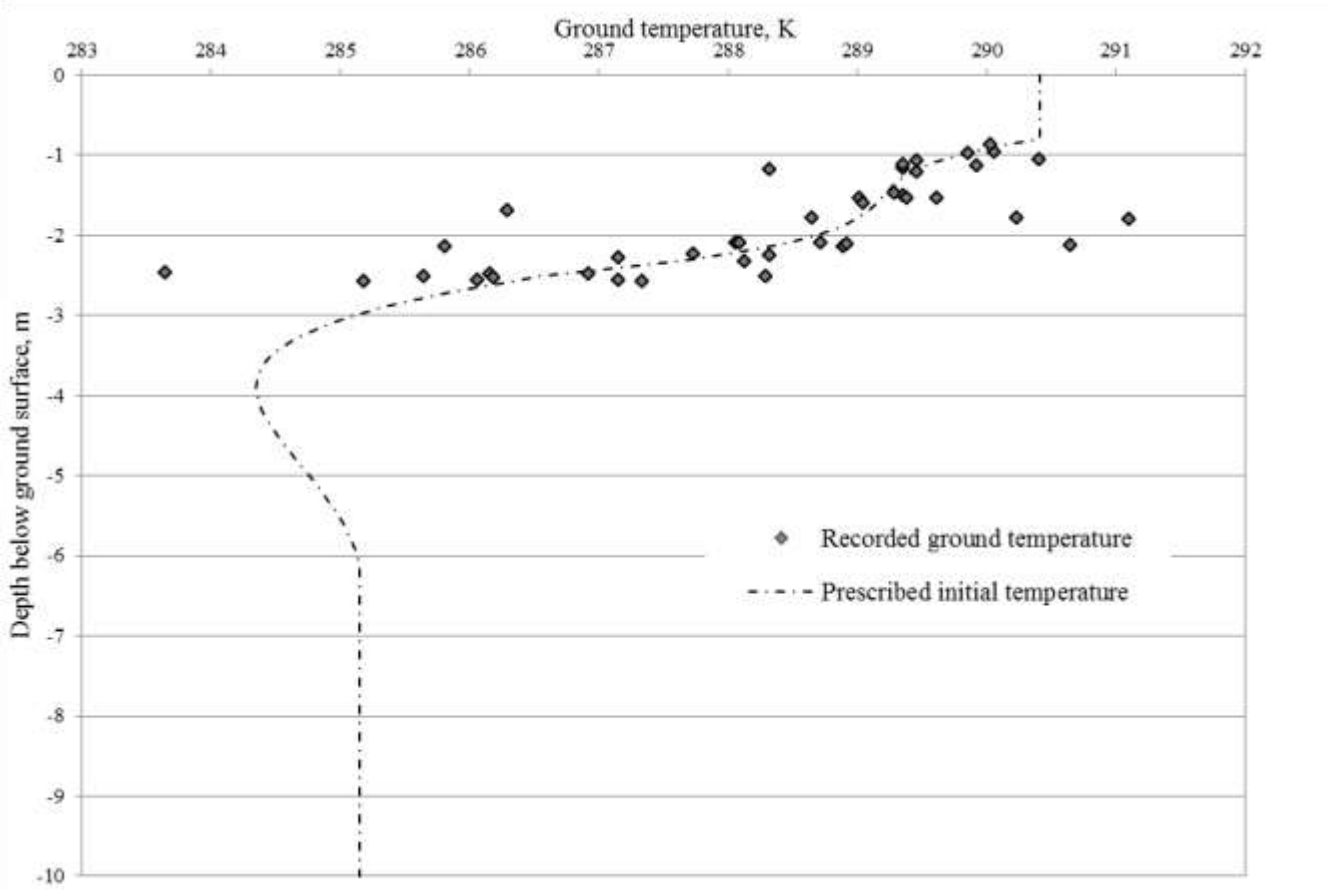

Figure 7.25 – Measured initial ground temperature on 1st September 2012 along with the initial ground temperature profile prescribed within the detailed cross-section BB validation exercise.

7.3.5 Material parameters

A total number of six soil samples were retrieved from both detailed cross-section AA and BB as part of ground investigations undertaken during the thermistor installation (see Chapter 3 for further details). The soil properties of the six samples reflected that of the overall site, i.e. the ground was heterogeneous and there was no apparent correlation between soil properties and spatial position. Based on these characteristics, a single material was prescribed within the two exercises. The material parameters were based on the six soil samples retrieved from each of the detailed cross-sections. The sample data can be found in Appendix C and the averaged material properties prescribed in the detailed cross-section AA and BB exercises can be found in Tables 7.6 and 7.7 respectively. The computation of the surface boundary condition required further material parameters related to the reflectivity, emissivity and aerodynamic drag of the ground surface (see Chapter 6 for further details regarding these parameters). For the current inspection period, the surface at the monitoring site could be described as long green grass (approximately 50 centimetres in length). The corresponding surface parameters prescribed in the model have been included within Tables 7.6 and 7.7.

Table 7.6 – Material parameters adopted within the detailed cross-section AA model.

Parameter	***Value***
Porosity	0.33
Density (solids)	2650 kg m^{-3}
Specific heat capacity (solids)	820 J kg K^{-1}
Thermal conductivity (solids)	2.93 W $m^{-1}K^{-1}$ (De Vries, 1966)
Saturated hydraulic conductivity	1 x 10^{-9} ms^{-1} (Gustafsson, 1946)
Shortwave reflection factor	0.22 (van Wijk & Scholte Ubing, 1966)
Longwave emissivity factor	0.97 (van Wijk & Scholte Ubing, 1966)
Aerodynamic drag at 2 meter height	0.05 m (Sheppard, 1947)

Table 7.7 – Material parameters adopted within the detailed cross-section BB model.

Parameter	***Value***
Porosity	0.4
Density (solids)	2650 kg m^{-3}
Specific heat capacity (solids)	820 J kg K^{-1}
Thermal conductivity (solids)	2.93 W $m^{-1}K^{-1}$ (De Vries, 1966)
Saturated hydraulic conductivity	1 x 10^{-9} ms^{-1} (Gustafsson, 1946)
Shortwave reflection factor	0.22 (van Wijk & Scholte Ubing, 1966)
Longwave emissivity factor	0.97 (van Wijk & Scholte Ubing, 1966)
Aerodynamic drag at 2 meter height	0.05 m (Sheppard, 1947)

7.3.6 Results

This section provides comparisons between the results from the validation simulations (detailed cross-sections AA and BB) and data collected at the monitoring site between September 1st and December 28th 2012. Ground temperatures collected at the monitoring site are compared with corresponding temperatures simulated within the models using the known thermistor positions. As previously discussed, and presented in Figures 7.16 and 7.17, each detailed cross-section contains a total of 41 thermistors. It proves unpractical to present results for all 41 thermistors for each detailed cross-section; therefore only salient results are presented in this section.

Based on Fourier's law of heat conduction, the ground closest to the ground-loop is subject to the greatest thermal gradients in a conduction dominant system. It can therefore be said that the ground-loop boundary condition has the greatest thermal impact within this ground region. Accordingly, the thermistors located in closest proximity to the ground-loop have been selected for greater scrutiny within this section. In addition to these, the far-field sensors have also been included to allow the model's performance beyond the ground-loops' thermal influence to be investigated. The far-field sensors are denoted AA12, AA13, AA14 and AA15 in Figure 7.16 and BA12, BA13, BA14 and BA15 in Figure 7.17. A full set of results presenting a comparison between the collected data and detailed validation models can be found in Appendix G. Figures 7.24, 7.25, 7.26, 7.27, 7.28, 7.29 and 7.30 present monitored and simulated ground temperatures for detailed cross-section A. The local coordinates (depth and x-displacement according to Figure 7.16) of the thermistors are contained within the Figure titles. The average absolute errors between the monitored and simulated results are also presented on the graphs.

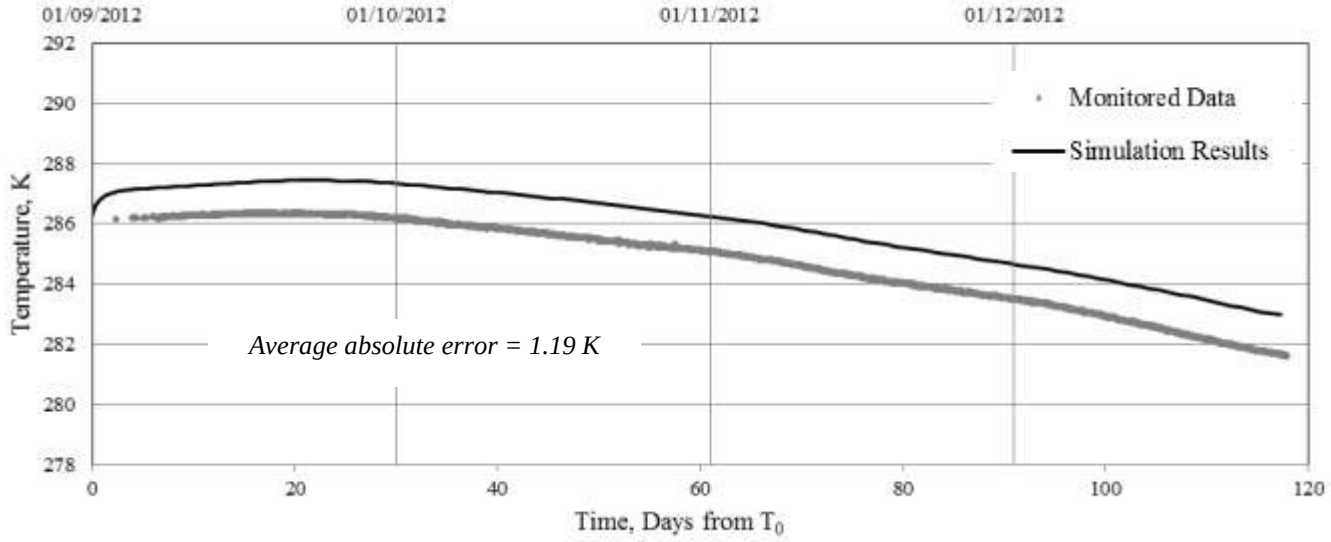

Figure 7.26 - Simulated and monitored ground temperature according to thermistor AA 12 (depth = 2.617m and x = -5.232m).

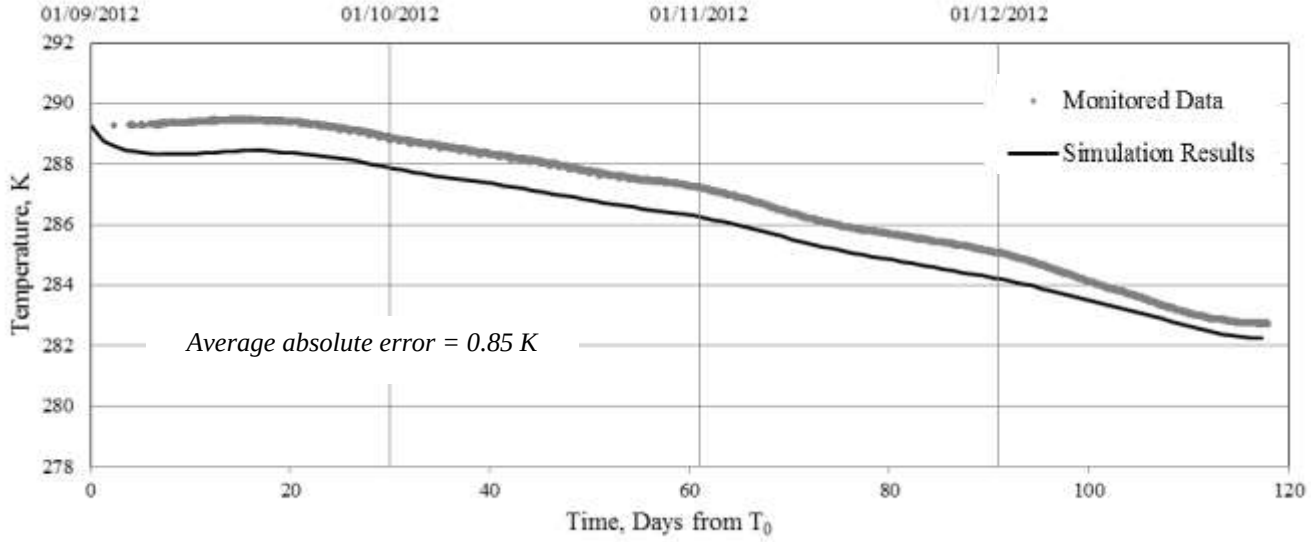

Figure 7.27 - Simulated and monitored ground temperature according to thermistor AA 13 (depth = 2.099m and x =-5.234m).

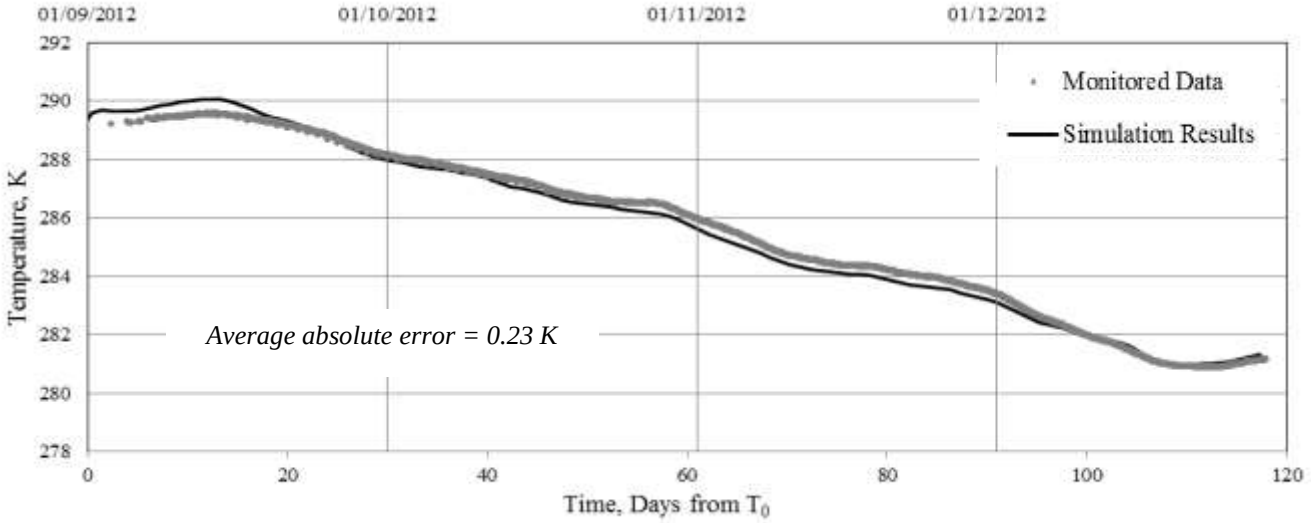

Figure 7.28 - Simulated and monitored ground temperature according to thermistor AA 14 (depth = 1.4m and x = -5.231m).

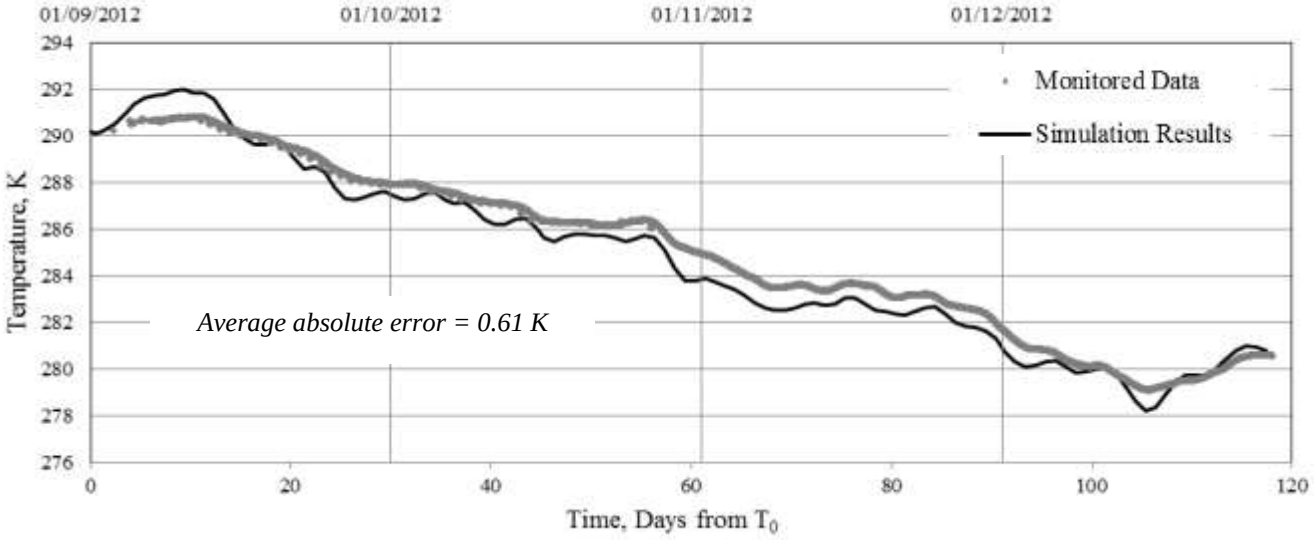

Figure 7.29 - Simulated and monitored ground temperature according to thermistor AA 15 (depth = 0.748m and x = -5.194m).

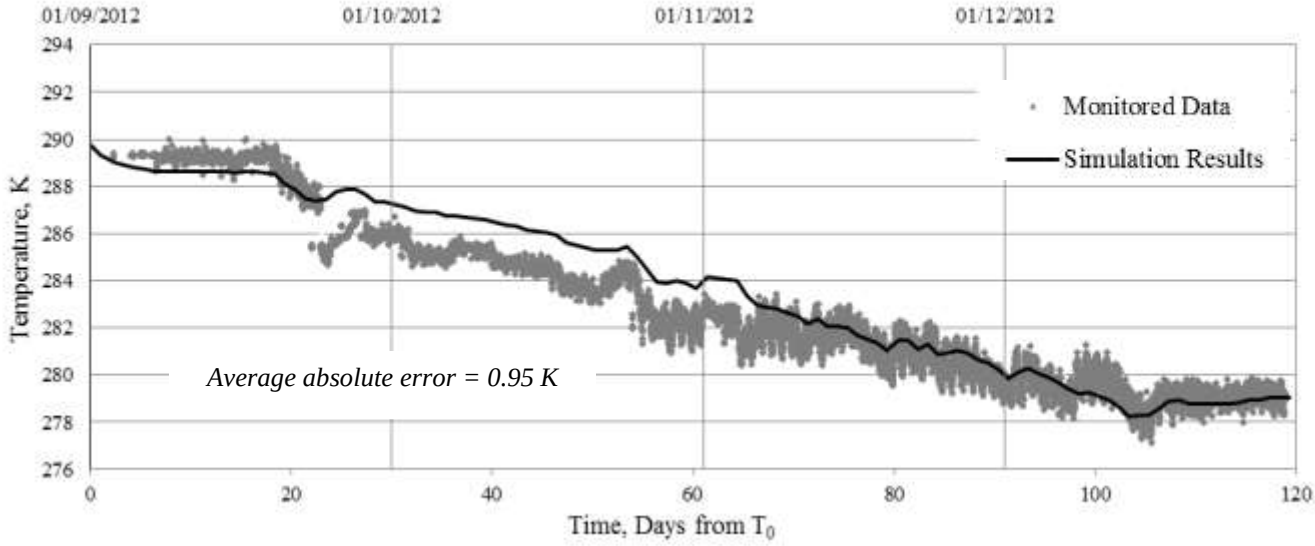

Figure 7.30 – Simulated and monitored ground temperature according to thermistor AB 4 (depth = 1.914m and x = -0.368m).

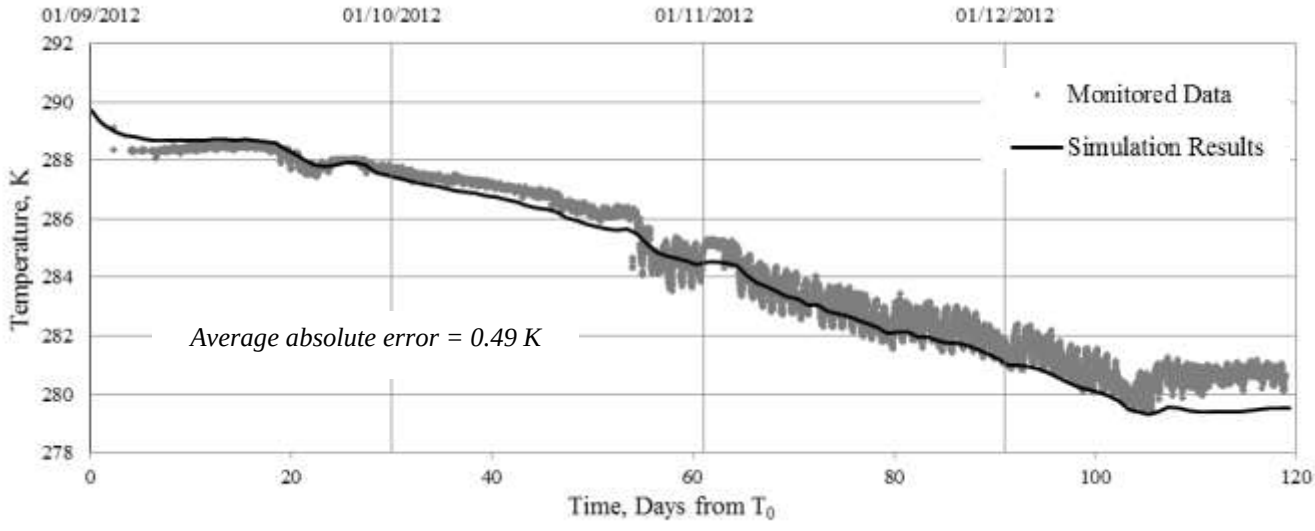

Figure 7.31 - Simulated and monitored ground temperature according to thermistor AB 12 (depth = 1.909m and x = 0.547m).

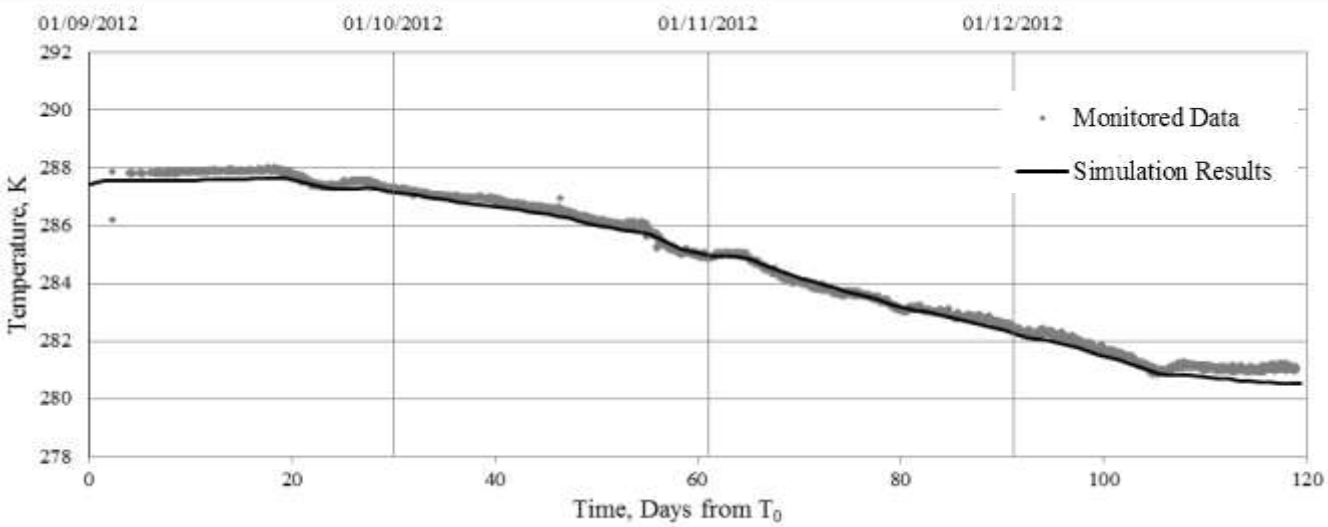

Figure 7.32 - Simulated and monitored ground temperature according to thermistor AB 14 (depth = 2.007m and x = 0.036m).

Figures 7.26 to 7.29 present the simulated and monitored ground temperatures for the far-field thermistors, beyond the thermal influence of the ground-loop. In general it can be said that the simulated ground temperatures are in good agreements with the collected ground data for the duration of the simulation period. This shows that beyond the ground loops' thermal influence, the ground temperatures predicted by the model are in close agreement within the collected data. This provides some confidence moving forward, that the surface boundary condition is functioning correctly within the model allowing the ground-loop boundary to be subsequently investigated.

The four thermistors located in closest proximity to the ground-loop within detailed cross-section AA are denoted AB4, AB7, AB12 and AB14. Thermistor AB7 failed after installation therefore no ground data is available for comparison. Figures 7.30 to 7.32 present the simulated and monitored ground temperature data for the remaining thermistors in close proximity to the ground-loop.

In general, it can be said that the trends exhibited by the monitored and simulated data are in close agreement for all three cases, particularly for the thermistor AB 14 (see Figure 7.32). The data collected by thermistors AB4 and AB12 (shown in Figure 7.30 and 7.31 respectively) however, showed short-term temperature fluctuations which were not predicted by the model. The two thermistors showing temperature fluctuations (i.e. AB4 and AB12) are located immediately adjacent to the ground-loop therefore it has been assumed that these fluctuations are due to the intermittent operational use of the ground source heat system. In comparison, thermistor AB14 (Figure 7.32) is located at a greater distance from the ground-loops and as a result it shows smaller fluctuations.

The omission of the fluctuations from the simulation results could be attributed to the resolution of the simulation data and maximum time-step prescribed within the model. Ground

temperature data was collected at 15 minute intervals whereas a 6 hour time-step was used for the majority of the simulation. The greater resolution of ground temperature data with time would allow short-term fluctuations, omitted by the simulation, to be recorded. This would explain why the general trends between the monitored and simulated data concur despite the omission of short-term fluctuations.

Figures 7.33, 7.34, 7.35, 7.36, 7.37, 7.38, 7.39 and 7.40 present monitored and simulated ground temperatures for detailed cross-section BB. The local coordinates (depth and x-displacement according to Figure 7.17) of the thermistors are contained within the Figure titles. The average absolute errors between the monitored and simulated results are also presented on the graphs.

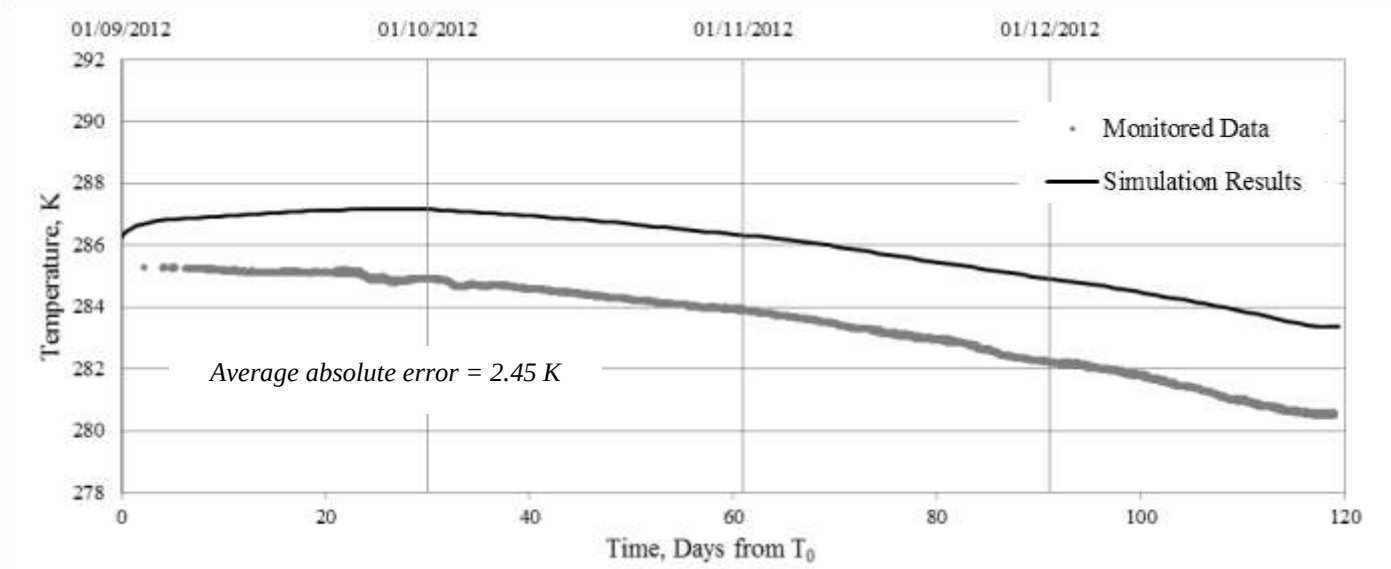

Figure 7.33 - Simulated and monitored ground temperature according to thermistor BA 12 (depth = 2.58m and x = -5.722m).

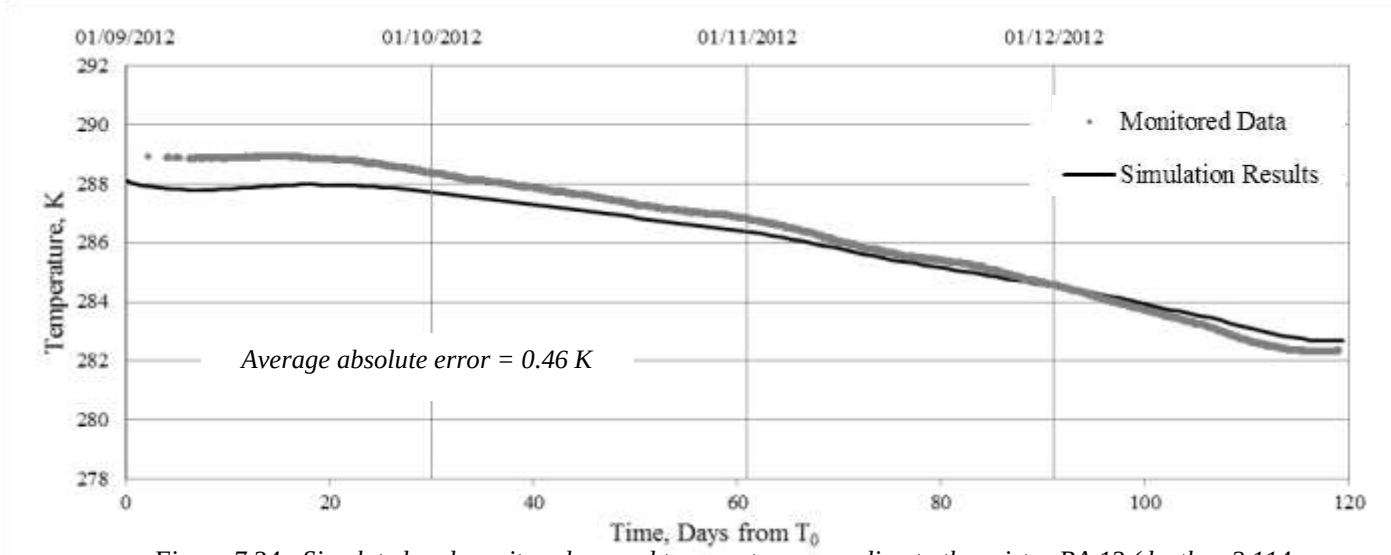

Figure 7.34 - Simulated and monitored ground temperature according to thermistor BA 13 (depth = 2.114m and x = -5.692).

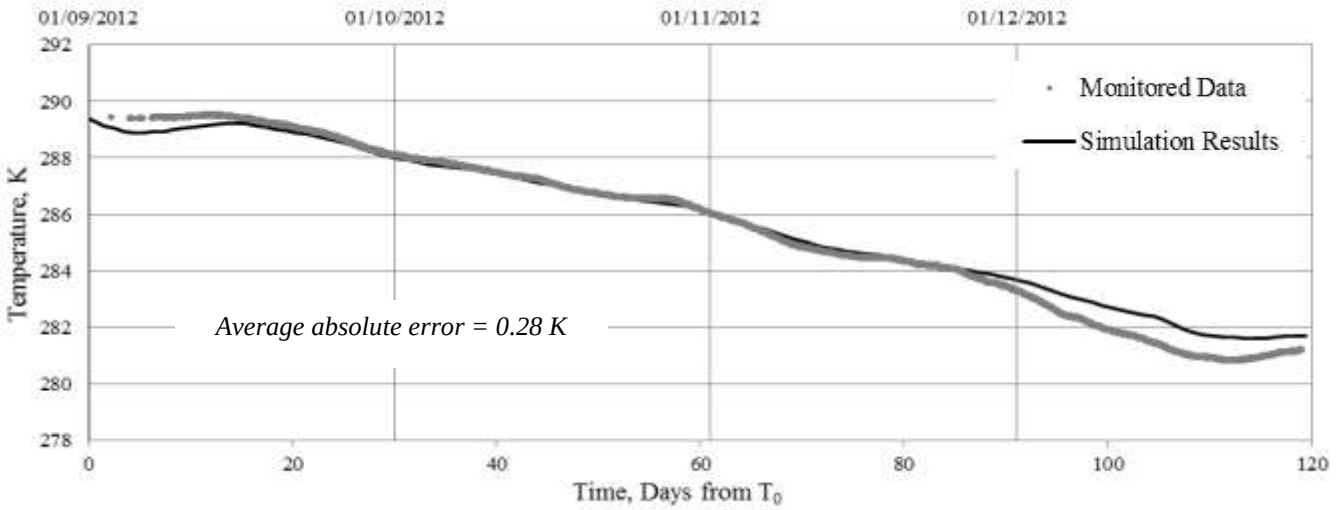

Figure 7.35 - Simulated and monitored ground temperature according to thermistor BA 14 (depth =1.535m and x = -5.723m).

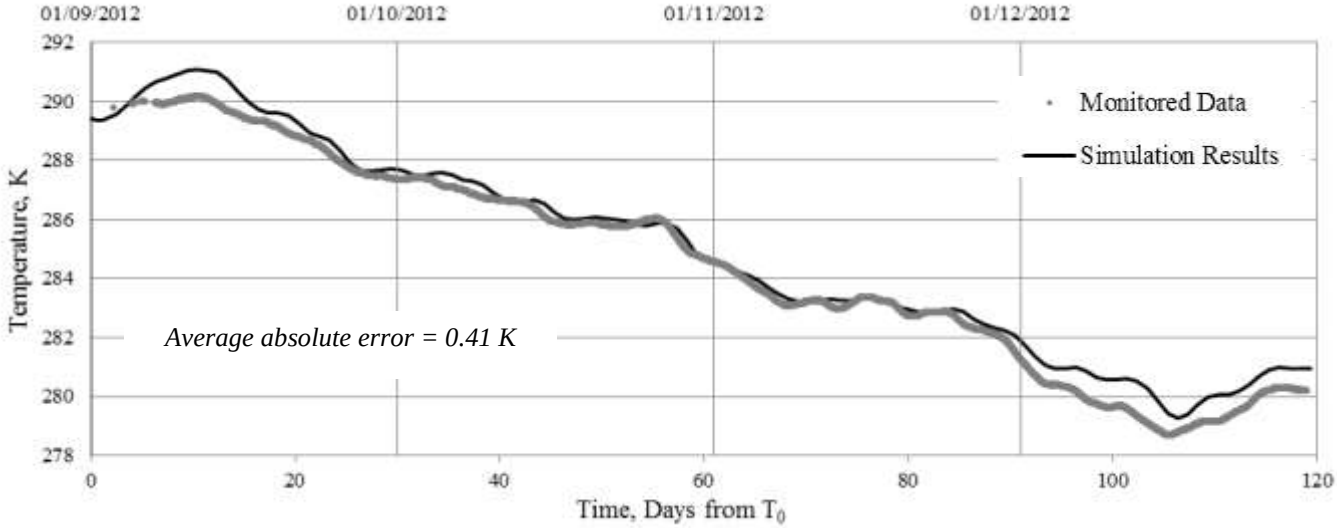

Figure 7.36 - Simulated and monitored ground temperature according to thermistor BA 15 (depth = 0.873m and x = -5.700m).

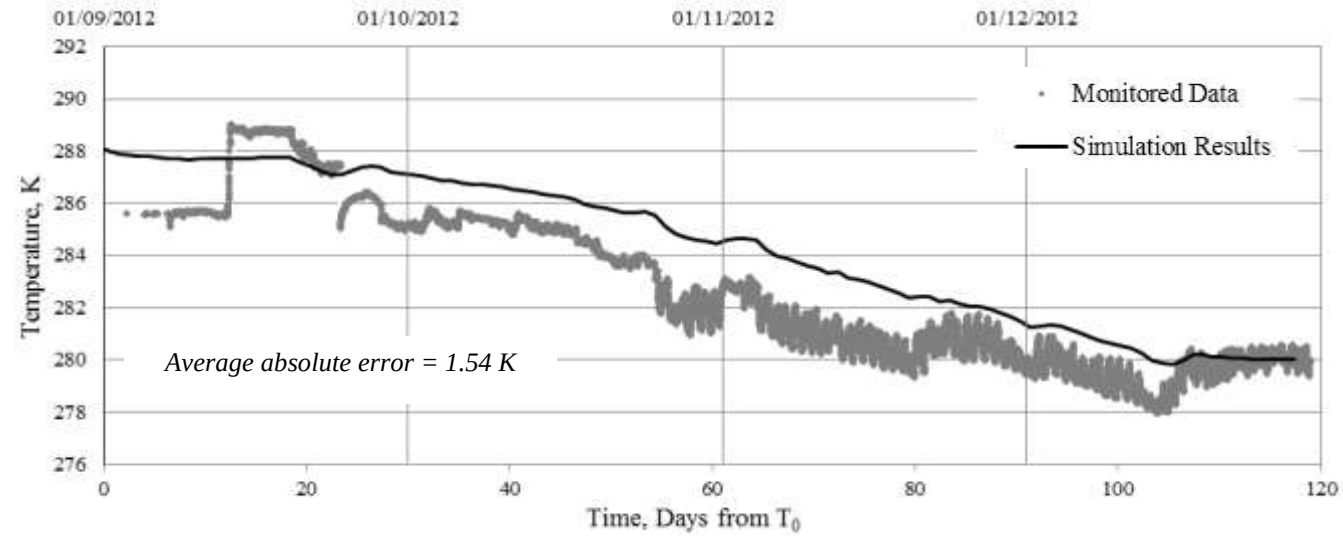

Figure 7.37 - Simulated and monitored ground temperature according to thermistor BB 4(depth = 2.136m and x = -0.541m).

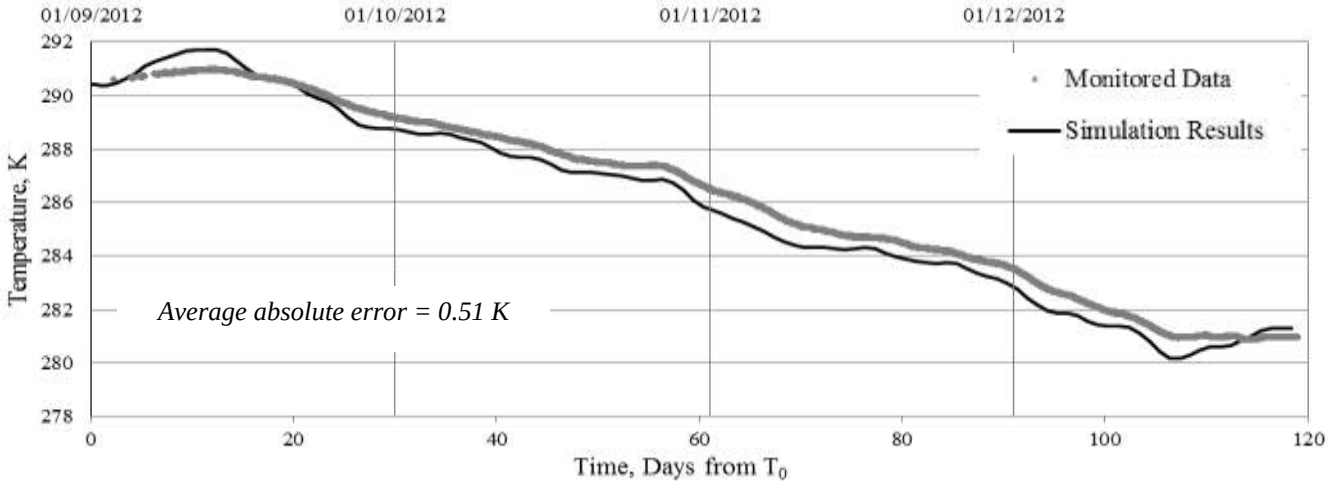

Figure 7.38 - Simulated and monitored ground temperature according to thermistor BB 7 (depth =2.131m and x =-0.113).

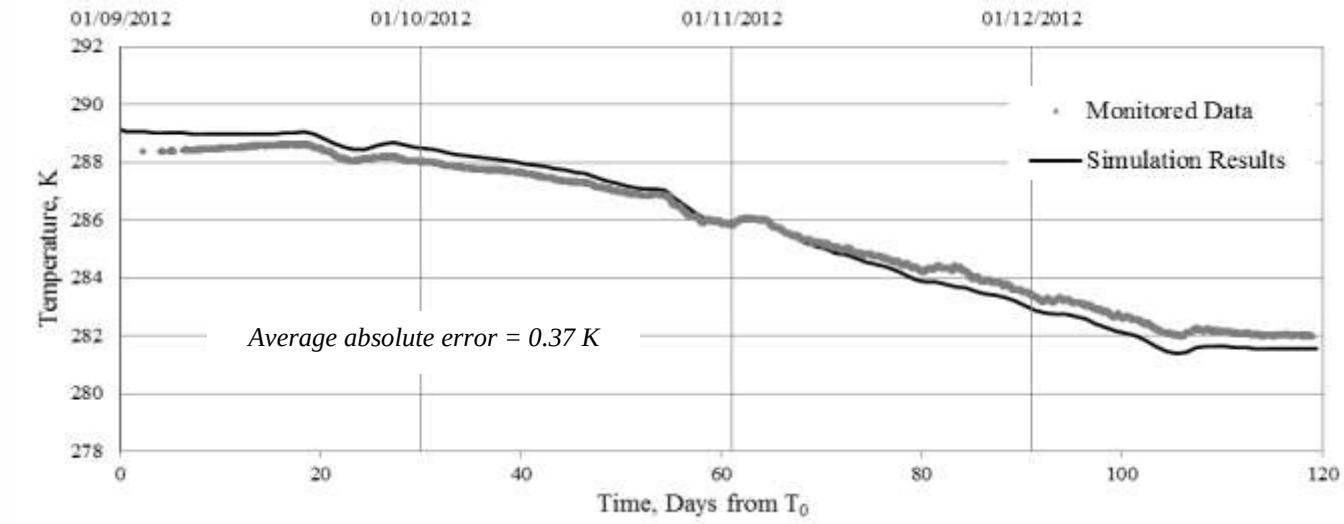

Figure 7.39 - Simulated and monitored ground temperature according to thermistor BB 10 (depth =2.56m and x = -0.067m).

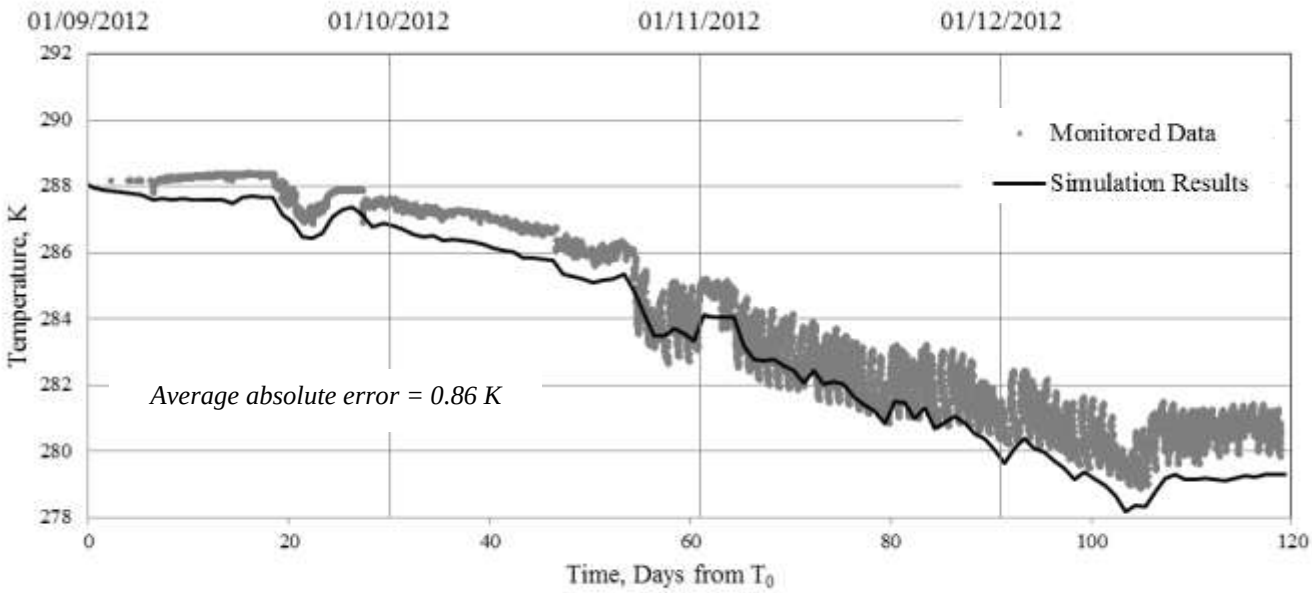

Figure 7.40 - Simulated and monitored ground temperature according to thermistor BB 12 (depth =2.144m and x = -0.331m).

Again the monitored far-field ground temperatures beyond the thermal influence of the ground-loop have been compared with simulation results in order to ascertain whether the surface boundary condition is performing correctly within the model. Figures 7.33 to 7.36 present the simulated and monitored ground temperatures for the far-field thermistors BA12 to BA15. It can be said that the simulated ground temperature shows good agreement with the monitored ground temperature at three of the four locations, with the one exception being thermistor BA12 (see Figure 7.33). At this location, there is an average absolute error of 2.45 K between the simulated and monitored data which is far greater than the remaining three far-field locations. Despite this, the general temperature trend exhibited by the monitored ground data was reflected by the simulated data, albeit at a lower temperature. Based on these results, it has been deduced that the surface boundary condition is functioning correctly within the model allowing the ground-loop boundary to be subsequently investigated with confidence.

The four thermistors located in closest proximity to the ground-loop within detailed cross-section BB are denoted BB4, BB7, BB10 and BB12. Figures 7.37 to 7.40 present the simulated and monitored ground temperature data for these thermistors. In general it can be said that the ground temperature trends exhibited by the simulation results concur with the monitored ground data, especially for thermistors BB7 and BB10. The thermistors BB4 and BB12 (found in Figures 7.37 and 7.40 respectively) did however show short-term fluctuations which were not predicted by the simulation. It is believed that this was due to the resolution of the monitored ground data and the minimum time-step adopted in the simulations as previously discussed. It is also noted that the monitored ground temperature data presented in Figure 7.37 is intermittent for approximately the first 30 days of the simulation period. This has been attributed to a poor wire connection between the multiplexer and data-logger. Further details regarding this problem have been presented in Chapter 3. Beyond the first 30 days, the connection was rectified and the quality of data subsequently improved.

Graphs containing the simulated and monitored ground data for the remaining thermistors located within detailed cross-sections AA and BB can be found in Appendix G. The results presented on these graphs generally reflect the findings previously presented within this section. In general it can be said that the monitored ground temperature data had good agreement with the simulation results.

The preceding sections have presented two validation exercises for the developed model under heat extraction conditions. The developed ground surface and ground-loop boundary conditions were prescribed within the models. After inspecting the results it can be deduced that the general ground temperature trends exhibited by the simulated results agreed with the monitored data. From the findings presented, it can be said that the developed model is capable of simulating the ground thermal behaviour under heat extraction conditions for the presented monitoring site. The

developed uniform ground-loop boundary condition has been deemed capable of representing the ground-loop boundary flux induced by the ground source heat system at the monitoring site and therefore validated.

7.4 Conclusions

This chapter presented the validation of the developed model which compromises of the previously developed TH formulations in conjunction with the ground surface and ground-loop boundary conditions. The model was validated against data collected at the monitoring site in a two stage process.

Stage I considered the pre-heat extraction phase at the monitoring site, during which no heat was extracted via the ground-loop. This allowed the model performance to be investigated when only the surface boundary condition was implemented. Comparisons between the simulated and monitored ground temperatures for a 110 day period showed that the developed models were capable of representing the ground behaviour in response to surface climatic conditions and heat extraction to a depth of 2.6 meters. The results thereby indicate that the theoretical and numerical formulations presented in Chapters 5 and 6 are representative of the ground behaviour at the monitoring site. In addition, the results indicate that the numerical parameters and conditions prescribed in the validation exercises were representative of the site conditions.

Stage II investigated the model performance during a 120 day period of heat extraction, employing both the developed ground surface and uniform ground-loop boundary conditions. Comparisons between simulated and monitored ground data during periods of zero and active heat extraction indicate that the model is capable of simulating the thermal recharge of the ground and cyclic/intermittent operational loads of a horizontal ground source heat system. Moving forward, this provides confidence in the developed model's ability to investigate the long term ground behaviour in response to heat extraction over a number of years. To the author's knowledge, the developed model has been subject to a more rigorous testing programme than previous related studies through comparisons with the collected data.

References

Busby, J., Kingdon, A. & Williams, J., 2011. *The measured shallow temperature field in Britain.* Nottingham: British Geological Survey.

De Vries, D. A., 1966. Thermal properties of soils. In: W. R. van Wijk, ed. *Physics of the Plant Environment.* Amsterdam: North Holland Publishing Co., p. 210.

Gustafsson, Y., 1946. *Die Stromungsverhaltnisse in gedrahntem Boden.* Stockholm: Acta Agricult, Suecana.

Hillel, D., 1980. *Applications of soil physics.* New York: Academic Press.

Kaye, G. W. C., Laby & M, T., 1973. *Tables of physical and chemical constants.* 14th ed. London: Longmans.

Kusuda, T., 1975. *The effect of ground cover on earth temperature.* Fort Worth, Texas, USA, Conference proceedings of 'Alternatives in energy conservation: The use of earth-covered buildings'.

Kusuda, T. & Achenbach, P. R., 1965. Earth temperature and thermal diffusivity at selected stations in the United States. *ASHRAE Trans,* 71(1), pp. 61-75.

ME Global, 2008. *Ethylene Glycol - Product Guide.* s.l.:ME Global Group of Companies.

Sheppard, P. A., 1947. The aerodynamic drag of the earth's surface and the value of von Karman's constant in the lower atmosphere. *Proceedings of the Royal Society,* pp. 208-222.

Siegfried, R., 2005. Ullmann's Encycolpedia of Industrial Chemistry. In: D. Mayer, ed. *Ethylene Glycol.* Weinheim: Wiley.

Thomas, H. R., 1987. Non-linear analysis of heat and moisture transfer in partly saturated soil. *Journal of Engineering Mechanics, American Society of Civil Engineering,* 1(113), pp. 1163-1180.

van Genuchten, M. T., 1980. A closed-form equation for predicting hydraulic conductivity of unsaturated soils. *Journal of Soil Society of America,* 44(1), pp. 892-898.

van Wijk, W. R. & Scholte Ubing, D. W., 1966. Radiation. In: W. R. van Wijk, ed. *Physics of the Plant Environment.* Amsterdam: North Holland Publishing Co., p. 87.

Chapter 8

Long-term ground behaviour and surface effects

8.1 Introduction

Numerical simulations investigating the long-term ground behaviour of horizontal ground source heat systems will be presented within this chapter. The meaning of the expression 'long-term' within the current scope of work corresponds to the anticipated operational life of horizontal ground source heat systems. Simulations have been performed using the coupled thermal-hydraulic (TH) numerical model previously validated within Chapter 7.

The long-term investigations presented within the scope of this chapter can be divided into four sections. Section 8.2 contains the long-term simulations of the monitoring site previously detailed in Chapter 3, to investigate the ground behaviour in response to heat extraction throughout the design life of the system.

Section 8.3 provides comparisons between the serial and parallel techniques previously detailed in Chapter 5. The performance of the techniques was quantitatively investigated by comparing the computational times from a series of long-term TH simulations.

Section 8.4 presents a series of simulations investigating the effects of ground surface properties on the long-term ground behaviour. Within this investigation, a number of different rural and urban surface types/materials are considered.

Finally, section 8.5 investigates the long-term validity of the MIS 3005 design standard currently endorsed by the UK government for the design and installation of horizontal ground source heat systems. The ground behaviour in response to two varying ground-loop configurations, designed accordance to the standard, is investigated and compared to the monitoring site ground behaviour. Concluding remarks are given in section 8.5.

8.2 Long-term simulations of the monitoring site

The following section aims to investigate the long-term ground behaviour of the monitoring site previously presented in Chapter 3. As previously described, the expression 'long-term' corresponds to the anticipated operational life of horizontal ground source heat systems. 'MIS (Micro-generation Installation Standard) 3005', the current design standard endorsed by the Department of Energy and Climate Change (DECC), suggests that horizontal ground source heat systems should be designed to efficiently operate for a minimum of 20 years (MCS, 2008). The simulations undertaken within the scope of this work have therefore being carried out for a period of 20 years. As described in Chapter 2, the majority of previous numerical investigations adopted a time period far smaller than this, often in the region of hours or days. The current section contains a simulation which will investigate the annual ground behaviour, including periods of heat extraction (i.e. winter) and thermal recovery (i.e. summer). Details regarding the model domains, initial conditions, boundary conditions and material properties are provided in the following subsections. The results attained from the simulation will then be collectively presented and discussed accordingly.

8.2.1 Domain and constitutive relationships

The long-term TH simulation presented within the current section has been performed using a two-dimensional domain. A two-dimensional domain has been selected following the ground temperature behaviour observed at the monitoring site (refer to Chapter 4) and validation results (refer

to Chapter 7). Upon review of the ground data presented in Chapter 4 and validation results presented in Chapter 7, it is possible to deduce that the ground behaviour trends exhibited across the site are very similar in nature despite the varying ground properties reported in Chapter 3. In order to avoid unnecessary repetition only one two-dimensional model has been produced for investigation here.

The two-dimensional model has been based on the system and ground characteristics found at detailed cross-section AA. Further details regarding the exact location of detailed cross-section AA can be found in Chapter 3. The selected domain extends downwards to a depth of 10 meters and across to a width of 10 meters. A schematic showing the domain, initial conditions, boundary conditions and prescribed material for the long-term simulation of the monitoring site is presented in Figure 8.1. The depth of the domain has been selected based on previous work undertaken by Kusuda & Achenbach (1965) and Kusuda (1975) which suggested there should be no appreciable ground temperature variation at a depth of 10 meters in response to seasonal climatic variations. The width of the domain has been selected such that the ground modelled at the horizontal extremity of the domain remains unaffected by ground-loop heat extractions. It can therefore be said that the ground simulated at the horizontal extremities represents undisturbed TH ground conditions.

Two circles with a diameter of 0.04 m have been used to represent the external circumference of the ground-loop within the two-dimensional domain (see Figure 8.1). The ground-loop itself has not been explicitly represented in the model; thereby its thermal capacity and resistance has been assumed negligible. This has been deemed acceptable based on the relatively thin polyethylene ground-loop pipe which measures 2.4 mm in thickness.

The constitutive relationships used to calculate the thermal conductivity, heat capacity, hydraulic conductivity and Soil Water Characteristic Curve (SWCC) are the same as those previously highlighted in Chapter 5. For convenience, they have been summarised in Table 8.1. Details regarding the parameters included within the equations can be sourced in Chapter 5.

The domain has been discretised using unstructured non-uniform linear triangular elements. As depicted in Figure 8.1, the elements are smaller at the top of the domain where the greatest thermal and hydraulic changes are expected, thus providing a finer mesh. A varying time-stepping algorithm was applied with an initial time-step of 1 second and the simulation period was 630,720,000 seconds, corresponding to a period of 20 years.

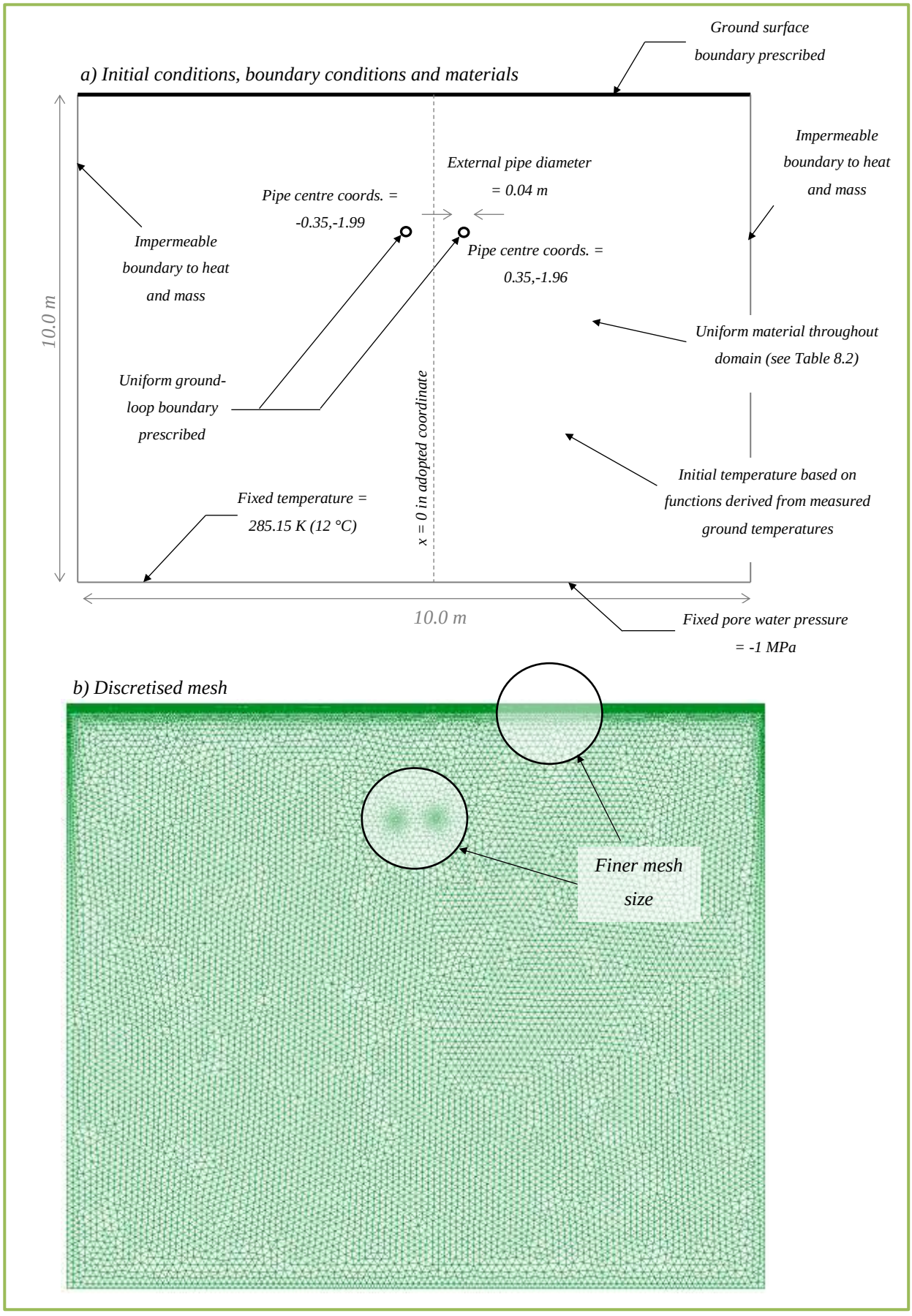

Figure 8.1 – Schematic showing the domain, initial conditions, boundary conditions, prescribed material (a) and discretised mesh used for the monitoring site long-term simulation (b).

Table 8.1 – Constitutive relationships used in the simulation.

Material parameter	*Relation*
Thermal conductivity	$\lambda = \prod_{i=1}^{3} \lambda_i^{\chi_i}$
Heat capacity	$H_c = (1-n)C_{ps}\rho_s + n\left(C_{pl}S_l\rho_l + C_{pv}S_a\rho_v + C_{pda}S_a\rho_{da}\right)$
Hydraulic conductivity	$K_l(h) = \frac{\{1 - (\alpha h)^{n-1}[1 + (\alpha h)^n]^{-m}\}^2}{[1+(\alpha h)^n]^{m/2}} \qquad \left(m = 1 - {}^1/_n\right)$
SWCC	$\theta = \theta_{res} + \frac{(\theta_{sat} - \theta_{res})}{[1 + (\alpha h)^n]^m}$

8.2.2 Initial and boundary conditions

The surface and uniform ground-loop boundary conditions, formulated in Chapter 6 and validated in Chapter 7, have been prescribed within the long-term simulation. In order to compute the surface boundary condition, the climatic variables of ambient air temperature, solar radiation, rainfall, relative humidity and wind speed need to be provided within model. Upon first inspection it seems logical to prescribe the climatic variables according to data recorded at the monitoring site however, prior to running the long-term simulations only 13 months of climatic data had been recorded. Analysis of the climatic data in Chapter 4 revealed that the 13 month period in question included some climatic irregularities (e.g. the abnormally cold March of 2013). To avoid prescribing climatic abnormalities throughout the 20 year simulation period, average annual data of the ambient air temperature, rainfall and relative humidity were prescribed according to historical climate data recorded in the region.

Unlike the previous climatic variables, solar radiation and wind speed are known to be particularly sensitive to bespoke site characteristics such as local structures and topography. In these instances, the uncertainty associated with a single years' worth of data was deemed to be outweighed by the influence of local site variables, therefore data collected from the monitoring site was prescribed within the model.

Ideally, climatic data for the ambient air temperature, rainfall and relative humidity would be sourced from a single local weather station however this was not possible due to the scarcity of suitable sources. Instead, the ambient air temperature and rainfall were based on measurements

recorded between 1981 and 2010 at a weather station located in Lyonshall outside Hay-on-Wye (MET Office, 2013). The relative humidity data used is based on measurements recorded between 2003 and 2013 from a Royal Air Force based located in Credenhill, again outside Hay-on-Wye (Tutiempo, 2013). The two weather stations are located at distances of 12 and 14 km from the monitoring site respectively. Figure 8.2 shows the ambient air temperature and rainfall prescribed within the model according to data recorded at the Lyonshall weather station while Figure 8.3 shows the relative humidity prescribed within the model according to data recorded at the Credenhill weather station. The solar radiation and wind speed data, based on measurements recorded at the monitoring site and prescribed within the long-term model, can be found in Figures 8.4 and 8.5 respectively.

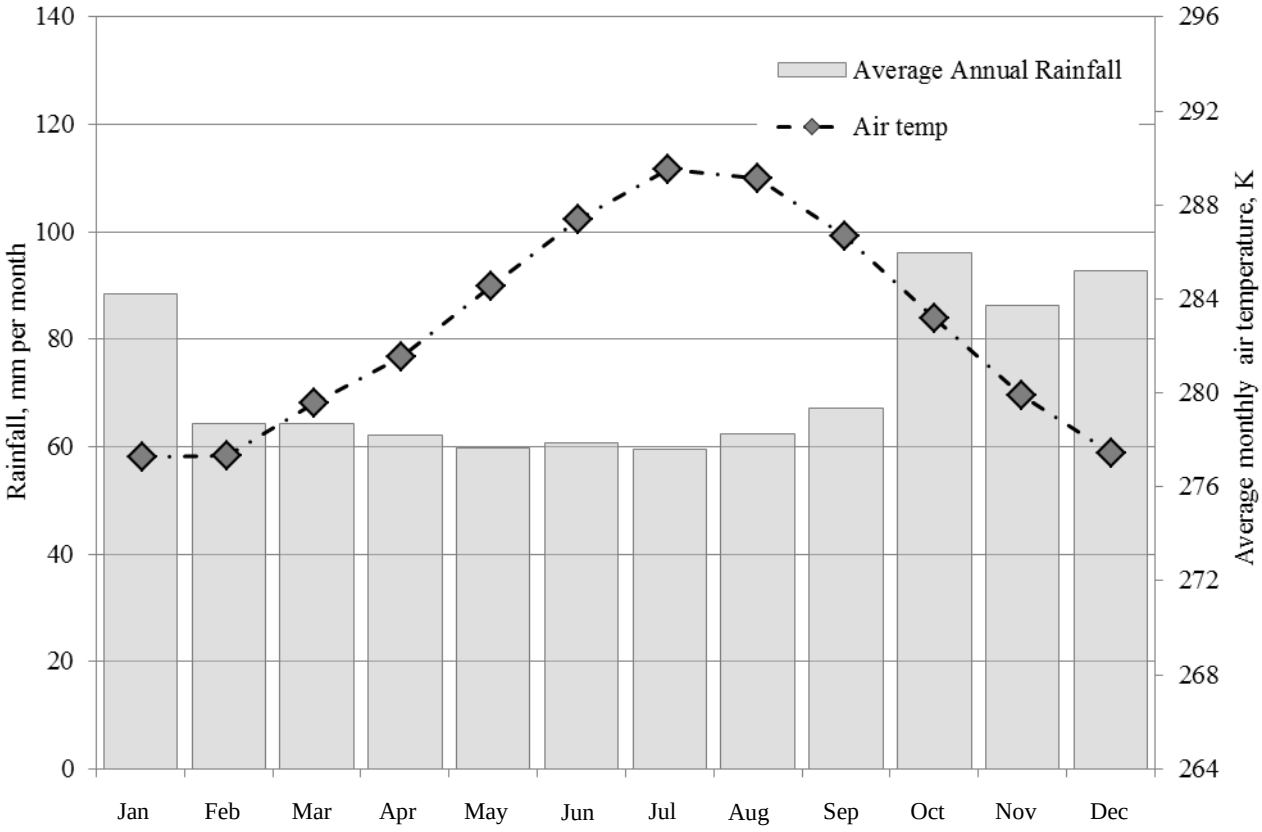

Figure 8.2 – Average monthly ambient air temperature and rainfall according to data recorded between 1981 and 2010 at Lyonshall (MET Office, 2013).

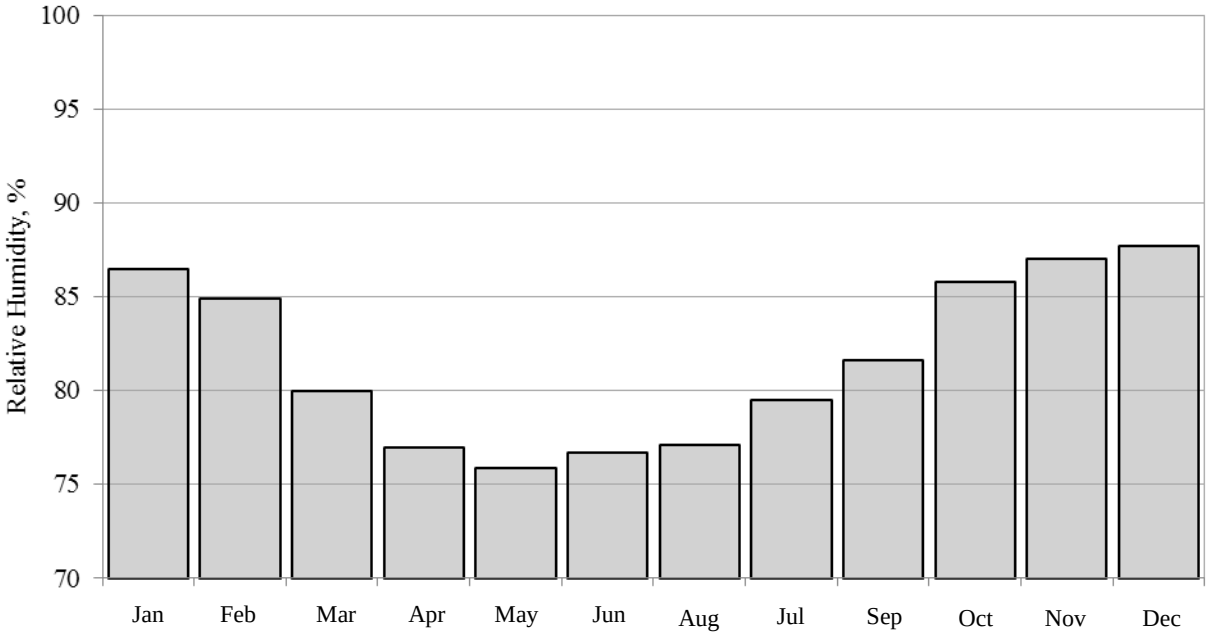

Figure 8.3 – Average monthly air relative humidity according to data recorded between 2003 and 2013 at Credenhill (Tutiempo, 2013).

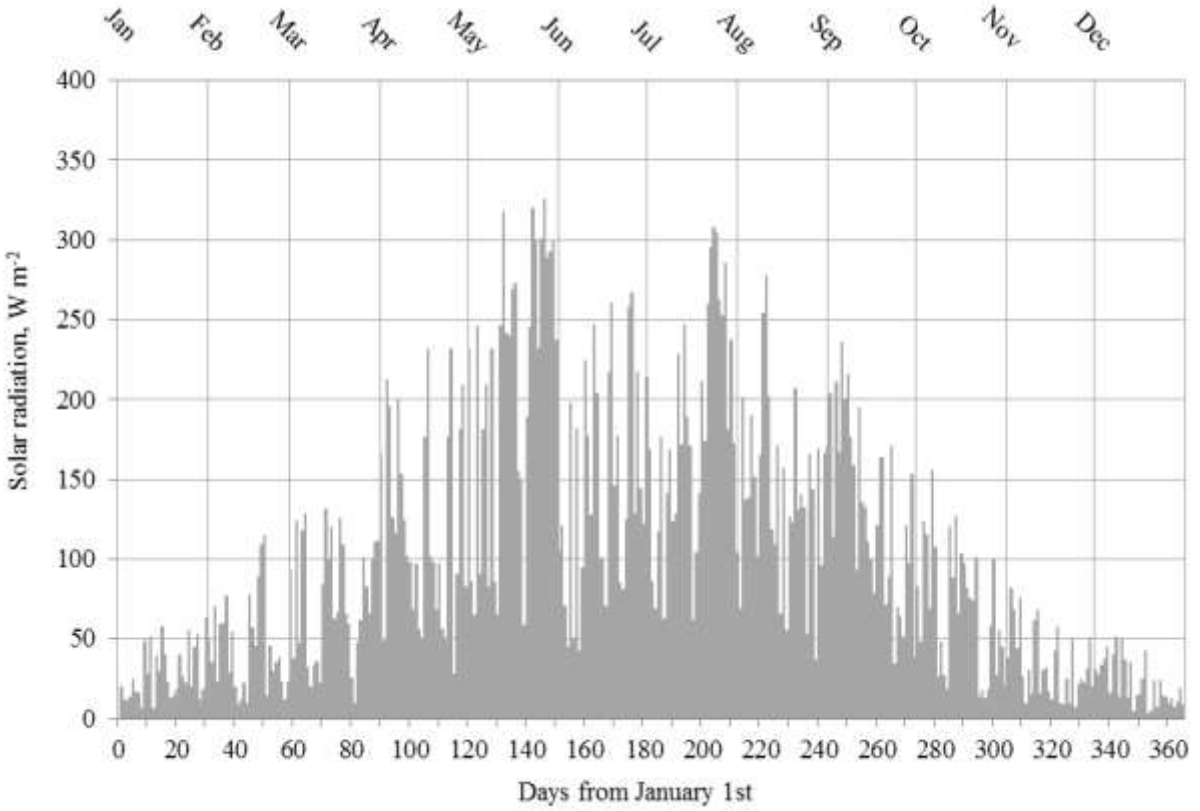

Figure 8.4 – Average daily solar radiation recorded at the monitoring site.

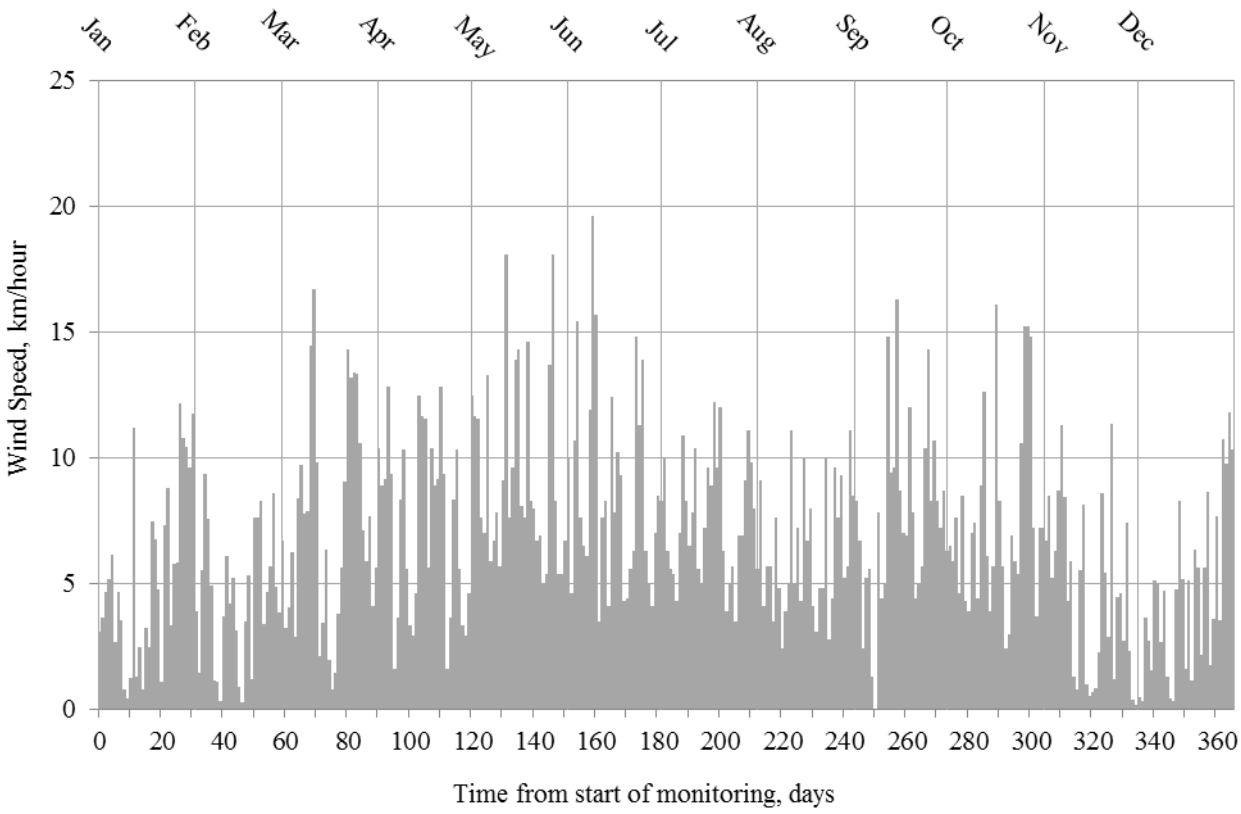

Figure 8.5 – Average wind speed recorded at the monitoring site.

Similar to the simulations presented in Chapter 7, the uniform ground-loop boundary condition has been prescribed to represent heat exchanged via the ground-loop. The computation of the uniform ground-loop boundary condition requires a heating load, representative of the horizontal ground source heat system in question. For the current case, a heating load has been calculated based on heat pump data (fluid flow and temperatures) recorded at the monitoring site. Further details regarding this calculation can be found in Chapter 6. Ideally, multiple years of data would be used in order to calculate an average annual heating load profile however this is not feasible within the time constraints of the current project. The heating load prescribed within the long-term simulations is presented in Figure 8.6.

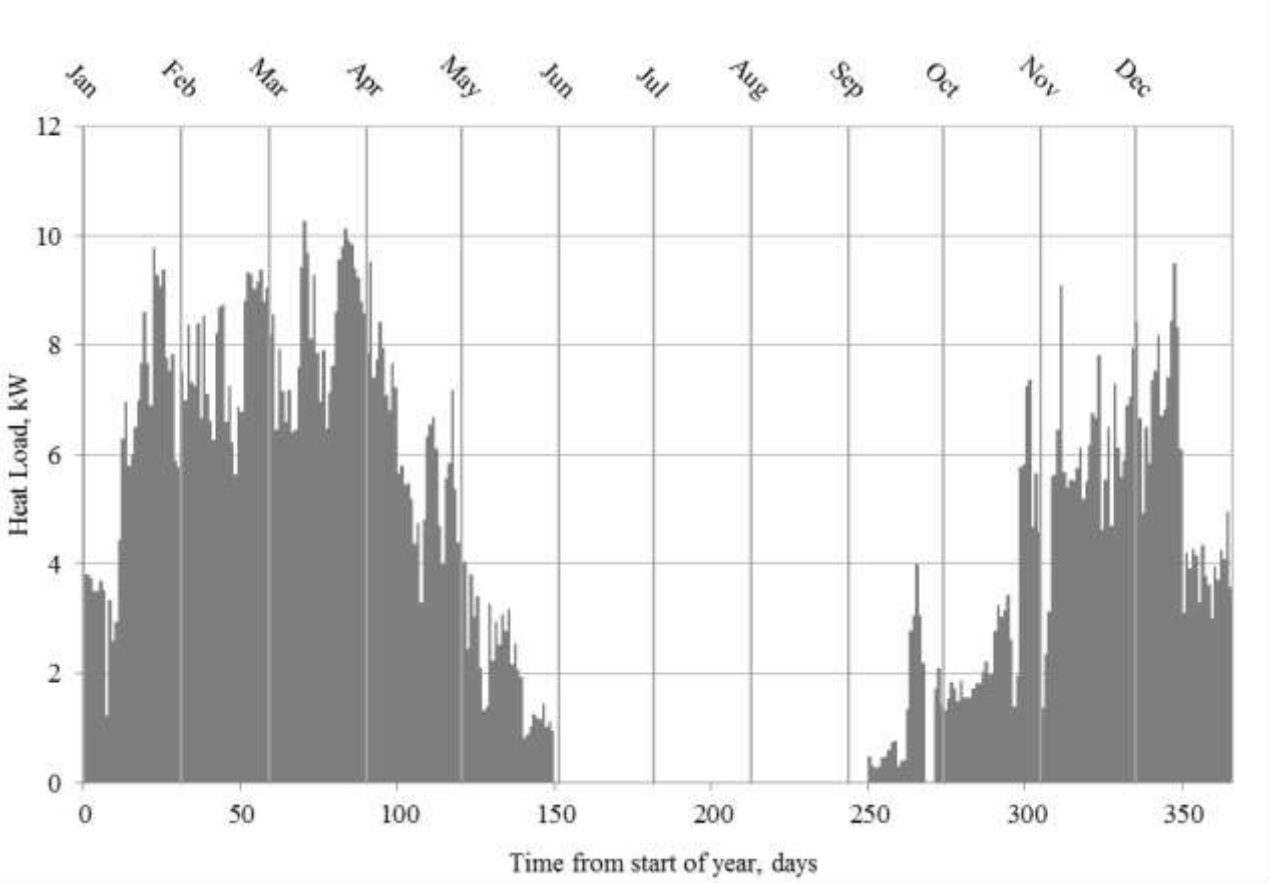

Figure 8.6 – Average daily heat load prescribed in the long-term simulations.

Figure 8.6 shows that only 9 months of heating data was recorded at the monitoring site during the inspection period, between September 2012 and June 2013. Unlike climatic data, horizontal ground source heat pumps are highly bespoke in their design and operation therefore the data recorded at the monitoring site is by far the most representative available. Although this period falls short of a whole calendar year, the heating system installed at the site was designed for space heating only (i.e. not for the provision of hot water) therefore it can be deduced that the inspection period has captured the majority of heat extraction anticipated for a single calendar year. Using knowledge regarding the operational characteristics of the system and the anticipated summer temperatures, a zero heating load has been assumed for the months of June, July and August (see Figure 8.6) in order to complete an annual heating load profile.

The heating load shown in Figure 8.6 represents the average daily heating load recorded at the monitoring site. Although the average daily heating load allows the heat extracted for a given day to be represented, it is important to recognise that it does not allow the intermittent operational behaviour of the heat pump to be explicitly represented. Chapter 4 previously discussed how the intermittent operational characteristics of the heat pump at the monitoring site can result in the system being turned on and off multiple times within one hour. Within current investigations the inclusion of

such behaviour would greatly restrict the maximum permissible simulation time-step, thus significantly increasing computational time and effort. Previous research efforts, most notably by Hellstrom (1991), have shown that long-term ground responses can be modelled using average heating loads. The application of daily heating loads has therefore been deemed acceptable within the current scope of work.

The initial ground temperature profile prescribed in the model is based on the ground temperatures recorded on 1st January 2013 (i.e. the starting point of the model). Figure 8.7 shows the ground temperature data recorded on 1st January 2013 at detailed cross-section AA, along with the approximated initial ground temperature profile prescribed within the model. A fixed ground temperature of 285.15 K (12 ºC) was prescribed to the lower boundary (see Figure 8.1) based upon a geothermal report of the area presented by the British Geological Society (Busby, et al., 2011). As previously discussed, the ground temperature at this depth should remain, to all intents and purposes, constant all year round and independent of seasonal climatic variations.

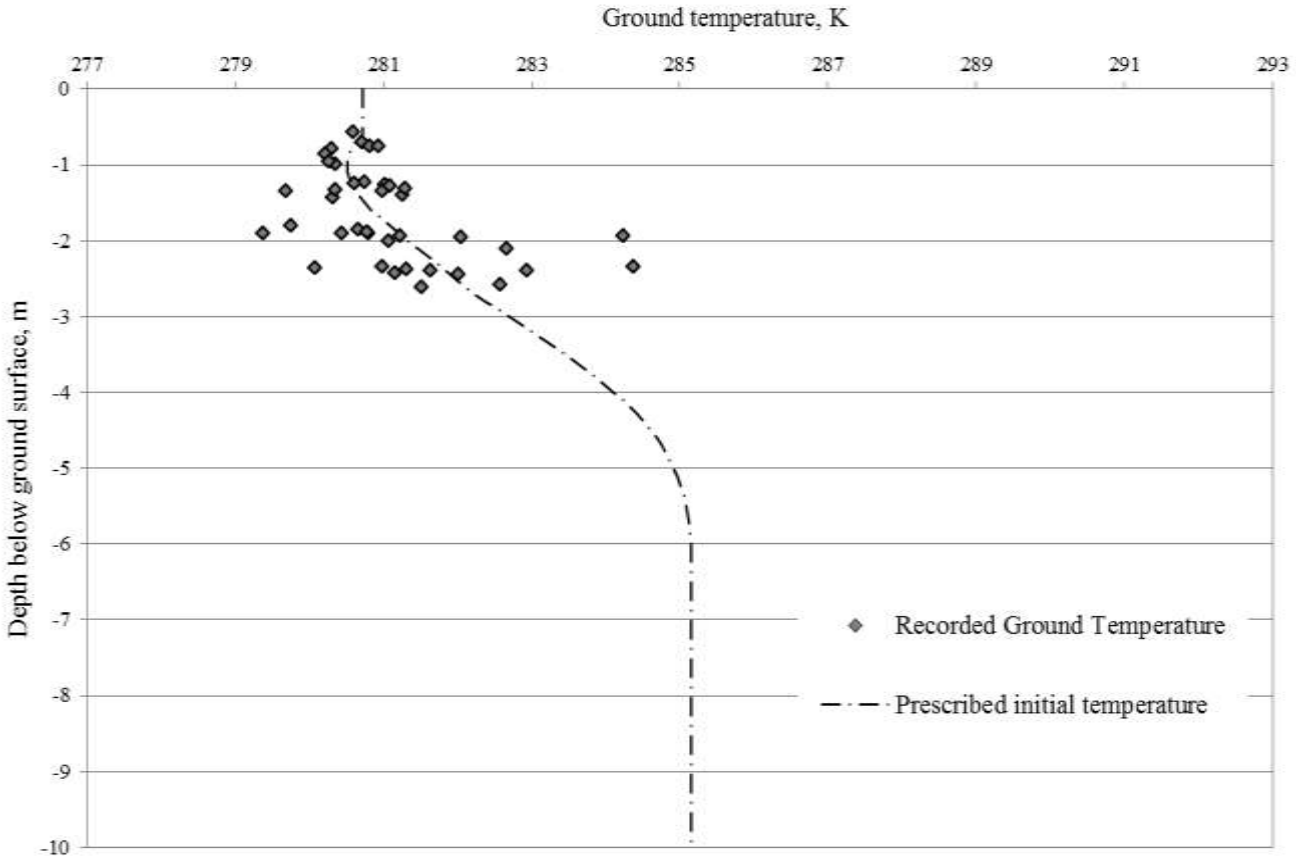

Figure 8.7 – Measured initial ground temperature values on 1st January 2013 along with the approximated initial ground temperature profile prescribed the long-term model.

The initial pore water pressure profile was based in the degree of saturation obtained from four samples retrieved from the monitoring site on January 23rd 2013 (see Chapter 3 for details). The pore water pressure was subsequently calculated according to van Genuchten's Soil Water Characteristic Curve (SWCC) (van Genuchten, 1980).

The measured degree of saturation was found to vary between 0.71 and 1 across the four samples, averaging 0.84. The results from the laboratory experiments can be found in Appendix F. The retrieved samples indicated that there was no clear relationship between the degree of saturation and sample depth at the time of sampling. Similar to the models presented in Chapter 7, a uniform initial pore water pressure was assumed throughout the model domain. The initial pore water pressure assumed was -1 MPa which corresponded to an initial degree of saturation of 0.82, concurring with the measured degree of saturation on January 23rd.

Similarly to the ground temperature, a fixed pore water pressure has been assigned at a depth of 10 meters within the long-term models. At this depth it is assumed that the hydraulic behaviour of the soil remains uninfluenced by annual variations in rainfall and evaporation. The pore water pressure at a depth of 10 meters could be calculated provided that either local pore water pressures or the water table depth (if it was shallower than 10 meters) were known; however neither parameter was measured at the monitoring site. Within the current model it has been assumed that the ground at 10 meters is unsaturated and above the water table with a degree of saturation equal to 0.82. This corresponded to a fixed pore water pressure of -1MPa based on the soil characteristics measured during the site installation.

8.2.3 Material parameters

A total of six soil samples were retrieved from detailed cross-section AA as part of an initial ground investigation performed during the thermistor installation (see Chapter 3 for details). The soil properties of the six samples reflected that of the overall site, i.e. the ground was heterogeneous and there was no apparent correlation between soil properties and spatial position. Based on these characteristics, a single material was prescribed within the long-term simulation. Average values of the porosity, moisture content and bulk density were determined and prescribed. Any obvious abnormal ground measurements were removed from the averaging process. Prescribing a single ground material based on the average soil properties reduces the chances of including extreme local heterogeneities within the model. The averaged material properties prescribed in the model can be found in Table 8.2.

In addition to the conventional geotechnical parameters displayed in Table 8.2, the computation of the surface boundary condition required further material parameters relating to the reflectivity, emissivity and aerodynamic drag of the ground surface (see Chapter 6 for further details). Within the long-term simulation, the surface was assumed to be short-grass, corresponding to the conditions found at site during the autumn of 2012. The surface parameters prescribed in the model have been included within Table 8.2.

Table 8.2 –Material parameters used in the long-term modelling.

Parameter	***Value***
Porosity	0.33
Density (solids)	2650 kg m^{-3}
Specific heat capacity (solids)	820 J kg K^{-1}
Thermal conductivity (solids)	2.93 W $m^{-1}K^{-1}$
Saturated hydraulic conductivity	1 x 10^{-7} ms^{-1}
Shortwave reflection factor	0.225 (van Wijk & Scholte Ubing, 1966)
Longwave emissivity factor	0.97 (van Wijk & Scholte Ubing, 1966)
Aerodynamic drag at a height of 2 meters	0.023 m (Sheppard, 1947)

8.2.4 Results

The following section investigates the long-term ground temperature and hydraulic behaviour. To facilitate the analysis of the results from the long-term simulation, specific locations from the model domain were identified for inspection. Upon review, it could be deduced that both the thermal and hydraulic simulation results were symmetrical either side domain centre line (denoted x=0 in Figure 8.1). The observed line of symmetry was used in order to reduce the number of inspection points by half (i.e. only one half of the domain was inspected). The inspection points selected for the following thermal and hydraulic analysis can be found in Figure 8.8.

Upon inspection of Figure 8.8 it can be seen that fewer inspection points were used to investigate the degree of saturation. This is a deliberate choice based on the visualisation of the simulation results which revealed that the degree of saturation varied predominantly with depth and that the ground-loop boundary had minimal impact. Based on this observation, the inspection points for the degree of saturation have been selected predominately as a function of depth whereas the inspection points for the thermal analysis have been selected as both a function of depth and displacement from the ground-loop.

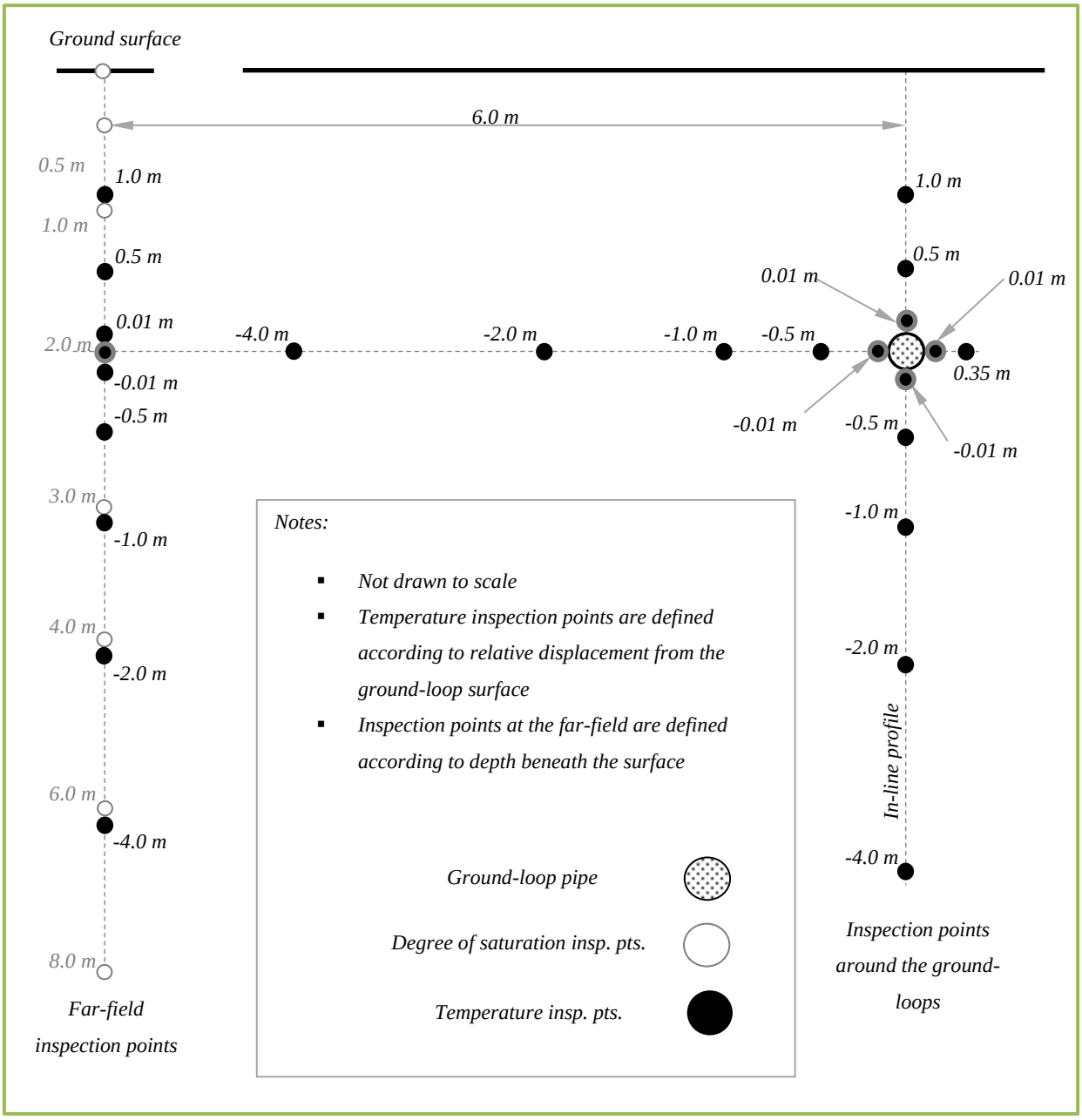

Figure 8.8 – Inspection locations selected for the thermal and hydraulic analysis of the long-term simulation results.

Results from the identified inspection points have been presented in the form of time evolution plots in Figures 8.9 to 8.13. Figures 8.9 and 8.10 contain time evolution data for the simulated degree of saturation whereas the remaining figures contain time evolution data for simulated ground temperature.

Upon the collective inspection of Figures 8.9 to 8.13 it can be seen that both the thermal and hydraulic ground behaviour reaches a steady annual cyclic state after approximately three years. Although the simulation was performed for a period of 20 years, only 5 years' worth of data has been presented in the following figures in order to improve the clarity of plots. The observed cyclic behaviour was expected based upon the annually prescribed climatic data and heating loads. With

respect to the ground temperature, this behaviour closely resembles the findings of previous work, most notably by Hellstrom (1991), which reported similar cyclic behaviour after only a few of years.

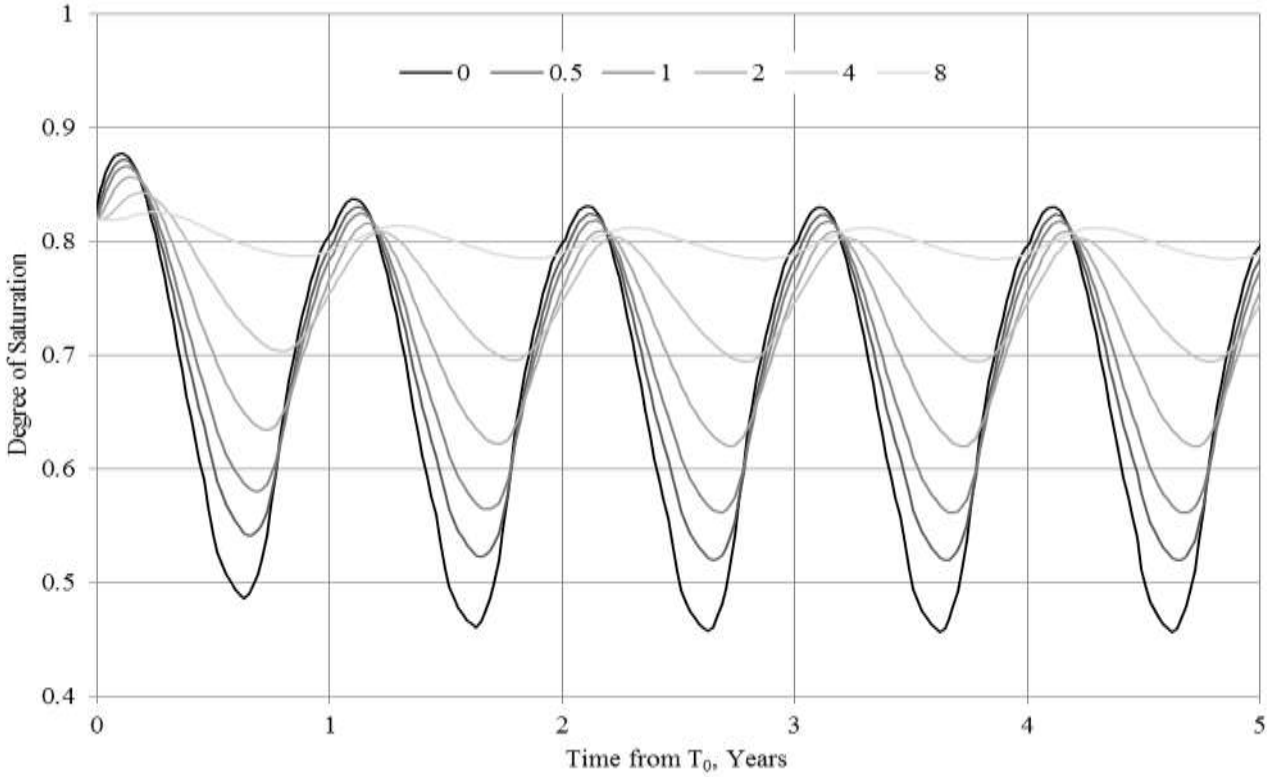

Figure 8.9 – Time evolution of the degree of saturation at various depths obtained from the long-term simulation.

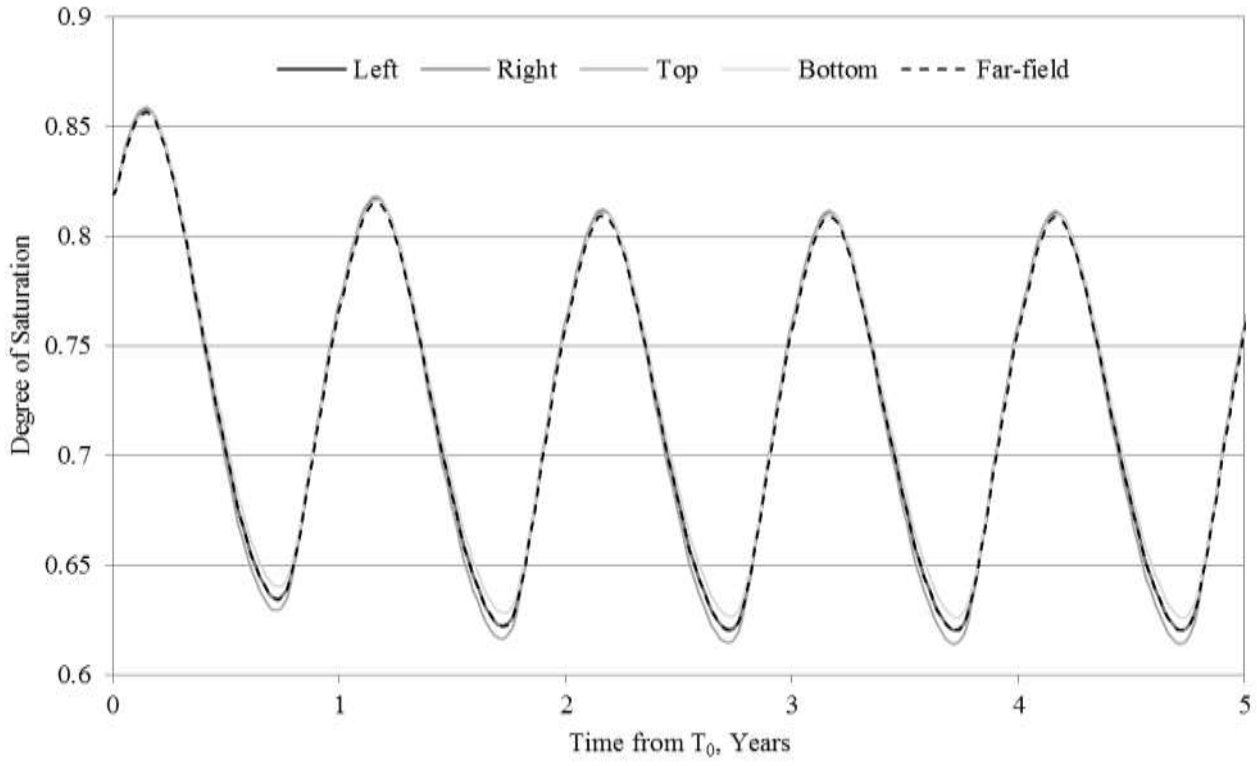

Figure 8.10 – Time evolution of the degree of saturation at various displacements from the ground-loop obtained from the long-term simulation.

Figure 8.9 shows the variations of the degree of saturation with time for the far-field inspection points detailed in Figure 8.8. As previously explained, the simulation results indicate that beyond an initial period of approximately three years, a steady annual cyclic state is reached. Upon reaching steady state, collective inspection of the curves reveals that the annual degree of saturation amplitude decreases with depth, measuring 0.37 at the ground surface and decreasing to 0.03 at a depth of 8 meters. The greatest annual amplitude found at the soil surface, ranged between 0.46 and 0.84 with the greatest value occurring in early February and the smallest value occurring in mid-August. In general, the decreasing amplitude with depth and the seasonal location of the greatest and lowest degree of saturation concurred with the expected outcomes.

One simulated feature which did not concur with the expected outcome was the greatest surface degree of saturation, which was equal to 0.84. Knowledge regarding the British climate and ground conditions would suggest that this value should actually be reaching 1 (i.e. saturation) at certain points during the year. In this particular instance, the lower than expected result has been attributed to the resolution of the monthly precipitation data prescribed within the model. Although this data represents the monthly precipitation, the resolution of the data fails to represent daily fluctuations which would inevitably occur in reality and lead to saturated ground conditions. It is recognised that this is not a direct reflection of reality however; it is stressed that within the current scope of work the surface boundary aimed to represent the long-term hydraulic exchange and not short term fluctuations.

Upon inspection of the curve profiles it can also be deduced that the individual curve peaks are off-set from one another with respect to depth. For example, the greatest degree of saturation at the ground surface is simulated in early February whereas the corresponding value at 8 meters is observed at mid-April, a lagging of 63 days. These characteristics mimic the anticipated ground behaviour which would occur in reality and is the expected outcome based on the prescribed model conditions.

In total, four locations were identified to investigate the impact, if any, of the heat exchange process via the ground-loop on the hydraulic behaviour of the ground immediately surrounding the ground-loop. The degree of saturation from these four locations has been presented via time evolution plots in Figure 8.10. The four points were labelled left, right, top and bottom in order to correspond with their locations as depicted in Figure 8.8. A fifth point representing the far-field degree of saturation at a depth of 2.0 meters has also been plotted to provide a baseline for comparisons. In general, it can be said that the plots in Figure 8.10 reveal there is very little difference between the simulated degree of saturation around the ground-loop and the simulated degree of saturation at the far-field location (i.e. beyond the thermal influence of the ground-loop). A minor difference between the degree of saturation immediately above and below the ground-loop and

far-field was observed however there was no observable difference between the left and right values and the far-field. This indicates that any observable difference was in fact due to the inspection point depth and not behaviour induced by the ground-loop. Based on the highlighted points, it has been deduced that the thermal interactions induced by the ground-loop had very little impact on the hydraulic behaviour of the surrounding ground.

Figure 8.11 shows the simulated ground temperatures for the far-field inspection points detailed in Figure 8.8. In order to facilitate future comparisons, the far-field temperatures have been presented in Figure 8.11 with respect to the corresponding displacements from the ground-loop surface (see Figure 8.8). It can be said that the simulated amplitude of the ground temperature was greatest at the ground surface, reducing with depth. Once the annual cyclic temperature regime had been established it can be said that the ground surface temperature (i.e. a displacement of 1.99 meters from the ground-loop) varied 19.2 K annually. This is significantly greater than at a depth of 6 meters (displacement of -4 meters from the ground-loop), where the ground temperature varied only 0.8 K annually. The general trends and values exhibited by the simulated ground temperatures concurred with theory previously presented by Kusuda & Achenbach (1965).

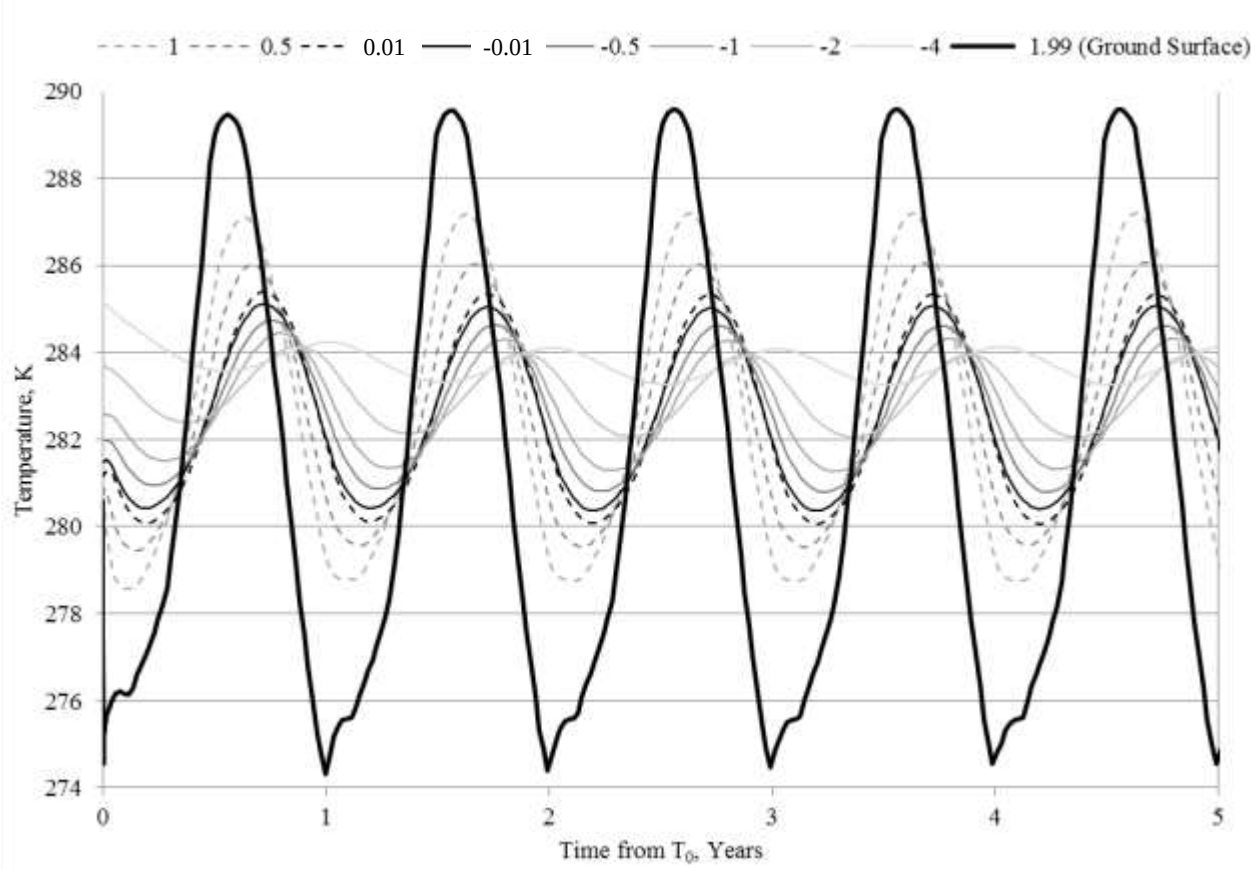

Figure 8.11 – Time evolution of the far-field ground temperature at various depths obtained from the long-term simulation.

Figures 8.12 and 8.13 show the simulated ground temperatures at a variety of horizontal and vertical displacements from the ground-loop surface respectively (see Figure 8.8). Beyond an initial three year period, the results indicate that a steady cyclic state is established in the ground thermal behaviour. The cyclic behaviour exhibited in the simulation results is expected based upon the annual climatic and heating loads prescribed within the model. Examination of the simulated ground temperatures in conjunction with the prescribed heating loads (see Figure 8.6) suggests that the cyclic ground behaviour can be divided into two distinct sections representing periods of so called 'heat extraction' and 'heat recovery'. The heat extraction period relates to the annual time period when heat is being extracted via the ground-loop whereas the heat recovery period relates to the annual time period when heat is not being extracted via the ground-loop according to the heating load profile. For clarity, the heat extraction and heat recovery periods have been graphically annotated in Figure 8.12.

Upon inspection of the heat extraction period, it is possible to identify a number of general trends associated with heat extraction. Firstly, the inspection points located closest to the ground-loop surface are the first to register a temperature decrease, followed by inspection points at greater horizontal and vertical displacements. Following on from this, it is possible to identify that the inspection points located closest to the ground-loop surface are subject to the greatest temperature variations with time. Both these ground thermal characteristics would be expected within a conduction dominant system.

In order to demonstrate the difference due to heat extraction, Figure 8.12 also includes the far-field temperature corresponding to the ground-loop depth. Once a steady cyclic system had been established, Figure 8.12 shows that the lowest simulated ground temperature in the horizontal was 274.0 K at the inspection point 0.01 meters from the ground-loop surface. This temperature was found at the very end of the heat extraction period, corresponding to the end of March. For the very same time, the simulated ground temperature for the opposing inspection point at -0.01 meters from the ground-loop surface was 0.5 K greater measuring 274.5 K. The slightly lower temperature at a displacement of 0.01 meters can be accredited to the thermal influence of the adjacent ground-loop leg. At the corresponding point in time (i.e. end of March), the simulated far-field temperature was 280.4 K. This indicates that the ground-loop induced a ground temperature change of approximately 6.4 K and 5.9 K respectively in the immediate ground region once the steady state cycle had been established.

When collectively inspecting the temperature evolution plots, it is also worth noting the ground temperature fluctuations which are exhibited during periods of heat extraction. The fluctuations can be predominantly found at displacements of 0.35, -0.01 and 0.01 meters although they are visible, to some extent, at greater displacements. By cross-referencing Figure 8.11 with Figure 8.6 it is possible to accredit these fluctuations to variations in the prescribed heating load. In a

conduction dominant system, it is expected that the fluctuations would be most prominent in the ground immediately surrounding the ground-loop, subsequently dissipating with displacement and the increasing thermal mass of the surrounding soil.

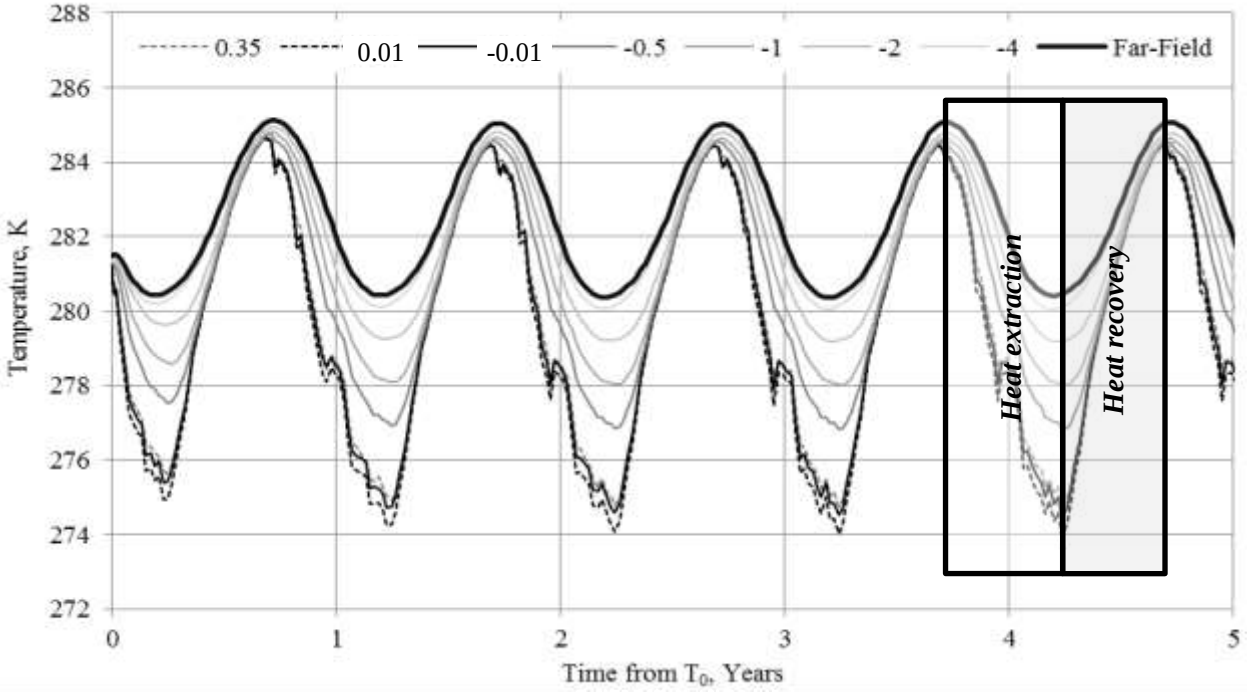

Figure 8.12 – Time evolution of the ground temperature at various horizontal displacements from the ground-loop obtained from the long-term simulation.

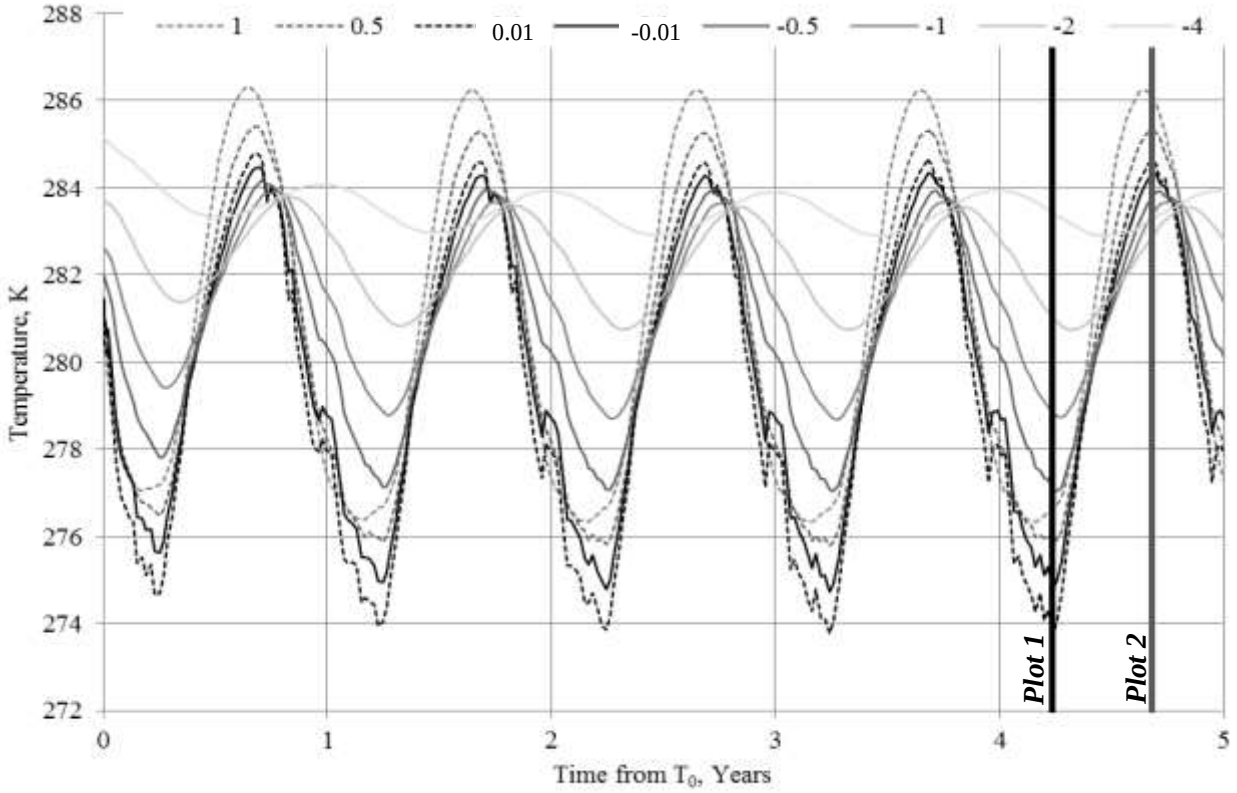

Figure 8.13 – Time evolution of the ground temperature at various vertical displacements from the ground-loop obtained from the long-term simulation.

The effect of heat extraction on the vertical ground temperature profile has been inspected by plotting the simulated far-field vertical temperature profile along with the so called 'in-line' vertical temperature profile. Within the current context of work, the term in-line refers to a vertical profile which dissects one of the ground-loops (see Figure 8.8). As the simulation results were symmetrical in the horizontal, it only proves necessary to plot a single in-line profile for subsequent inspections.

The two curves presented in Figure 8.14 represent the vertical temperature profiles at the far-field and in-line with the ground-loop at the very end of the heat extraction period (Plot 1 in Figure 8.13). When inspecting the vertical ground temperature profiles in Figure 8.14 a number of general observations can be made. Similarly to the horizontal case, the lowest ground temperatures were simulated in the ground region immediately adjacent to the ground-loop. In addition to this feature, the profiles also reviled that the surface ground temperature immediately above the ground-loop was 2.5 K lower than that found at the far-field. This indicated that the ground-surface temperature immediately above the ground-loop was subject to noticeable thermal change due to heat extraction. From a design perspective, this is an important system characteristic as it shows that this ground region will influence the performance of horizontal ground source heat systems. It can therefore be said that the backfilling procedure and material type used during the system installation will influence the ground behaviour.

The lowest simulated ground temperature was 273.8 K at a displacement of 0.01 meters above the ground-loop surface. For the same time, the simulated ground temperature at the inspection point 0.01 meters below the ground-loop surface was 0.97 K greater. Unlike the horizontal case, this temperature difference cannot be attributed to the remaining ground-loop leg due to the vertical position of the inspection points and the symmetrical model domain in the horizontal. Instead, this temperature difference must be due to the influence of the surface boundary condition and the ground thermal gradient immediately above/below the ground-loop.

Inspection of the in-line temperature profile reveals that the induced thermal gradient beneath the ground-loop is steeper than that above it. This concurs with ground data collected at the monitoring site, previously discussed within Chapter 4. From an operational point of view, these results suggest that more thermal energy will be extracted from beneath the ground-loop than above it, a feature which was also alluded to in Chapter 4. The difference in the thermal gradient above/below the ground-loop is another behavioural characteristic which could be applied to improve/optimise system performance.

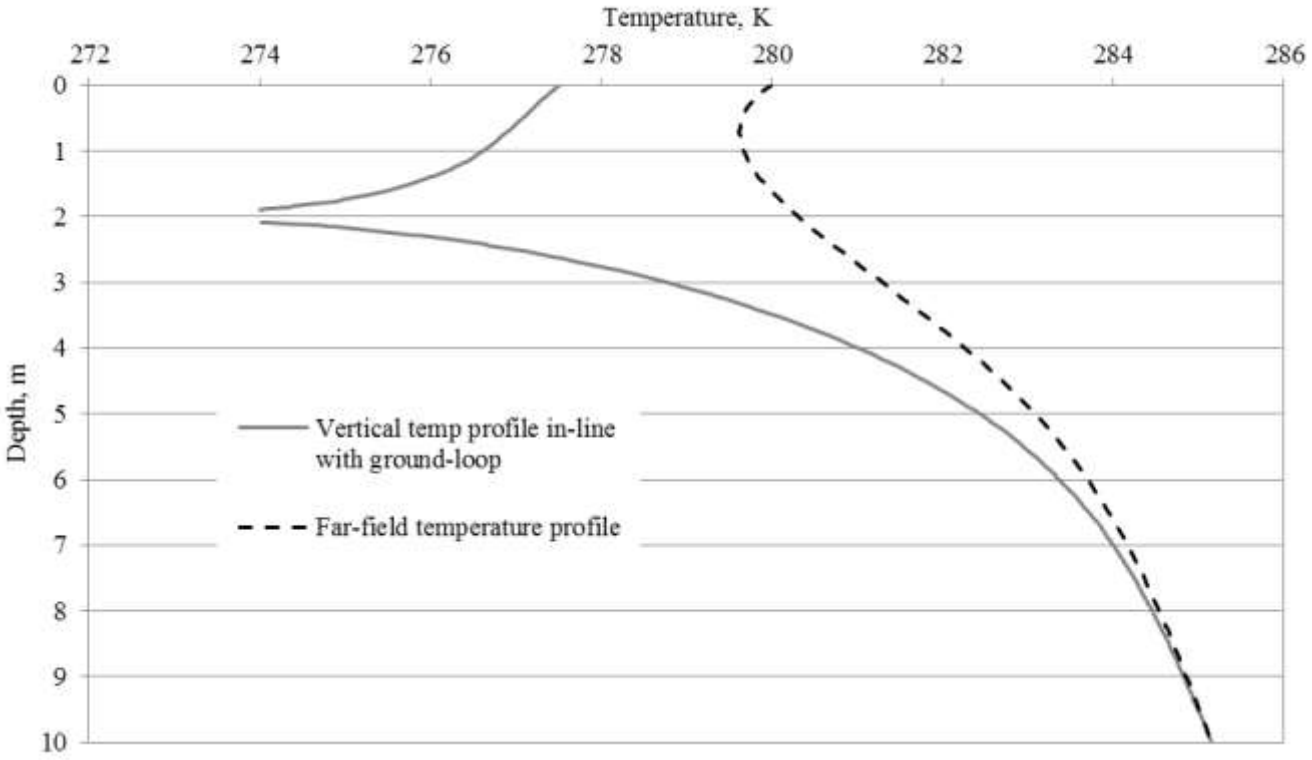

Figure 8.14 – Vertical temperature plot for the line denoted plot 1 in Figure 8.13.

When collectively analysing the vertical and horizontal analysis for the heat extraction period it is worth noting that the ground temperatures remained above 273.0 K, the minimum adjacent ground-loop temperature suggested by the MIS 3005 design standard. This indicates that the system has been suitably sized to meet the current heating demands of the occupants.

As previously discussed, the heat recovery period depicted in Figure 8.12 represents the annual period when no thermal energy is being extracted via the ground source heat system. Broadly speaking, the thermal gradients induced by the ground-loop during heat extraction are allowed to dissipate within the heat recovery period.

Upon inspection of Figure 8.12 it is possible to deduce that the temperature difference between the far-field and the remaining inspection points decreases during the heat recovery period. By the end of the recovery period, Figure 8.12 shows that the ground temperatures either approach or reach that of the far-field indicating that the thermal gradients induced by the ground-loop have almost completely dissipated. As expected, the greatest temperature recovery occurs in the ground immediately surrounding the ground-loop (i.e. at displacements of -0.01, 0.01 and 0.35). The greatest temperature change occurs at a displacement of -0.01 meters where the ground temperature increases 10.4 K. From a system recovery point of view, a more important value is with regards to the temperature difference between the ground immediately surrounding the ground-loop and the far-field as this indicates the true level of recovery with respect the natural in-situ ground conditions.

Considering the same point at a displacement of -0.01 meters, the difference with respect to the far-field ground temperature at the beginning of the recovery period is 6.5 K whereas as the end of the recovery period this has reduced to 0.3 K. This shows that once the cyclic state has been established, the simulated ground temperatures are almost completely returning to their natural states prior to the onset of the heat extraction phase. From an operation point of view, this suggests that the system performance would not diminish with time for the current heating loads.

In order to analyse the vertical ground temperature changes associated with the recovery period, Figure 8.15 has been produced showing the vertical temperature profile at the end of the recovery period.

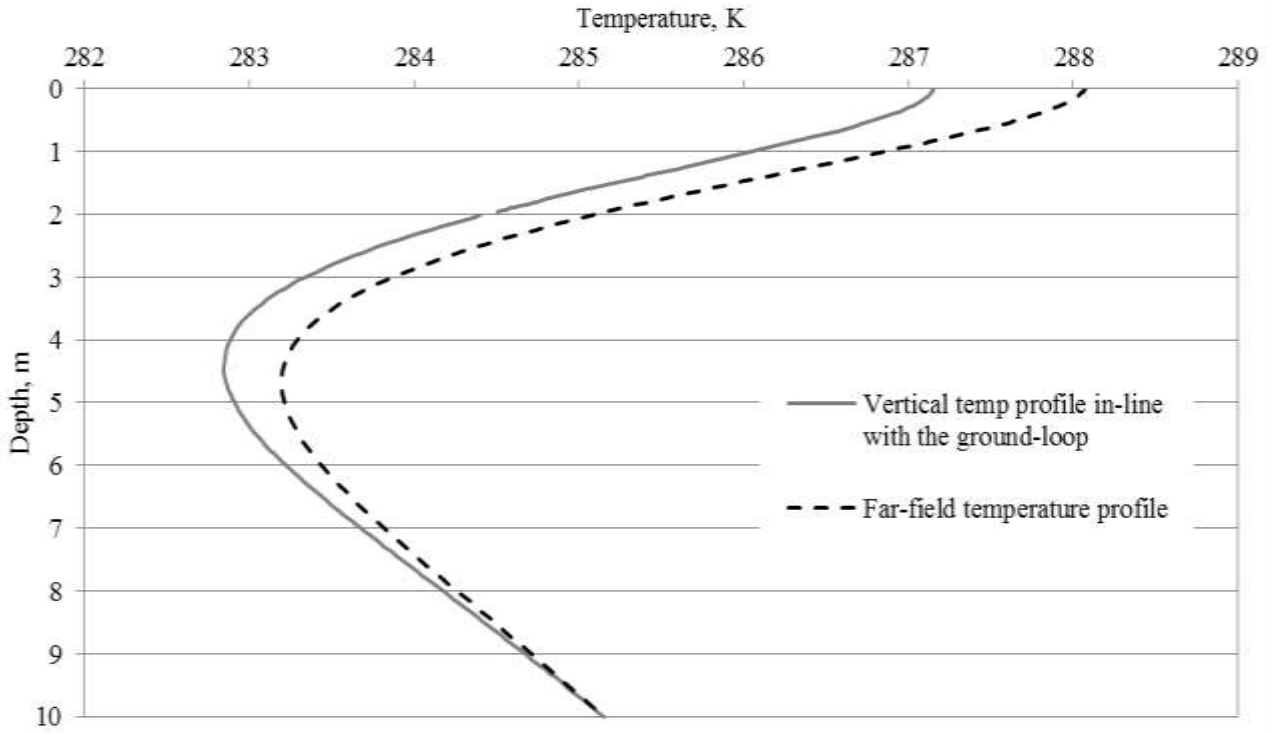

Figure 8.15 – Vertical temperature plot for the line denoted plot 2 in Figure 8.13

By comparing Figures 8.14 and 8.15 it can be seen that the vertical temperature profile has almost returned to that of the far-field vertical profile by the end of the recovery period. Interestingly, the model predicts that the greatest difference between the vertical temperature profile and the far-field occurs at the surface where there is a temperature difference of 0.92 K. Below the ground-loop, the greatest difference between the vertical temperature profile and the far-field profile is found at a depth of 4 meters where the temperature difference is 0.41 K. The profile therefore suggests that the ground thermal recovery is coming from both beneath and above the ground-loop. With regards to system optimisation, this is an important aspect of system behaviour to recognise.

When comparing the temperature evolution and vertical temperature profiles coinciding with the end of the heat recovery period it is possible to identify that the greatest thermal differences, with regards to the far-field temperatures, occur in the vertical. This suggests that the thermal recharge of the ground immediately surrounding the ground-loop occurs predominantly in the vertical as a result of the fixed ground temperature at depth and the surface boundary conditions.

In summary, the thermal and hydraulic simulation results reached a steady cyclic state after approximately three years of operation. Upon reaching steady state, all ground temperatures in the in the vicinity of the ground-loop were above the 273.0 K threshold defined in MIS 3005, suggesting that the system had been designed appropriately for the operational loads. The thermal gradient induced by the ground-loop not only resulted in a notable temperature decrease surrounding the ground-loop but also at the ground surface. The thermal interference from the adjacent ground-loop resulted in lower temperatures on the associated side. The thermal distribution induced by heat extraction depicted a steeper thermal gradient below the ground-loop. From an operation point of view, this suggested that more thermal energy was being extracted from beneath the ground-loop than above. The horizontal thermal recovery of the ground almost approached the far-field value however, there were some differences in the vertical profiles.

The results showed that the degree of saturation predominantly varies with depth. The thermal gradient induced by the ground-loop was shown to have little measurable effect on the degree of saturation simulated adjacent to the ground-loop surfaces.

8.3 Computational performance

The long-term TH simulations presented within the scope of this thesis result in computationally expensive models which can take significant time to run. Chapter 5 previously described the serial and parallel code developments which have been implemented specifically with the aim of reducing computational times. In this section the performance of the implemented parallel techniques will be analysed within the scope of the current investigation.

The main objective of the parallel formulation, previously detailed in Chapter 5, was to reduce computational times by utilising the full processing power available to modern desktop computers. The computational performance has been analysed here by comparing the computational times of four simulations which utilised one, two, three and four cores of a modern desktop quad-core machine. In order to provide a fair basis for comparison, the only variable altering between the four case simulations was the numbers of processors engaged. The long-term simulation previously detailed as part of section 8.2 was used, and remained constant, in all four cases. The relevant

hardware specifications for the quad-core machine used in the current investigation have been summarised in Table 8.3.

Table 8.3 – Relevant hardware specifications for the desk-top machine used in the computational performance investigation.

Hardware	*Specification*
Processor	Intel Core – Quad CPU Q9550 (283GHz)
RAM	4.00 GB
System Architecture	64-bit

The results from the computational investigation have been presented in terms of the total time taken to complete the subject simulation. These results have been summarised in Table 8.4. Due to the size of the simulation, details regarding the initialisation time and post processing have been omitted as these represent a very small fraction of the overall computation. For example, the initialisation took in the region of 30 seconds to complete. For the current analysis, the single core time has been used as a benchmark to compare the performance of the subsequent multi-core simulations. Figure 8.16 graphically relates the performance of the multi-core simulations to the single core simulation in terms of the single core simulation time.

Table 8.4 - Measured computational times associated with the one, two, three and four core simulations.

No. of cores utilized	***Time (seconds)***	***Time (hours)***	***Percentage of single core time***
1	355,920	98.87	-
2	252,858	70.24	71.0
3	218,619	60.73	61.4
4	196,680	54.63	55.3

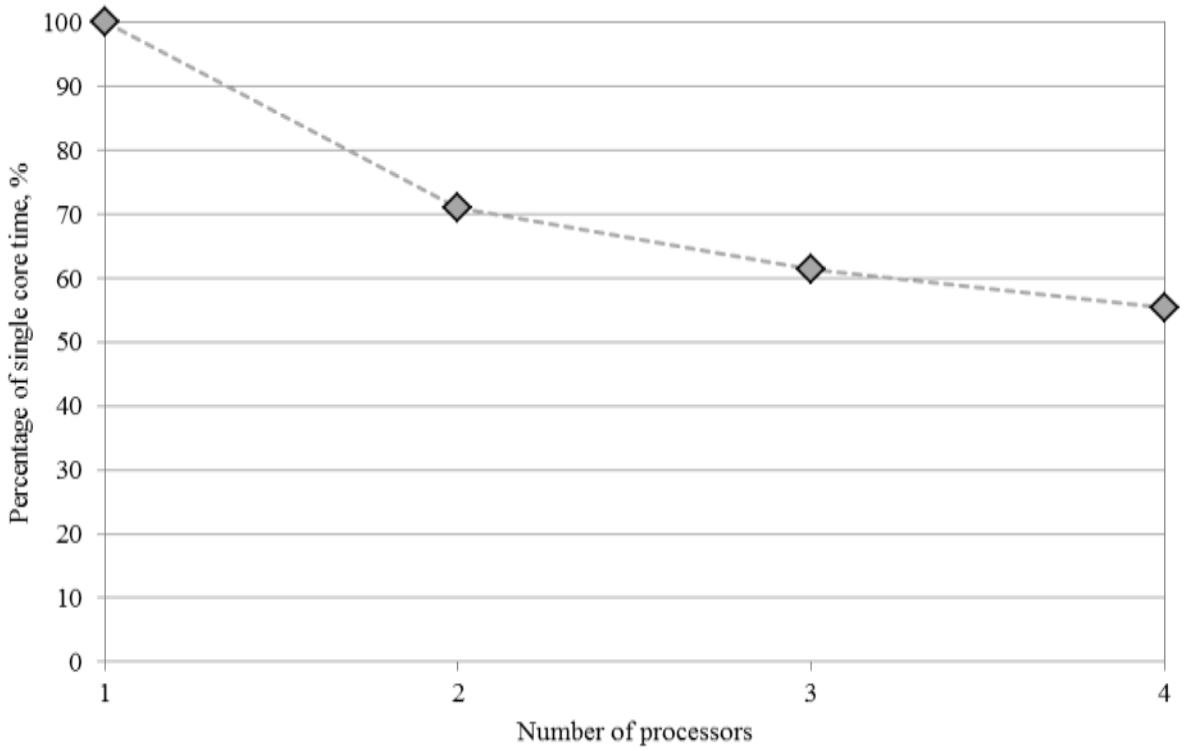

Table 8.16 - Measured computational times in terms of the single core simulation time.

As expected, Figure 8.16 shows that computational times decreases with the inclusion of additional cores. By using the single core as a benchmark it is possible to quantify the time saving associated with the inclusion of additional cores. From Figure 8.16 it can be seen that the greatest time saving occurs when the number of utilised processors increases from one to two, resulting in a 30% reduction in simulation time. Beyond this, further time reductions are registered with the inclusion of three and four processors however the overall time reductions are considerable lower measuring 8.6% and 6.1% respectively. The shape of the graph depicted in Figure 8.16 can be attributed to a number of system variables, most notably the system architecture. When running a desktop computer there are a number of computational processes already running prior to the initialisation of any applications, for example, the operating system, security clients, firewalls etc. Depending upon the system architecture, these processes may be running completely or partially on the same processor as an application which is utilising a single core. The greatest performance increase observed between the single and dual processor tests could be a result of such system architecture. It is important recognise at this stage that these results are associated with the specific hardware employed in this investigation. Alternative hardware and system architecture may result in differing outcomes.

8.4 The effects of ground surface properties on ground behaviour

In Chapter 2, a salient review of existing horizontal ground source heat numerical investigations was presented. The findings of this review highlighted that the majority of previous numerical investigations have simplified the interactions between the ground and atmosphere. The theoretical surface boundary presented in Chapter 6 required the consideration of a range of ground surface properties, namely; heat capacity, thermal conductivity, shortwave reflection, longwave reflection, longwave emissivity, aerodynamic drag and permeability. Consideration of these parameters not only allows a greater number of climatic variables to be represented within the models but also allows the inclusion of a greater number of surface material properties. The following section aims to investigate the influence of some surface materials on the long-term TH ground behaviour. The long-term simulations of the monitoring site contained in section 8.2 have assumed the surface type as short-grass, based on field conditions found at the monitoring site. Building on these simulations, a further three surface types have also been selected for the investigations presented here. These surface types are as follows:

- *Barley crops*
- *Asphalt road surface*
- *Brick paving*

The surface materials have been selected in order to cover a range of common surface types which would typically be encountered in rural and urban horizontal ground source heat systems. For coherency between the previous long-term model and those presented in this section, the models developed for all three cases listed above have been predominantly based on the simulation detailed in section 8.2. The only model characteristics which have been altered for the current investigations are with regards to the ground surface materials prescribed and surface material characteristics. To avoid repetition, only details regarding the surface material profile and properties will be discussed in the following subsections. Details regarding the model domain, initial conditions and boundary conditions have been previously outlined in section 8.2. The results from the three simulation cases will be collectively discussed in section 8.4.4.

8.4.1 Barley crops

The installation of a horizontal ground source heat system may require access to a large plan footprint in order to bury the designed ground-loops. Rural properties with access to adjoining fields are ideally suited for the installation of horizontal ground source heat systems. WDS Environmental

(Seren Projects industrial partners) have found that the overwhelming majority of horizontal ground source heat systems they install are at rural properties and in particular farms. Using this knowledge, it proves logical to investigate what impact, if any, surface agricultural use will have on the performance of the ground source heat systems. Within the scope of this particular study the properties of the surface correspond to the barley crop cycle. The only parameters which differ between the current model and that previously detailed in section 8.2, are the surface properties of solar reflection, longwave emissivity and aerodynamic drag at the surface (see Chapter 6 for parameter details). These have been listed in Table 8.7.

Table 8.7 – Table of material parameters used in the barley surface model.

Parameter	***Value***
Ploughed field:	
Shortwave reflectivity	0.15 (van Wijk & Scholte Ubing, 1966)
Longwave emissivity	0.96 (van Wijk & Scholte Ubing, 1966)
Aerodynamic resistance at 2 meter height	0.021 m
Long grass:	
Shortwave reflectivity	0.16 (van Wijk & Scholte Ubing, 1966)
Longwave emissivity	0.97 (van Wijk & Scholte Ubing, 1966)
Aerodynamic resistance at 2 meter height	0.039 m
Barley:	
Shortwave reflectivity	0.17 (van Wijk & Scholte Ubing, 1966)
Longwave emissivity	0.97 (van Wijk & Scholte Ubing, 1966)
Aerodynamic resistance at 2 meter height	0.045 m

In order to model the TH ground effects of barley at the monitoring site, it is necessary to consider the crop cycle of barley within the UK. For the current case, the cycle has been simplified into three stages; namely ploughed field, long grass and full grown barley. The annual variation in surface type has been based on the winter barley cycle (HGCA, 2006) and is summarised in Table 8.8. During each of the three stages the associated surface properties listed in Table 8.7 are assumed to remain constant.

Table 8.8 – Table showing the annual variation in surface type based on the winter barley cycle.

Surface type & length	***Sept***	***Oct***	***Nov***	***Dec***	***Jan***	***Feb***	***Mar***	***Apr***	***May***	***Jun***	***Jul***	***Aug***
Barley, 0.75 m												
Long grass, 0.5 m												
Ploughed field, 0 m												

8.4.2 Asphalt road surface

The second scenario considered for the surface condition aims to inspect the performance of a horizontal ground source heat system in an urban environment. It is logical to presume that a horizontal ground source heat system would only be economically viable in an urban environment so long as the surface was utilised in some capacity. The model presented within this subsection aims to investigate the TH ground behaviour if the surface was used for a car park covered in asphalt. The materials within the model domain have been prescribed according to a generic car-park construction design (Chudley, 1988). Figure 8.17 shows the materials prescribed in the model along with the initial conditions and boundary conditions. Only the surface material properties have altered from the long-term simulations presented in section 8.2.

In total three separate materials have been prescribed in the model according to a typical car-park construction. The surface layer corresponds to asphalt, measuring 30 mm in depth. Beneath this is the so called binder layer, which is made up of concrete and measures 80 mm in depth. The final and deepest layer is the so called sub-base which compromises of un-bound concrete gravel. Table 8.9 contains the material properties prescribed in the model along with the surface properties of asphalt; namely shortwave reflection, longwave emissivity and aerodynamic drag required for the computation of the surface boundary condition. No exact value for the surface drag of asphalt could be sourced in literature therefore a value was inferred from those provided by Shepherd (1947).

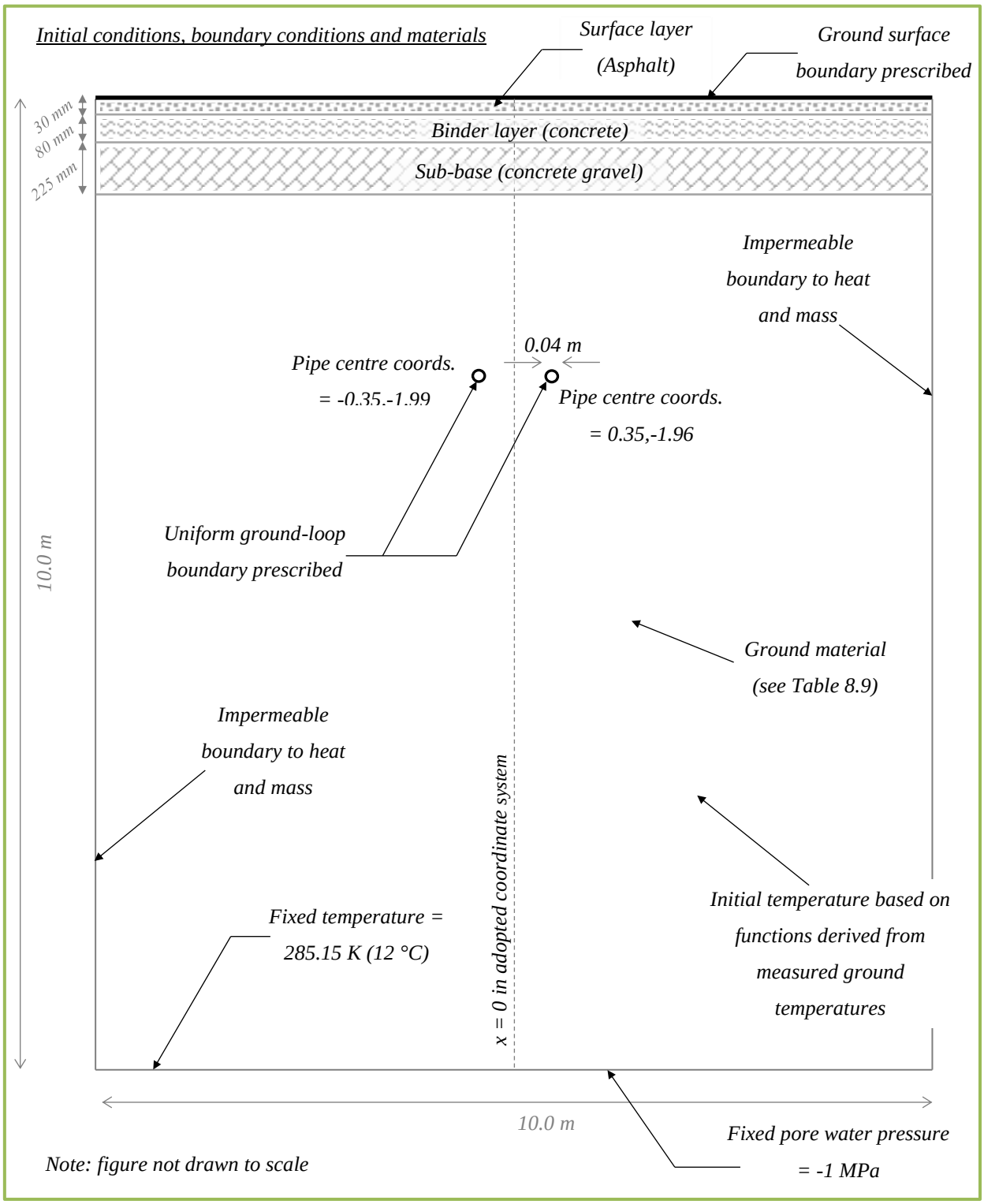

Figure 8.17 – Schematic showing the domain, initial conditions, boundary conditions, prescribed material and discretised mesh used for the asphalt surface simulations.

Table 8.9 – Material parameters used in the asphalt surface model.

Parameter	***Value***
Surface layer: *Asphalt*	
Porosity	0.22 (Gruber, et al., 2012)
Density (solids)	2500 kg m^{-3} (Gruber, et al., 2012)
Specific heat capacity (solids)	920 J kg K^{-1} (Yavuzturk & Ksaibati, 2002)
Thermal conductivity (solids)	1.3 W $m^{-1}K^{-1}$ (Yavuzturk & Ksaibati, 2002)
Saturated hydraulic conductivity	1 x 10^{-5} ms^{-1} (Gruber, et al., 2012)
Shortwave reflectivity	0.075 (Levinson & Akbari, 2001)
Longwave emissivity	0.81 (Yavuzturk & Ksaibati, 2002)
Aerodynamic resistance at 2 meter height	0.0001 m
Binder layer: *Concrete*	
Porosity	0.1 (Zadrazil, et al., 2004)
Density (solids)	2700 kg m^{-3} (De Vries, 1966)
Specific heat capacity (solids)	1000 J kg K^{-1} (Khudhair & Farid, 2004)
Thermal conductivity (solids)	1.5 W $m^{-1}K^{-1}$ (Kaye, et al., 1973)
Saturated hydraulic conductivity	1 x 10^{-15} ms^{-1} (Kondraivendhan, et al., 2011)
Sub-base layer: *Concrete gravel (un-bound)*	
Porosity	0.4 (Barnes, 2000)
Density (solids)	2700 kg m^{-3} (De Vries, 1966)
Specific heat capacity (solids)	812 J kg K^{-1} (De Vries, 1966)
Thermal conductivity (solids)	1.5 W $m^{-1}K^{-1}$ (Kaye, et al., 1973)
Saturated hydraulic conductivity	1.0 ms^{-1} (Barnes, 2000)

8.4.3 Brick paving

Similar to the previous case, the current scenario aimed to simulate the TH ground behaviour of a horizontal ground source heat system in an urban environment, this time beneath brick paving. Permeable brick paving has been selected within the scope of this work in order to represent a permeable urban surface. Within the UK the use of permeable brick paving has increased in recent years in response to sustainable urban drainage legislation (DEFRA, 2010). Figure 8.18 shows two typical examples of permeable brick paving similar to that being studied in the current model.

Figure 8.18 – Typical examples of permeable brick paving (Holland Stone, 2013; Quient Nature, 2013).

The materials within the current domain have been prescribed according to a conventional brick paving construction design (Chudley, 1988). Figure 8.19 shows the materials prescribed in the model along with the initial conditions and boundary conditions. The only model characteristics which have altered from the long-term simulations presented in section 8.2 are with regards to the surface material properties therefore only these shall be discussed at length here.

In total three materials have been prescribed within the model corresponding to a brick/sand layer (i.e. permeable brick paving), base layer and sub-base. The surface layer compromises of 80% conventional clay fired bricks and 20% sand by surface area. Beneath this, the base layer compromises of sand 30 mm in depth while the sub-base is made up of unbound concrete gravel measuring 125 mm in depth. Table 8.10 contains the material properties prescribed in the model along with the prescribed surface properties of shortwave reflection, longwave emissivity and aerodynamic drag required for the computation of the surface boundary condition. The thermal properties of the brick/sand surface layer have been weighted according to the constituent values. Unlike the thermal properties, the hydraulic permeability of the two surface constituents varies considerably therefore the surface drainage and water exchange has been assumed to take place solely in sand. No values representing the shortwave reflection, longwave emissivity and aerodynamic drag of a hybrid brick/sand surface could be sourced; therefore, the prescribed surface properties have been calculated according to the brick and sand values sourced in literature.

Table 8.10 – Material parameters used in the brick surface model.

Parameter	***Value***
Surface layer: ***80% Brick, 20% Sand***	
Porosity	0.37 (Cultrone, et al., 2004) (Ewen & Thomas, 1987)
Density (solids)	2655 kg m^{-3} (De Vries, 1966)
Specific heat capacity (solids)	840 J kg K^{-1} (Kaye, et al., 1973) (De Vries, 1966)
Thermal conductivity (solids)	4.1 W $m^{-1}K^{-1}$ (De Vries, 1966)
Saturated hydraulic conductivity (based on sand alone)	1.9^{-3} ms^{-1} (van Wijk & De Vries, 1966)
Shortwave reflectivity	0.15 (van Wijk & Scholte Ubing, 1966)
Longwave emissivity	0.95 (van Wijk & Scholte Ubing, 1966)
Aerodynamic resistance at 2 meter height	0.0001 m
Base layer: ***Sand***	
Porosity	0.39 (Ewen & Thomas, 1987)
Density (solids)	2660 kg m^{-3} (De Vries, 1966)
Specific heat capacity (solids)	800 J kg K^{-1} (De Vries, 1966)
Thermal conductivity (solids)	8.8 W $m^{-1}K^{-1}$ (De Vries, 1966)
Saturated hydraulic conductivity	1.9^{-3} ms^{-1} (van Wijk & De Vries, 1966)
Sub-base layer: ***Concrete gravel (un-bound)***	
Porosity	0.4 (Barnes, 2000)
Density (solids)	2700 kg m^{-3} (De Vries, 1966)
Specific heat capacity (solids)	812 J kg K^{-1} (De Vries, 1966)
Thermal conductivity (solids)	1.5 W $m^{-1}K^{-1}$ (Kaye, et al., 1973)
Saturated hydraulic conductivity	1.0 ms^{-1} (Barnes, 2000)

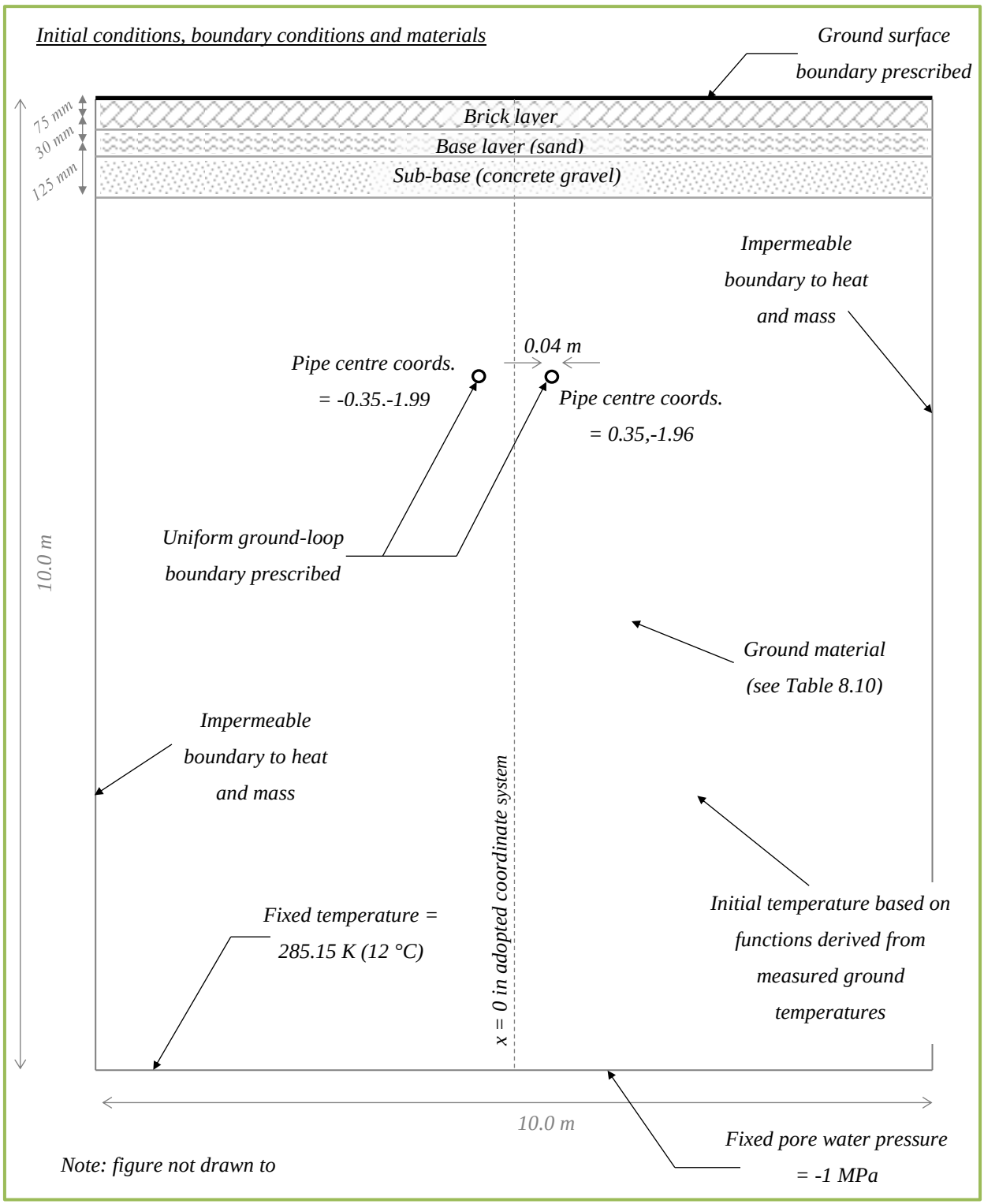

Figure 8.19 – Schematic showing the domain, initial conditions, boundary conditions, prescribed material and discretised mesh used for the brick surface simulations.

8.4.4 Results

The thermal and hydraulic results of the long-term simulations using the preceding three surface models are presented in the following sections. The results will be analysed in conjunction with the long-term model, previously presented in section 8.2, which simulated the TH behaviour considering short-grass as the surface boundary. Collective analysis of the results reviled that the cyclic behaviour exhibited by the original TH simulation (see section 8.2) was also found within the surface model results. Based on these observations, thermal comparisons between the three surface models and the original TH model have been made via vertical temperature profiles at the far-field and in-line with the ground-loop. The term in-line has been previously discussed in section 8.2.4. The vertical temperature profiles have been presented for two instances in time, coinciding with the end of the end of the so called heat extraction and heat recovery periods previously defined in section 8.2.4.

Hydraulic comparisons on the other hand have been made by solely comparing the vertical degree of saturation profile at the far-field. This is based on the findings in section 8.2 which showed that the ground-loop thermal interactions had minimal impact on the surrounding hydraulic behaviour of the ground. Results regarding the hydraulic behaviour of the ground will be presented first, followed by an analysis of the thermal behaviour.

The vertical degree of saturation profiles for the short-grass, barley, asphalt and brick models are presented in Figure 8.20 and 8.21. The figures show the simulated degree of saturation at two points during a year, once a steady cyclic hydraulic state had been established. The two points correspond to February 1st and August 1st. These points in time were selected based on the results from section 8.2, which found that the surface reached its greatest and least states of saturation at these annual times.

Comparisons between Figures 8.20 and 8.21 indicate that the short-grass and barley models exhibited very similar hydraulic profiles. In both instances, the greatest and lowest degree of saturation was found at the surface, simulated to be 0.83 and 0.46 respectively. Beneath the surface, the profiles did not exactly match one another; however the simulated difference never exceeded 0.01. As the soil properties prescribed were identical to each other, the slight variation in profile can be attributed to the surface properties, namely; shortwave reflectivity, longwave emissivity and aerodynamic resistance.

Inspection of Figures 8.20 and 8.21 reveal that the simulated degree of saturation for the brick model is greater than the short-grass and barley cases. The greatest and lowest degrees of saturation were found at the ground surface measuring 0.93 and 0.77 respectively in Figures 8.20 and 8.21. The greater degree of saturation, when compared to the short-grass and barley cases, can partially be

attributed to the increased hydraulic conductivity of the upper regions, modified to represent the brick and sand surface. This region contains comparatively higher permeable materials which increase hydraulic conductivity and facilitate the transport of water to deeper regions. In addition to this, the surface roughness is smoother than the short-grass and barley models, reducing evaporation rates.

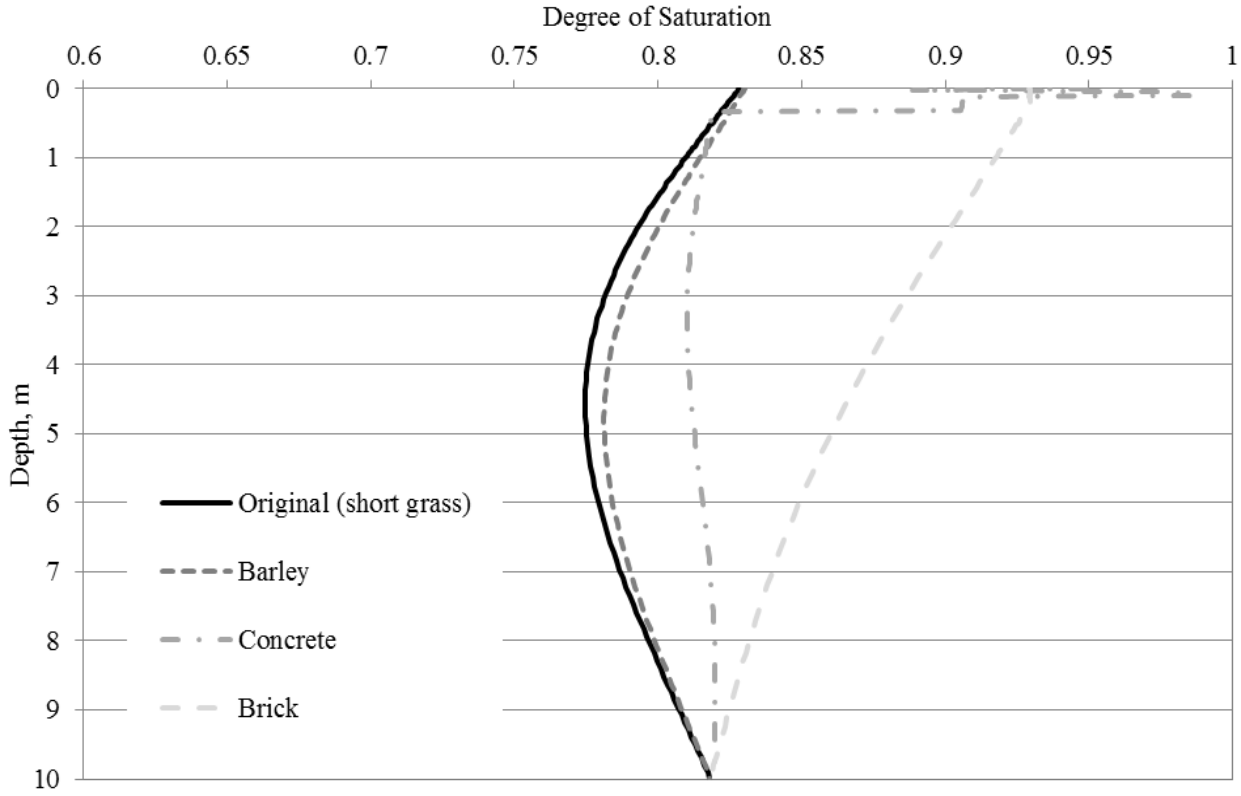

Figure 8.20 –Far-field vertical degree of saturation profile at the wettest cyclic point for the original, barley, asphalt and brick surface models.

The degree of saturation curve exhibited by the asphalt model differs greatly from the remaining three surface models. Upon further inspection of Figures 8.20 and 8.21 it can be seen that there is very little change in the degree of saturation below a depth of approximately 0.2 meters. This corresponds to the depth of a relatively impermeable concrete layer prescribed according to the adopted car-park construction profile. Above the impermeable concrete layer, the simulated degree of saturation range is greater than the remaining three cases reaching as low as 0.24 and as high as 1. The more extreme degree of saturation range has again been attributed to the impermeable concrete layer which restricts the vertical flow of moisture between the surface layers and deeper ground regions.

Applying knowledge of the relatively impermeable concrete layer, it can be deduced that the degree of saturation changes beneath the impermeable layer are primarily induced by the thermal ground behaviour and not hydraulic exchanges at the ground surface. In reality, it would be expected that lateral moisture flow would alter the degree of saturation in this region however; this has not been accounted for in the current model.

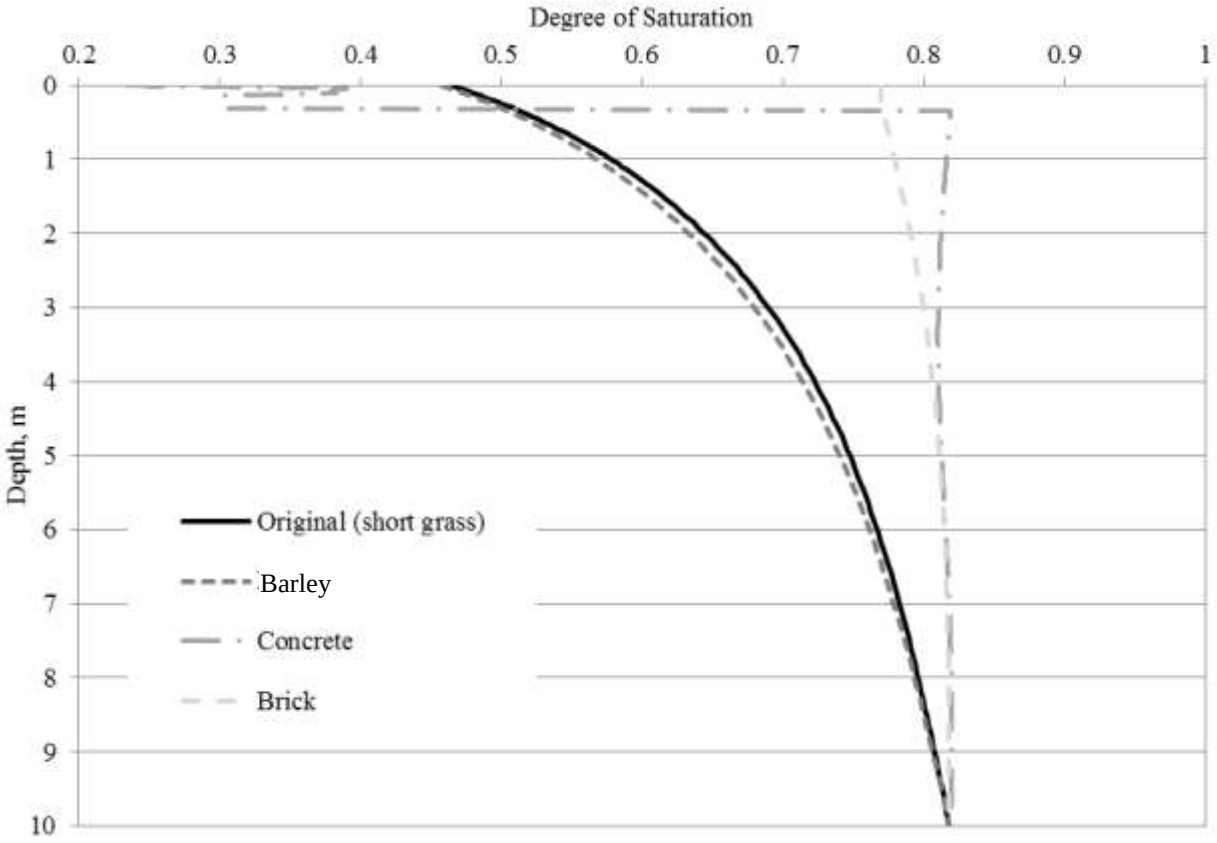

Figure 8.21 –Far-field vertical degree of saturation profile at the driest cyclic point for the original, barley, asphalt and brick surface models.

The thermal results from the four models representing surface conditions associated with short-grass, barley, brick and asphalt have been presented using four vertical temperature profiles. Figures 8.22 and 8.23 show vertical temperature profiles coinciding with the end of the heat recovery period (see Figure 8.12), while Figures 8.24 and 8.25 show vertical temperature profiles coinciding with the end of the heat extraction period (see Figure 8.12). In each case, Figures 8.22 and 8.24 show the fair-field temperature profiles for the four simulations while Figures 8.23 and 8.25 show the in-line temperature profiles. The following paragraphs will discuss Figures 8.22 and 8.23 first, followed by 8.24 and 8.25.

Upon inspection of Figures 8.22 and 8.23, it is possible to highlight a number of general trends. First, it can be said that the simulated profiles for short-grass and barley closely match each another. Within Figures 8.20 and 8.21, the simulated temperature difference between these two curves never exceeds 0.1 K. The identical soil properties prescribed in both the short-grass and barley model could explain the similarity between the simulated vertical profiles. The small differences observed can therefore be attributed to the surface conditions, namely; shortwave reflectivity, longwave emissivity and aerodynamic resistance.

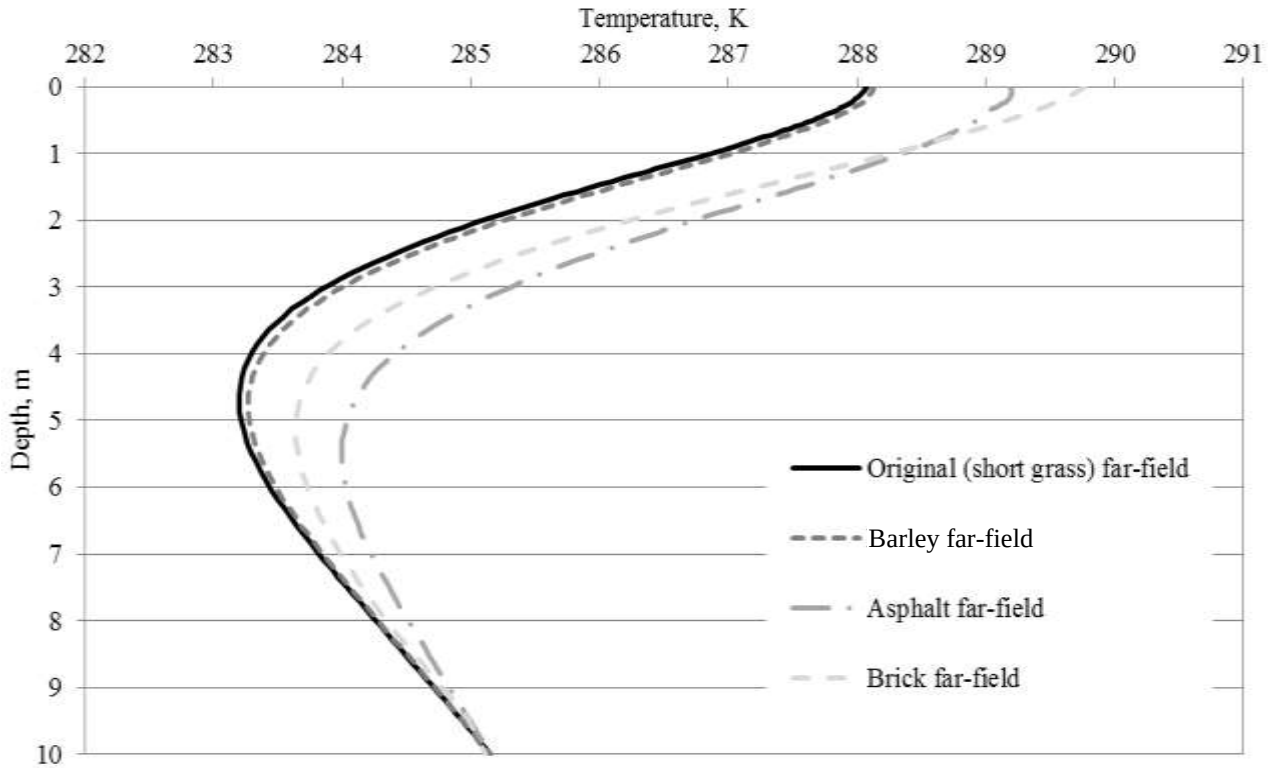

Figure 8.22 – Far-field vertical temperature profile at the end of the heat recovery period for the original, barley, asphalt and brick surface models.

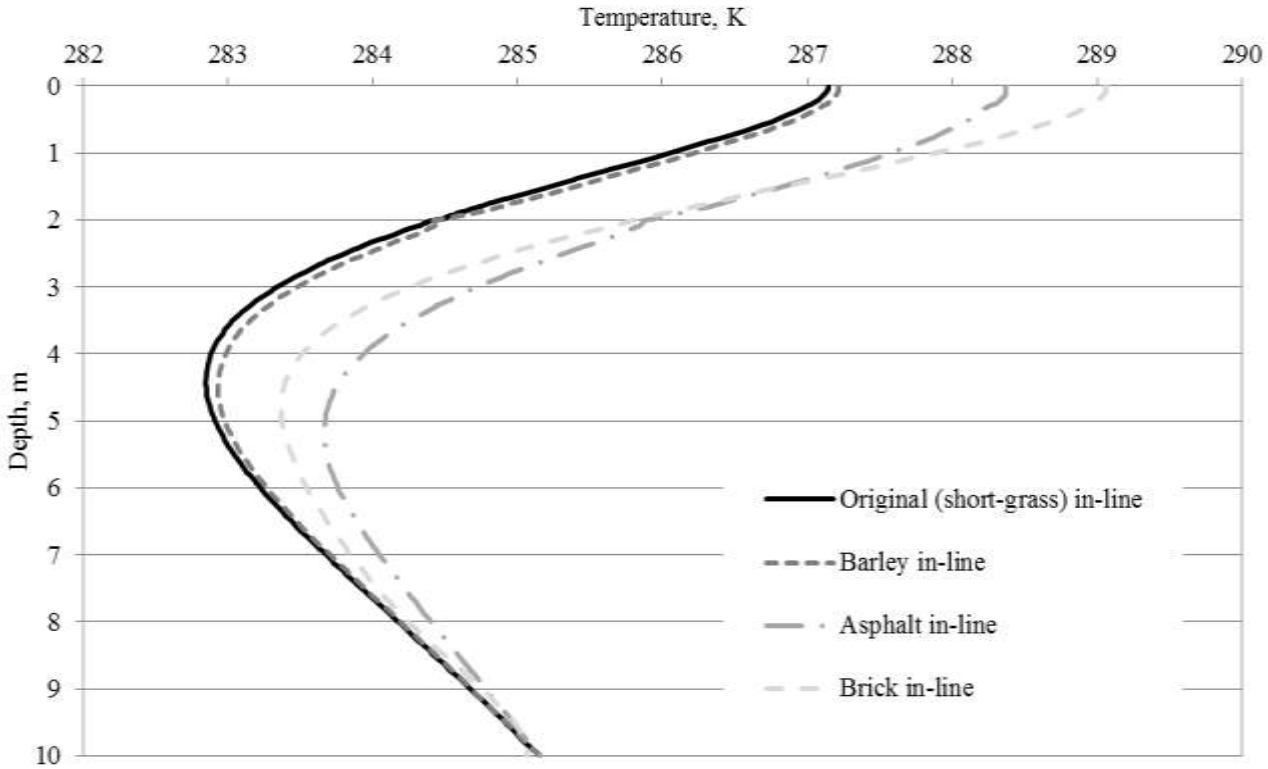

Figure 8.23 – In-line vertical temperature profile at the end of the heat recovery period for the original, barley, asphalt and brick surface models.

From the results obtained, it can be said that the vertical temperature profiles of the urban surfaces (i.e. asphalt and brick) were greater than those associated with the rural surfaces (i.e. short-grass and barley). As this trend was observed both at the far-field and in-line, it can be deduced that the difference in profile was due to the surface boundary and not heat extraction via the ground-loop. In both figures, the greatest difference between the urban and rural cases was simulated at the ground surface. For example, Figure 8.23 shows that the simulated ground temperature for the brick case is 1.9 K greater than the short-grass, whereas the asphalt case is 1.2 K greater than the short-grass. Despite the temperature differences, it can be said that the general shape of the vertical profiles exhibited by the four materials in both Figure 8.22 and 8.23 broadly correlate with each other.

The difference in ground temperature associated with the surface materials is not unexpected. Philippe et al. (2010) presented data regarding the ground temperature beneath short-grass and an adjacent car-park. Within this research, ground temperature data at a depth of 1.5 meters was presented for May 2009. At a depth of 1.5 meters, the undisturbed ground temperatures reported under the car park were approximately 1.0 K greater than short-grass. The temperature differences simulated in the current investigations approximately concur with these findings.

As previously discussed, the only difference between the four models is with regards to the surface materials and associated properties. The ground temperature difference observed at the ground surface is therefore, to some extent, expected. The following paragraphs will discuss the observed differences between the brick/asphalt cases and the rural cases.

When inspecting the asphalt case it is possible to deduce that the temperature increase from the rural models is due to a combination of the material properties and surface properties. Although the thermal properties of the constituent surface materials are similar, the simulated degree of saturation was greater in the asphalt case. The increased degree of saturation leads to an increase in thermal conductivity which could be identified as a contributing factor. Unlike the constituent materials, the surface short-wave reflection factor differs greatly for the rural and asphalt models. This results in the asphalt absorbing approximately 15% more short-wave radiation than the short-grass and barley models.

When inspecting the brick case, it is possible to deduce that temperature increase from the rural models is again due to a combination of surface reflection and thermal properties. Unlike the asphalt, the sand contained in the brick surface has a greater thermal conductivity than the short-grass model, promoting heat conduction. Further to this, Figures 8.20 and 8.21 show that the simulated ground has a greater degree of saturation than the rural cases. This also leads to an increase in the thermal conductivity of the ground. When comparing the surface reflection properties, it can be seen that the short-wave reflection factor of the brick results in the brick absorbing approximately 7.5% more short-wave radiation than the rural cases.

Figures 8.24 and 8.25 show the vertical temperature profiles at the at far-field and in-line locations respectively, at the end of the heat extraction period. The trends exhibited by the four cases in Figures 8.24 and 8.25 concur with those previously discussed, namely, that the ground temperature profiles associated with the urban surfaces (asphalt and brick) are greater than those for the rural surfaces (short-grass and barley), and; that the vertical profiles for barley and short-grass closely resemble one another.

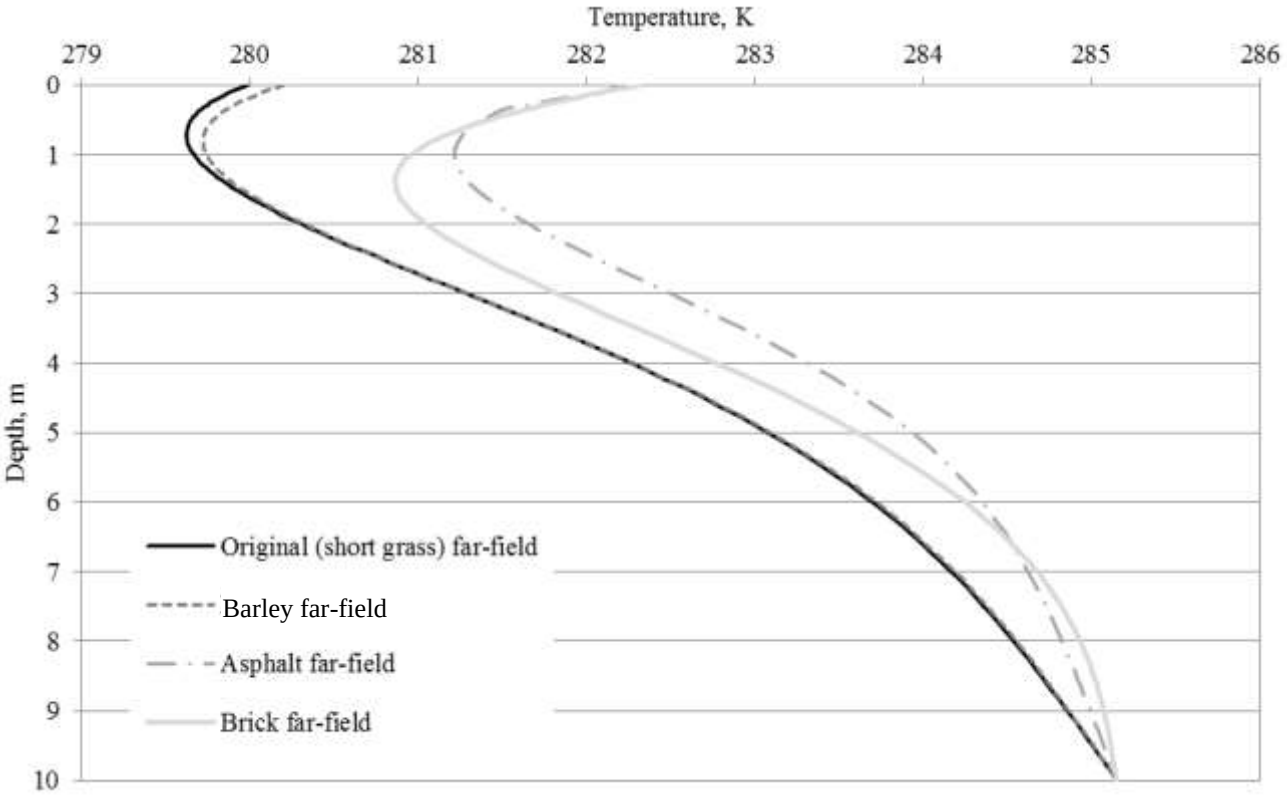

Figure 8.24 – Far-field vertical temperature profile at the end of the heat extraction period for the original, barley, asphalt and brick surface models.

Closer inspection of Figure 8.25 allows the impact of the surface materials on ground source heat performance to be further investigated. The greater far-field temperatures simulated for urban surface materials have resulted in an increased ground temperature immediately adjacent to the ground-loop. The ground temperature adjacent to the ground-loop for the short-grass cases measures 274.0 K whereas in the asphalt case this has increased to 275.0 K and in the brick case this has further increase to 276.0 K. From the perspective of the ground-loop performance, these are important findings as they suggest that surface materials, and their associated properties, are capable of influencing ground source heat extraction. The increased ground temperatures would enable a greater amount of heat energy to be extracted from the ground, while the ground temperature itself remained above the 273.0 K threshold (the minimum ground temperature as suggested by the design standard MIS 3005).

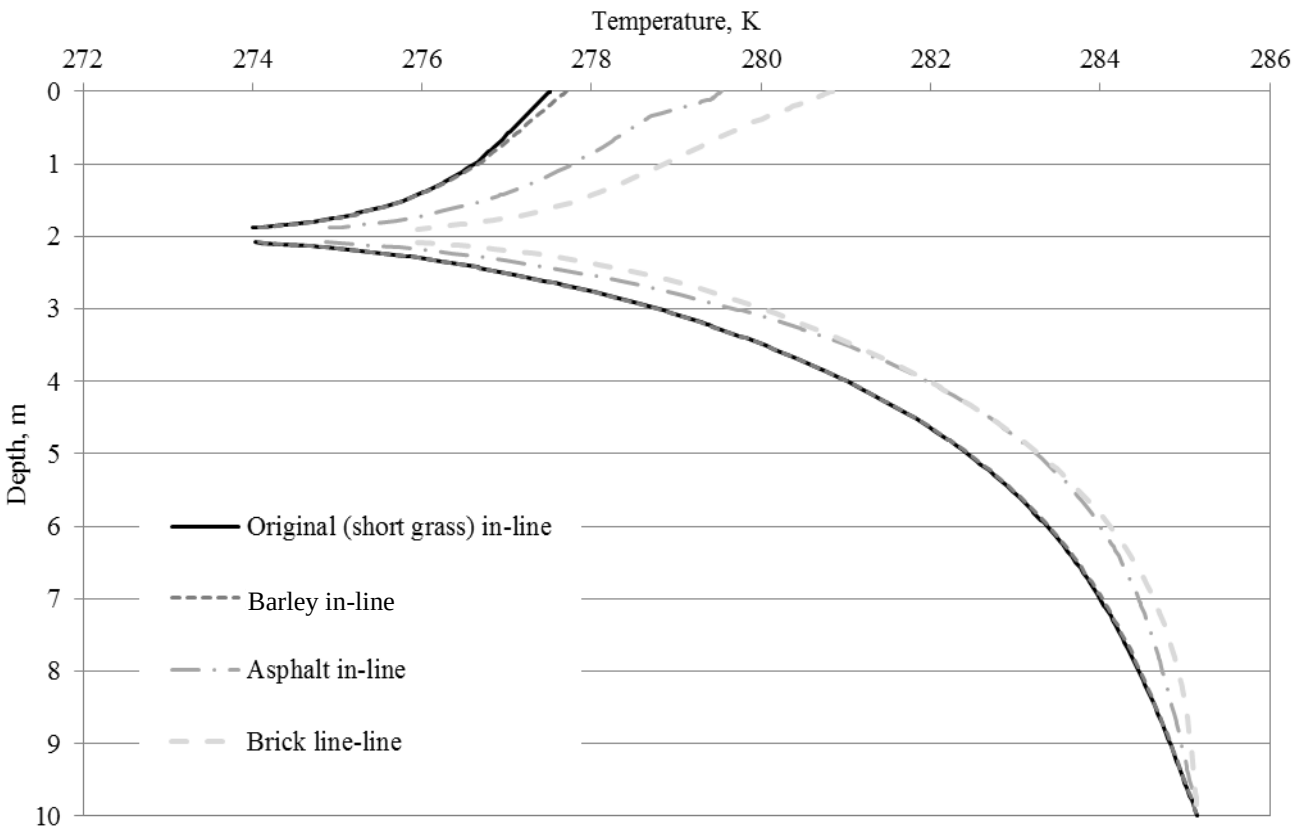

Figure 8.25 – In-line vertical temperature profile at the end of the heat extraction period for the original, barley, asphalt and brick surface models.

The preceding sections have found that surface thermal and hydraulic behaviour exhibited by both the barley and short-grass model closely resembled each other. Before drawing any conclusions, it proves necessary to draw attention to the current model limitations. Although the model is able to account for the varying short-wave and longwave radiation factors associated with the annual barley cycle, the model is unable to completely account for the air behaviour once the crop exceed approximately 0.5 m. Geiger (1950) showed that in such circumstances (i.e. when the crop cover exceeds 0.5 m), the near ground air behaviour would noticeably influence ground temperature simulations. To give a sense of perspective, Geiger reported a difference in temperature between the near ground and ambient air temperature of up to 3 K in maize crops planted in Germany. Although the model did not consider the modified air temperature associated with barley this should only adversely affect the model performance for the months of May, June, July and August (i.e. when the barley is greater than 0.5 meters in height) (Geiger, 1950). The air behaviour above the ground is further discussed in Chapter 9 as a potential avenue for further works.

In summary, the findings from the preceding investigation revealed that surface materials are capable of influencing the ground thermal behaviour subject to heat extraction via ground source heat systems. The surface materials of asphalt and brick resulted in higher ground temperatures within the

far-field and in-line vertical profiles. On the other hand, there was limited thermal difference between the barley and short grass models. At the end of the heat extraction period, the ground immediately surrounding the ground-loop was 1.0 and 2.0 K higher for the asphalt and brick surfaces respectively. From a performance perspective, this suggests that a greater amount of thermal energy could be viably extracted from these two scenarios.

There was very little difference between the hydraulic behaviour simulated in the short-grass and barley cases. The lower permeability of the concrete layer in the asphalt model prevented the surface mass exchanges from influencing the degree of saturation of the ground. The resulting degree of saturation variations were therefore induced by thermal gradients alone. The brick surface had a greater permeability than the short-grass and barley cases, leading to a general increase in the degree of saturation throughout the inspection period.

8.5 Investigation into MIS 3005 standard

As previously discussed, the standard currently endorsed by the UK government for the design and installation of horizontal ground source heat systems is the MIS 3005 standard (MCS, 2008). This section presents an investigation into the validity of the standard with regards to the horizontal ground source heat system detailed in Chapter 3.

The ground behaviour in response to two ground-loop configurations has been simulated using the model developed and validated within the scope of this study. Both ground-loops have been designed to meet the design heating loads for the monitoring site detailed in Chapter 3. The first model investigates the ground behaviour in response to a ground-loop designed fully in accordance with the MIS 3005 standard, installed at the maximum suggested depth of 1.2 meters. This simulation will be referred to as ‘MIS 1.2m’ within this section. The second model investigates the ground behaviour in response to a ground-loop length designed in accordance with MIS 3005 but installed at a 2 meter burial depth (i.e. beyond the maximum depth specific by MIS 3005). This is similar to the ground-loop burial depth adopted at the monitoring site. This simulation is referred to as ‘MIS 2m’ within this section. Results achieved from the two models are subsequently compared with the long-term simulations of the monitoring site previously presented in section 8.2.

8.5.1 Domain and constitutive relationships

The domain and constitutive relationships adopted within the 'MIS 1.2' and 'MIS 2m' simulations are similar, if not identical, as those previously used within the long-term simulations detailed in section 8.2.1. To avoid repetition, only the model differences will be discussed in detail here. Further details can be found in section 8.2.1 for the remaining simulation details.

The domain and constitutive relationships adopted within the 'MIS 2m' model is identical to those previously presented in section 8.2.1 and will therefore not be discussed further. The only difference with regard to the 'MIS 1.2m' model is the ground-loop depth. As previously mentioned, the ground-loop has been simulated at a depth of 1.2 meters. The central pipe coordinates depicted on Figure 8.1 have therefore been altered to (-0.35, -1.2) and (0.35, 1.2) respectively. The constitutive relationships prescribed in both models have been previously summarised in Table 8.1.

8.5.2 Initial and boundary conditions

All initial and boundary conditions have remained the same as those detailed in section 8.2.2 with the exception of the ground-loop boundary flux. Re-designing the ground-loop in accordance with MIS 3005 resulted in a ground-loop 667 meters in length, 11.1% shorter than the 750 meter ground-loop installed at the monitoring site. The ground-loop external diameter (measuring 0.04 meters) and material on the other hand remained the same. The design calculations for the ground-loop can be in Appendix H.

Similar to the long-term simulations detailed in section 8.2, the uniform ground-loop boundary has been prescribed within the models. The prescribed heat flux has been based on the average daily heating loads recorded at the monitoring site (previously depicted in Figure 8.6). The change in the ground-loop length increased the heat flux per unit length being extracted by the ground-loop by 12.4%. The resulting heat flux has been presented in Figure 8.26.

8.5.3 Material parameters

The material parameters prescribed in both the 'MIS 1.2m' and 'MIS 2m' models are the same as those previously detailed in section 8.2.3. The material parameters have been previously summarised in Table 8.2.

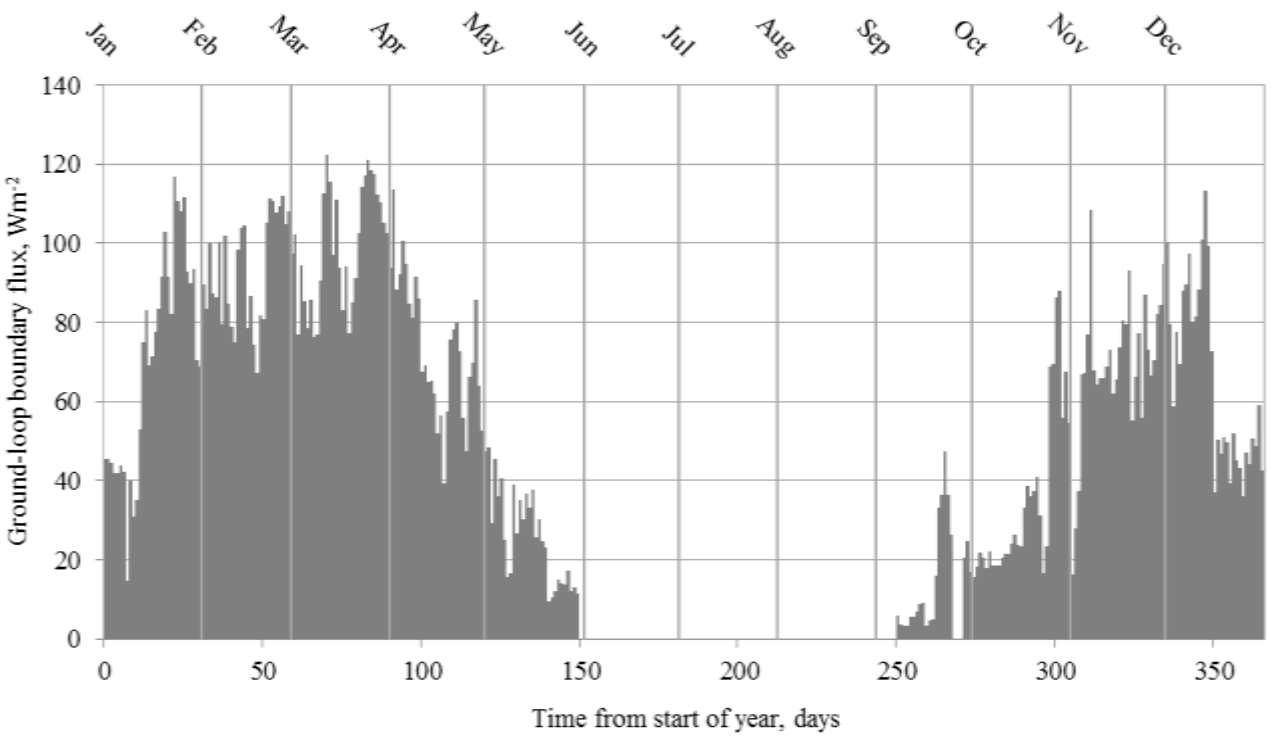

Figure 8.26 – Ground-loop heat flux based upon the heating loads recorded at the monitoring site and ground-loop length according to the MIS 3005 design standard.

8.5.4 Results

The following section will discuss the results obtained from the MIS 1.2m and MIS 2m models. The ground behaviour in response to these ground-loop configurations is also compared with the long-term simulations previously detailed in section 8.2 (i.e. the actual ground-loop configuration installed at the monitoring site). The hydraulic ground behaviour simulated in response to both the MIS 1.2m and MIS 2m models was similar to the findings previously discussed in section 8.2. For example, the ground-loop flux in both cases was insufficient to induce noticeable changes in the degree of saturation in the vicinity of the ground-loop. To avoid repetition, the reader is referred to section 8.2.4 for a more detailed inspection of the long-term hydraulic ground behaviour in response to heat extraction. Where the models did differ was with regards to the ground thermal behaviour in the ground immediately surrounding the ground-loop. The remainder of this section will focus of this aspect.

Similar to the findings in section 8.2, the ground behaviour was found to exhibit annual cyclic behaviour after approximately 3 years. To improve the clarity of the results, ground behaviour from only the first 3 years is presented. The simulation also showed that the greatest thermal differences occurred in the ground region immediately surrounding the ground-loop. This region shall therefore be as the basis for the following discussion. Figure 8.27 shows the ground temperature behaviour for

all three design cases (i.e. the original design, MIS 1.2m and MIS 2m designs), at a horizontal displacement of 0.01 meters.

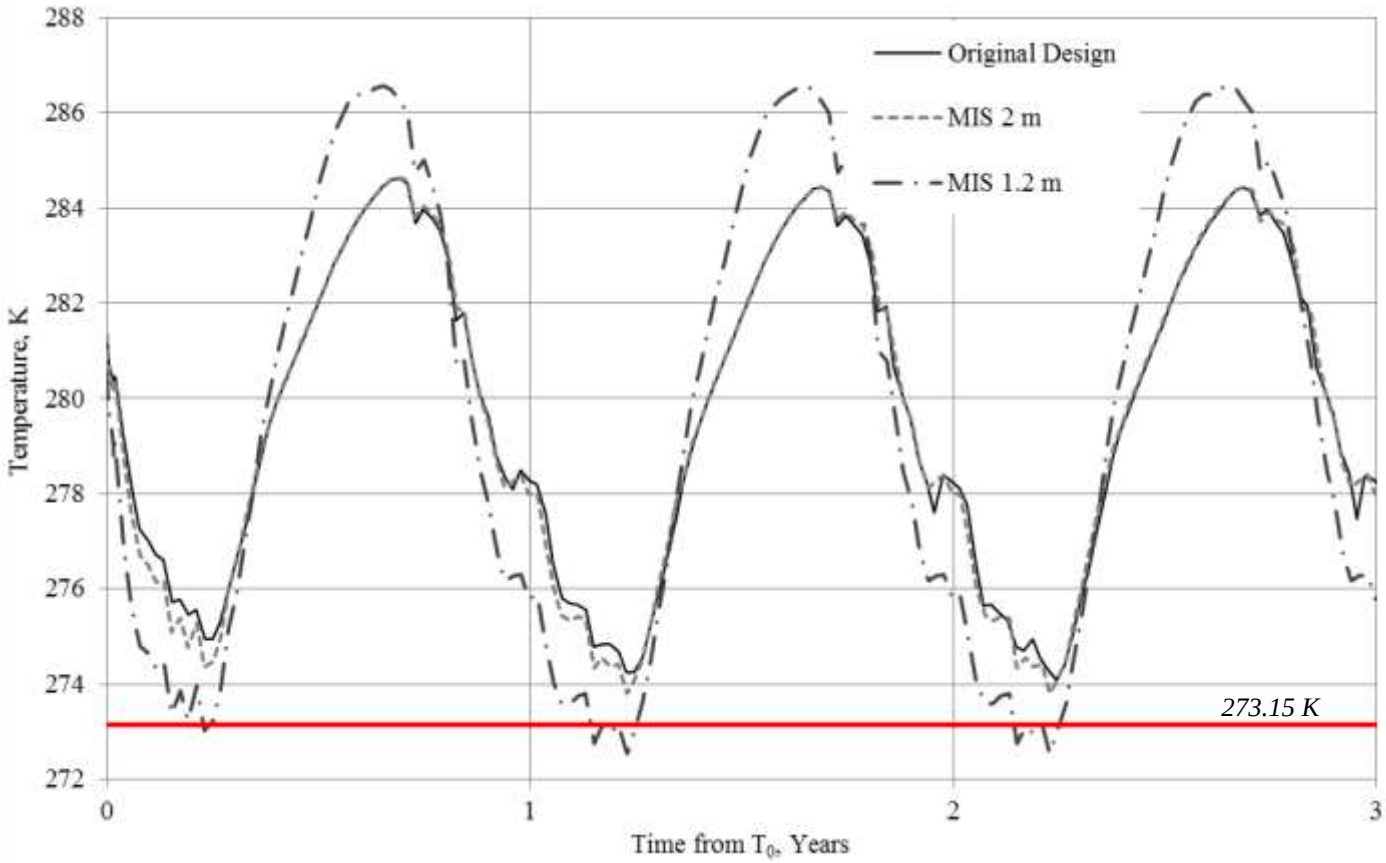

Figure 8.27 – Ground temperature at a horizontal displacement of 0.01 m from the ground-loop surface for the MIS 1.2, MIS 2 and Original ground-loop configurations.

Figure 8.27 shows that the ground thermal behaviour in response to the MIS 2m design was similar to the behaviour found when inspecting the original long-term model, simulating the real system. At a displacement of 0.01m, the ground thermal behaviour only noticeably differs during periods of prolonged heating (i.e. during the winter months). The greater ground-loop flux induced by the MIS 2m model results in ground temperatures dipping to 273.6 K, 0.6 K lower than the original long-term model. Outside periods of prolonged heating, there is little, if any, difference between the original and MIS 2 m simulation results.

When comparing the original and MIS 1.2m model, it becomes apparent that there are far greater differences than the preceding discussion. When inspecting periods of prolonged heat extraction, it can be deduced that the ground temperatures in response to heat extraction are notably lower for the MIS 1.2 meter model when compared to the remaining models. For example, the MIS 1.2m model predicts ground temperatures as low as 272.6 K, 1.0 K lower than the MIS 2m model and 1.6 K lower than the original long-term model. An identical ground-loop flux is prescribed in the

MIS 1.2m and MIS 2m models, therefore the ground temperature difference can be accredited to the difference in ground-loop depth.

The differences between the original and MIS 1.2m model are not confined to periods of prolonged heating. For example, during the summer months the ground temperature increases to 286.5 K, 1.9 K greater than the ground found at a depth of 2.0 meters. It can therefore be said that the annual ground temperature amplitude is greater in the MIS 1.2m model. This reflects the behaviour of the surrounding ground and the increased influence of the surface boundary at a depth of 1.2 meters. Although the summer months subject the ground region at a depth of 1.2 meters to greater ground temperatures, promoting thermal recharge and sustainability, the winter months give rise to lower temperatures than those found at a depth of 2 meters.

The ground behaviour in response to the three ground-loop configurations can be further investigated with comparisons between the design criterion 4.2.13 within MIS 3005 (MCS, 2008). This criterion states than the ground temperature adjacent to the ground-loop must remain above 273.15 K throughout the design life of the system, where the design life is a minimum of 20 years. As will be discussed, this criterion becomes of particular importance within the context of the preceding findings. Although the ground temperatures were found to decrease in the MIS 2m simulation, they remain above to 273.15 K threshold and therefore the system conformed to the criterion. The same cannot be said for the MIS 1.2m model which simulated ground temperatures below the 273.15 K threshold, thereby failing to meet the design criterion.

As previously highlighted, the ground-loop configuration modelled within the MIS 1.2m model was in full accordance with the MIS 3005 design codes (lay to the maximum specified depth). The results presented here show that the ground-loop design specified by the MIS 3005 standard was invalid for the heat loads and ground conditions encountered at the monitoring site. Despite this, the MIS 2m model did show that a ground-loop length designed in accordance with MIS 3005 would meet the criterion provided that it was lay at a depth of 2.0 meters, beyond the maximum depth of 1.2 meters specific in the current standard. The difference between the MIS 1.2m and MIS 2m models has demonstrated the impact of ground-loop depth, and its importance within the ground-loop design. At present there is no consideration of ground depth made within the ground-loop calculation.

In summary, a ground-loop was designed in accordance with MIS 3005 to meet the design heat load of the property found at the monitoring site. The resulting ground-loop was 667 meters long, 83 meters shorter than the installed ground-loop, resulting in a greater ground-loop flux. Two models were developed to simulate the ground-loop configuration at a depth of 1.2 meters (the maximum depth specified by the standard) and a depth of 2.0 meters. It was found that the ground-loop lay at 2 meters resulted in lower ground temperatures than the original long-term model; however they remained above the ground temperature criterion specific by MIS 3005. The ground-

loop lay in full accordance with the standard, at a depth of 1.2 meters, was found to fail the criterion. This indicates that the ground-loop configuration was unable to sustainably meet the heating loads of the system considered in this study.

8.6 Conclusions

This chapter first presented long-term simulations which investigated the TH ground behaviour at the monitoring site in response to heat extraction over a period of 20 years. It was found that both the thermal and hydraulic ground behaviour reached a steady cyclic state after approximately 3 years. Identification of this cyclic response can be applied within future investigations to reduce simulation and computational times.

Investigation of the hydraulic ground behaviour revealed that it varied predominantly as a function of depth. The heat flux induced by the ground-loop (due to heat extraction) was found to be insufficient in the current case to induce a noticeable change in the ground hydraulic behaviour. These results show that the current heat extraction does not influence the thermal properties (namely thermal conduction and specific heat capacity) of the ground adjacent to the ground-loop.

Inspection of the simulated ground thermal distributions highlighted two important features. Firstly, heat extraction via the ground-loop noticeably influenced the ground behaviour up to, and including, the surface. Secondly, the thermal gradient induced by heat extraction was steeper beneath the ground-loop than above it, concurring with findings previously presented in Chapter 4. Identification of these distributions has not only enhanced knowledge of the ground thermal response to heat extraction but also highlighted potential avenues for future system optimisation.

During the summer months (i.e. the so-called heat recovery period) the simulated ground temperature almost recovered to the far-field ground temperatures. For the current system, this shows that heat being extracted during the winter is being replenished and therefore the system is sustainable. From a holistic perspective, this demonstrates that ground source heat is a viable and sustainable approach to provide space heating.

Following the long-term simulations, an investigation into the computational performance of the developed parallel algorithm was conducted. Using the serial code as a benchmark, the performance of the parallel algorithm using two, three and four processors was investigated. It was found that the application of the parallel algorithm reduced computational times, although the relationship between the time reduction and utilised processors was non-linear. The utilisation of four processors reduced computational times to 55.3% of the benchmark simulation. The results show that

computational capability is no longer a significant barrier to the simulation of horizontal ground source heat systems.

An investigation into the effects of surface properties on the TH ground behaviour was undertaken. In addition to the original long-term simulation (considering the surface as short-grass), three cases considering a brick, asphalt and barley crop cover were simulated. The TH ground behaviour exhibited by the original and barley crop covering were very similar. It was found that the brick and asphalt surface covering led to greater ground temperatures both at the far-field and in the ground immediately surrounding the ground-loop. The results show that more heat can be sustainably extracted from horizontal ground source heat systems which have urban surface coverings. From a design perspective, this finding has a number of implications. For example, the greater ground temperature would reduce the ground-loop length required to meet the heating load of the system. The current design standards do not take account of the surface type/material. The results presented have demonstrated that this simplification could result in ground-loops being over-sized.

Finally, investigations were undertaken into the validity of the current design code (MIS 3005) with respect to ground-loop design considered in this study. It was found that the ground-loop configuration in full accordance with the design standard (i.e. buried at a depth of 1.2 meters), failed a ground temperature criterion specified by the standard. From a holistic perspective, this indicates that design recommendations provided did not lead to a sustainable design which can meet the ground temperature criterion specified. When modelled at a depth of 2.0 meters, the ground-loop configuration was found to meet the design standards. This not only highlighted the importance of the ground-loop depth on the sustainable performance of systems but also that the current design code has over simplified the aspect of ground-loop burial depth.

The nature of the long-term investigations presented are unlike any others previously undertaken in the research area, therefore it can be said that the findings have increased the available knowledge base. In doing so, potential avenues for future investigations have been highlighted particularly with regard to the influence of the surface material on ground behaviour and system design codes.

References

Barnes, G. E., 2000. *Soil Mechanics - Principle and Practice.* New York: Palgrave.

Busby, J., Kingdon, A. & Williams, J., 2011. *The measured shallow temperature field in Britain.* Nottingham: British Geological Survey.

Chudley, R., 1988. *Building Construction Handbook.* 1st ed. Oxford: Heinemann Newnes.

Cultrone, G. et al., 2004. Influence of mineralogy and firing temperature on the porosity of bricks. *Journal of the European Ceramic Society,* 24(1), pp. 547-564.

De Vries, D. A., 1966. Thermal properties of soils. In: W. R. van Wijk, ed. *Physics of plant environment.* 2nd ed. Amsterdam: North Halland Publishing Co., pp. 215-235.

Department for Environment, Food and Rural Affairs (DEFRA), 2010. *Flood and Water Management Act 2010.* London: Crown.

Ewen, J. & Thomas, H. R., 1987. The thermal probe - a new method and its use on an unsaturated sand. *Geotechnique,* 37(1), pp. 91-105.

Geiger, R., 1950. *The Climate Near the Ground.* 2nd ed. Cambridge, Massachusetts: Harvard University Press.

Gruber, I. et al., 2012. A computational study of the effect of structural anisotropy of porous asphalt on hydraulic conductivity. *Construction and Building Materials,* 36(1), pp. 66-77.

Hellstrom, G., 1991. *Ground heat storage: Thermal analysis of duct storage systems.* Lund: Department of Mathematics Physics University of Lund.

HGCA, 2006. *The barley growth guide,* London: Scottish Executive Enironmental and Rural Affairs Department.

Holland Stone, 2013. [Online]
Available at: www.hollandstone.com/our_work.html
[Accessed 13 5 2013].

Hunt, W. F. & Collins, K. A., 2008. *Urban Waterways - Permeable Pavement: Research Update and Design Implications,* Raleigh: North Carolina Cooperative Extension Service.

Kaye, G. W. C., Laby & M, T., 1973. *Tables of physical and chemical constants.* 14th ed. London: Longmans.

Khudhair, A. M. & Farid, M. M., 2004. A review on energy conservation in building applications with thermal storage by latent heat using phase change materials. *Energy Conversion and Management,* 45(2), pp. 263-275.

Kondraivendhan, B., Sabet Divsholi, B. & Susanto, T., 2011. *Assessment of strength, permeability and hydraulic diffusivity of concrete through mercury intrusion porosimetry.* Singapore, 36th Conference on Our World in Concrete and Structures.

Kusuda, T., 1975. *The effect of ground cover on earth temperature.* Fort Worth, Texas, USA, Conference proceedings of 'Alternatives in energy conservation: The use of earth-covered buildings'.

Kusuda, T. & Achenbach, P. R., 1965. Earth temperature and thermal diffusivity at selected stations in the United States. *ASHRAE Trans,* 71(1), pp. 61-75.

Levinson, R. & Akbari, H., 2001. *Effects of composition and exposure on the solar reflectance of Portland cement concrete,* Berkeley, CA, USA: Lawrence Berkeley National Laboratory Report.

MET Office, 2013. *Met Office: Regional Climates.* [Online]
Available at: http://www.metoffice.gov.uk/climate/uk/wl/
[Accessed 27 2 2013].

Microgeneration Certification Scheme (MCS), 2008. *Microgeneration Installation Standard: MIS 3005 Issue 3.0.* London: Department of Energy and Climate Change (DECC).

Quiet Nature, 2013. [Online]
Available at: http://www.quietnature.ca/sustainable-landscape-design-elements-permeable-paving-and-green-driveways/
[Accessed 13 5 2013].

Sheppard, P. A., 1947. The aerodynamic drag of the earth's surface and the value of von Karman's constant in the lower atmosphere. *Proceedings of the Royal Society,* pp. 208-222.

Tutiempo, 2013. *Hereford/Credenhill historical weather.* [Online]
Available at: http://www.tutiempo.net/en/Climate/HEREFORD_CREDENHILL/2012/35220.htm
[Accessed 10 4 2013].

van Genuchten, M. T., 1980. A closed-form equation for predicting hydraulic conductivity of unsaturated soils. *Journal of Soil Society of America,* 44(1), pp. 892-898.

van Wijk, W. R. & De Vries, D. A., 1966. The Atmosphere and the Soil. In: W. R. van Wijk, ed. *Physics of Plant Evironment.* Amsterdam: North Amsterdam Publishing Co., p. 52.

van Wijk, W. R. & Scholte Ubing, D. W., 1966. Radiation. In: W. R. van Wijk, ed. *Physics of the Plant Environment.* Amsterdam: North Holland Publishing Co., p. 87.

Yavuzturk, C. & Ksaibati, K., 2002. *Assessment of temperature fluctuations in asphalt pavements due to thermal environmental conditions using a two-dimensional, transient finite difference approach,* Wyoming, USA: University of Wyoming.

Zadrazil, T., Vodak, F. & Kapickova, O., 2004. Effect of temperature and age of concrete on strength - Porosity relation. *Acta Polytechnica,* 44(1), pp. 53-56.

Chapter 9

Conclusions

9.1 Introduction

Specific conclusions pertinent to each respective chapter have been presented throughout this thesis. This chapter aims to synthesise these conclusions and relate them to the research objectives as specified at the start of this work. With regards to the current work, key scientific developments will be highlighted in the following sections. Following this, potential research and scientific development for further work will be discussed.

The aim of the presented thesis was to obtain a better understanding of the ground thermal behaviour in response to heat extraction from horizontal ground source heat systems. The overall aim was sub-divided into a number of specific study objectives which have been previously detailed in Chapter 1. For clarity, the developments and achievements of this thesis will be broadly discussed in two sections (9.2 and 9.3), with respect to: *i) Field-scale experimental study and ii) Numerical study*. Where necessary, references to the respective chapters containing the work will be made. Following

this, the overall conclusions of the thesis will be discussed in section 9.4 and suggestions for further work will be made in section 9.5.

9.2 Field-scale experimental study

A literature review contained in Chapter 2 highlighted that there was a limited number of sites monitoring the ground behaviour of horizontal ground source heat systems. Further to this, the majority of the existing monitoring systems were found to focus on the mechanical aspects of the system either simplifying ground measurements or overlooking them all together.

The monitoring scheme designed and implemented within the scope of this thesis provided a more detailed and comprehensive ground data-set than any previous examples sourced in literature. The scheme was implemented to continuously monitor the ground, climatic and system characteristics of a working horizontal ground source heat system which was the sole provider of space heating to a habited domestic property in Powys, UK. The nature of the system addressed many of the limitations associated with previous monitoring sites, namely the site was: *i) full-scale, ii) subject to real heating loads and cycles;* and *iii) provided space heating only*. The number of ground thermistors installed was far greater than previous monitoring sites, allowing a greater resolution of ground thermal data to be collected. Unlike previous work, a full set of climate data capable of influencing diurnal and annual ground thermal-hydraulic behaviour was collected along with system information sufficient to calculate the heat load, facilitating a more complete analysis of the overall system. In addition to this, a ground investigation was undertaken to characterise the soil at the experimental site the results of which were applied within the numerical aspect of the thesis. The ground investigation was more comprehensive and investigated a wider range of parameters than those previously presented in literature.

The scale and location of the monitoring site raised further issues regarding the checking, downloading and analysis of the collected data. To address the displacement of the monitoring site from the university campus, appropriate remote monitoring capabilities were installed to allow the continual checking and communication of data. At the university end, a data management tool was produced to store, check, structure and interrogate the incoming raw data. The successful design and implementation of this data strategy is important for future research, demonstrating that large volumes of data can be efficiently collected, stored and subsequently analysed from a single location.

The global scarcity of similar monitoring sites within the research area raises the significance of the current scheme. In addition to providing a unique data-set, the design process outlined in

Chapter 3 along with the remote communication capabilities and data management approach can be used to provide a template for similar schemes.

Through the analysis of the collected data, a more substantial understanding of ground thermal behaviour in response to energy extraction via horizontal ground source heat systems has been obtained. The results obtained from the 13 month observation period provide a greater insight into the behaviour of horizontal ground source heat systems than previous studies. The key findings, as discussed in Chapter 4 have been concluded in the following paragraphs.

For the system in question, the climatic conditions were found to significantly influence the temperature of the ground immediately adjacent to the ground-loop surface, more so than the heat extraction via the ground-loop. Inspecting the undisturbed ground temperatures beyond the thermal influence of the ground-loop highlighted the potential performance improvement which would be gained by installing a ground-loop at a depth of 2 meters as oppose to the 1.2 meter maximum currently defined in the MIS 3005 design standards (MCS, 2008).

The greater resolution of the ground temperature data allowed for a more detailed analysis of the ground thermal behaviour than previous investigations. The data resolution enabled a more comprehensive inspection into the size and shape of the thermal distributions induced around ground-loop surfaces. Examination of these distributions revealed that the thermal gradients induced around the ground-loop were non-symmetrical. The thermal gradients observed beneath the ground-loop were steeper than those above. The differing thermal gradients suggest that the energy extraction from the ground is also non-symmetrical and that more thermal energy is being extraction from beneath the ground-loop. Application of this knowledge can be used to improve the system design and performance assessment.

A series of thermistors were spatially positioned within the monitoring scheme to collect ground temperature data immediately adjacent to the ground-loop surface. Collective analysis of this data revealed that the varying fluid temperature along the ground-loop length had little observable impact on the adjacent ground temperatures. This observation has significant implication from both a monitoring and modelling point of view. Firstly, this finding highlights that a systems thermal behaviour can be sufficiently monitored via a single ground cross-section provided that conventional ground-loop configurations are adopted and significant ground heterogeneities do not exist which would otherwise influence ground thermal behaviour. This has implications for future research, implying that high resolution ground data can be obtained from a fewer number of ground sensors than that used in the current scheme, financially improving the viability of monitoring sites. From a numerical perspective, the finding suggests that horizontal ground source heat systems can be simulated using two-dimensional analysis, as oppose to three-dimensional analysis, without incurring

errors associated with a varying fluid temperature profile. The will reduce the computation effort and time associated with simulations, facilitating more efficient research.

9.3 Numerical study

A coupled thermal-hydraulic modelling investigation was undertaken by developing the coupled numerical tool COMPASS. The model was developed to include boundary conditions that are representative of horizontal ground source heat systems; namely the so-called ground surface and ground-loop boundary conditions.

The developed surface boundary condition represents the coupled thermal-hydraulic interaction between the ground surface and atmosphere, considering a range of climatic variables and mechanisms. The development and implementation of this boundary allows climatic variables capable of influencing ground regions, within which the ground-loop is positioned, to be considered. The developed boundary is more sophisticated than examples found in literature, not only allowing consideration of the climatic variables but also surface material properties. The application of this boundary within a numerical model will allow a better representation of surface materials and climatic conditions.

Two separate boundary conditions were developed to represent the interaction between the ground-loop and ground matrix, namely; the so called ‘uniform’ and ‘non-uniform’ ground-loop boundary conditions. The uniform ground-loop boundary was based on the total heat load at a point in time whereas the non-uniform ground-loop was based on the fluid temperature profile within the ground-loop. The boundary conditions, and their implementation within the numerical model, allowed the heat exchange via the ground-loop to be represented in multiple ways. To the author’s knowledge, this is the first model which has had the capability of representing heat extraction via these two approaches allowing the differences to be quantitatively investigated.

The high resolution of ground temperature data obtained through field-scale monitoring provided an appropriate and complete benchmark to validate the developed numerical model. Through a two stage validation procedure, the model accuracy was tested against real in-situ ground data collected at the site. Comparisons collectively revealed that the simulation results concurred with the ground data, thereby indicating that the model is able to simulate ground behaviour during periods of both surface influence and active heat extraction. This demonstrated the model’s capability to simulate the ground behaviour in response to ground source heat systems, providing confidence in the model’s capability to simulate long-term ground behaviour in response to such systems.

In addition to the previous numerical advances, existing high performance algorithms already contained within COMPASS were further developed and tailored specifically towards the simulation of ground source heat systems on desktop machines. The developed numerical algorithm employed parallel techniques and resulted in a time saving of 44.7% over a comparable serial simulation on the quad-core machine utilised for testing. The development of this algorithm shows that significant computational time savings can be made with the application of parallel techniques on desktop machines. Despite the fact that it is widely acknowledged that computational performance constrains the numerical solutions which can be feasibly applied to ground source heat systems, prior to this study no attempts have been made to apply high performance computational techniques to the simulation of ground source heat systems. The presented work is therefore a first within the research field.

A series of long-term investigations were performed as part of Chapter 8, applying the validated model. The coupled thermal-hydraulic behaviour of the ground was investigated for a period of 20 years, coinciding with the minimum design life of horizontal ground source heat systems as specified in the design standard MIS 3005 (MCS, 2008). This simulation period was greater than the majority presented in literature which typically studied ground behaviour for a period of only hours or days. It was found that both the thermal and hydraulic behaviour of the ground reached a cyclic state after approximately 3 years. To the author's knowledge, this is the first work which has proved through numerical analysis that horizontal systems reach a cyclic state. From a modelling perspective this finding could be used to justify a reduction in the necessary simulation period in order to investigate the operational behaviour of horizontal ground source heat systems.

During the summer months, the ground distributions surrounding the ground-loop were found to almost completely dissipate and ground temperatures returned to their undisturbed values. This is an important system aspect as it shows that the system is sustainable and could meet the current heating demands indefinitely. From a more holistic stand point, this demonstrates that horizontal ground source heat systems can provide a sustainable means of providing space heating.

Investigation of the ground hydraulic behaviour indicated that it varied predominantly with depth and the thermal gradients induced by the ground-loop were insufficient to induce noticeable hydraulic changes in the vicinity of the ground-loop. With regards to horizontal ground source heat systems, this shows that the surface boundary governs the ground hydraulic behaviour and therefore the associated thermal property changes which will be subsequently induced in the ground (i.e. thermal conductivity and specific heat capacity changes with moisture content).

Inspection of the ground thermal behaviour highlighted a number of key behavioural trends. The simulation results highlighted that the vertical temperature gradient associated with heat extraction via the ground-loop was non-symmetrical. The vertical gradient beneath the ground-loop

was found to be steeper than that above it, concurring with monitoring site findings presented in Chapter 4. This indicated that the thermal energy extraction is also non-symmetrical and that more thermal energy is being extracted from beneath the ground-loop than above it. Further to this, the simulated vertical temperature gradient also indicated that the effect of heat extraction via the ground-loop extended to the surface boundary. Despite the previous points, comparison of the simulated ground temperature revealed that the majority of the ground temperature decrease at the ground-loop surface was in fact due to the surface climatic influences and not heat extraction, again concurring with the findings of Chapter 4.

The characteristics observed in the simulated vertical temperature profile could be subsequently applied within the design process. Knowledge regarding the thermal gradients could be applied to optimise the system design such that it fully utilises the shape induced gradients.

The validated model was also applied to investigate the influence of surface material types (and associated properties) on ground behaviour subject to heat extraction. Simulation results indicated that urban surfaces, namely brick and asphalt, had a noticeable effect on the thermal-hydraulic ground behaviour. In particular the simulation results indicated that the urban surfaces led to a general increase in ground temperature. It was shown that the surface type would increase ground temperatures, thereby increasing the amount of thermal energy which could be sustainably extracted from horizontal ground source heat systems. At present the design standard MIS 3005 (MCS, 2008) does not consider the surface material type within the ground-loop design process. The numerical findings of this study have shown that the surface material type would influence the ground temperature in the region of a horizontal ground-loop and thus the ground-loop design (e.g. the ground-loop length required to meet the design loads).

Finally, investigations were undertaken into the validity of the current design codes with respect to ground-loop design. A ground-loop configuration designed in accordance with the MIS 3005 design standard (MCS, 2008) was found to result in thermal conditions which failed a design criterion contained within the same standard (i.e. ground temperatures adjacent to the ground-loop fell below 273.15 K). Further investigations revealed that the ground-loop configuration conformed to the same ground temperature criterion when modelled at a greater depth of 2.0 meters. The difference in the outcomes clearly demonstrates that the current design code does not fully consider the influence of the ground-loop burial depth on the systems performance and sustainability.

The numerical and ground studies presented have provided a more comprehensive long-term study of the ground behaviour than previous research, fully accounting for both the thermal and hydraulic behaviour. This in conjunction with the surface and MIS investigations has bridged knowledge gaps which were present in the field, furthering the understanding of ground behaviour in response to horizontal ground source heat systems.

9.4 Overall conclusions

In terms of overall conclusions that can be drawn from the research performed, the following observations are presented:

- A significant data-set inspecting the ground behaviour in response to heat extraction via horizontal ground source heat systems has been collated through the implementation of the monitoring site presented in this work. The resulting data-set provides a more detailed resolution of ground thermal data than previous examples in literature. Further to this, the data-set currently provides a continuous data-set for an 18 month period, greater than the majority of previous studies. The data-set in its own right is a significant contribution to the scientific community and is able to provide a means of validation for future models developed within the research area. Within the scope of this study, the data-set has highlighted ground temperature behaviour which has previously not being observed or reported in literature.

- A coupled thermal-hydraulic model was extended to include boundary conditions representing the ground's interaction with the atmosphere and buried ground-loop, allowing for the simulation of ground behaviour in response to horizontal ground source heat systems. The implemented boundaries allow for more detailed investigations of the ground behaviour than previous models developed within the research area.

- Validations of the model, perused through comparisons with the collected data, were more rigorous than previous investigations undertaken within the research area. This not only demonstrates the validity of the developed model but also the scientific value of the collated data-set for validation purposes.

- Application of the model and developed boundary conditions allowed the long-term ground behaviour in response to horizontal ground source heat systems to be inspected, furthering the knowledge within the research area. Results highlighted that both the thermal and hydraulic behaviour reached a cyclic state after approximately 3 years, the knowledge of which can be applied to justify shorter simulation periods in future studies. Investigations also revealed that the induced ground-loop flux was insufficient to noticeably change the thermal conductivity or specific heat capacity of the surrounding ground. To the author's knowledge, this feature has not been previously discussed in literature with respect to ground source heat systems.

- Simulations undertaken have demonstrated that horizontal ground source heat systems can provide a sustainable means of providing space heating. Further to this, surface investigations highlighted that more energy can be sustainably extracted from systems with an urban surface covering (i.e. asphalt and brick paving) due to the increased ground temperatures associated with the material properties. Previous research within the topic area has not numerically investigated the influence of the surface type on horizontal ground source heat systems; therefore the findings presented expand the current knowledge base.

- Investigations into an existing design code demonstrated that the ground-loop design procedure resulted in unsustainable heat extraction (i.e. ground temperatures fell below the 273.15K design criterion). Simulation results highlighted the importance of the consideration of ground-loop burial depth within the design process, a feature which is currently over simplified.

- As a result of this study, it is claimed that a better understanding of horizontal ground source heat systems has been achieved through the collection and analysis of field-data. Further to this, the boundary developments and validation undertaken within the scope of this study has allowed for a more thorough investigation of the long-term ground behaviour and sustainability.

9.5 Suggestions for future work

The research findings presented within the scope of this thesis have highlighted a number of potential avenues for future research works. Applying the conclusions from this work, the following suggestions for future developments have been identified.

First and foremost, it is suggested that data from the implemented monitoring site is continued to be collected and added to the overall data-base. The value of the data-base will increase with time, allowing the long-term ground behaviour in response to heat extraction to be investigated at the site.

It is suggested that the field-scale approach and methodology developed to monitor ground source heat systems in this study is applied to further sites with differing heat loads and ground conditions. This would not only assist with the validation of models but also allow thermal distributions induced by different systems to be inspected. The resulting data-sets alone would provide valuable information which is currently lacking within the research area.

The potential of ground source heat as an alternative energy source for space heating is widely recognised. Despite this and growing environmental concerns, uptake of the technology has been slow. One of the main reasons cited for slow uptake, besides the large installation costs, are the vague design codes leading to some poorly performing new installations. Although the fundamental processes associated with heat transfer are well understood, the current design standards greatly simplify the influence of local ground characteristics and temperatures on system design and performance. For example, MIS 3005 (MCS, 2008) assumes ground temperatures on a regional basis, without taking consideration of the surface type and greatly simplifying the influence of burial depth. Through the current research, it was found that both of the previous characteristics could greatly influence ground temperature and thus system performance. Further research is suggested with the aim to further investigate the validity of the existing design standards and extend them further to account for surface type and ground-loop depth. The implication of such research could significantly impact the sector leading to more efficient designs and better performing systems, helping to diffuse the use of the technology.

As previously touched upon, the installation cost of ground source heat systems is widely recognised to be a market barrier. One way to reduce the initial capital cost is to improve the economic efficiency of designs. Despite this, current design codes do not include any references to economic optimisation, for example considering the cost of excavation versus the performance increase with depth for a given heat load. Research presented in the scope of this thesis demonstrated that the thermal distributions arising from heat extraction were non-symmetrical, particularly in the vertical. Further examination of this behaviour in conjunction with an investigation into the ground-loop depth would highlight potential for design and economic optimisation.

Numerical simulations investigating the influence of a barley crop on the thermo-hydro ground behaviour were conducted within the scope of this research. Results highlighted that the current model fails to fully account for the ambient air temperature associated with surface crop textures. Horizontal ground source heat systems are ideally suited for rural areas where the large ground requirements can be met. It is therefore suggested that the current surface boundary is developed in order to allow agricultural surfaces to be further inspected.

The model developed within the scope of this study has been applied to simulate horizontal ground source heat systems. It is suggested that the numerical works are applied to investigate the ground behaviour in response to alternative ground-loop orientations and types, for example vertical borehole systems and energy piles.

9.6 References

Microgeneration Certification Scheme (MCS), 2008. *Microgeneration Installation Standard: MIS 3005 Issue 3.0*. London: Department of Energy and Climate Change (DECC).

Appendix A

Monitoring Equipment Specifications

Property	*Details*
Measurement precision	±0.2º C
Operating temp. range	-80º C to +75ºC
Stability	0.01 ºC or better per 100 months at 0 ºC
Resistance at 25º C	2252, 3k, 5k, 10k ohms
Cable type	Direct burial rated 22 gauge water blocked instrumentation cable

Source: http://www.mgs.co.uk/data/pdf/70.pdf{Accessed on 12/8/2011}

Table A1 – Manufacturer specifications for the thermistor string installed at the monitoring site.

Property	*Details*
Absolute accuracy	±5 %
Uniformity	± 3 %
Sensitivity	Custom calibrated to exactly 5.00 W m^{-2} per mV
Dimensions	2.40 cm diameter by 2.75 cm high
Mass	70 g (excluding signal wire)
Input power	None, self-powered
Materials	Anodized aluminum with cast acrylic lens
Cable	5 meters twisted wire pair with Santoprene jacket

Source: Pyranometer SP-110 user manual, Apogee Instruments

Table A2 – Manufacturer specifications for the silicon-cell pyranometer used to measure the solar radiation.

Property	*Details*
Relative humidity (RH):	
Operational range	0% to 100% RH
Output resolution	0.03%
Accuracy at 25ºC	±2% (10% - 90% RH), ±4% (0% - 100% RH)
Stability	±1.0 % per year
Temperature:	
Operational range	-40°C to +70°C
Output resolution	0.01 °C
Accuracy at 25ºC	±0.3ºC at 25ºC

Source: Campbell Scientific – CS215-L specifications and technical data. http://www.campbellsci.com/cs215-specifications {Accessed on 9/11/12}

Table A3 – Manufacturer specifications for combined temperature and relative humidity probe installed at the monitoring site.

Property	*Details*
Accuracy (4 to 10 mph)	±0.25 mph
Accuracy (10 to 50 mph)	±4%
Pulse interpretation	2.5 mph per Hz

Source: Audon electronics – technical specifications for VORTEX wind speed sensor http://www.audon.co.uk/weather_sensors/vortex.html {Accessed on 9/11/12}

Table A4 – Manufacturer specifications for the cup anemometer used to measure the wind-speed at the monitoring site.

Property	*Details*
Accuracy	2 % up to 25 mm/hr, 3 % up to 50 mm/hr
Operating temperature	-20ºC to +50^{O}C
Resolution	0.1 mm per tip
Catchment area	200 cm^{2}
Dimensions	18 cm diameter, 39 cm high (including mounting base)
Output	Magnetic read switch (N.O), rating 24V AC/DC 500 mA

Source: Young tipping bucket rain gauge – Model 52202/52203 technical specification, http://www.youngusa.com/products/3/18.html {Accessed 11/07/2012}

Table A5 – Manufacturer specifications for the tipping bucket rain gauge used to measure the rainfall at the monitoring site.

Property	*Details*
Analogue inputs	16 single-ended or 8 differentially individually configured
Maximum scan rate	100 Hz
Digital ports	8 I/Os or 4 RS232 COM
Memory	2 MB Flash (operating system)
	4 MB (CPU usage, program storage and data storage)
Power requirements	9.6 – 16 V dc
Dimensions	23.9 x 10.2 x 6.1 cm

Source: Campbell-Scientific CR1000 technical specification, http://www.campbellsci.com/cr1000-specifications {Accessed 11/07/2012}

Table A6 – Manufacturer specifications for Campbell-Scientific data-logger installed at the monitoring site.

Property	*Details*
Pipe Diameter	25 mm
Minimum flow	70 lt/hr
Maximum flow	7 m^3/hr
Maximum operation temperature	90ºC
Minimum	N/A

Source: Metron FMC flow meter specifications: http://www.metronfmc.com/watermeter.html {Accessed 21/8/2012}

Table A7 – Manufacturer specifications for mechanical hot water meter BSP, 25mm connection.

Appendix B

KD2 Probe device specifications

Property	*Details*
Devise Model	KD2 Pro Controller Model KD2 Pro-C
Specific heat capacity reading accuracy	±2.5 %
Thermal conductivity reading accuracy	±2.5 %
Thermal diffusivity reading accuracy	±5.0 %
Temp. operating range of sensors	-50ºC to +150ºC
Range of conductivity measurements	0.02 to 4 $Wm^{-1}K^{-1}$
Range of specific heat capacity measurements	0.5 to 4 $MJm^{-3}K^{-1}$
Probe dimensions	100mm long, 2.4mm diameter

Source: KD2 Pro user Manual, Decagon Devices Inc., 2006

Table B1 – Manufacturer specifications for KD2 thermal resistivity probe.

Appendix C

Site investigation experimental results

Location	Depth, *m*	Reference Temperature, *K*	Specific heat capacity, $J\,kg^{-1}\,K^{-1}$	Thermal conductivity, $Wm^{-1}\,K^{-1}$
1A	†			
1B	1.49401	14.64	1331	2.52
1C	1.08916	14.58	1061	2.145
1D	1.88756	14.36	1302	0.488
2A	1.16965	14.34	1402	2.374
2B	1.82795	14.24	1143	2.874
2C	†			
2D	†			
3A	1.16089	14.82	1054	2.443
3B	1.74755	14.59	1040	2.694
3C	1.1216	14.85	1157	2.318
3D	1.99848	14.5	1202	2.512
4A	1.18495	14.77	1079	2.538
4B	1.74906	14.49	1091	2.525
4C	1.06857	14.63	1222	2.279
4D	1.94471	14.42	1338	2.543
5A	1.07357	14.65	1052	2.566
5B	1.72557	14.36	1428	2.385
5C	1.08236	14.41	1200	2.583
5D	1.78073	14.22	1183	2.632
6B	1.95657	14.18	1078	2.479
6A	1.2959	14.43	1133	0.476
6A	1.14858	14.33	1352	1.878
6B	1.77243	14.07	1167	2.493
6C	1.10391	14.27	1177	2.401
6D	1.7009	14.22	971	2.359
7A	1.22284	14.22	1126	2.429
7B	†			
7C	†			
7D	†			
8A	1.27819	14.35	1343	2.75
8B	2.38988	13.96	1164	2.222
8C	†			
8D	†			
9A	1.36989	14.52	1108	2.157
9B	2.51843	13.9	1166	2.114
9C	†			
9D	†			
10A	1.31886	14.35	1304	2.552
10B	1.9544	14.39	1102	2.217

10C	†				
10D	†				
11A		1.48333	14.28	1083	2.591
11B		1.98546	14.48	1173	2.057
11C	†				
11D	†				
12A	†				
12B	†				
12C		1.1964	14.04	1298	2.515
12D		2.0793	14.12	1173	2.398
13A	†				
13B	†				
13C		1.46532	13.81	983	2.369
13D		2.01341	13.88	1175	2.628
14A	†				
14B	†				
14C		1.27958	13.58	1147	2.314
14D		2.01158	13.66	1191	2.24
15A		1.36034	13.44	1118	2.115
15B		2.22382	13.47	1123	2.479
15C		1.29226	14	1196	2.524
15D		2.14098	14.14	1102	2.526
16A		1.23059	14.97	932	2.242
16B		2.11859	14.37	1354	2.268
16C	†				
16D	†				
17A		1.34935	15.17	1187	1.704
17B		2.08502	14.41	1098	2.257
17C	†				
17D	†				
18A		1.37578	14.73	1347	2.618
18B		2.1519	14.28	1120	2.578
18C	†				
18D	†				
19A		1.14164	14.35	1212	2.261
19B		2.001	14.3	1197	2.056
19C	†				
19D	†				
20A		1.30478	14.47	1105	1.63
20B		1.94498	14.23	1131	1.973
20C	†				
20D	†				

† - the in-situ thermal properties at these points were not obtained

Table C1 – Measured in-situ thermal properties at the monitoring site.

Location	Depth, *m*	Bulk unit weigh, $kN\ m^{-3}$	Moisture Content, *%*	Porosity, *dimensionless*
1.1	2.052	20.290	15.0	0.219
1.2 (a)	1.138	17.905	17.0	0.311
1.2 (b)	1.138	18.818	17.0	0.276
2.1	-	-	-	-
2.2	0.986	17.862	11.1	0.313
3.1	1.035	12.420	7.3	0.522
3.2	1.954	21.256	15.7	0.182
4.1 (a)	1.825	20.325	13.9	0.218
4.1 (b)	1.825	19.395	13.9	0.254
4.2	1.140	14.873	13.0	0.428
5.1 (a)	0.745	18.255	12.6	0.298
5.1 (b)	0.745	13.367	12.6	0.486
5.2	1.519	18.976	13.2	0.270
6.1 (a)	0.094	15.805	29.1	0.392
6.1 (b)	0.094	13.733	29.1	0.472
6.2	1.697	22.179	13.9	0.147
7.1	1.461	18.874	14.2	0.274
7.2 (a)	1.797	19.446	10.3	0.252
7.2 (b)	1.797	17.392	10.3	0.331
8.1	1.930	21.508	13.8	0.172
8.2	0.880	18.666	12.8	0.282
9.1	1.141	19.776	8.4	0.239
9.2	2.302	16.823	6.1	0.353
10.1	2.469	18.665	13.9	0.282
10.2	1.125	20.806	12.6	0.199
11.1	2.031	17.505	9.4	0.326
11.2	1.251	14.428	11.9	0.445
12.1	2.086	15.413	11.8	0.407
12.2	1.188	17.758	17.7	0.317
12.3	1.829	16.693	8.5	0.358

Table C2 – Measured ground properties of the samples extracted from the monitoring site.

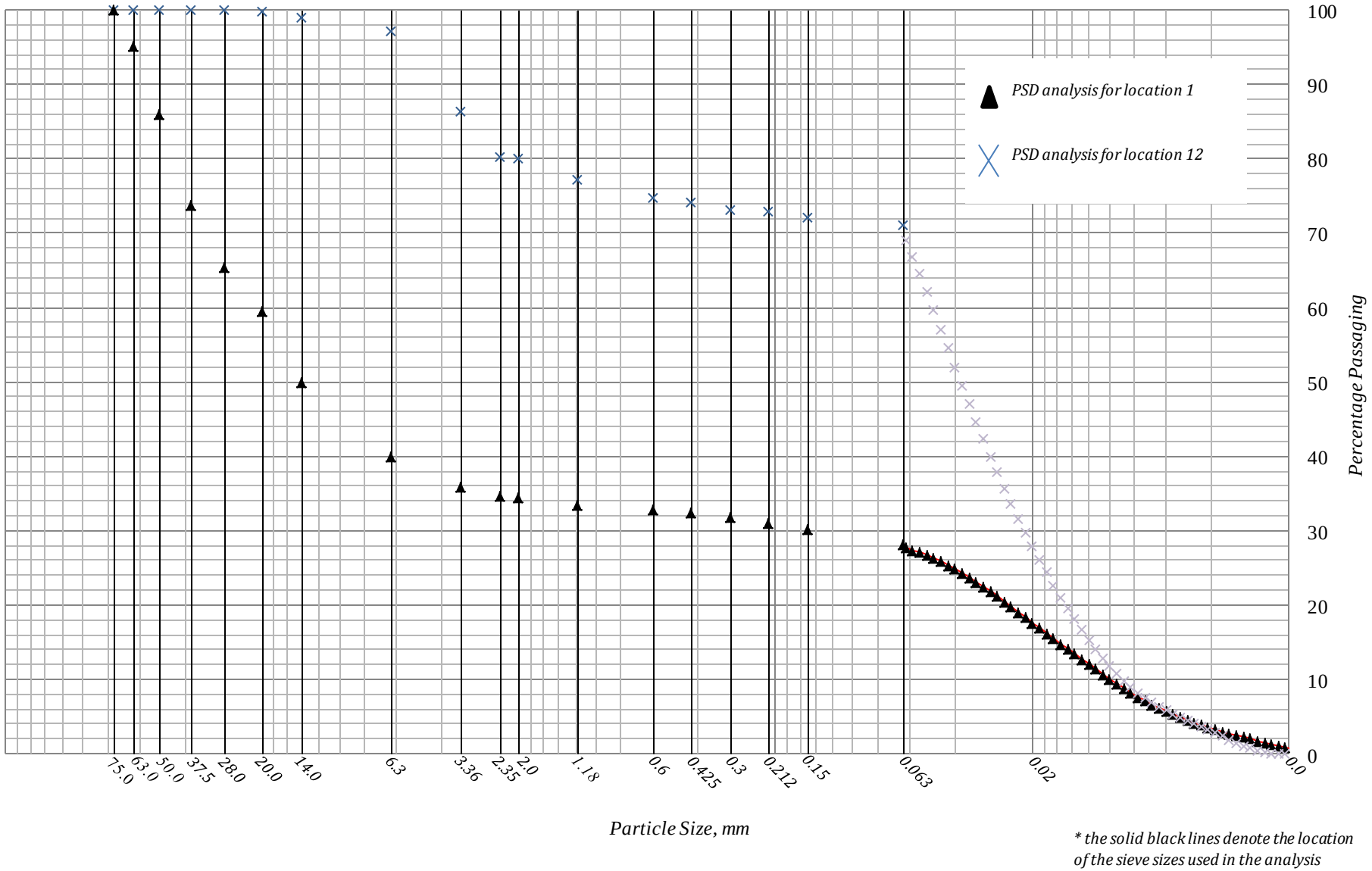

Figure C1 – Particle size distribution curve for the two samples extracted from the monitoring site.

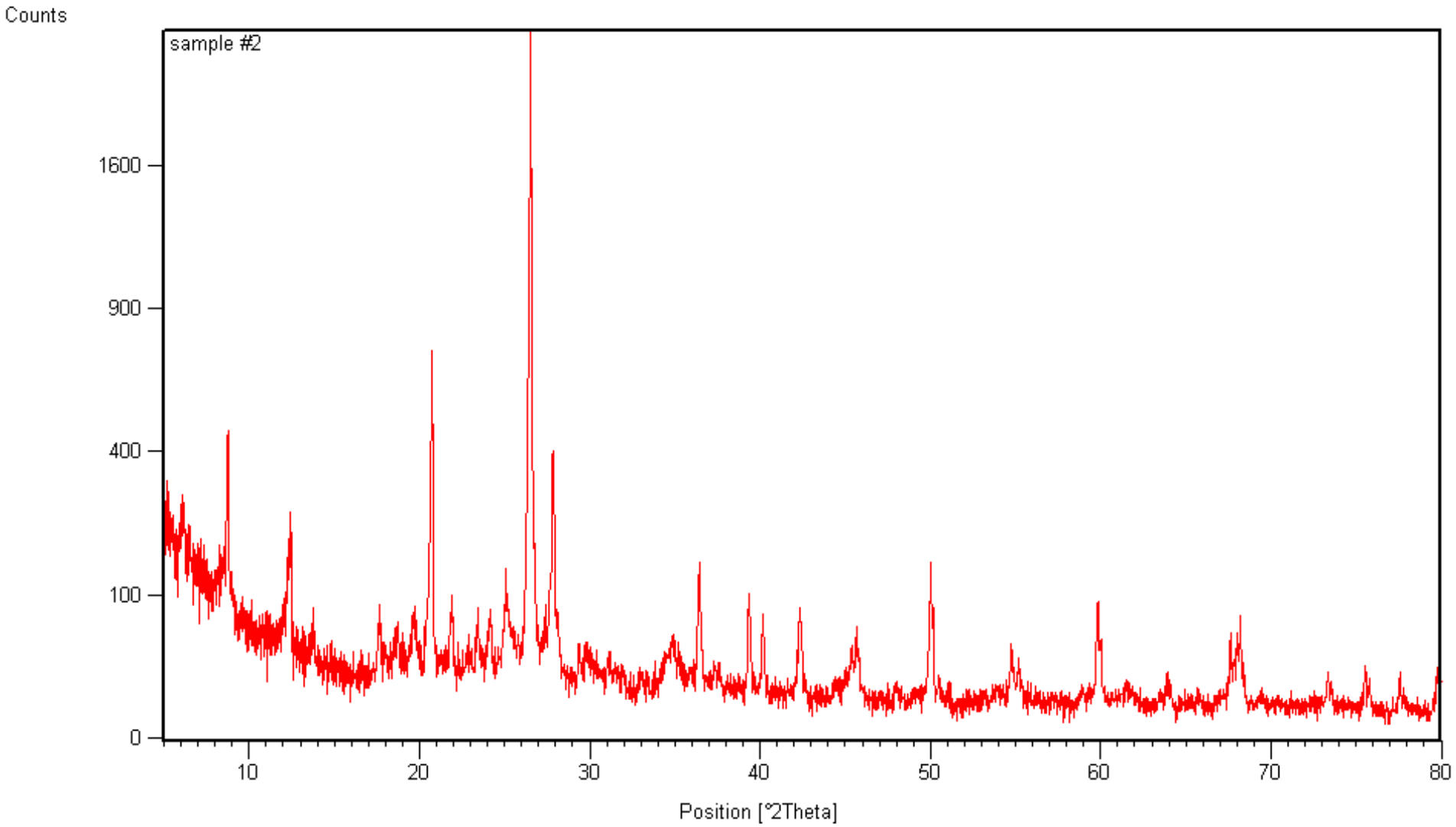

Figure C2 – X-Ray diffraction results for sample location 1.

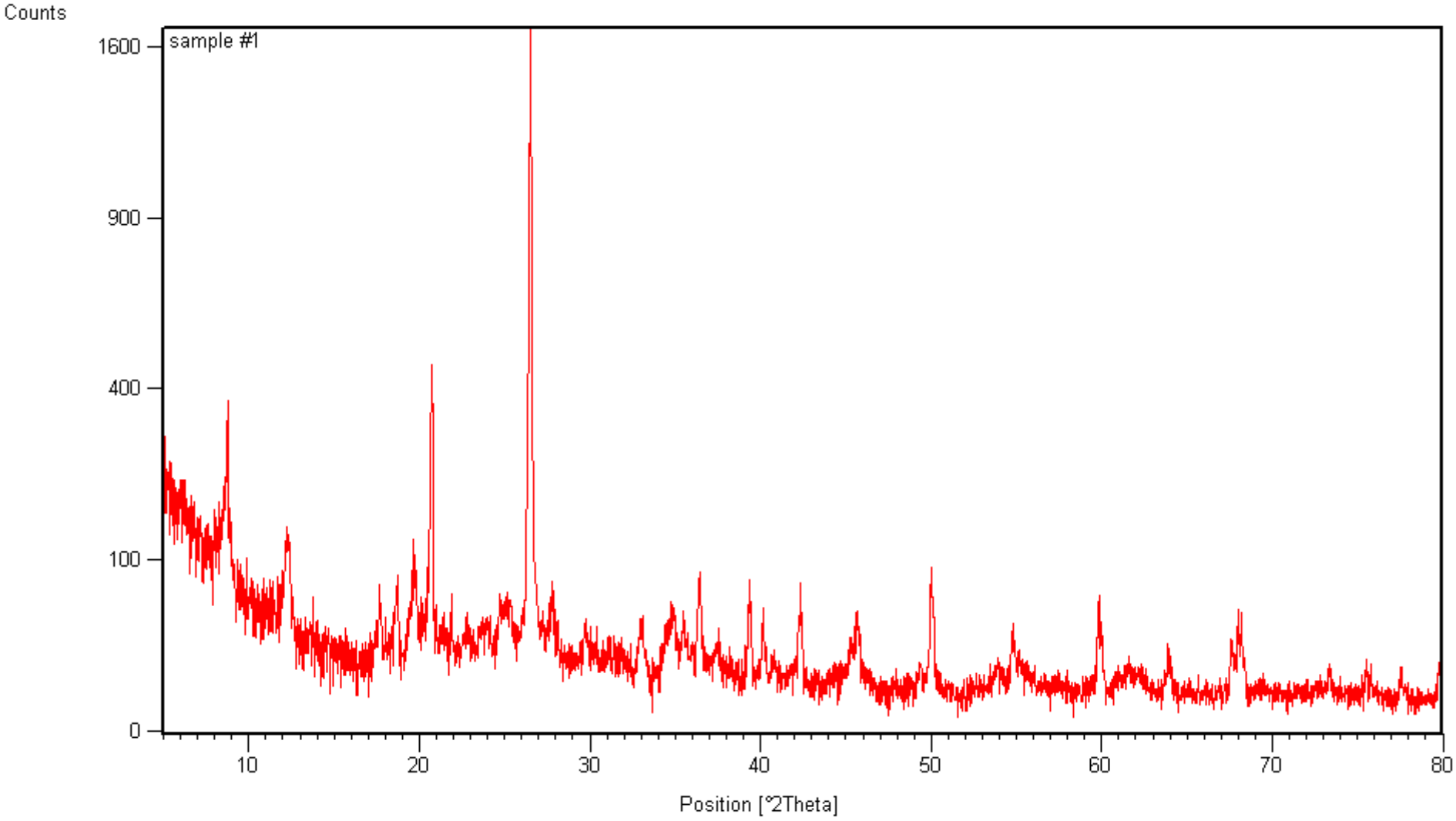

Figure C3 – X-Ray diffraction results for sample location 12.

Appendix D

Raw ground temperature data recorded at the monitoring site between May 2012 and June 2013

- The ground temperature data obtained from the intermediate cross-sections A, B, C, D, E and F has been denoted according to the thermistor notation provided in Figure D1.

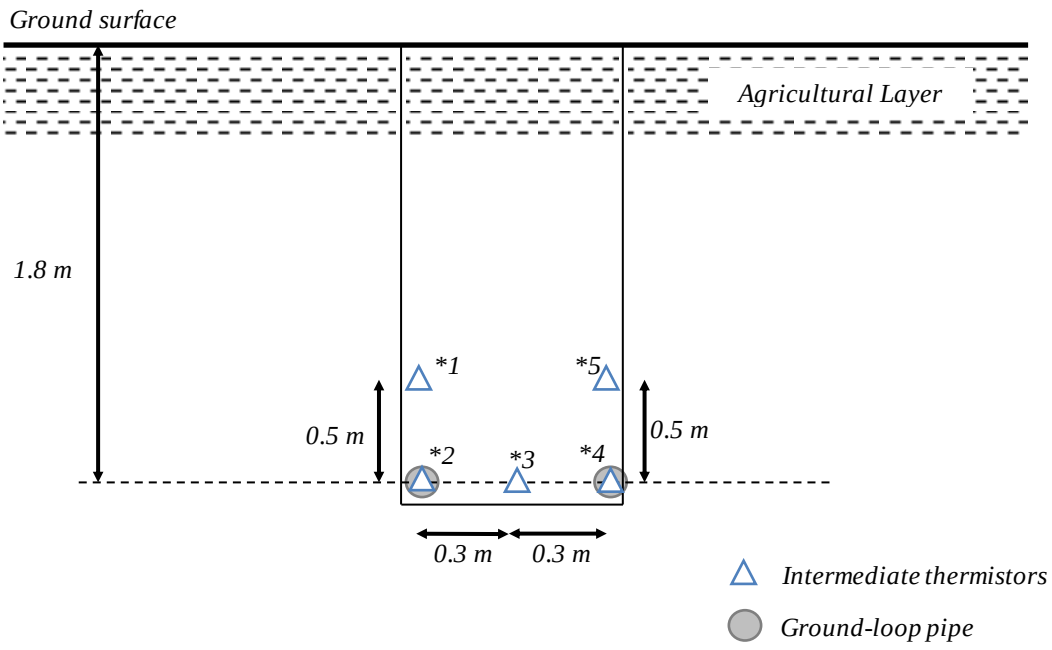

Notes

1. Figure not drawn to scale
2. Figure shows the vertical cross-sectional viewpoint facing a northward direction (see Chapter 3, Figure 3.2)
3. The '*' is replaced by the respective intermediate section letter
4. The plan location of these intermediate cross sections can be found in Chapter 3, Figure 3.2

Figure D1 – Thermistor notation used to present the raw temperature data for the intermediate cross-section A, B, C, D, E and F.

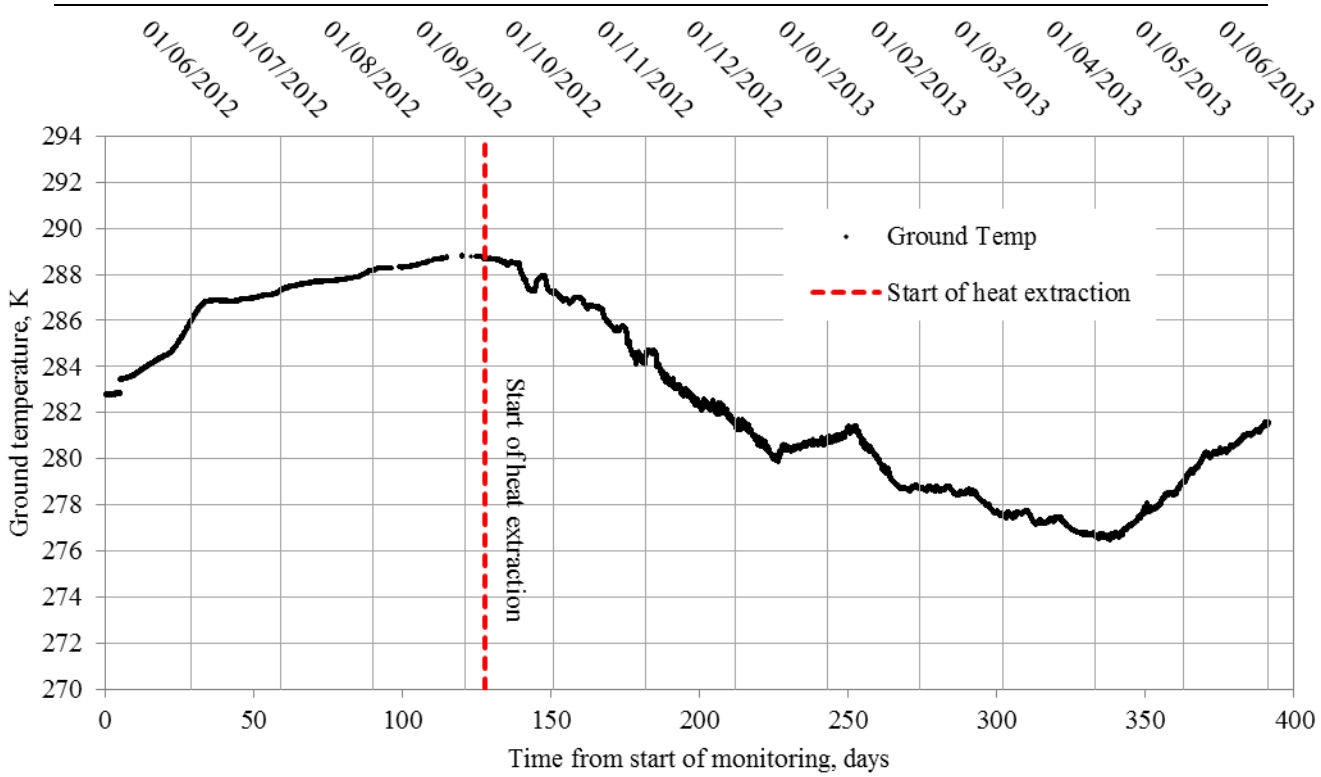

Figure D2 – Time evolution showing the monitored ground temperature data at sensor A1.

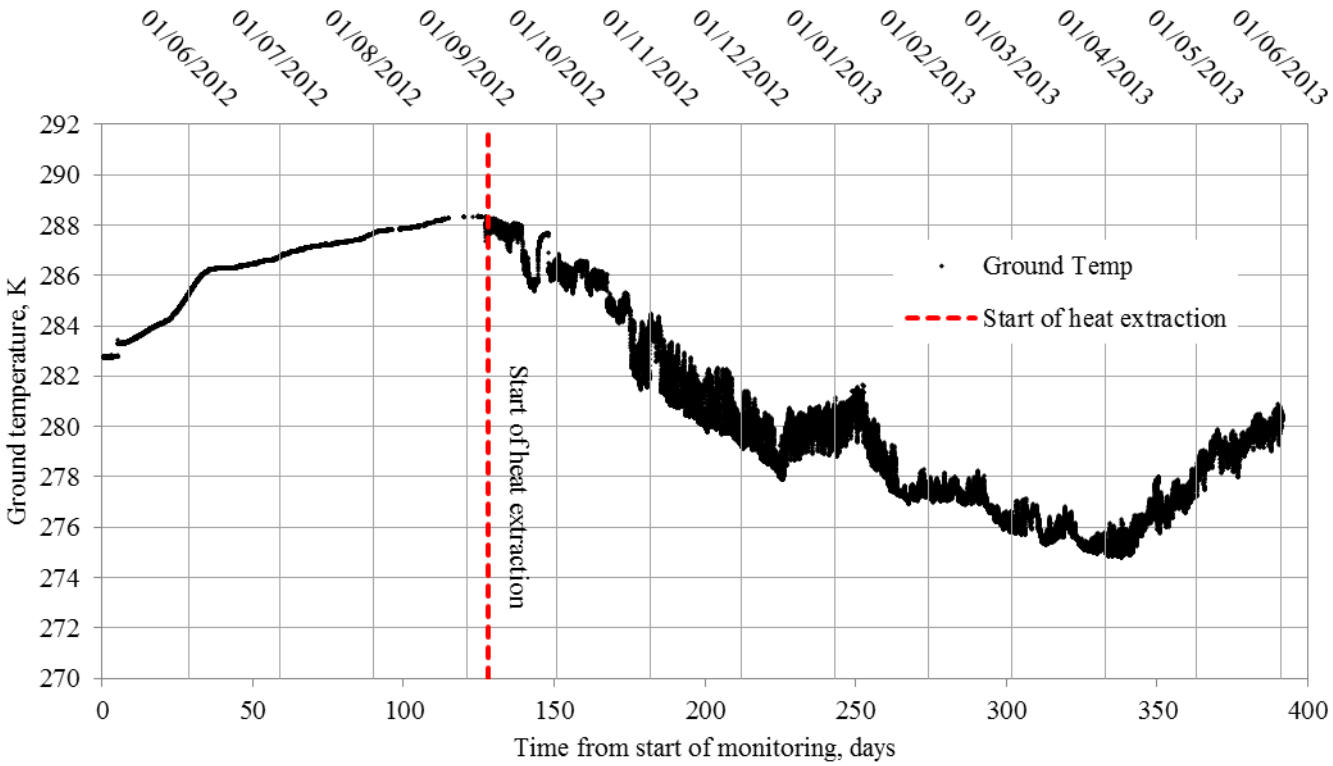

Figure D3 – Time evolution showing the monitored ground temperature data at sensor A2.

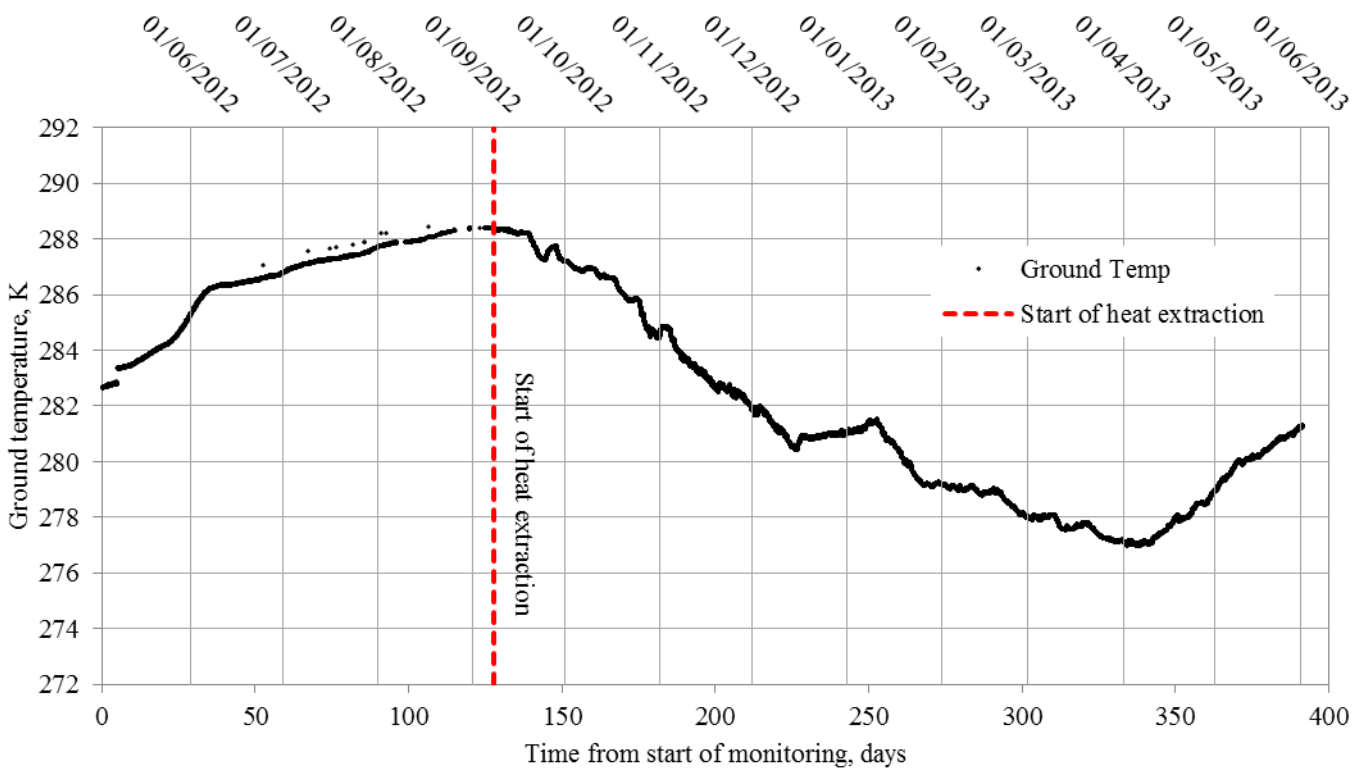

Figure D4 – Time evolution showing the monitored ground temperature data at sensor A3.

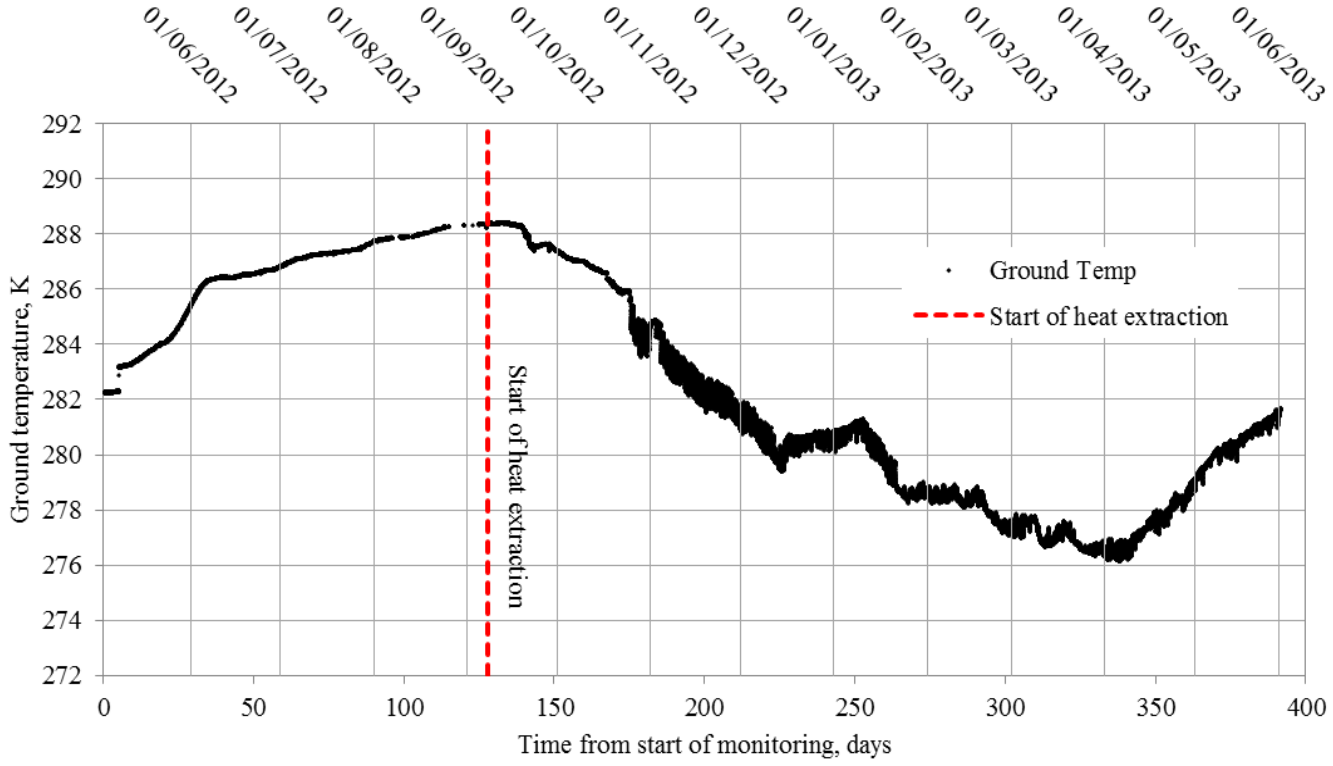

Figure D5 – Time evolution showing the monitored ground temperature data at sensor A4.

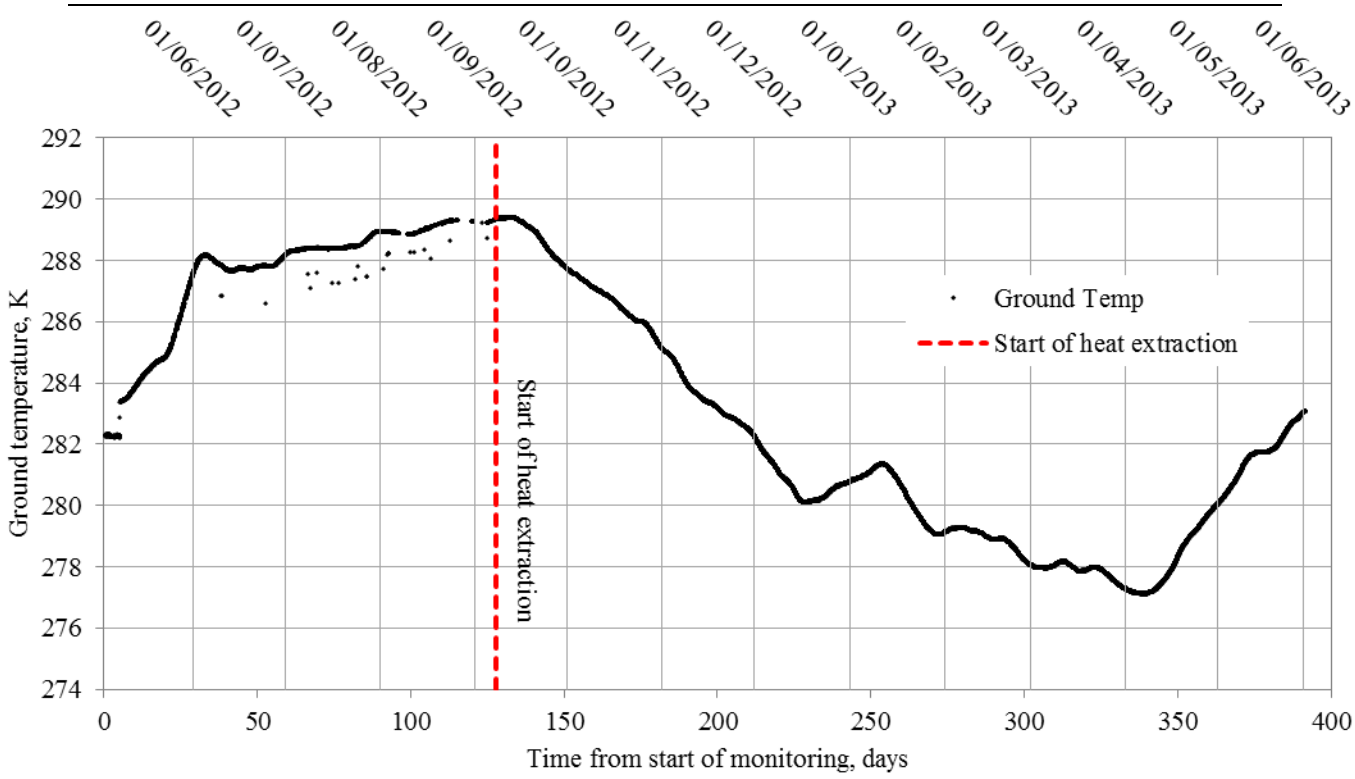

Figure D6 – Time evolution showing the monitored ground temperature data at sensor A5.

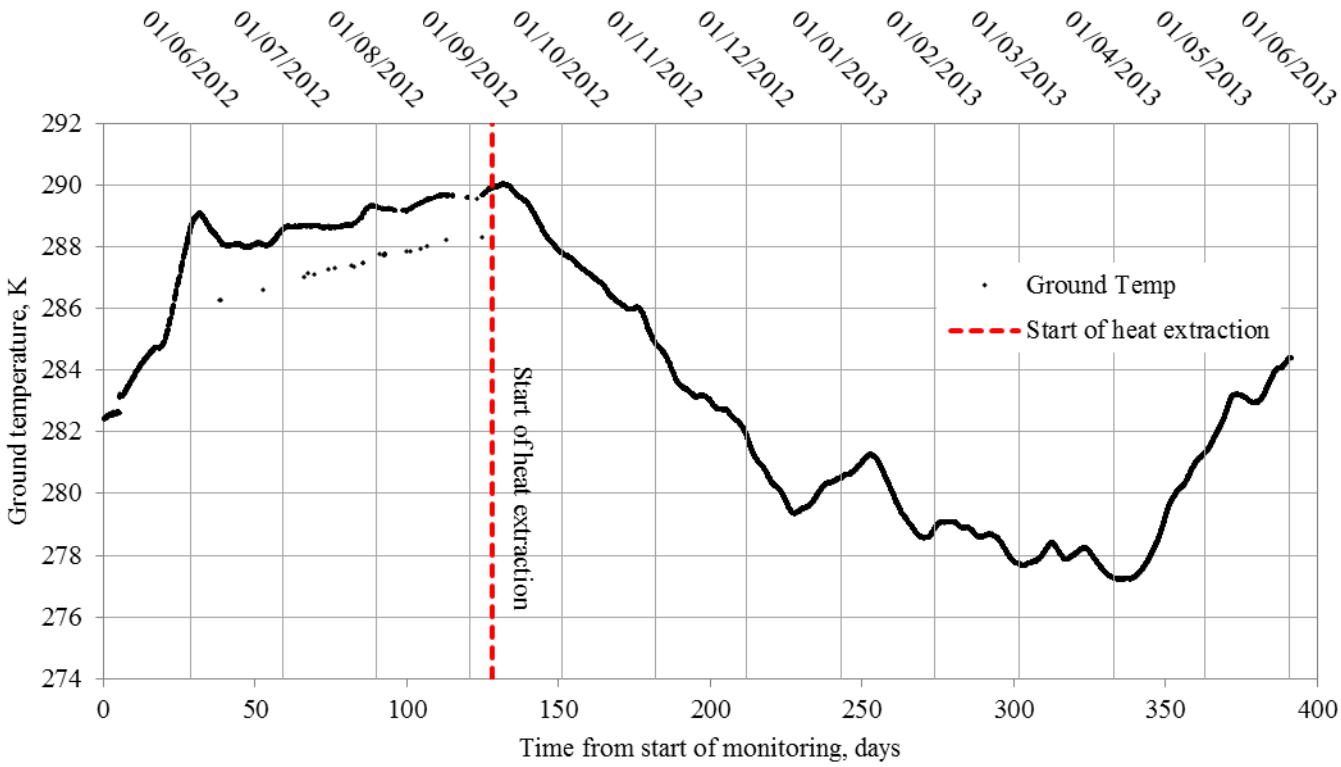

Figure D7 – Time evolution showing the monitored ground temperature data at sensor B1.

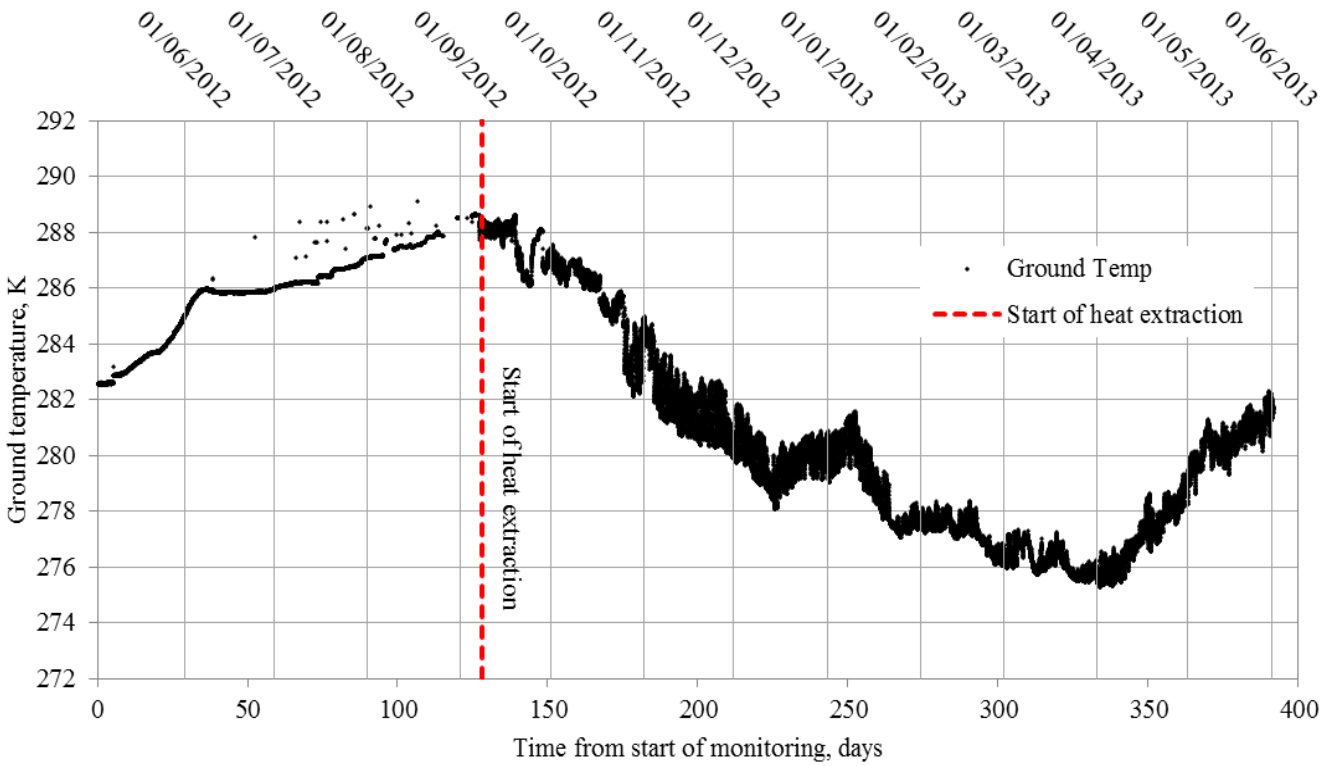

Figure D8 – Time evolution showing the monitored ground temperature data at sensor B2.

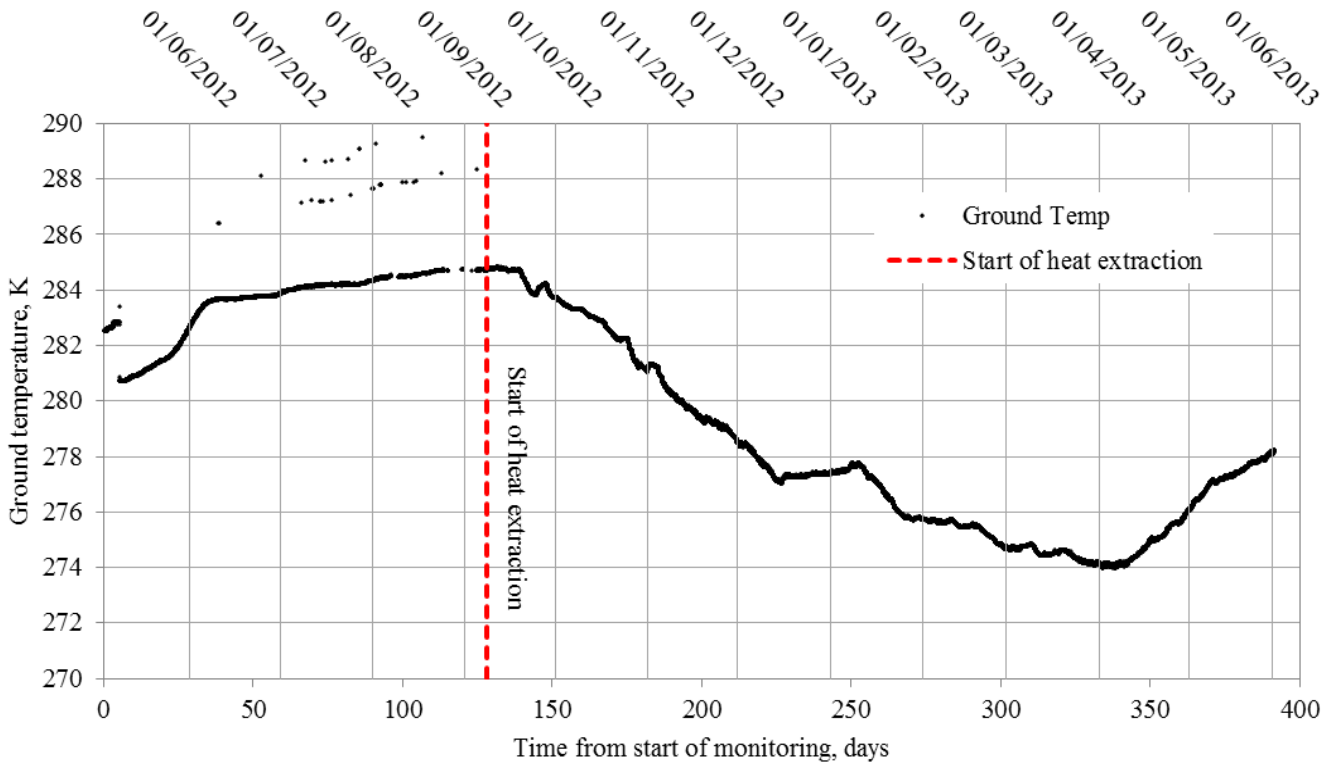

Figure D9 – Time evolution showing the monitored ground temperature data at sensor B3.

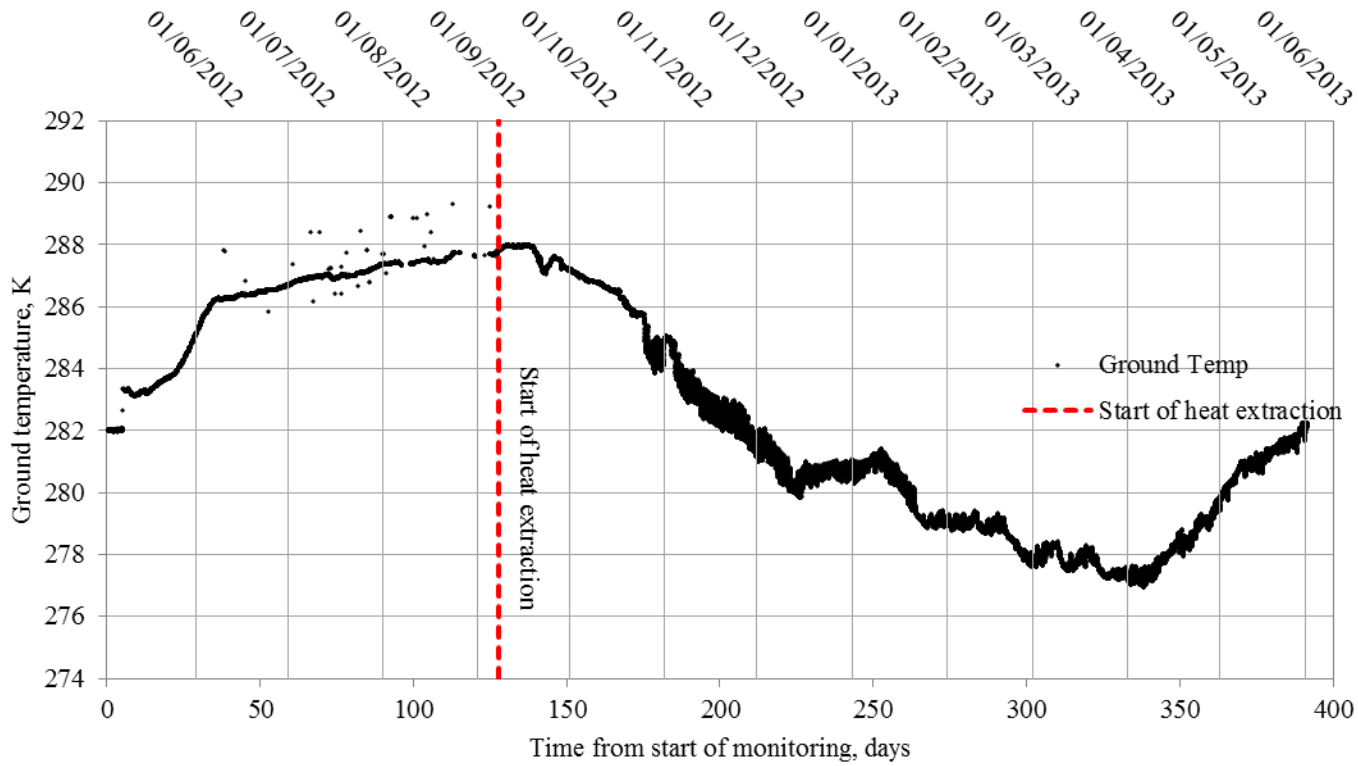

Figure D10 – Time evolution showing the monitored ground temperature data at sensor B4.

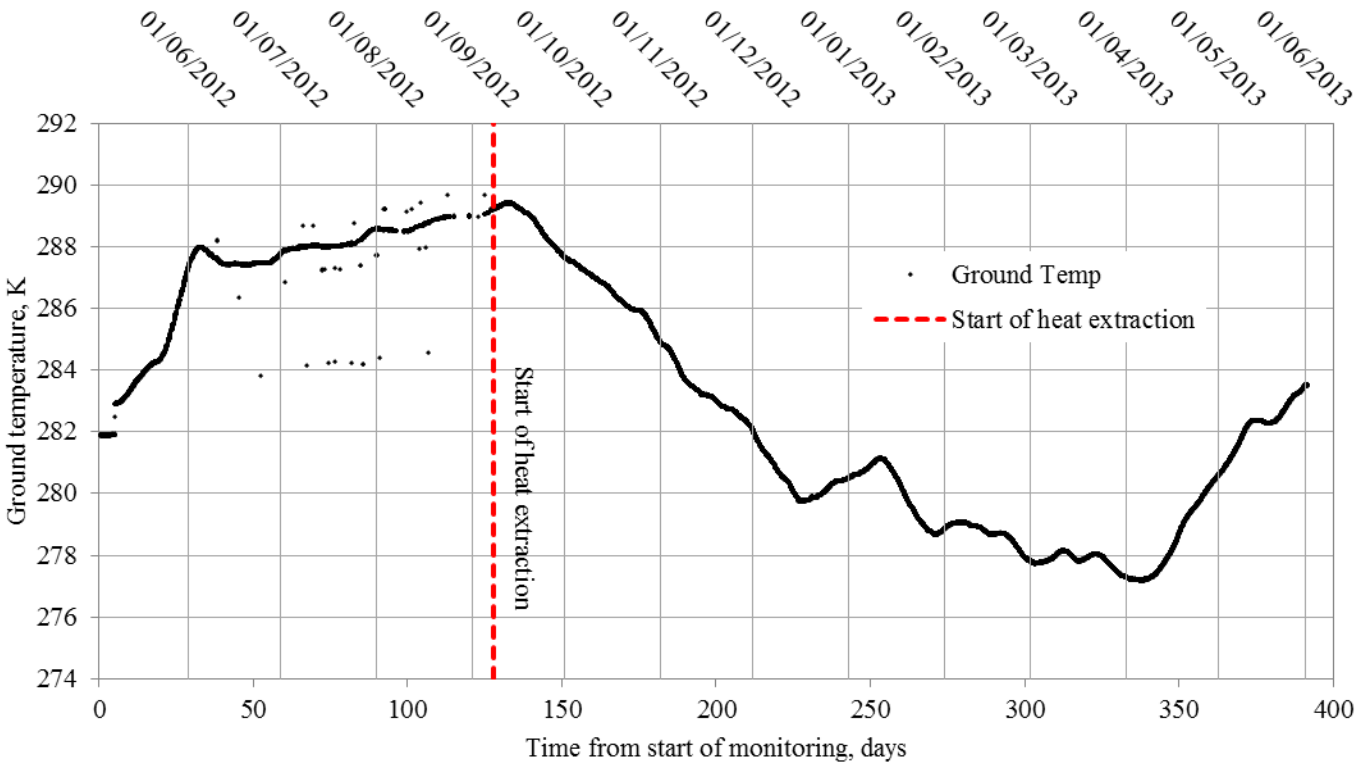

Figure D11 – Time evolution showing the monitored ground temperature data at sensor B5.

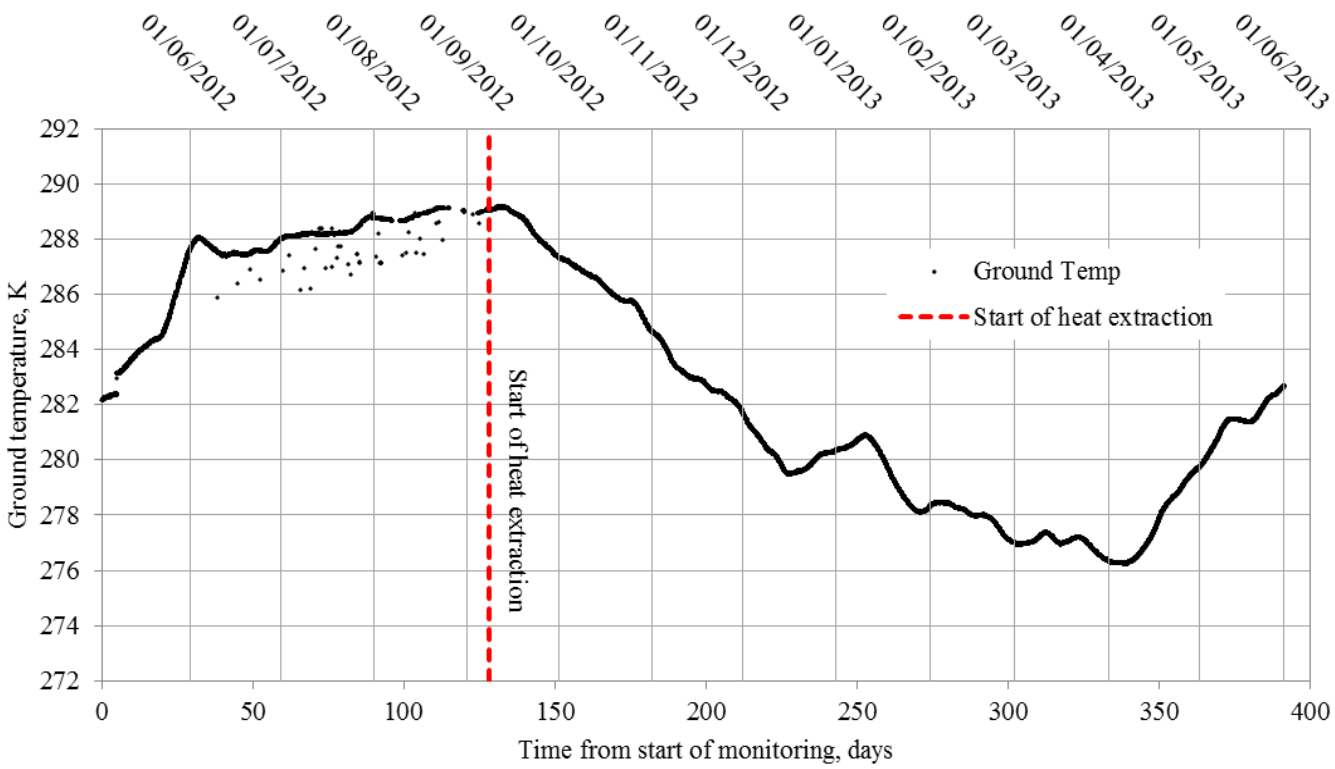

Figure D12 – Time evolution showing the monitored ground temperature data at sensor C1.

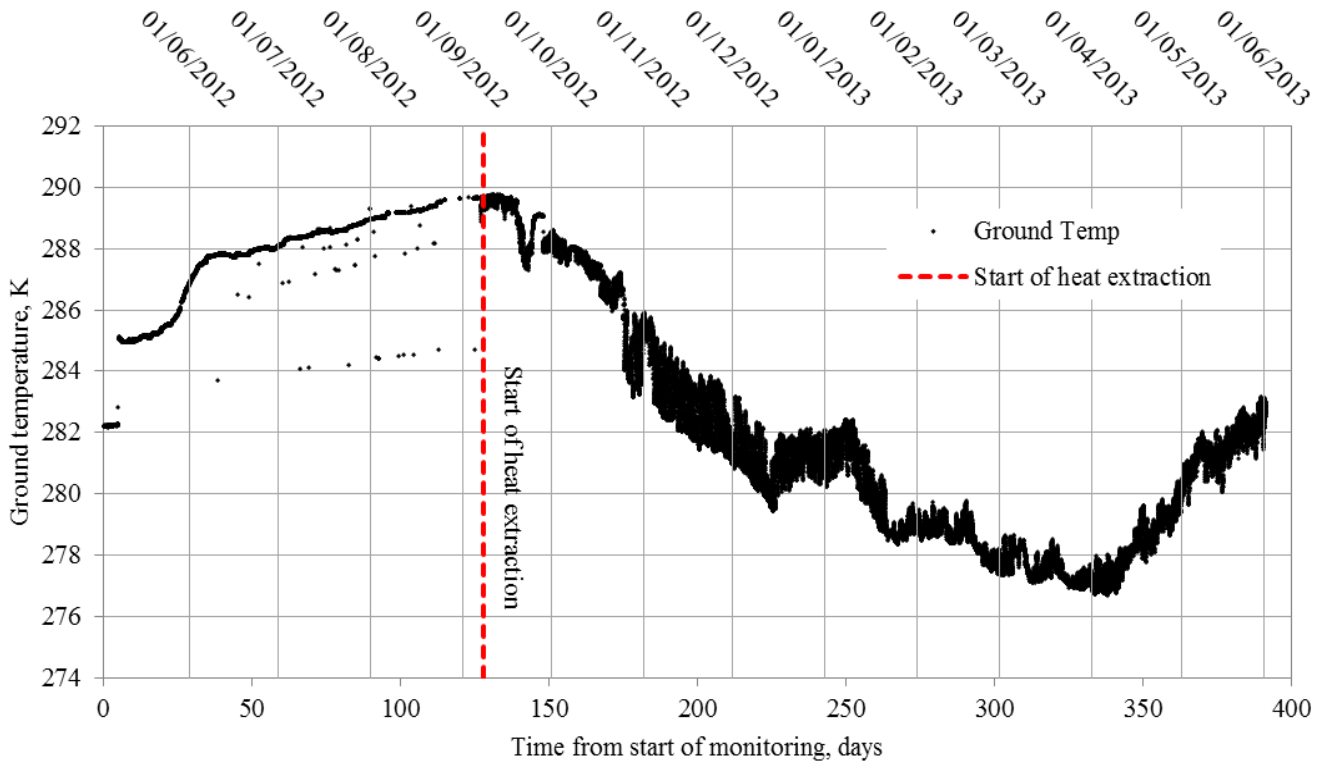

Figure D13 – Time evolution showing the monitored ground temperature data at sensor C2.

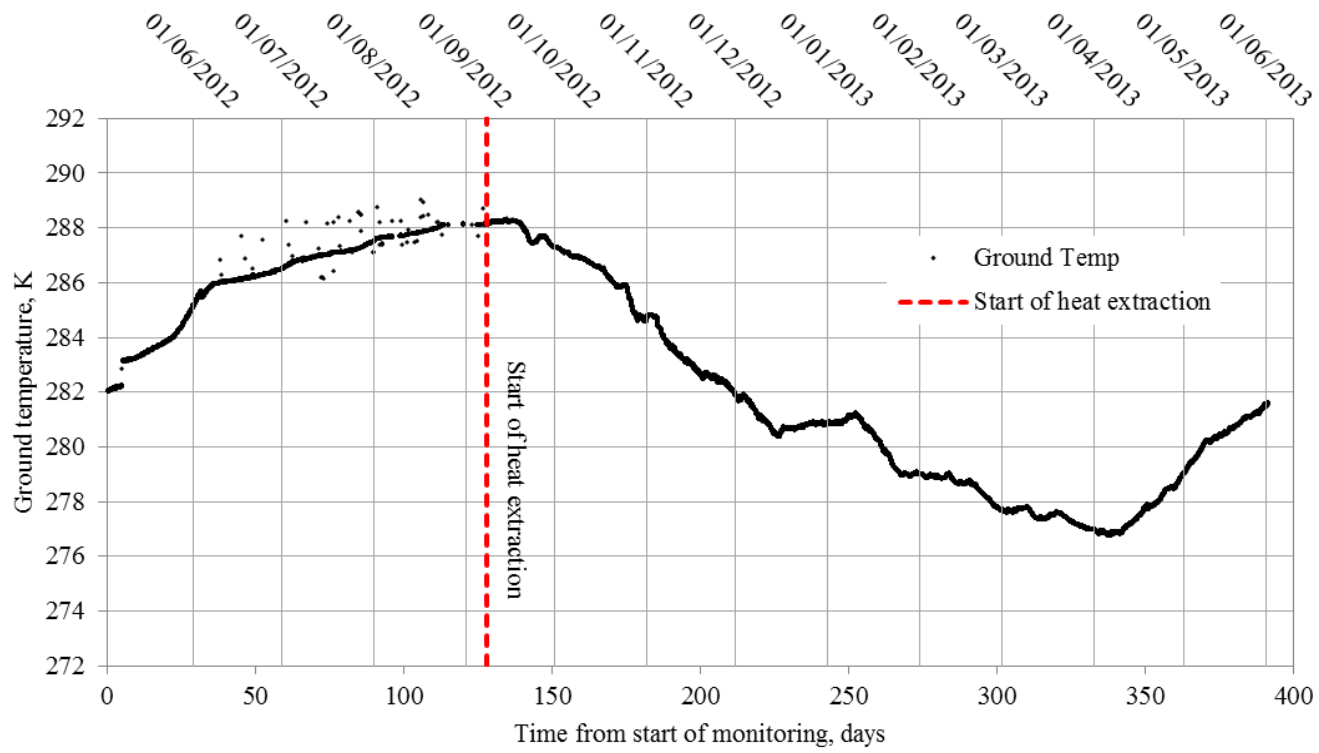

Figure D14 – Time evolution showing the monitored ground temperature data at sensor C3.

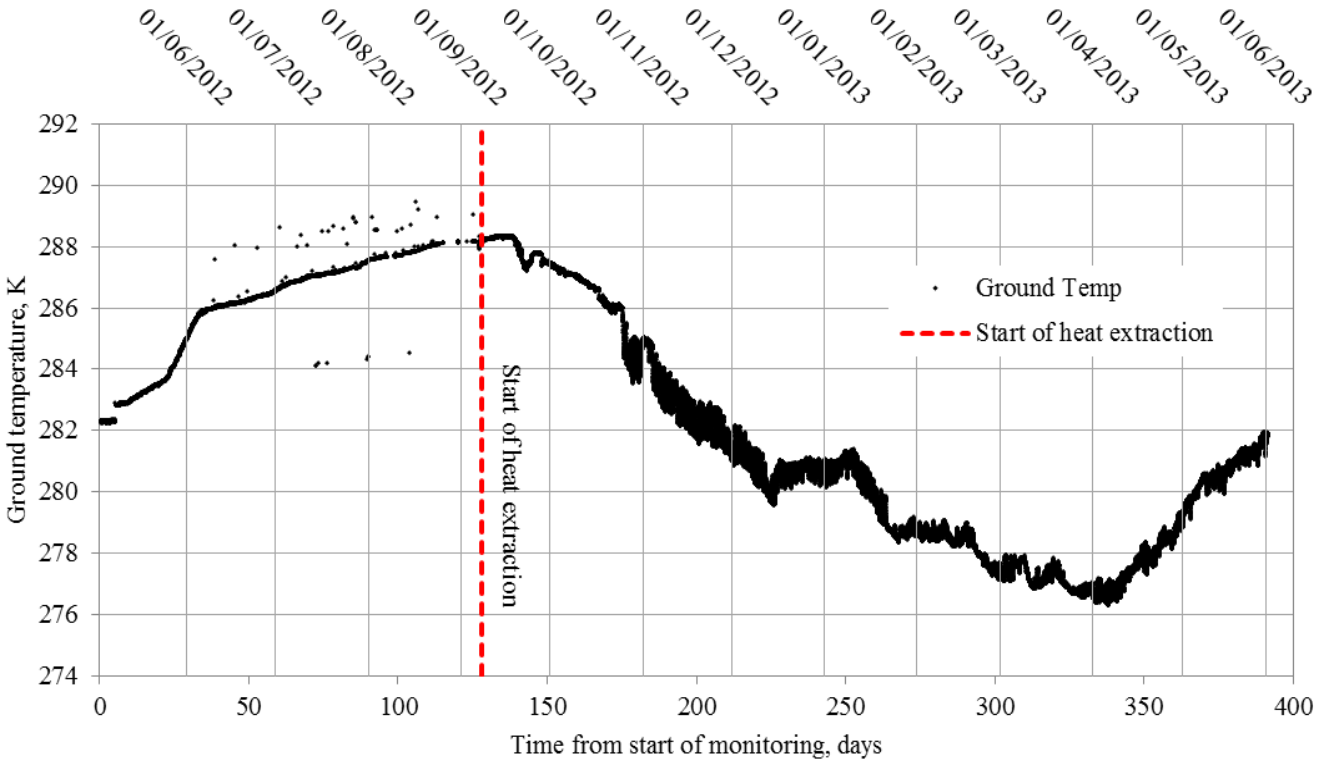

Figure D15 – Time evolution showing the monitored ground temperature data at sensor C4.

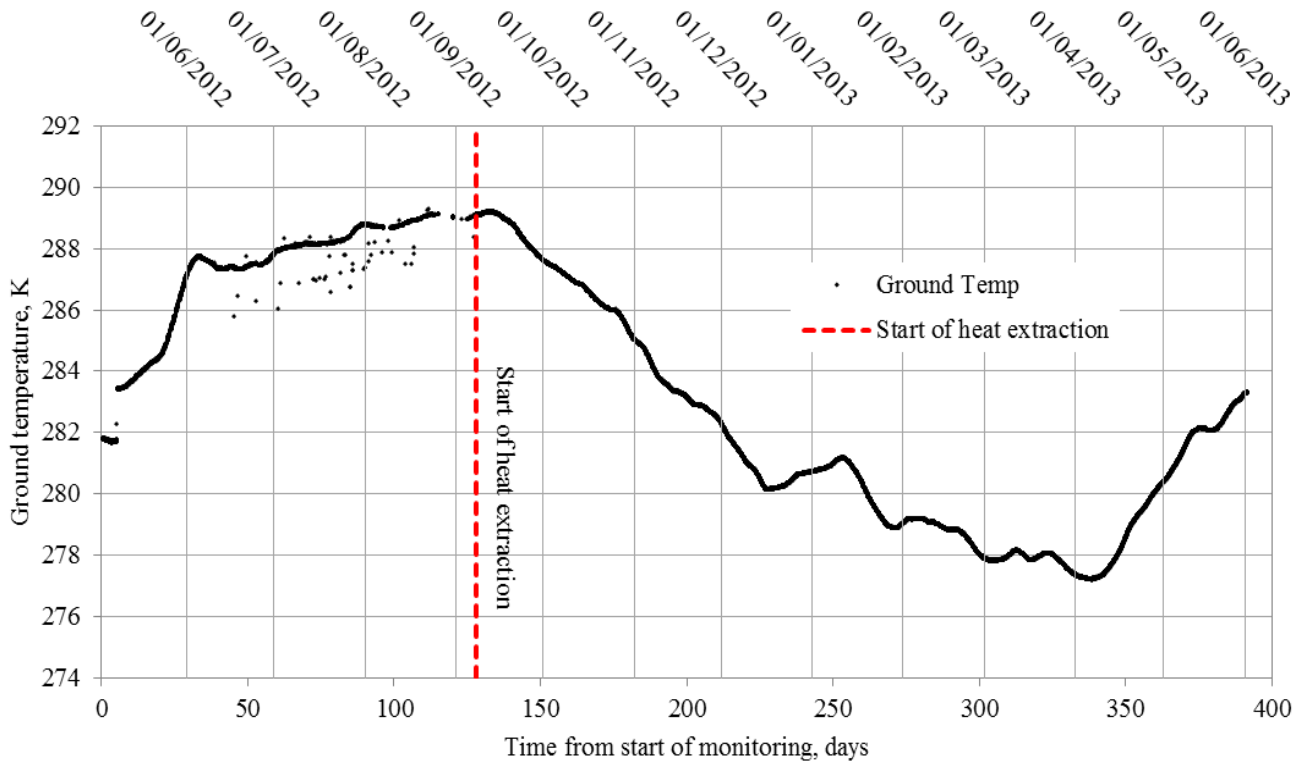

Figure D16 – Time evolution showing the monitored ground temperature data at sensor C5.

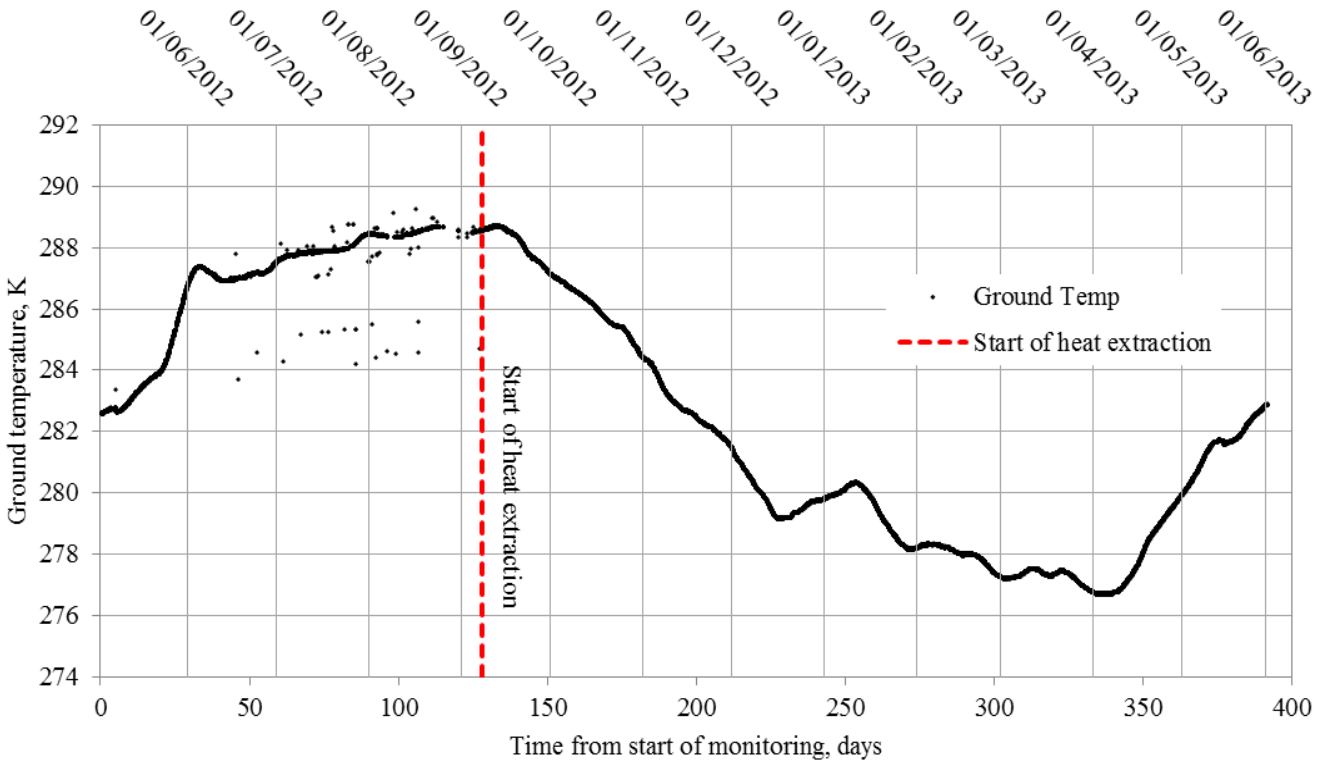

Figure D17 – Time evolution showing the monitored ground temperature data at sensor D1.

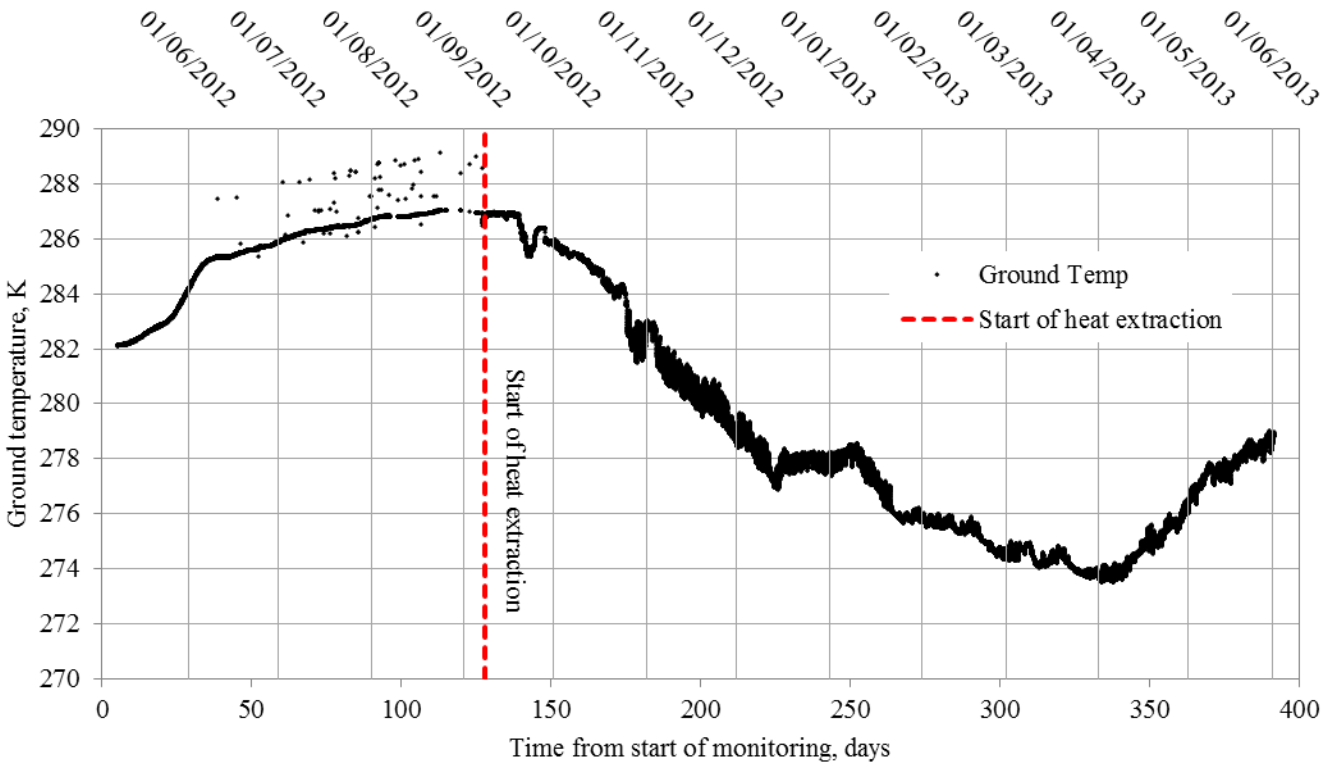

Figure D18 – Time evolution showing the monitored ground temperature data at sensor D2.

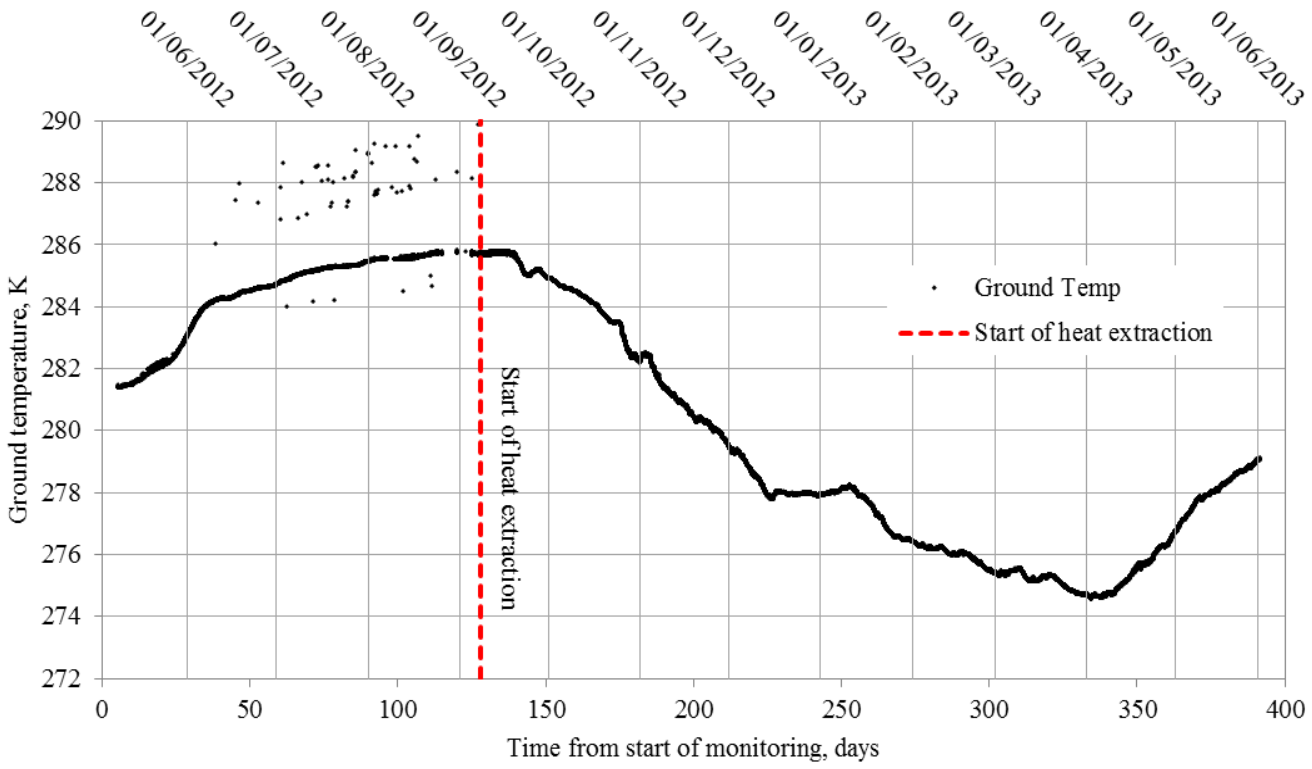

Figure D19 – Time evolution showing the monitored ground temperature data at sensor D3.

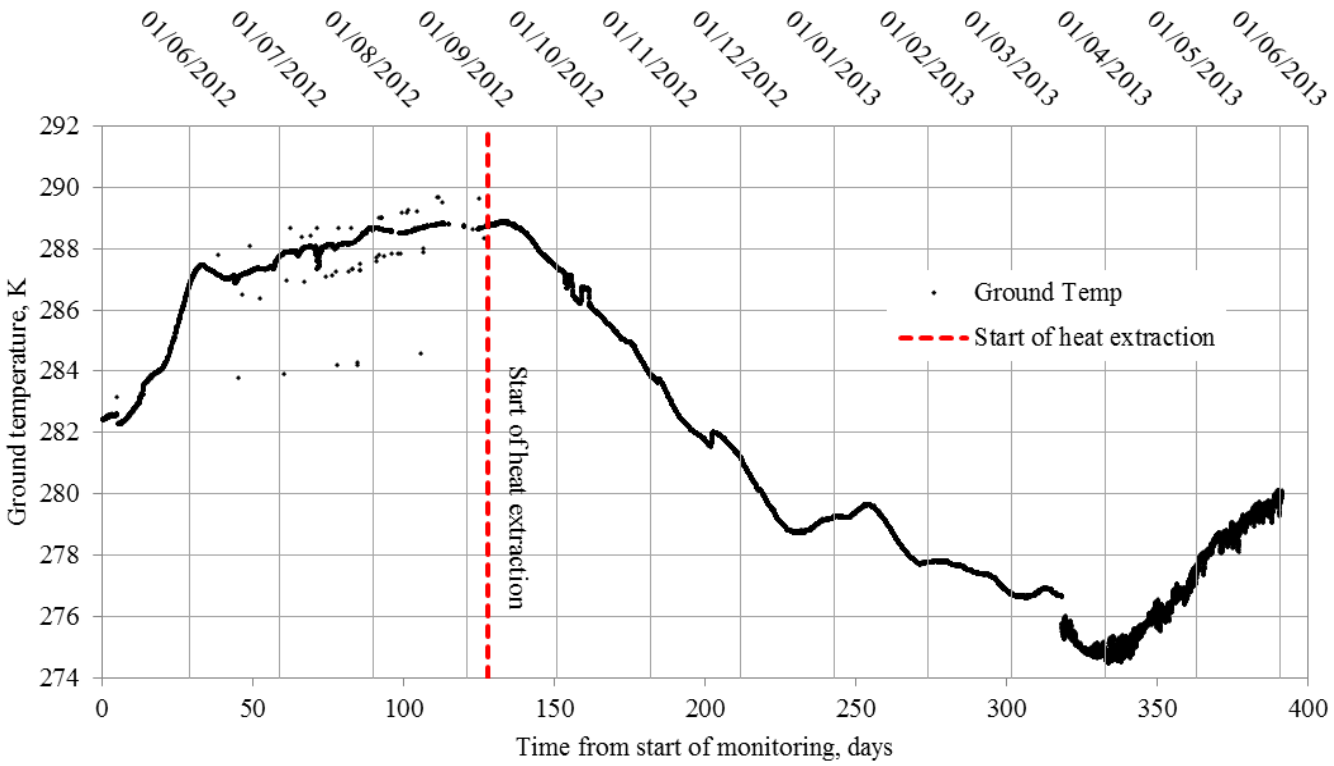

Figure D20 – Time evolution showing the monitored ground temperature data at sensor D4.

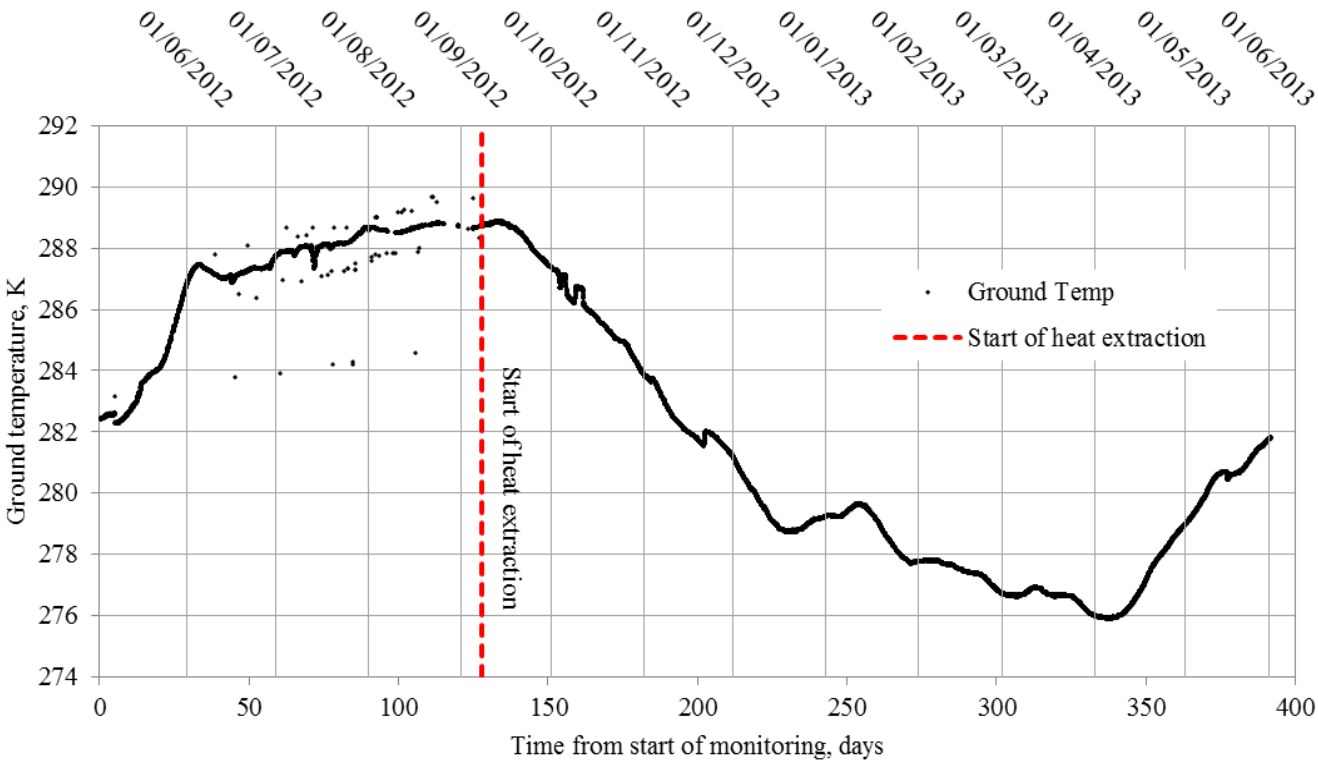

Figure D21 – Time evolution showing the monitored ground temperature data at sensor D5.

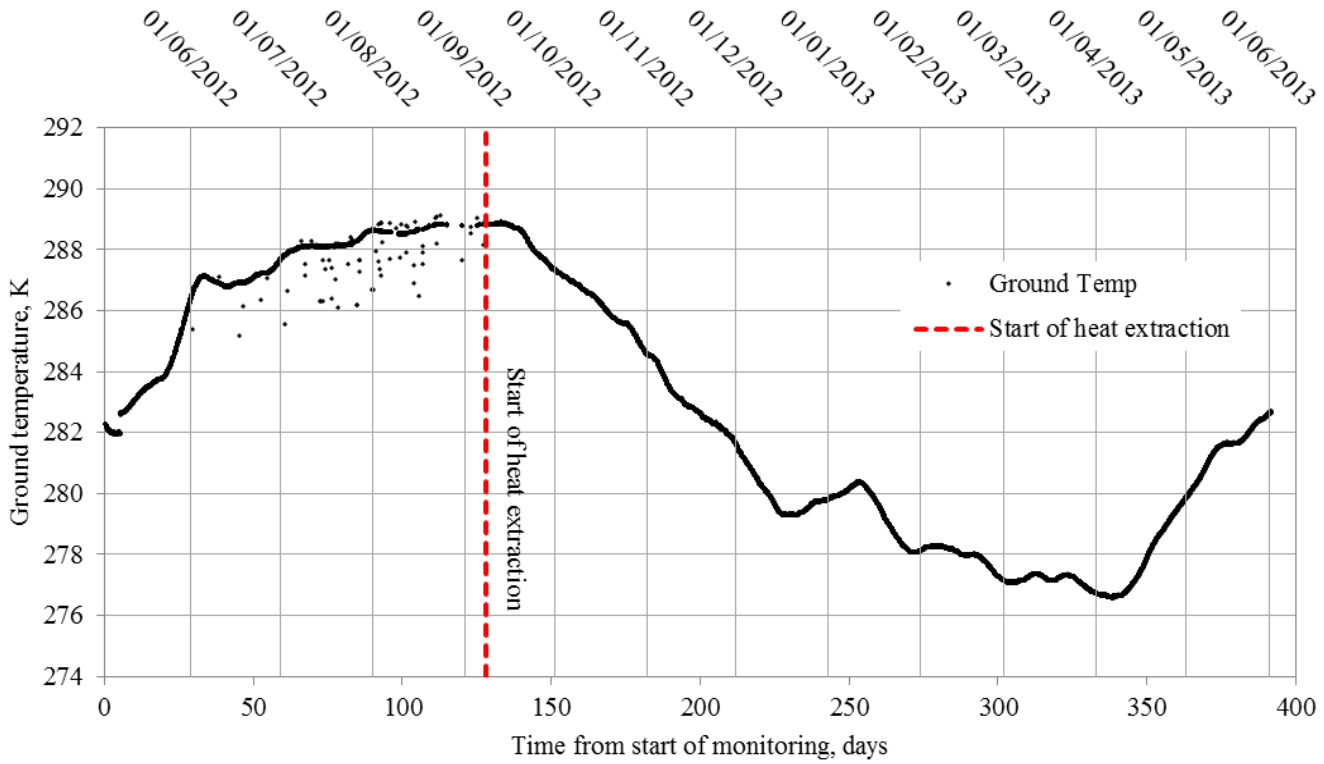

Figure D22 – Time evolution showing the monitored ground temperature data at sensor E1.

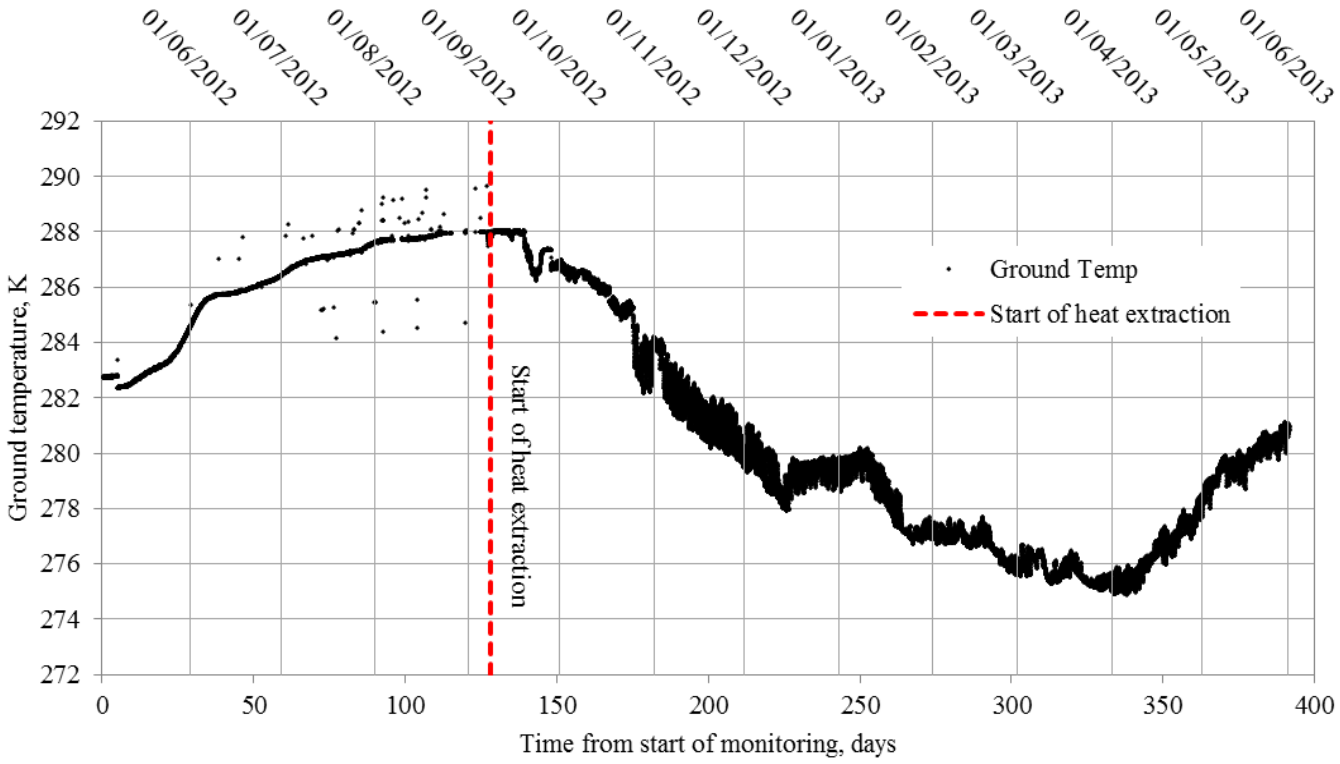

Figure D23 – Time evolution showing the monitored ground temperature data at sensor E2.

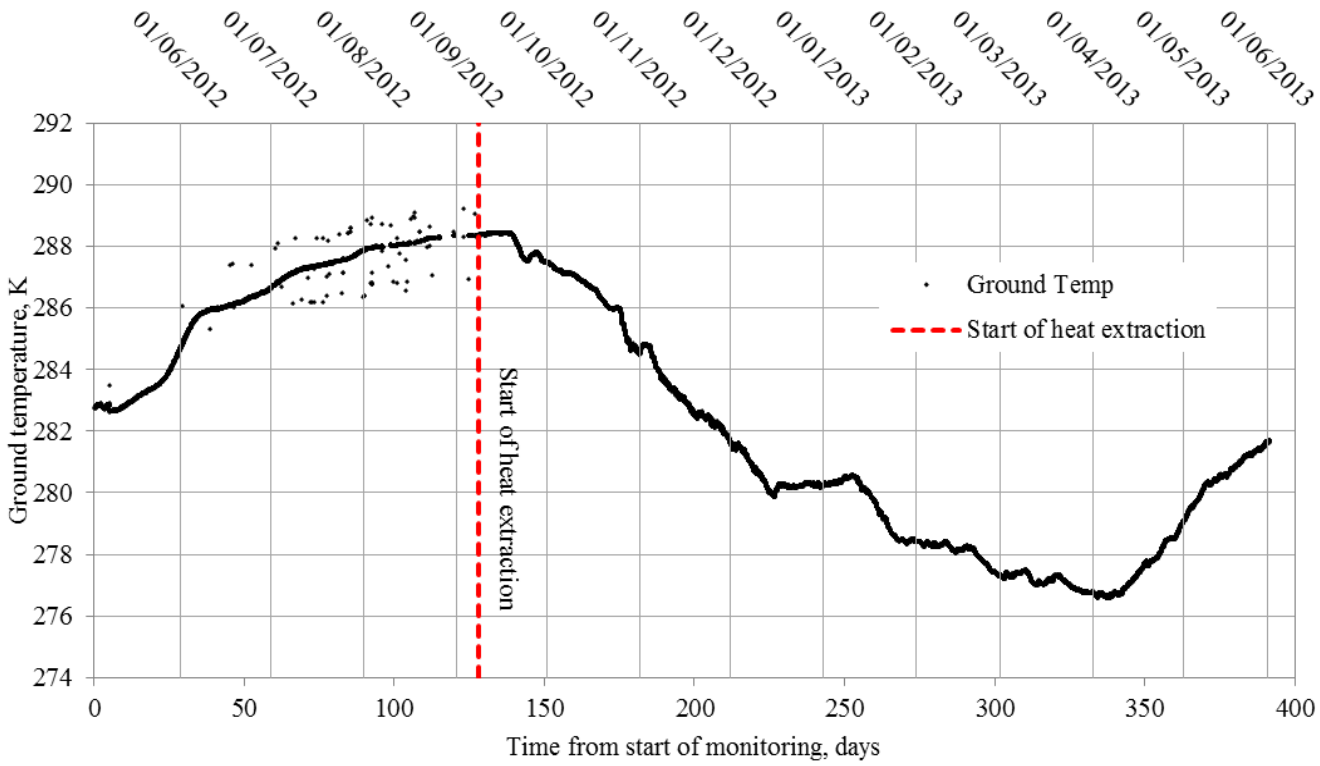

Figure D24 – Time evolution showing the monitored ground temperature data at sensor E3.

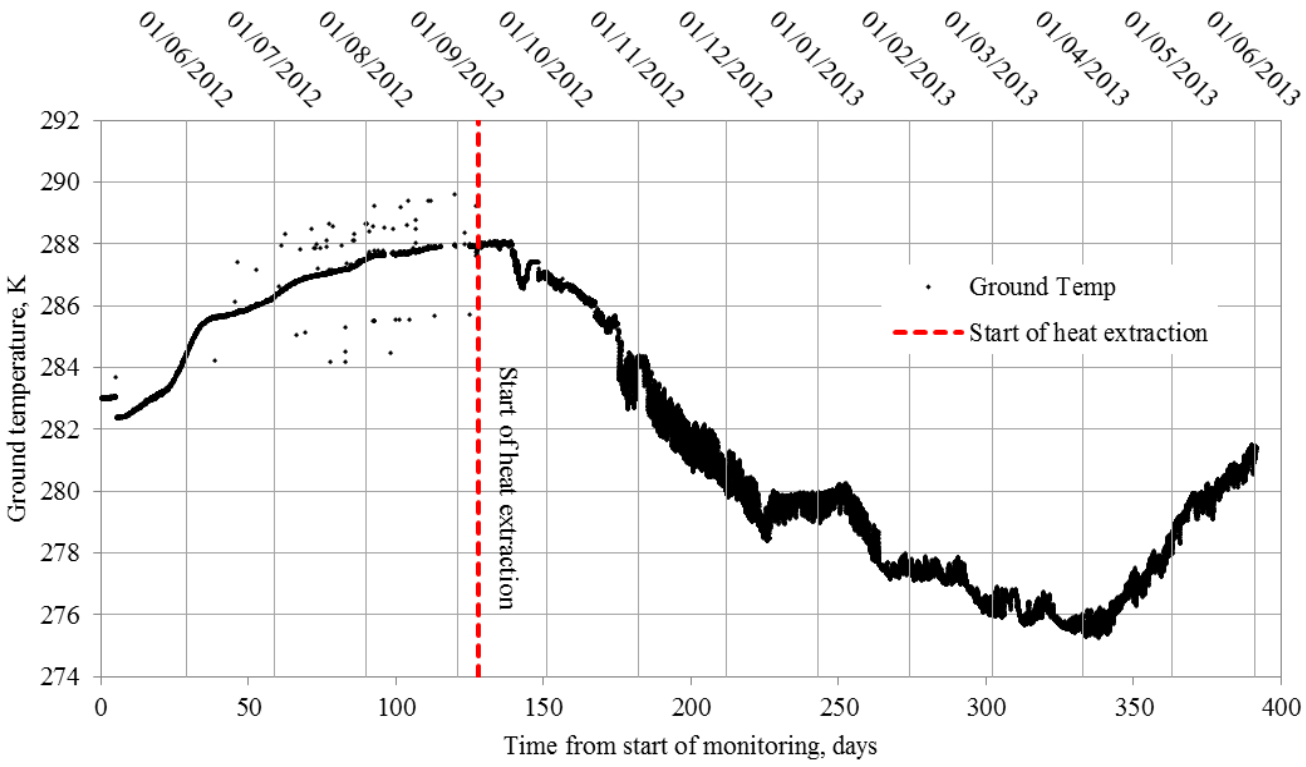

Figure D25 – Time evolution showing the monitored ground temperature data at sensor E4.

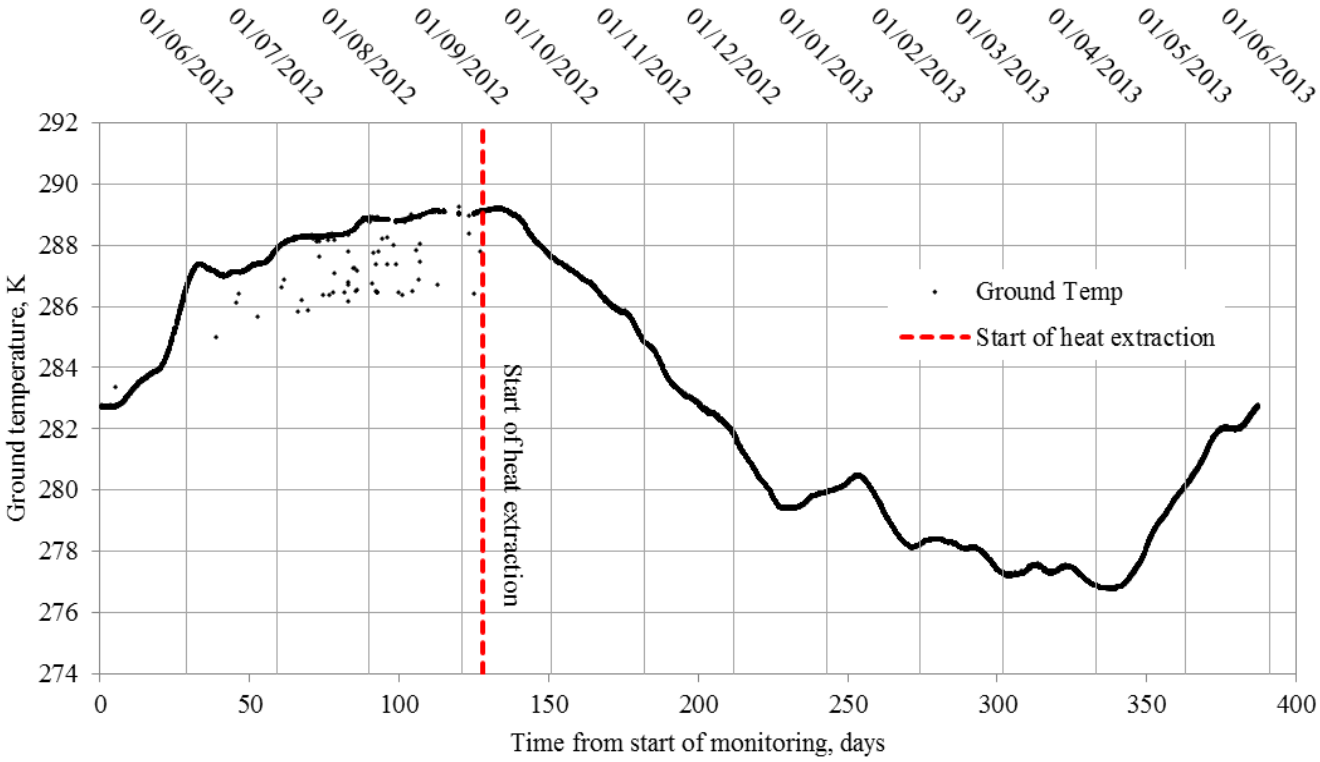

Figure D26 – Time evolution showing the monitored ground temperature data at sensor E5.

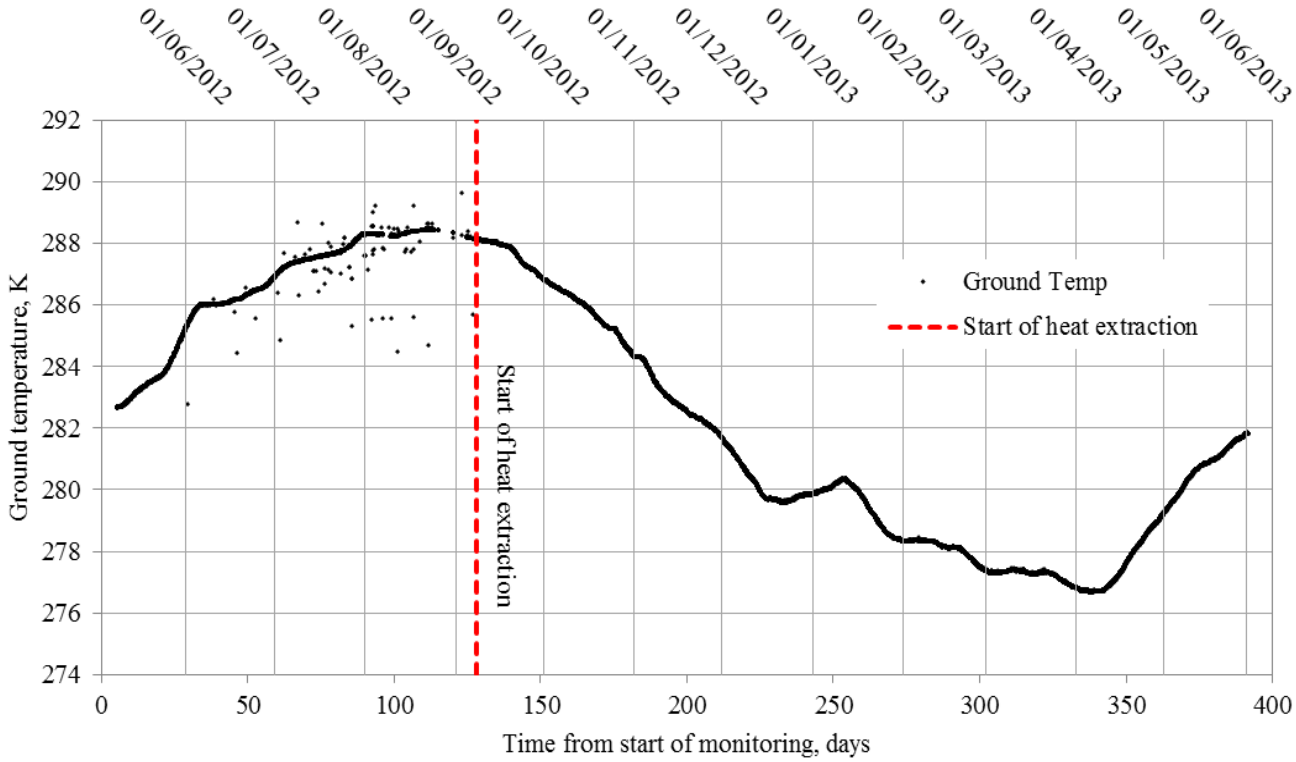

Figure D27 – Time evolution showing the monitored ground temperature data at sensor F1.

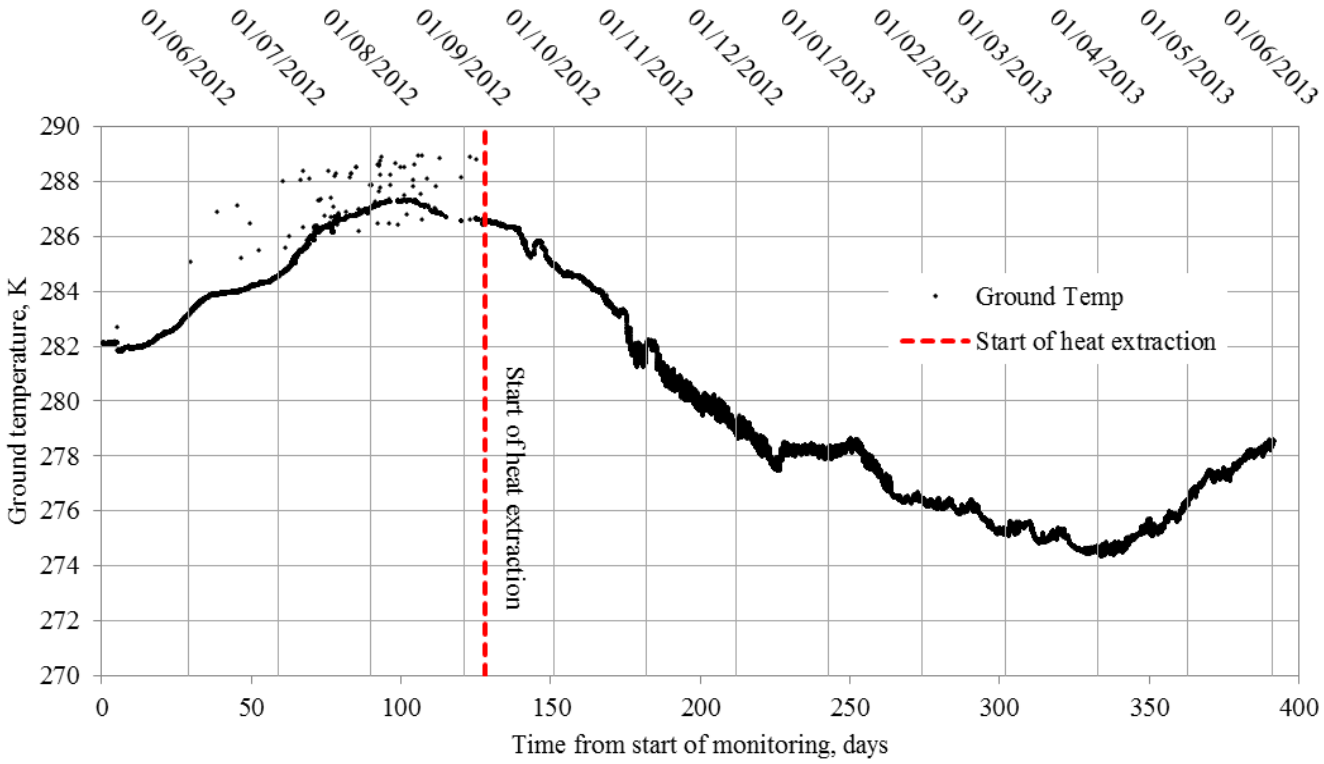

Figure D28 – Time evolution showing the monitored ground temperature data at sensor F2.

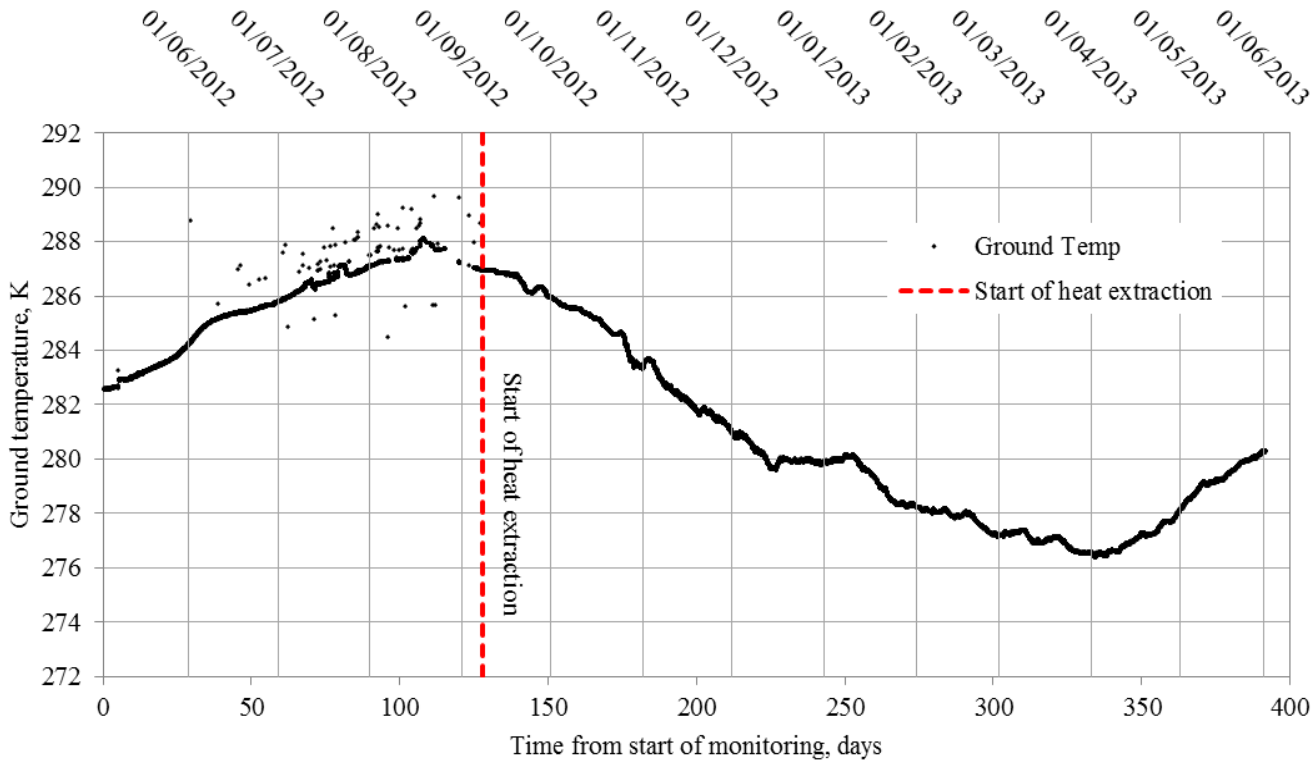

Figure D29 – Time evolution showing the monitored ground temperature data at sensor F3.

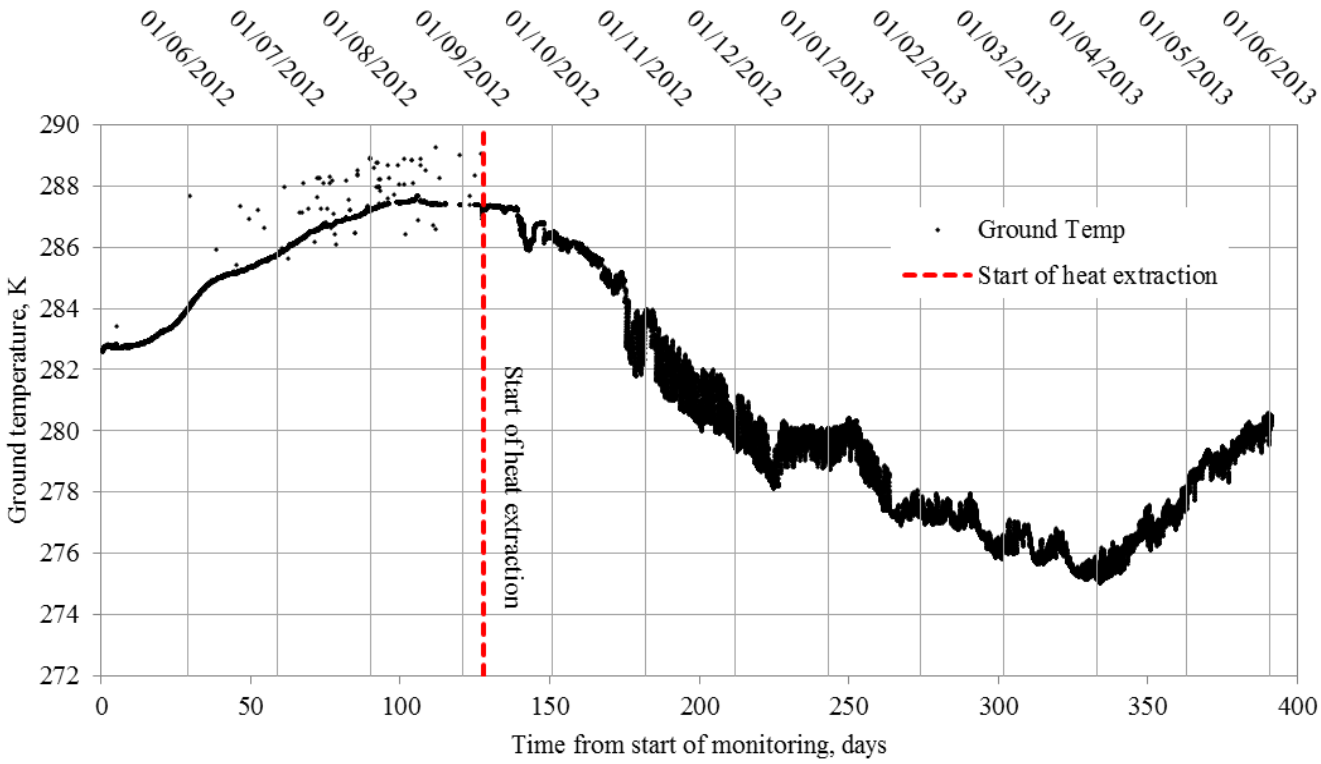

Figure D30 – Time evolution showing the monitored ground temperature data at sensor F4.

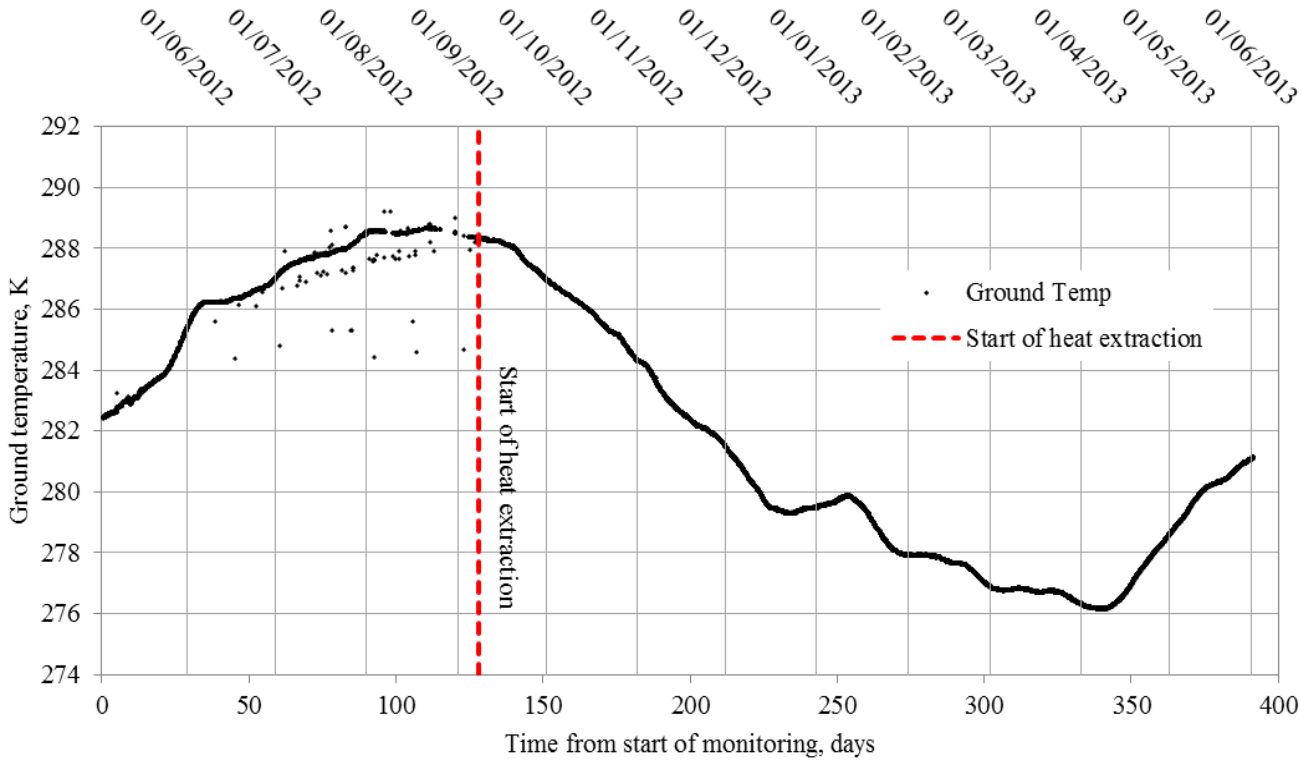

Figure D31 – Time evolution showing the monitored ground temperature data at sensor F5.

- The ground temperature data obtained from detailed cross-section AA has been denoted according to the thermistor notation provided in Figure D32.
- Figure D32 shows the spatial position of the thermistors, as recorded during a topographical survey of the site, along with the thermistor notation used.
- The letters 'AA', 'AB' and 'AC' correspond to the thermistor string which the respective thermistors are part of (see Chapter 3 for more details).

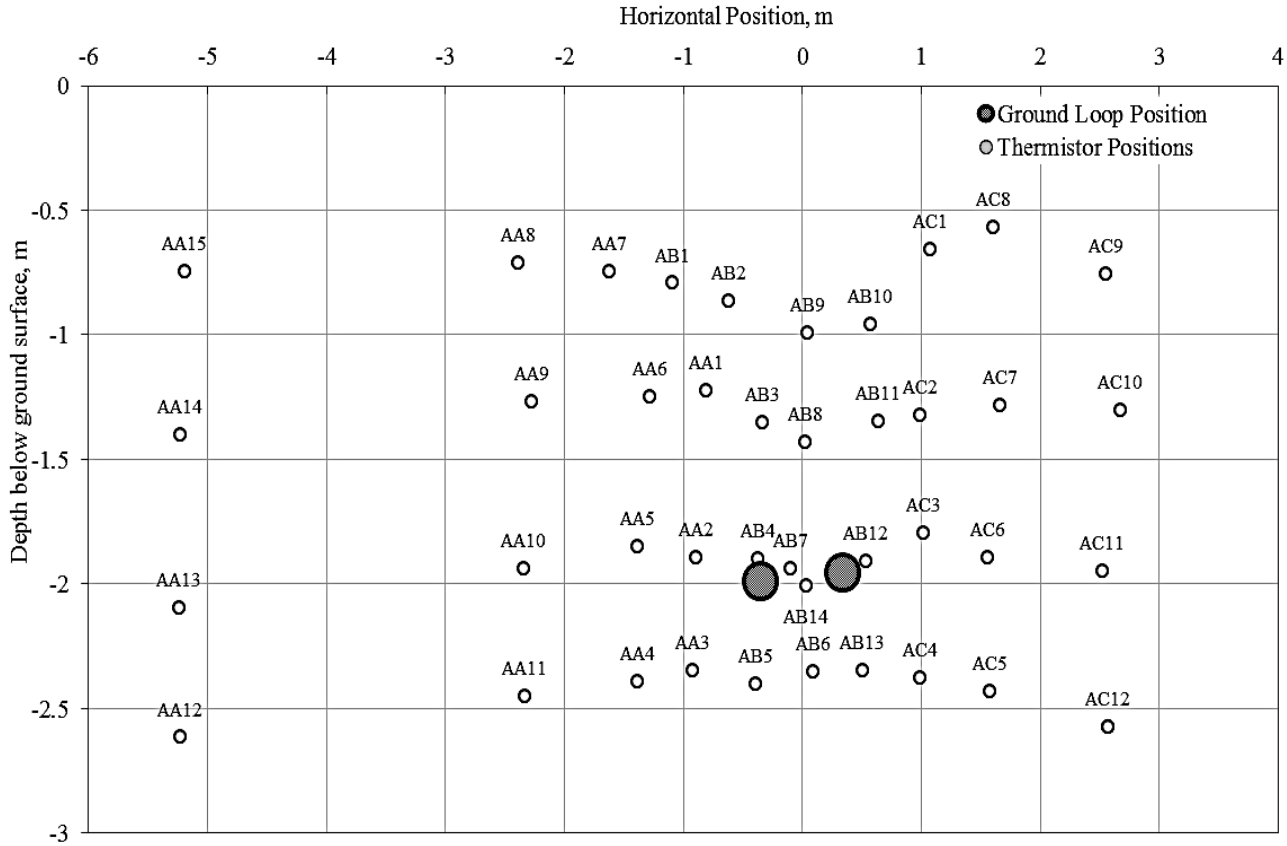

Figure D32 – Spatial position and adopted notation of the thermistors located in detailed cross-section AA.

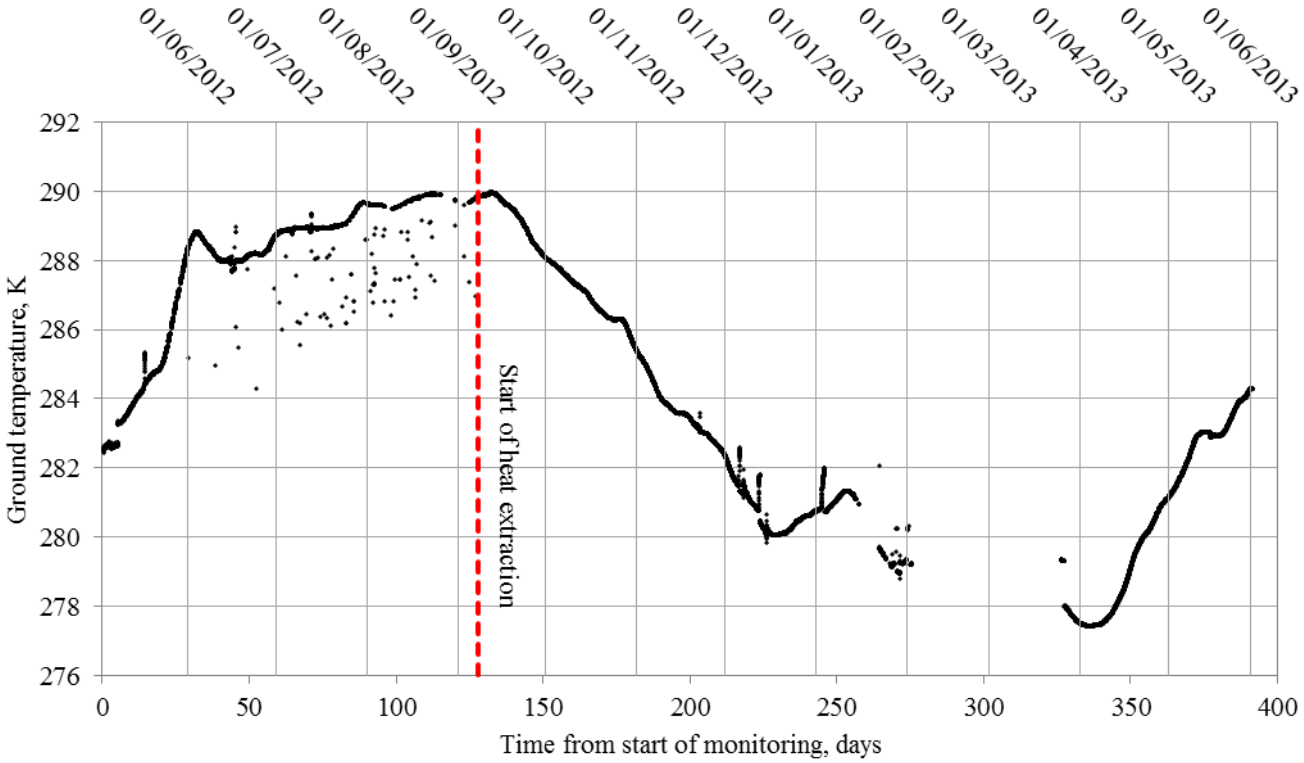

Figure D33 – Time evolution showing the monitored ground temperature data at sensor AA1.

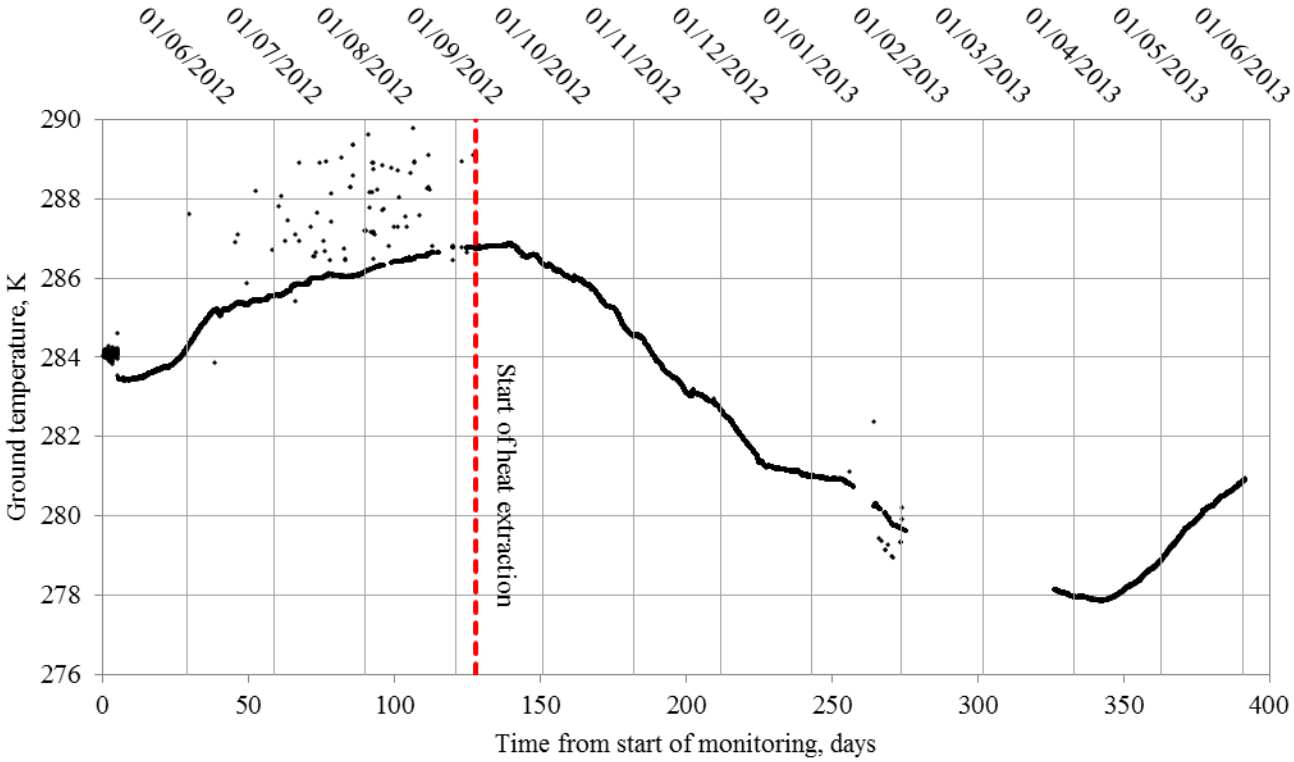

Figure D34 – Time evolution showing the monitored ground temperature data at sensor AA3.

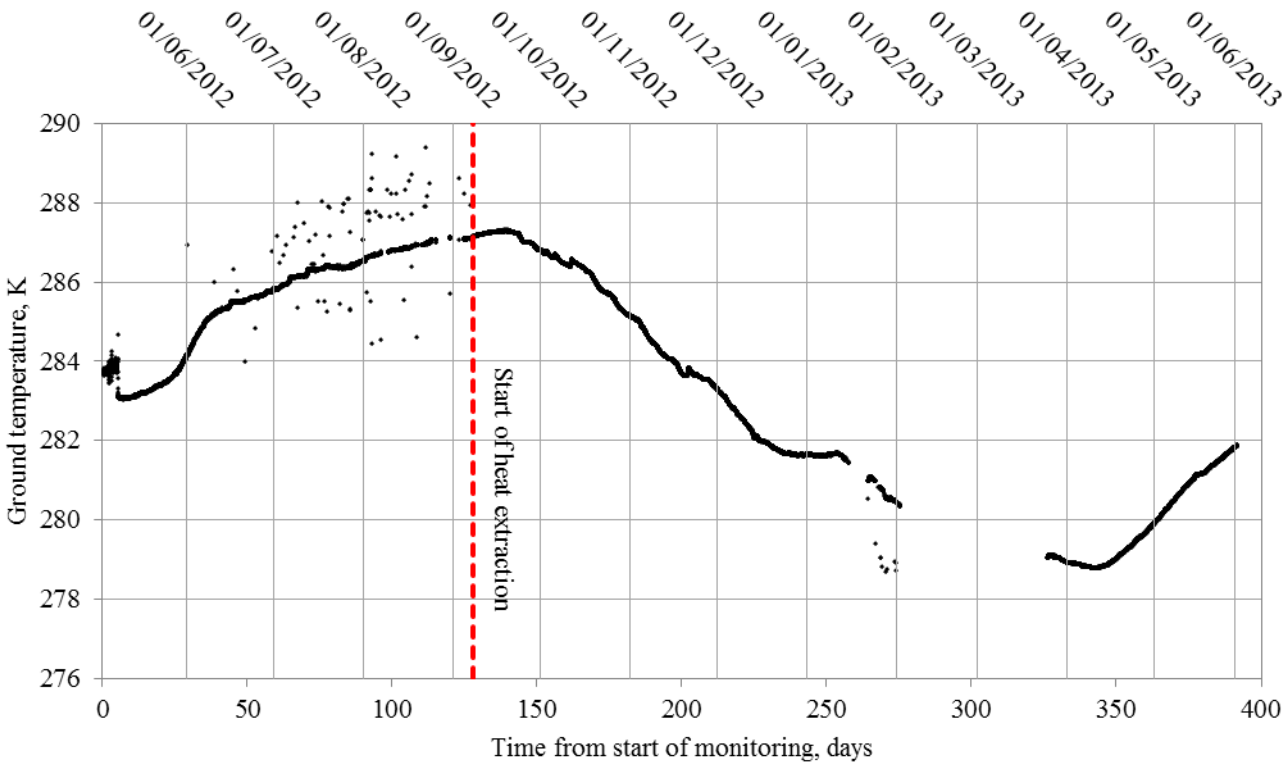

Figure D35 – Time evolution showing the monitored ground temperature data at sensor AA4.

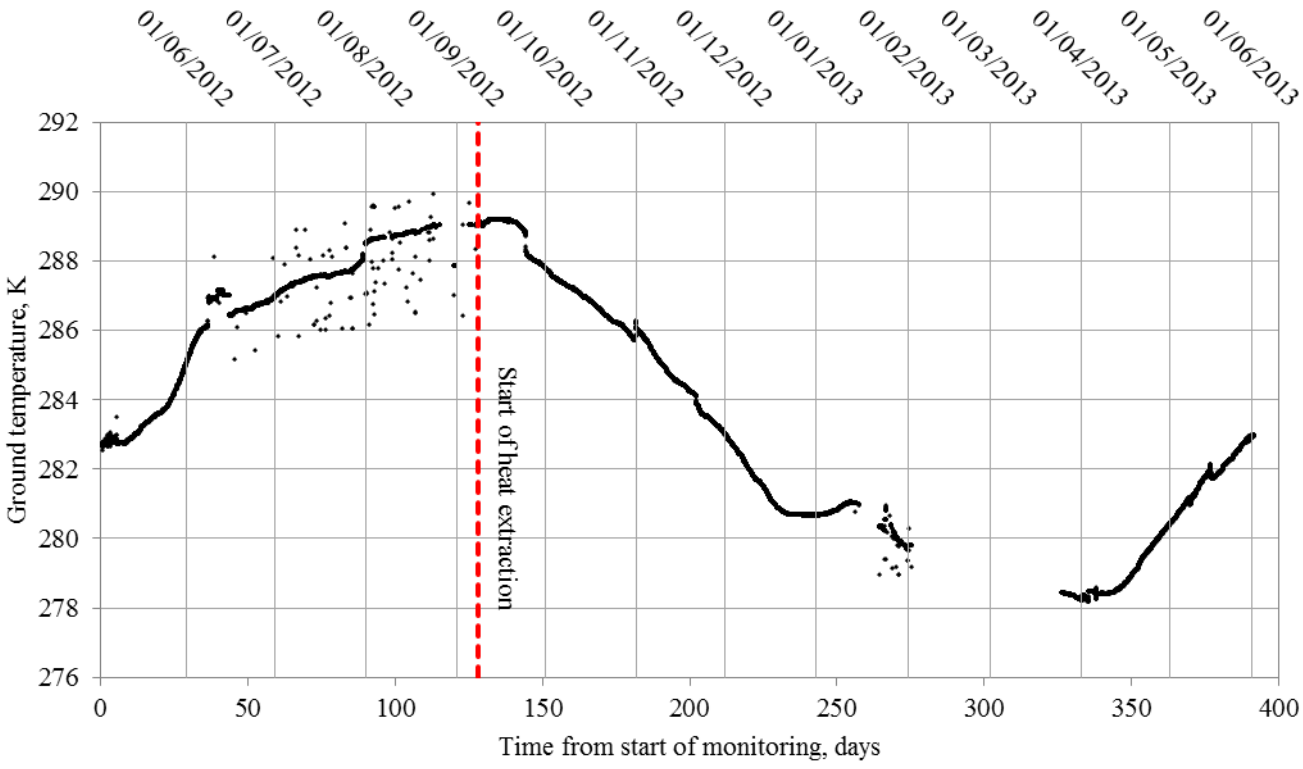

Figure D36 – Time evolution showing the monitored ground temperature data at sensor AA5.

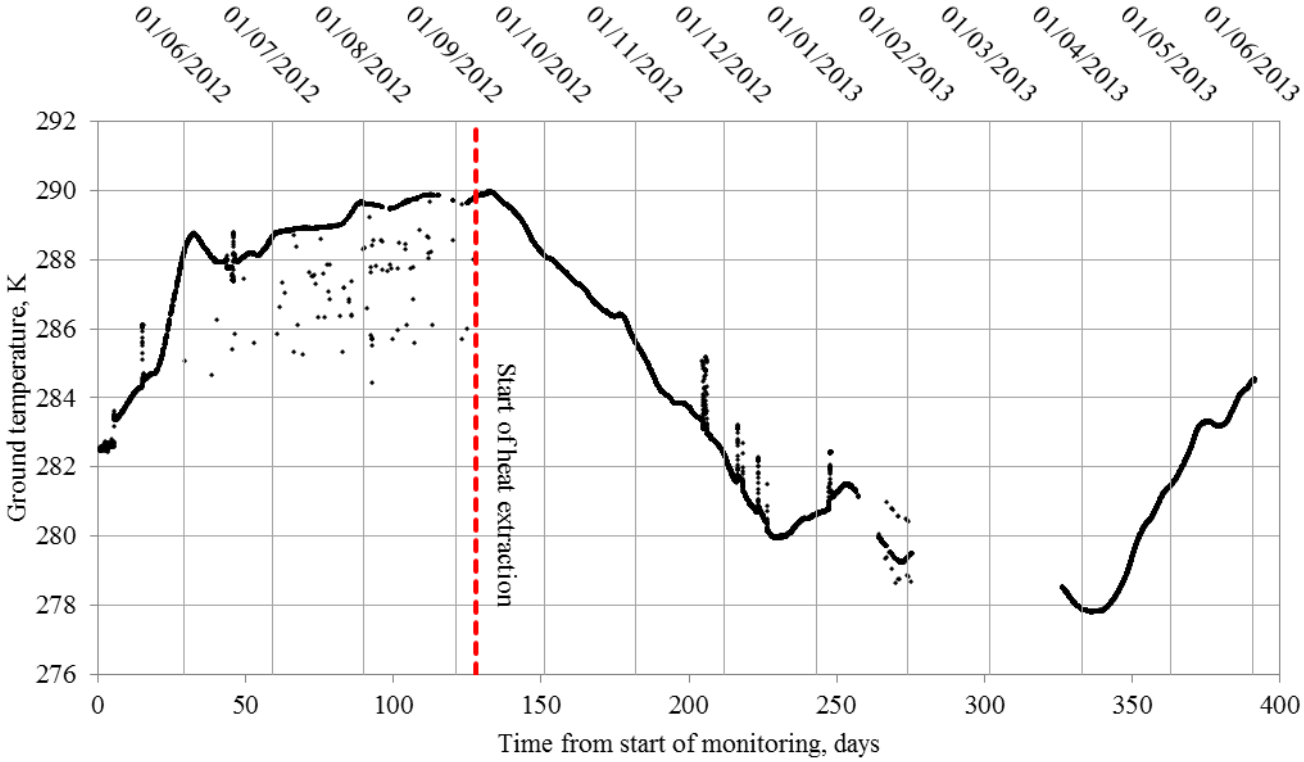

Figure D37 – Time evolution showing the monitored ground temperature data at sensor AA6.

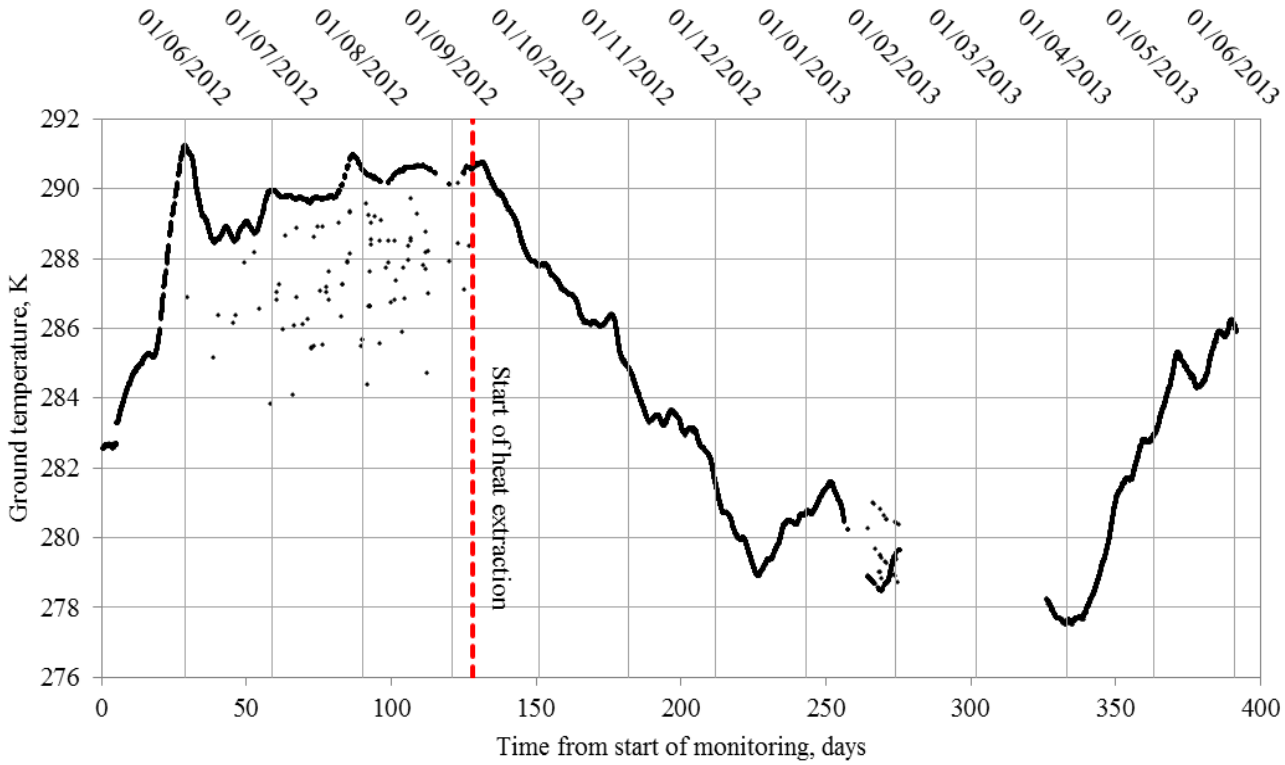

Figure D38 – Time evolution showing the monitored ground temperature data at sensor AA8.

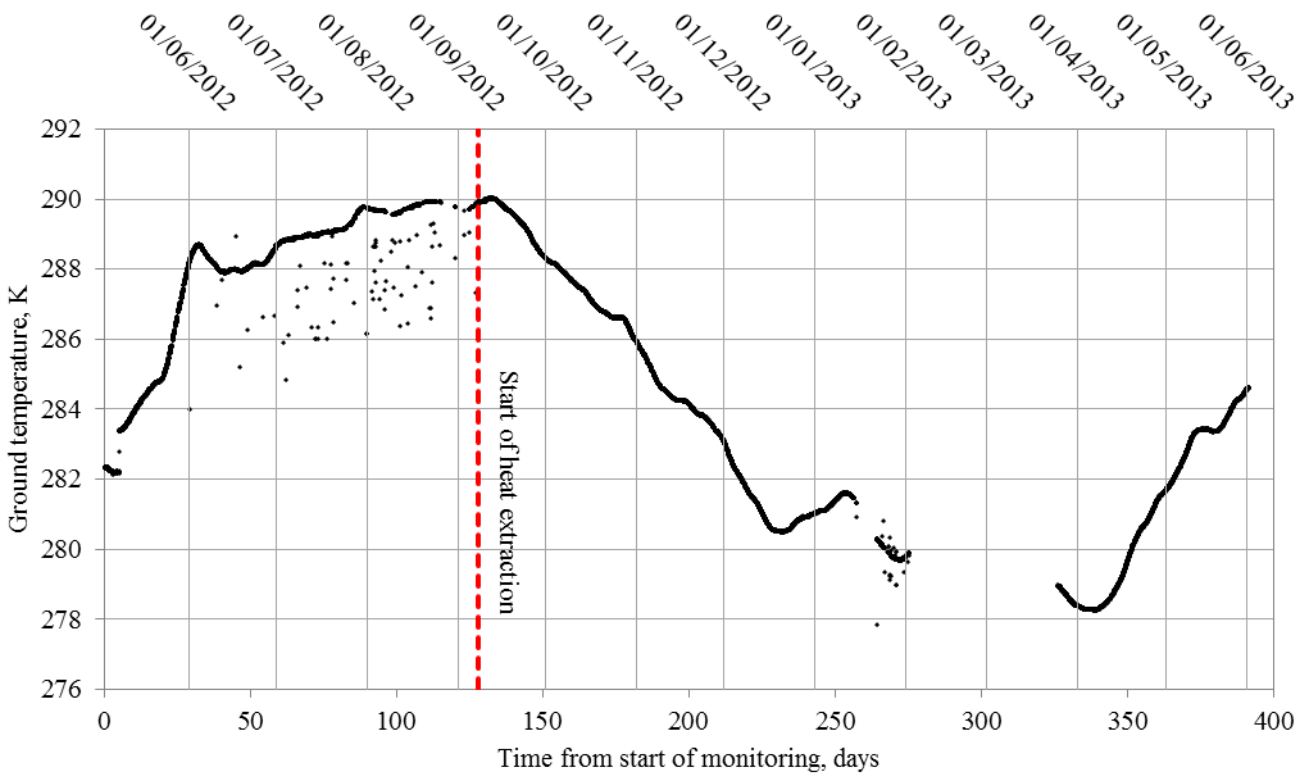

Figure D39 – Time evolution showing the monitored ground temperature data at sensor AA9.

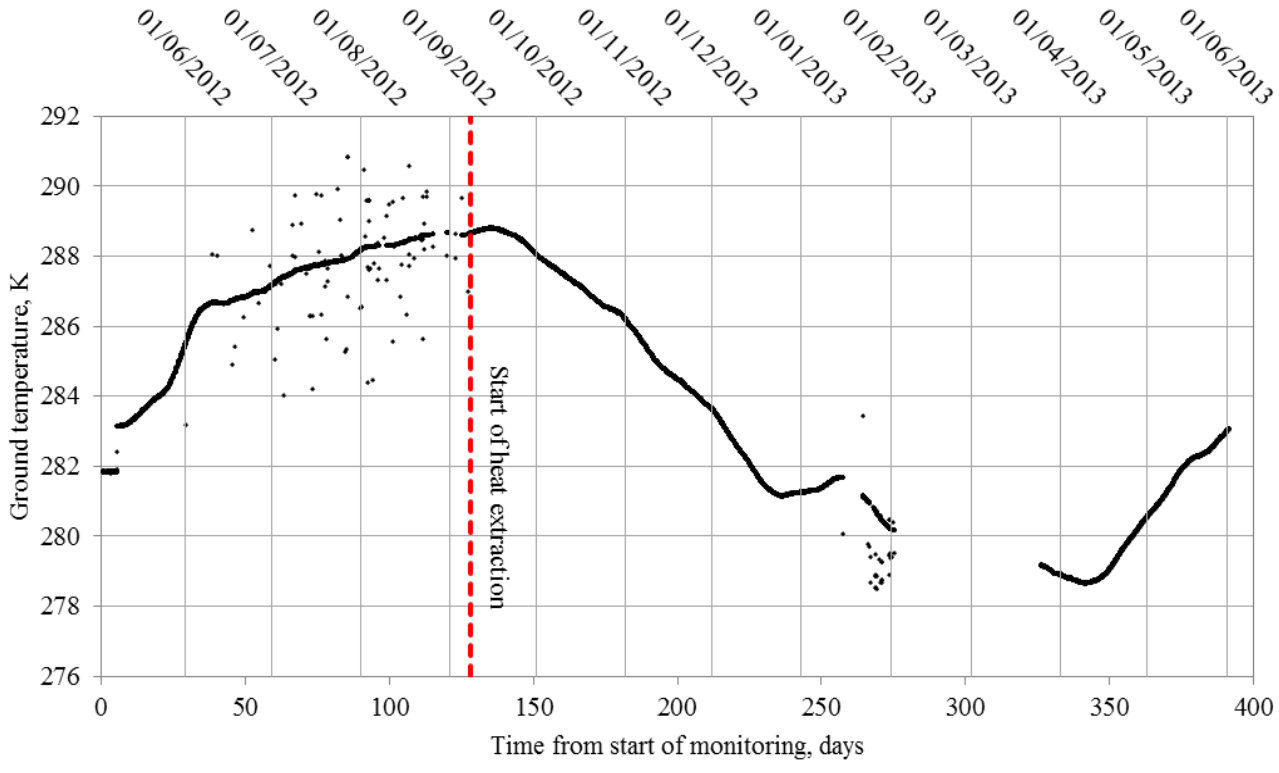

Figure D40 – Time evolution showing the monitored ground temperature data at sensor AA10.

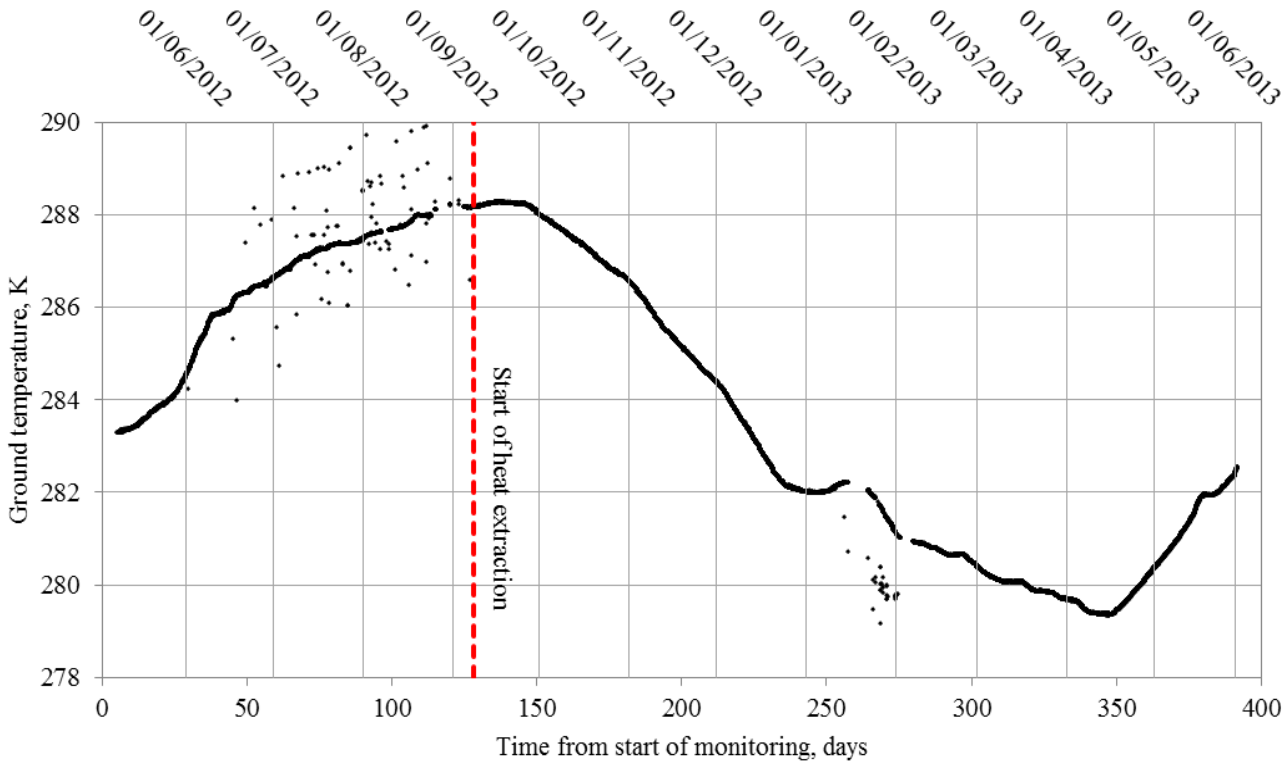

Figure D41 – Time evolution showing the monitored ground temperature data at sensor AA11.

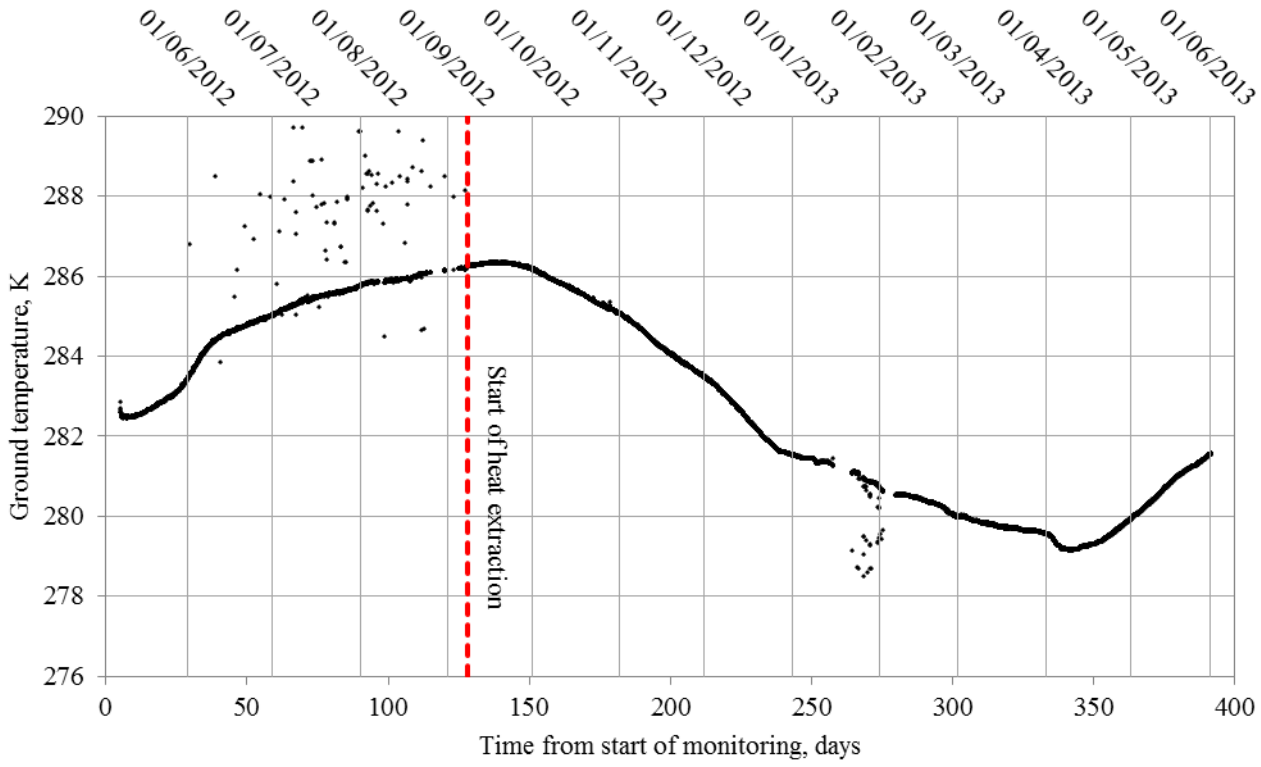

Figure D42 – Time evolution showing the monitored ground temperature data at sensor AA12.

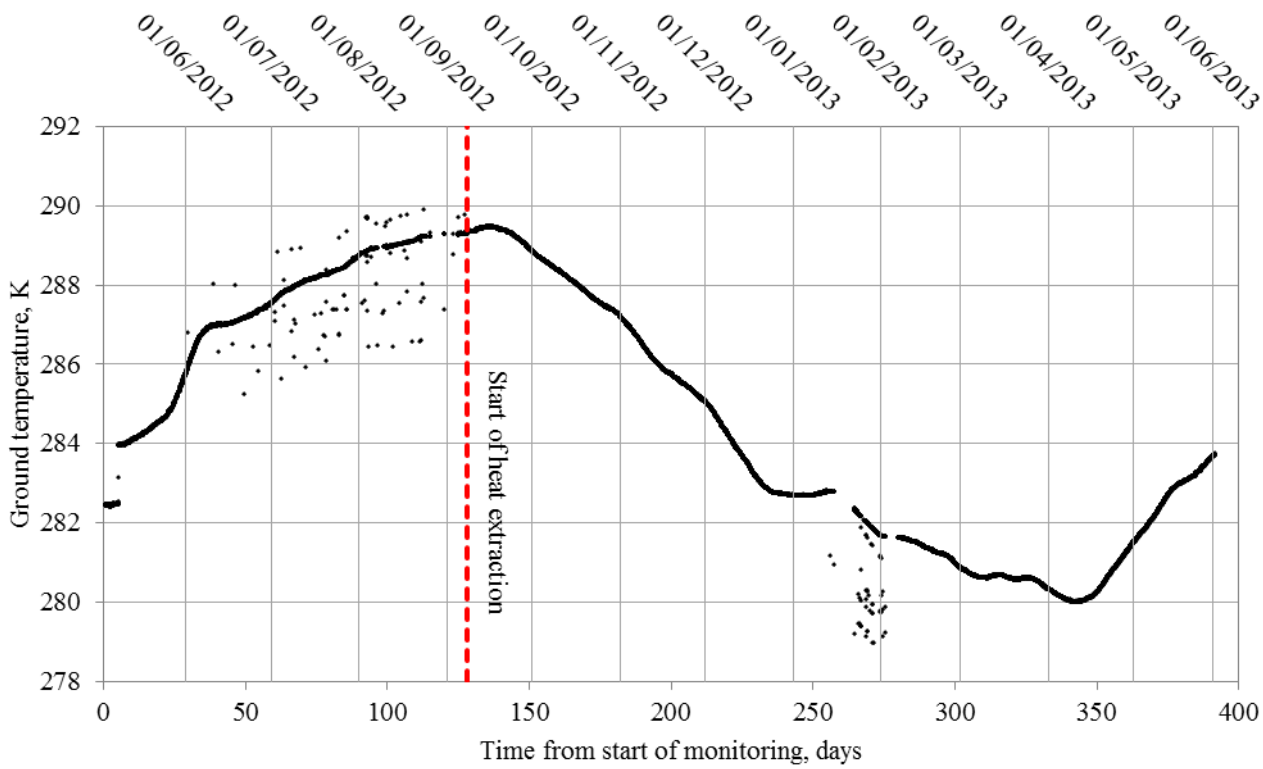

Figure D43 – Time evolution showing the monitored ground temperature data at sensor AA13.

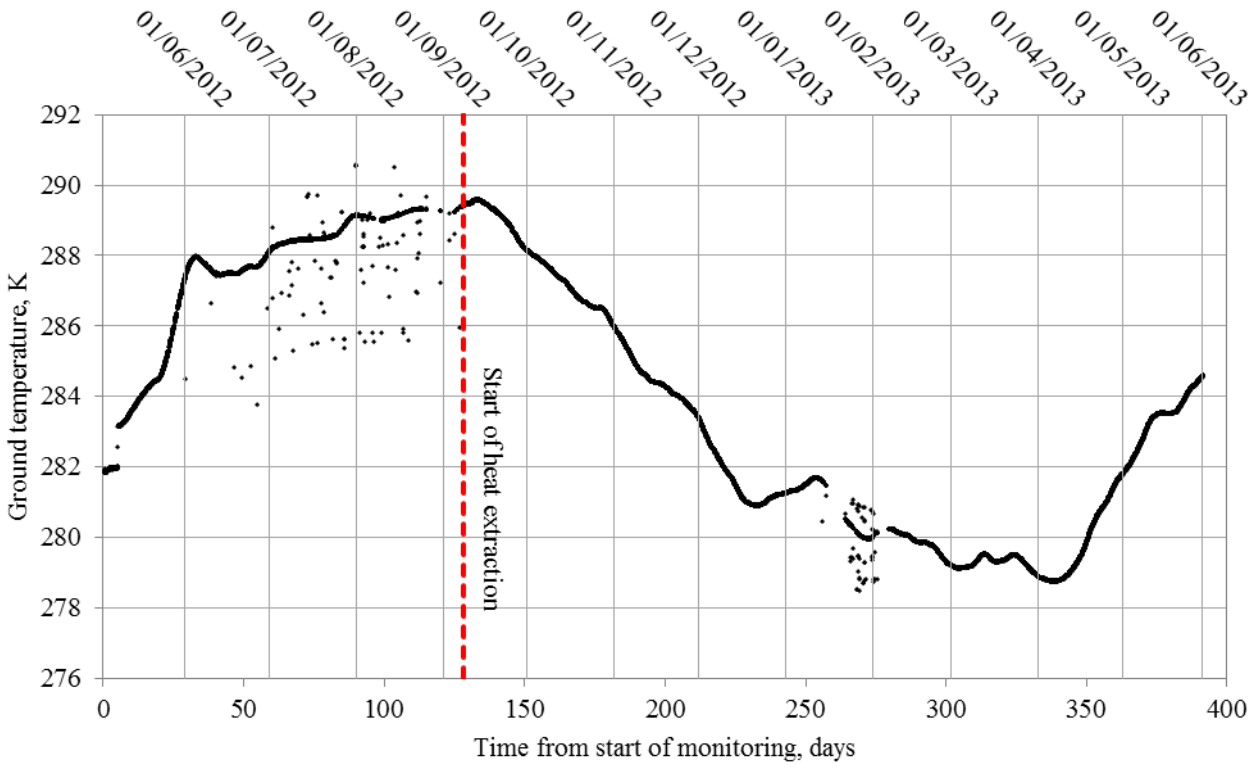

Figure D44 – Time evolution showing the monitored ground temperature data at sensor AA14.

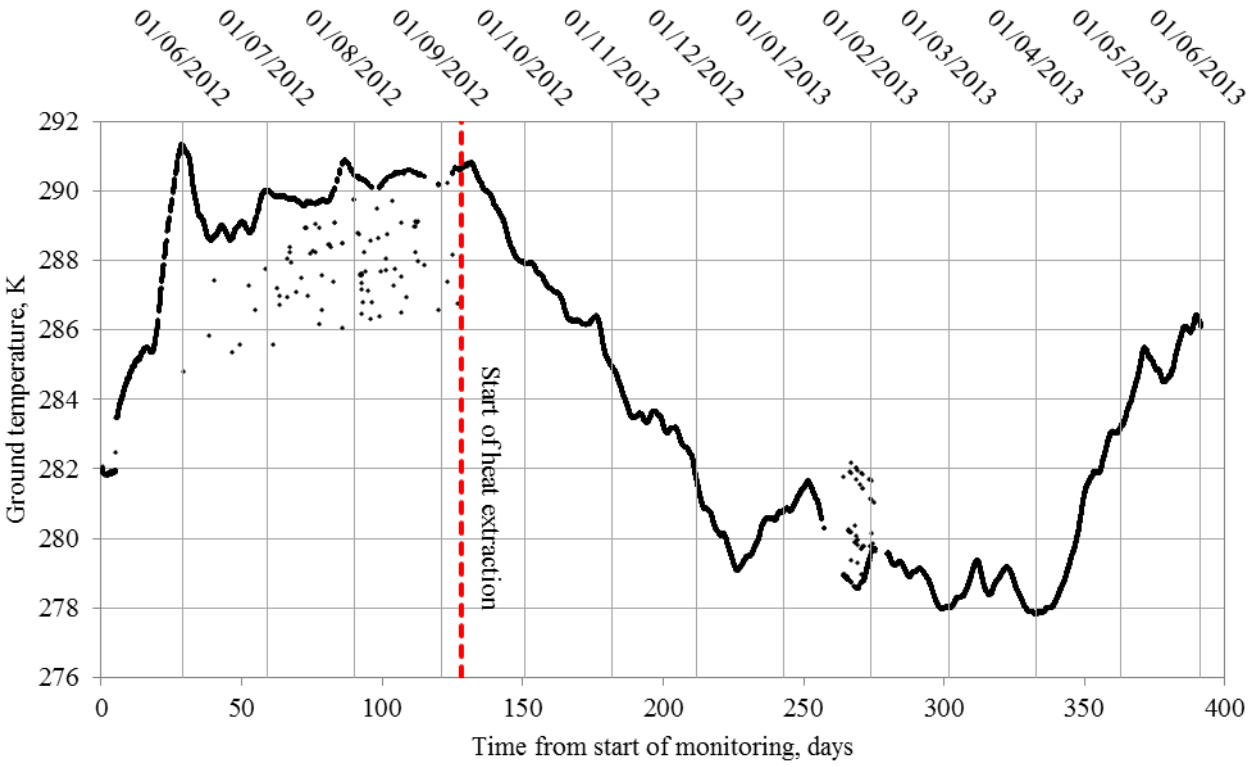

Figure D45 – Time evolution showing the monitored ground temperature data at sensor AA15.

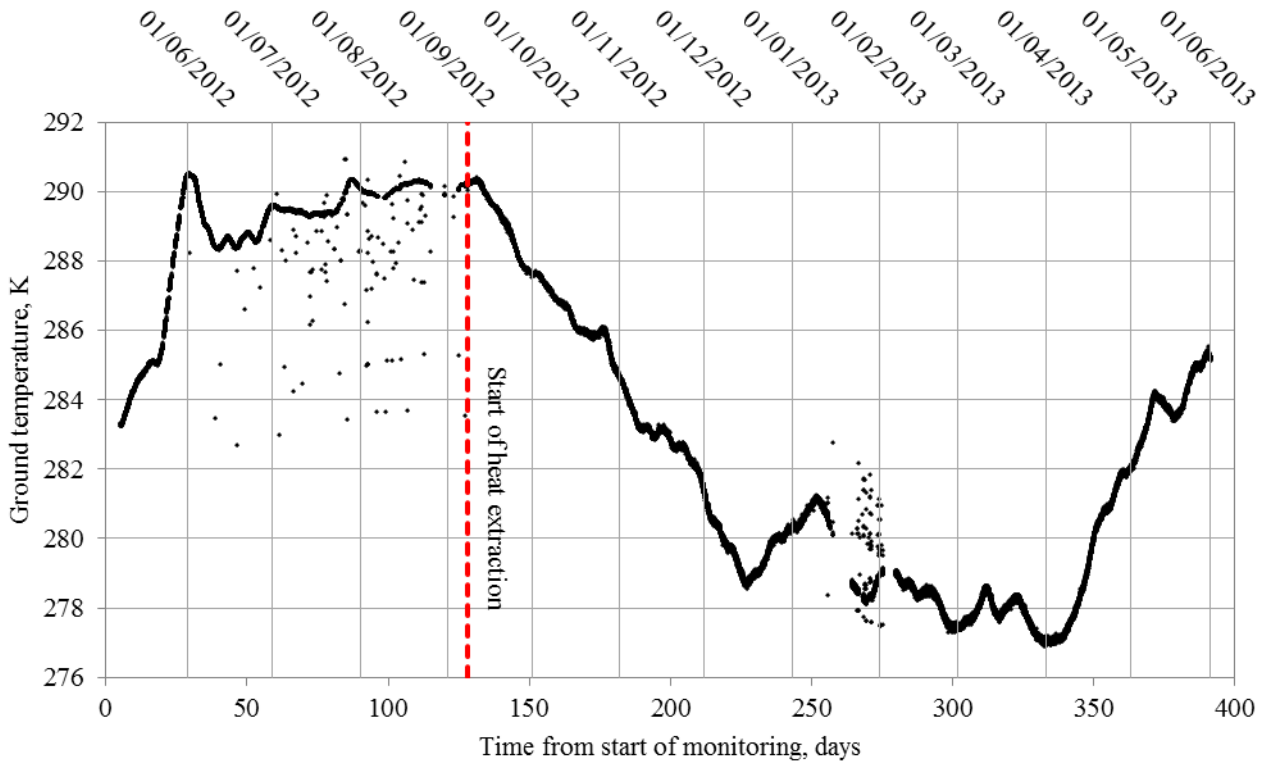

Figure D46 – Time evolution showing the monitored ground temperature data at sensor AB1.

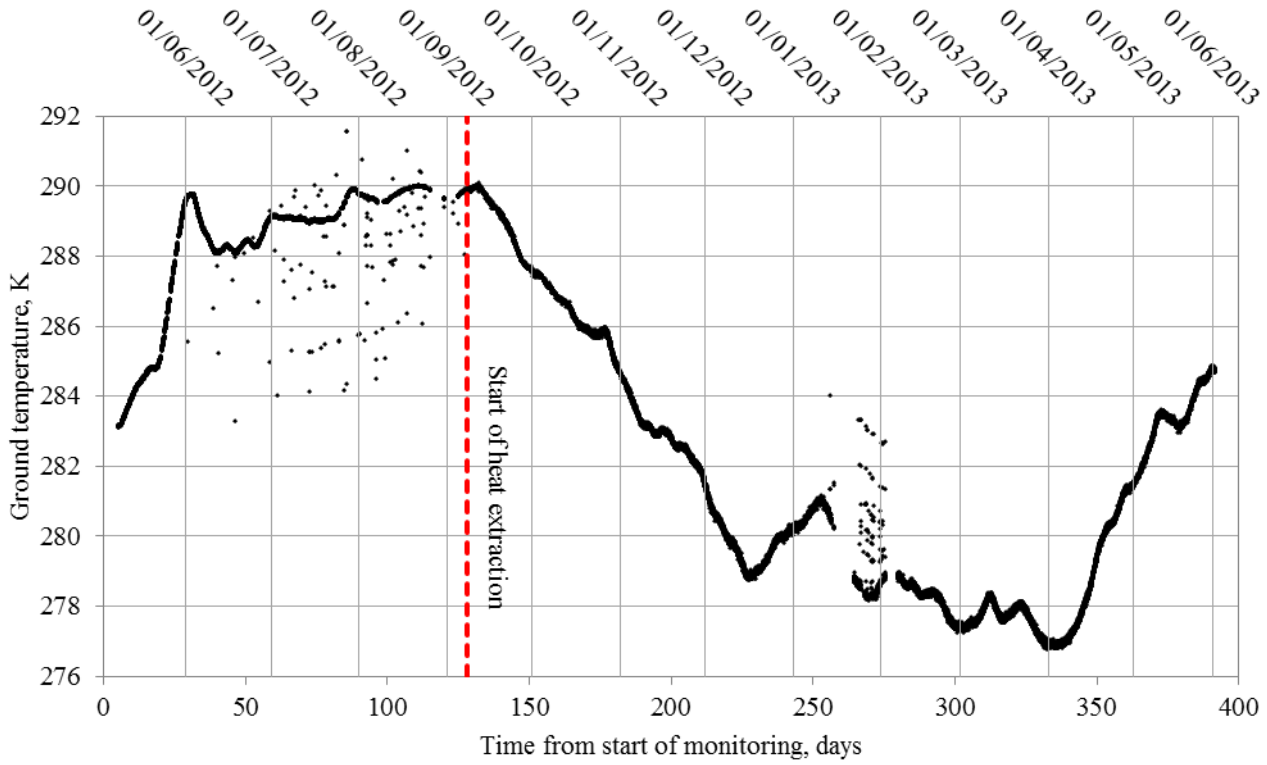

Figure D47 – Time evolution showing the monitored ground temperature data at sensor AB2.

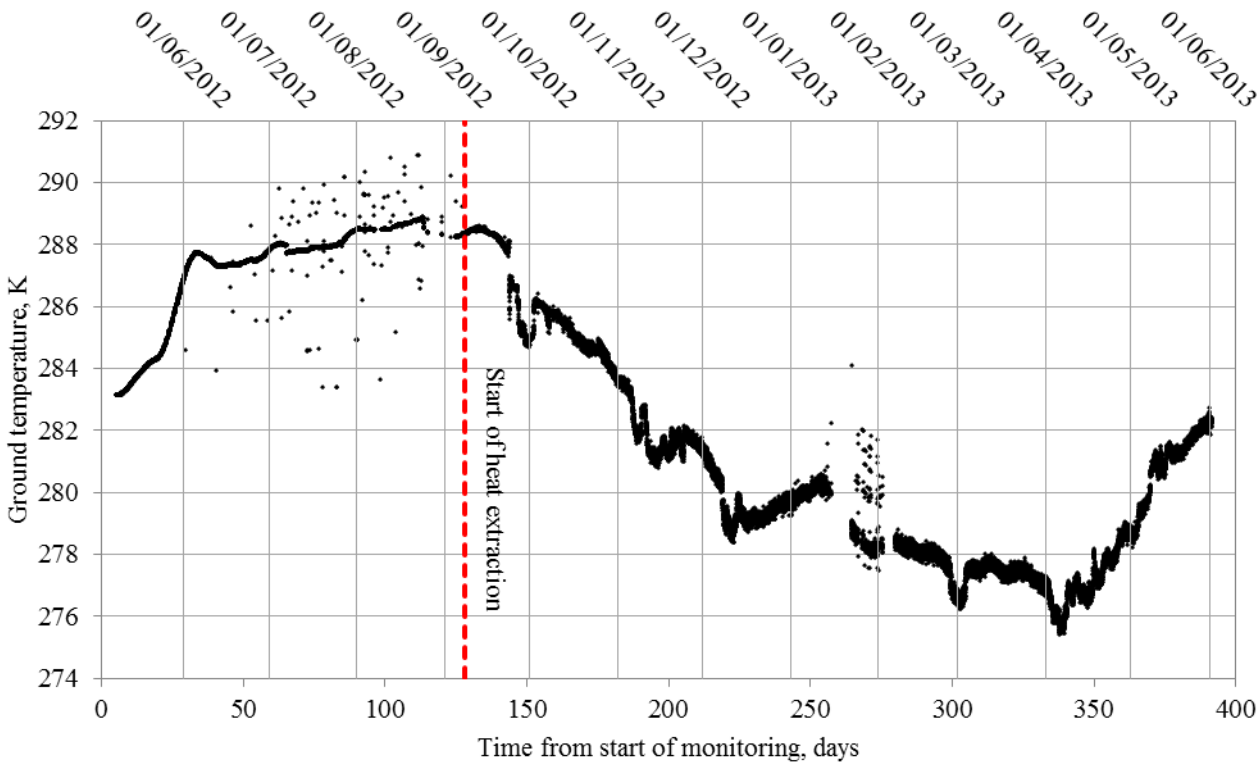

Figure D48 – Time evolution showing the monitored ground temperature data at sensor AB3.

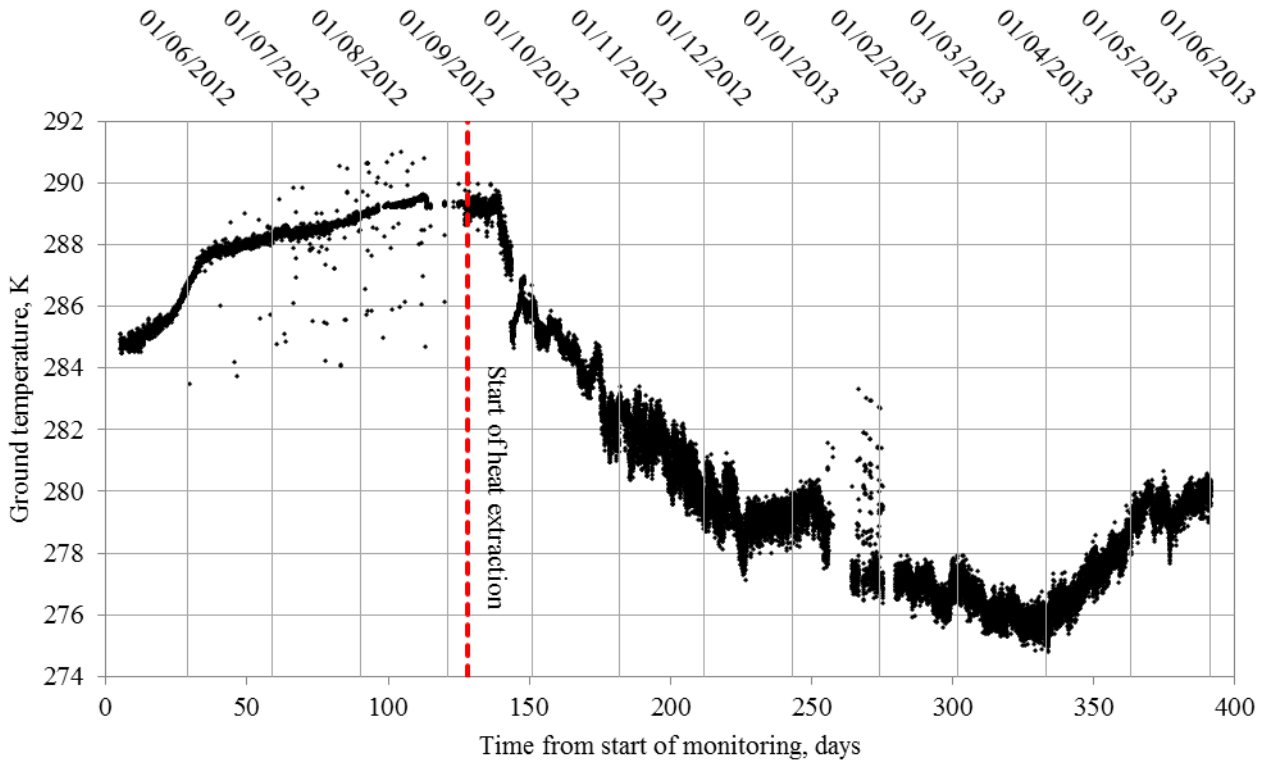

Figure D49 – Time evolution showing the monitored ground temperature data at sensor AB4.

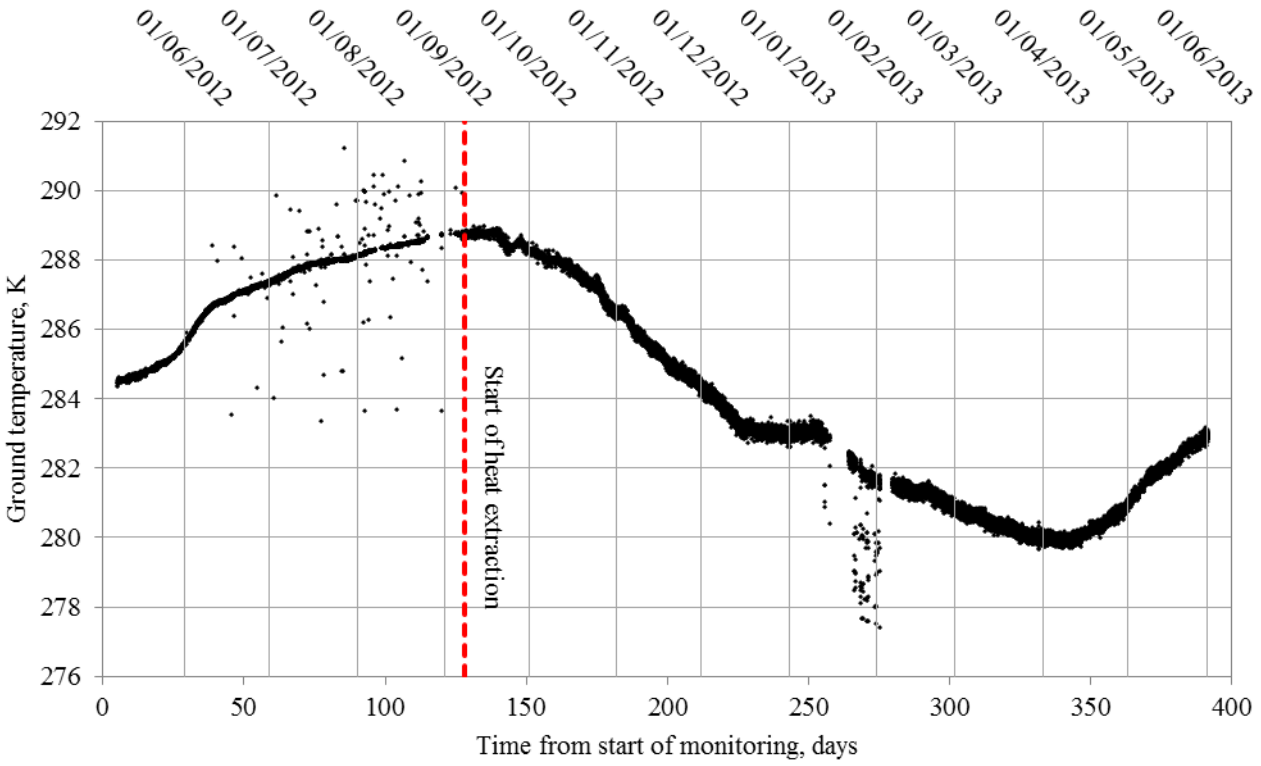

Figure D50 – Time evolution showing the monitored ground temperature data at sensor AB5.

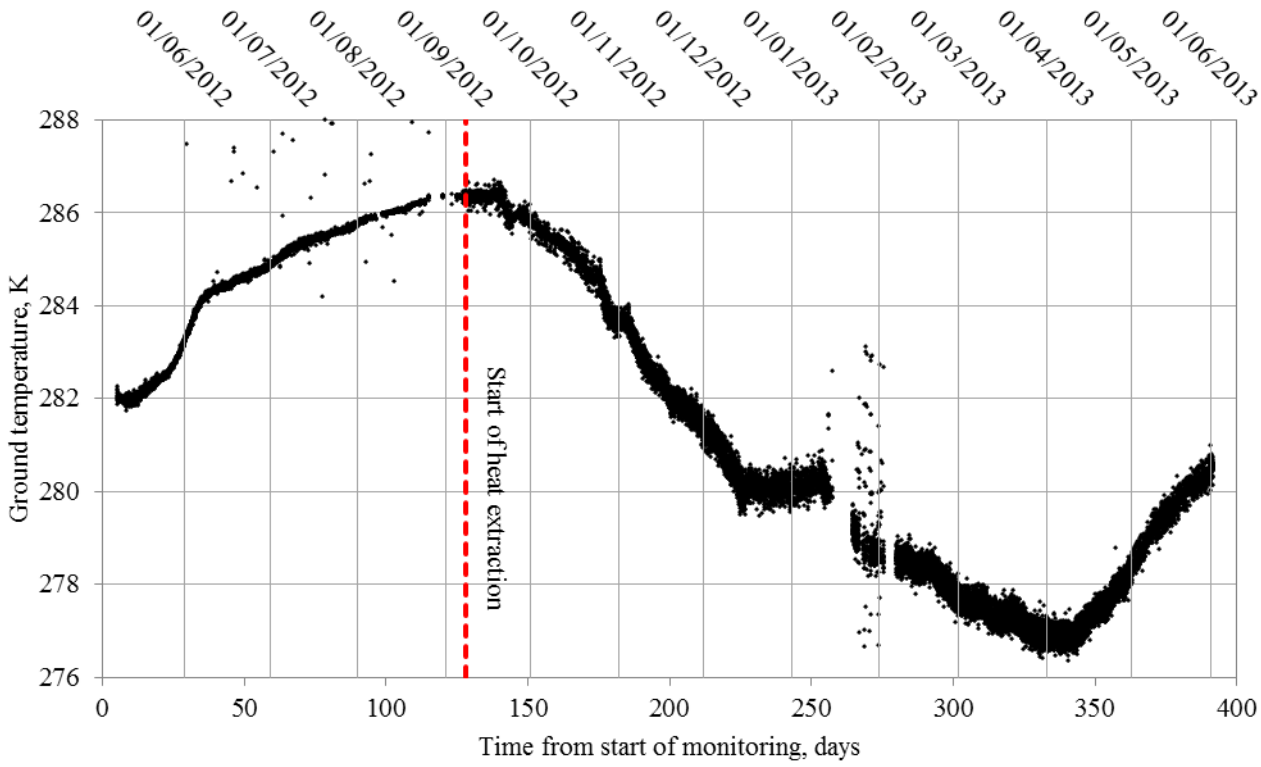

Figure D51 – Time evolution showing the monitored ground temperature data at sensor AB6.

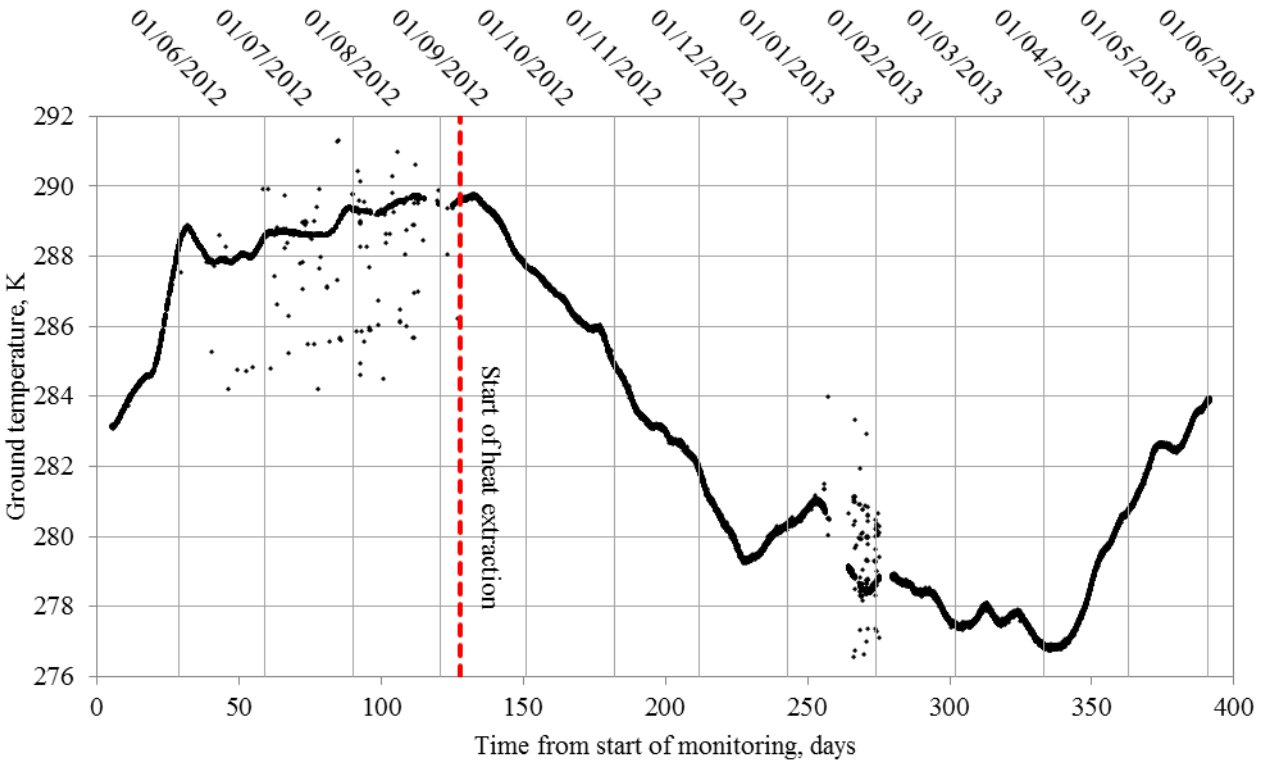

Figure D52 – Time evolution showing the monitored ground temperature data at sensor AB8.

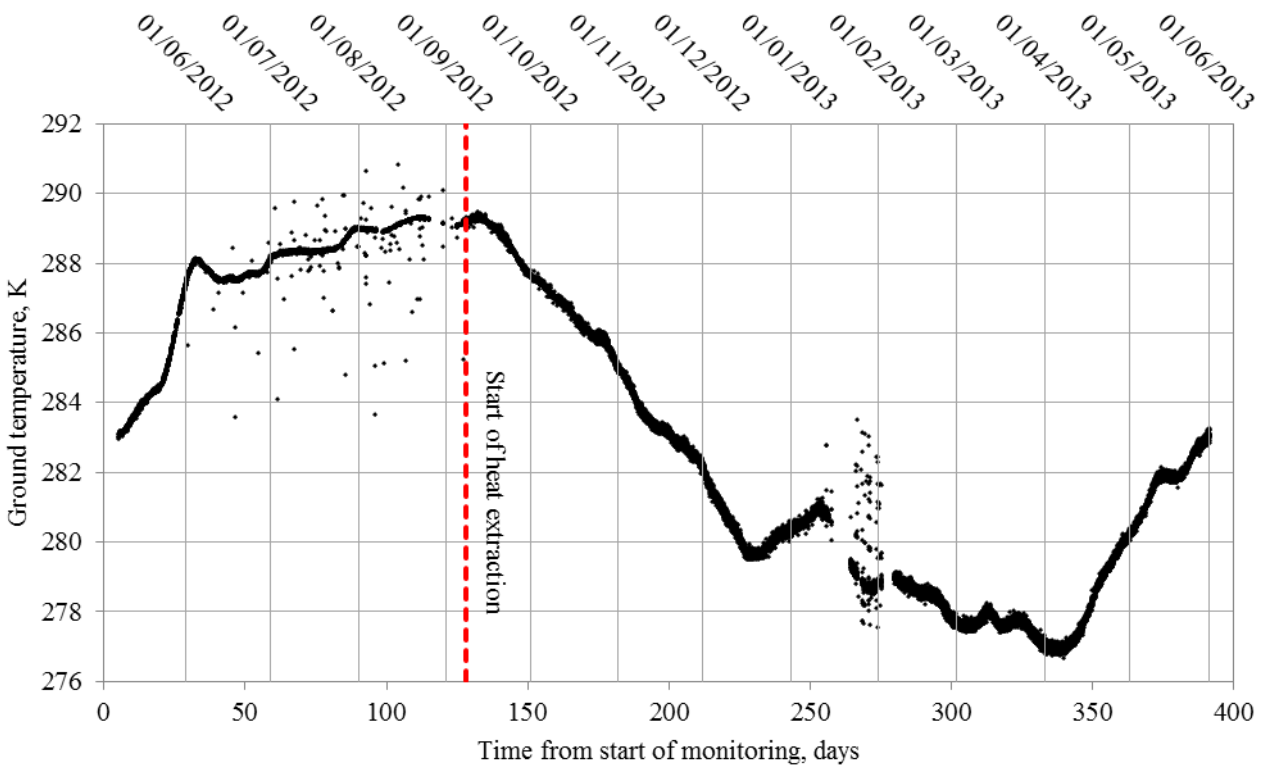

Figure D53 – Time evolution showing the monitored ground temperature data at sensor AB9.

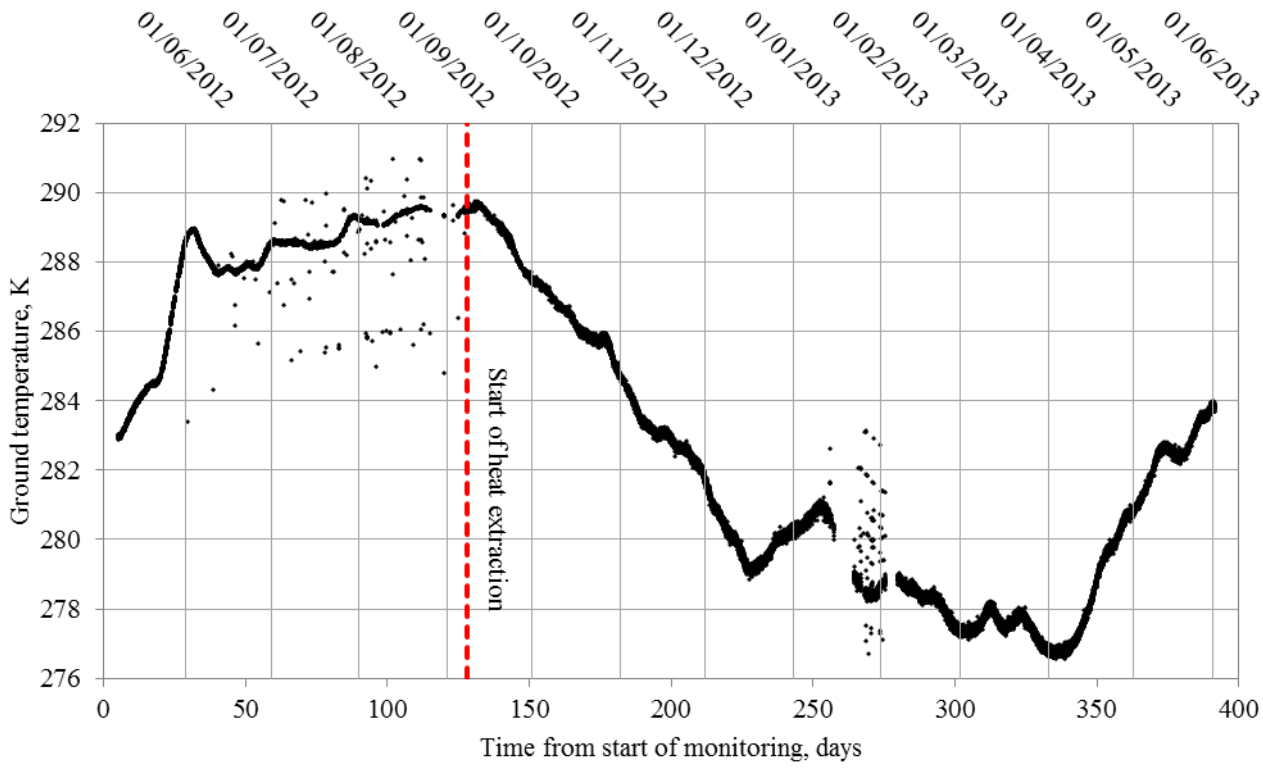

Figure D54 – Time evolution showing the monitored ground temperature data at sensor AB10.

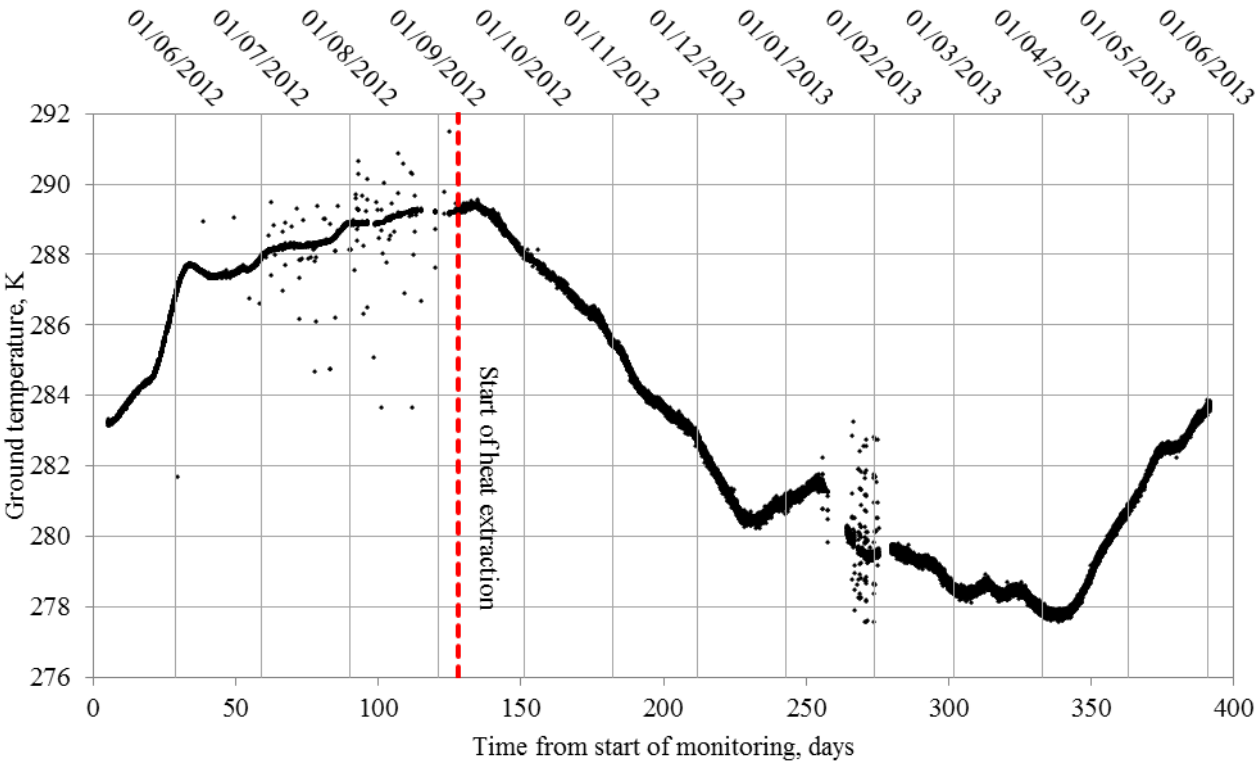

Figure D55 – Time evolution showing the monitored ground temperature data at sensor AB11.

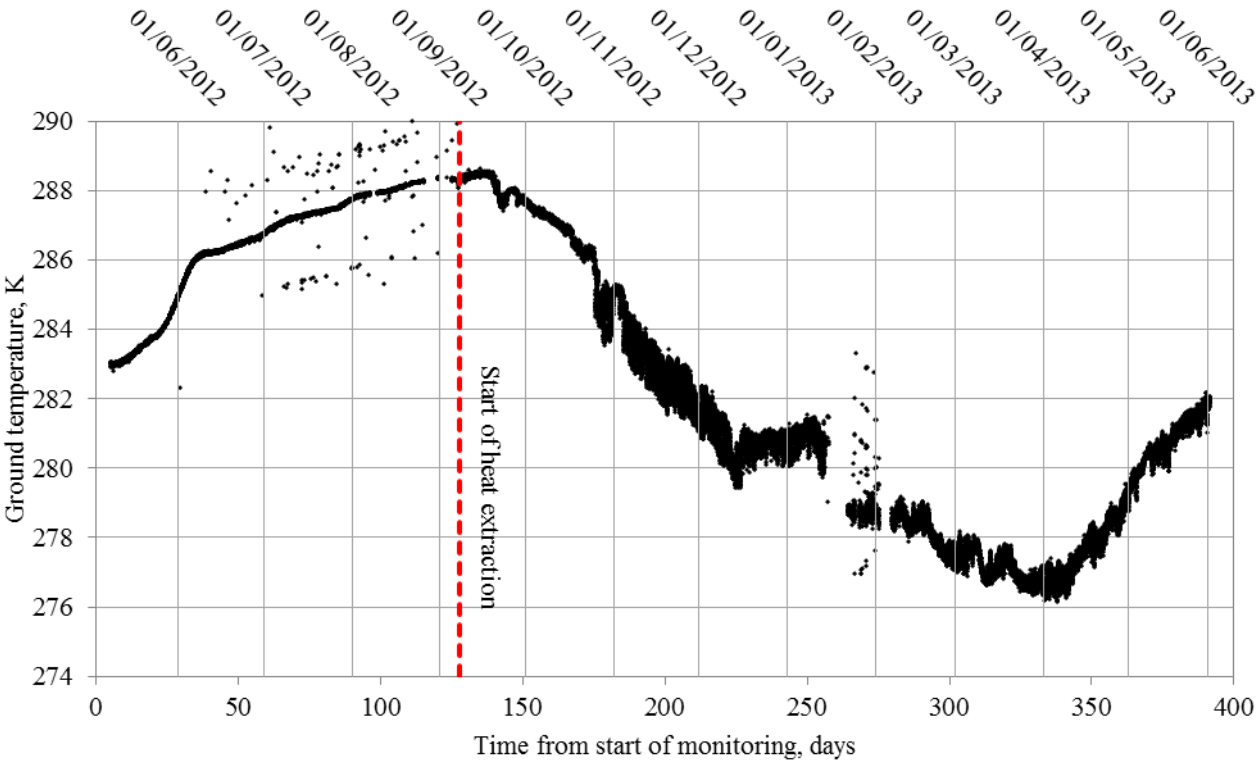

Figure D56 – Time evolution showing the monitored ground temperature data at sensor AB12.

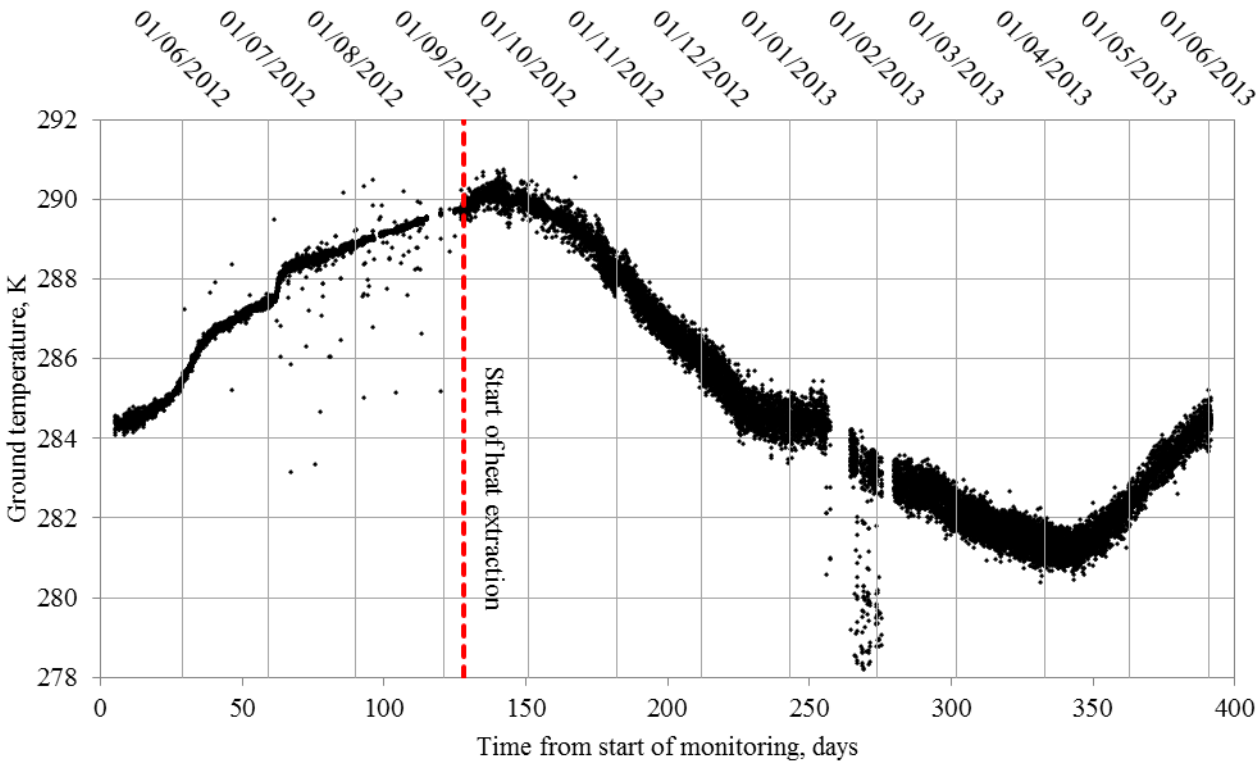

Figure D57 – Time evolution showing the monitored ground temperature data at sensor AB13.

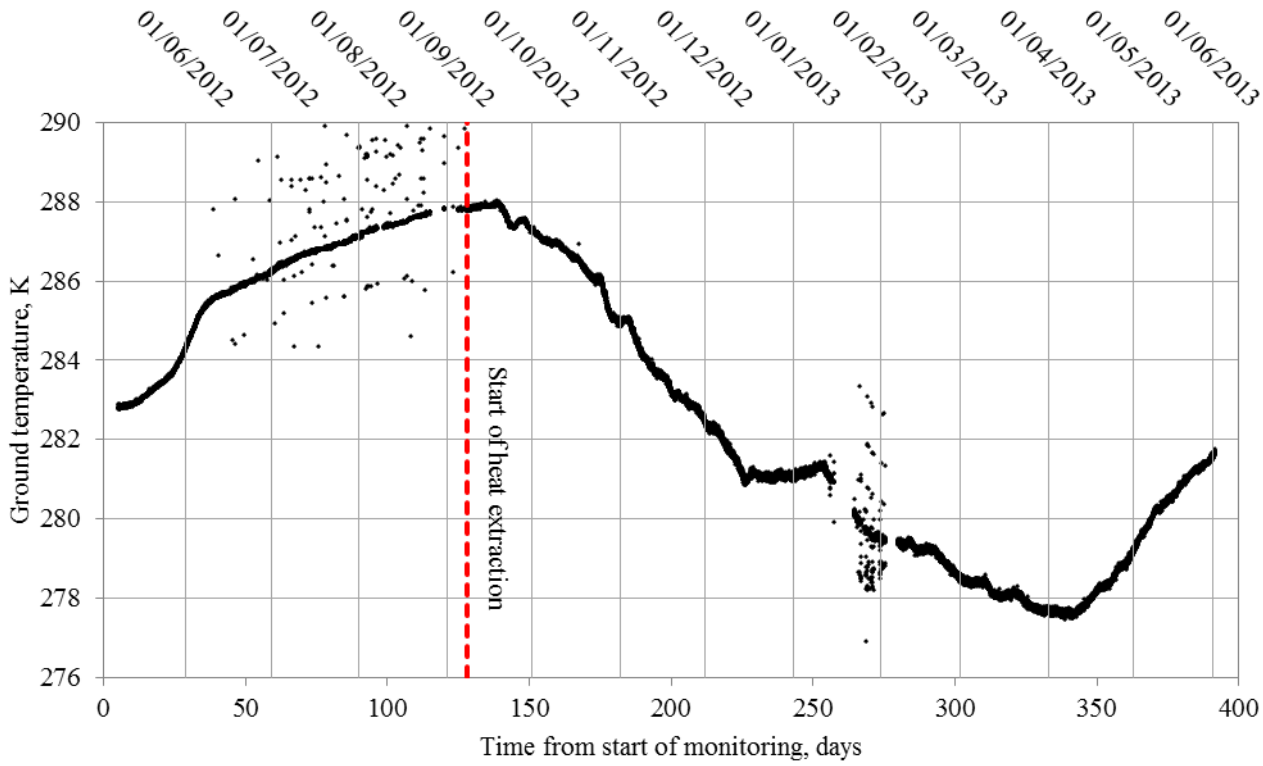

Figure D58 – Time evolution showing the monitored ground temperature data at sensor AB14.

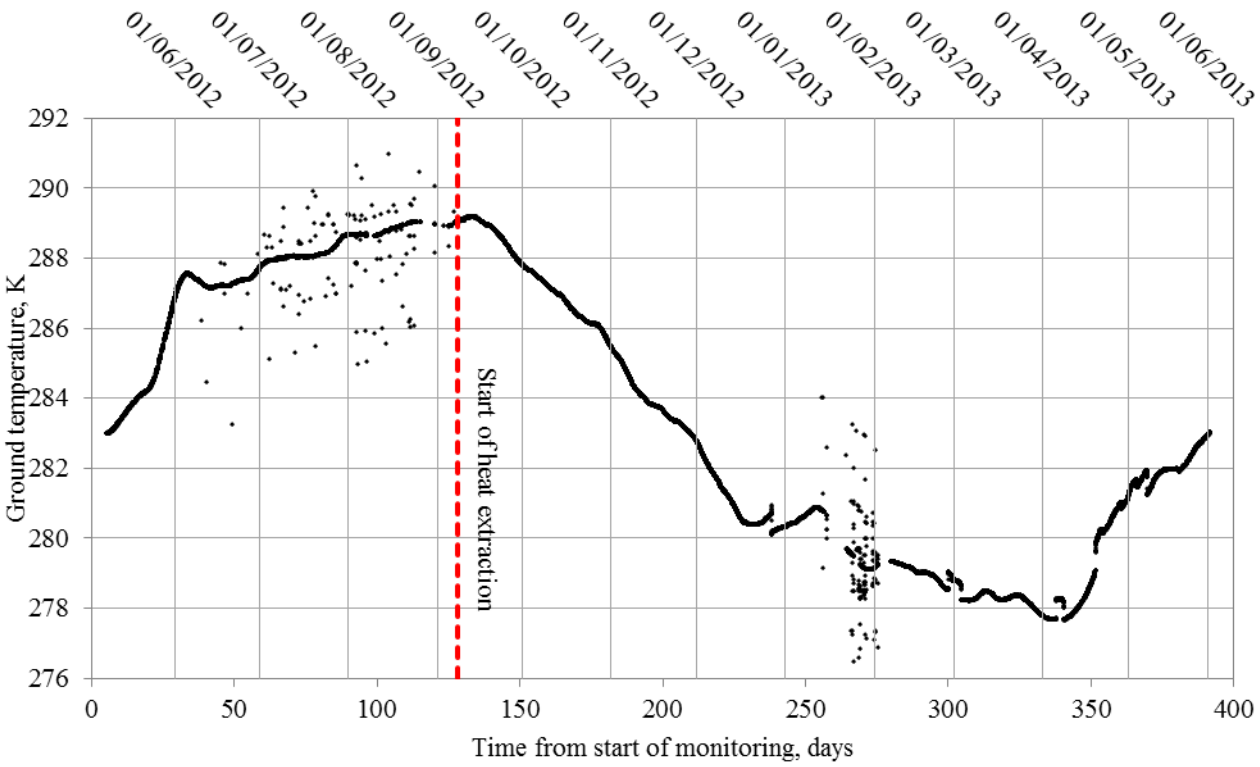

Figure D59 – Time evolution showing the monitored ground temperature data at sensor AC2.

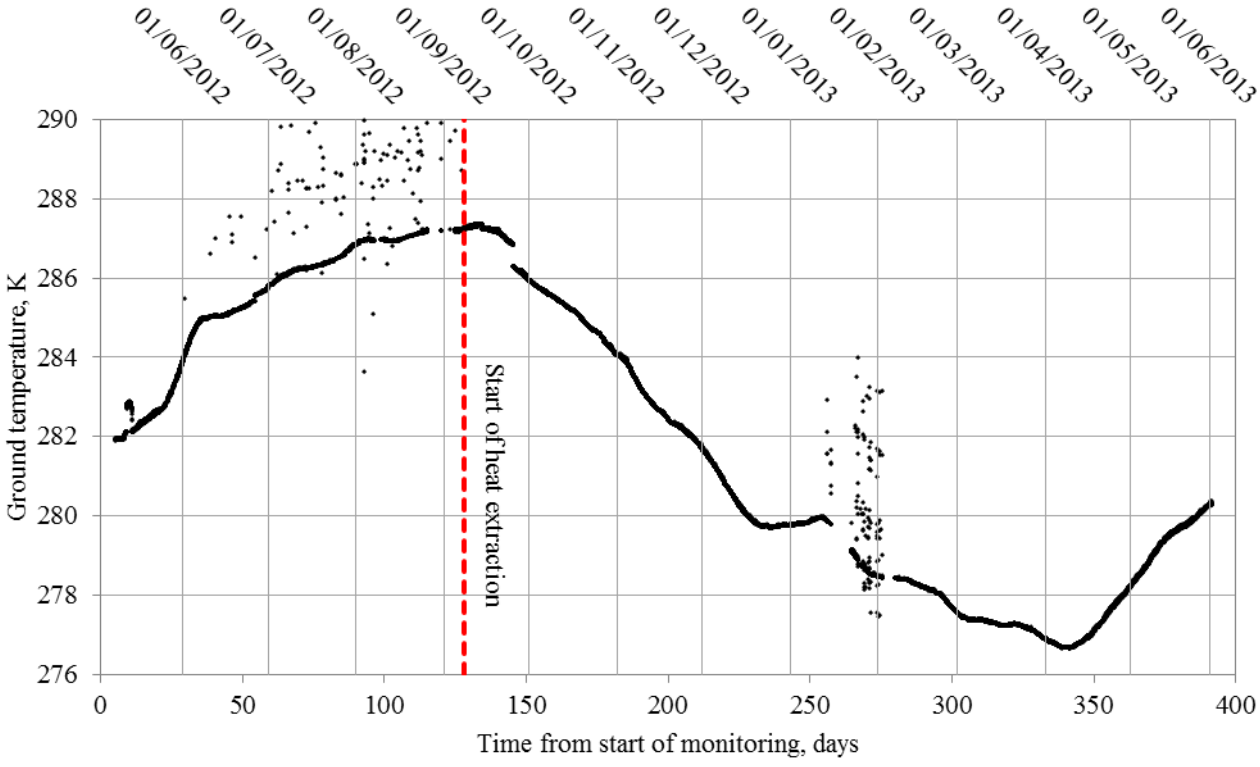

Figure D60 – Time evolution showing the monitored ground temperature data at sensor AC3.

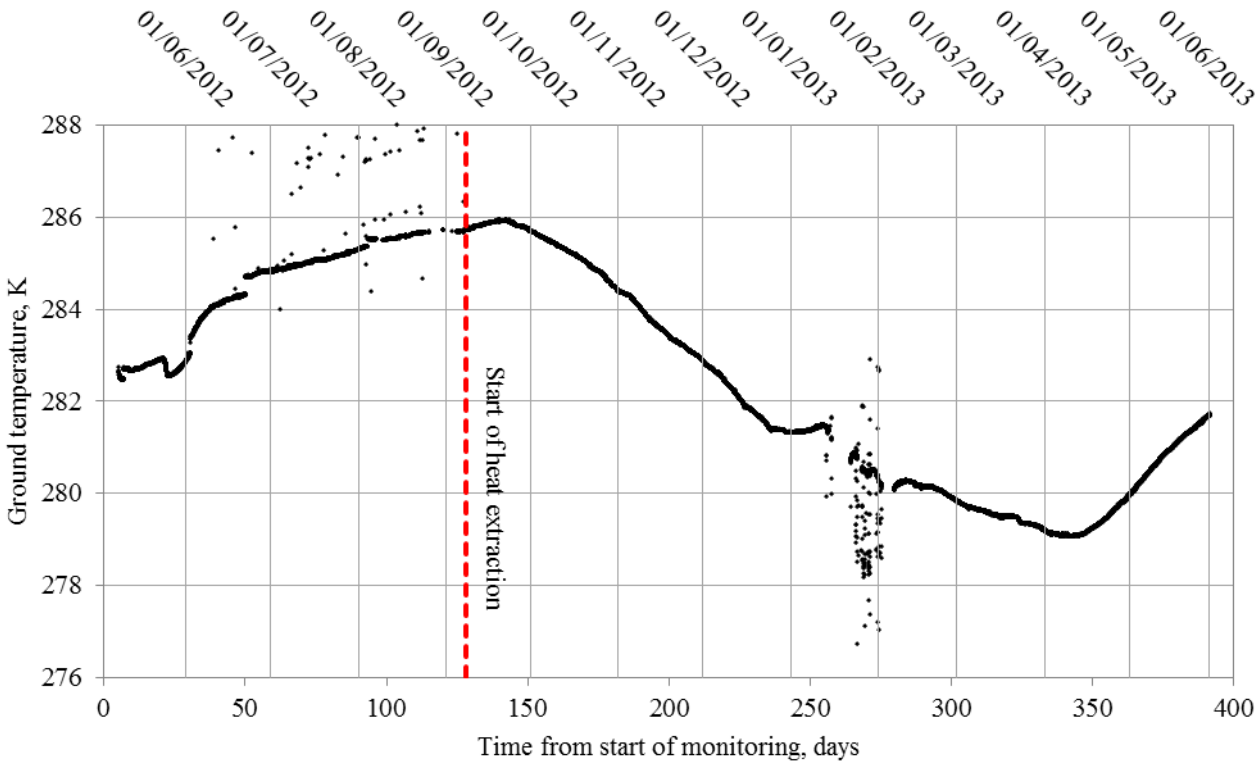

Figure D61 – Time evolution showing the monitored ground temperature data at sensor AC4.

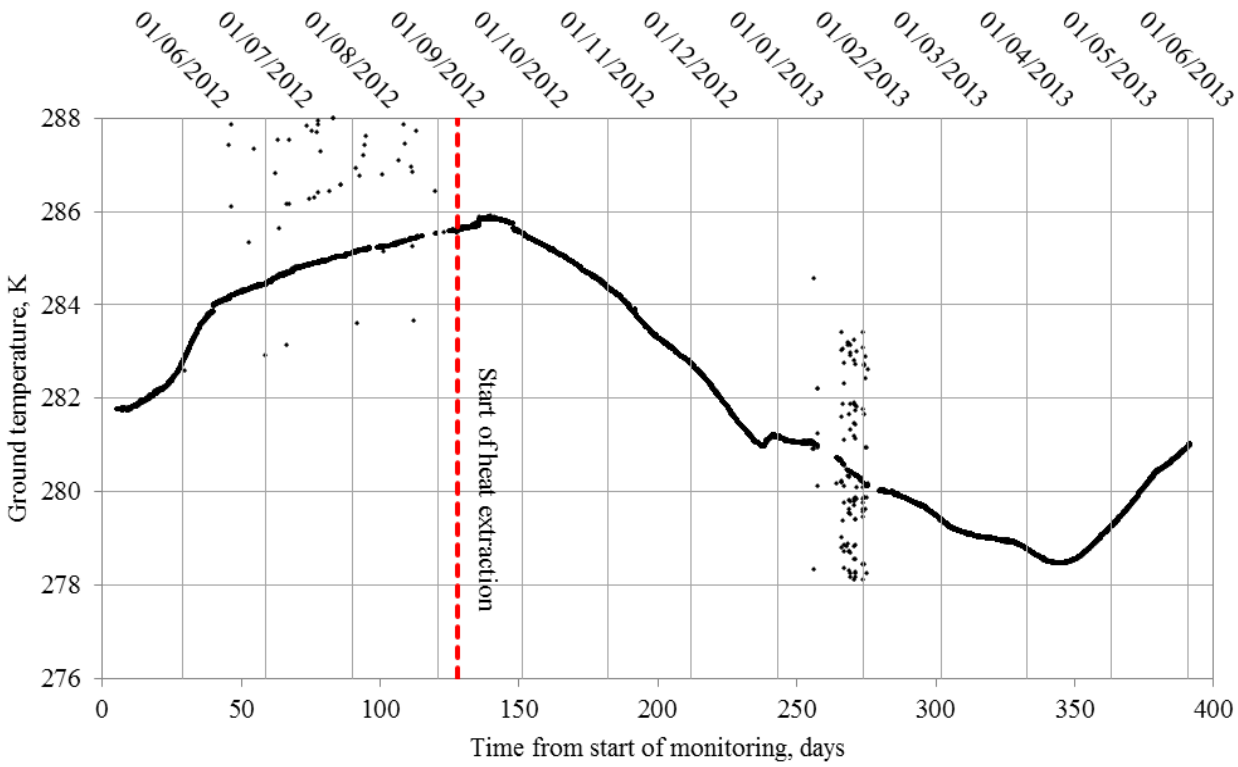

Figure D62 – Time evolution showing the monitored ground temperature data at sensor AC5.

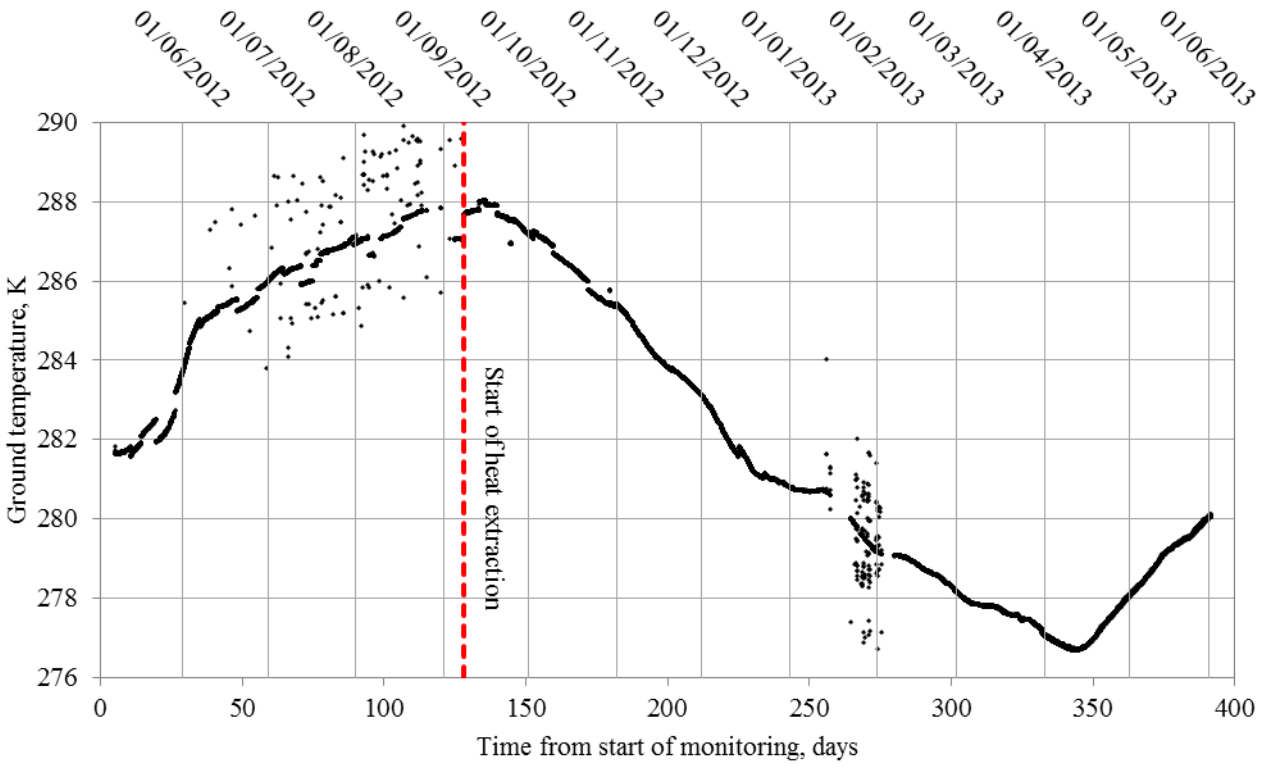

Figure D63 – Time evolution showing the monitored ground temperature data at sensor AC6.

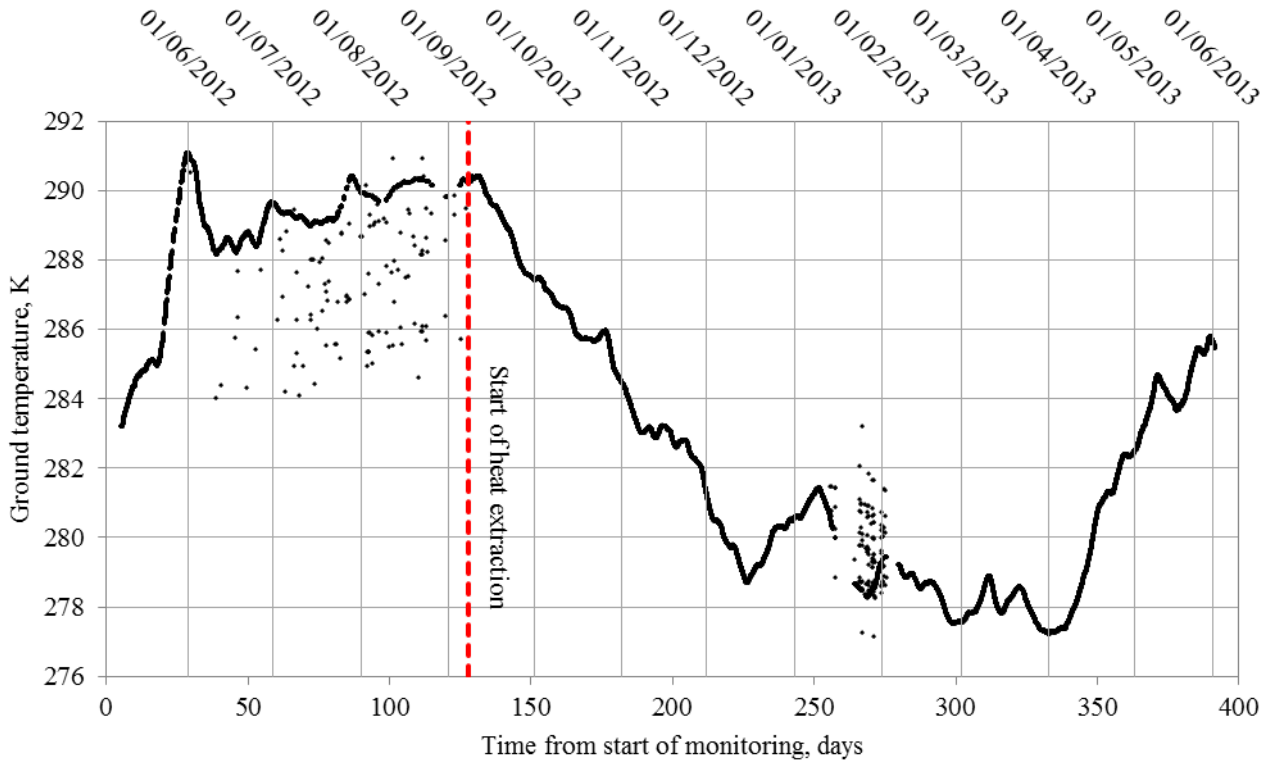

Figure D64 – Time evolution showing the monitored ground temperature data at sensor AC8.

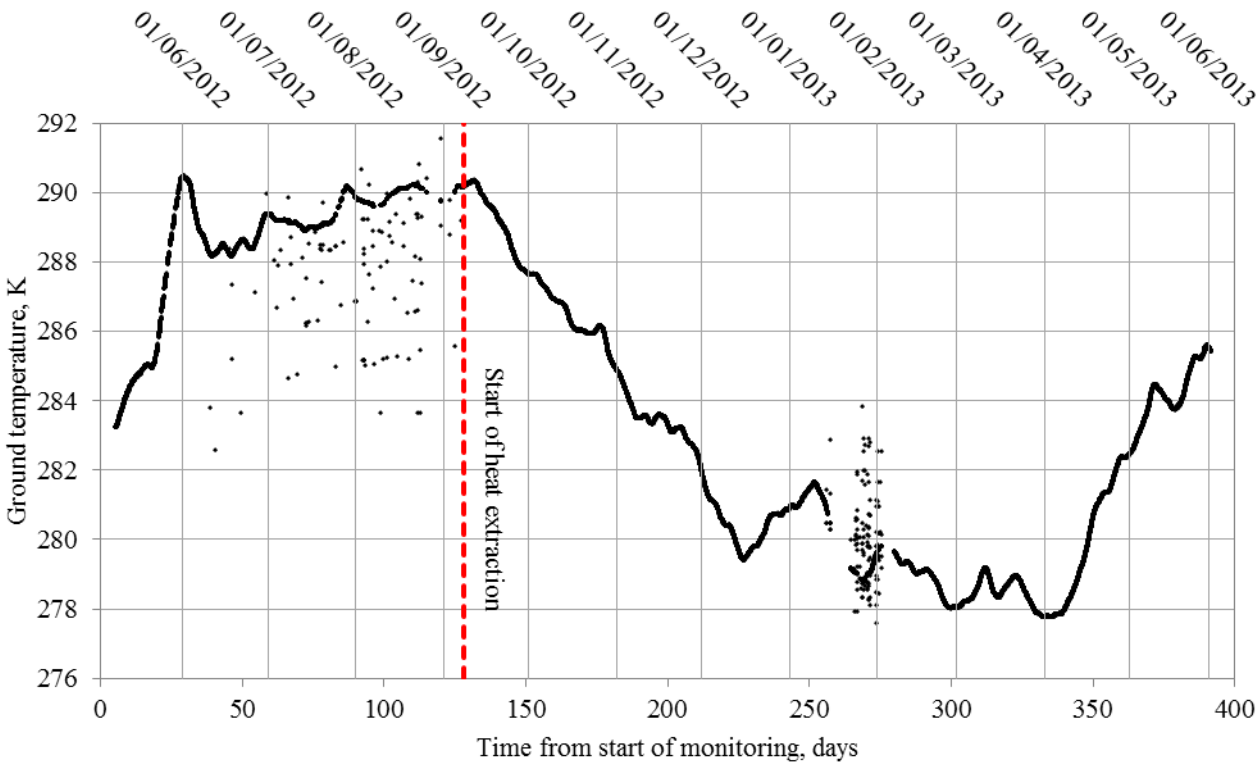

Figure D65 – Time evolution showing the monitored ground temperature data at sensor AC9.

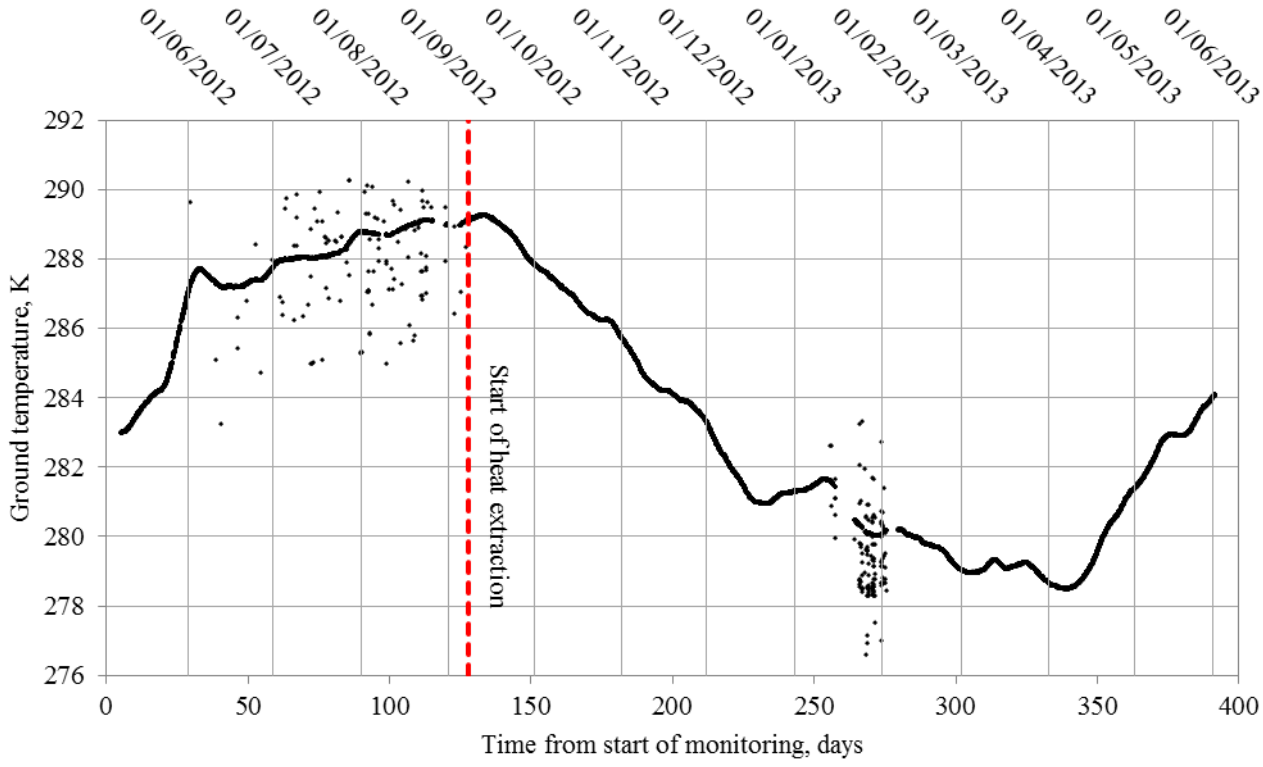

Figure D66 – Time evolution showing the monitored ground temperature data at sensor AC10.

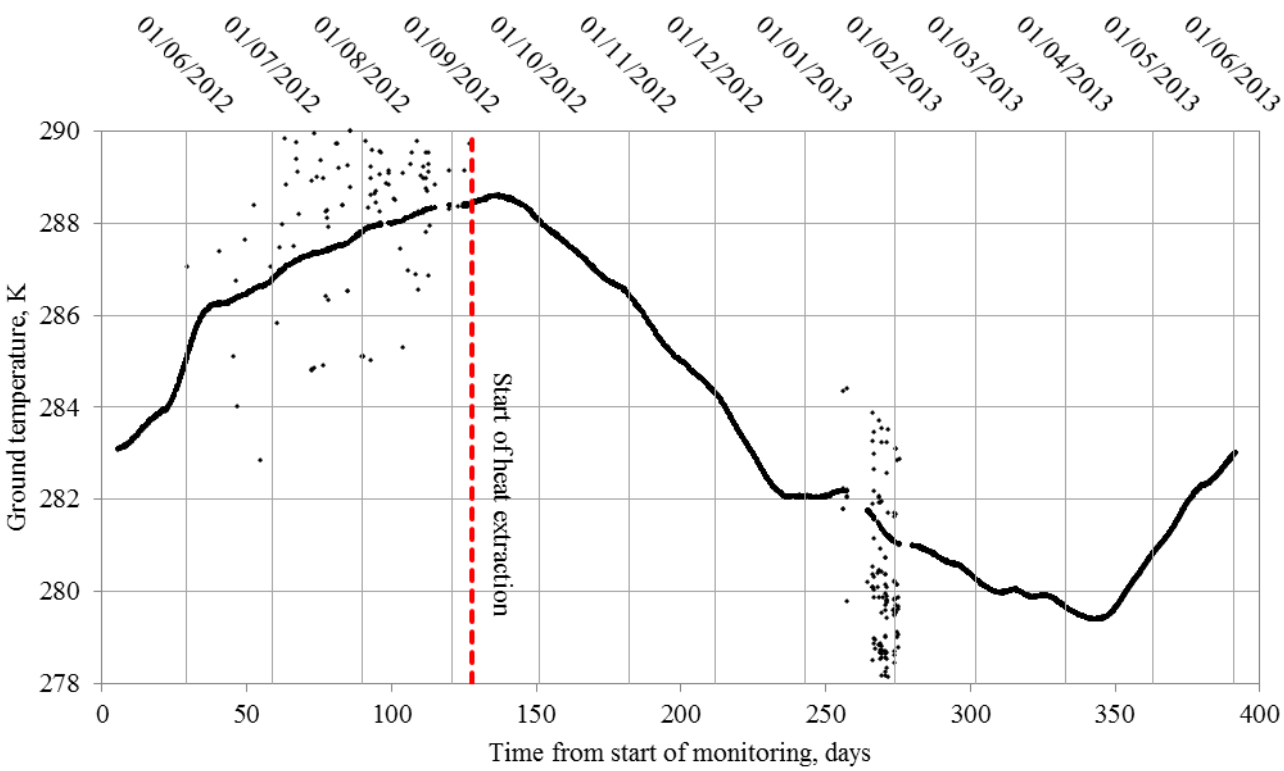

Figure D67 – Time evolution showing the monitored ground temperature data at sensor AC11.

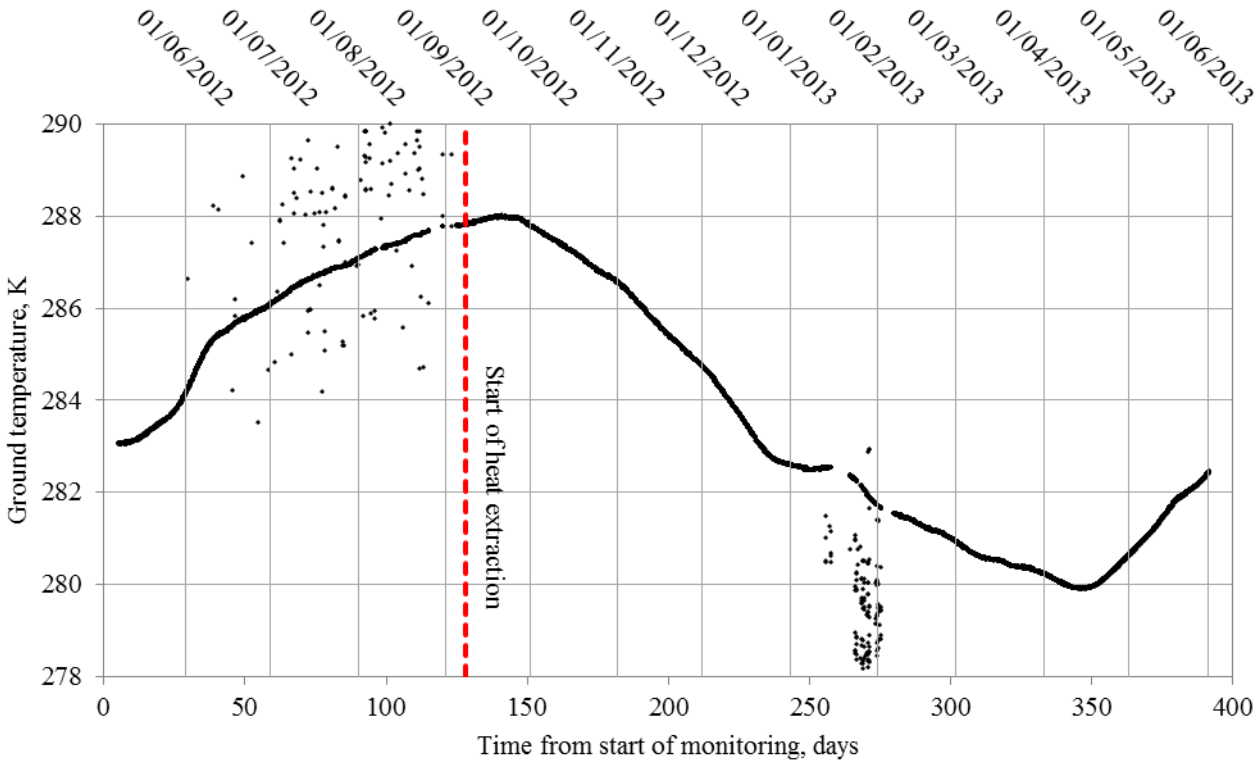

Figure D68 – Time evolution showing the monitored ground temperature data at sensor AC12.

- The ground temperature data obtained from detailed cross-section BB has been denoted according to the thermistor notation provided in Figure D69.
- Figure D69 shows the spatial position of the thermistors, as recorded during a topographical survey of the site, along with the thermistor notation used.
- The letters 'BA', 'BB' and 'BC' correspond to the thermistor string which the respective thermistors are part of (see Chapter 3 for more details)

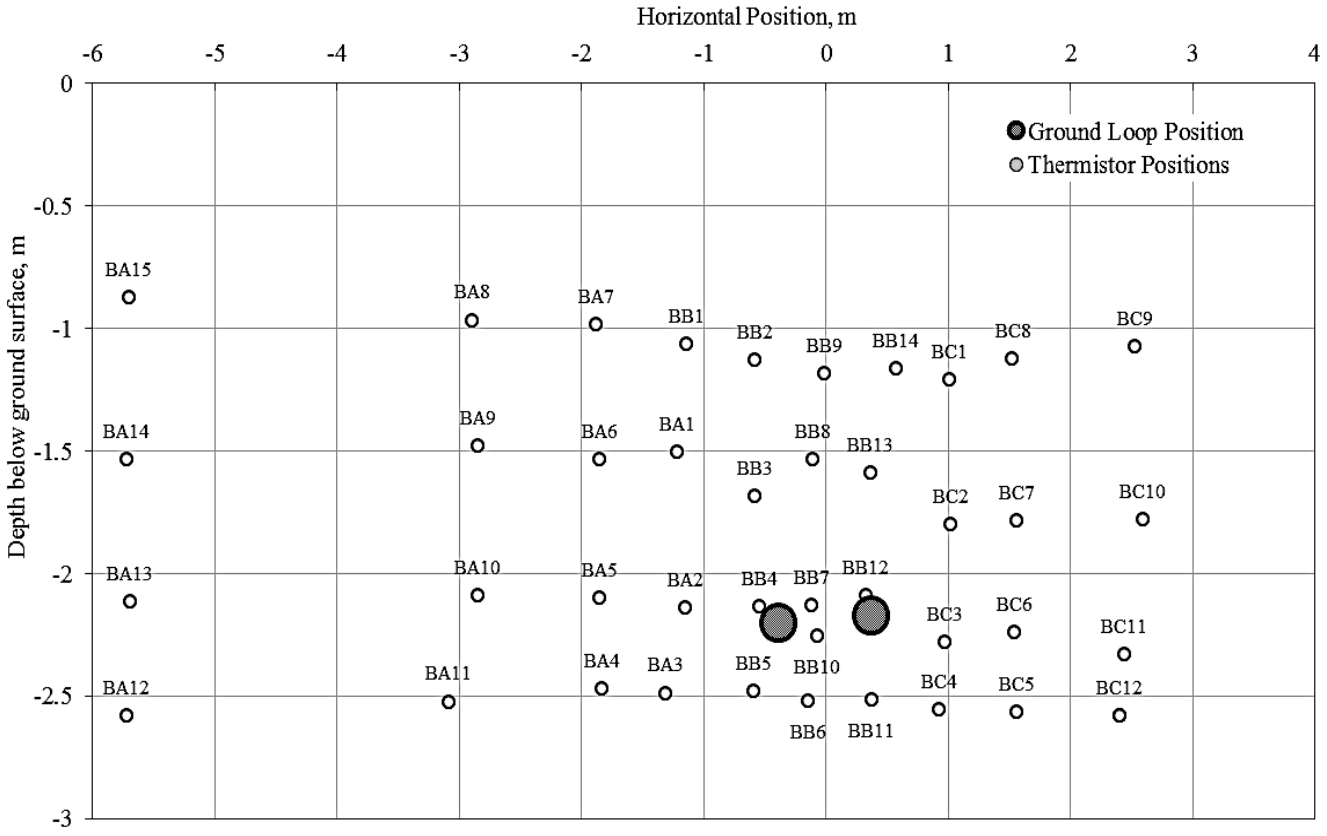

Figure D69 – Spatial position and adopted notation of the thermistors located in detailed cross-section BB.

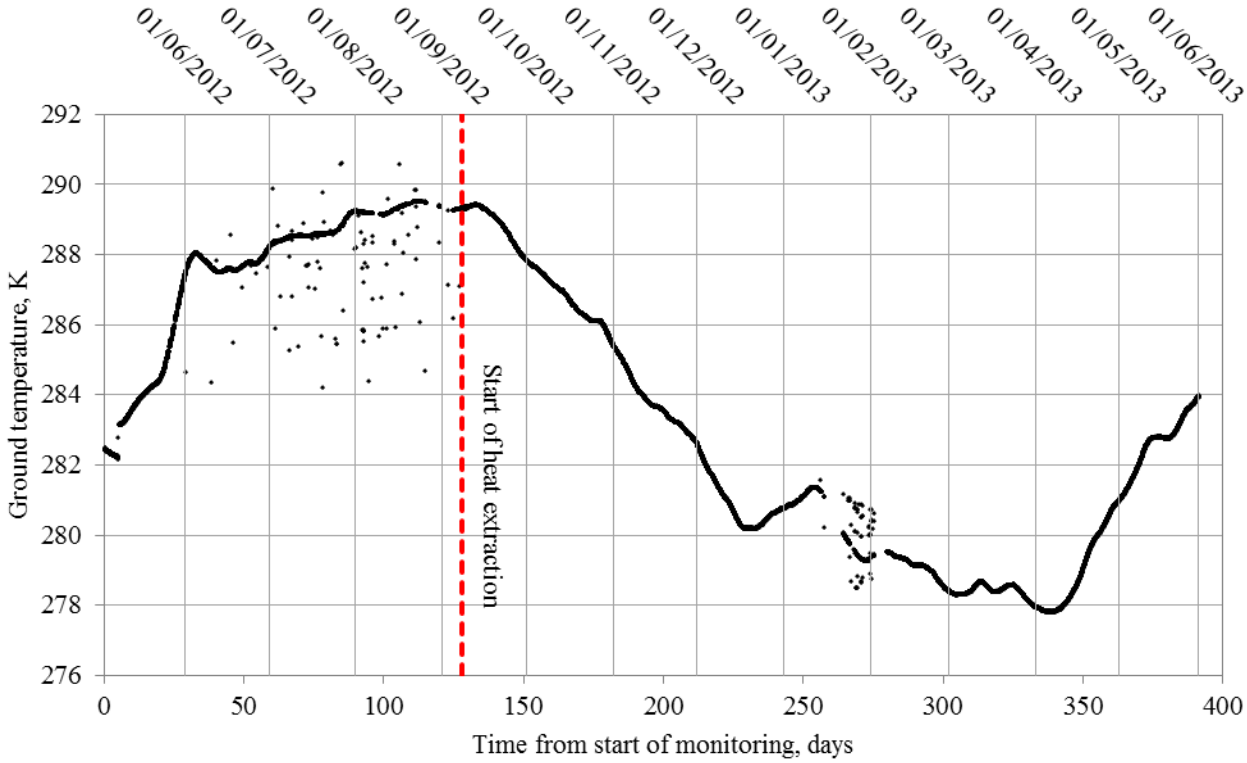

Figure D70 – Time evolution showing the monitored ground temperature data at sensor BA1

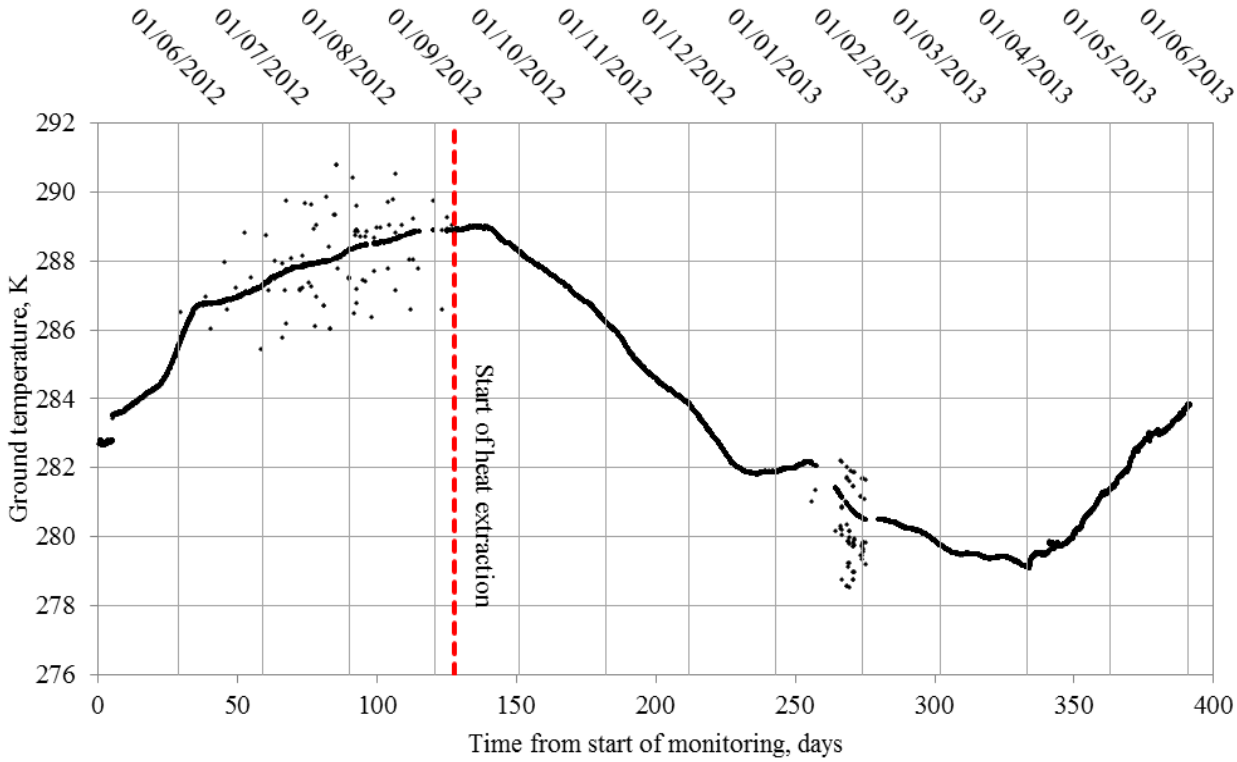

Figure D71 – Time evolution showing the monitored ground temperature data at sensor BA2

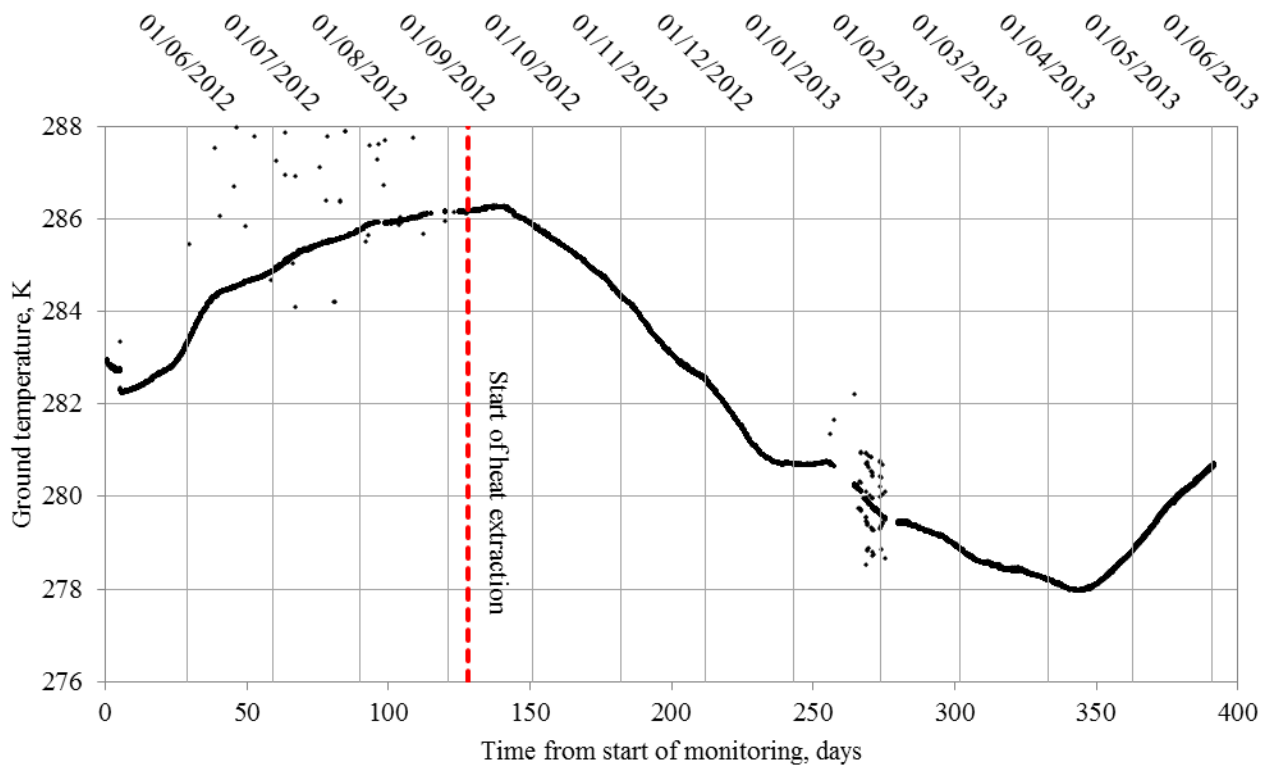

Figure D72 – Time evolution showing the monitored ground temperature data at sensor BA3

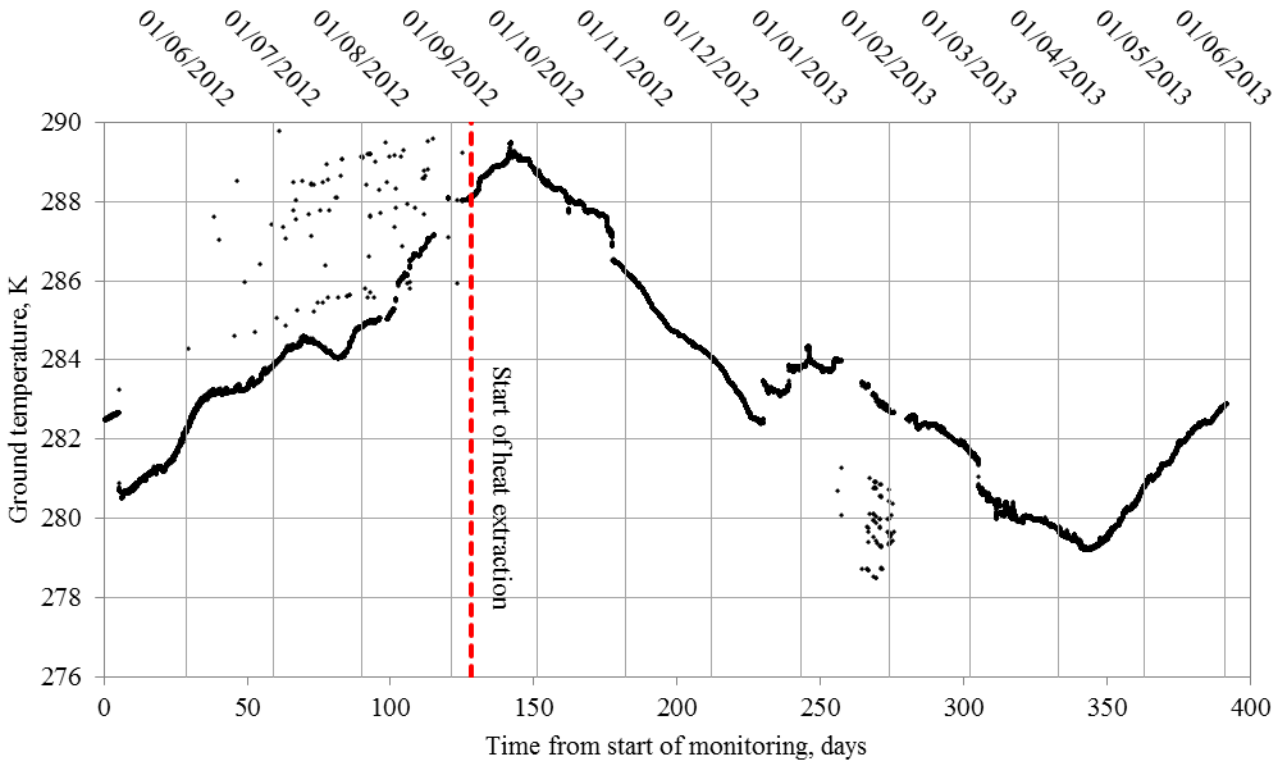

Figure D73 – Time evolution showing the monitored ground temperature data at sensor BA5

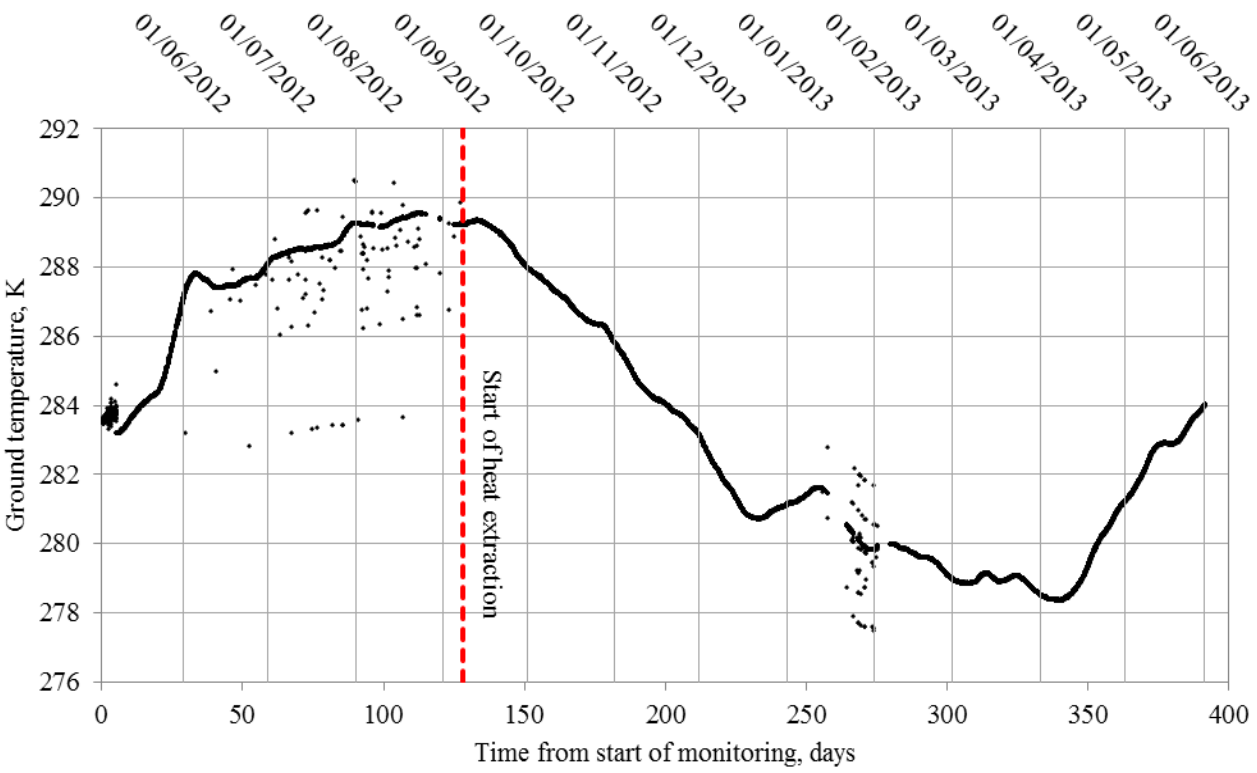

Figure D74 – Time evolution showing the monitored ground temperature data at sensor BA6

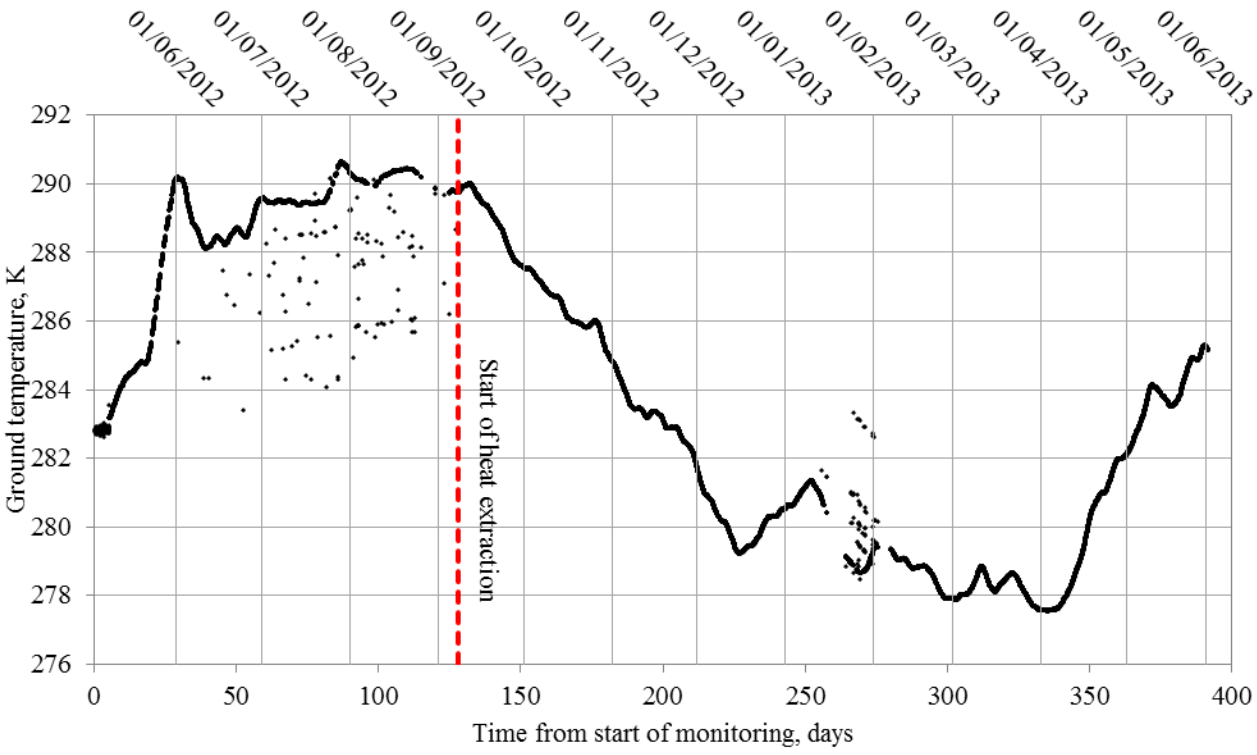

Figure D75 – Time evolution showing the monitored ground temperature data at sensor BA7

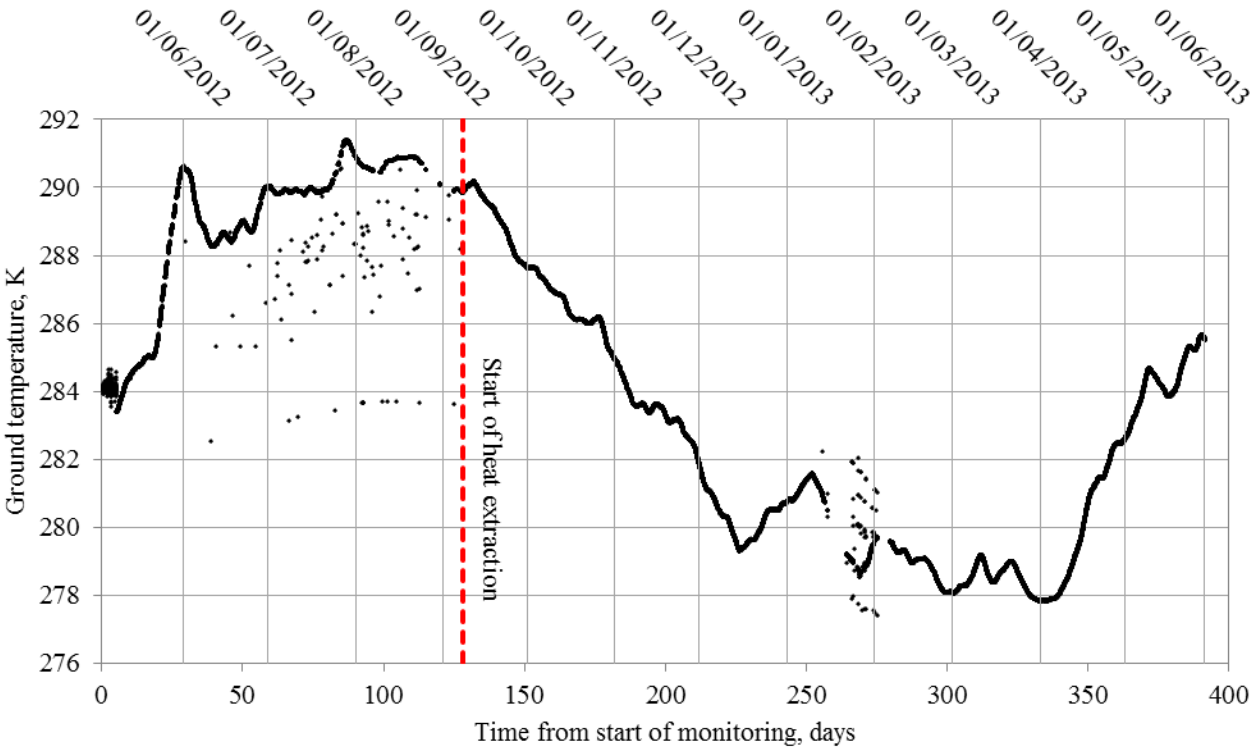

Figure D76 – Time evolution showing the monitored ground temperature data at sensor BA8

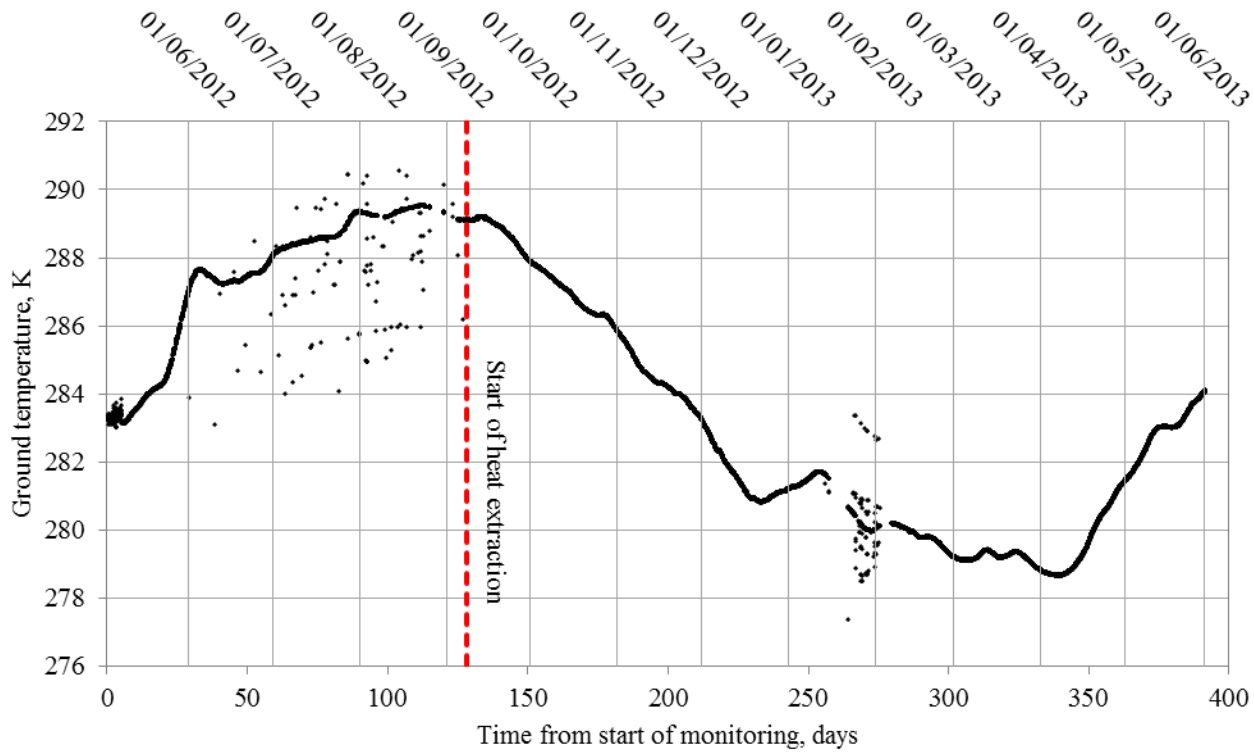

Figure D77 – Time evolution showing the monitored ground temperature data at sensor BA9

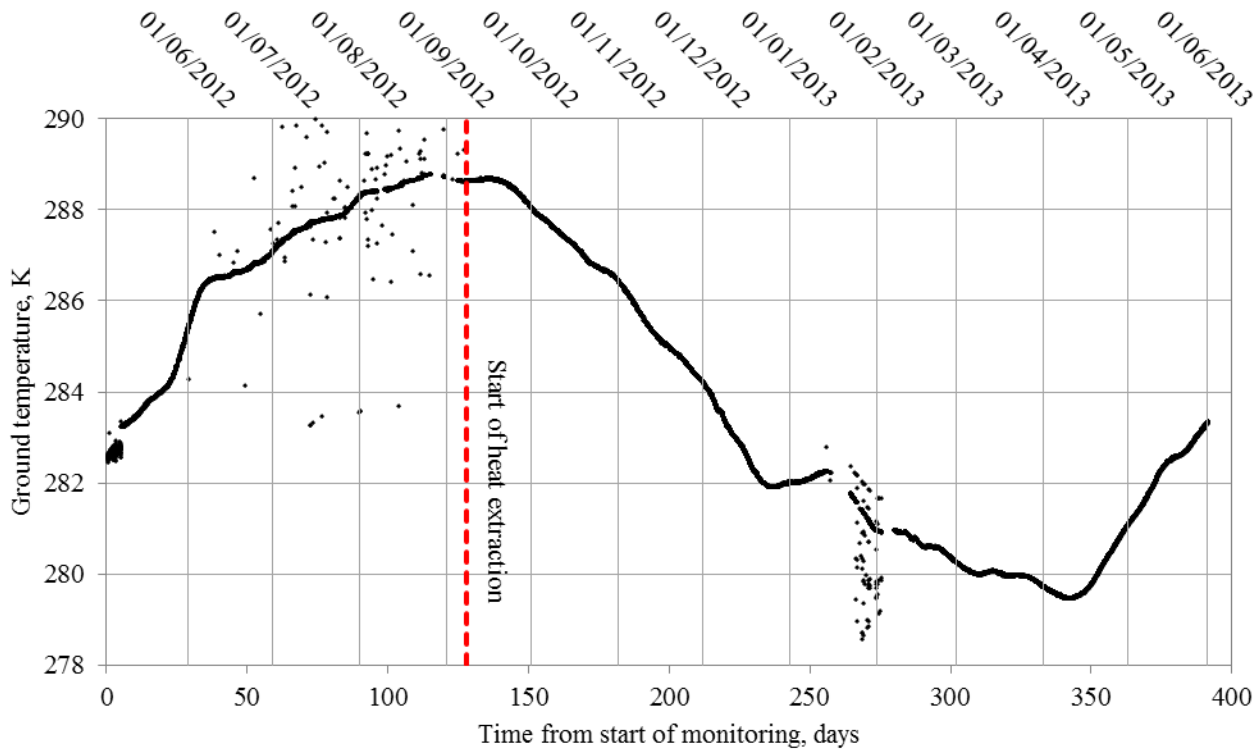

Figure D78 – Time evolution showing the monitored ground temperature data at sensor BA10

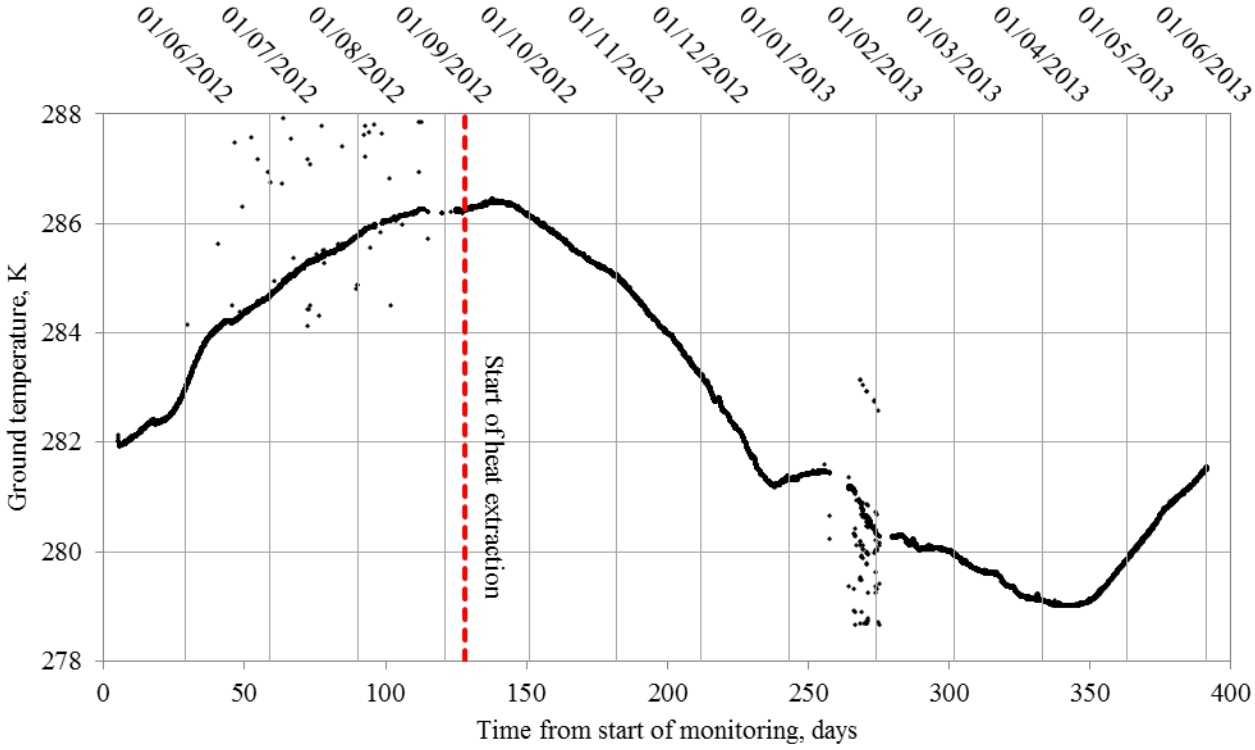

Figure D79 – Time evolution showing the monitored ground temperature data at sensor BA11

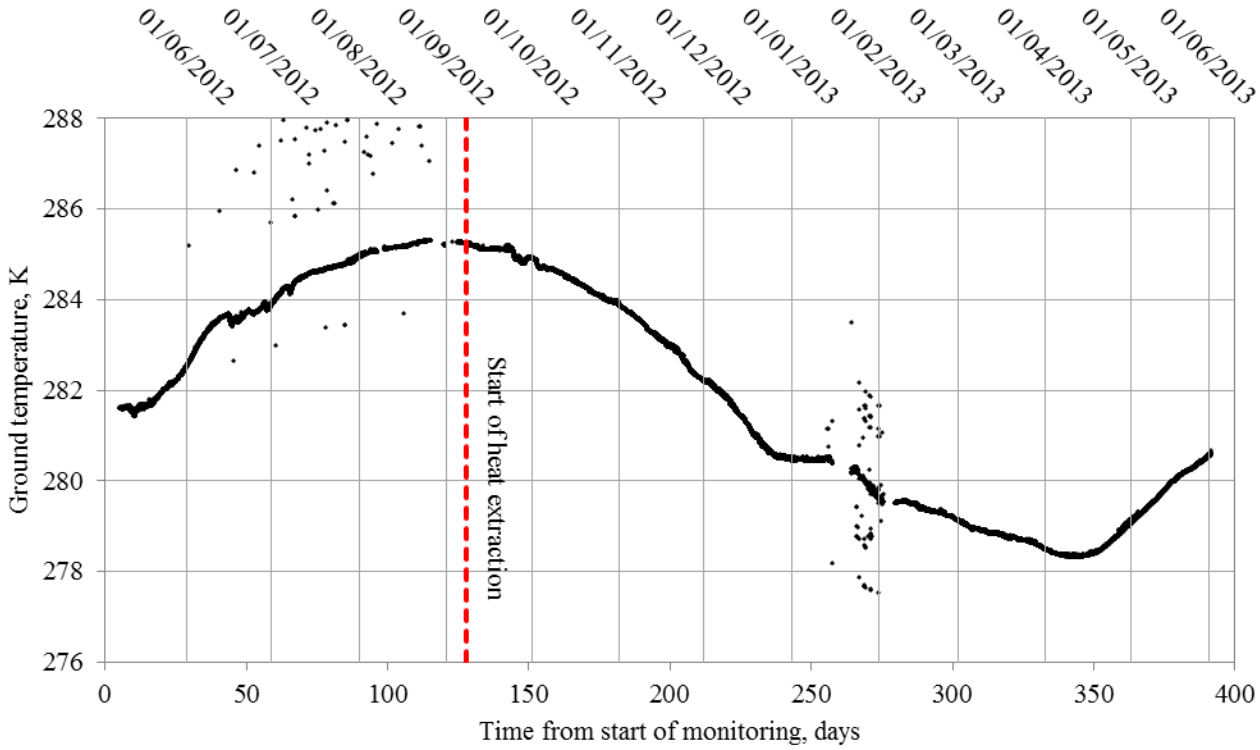

Figure D80 – Time evolution showing the monitored ground temperature data at sensor BA12

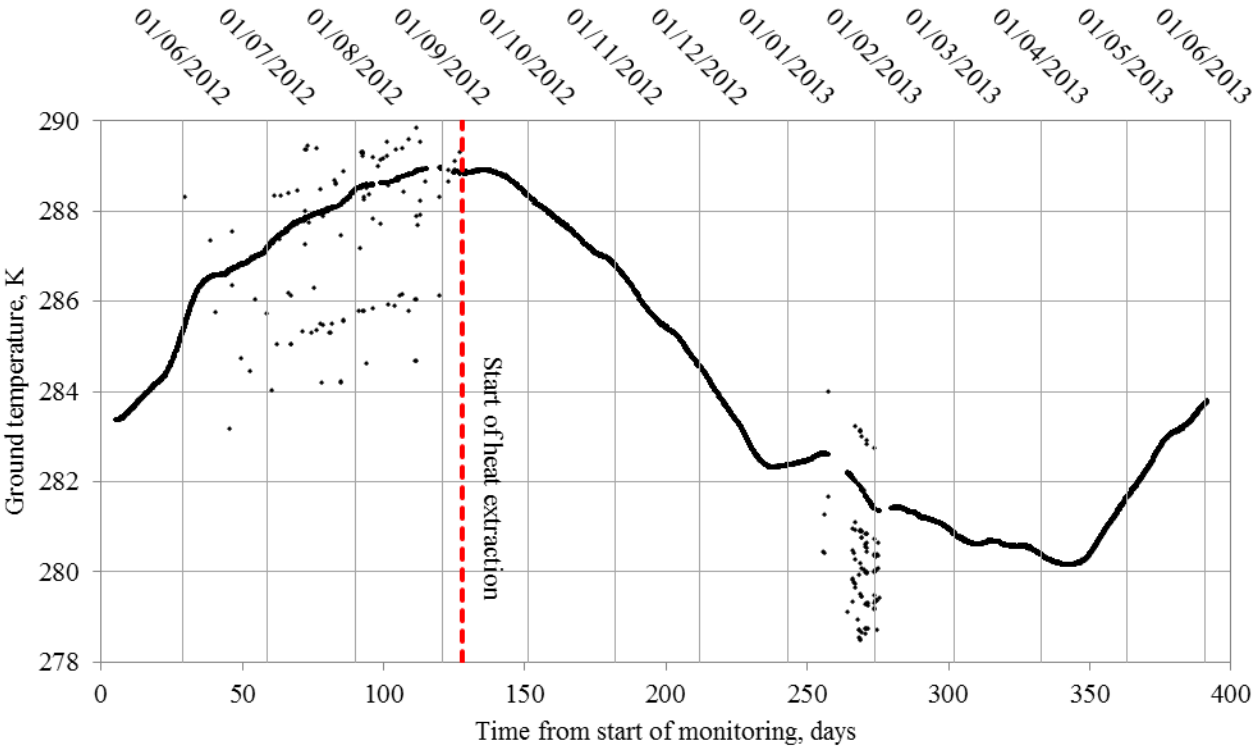

Figure D81 – Time evolution showing the monitored ground temperature data at sensor BA13

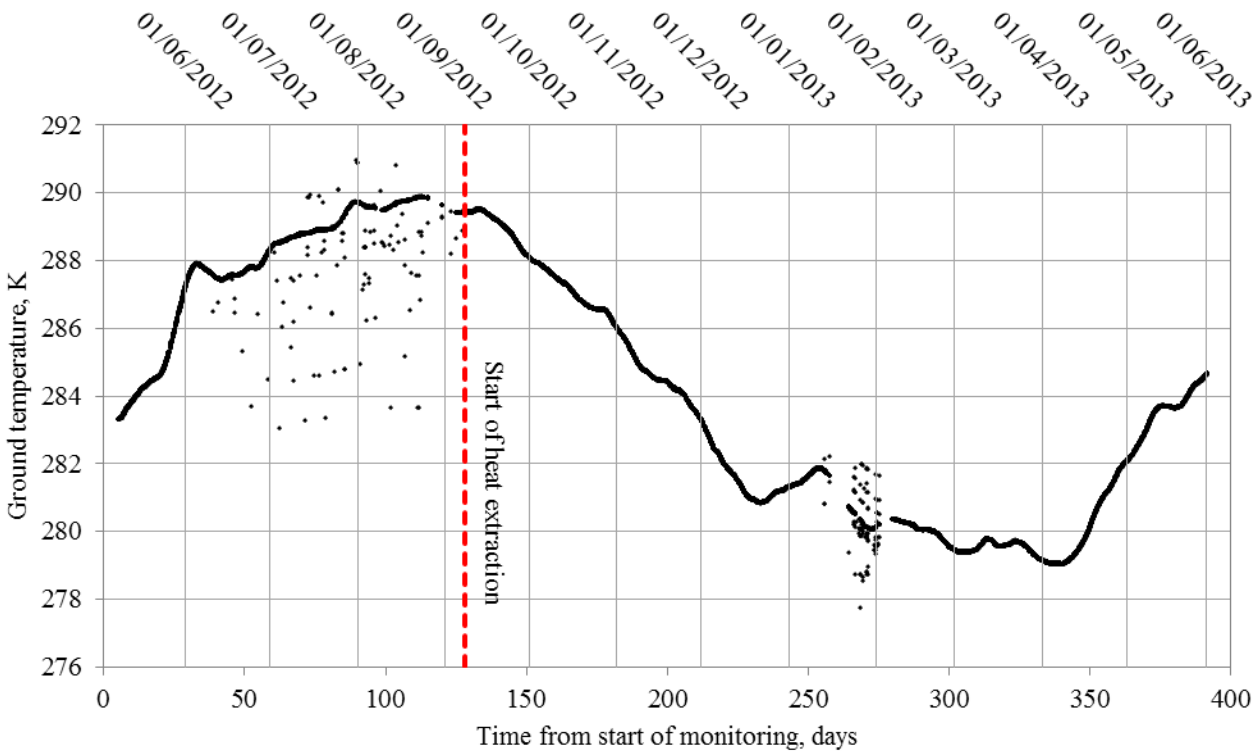

Figure D82 – Time evolution showing the monitored ground temperature data at sensor BA14

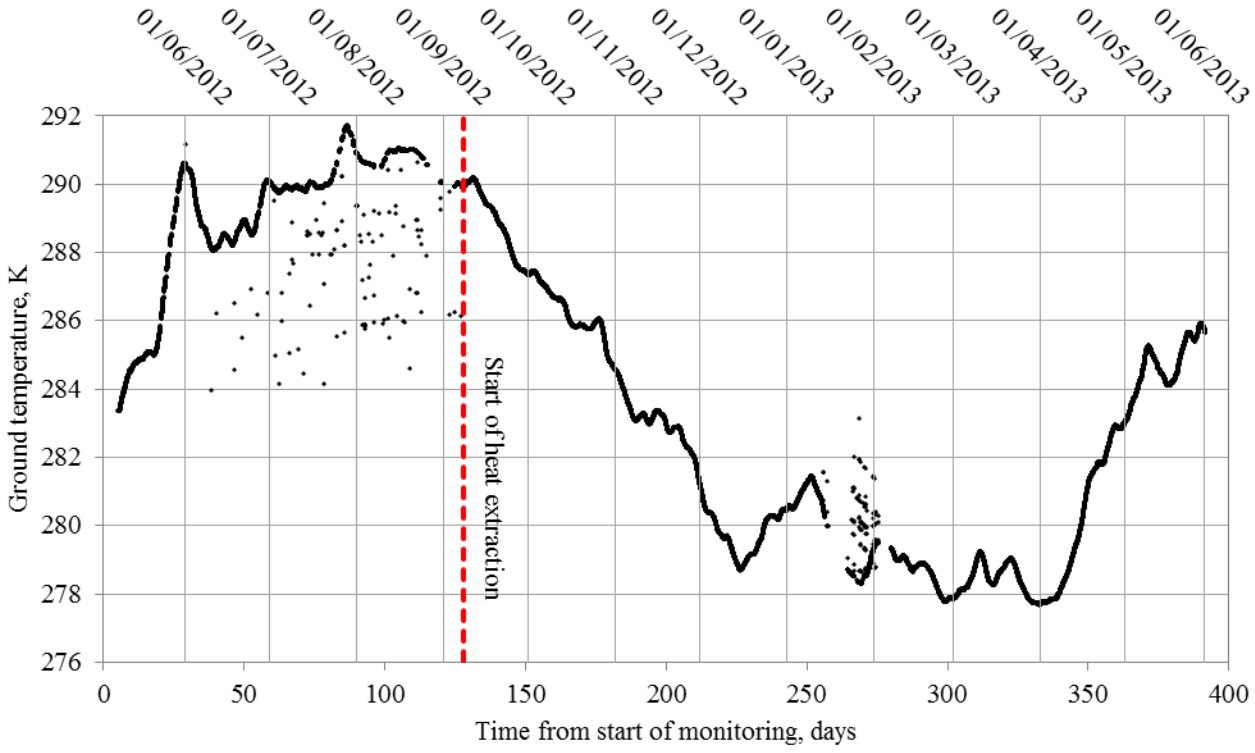

Figure D83 – Time evolution showing the monitored ground temperature data at sensor BA15

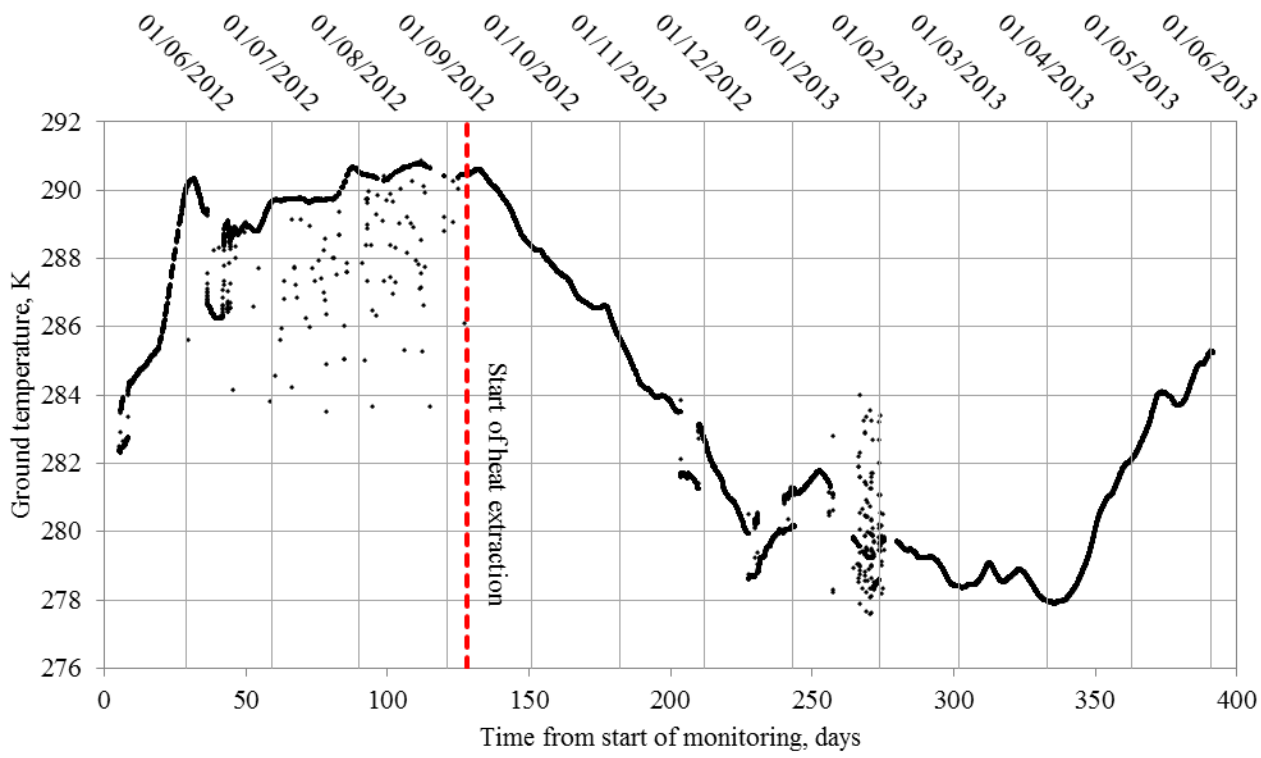

Figure D84 – Time evolution showing the monitored ground temperature data at sensor BB1

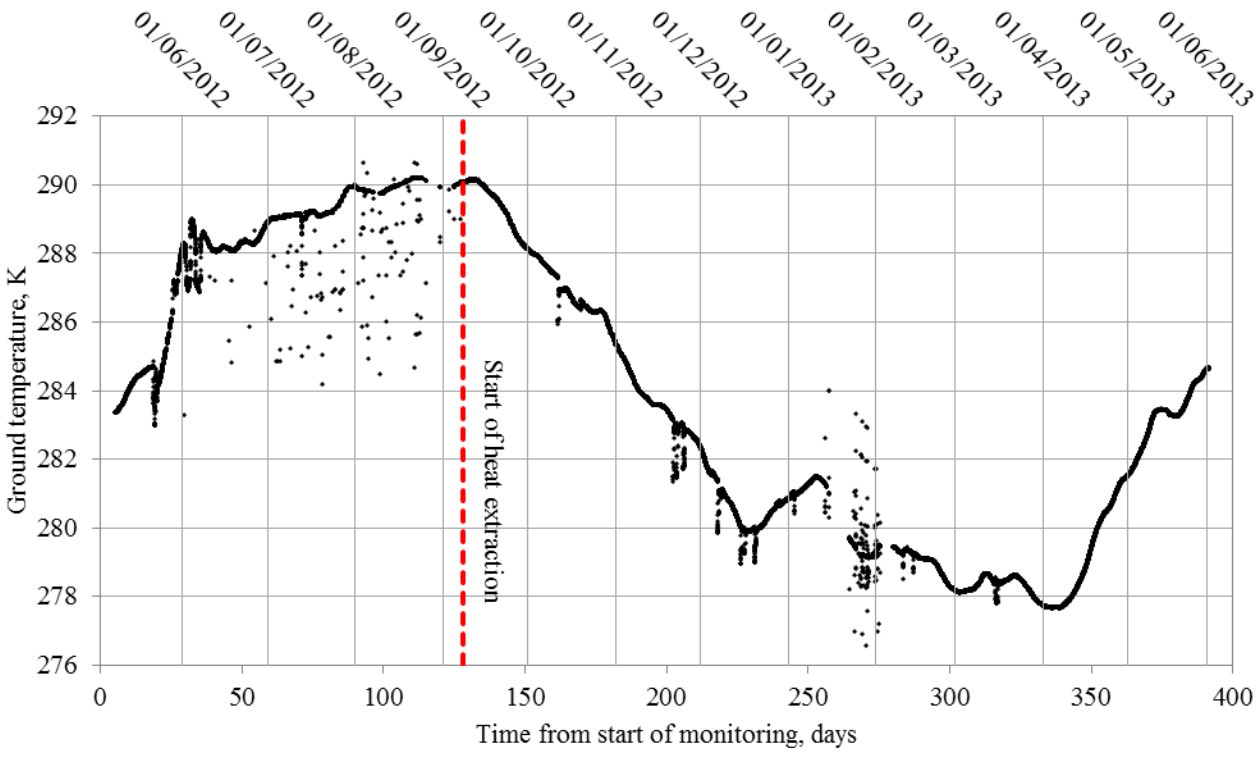

Figure D85 – Time evolution showing the monitored ground temperature data at sensor BB2

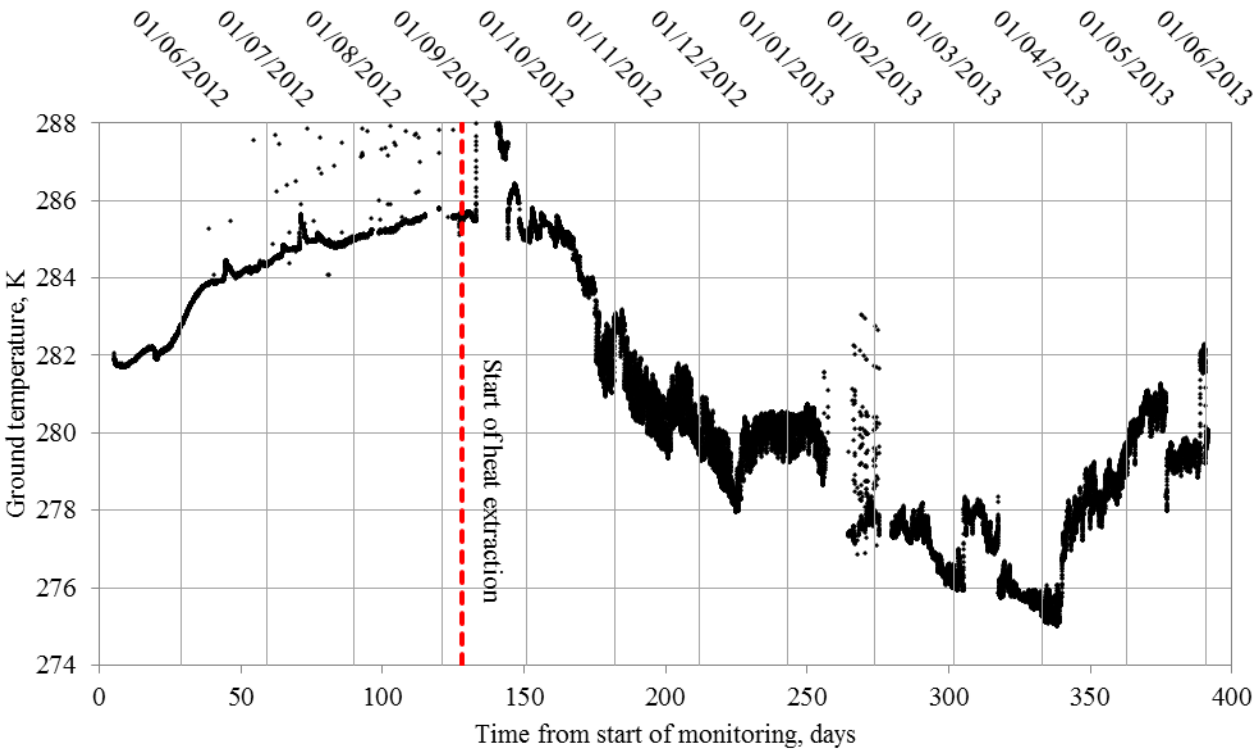

Figure D86 – Time evolution showing the monitored ground temperature data at sensor BB4

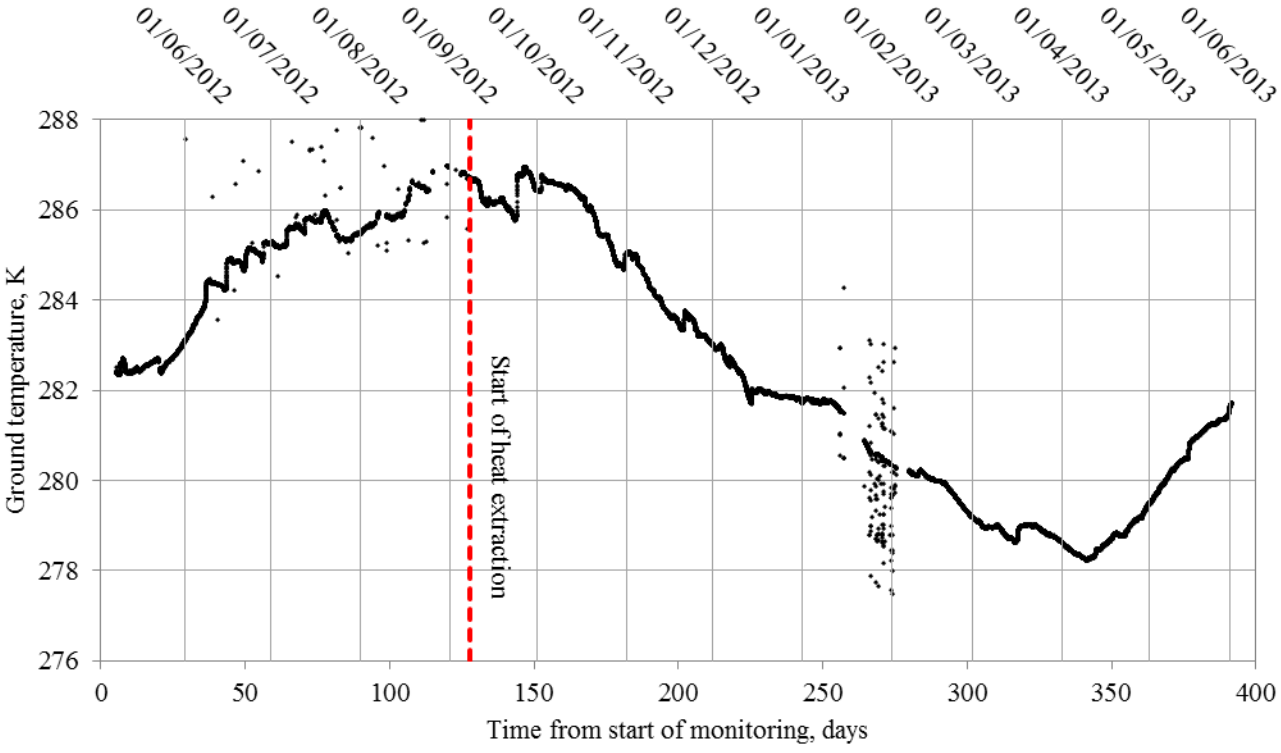

Figure D87 – Time evolution showing the monitored ground temperature data at sensor BB5

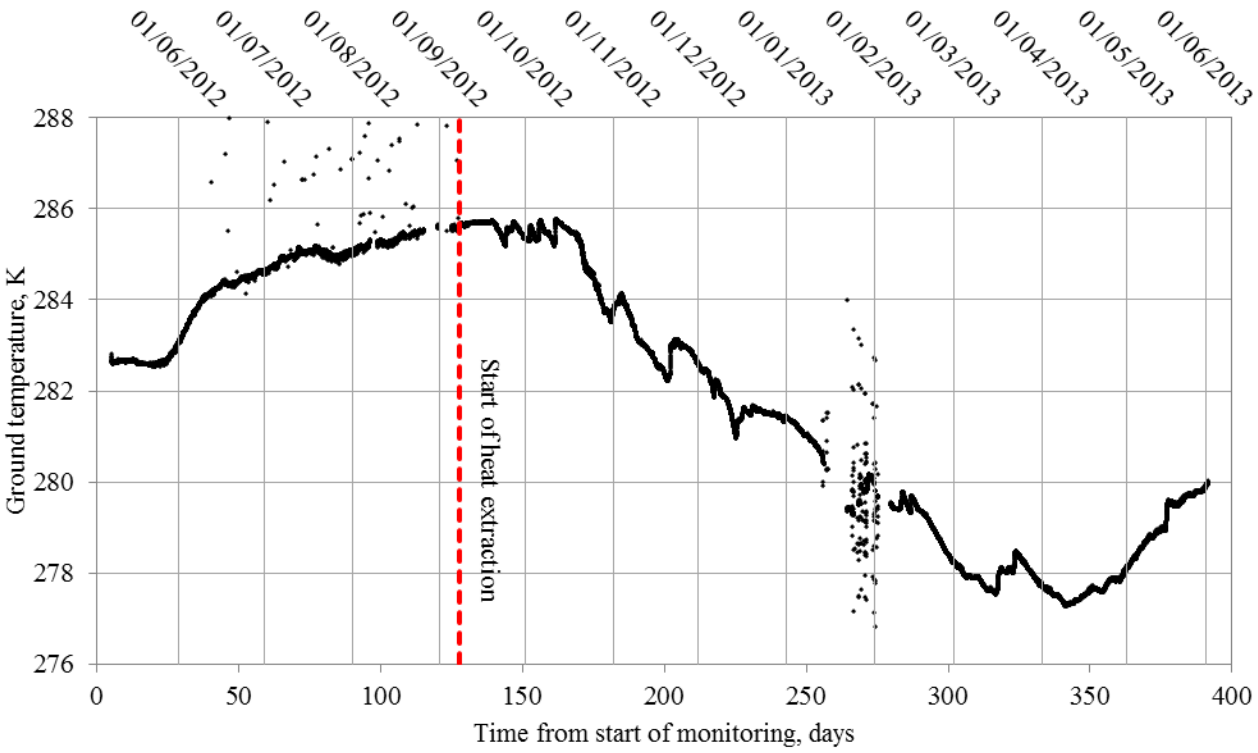

Figure D88 – Time evolution showing the monitored ground temperature data at sensor BB6

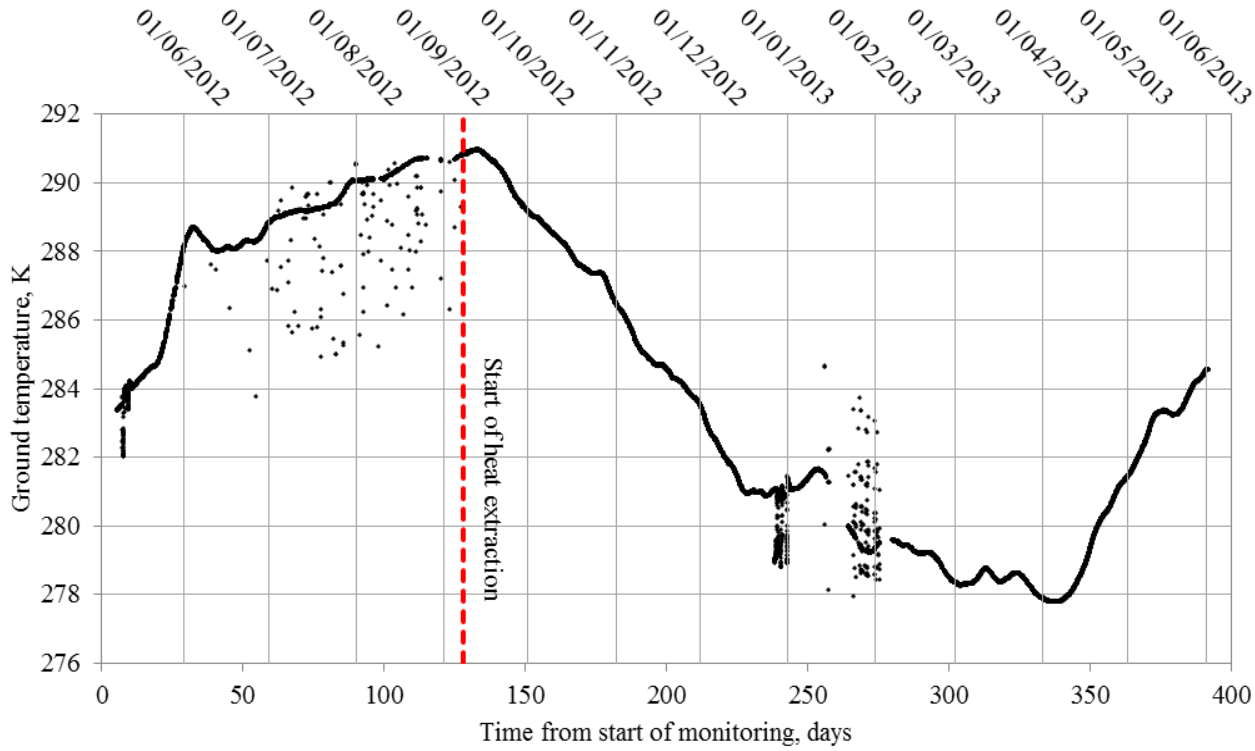

Figure D89 – Time evolution showing the monitored ground temperature data at sensor BB7

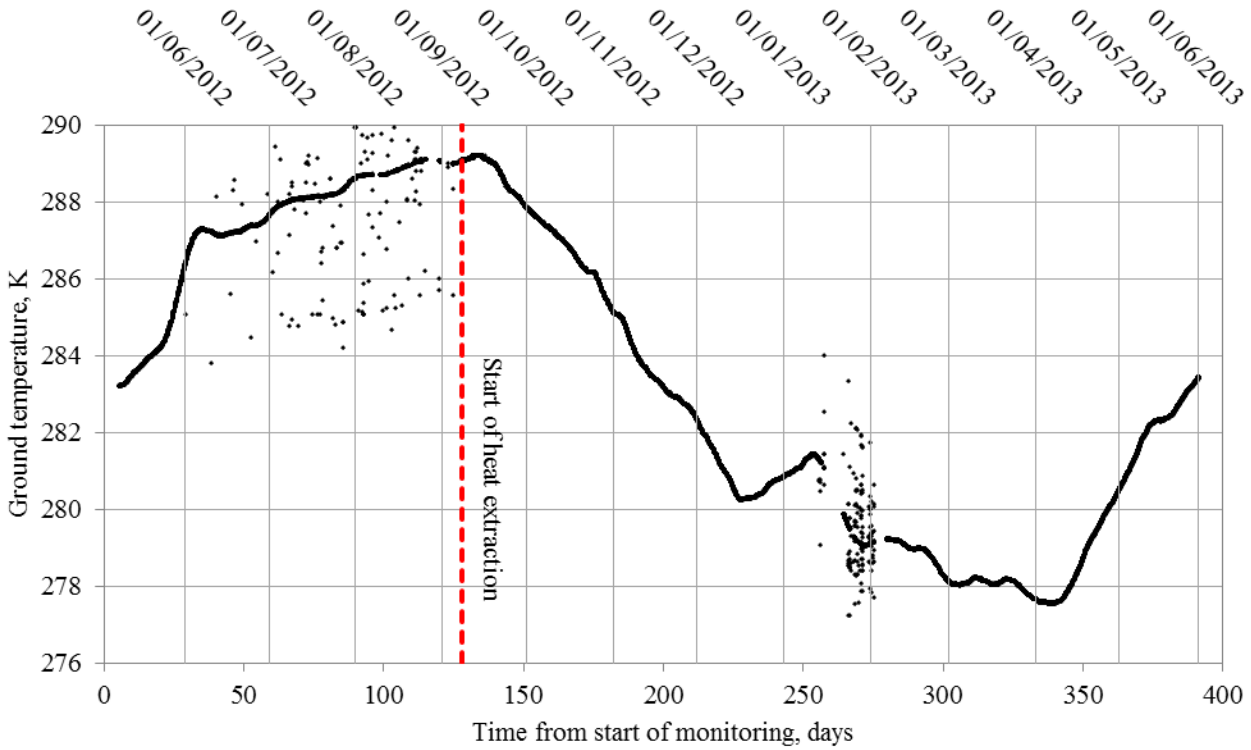

Figure D90 – Time evolution showing the monitored ground temperature data at sensor BB8

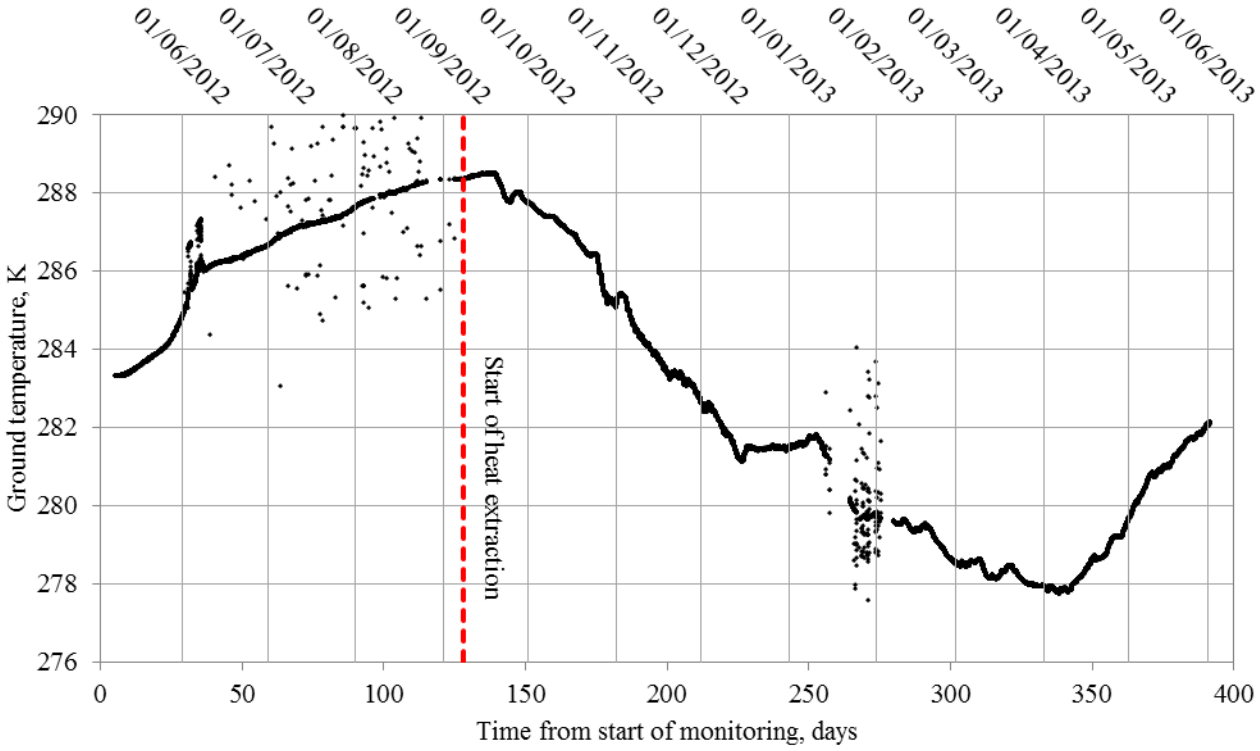

Figure D91 – Time evolution showing the monitored ground temperature data at sensor BB9

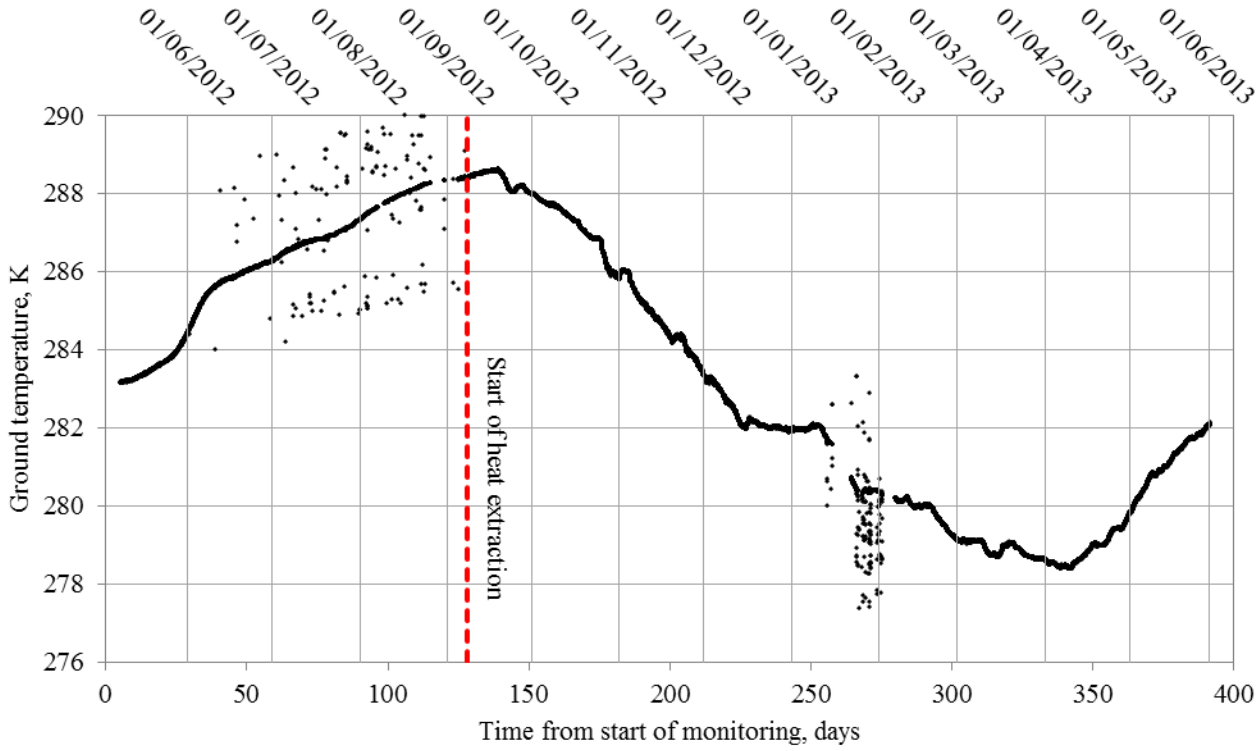

Figure D92 – Time evolution showing the monitored ground temperature data at sensor BB10

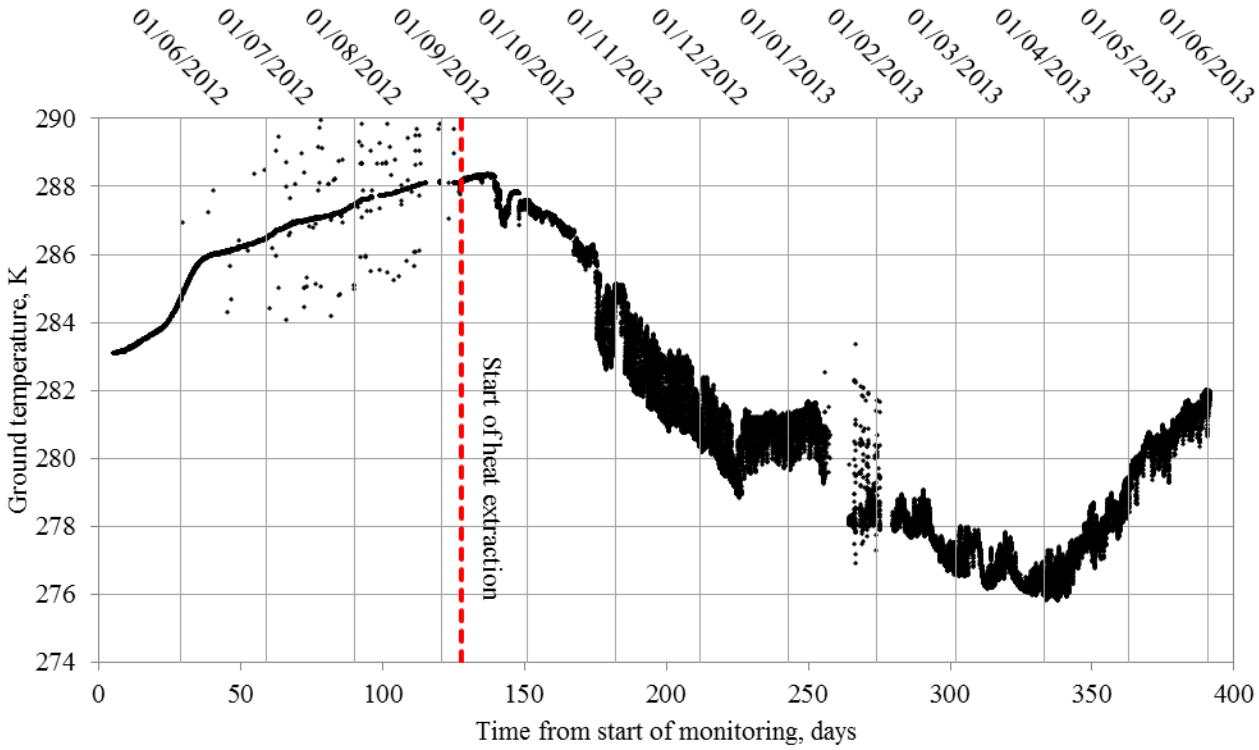

Figure D93 – Time evolution showing the monitored ground temperature data at sensor BB12

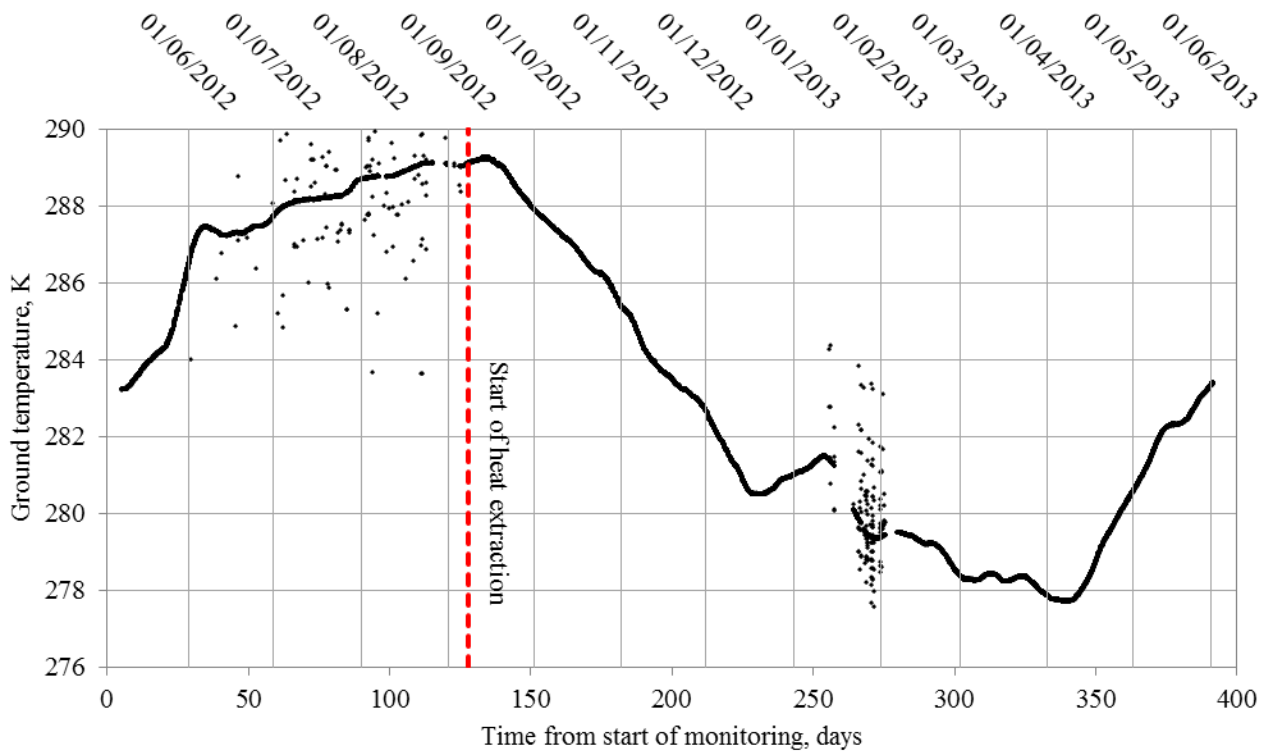

Figure D94 – Time evolution showing the monitored ground temperature data at sensor BB13

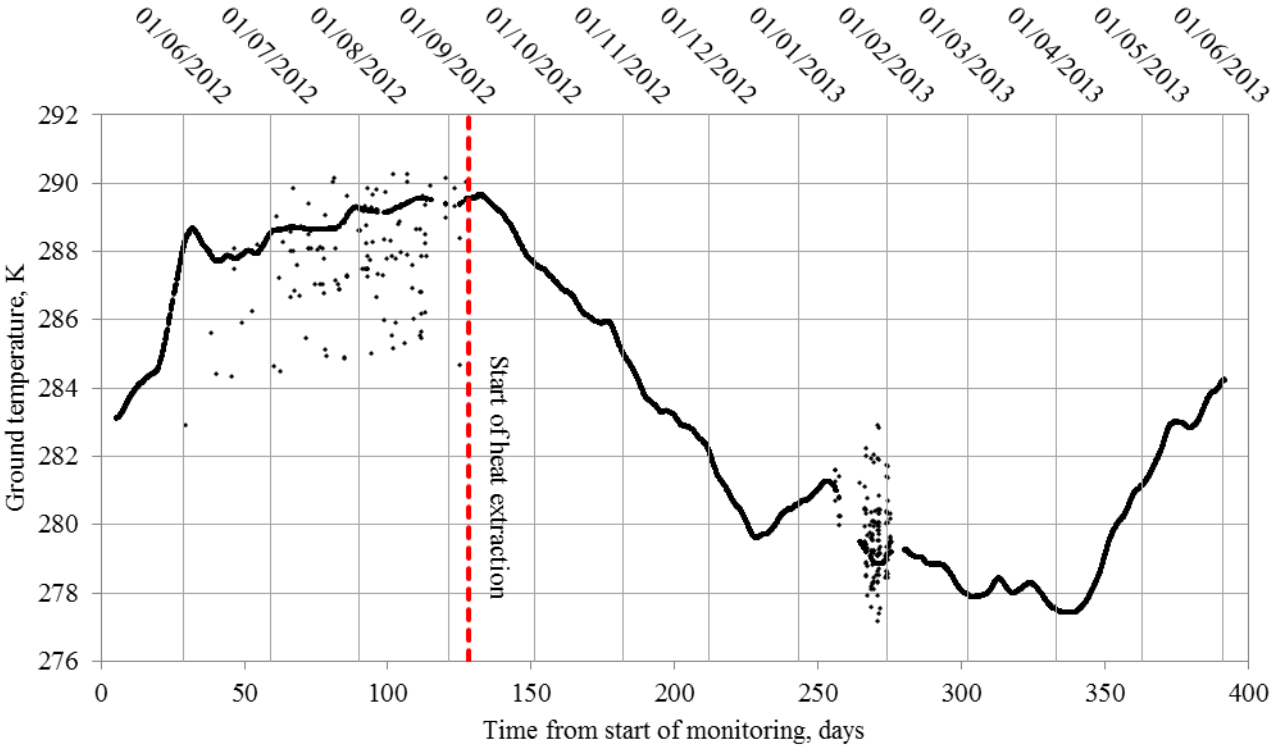

Figure D95 – Time evolution showing the monitored ground temperature data at sensor BB14

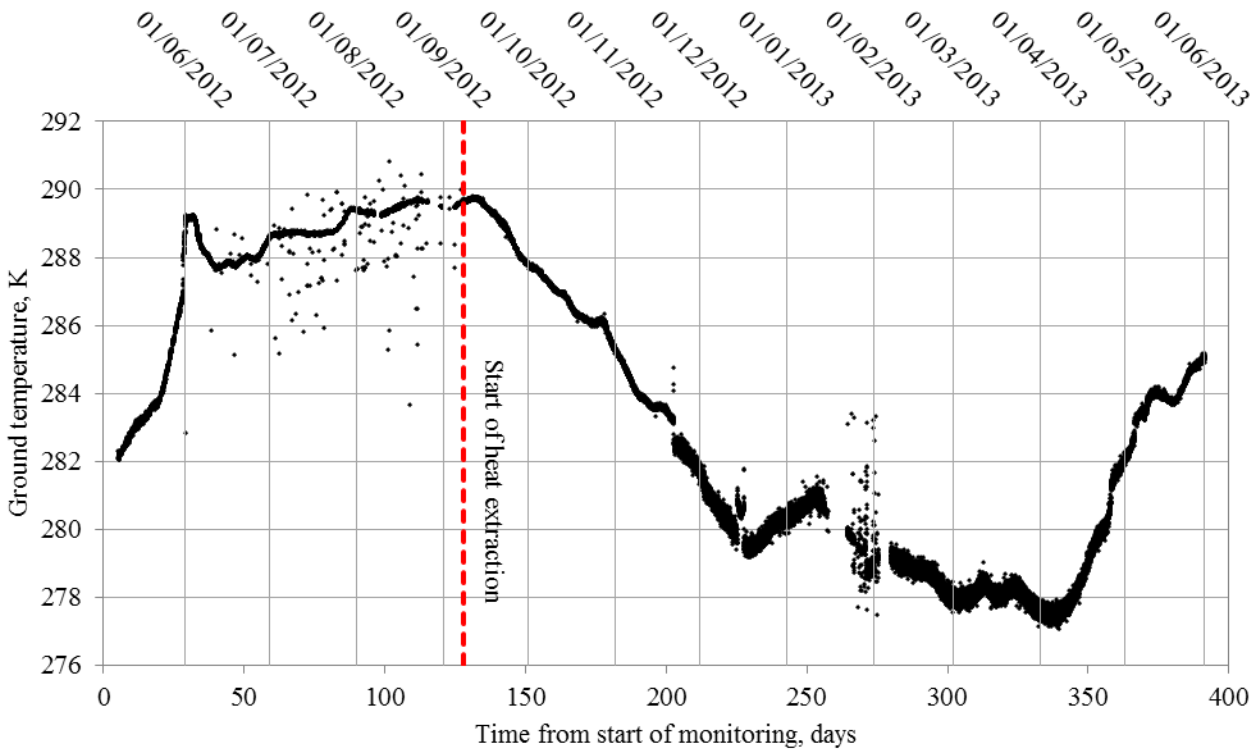

Figure D96 – Time evolution showing the monitored ground temperature data at sensor BC1

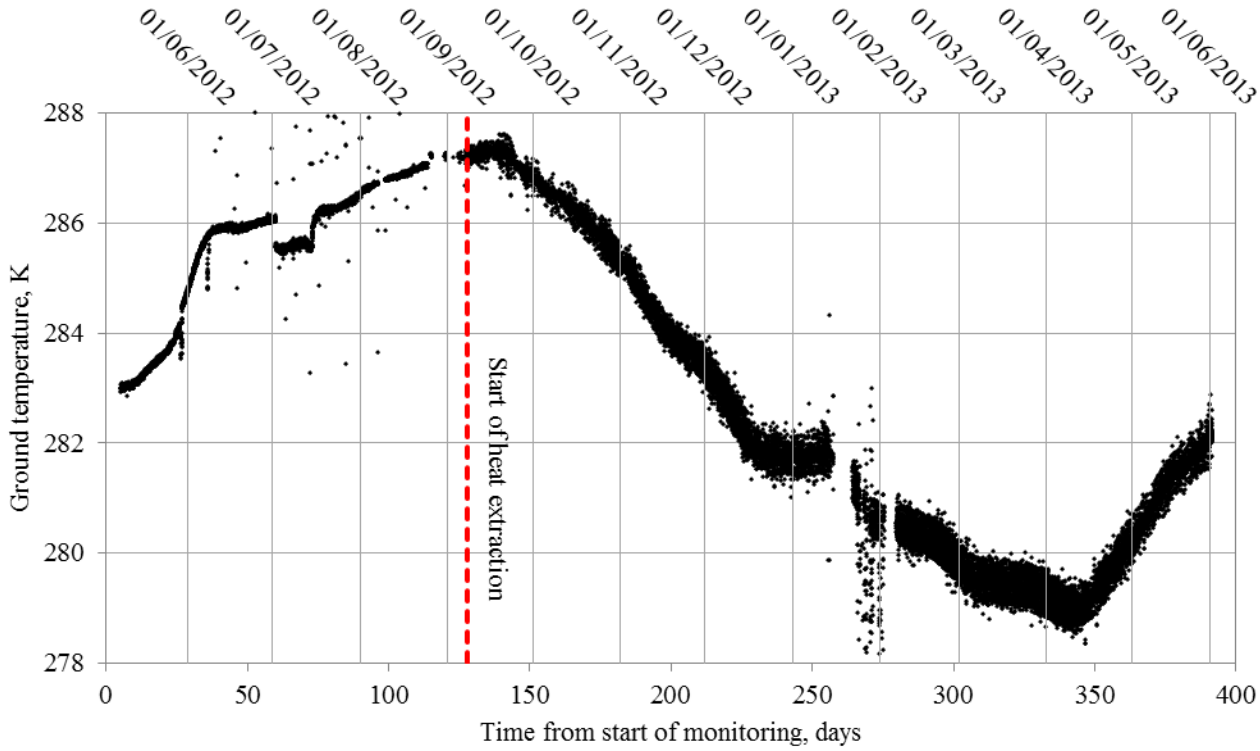

Figure D97 – Time evolution showing the monitored ground temperature data at sensor BC3

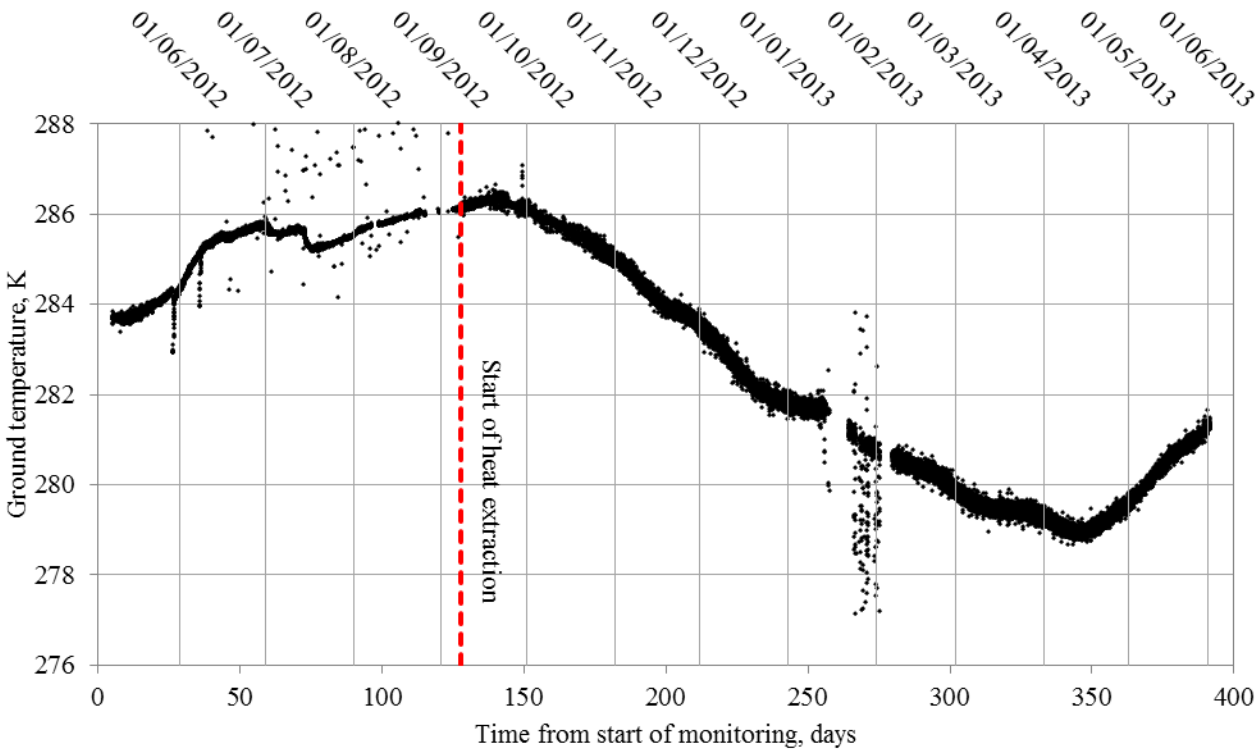

Figure D98 – Time evolution showing the monitored ground temperature data at sensor BC4

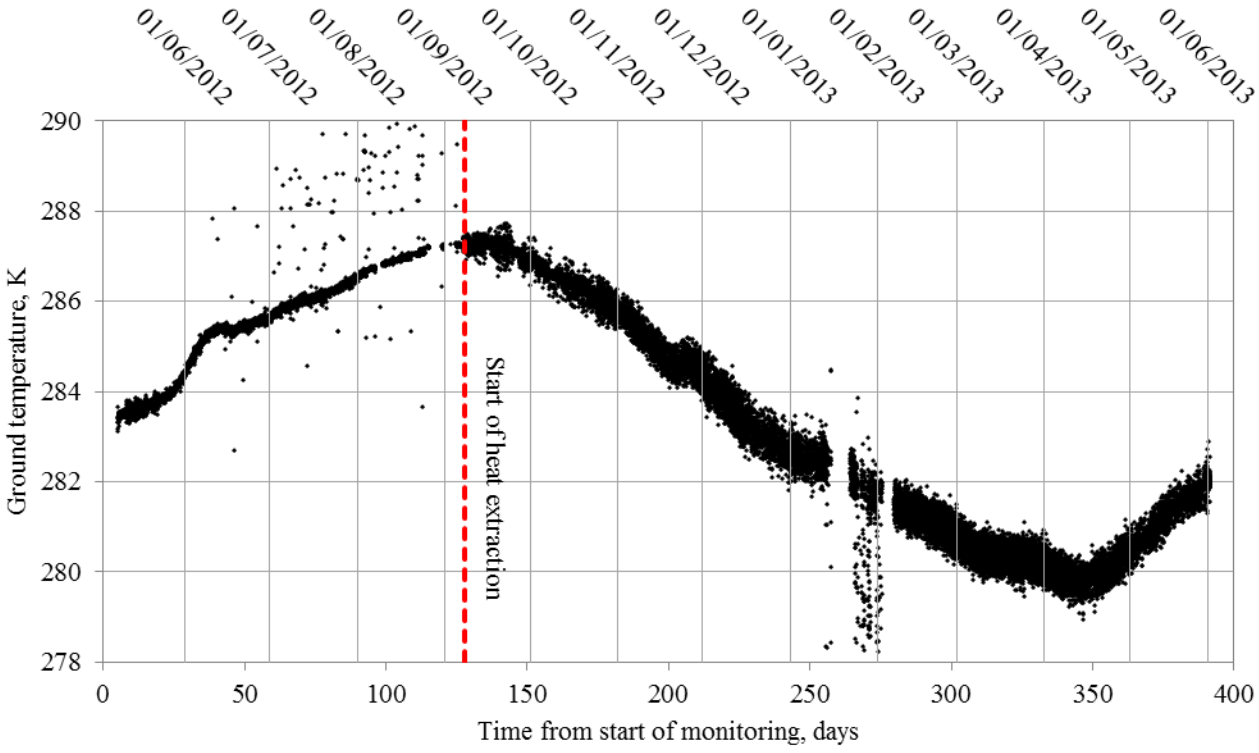

Figure D99 – Time evolution showing the monitored ground temperature data at sensor BC5

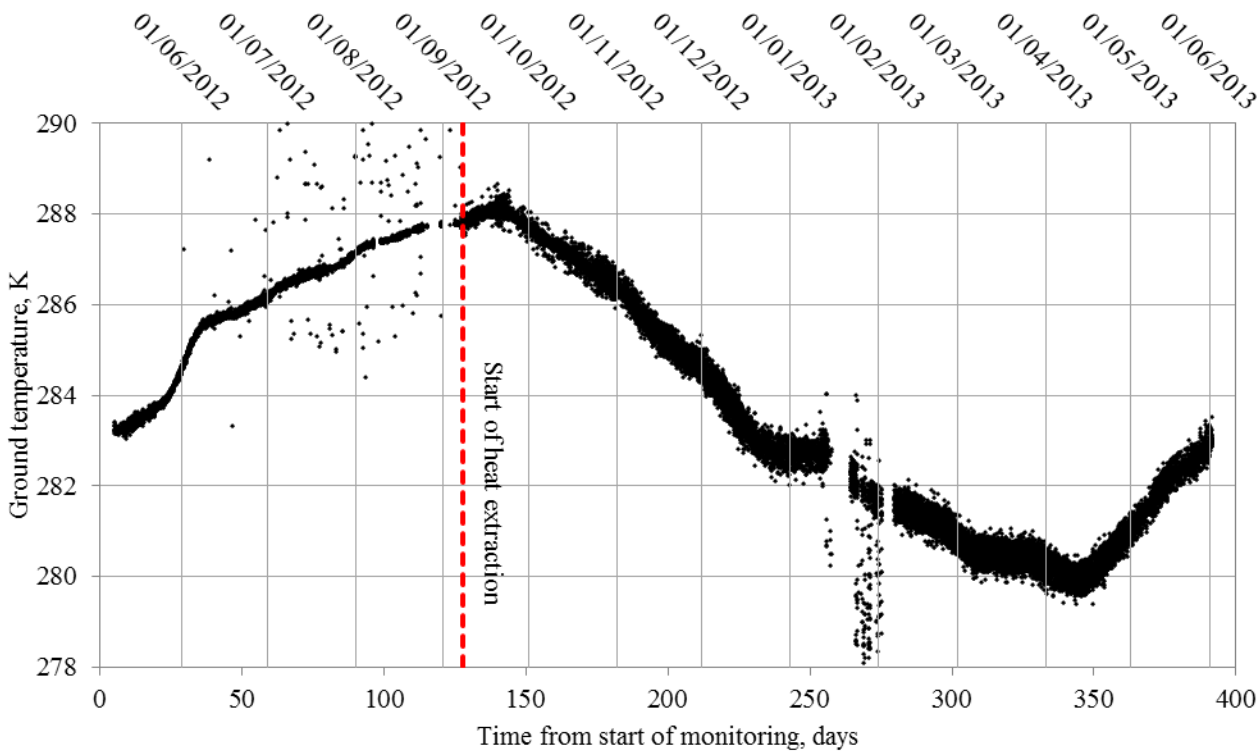

Figure D100 – Time evolution showing the monitored ground temperature data at sensor BC6

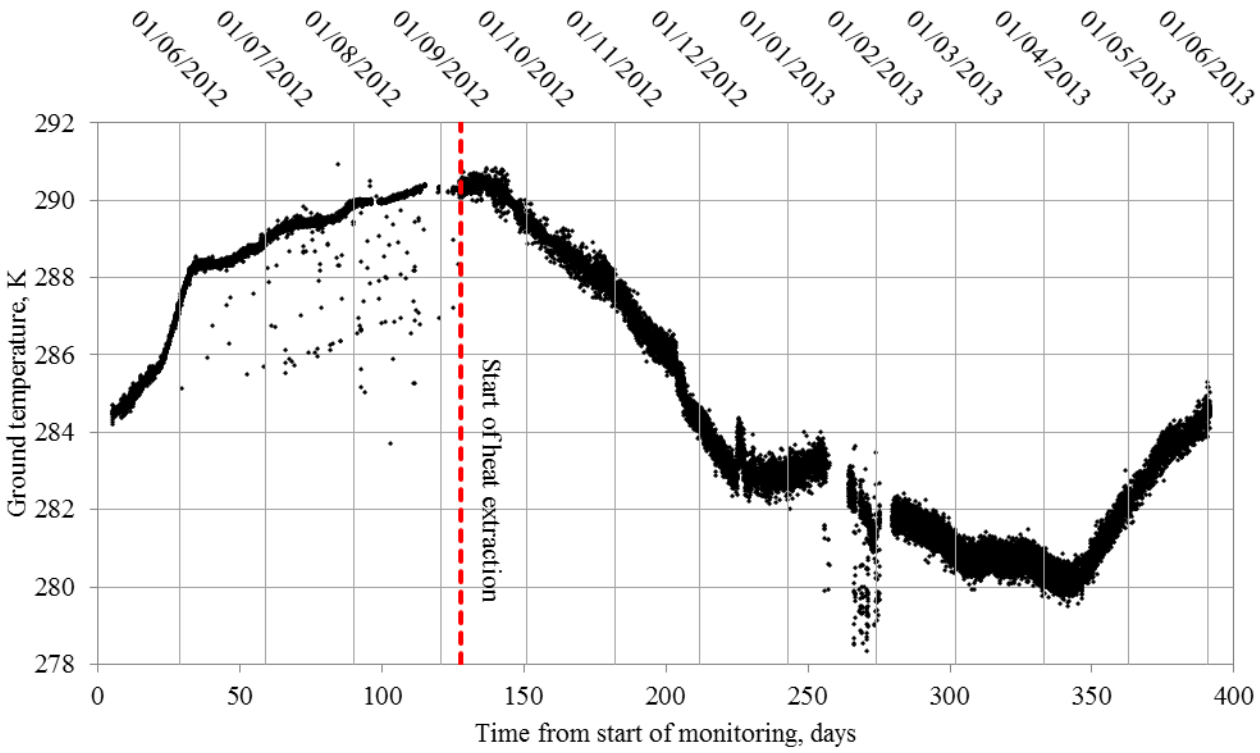

Figure D101 – Time evolution showing the monitored ground temperature data at sensor BC7

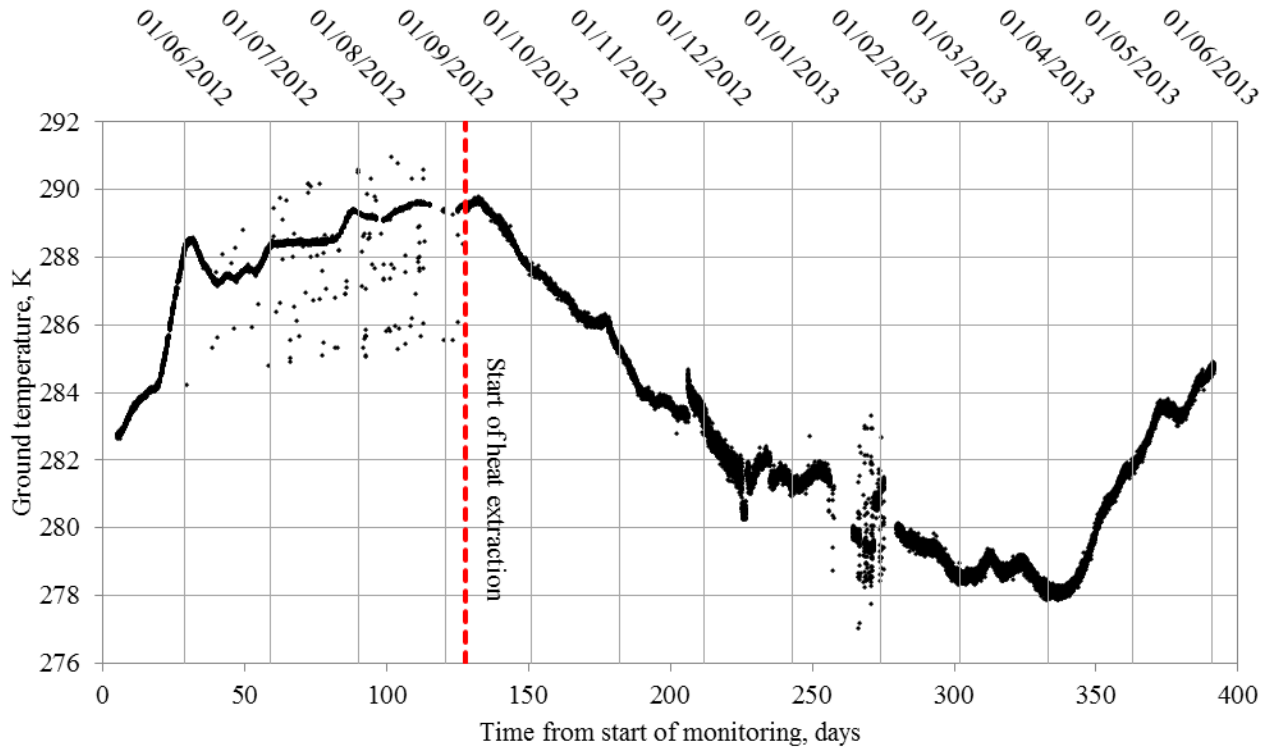

Figure D102 – Time evolution showing the monitored ground temperature data at sensor BC8

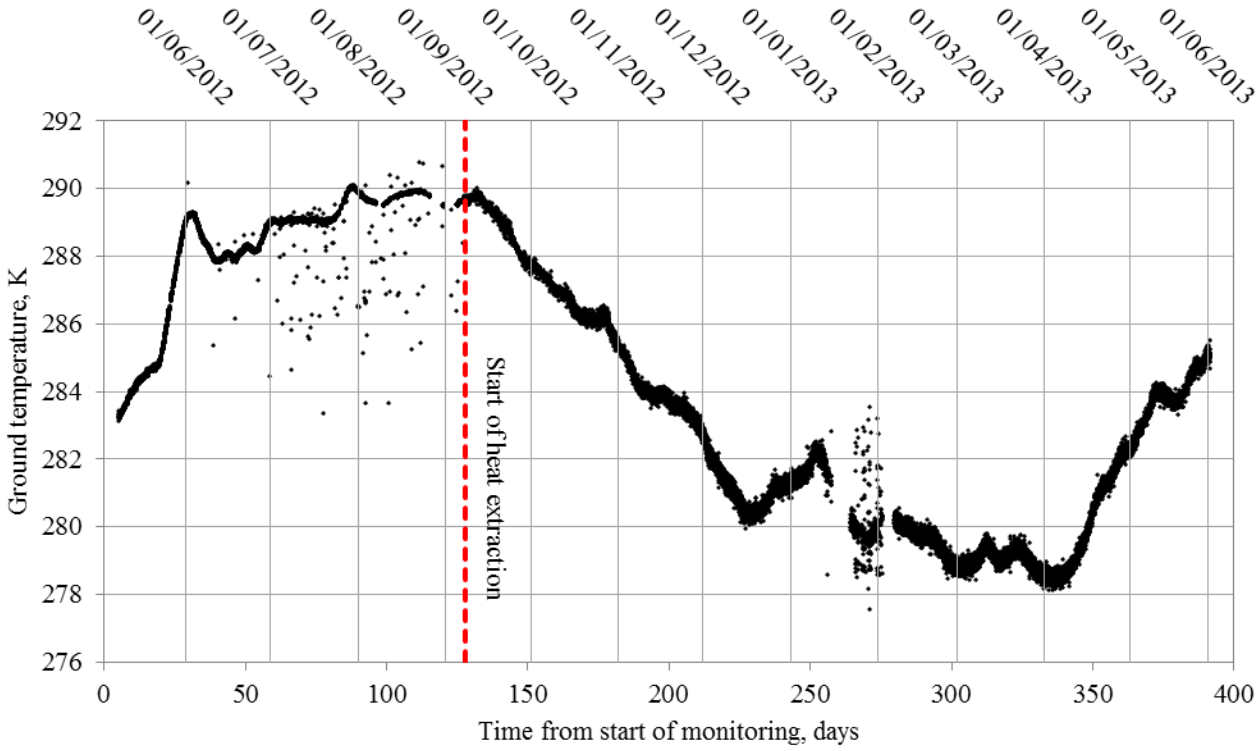

Figure D103 – Time evolution showing the monitored ground temperature data at sensor BC9

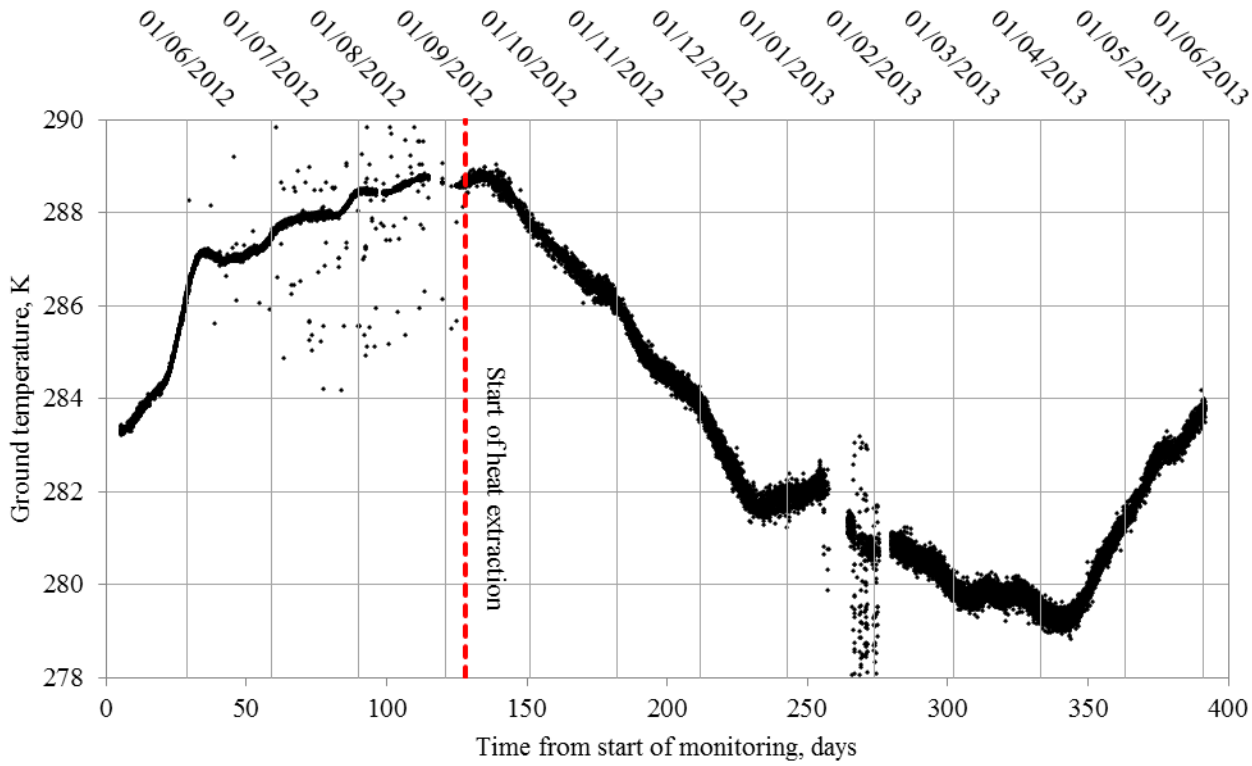

Figure D104 – Time evolution showing the monitored ground temperature data at sensor BC10

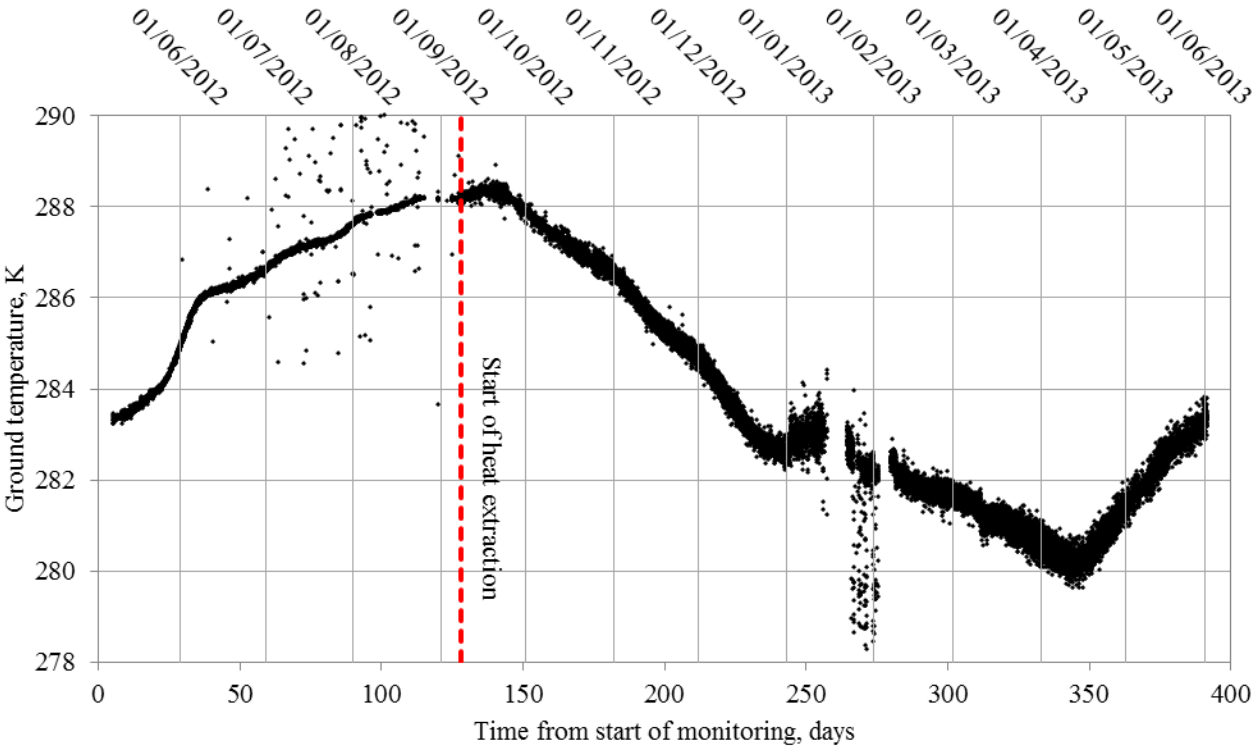

Figure D105 – Time evolution showing the monitored ground temperature data at sensor BC11

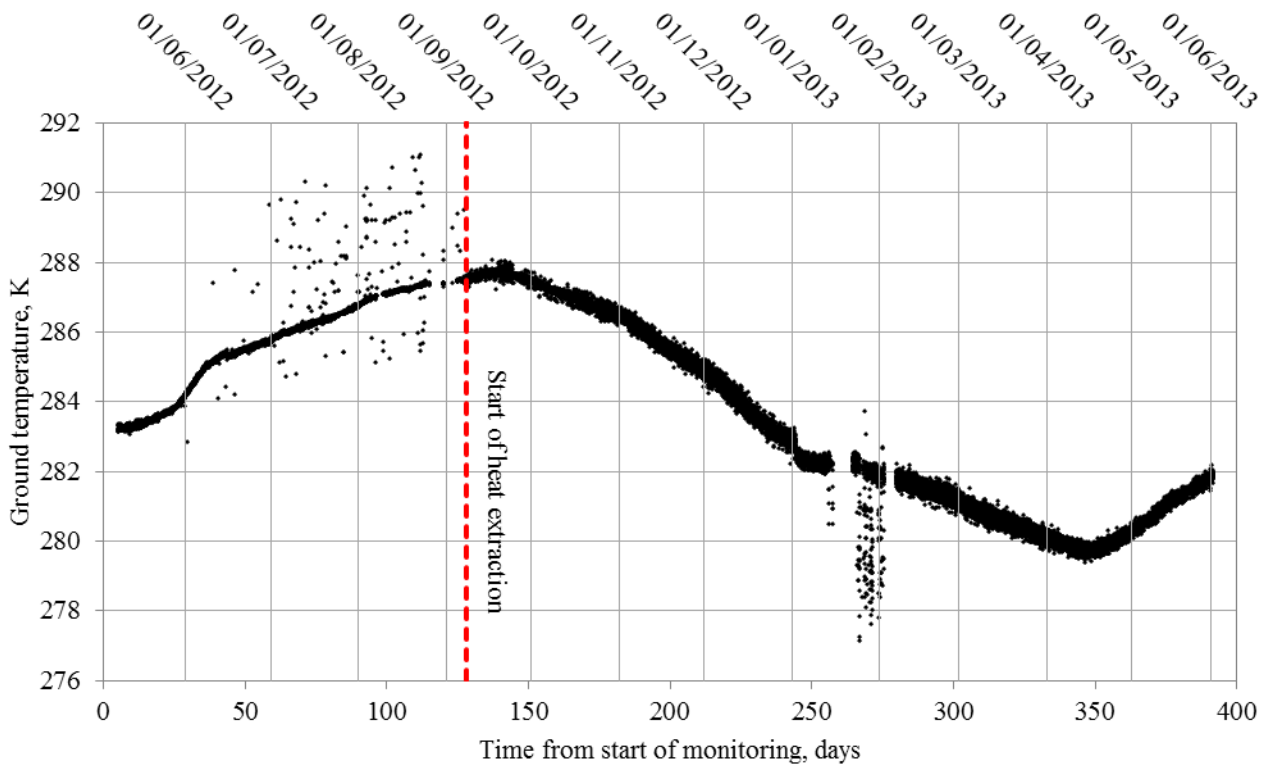

Figure D106 – Time evolution showing the monitored ground temperature data at sensor BC12

Appendix E

Contour plots showing the two-dimensional ground temperature distribution at detailed cross-section BB

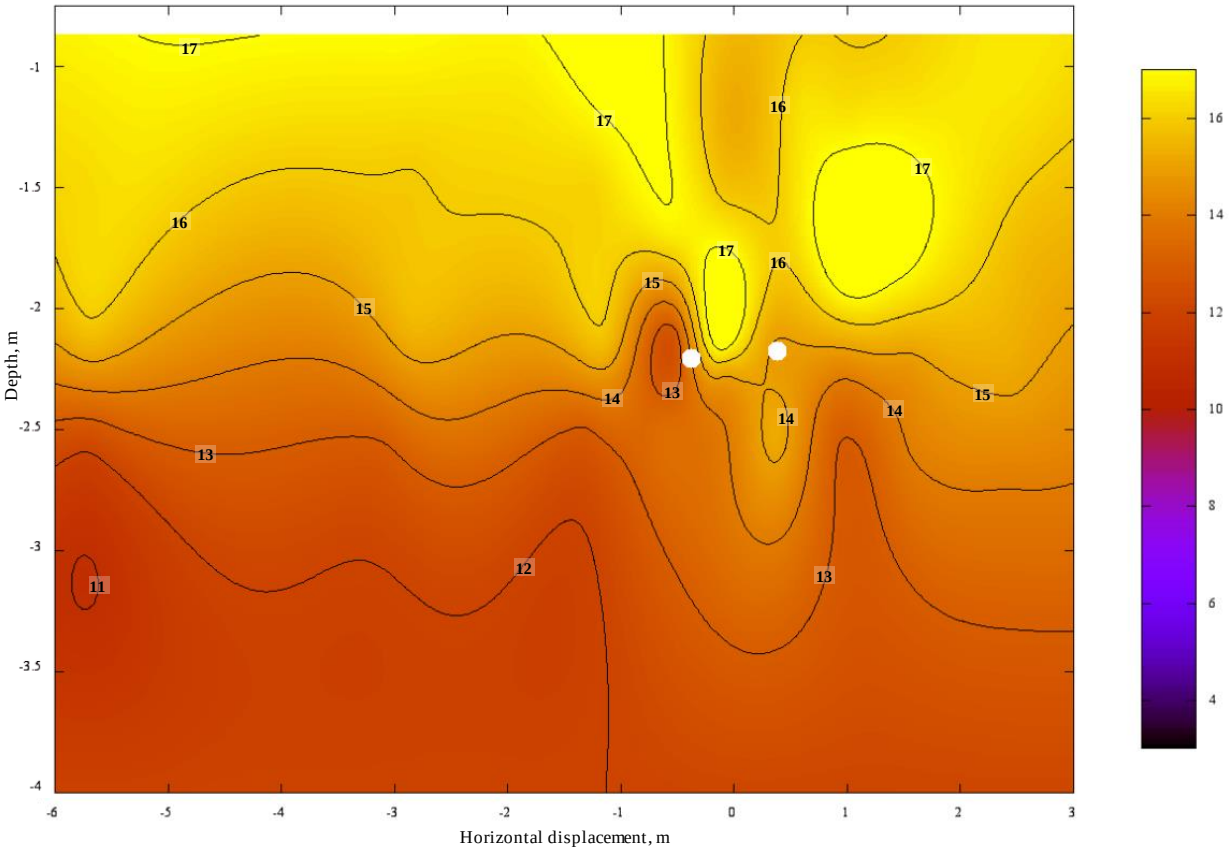

Figure E1 - Two-dimensional ground temperature distribution at detailed cross-section BB on September 1st 2012.

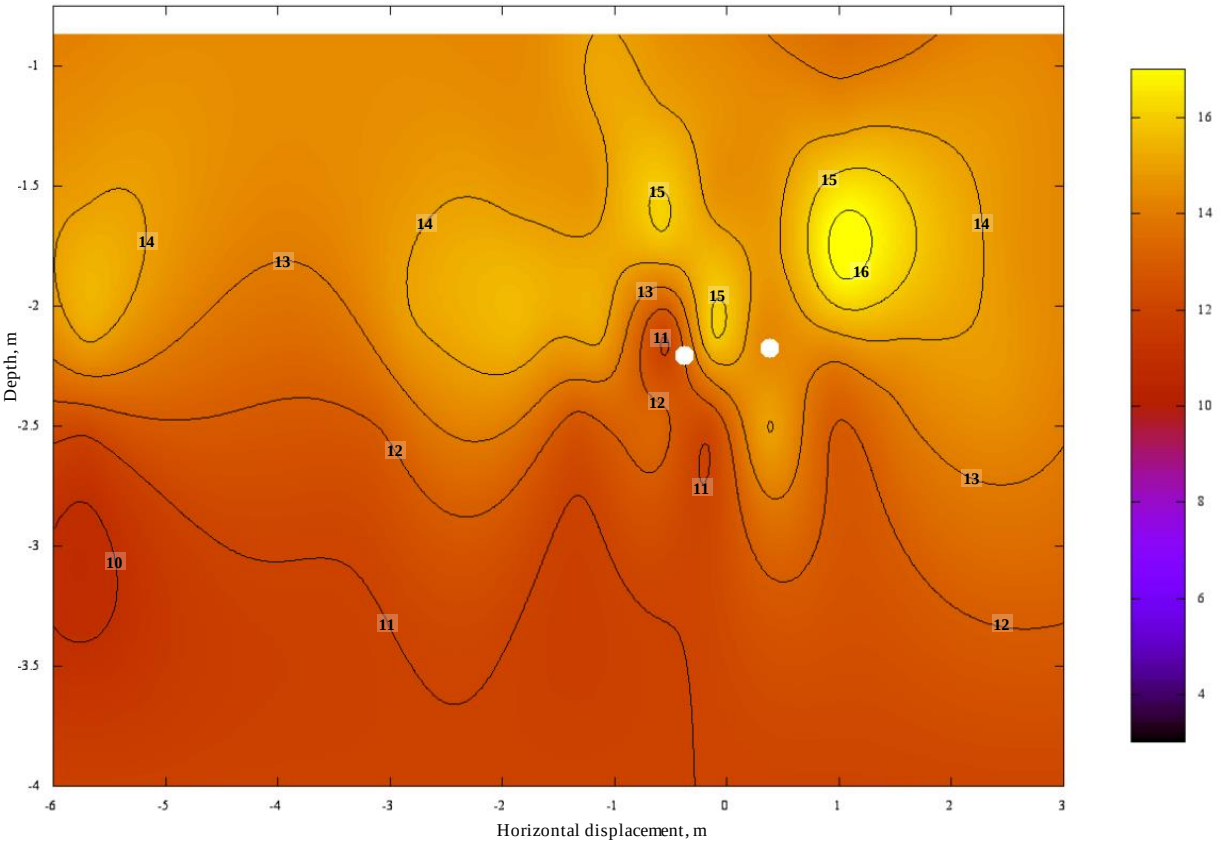

Figure E2 - Two-dimensional ground temperature distribution at detailed cross-section BB on October 1st 2012.

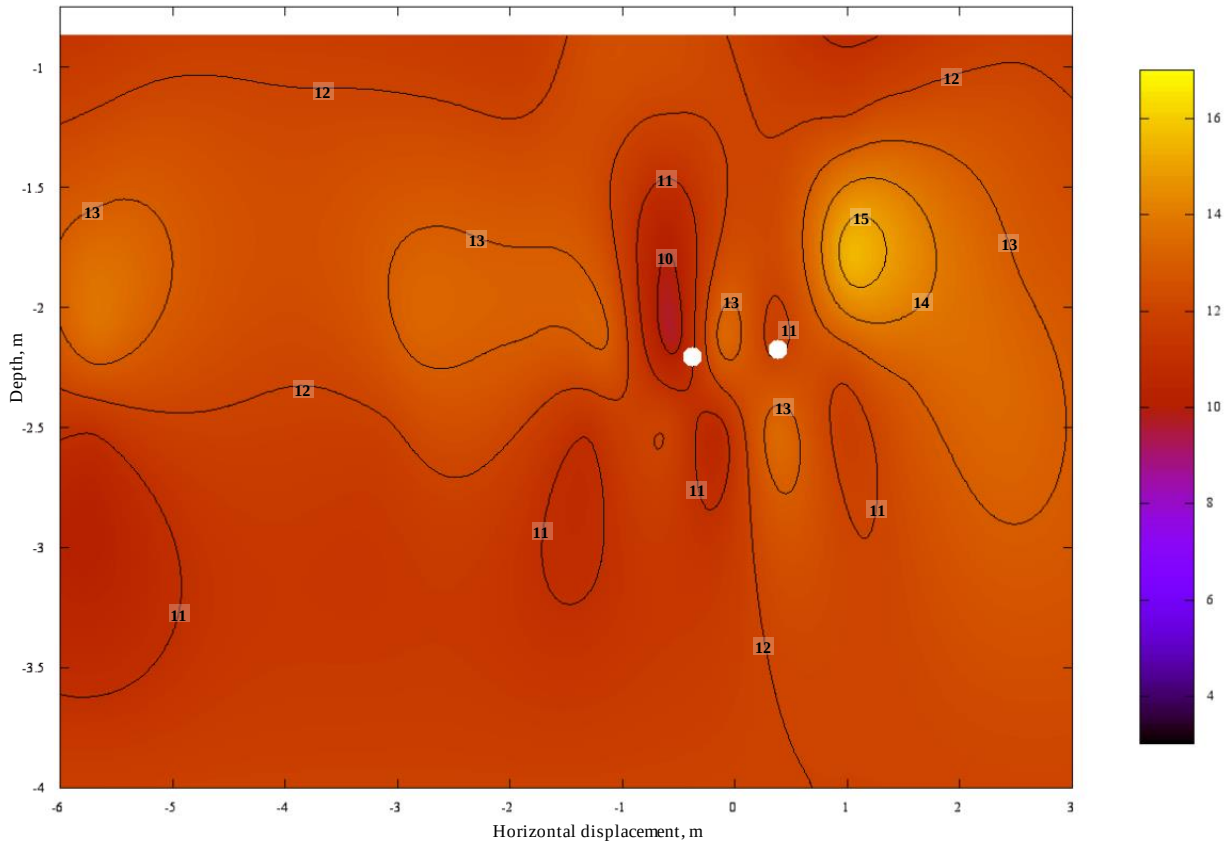

Figure E3- Two-dimensional ground temperature distribution at detailed cross-section BB on November 1st 2012.

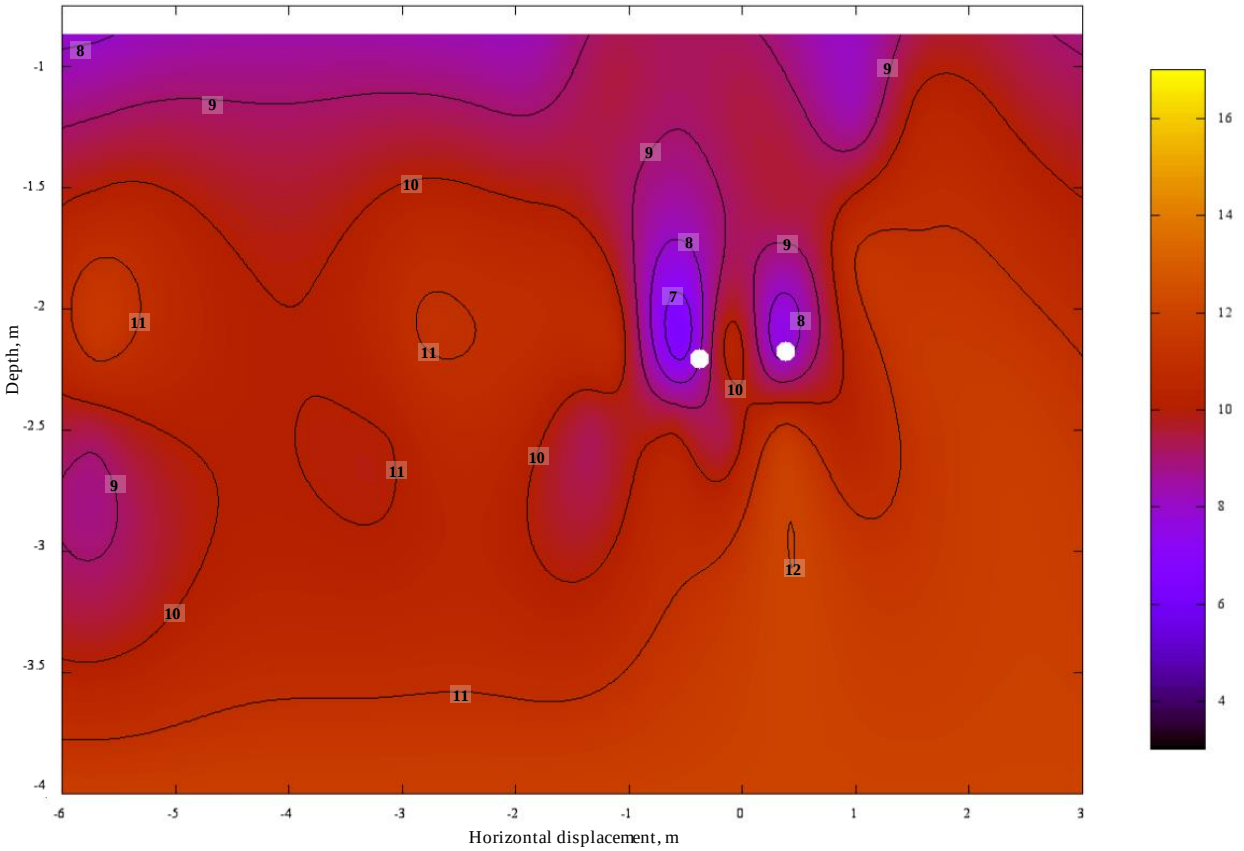

Figure E4- Two-dimensional ground temperature distribution at detailed cross-section BB on December 1st 2012.

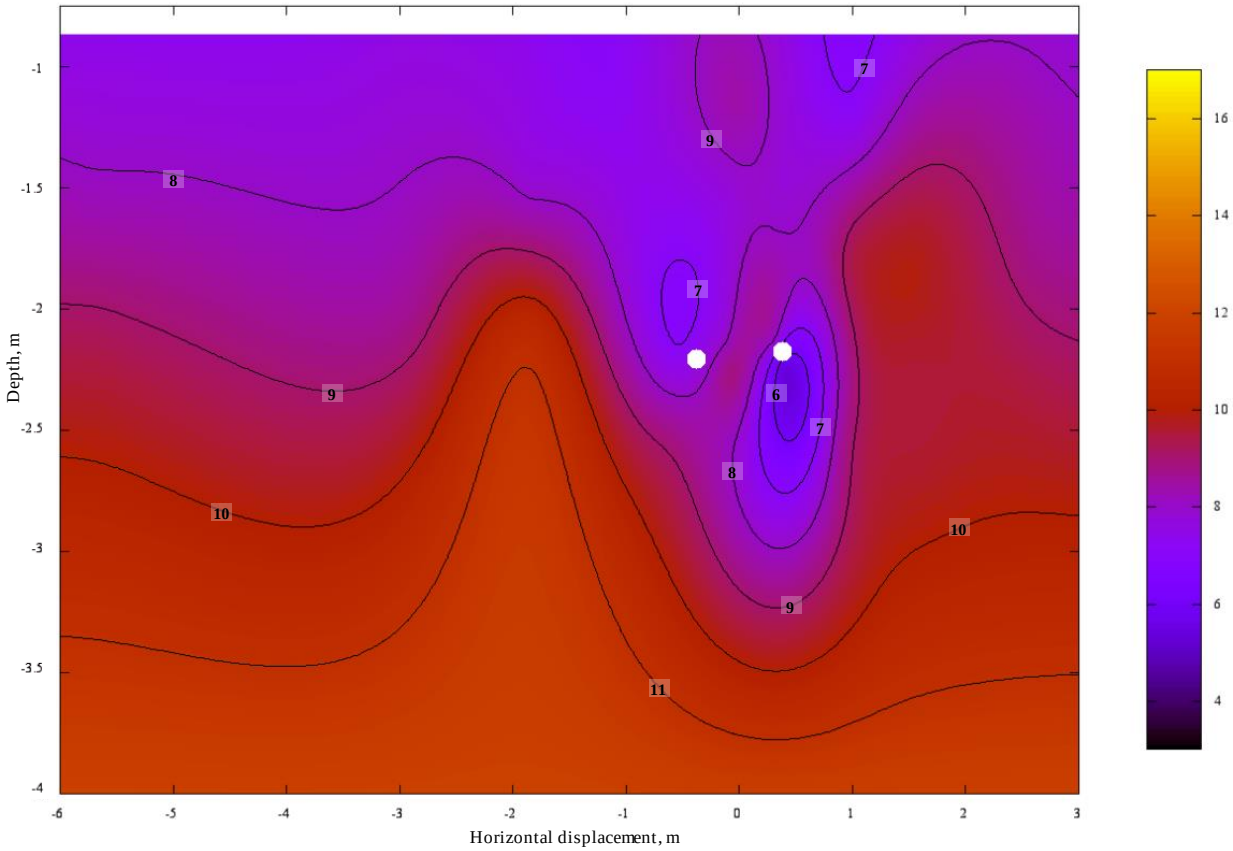

Figure E5- Two-dimensional ground temperature distribution at detailed cross-section BB on January 1st 2013.

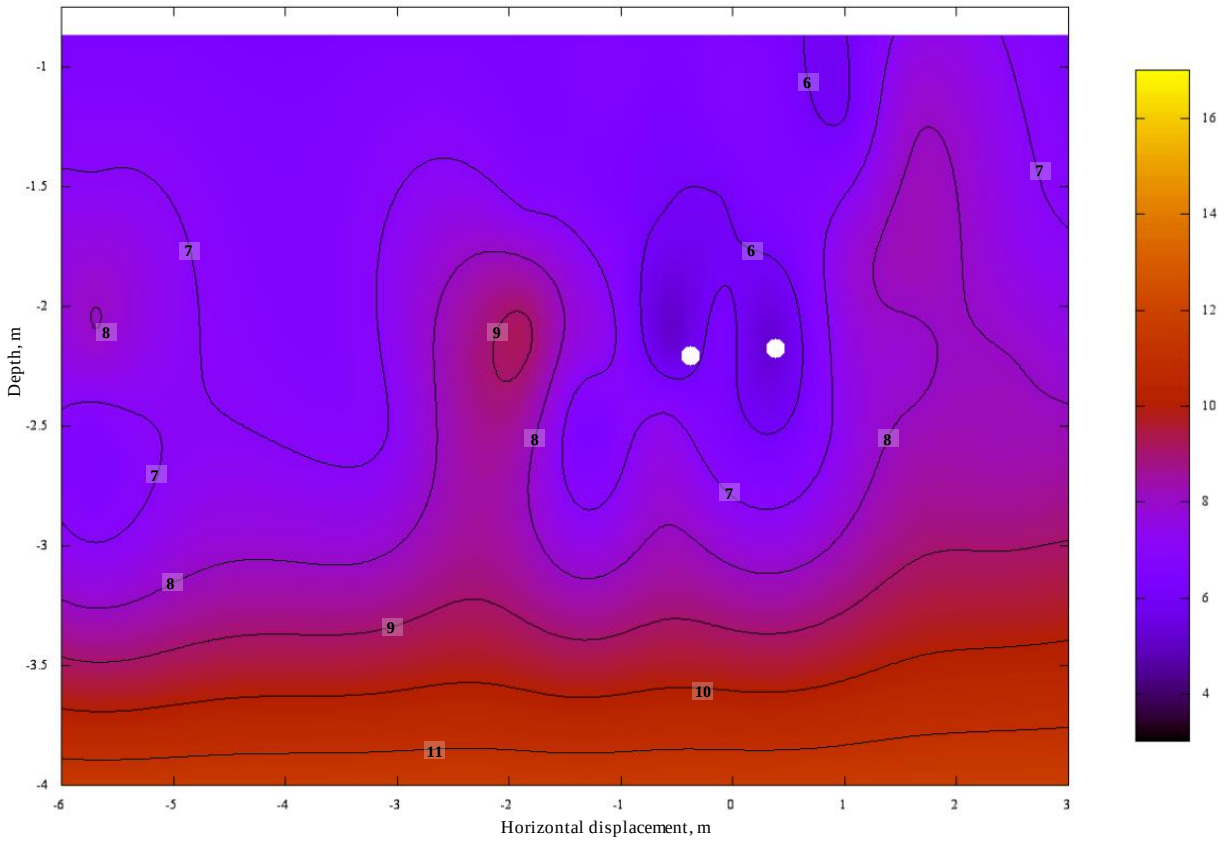

Figure E6- Two-dimensional ground temperature distribution at detailed cross-section BB on February 1st 2013.

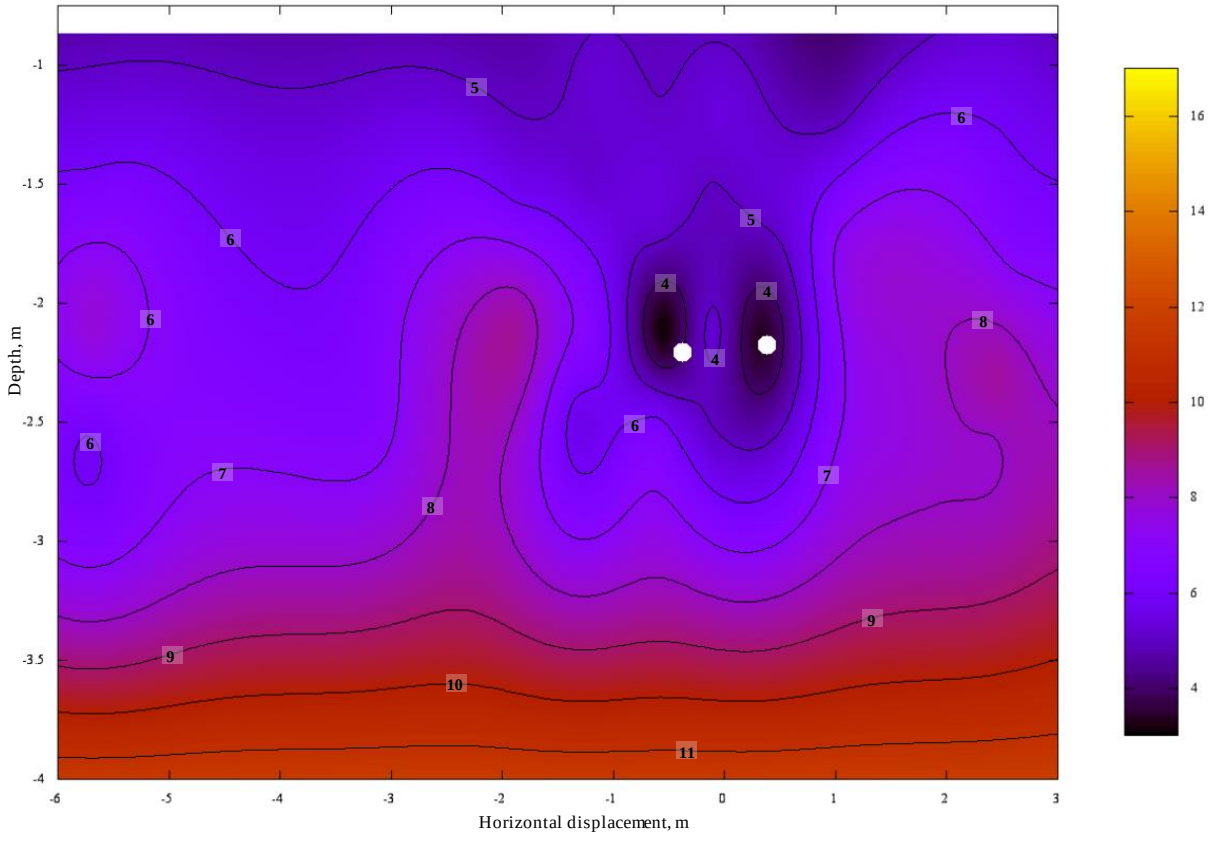

Figure E7- Two-dimensional ground temperature distribution at detailed cross-section BB on March 1st 2013.

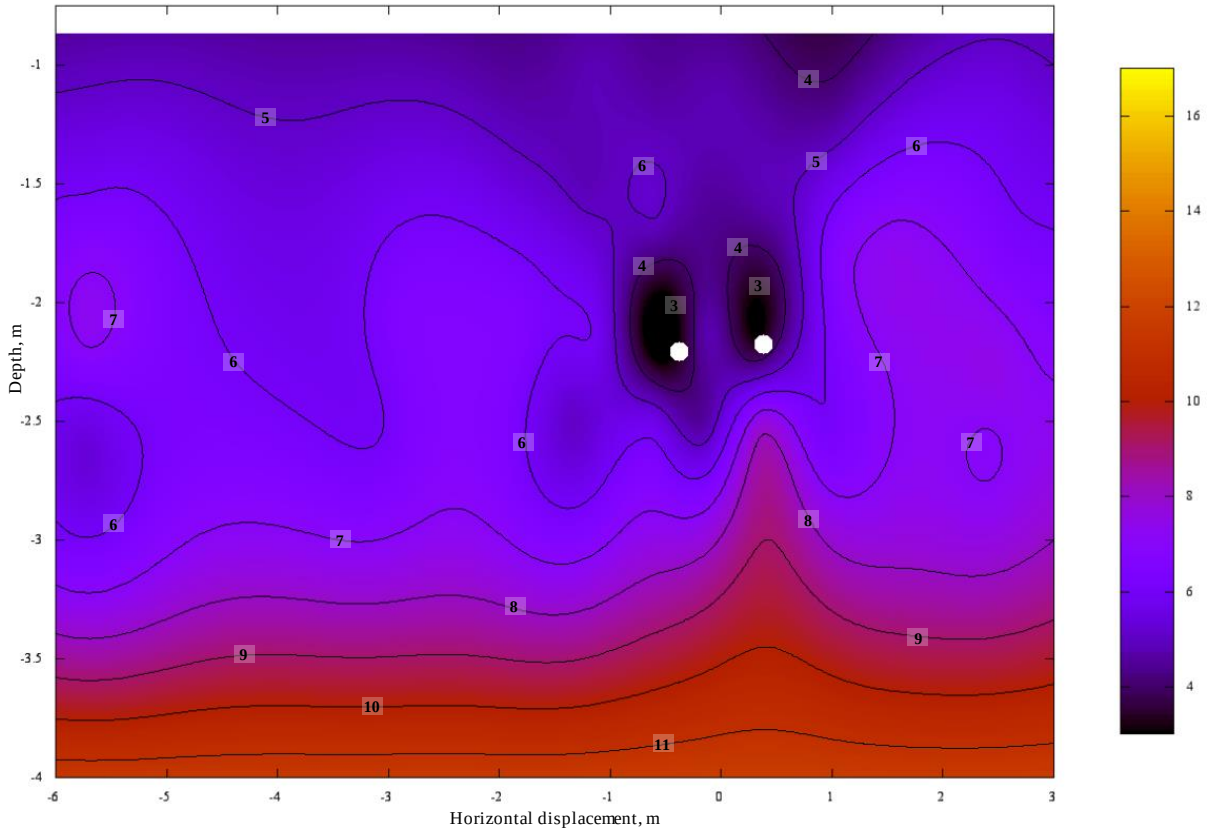

Figure E8- Two-dimensional ground temperature distribution at detailed cross-section BB on April 1st 2013.

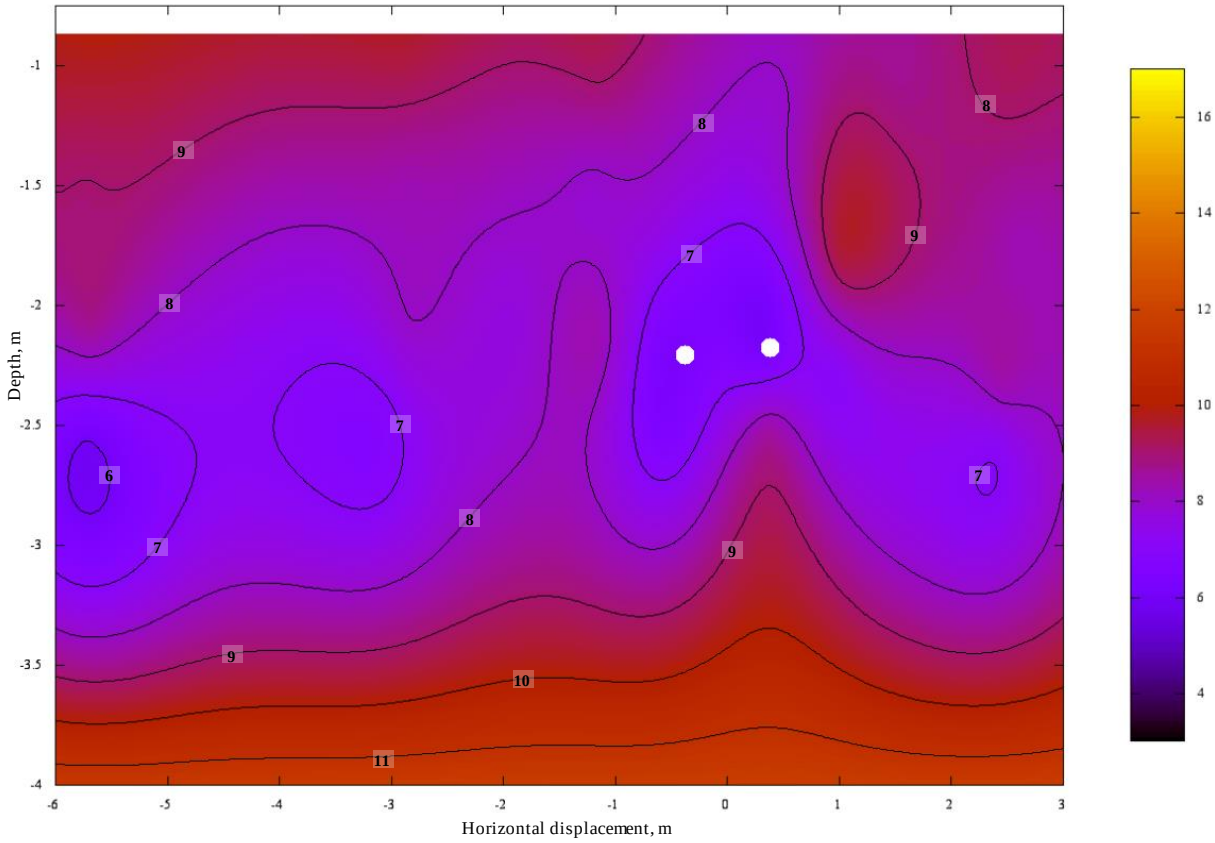

Figure E9- Two-dimensional ground temperature distribution at detailed cross-section BB on May 1st 2013.

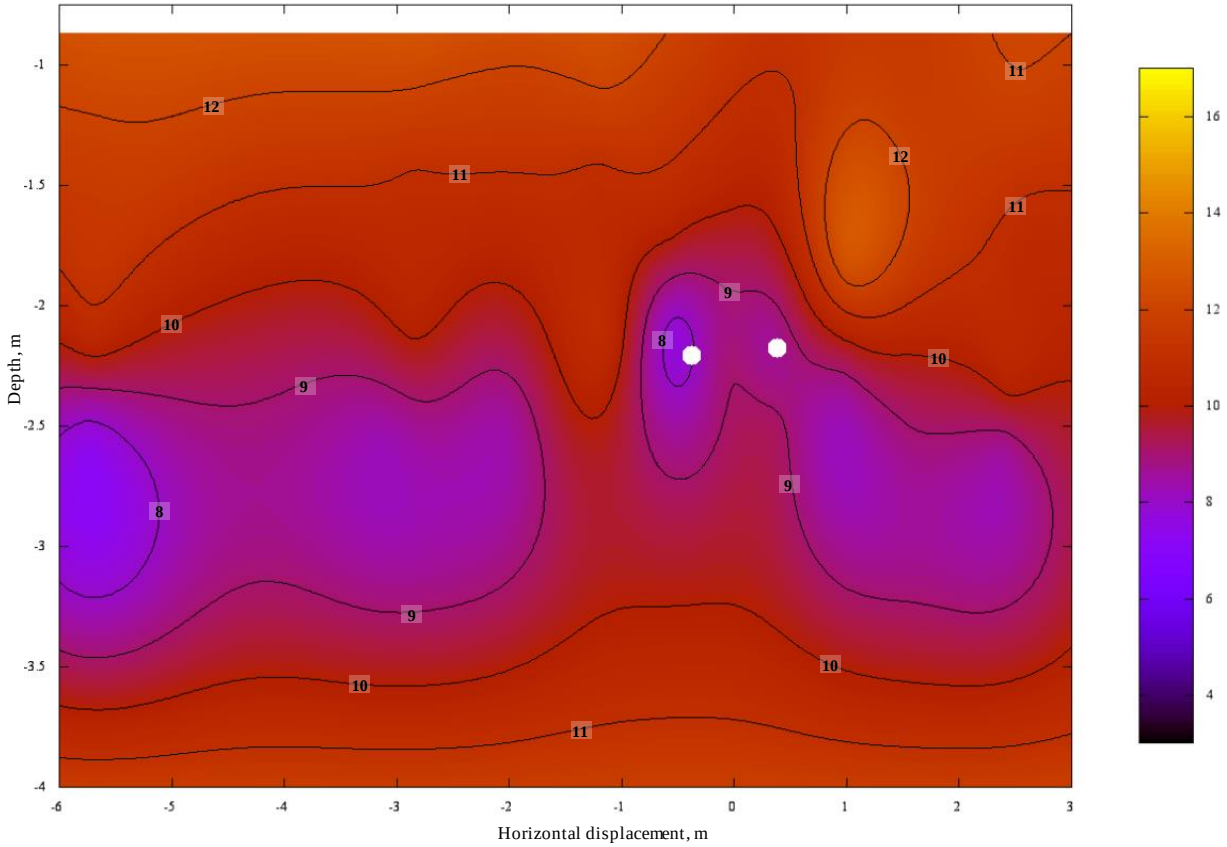

Figure E10- Two-dimensional ground temperature distribution at detailed cross-section BB on June 1st 2013.

Appendix F

Exploratory samples retrieved from the monitoring site

Depth of sample beneath ground surface, m	*Moisture content, %*	*Porosity*	*Degree of saturation*
0.28	40.4	0.47	0.86
0.38	23.6	0.40	0.59
0.62	21.7	0.35	0.62
0.78	30.8	0.41	0.75

Table F1 – Measured and calculated soil properties from exploratory samples taken on 4th May 2012 from the monitoring site.

Depth of sample beneath ground surface, m	*Moisture content, %*	*Porosity*	*Degree of saturation*
0.19	30.4	0.51	0.66
0.35	13.0	0.42	0.31
0.52	27.7	0.39	0.71
0.70	27.0	0.36	0.75

Table F2 – Measured and calculated soil properties from exploratory samples taken on 7th September 2012 from the monitoring site.

Depth of sample beneath ground surface, m	*Moisture content, %*	*Porosity*	*Degree of saturation*
0.21	46.0	0.46	1.0
0.41	38.6	0.42	0.91
0.63	27.7	0.35	0.77
0.84	19.9	0.28	0.71

Table F3 – Measured and calculated soil properties from exploratory samples taken on 23rd January 2013 from the monitoring site.

Appendix G

Simulated and monitored ground temperatures from validation Stage II (Chapter 7)

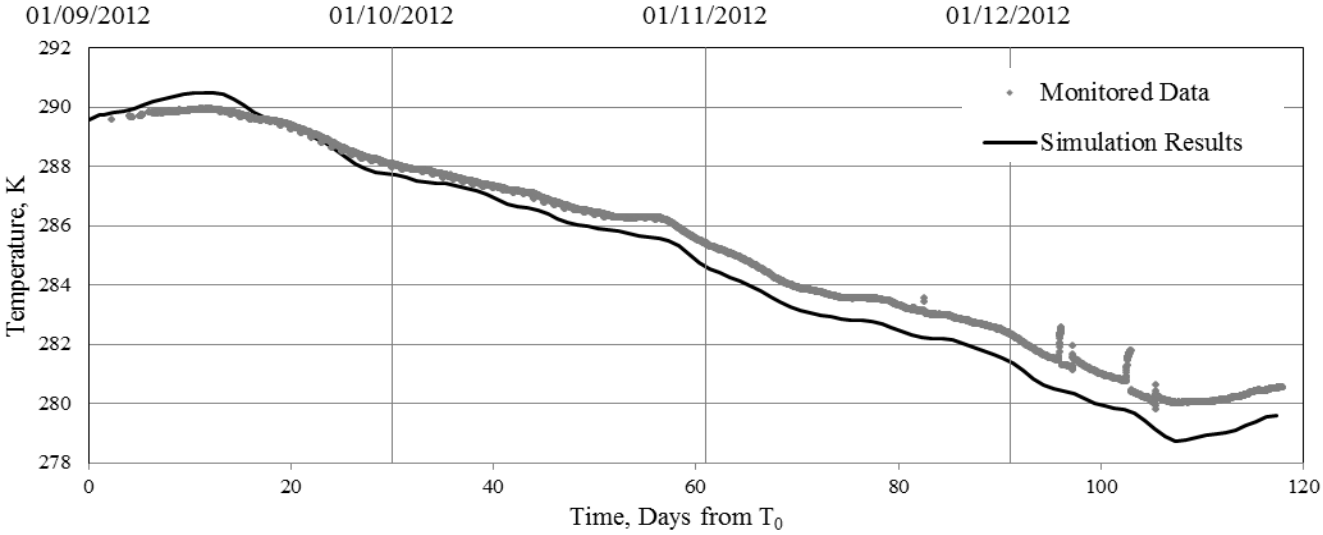

Figure G1- Simulated and monitored ground temperatures at thermistor location AA1.

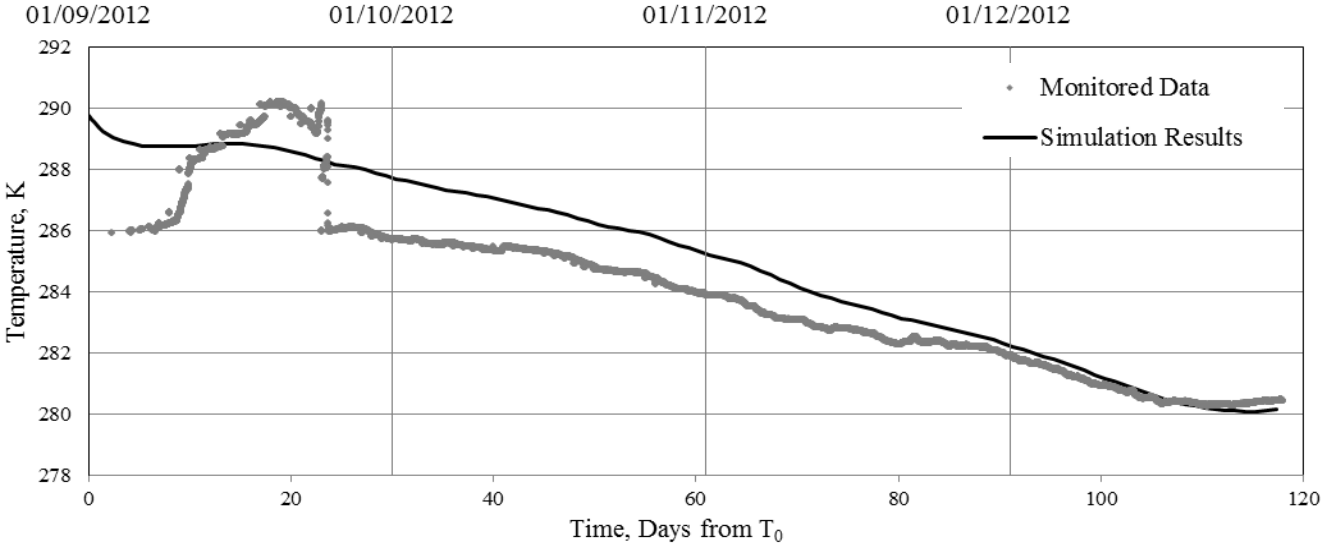

Figure G2 - Simulated and monitored ground temperatures at thermistor location AA2.

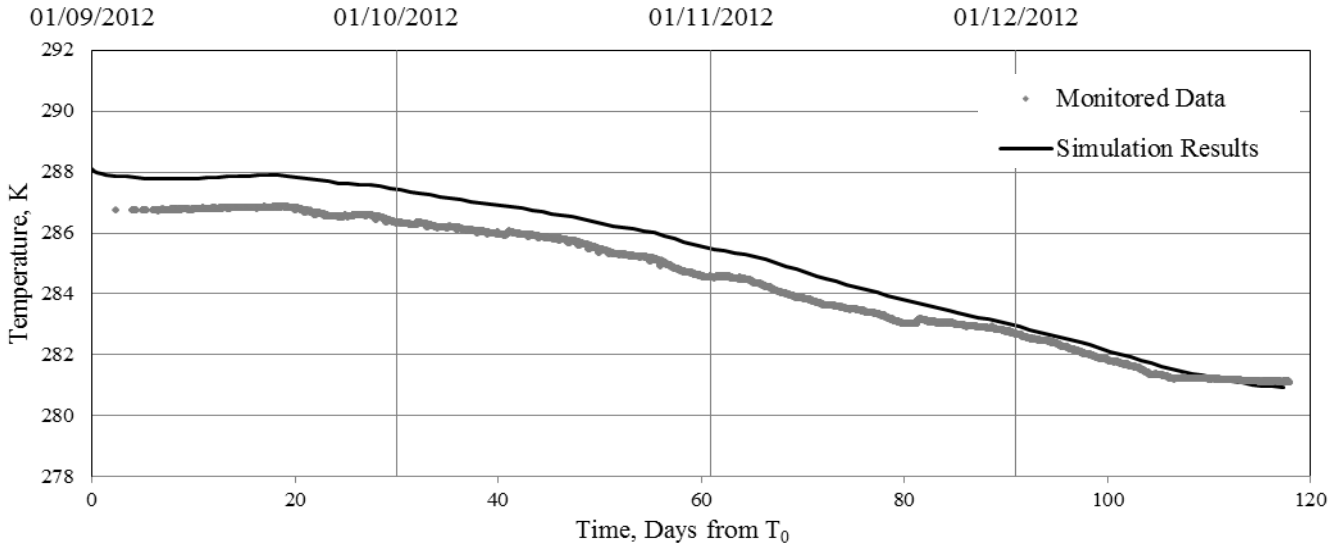

Figure G3- Simulated and monitored ground temperatures at thermistor location AA3.

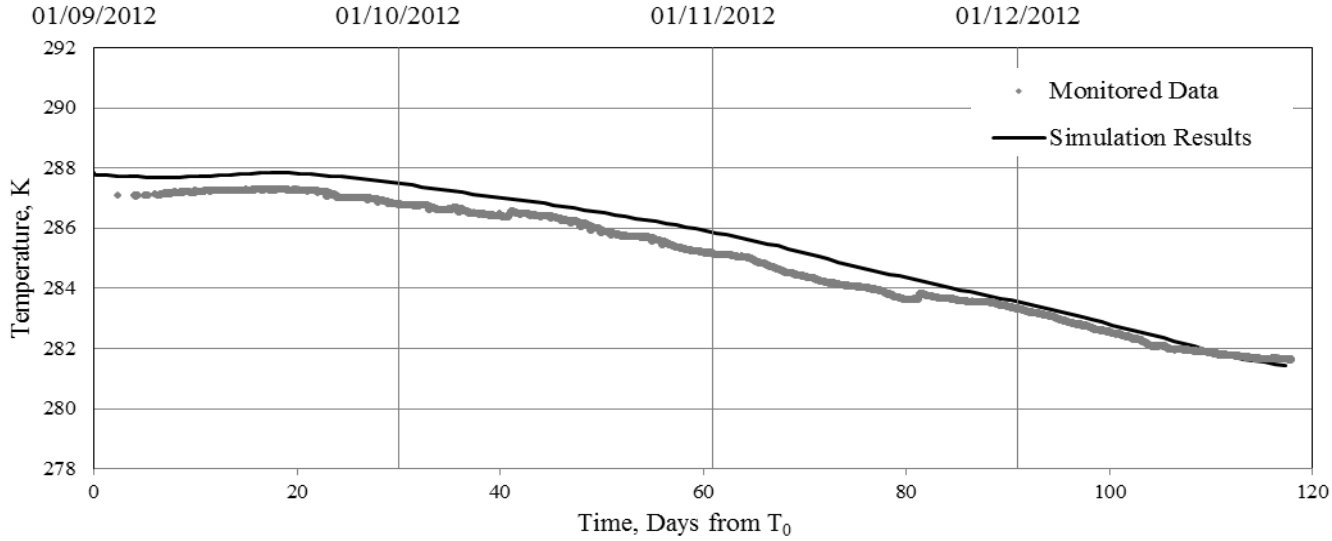

Figure G4- Simulated and monitored ground temperatures at thermistor location AA4.

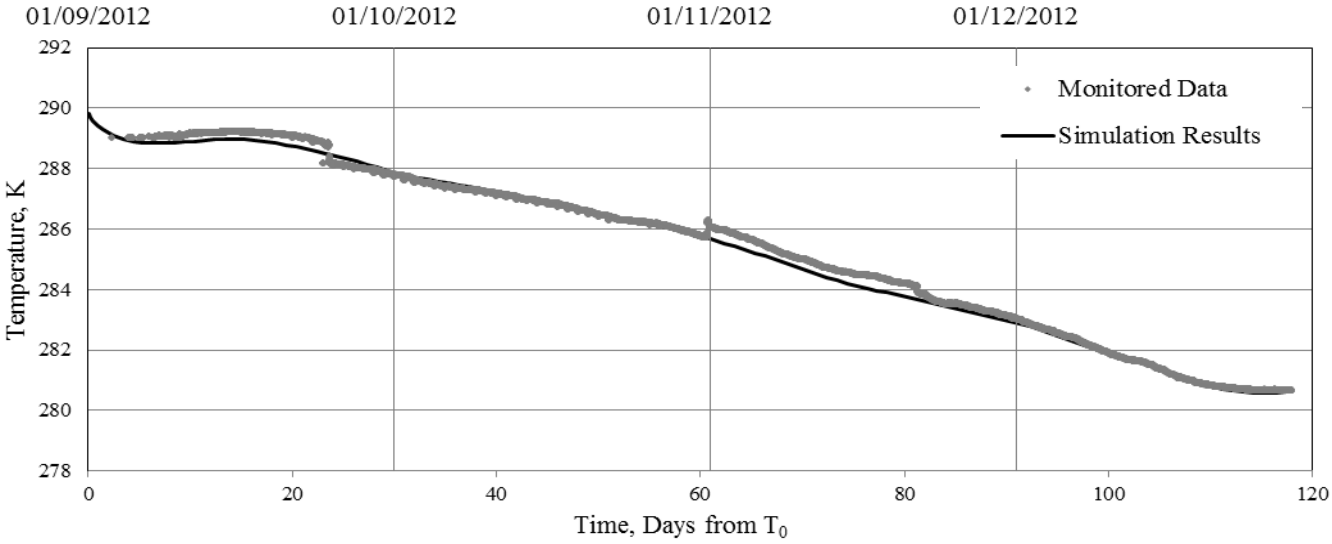

Figure G5 - Simulated and monitored ground temperatures at thermistor location AA5.

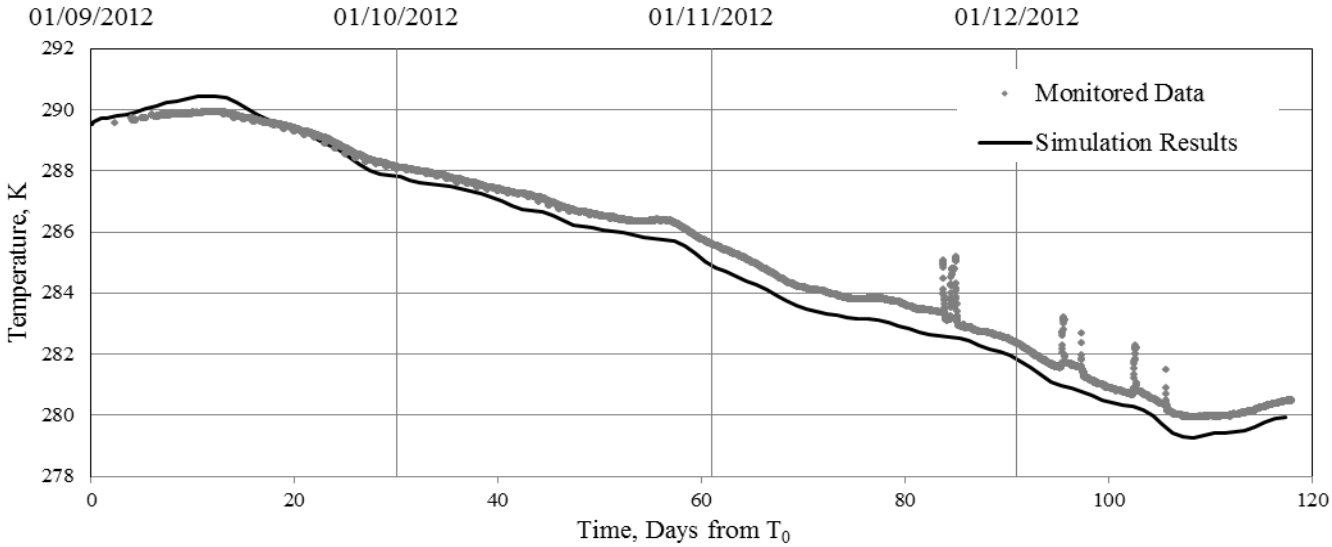

Figure G6 - Simulated and monitored ground temperatures at thermistor location AA6.

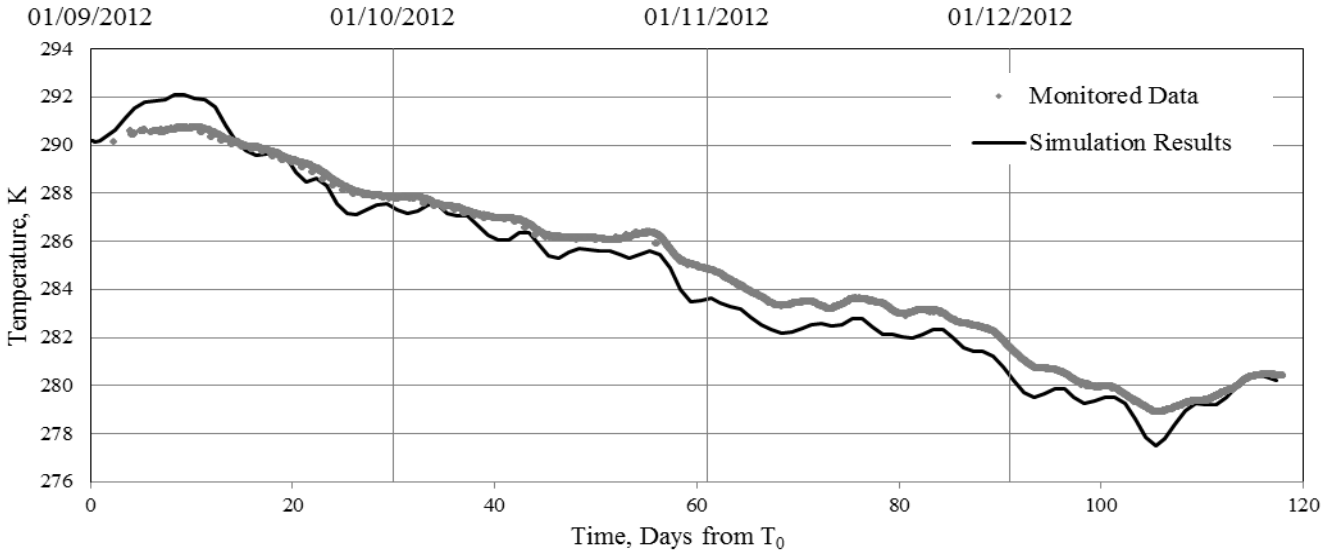

Figure G7 - Simulated and monitored ground temperatures at thermistor location AA8.

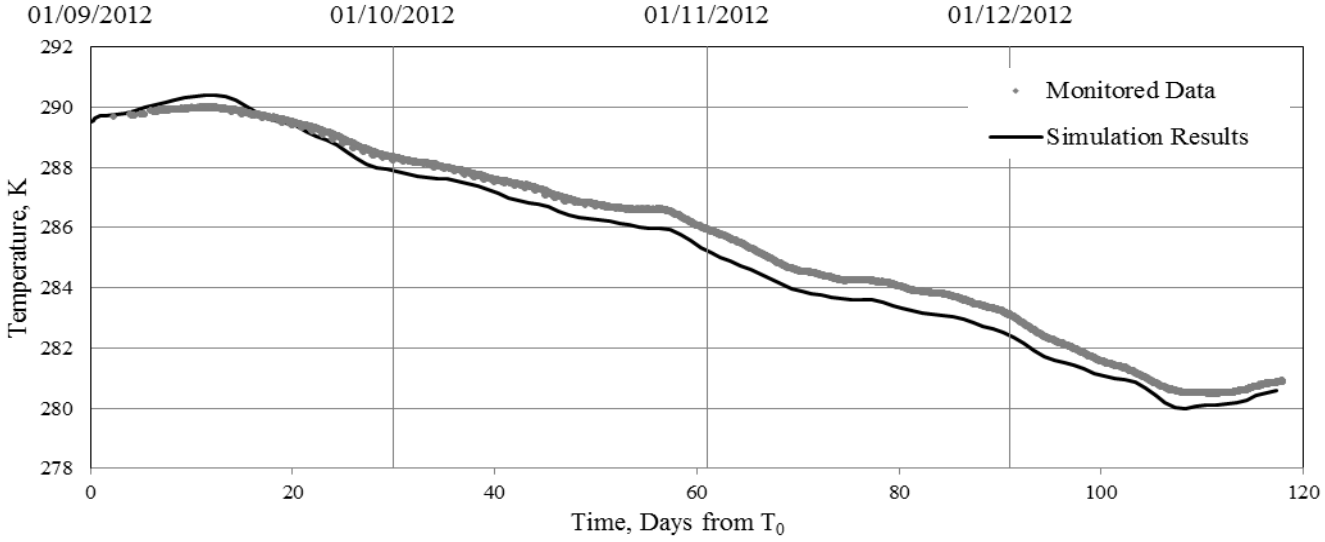

Figure G8 - Simulated and monitored ground temperatures at thermistor location AA9.

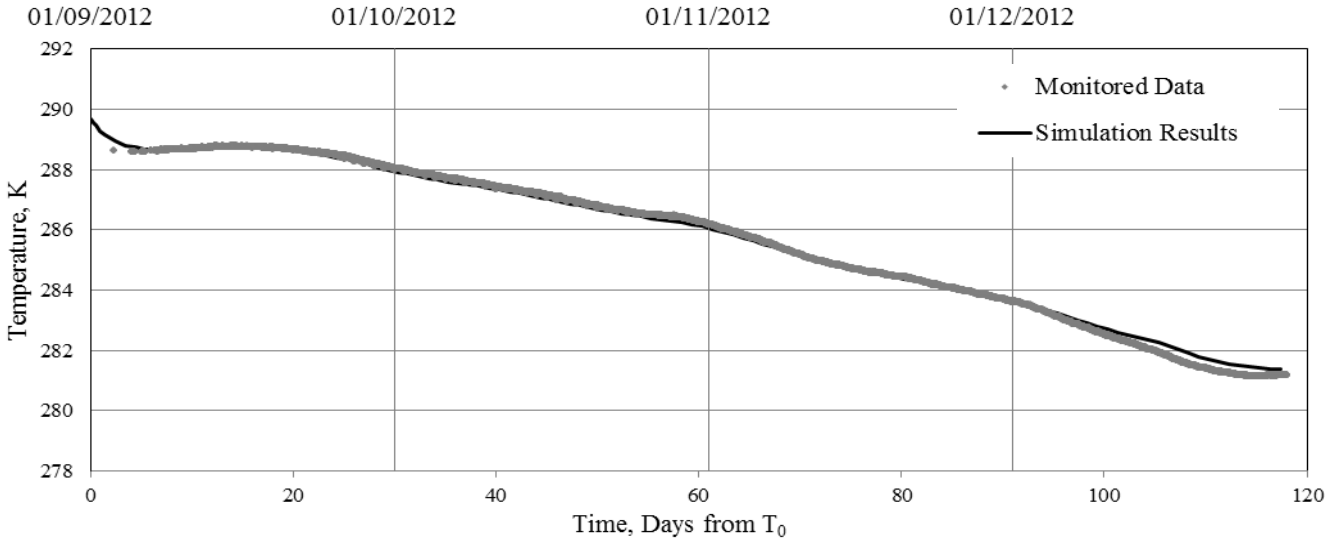

Figure G9 - Simulated and monitored ground temperatures at thermistor location AA10.

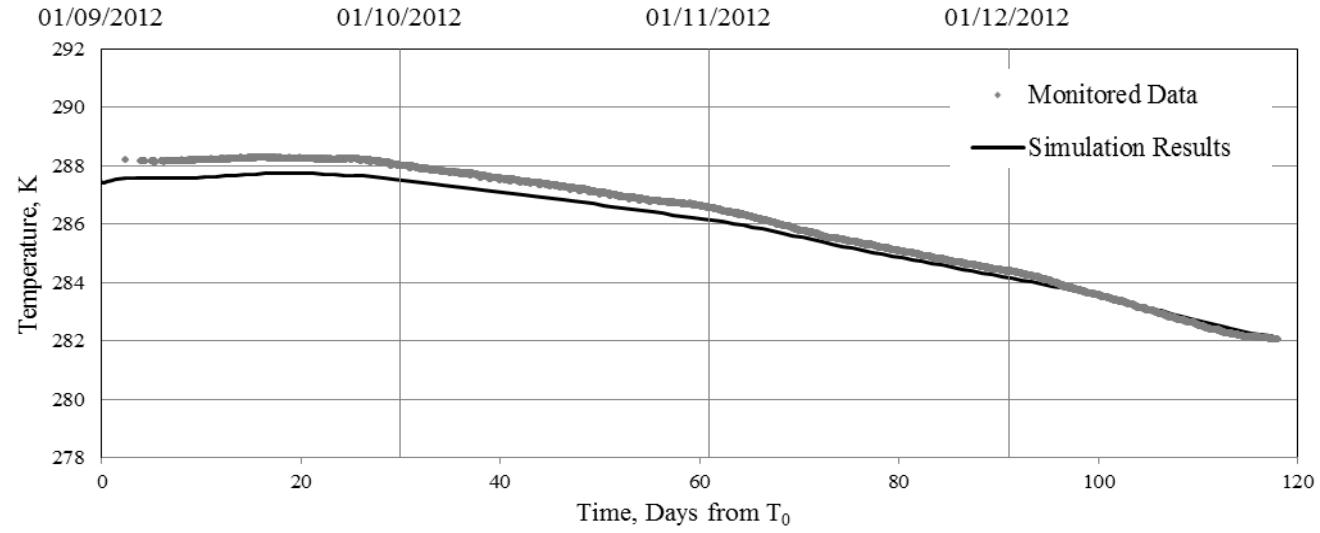

Figure G10 - Simulated and monitored ground temperatures at thermistor location AA11.

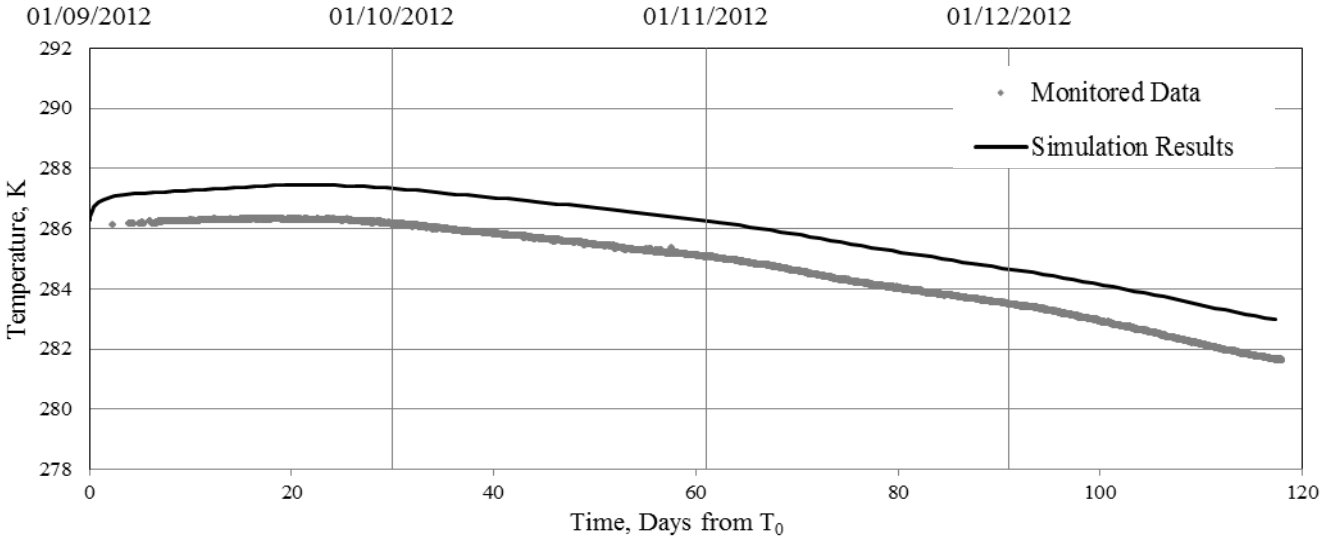

Figure G11 - Simulated and monitored ground temperatures at thermistor location AA12.

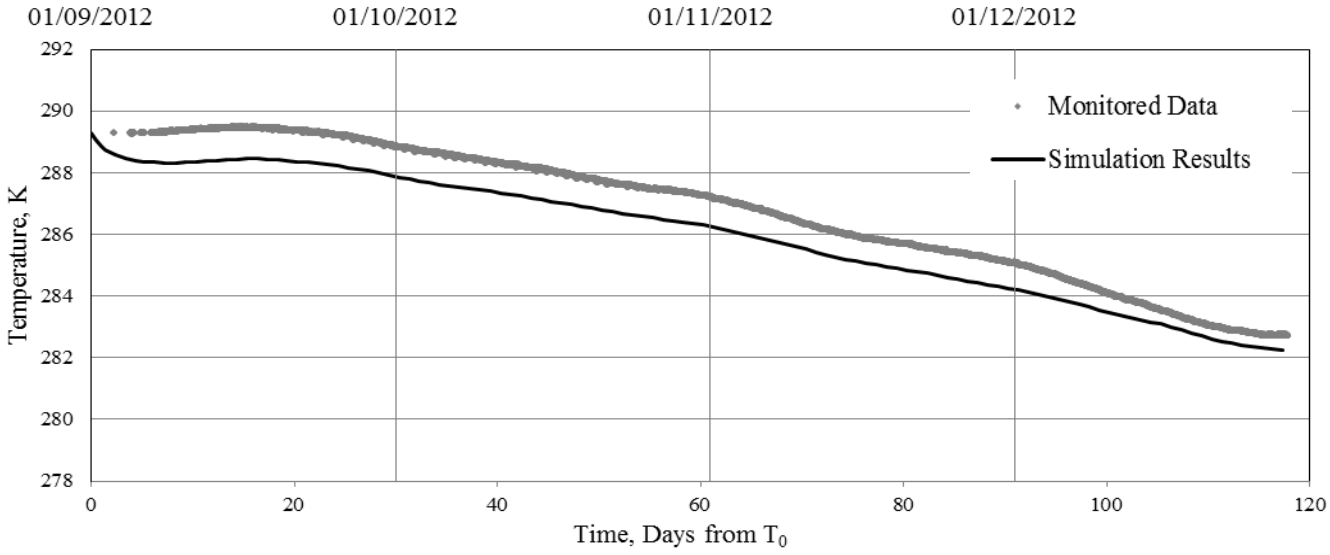

Figure G12 - Simulated and monitored ground temperatures at thermistor location AA13.

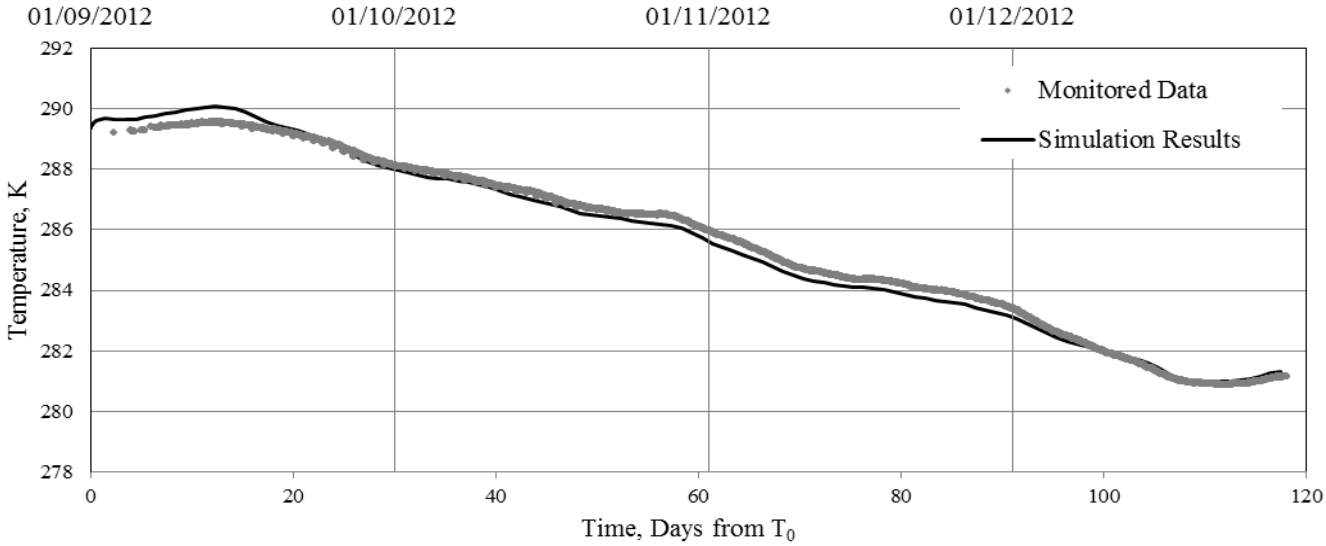

Figure G13 - Simulated and monitored ground temperatures at thermistor location AA14.

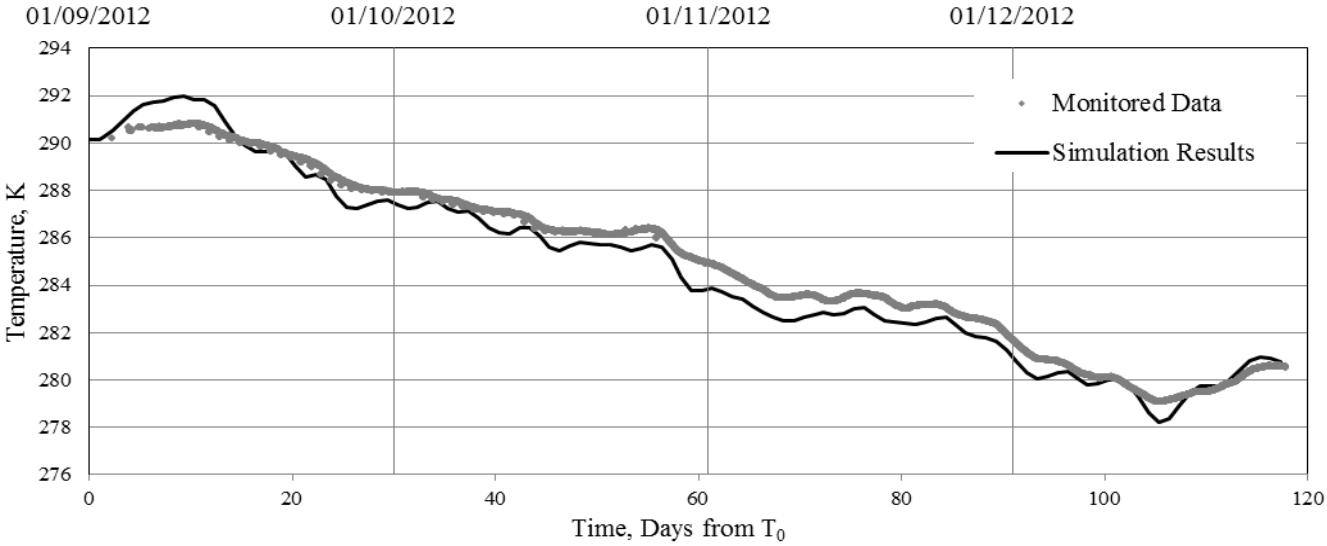

Figure G14 - Simulated and monitored ground temperatures at thermistor location AA15.

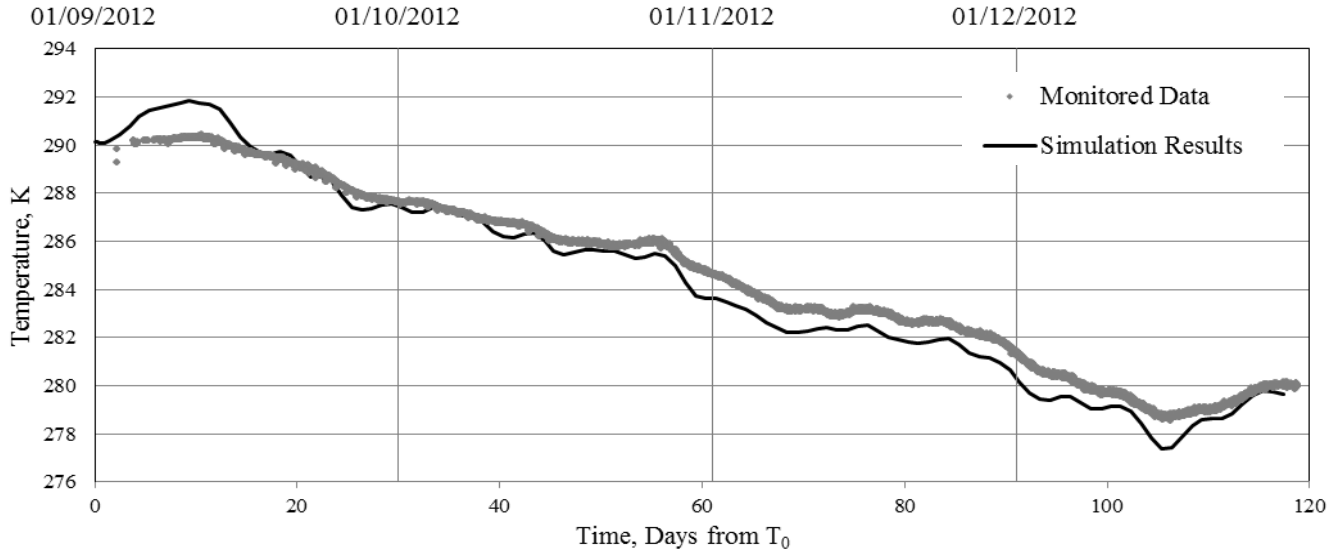

Figure G15 - Simulated and monitored ground temperatures at thermistor location AB1.

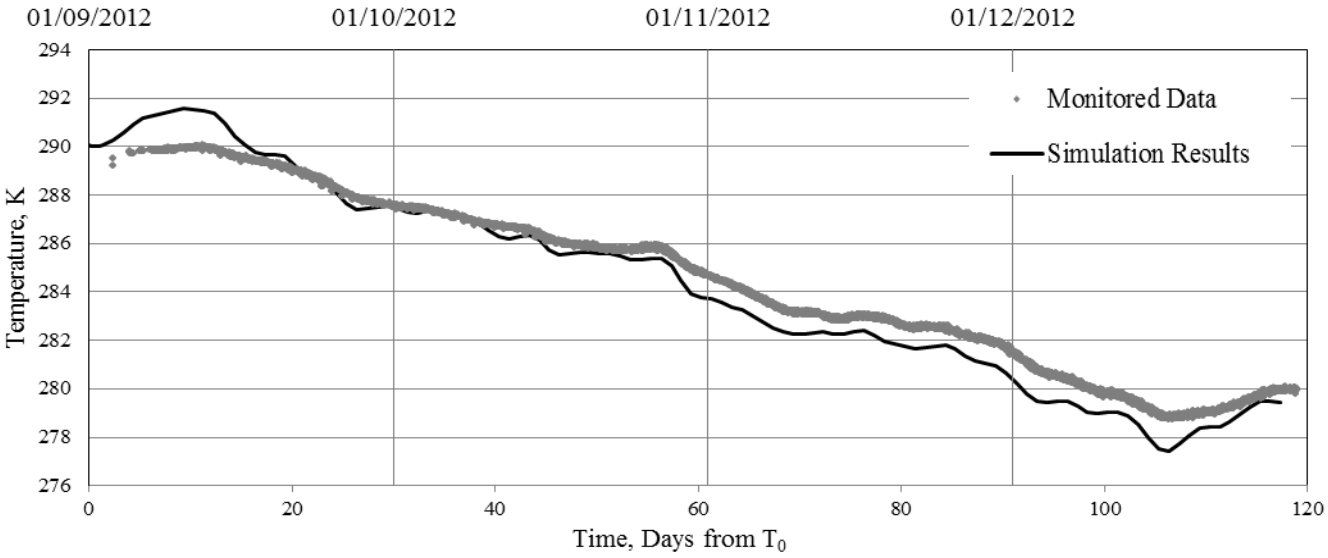

Figure G16 - Simulated and monitored ground temperatures at thermistor location AB2.

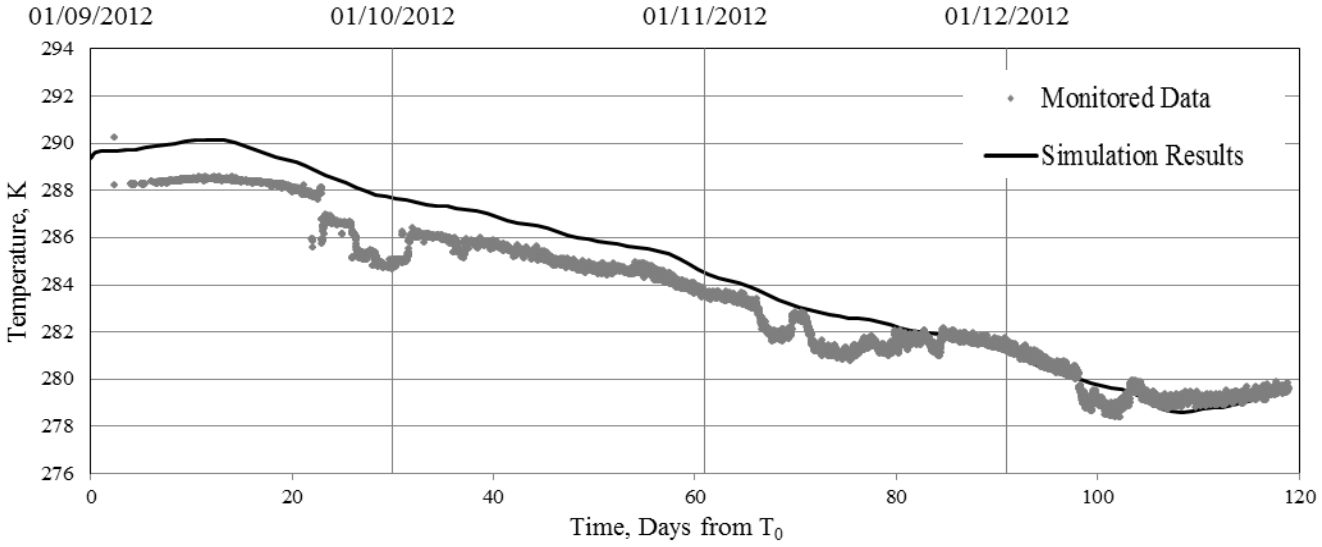

Figure G17 - Simulated and monitored ground temperatures at thermistor location AB3.

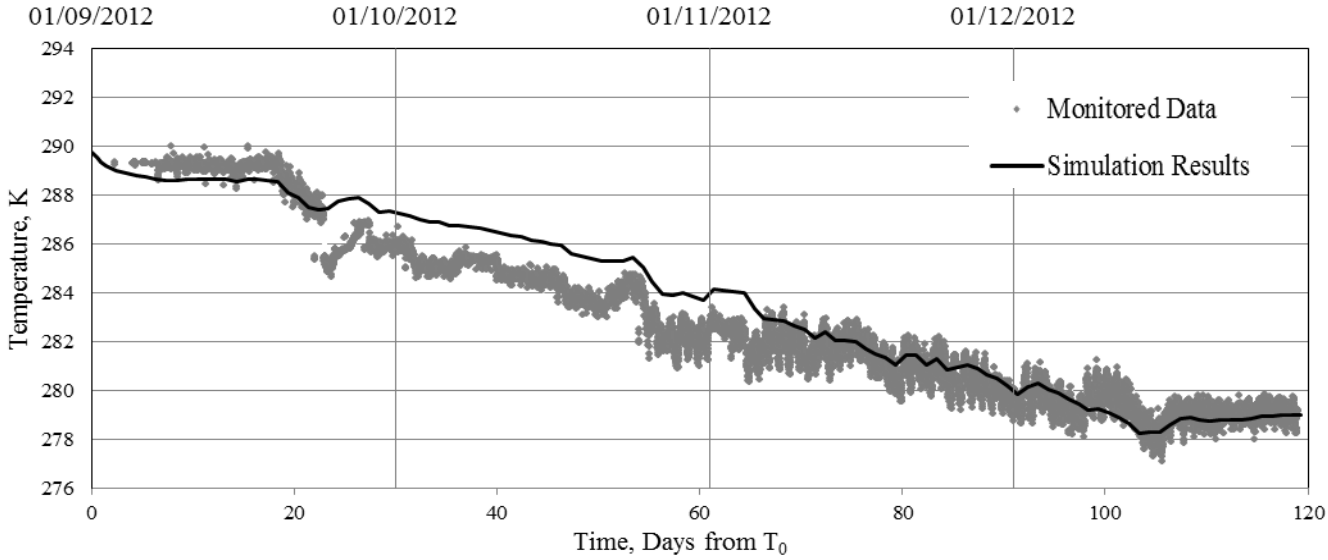

Figure G18 - Simulated and monitored ground temperatures at thermistor location AB4.

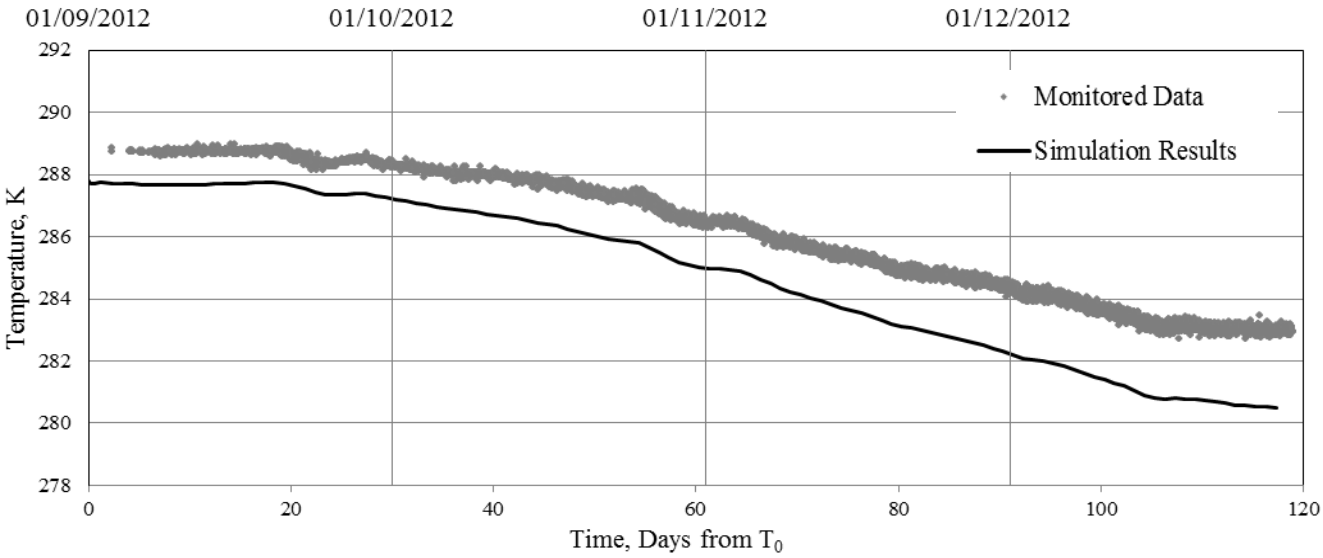

Figure G19 - Simulated and monitored ground temperatures at thermistor location AB5.

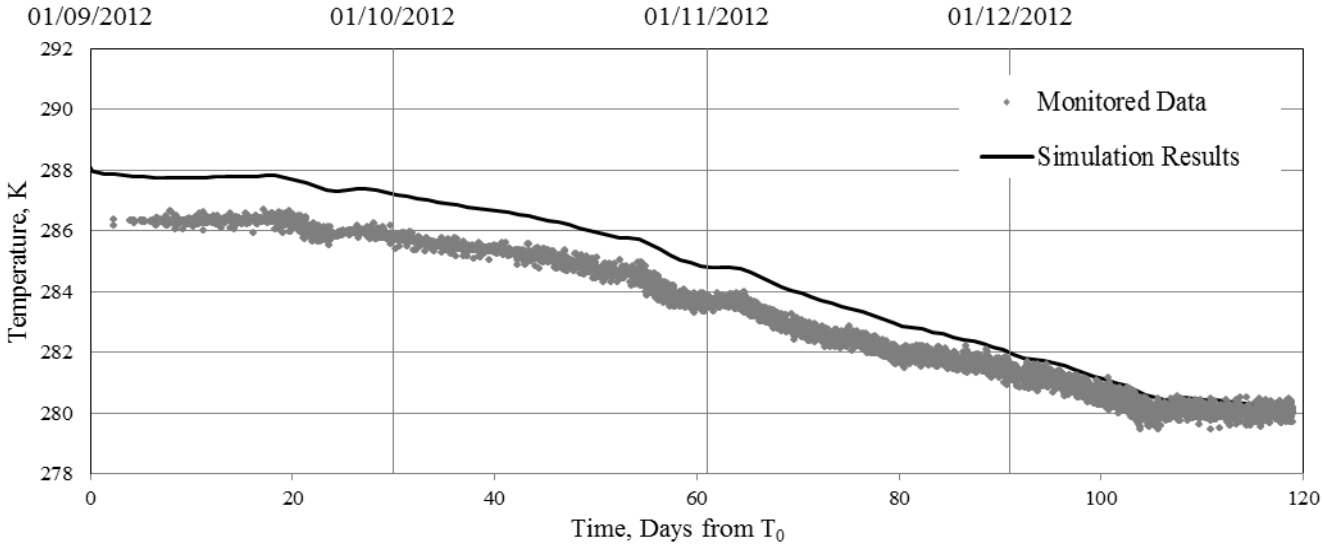

Figure G20 - Simulated and monitored ground temperatures at thermistor location AB6.

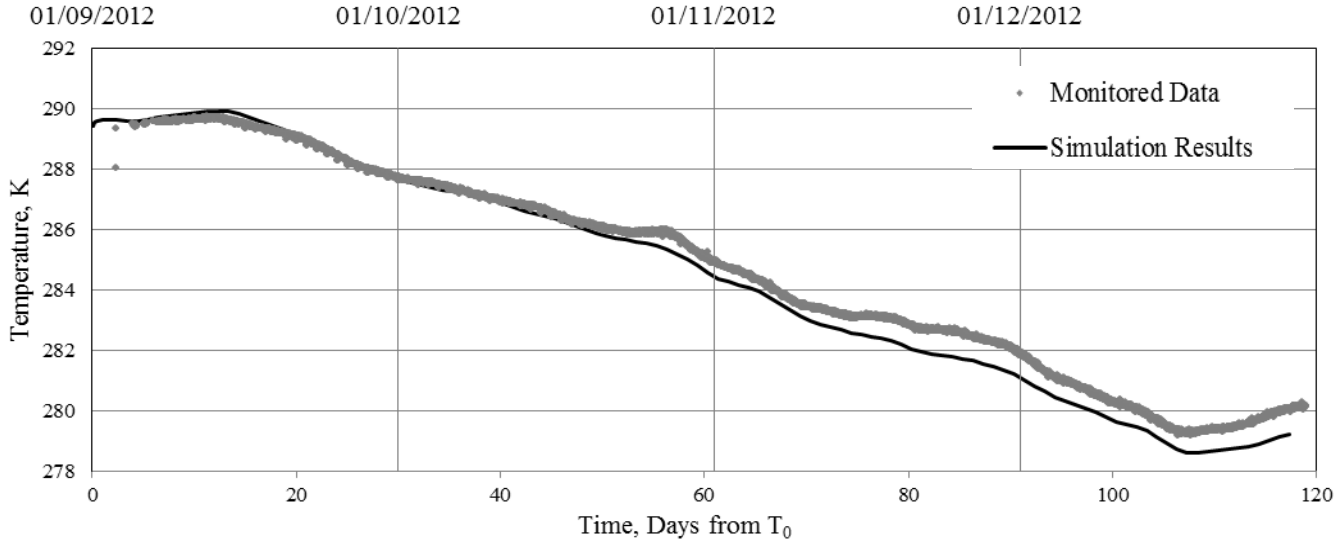

Figure G21 - Simulated and monitored ground temperatures at thermistor location AB8.

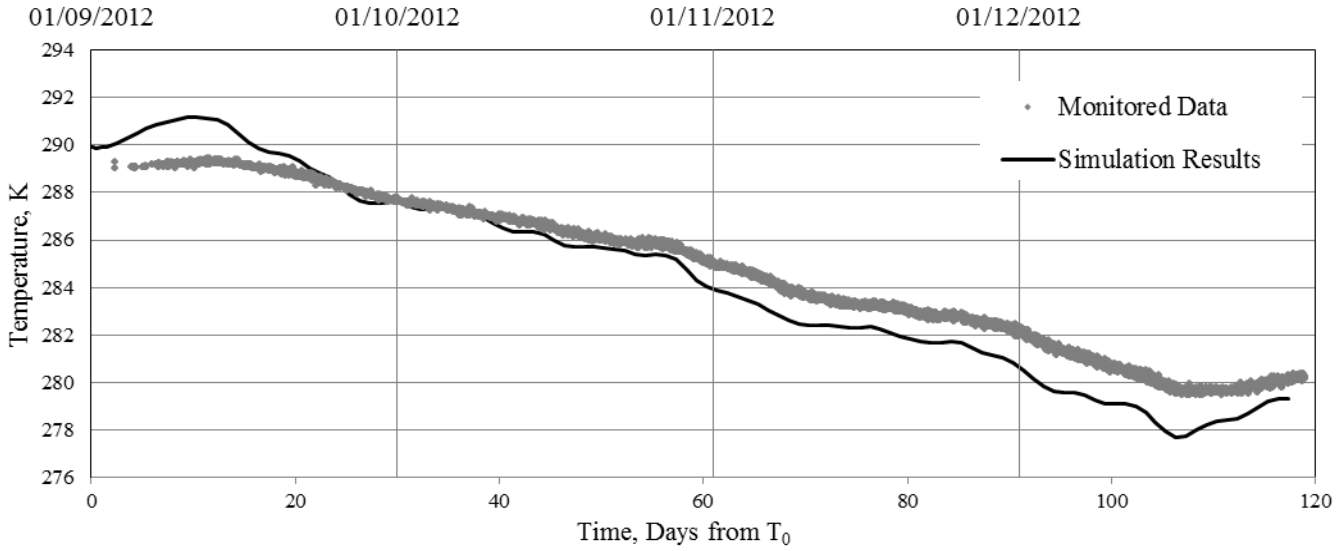

Figure G22 - Simulated and monitored ground temperatures at thermistor location AB9.

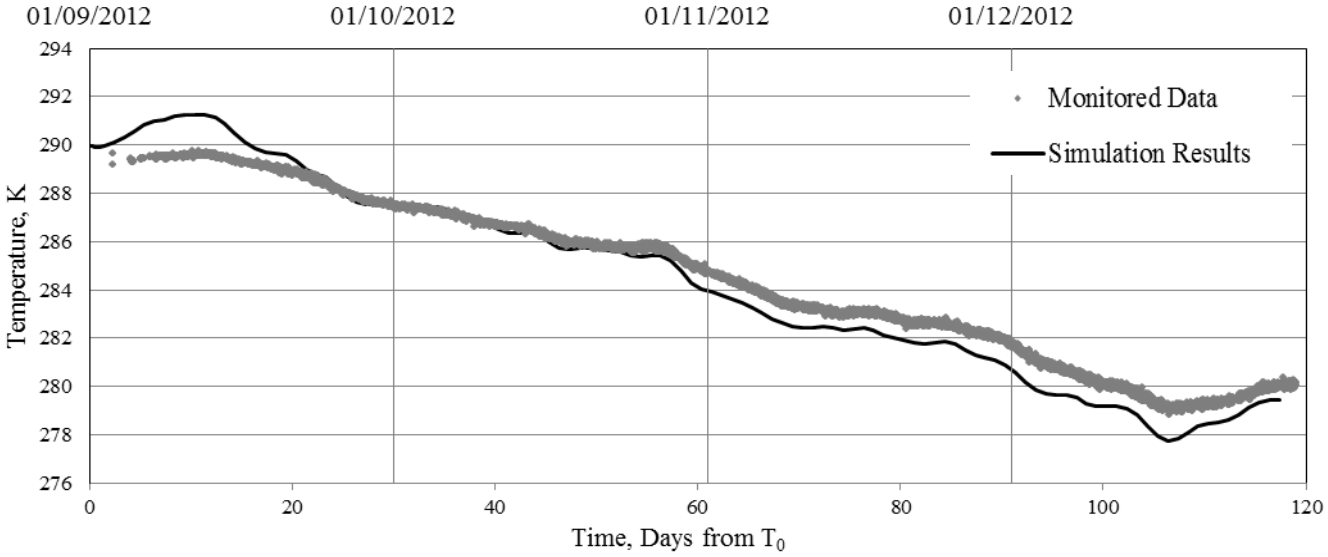

Figure G23 - Simulated and monitored ground temperatures at thermistor location AB10.

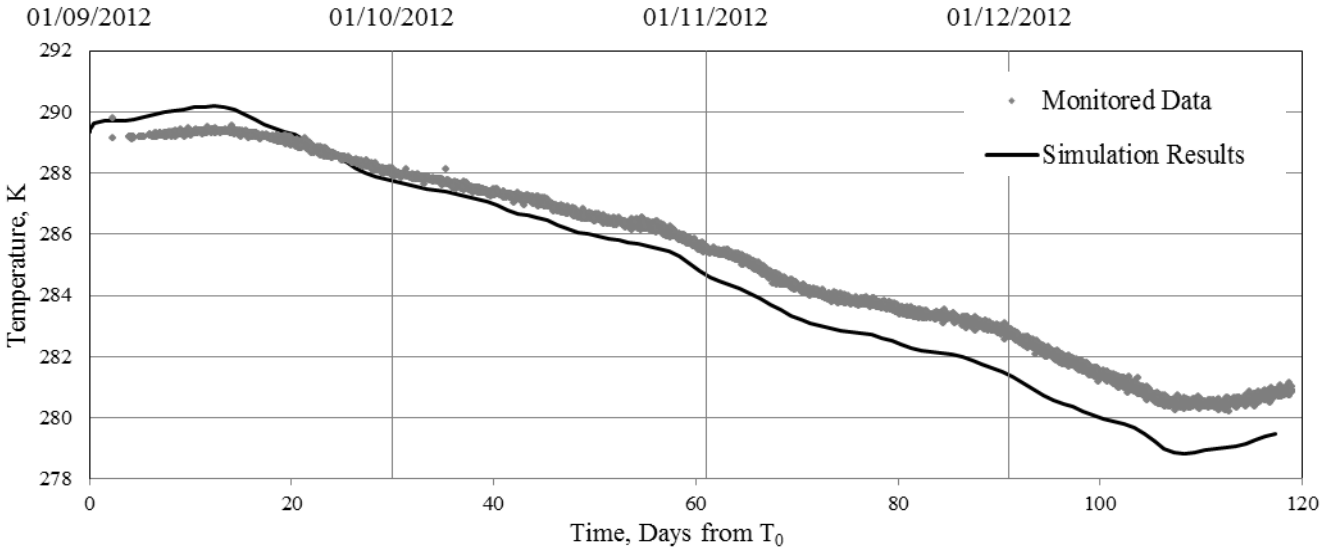

Figure G24 - Simulated and monitored ground temperatures at thermistor location AB11.

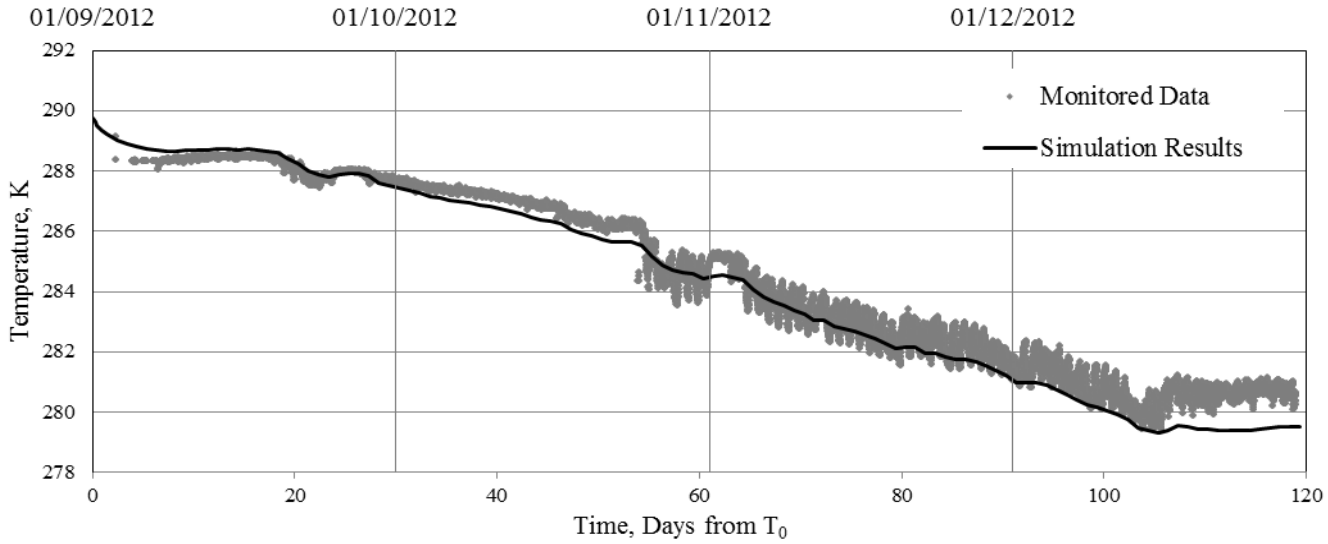

Figure G25 - Simulated and monitored ground temperatures at thermistor location AB12.

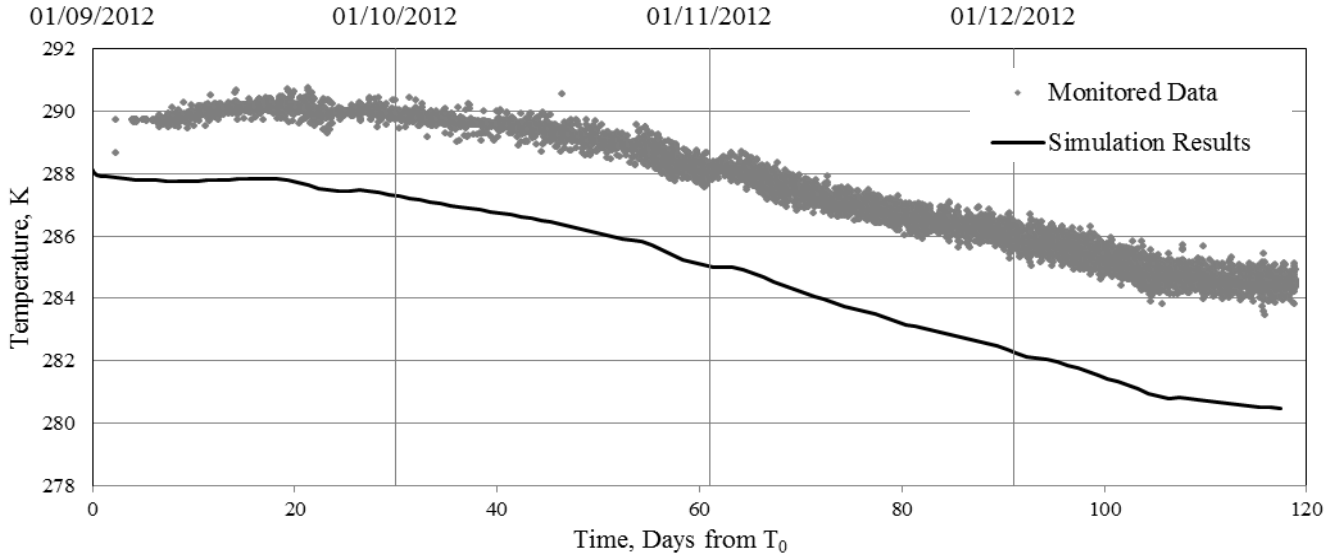

Figure G26 - Simulated and monitored ground temperatures at thermistor location AB13.

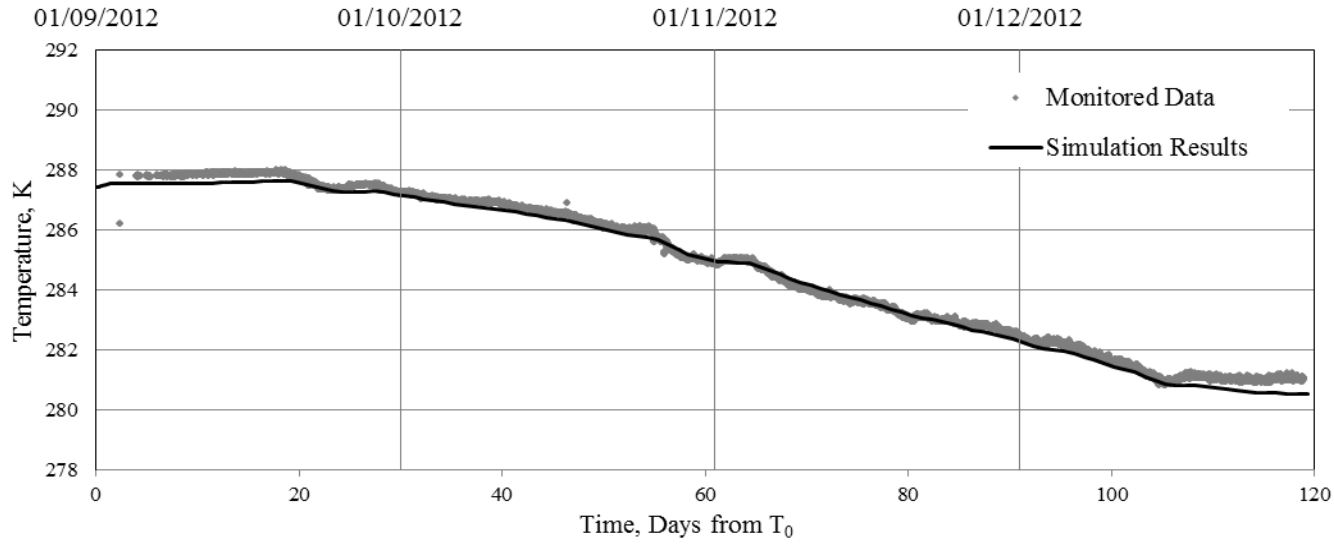

Figure G27 - Simulated and monitored ground temperatures at thermistor location AB14.

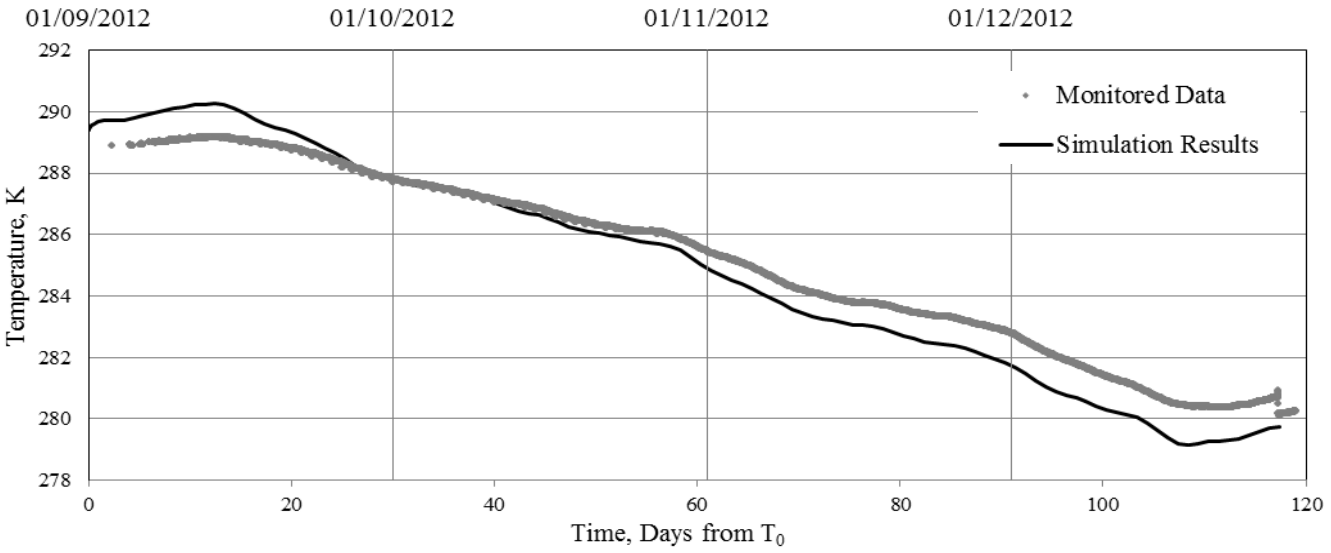

Figure G28 - Simulated and monitored ground temperatures at thermistor location AC2.

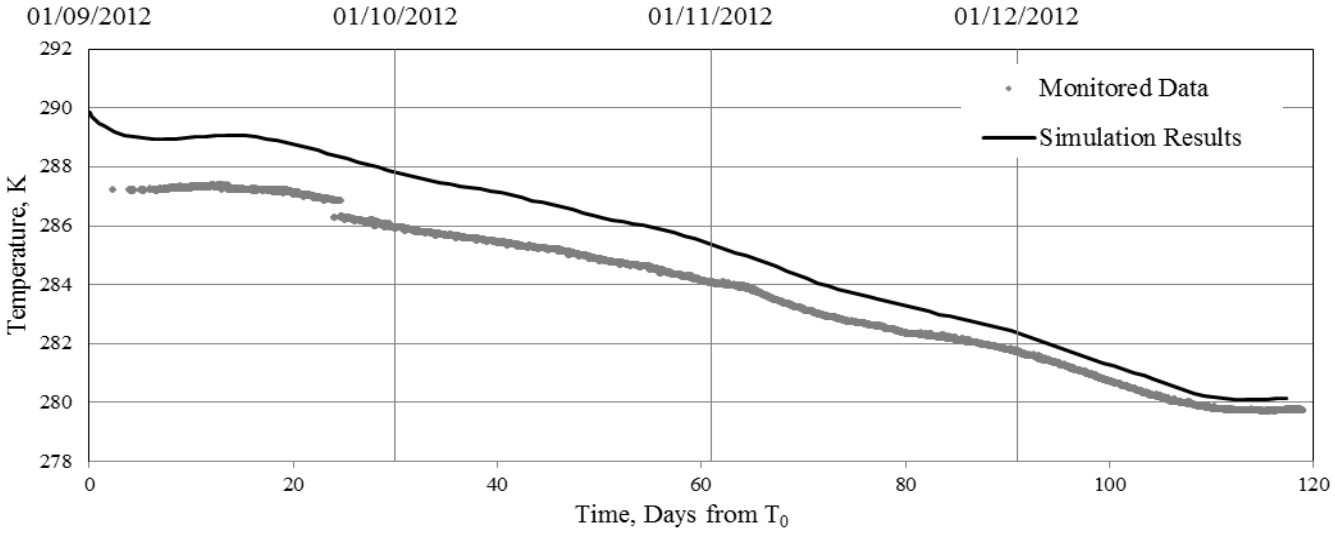

Figure G29 - Simulated and monitored ground temperatures at thermistor location AC3.

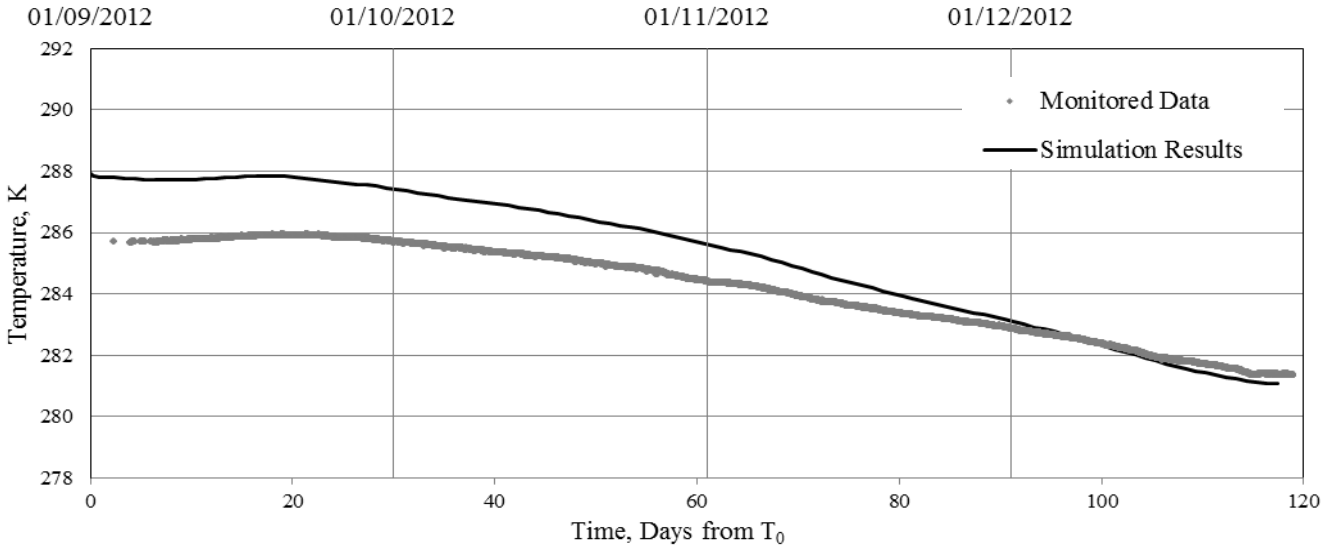

Figure G30 - Simulated and monitored ground temperatures at thermistor location AC4.

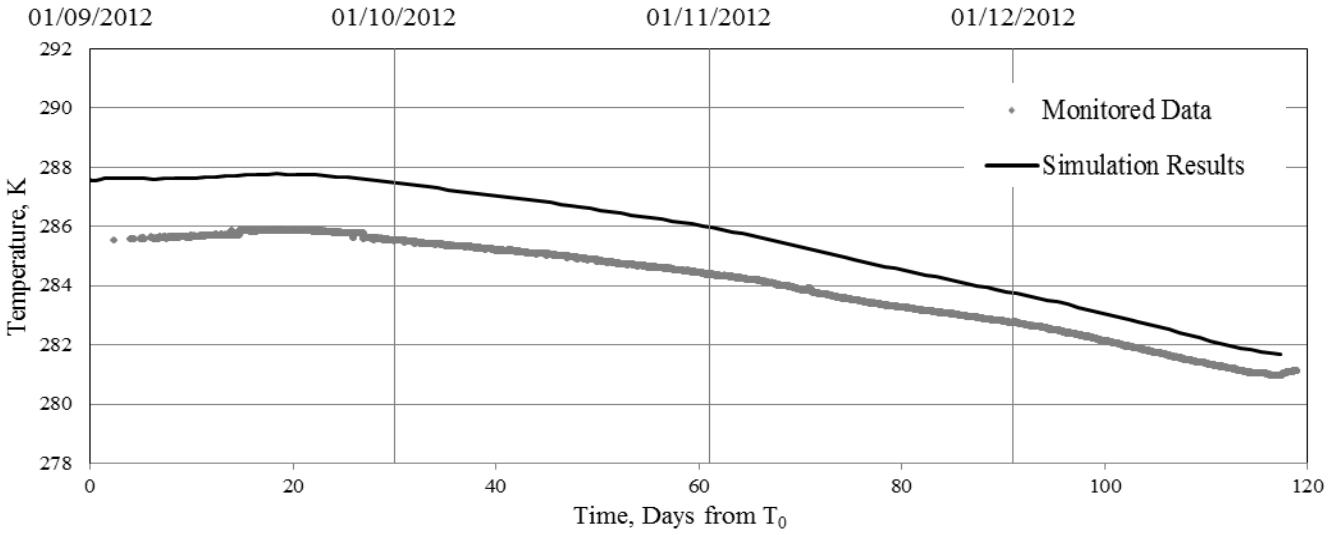

Figure G31 - Simulated and monitored ground temperatures at thermistor location AC5.

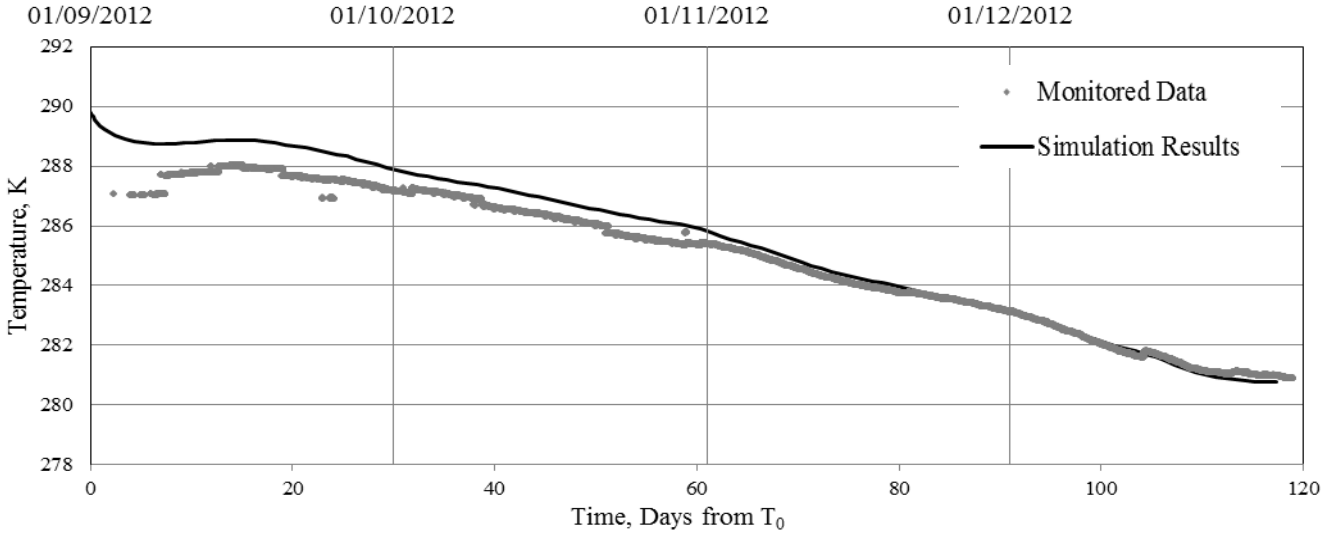

Figure G32 - Simulated and monitored ground temperatures at thermistor location AC6.

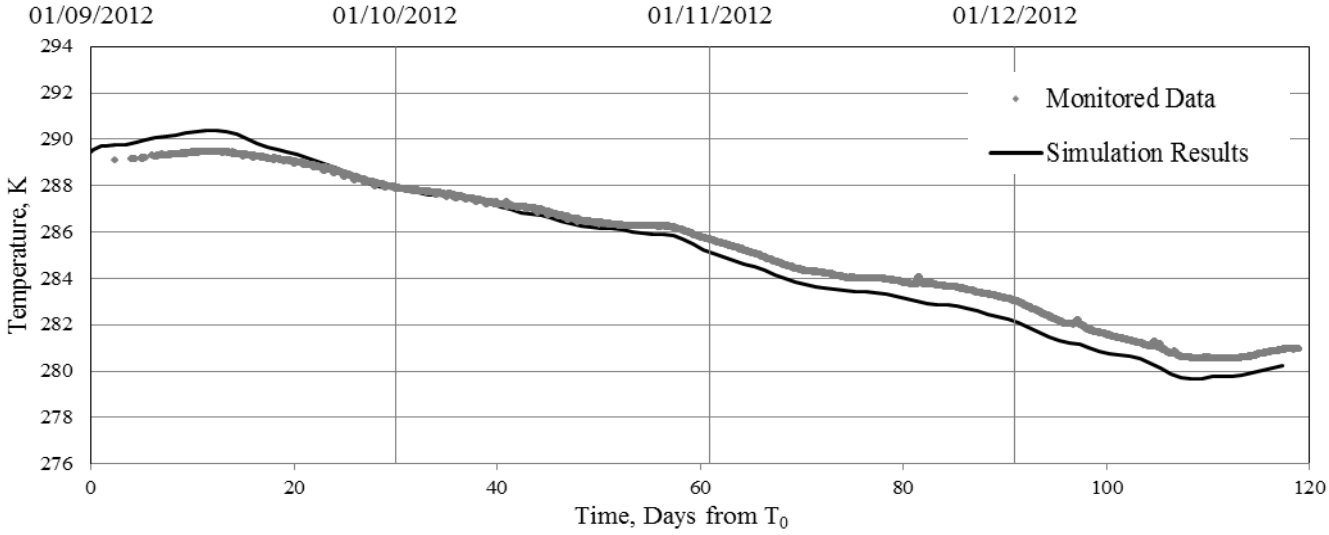

Figure G33 - Simulated and monitored ground temperatures at thermistor location AC7.

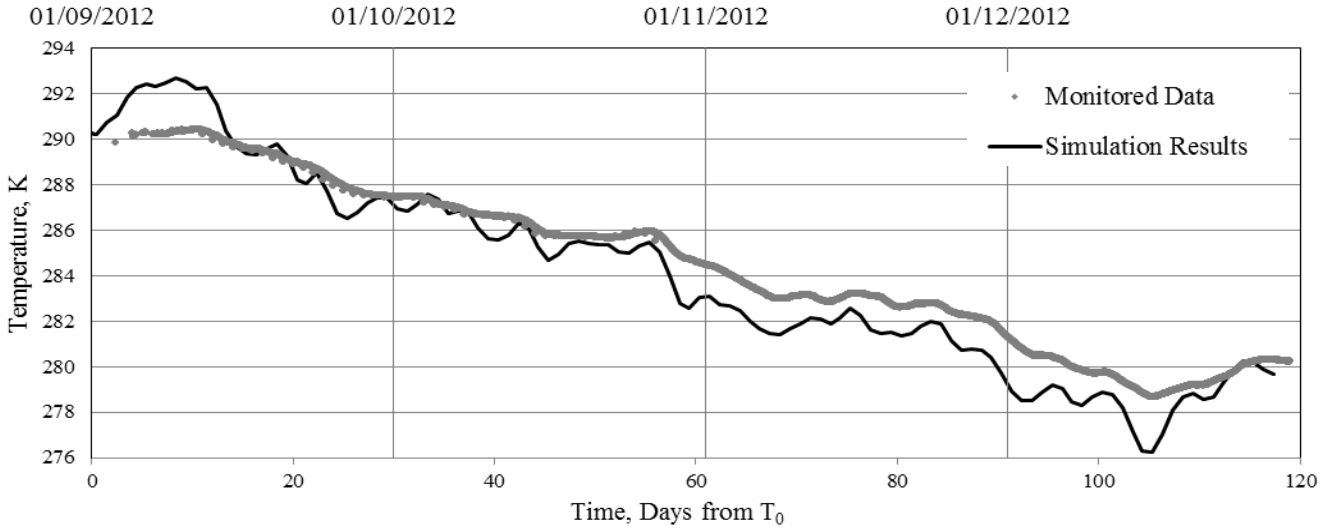

Figure G34 - Simulated and monitored ground temperatures at thermistor location AC8.

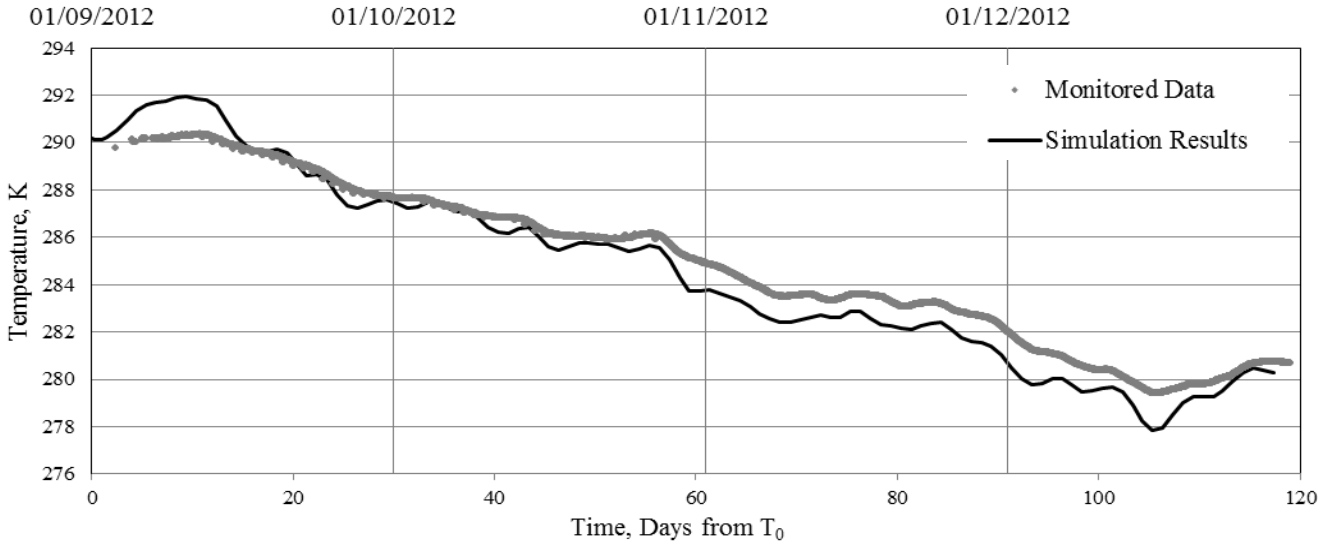

Figure G35 - Simulated and monitored ground temperatures at thermistor location AC9.

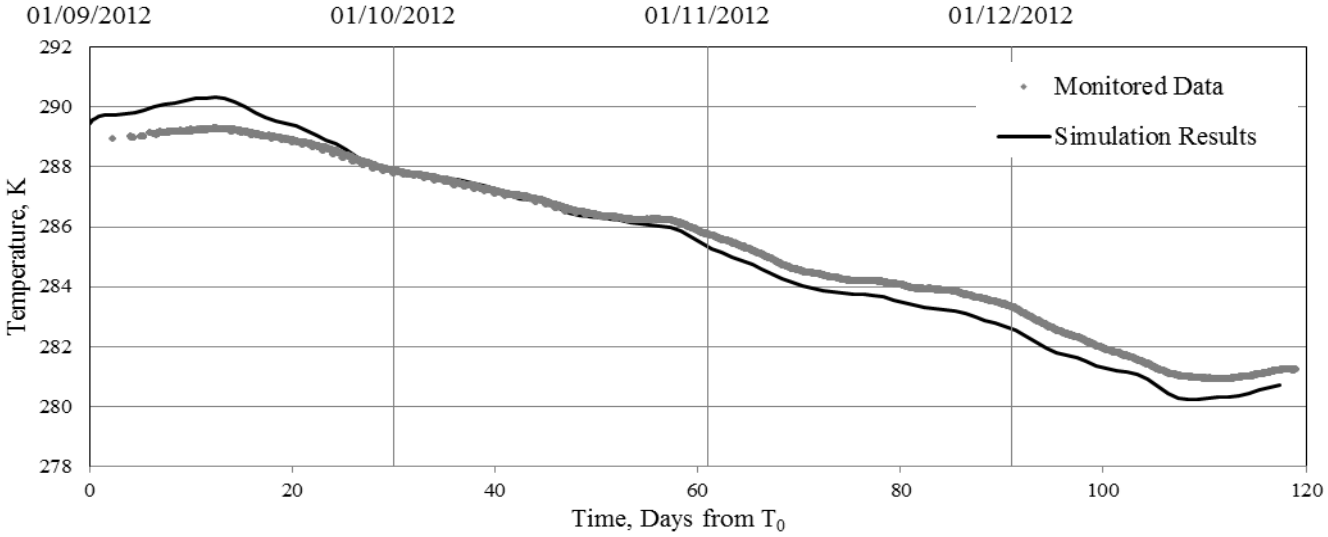

Figure G36 - Simulated and monitored ground temperatures at thermistor location AC10.

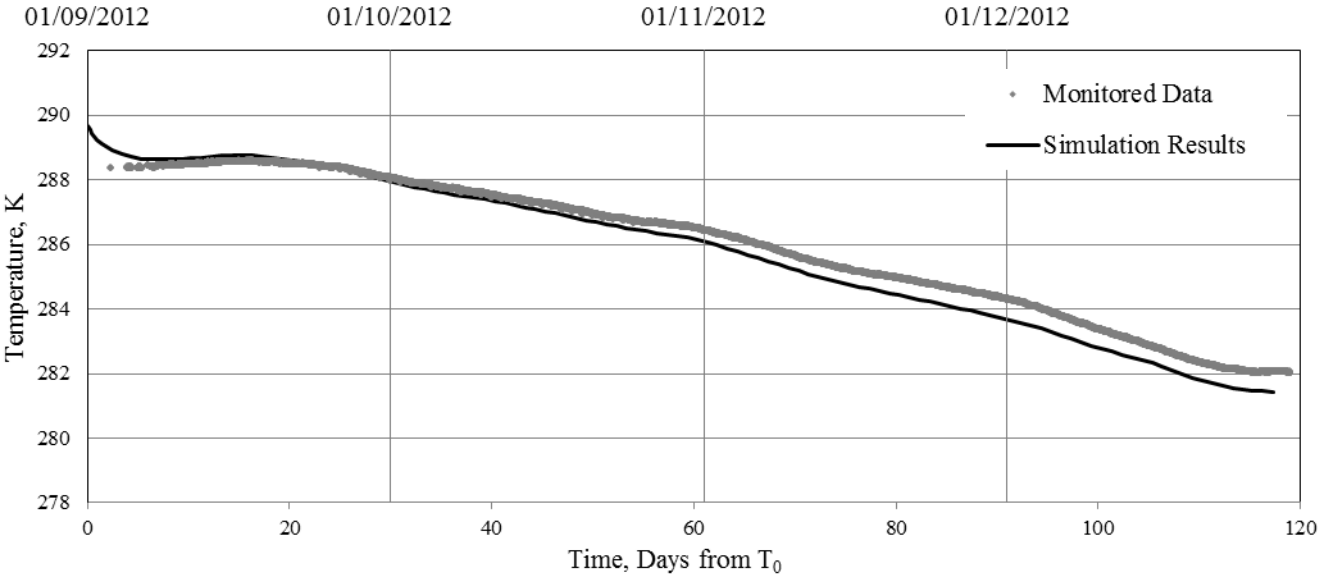

Figure G37 - Simulated and monitored ground temperatures at thermistor location AC11.

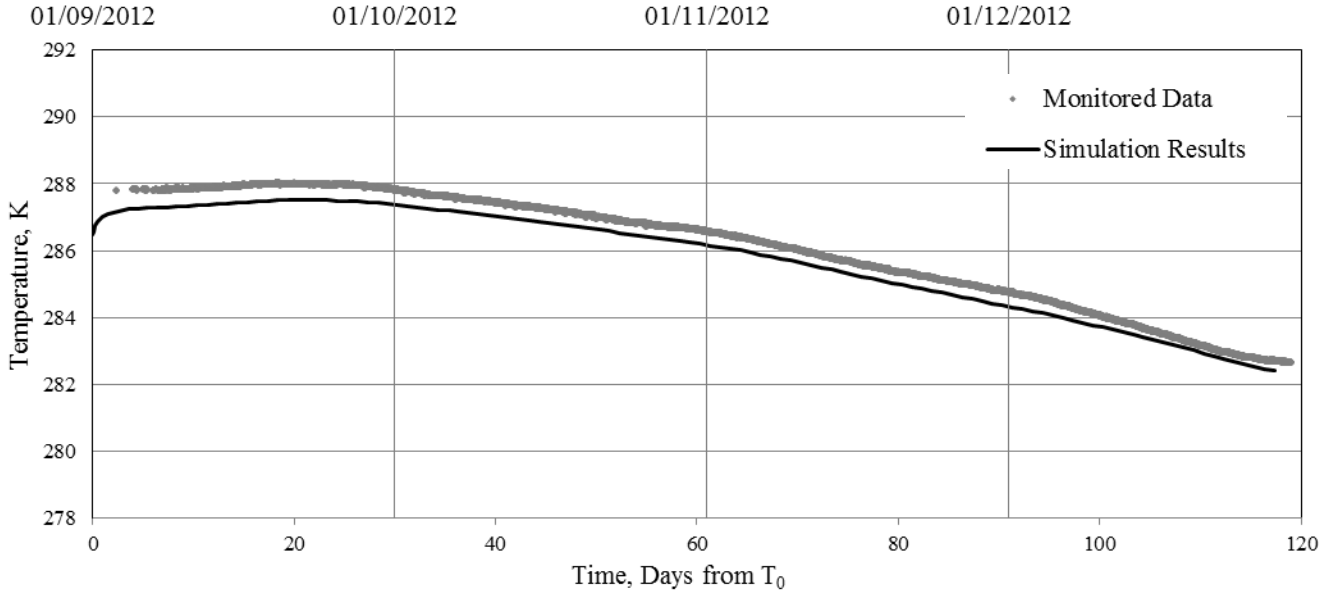

Figure G38 - Simulated and monitored ground temperatures at thermistor location AC12.

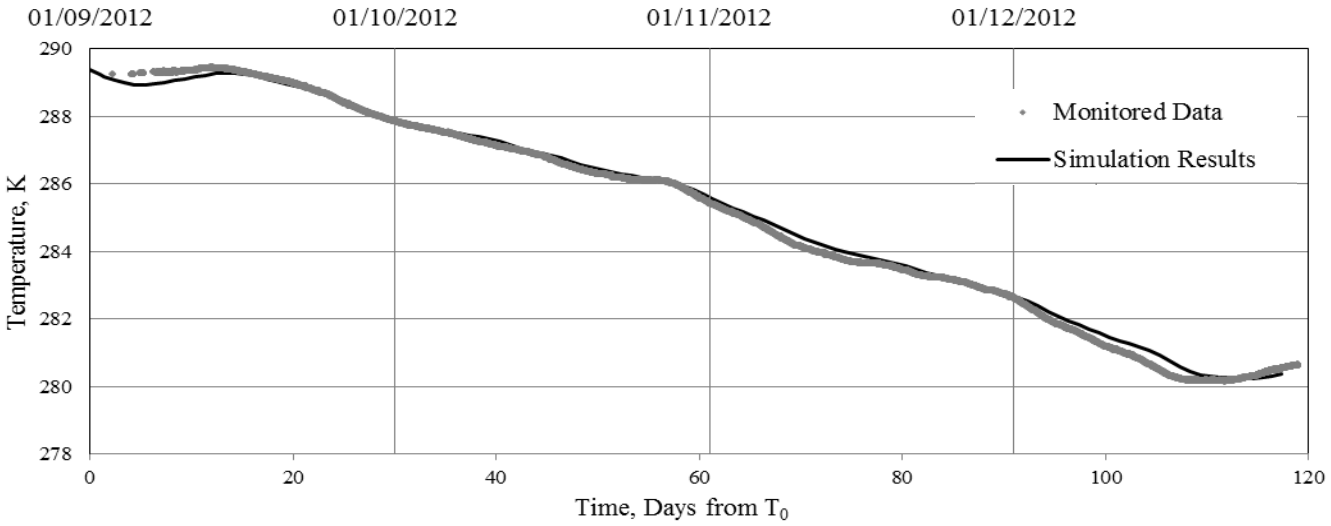

Figure G39 - Simulated and monitored ground temperatures at thermistor location BA1.

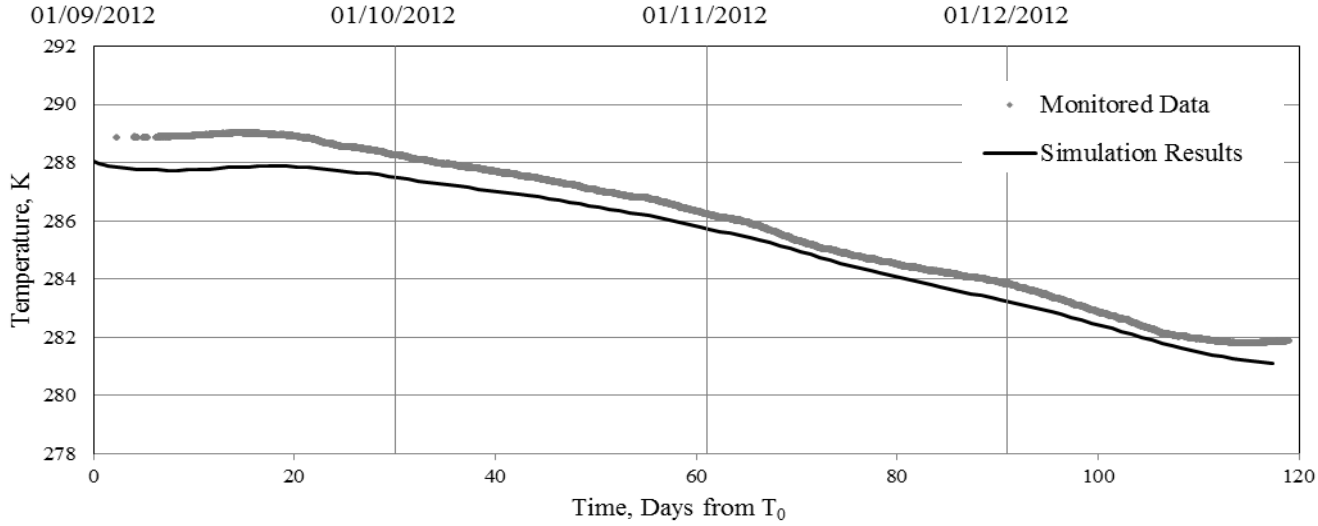

Figure G40 - Simulated and monitored ground temperatures at thermistor location BA2.

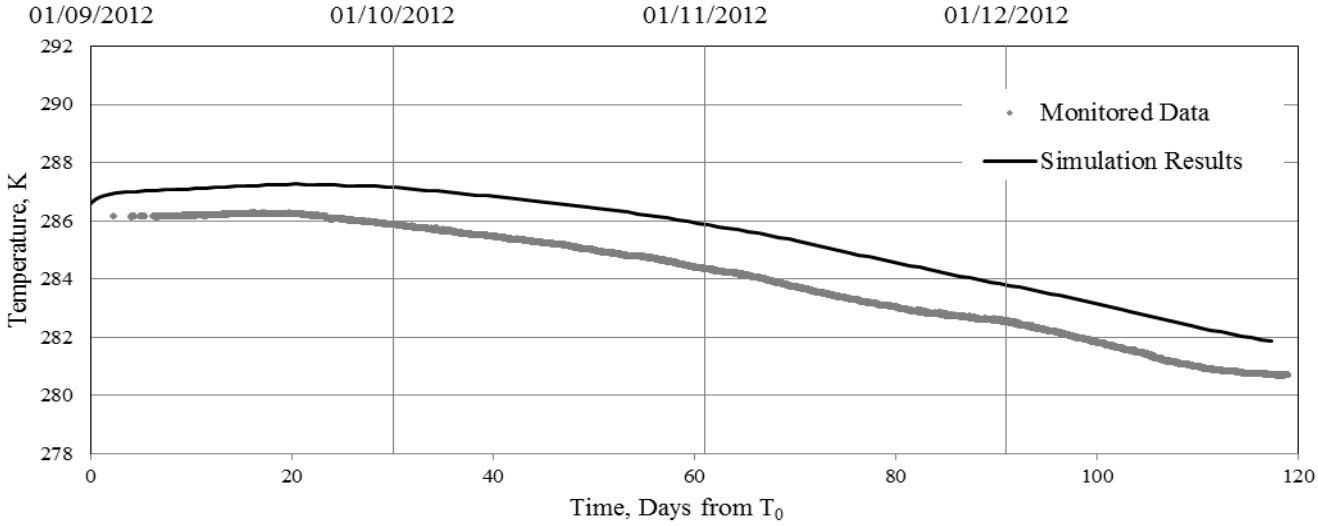

Figure G41 - Simulated and monitored ground temperatures at thermistor location BA3.

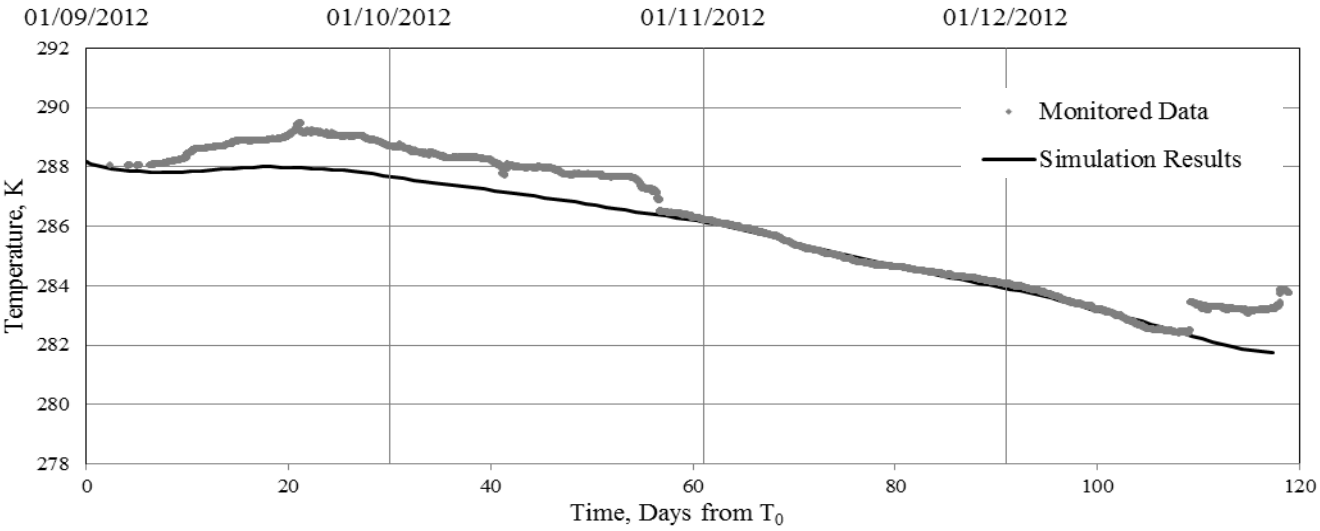

Figure G42 - Simulated and monitored ground temperatures at thermistor location BA5.

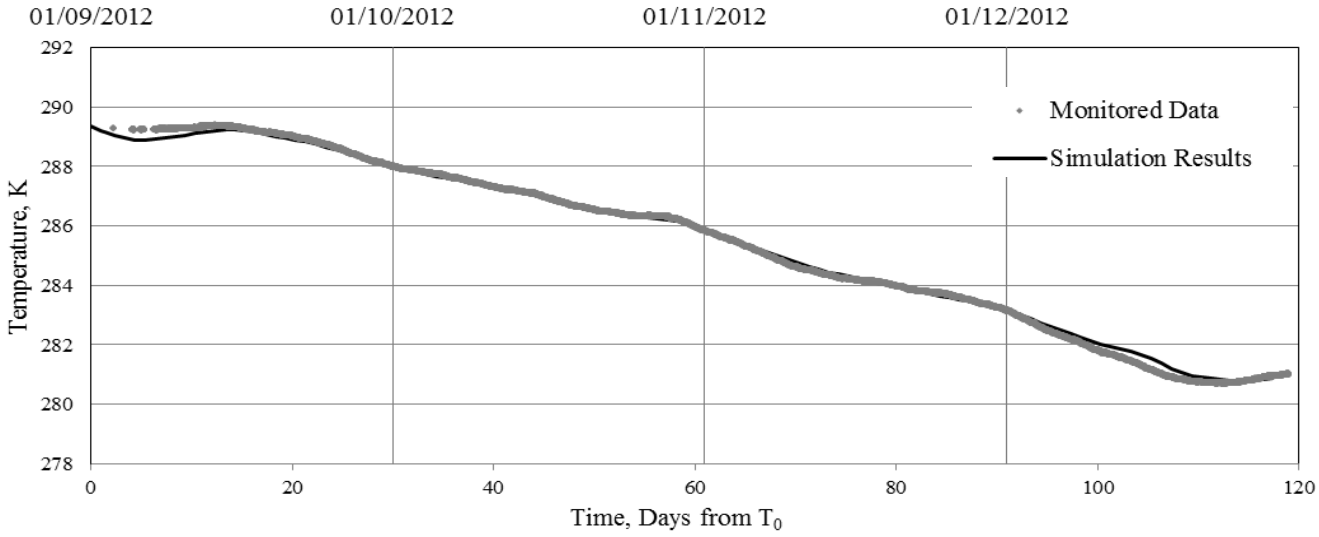

Figure G43 - Simulated and monitored ground temperatures at thermistor location BA6.

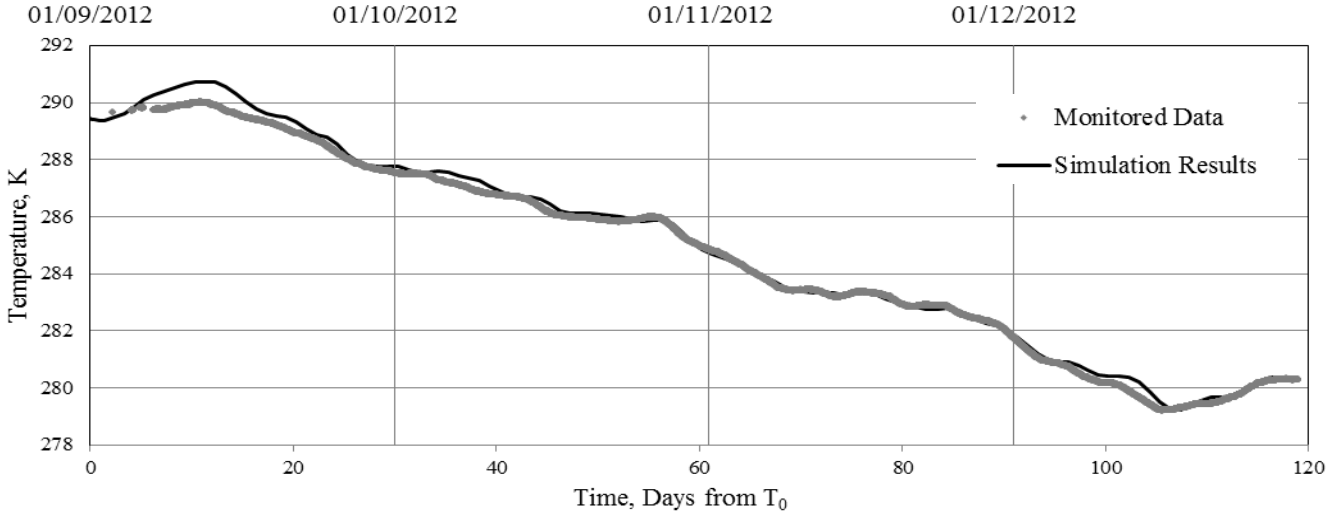

Figure G44 - Simulated and monitored ground temperatures at thermistor location BA7.

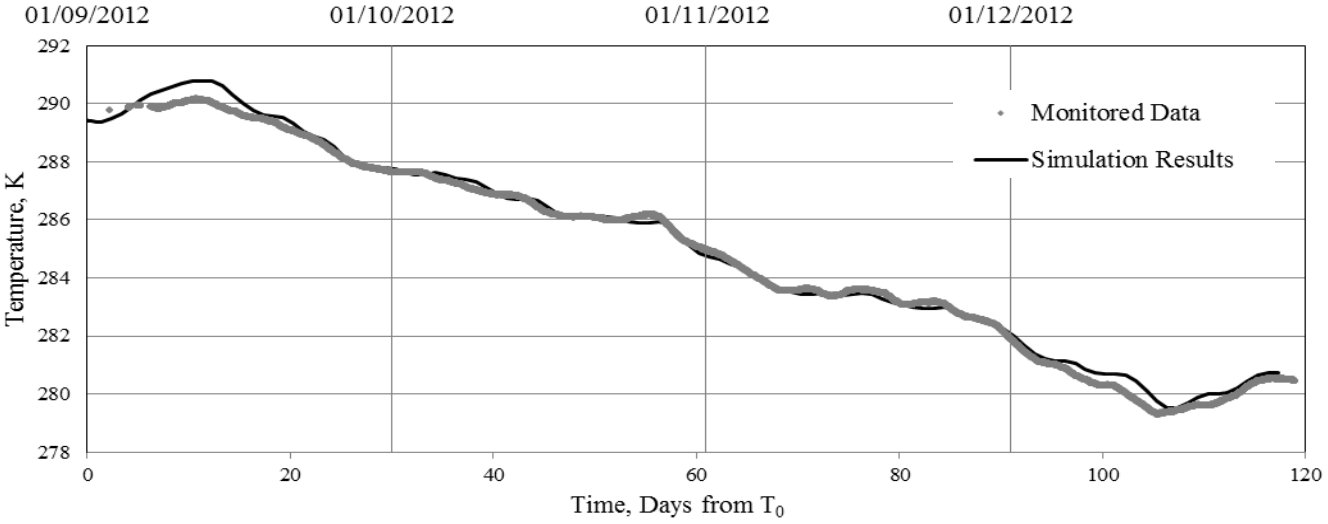

Figure G45 - Simulated and monitored ground temperatures at thermistor location BA8.

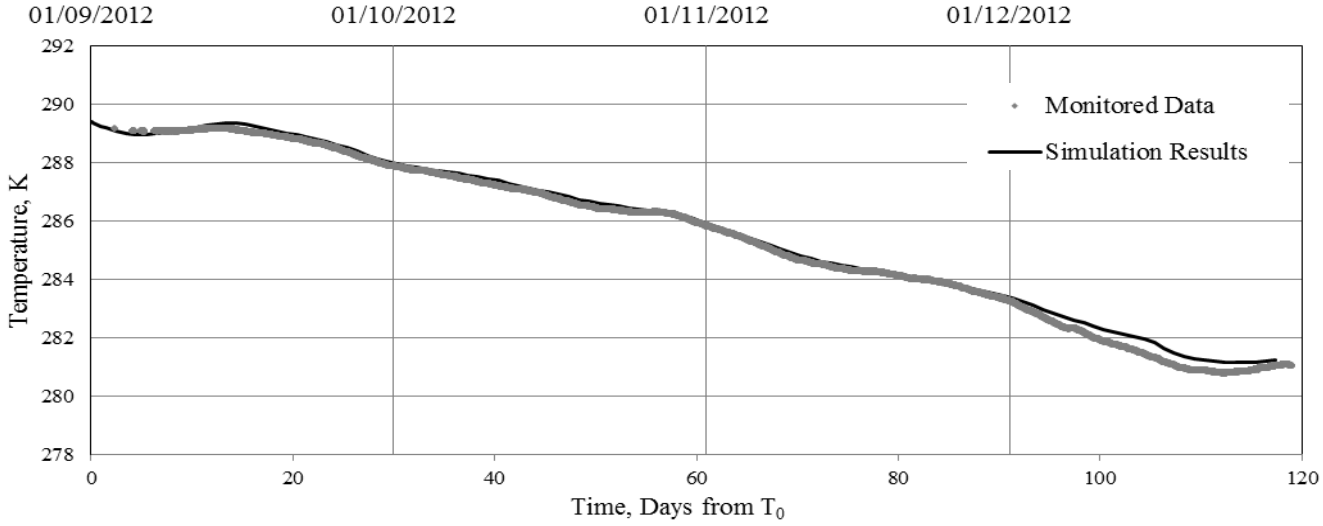

Figure G46 - Simulated and monitored ground temperatures at thermistor location BA9.

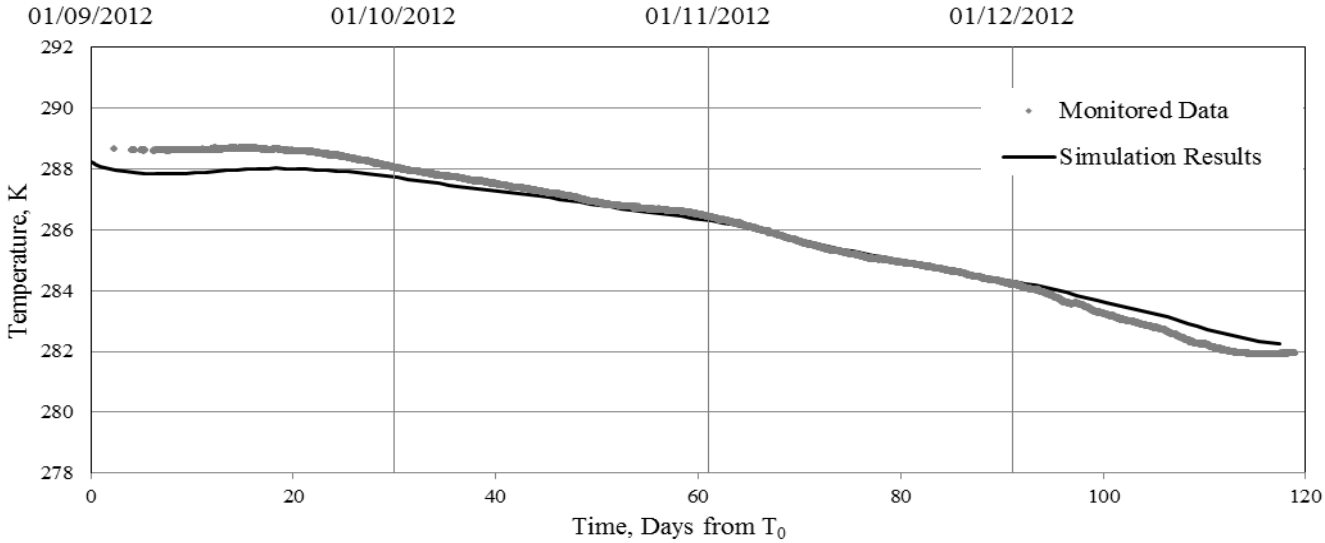

Figure G47 - Simulated and monitored ground temperatures at thermistor location BA10.

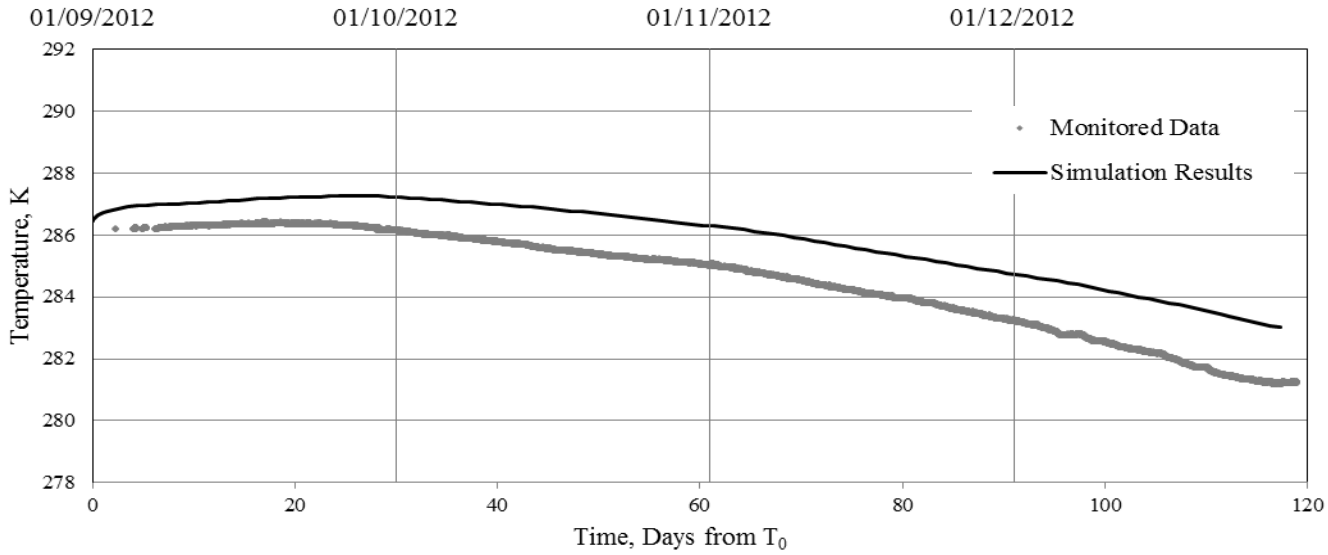

Figure G48 - Simulated and monitored ground temperatures at thermistor location BA11.

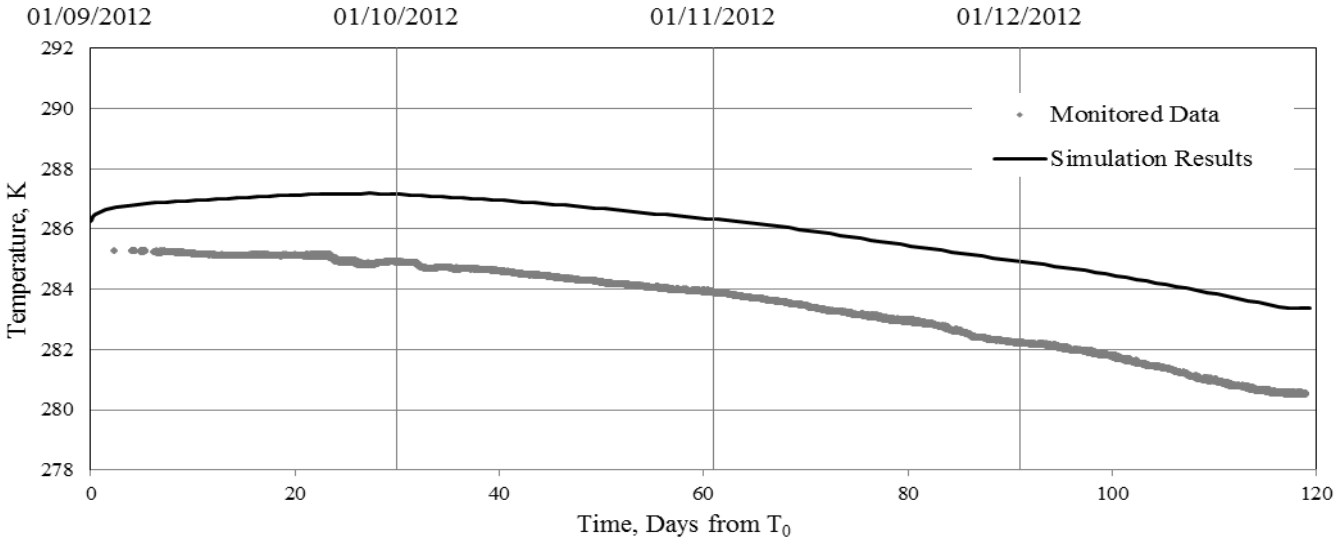

Figure G49 - Simulated and monitored ground temperatures at thermistor location BA12.

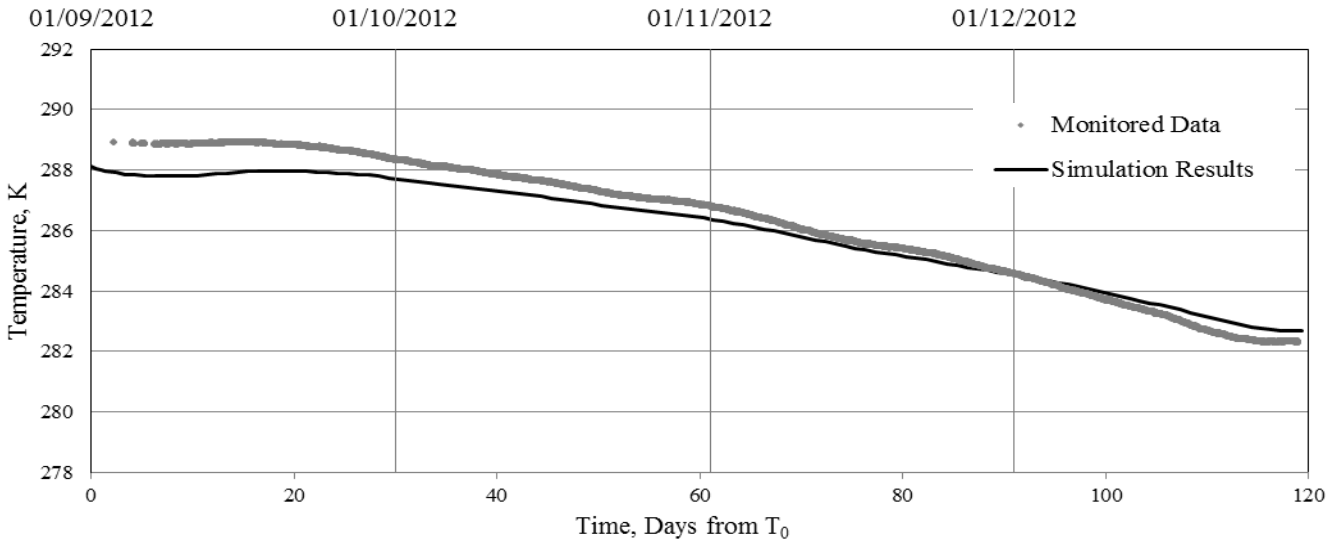

Figure G50 - Simulated and monitored ground temperatures at thermistor location BA13.

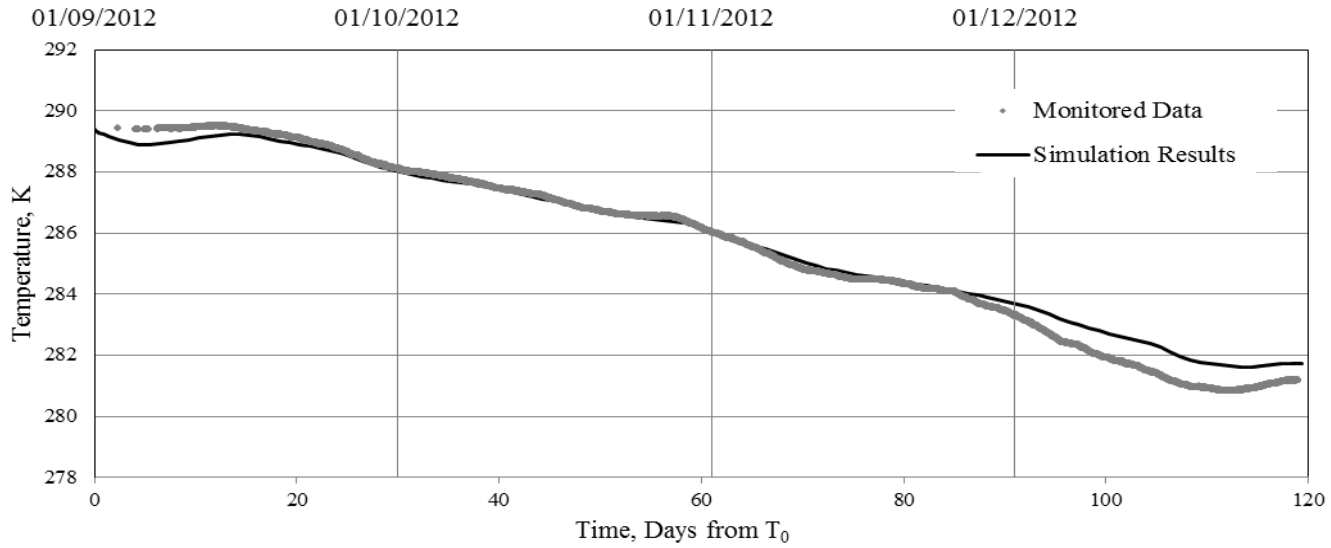

Figure G51 - Simulated and monitored ground temperatures at thermistor location BA14.

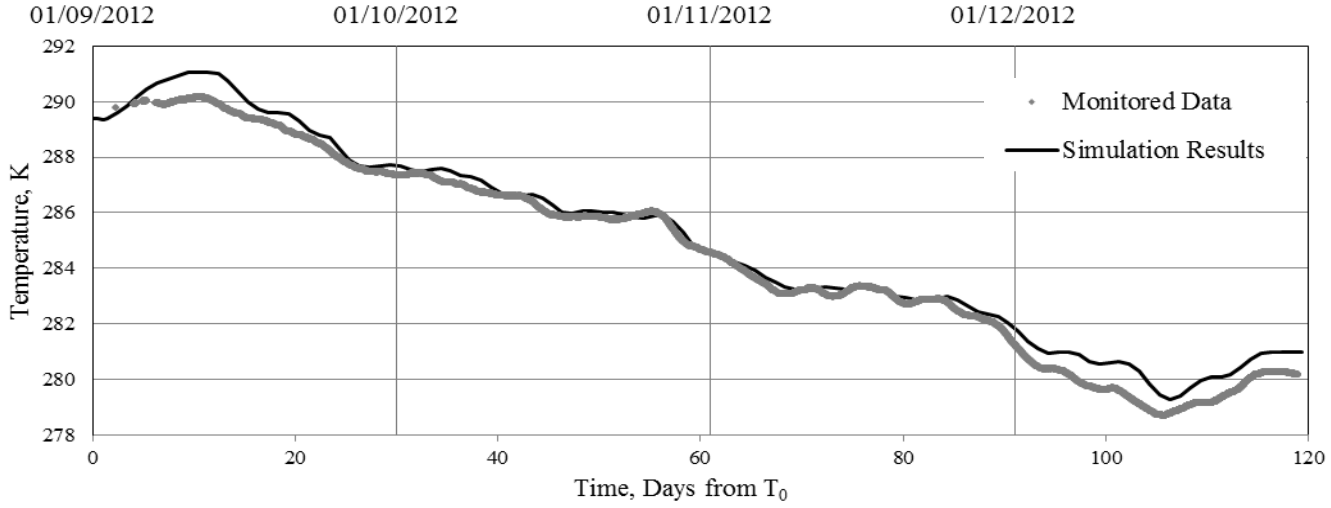

Figure G52 - Simulated and monitored ground temperatures at thermistor location BA15

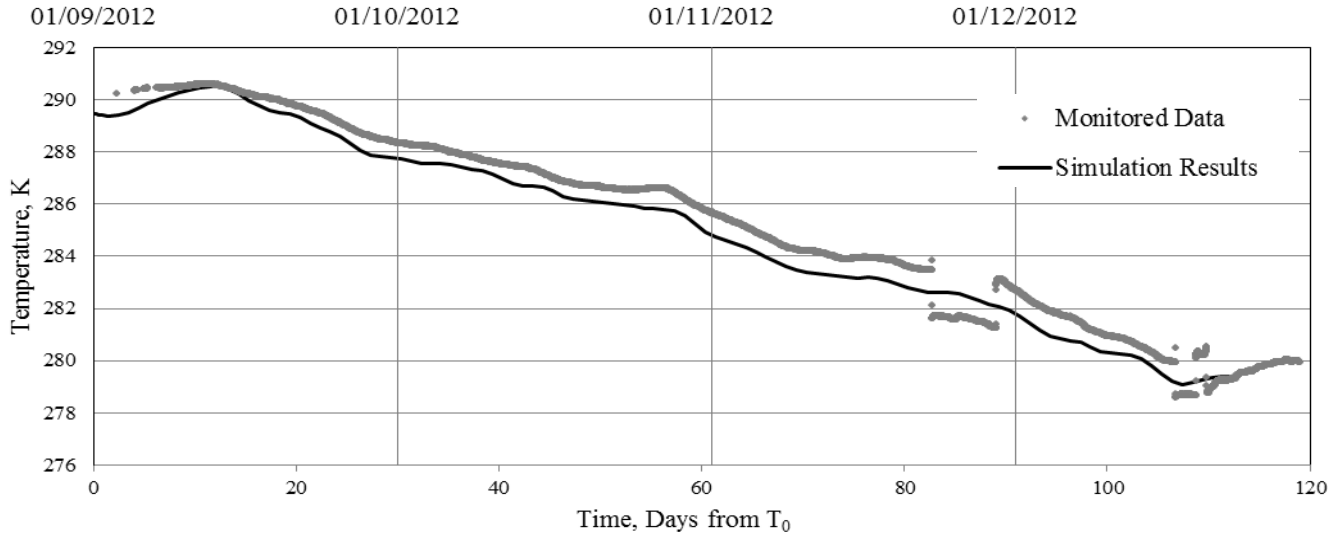

Figure G53 - Simulated and monitored ground temperatures at thermistor location BB1.

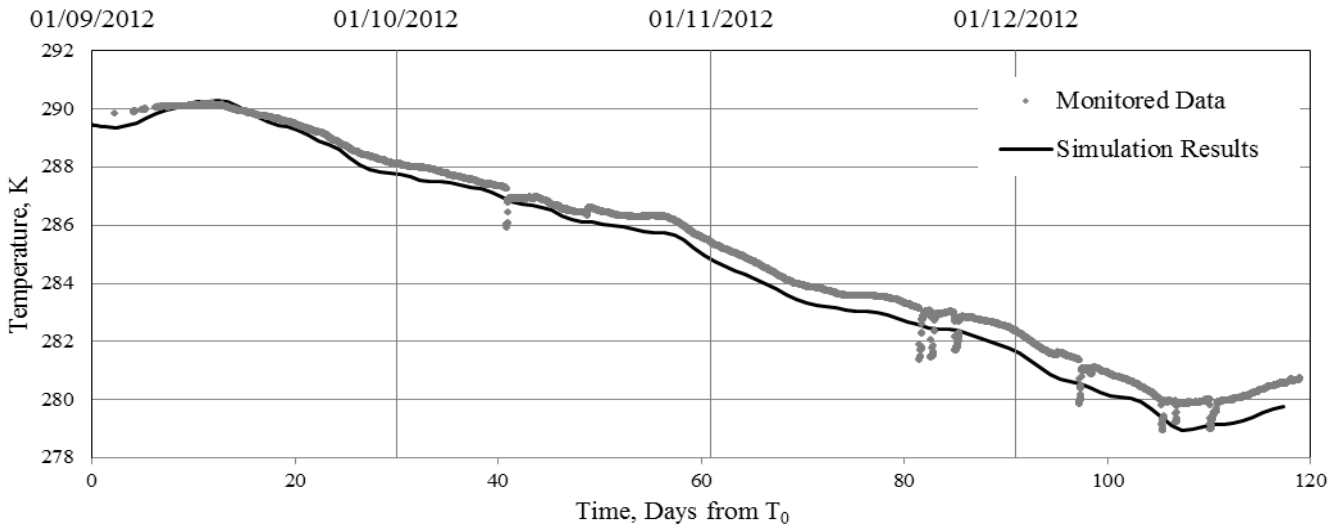

Figure G54 - Simulated and monitored ground temperatures at thermistor location BB2.

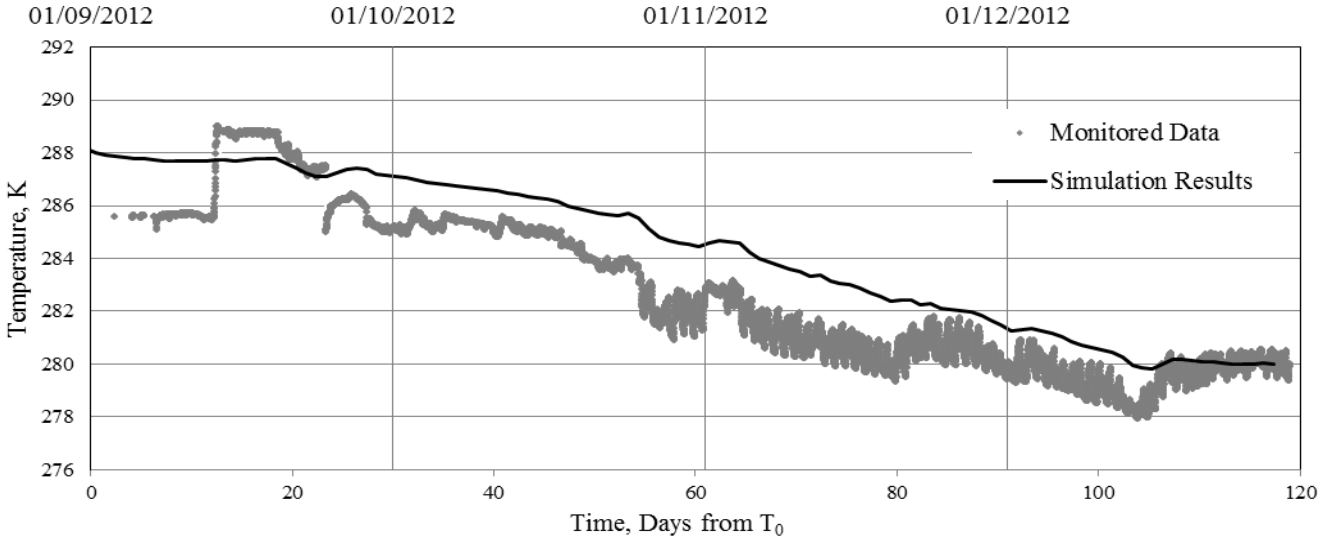

Figure G55 - Simulated and monitored ground temperatures at thermistor location BB4.

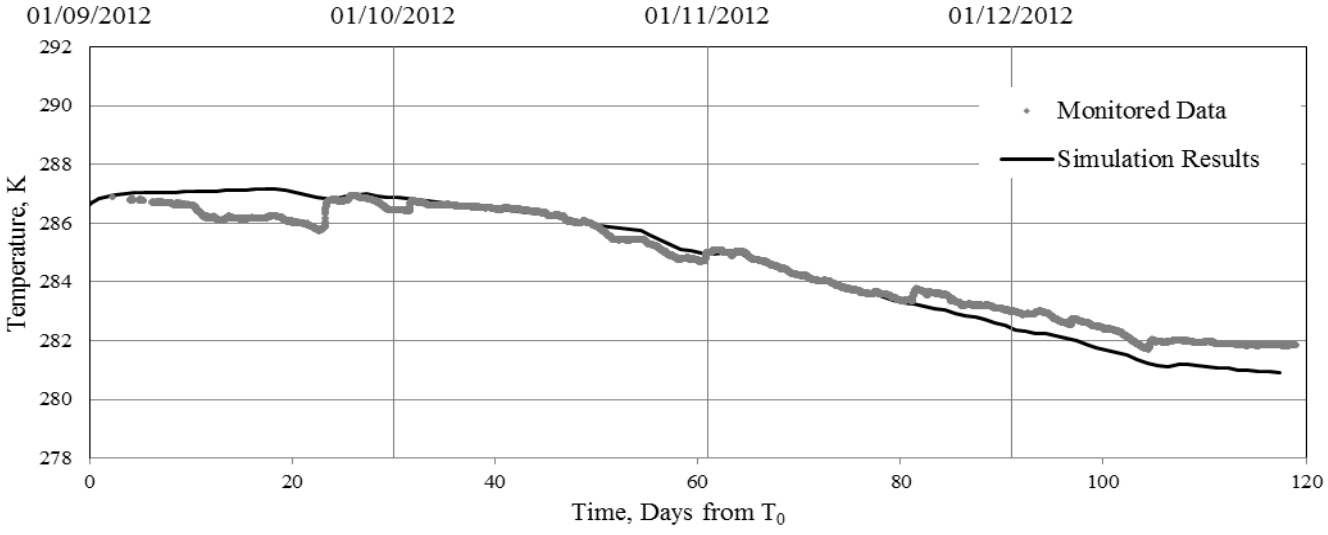

Figure G56 - Simulated and monitored ground temperatures at thermistor location BB5.

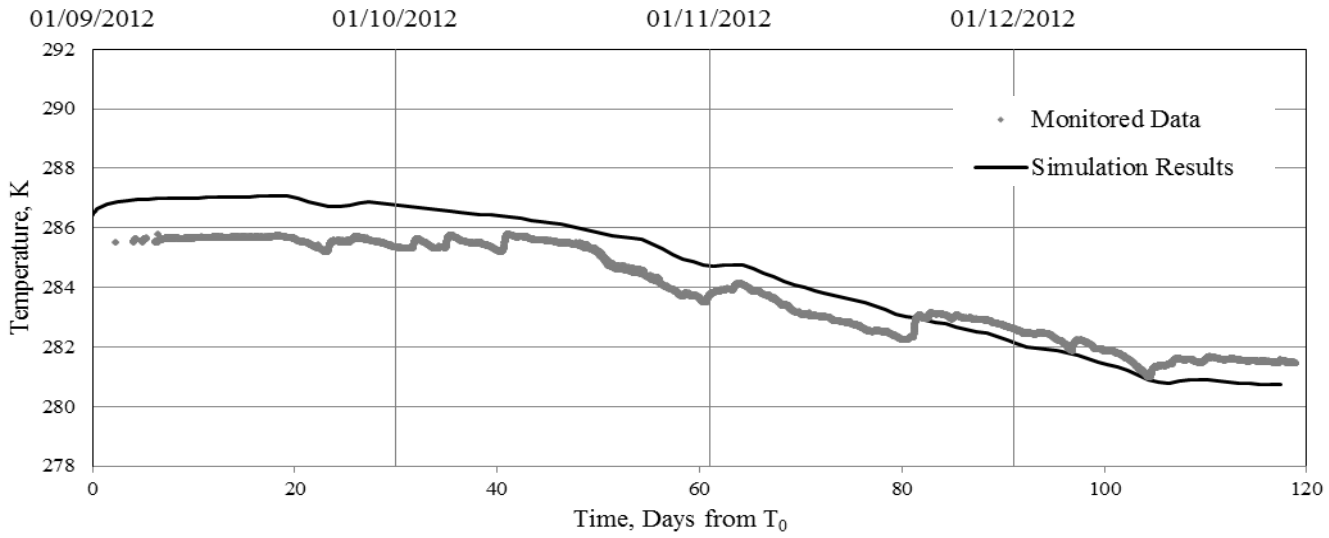

Figure G57 - Simulated and monitored ground temperatures at thermistor location BB6.

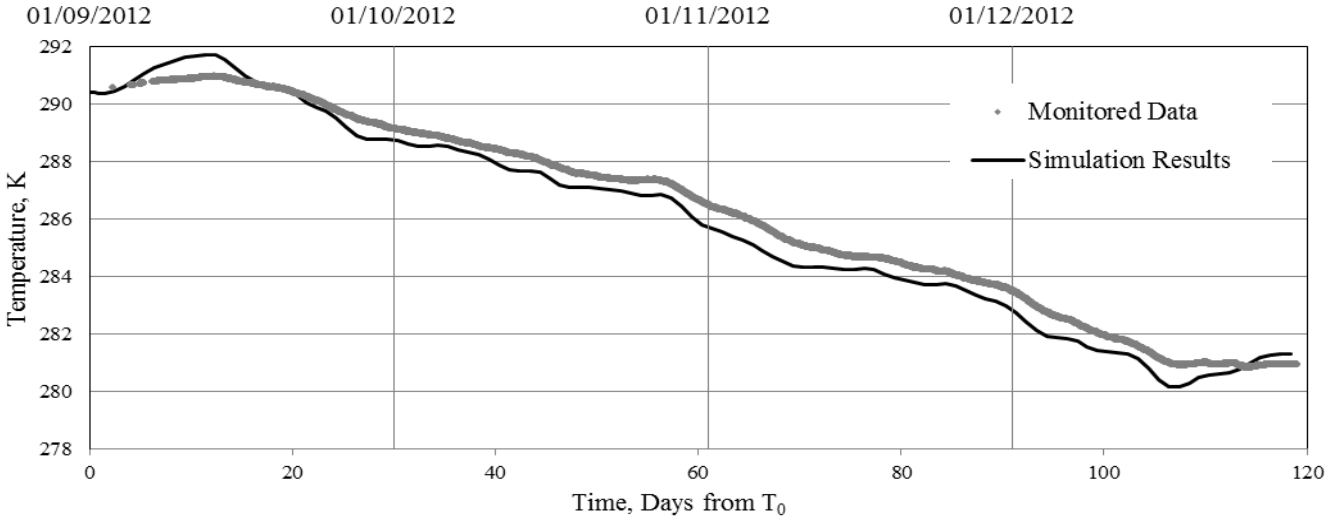

Figure G58- Simulated and monitored ground temperatures at thermistor location BB7.

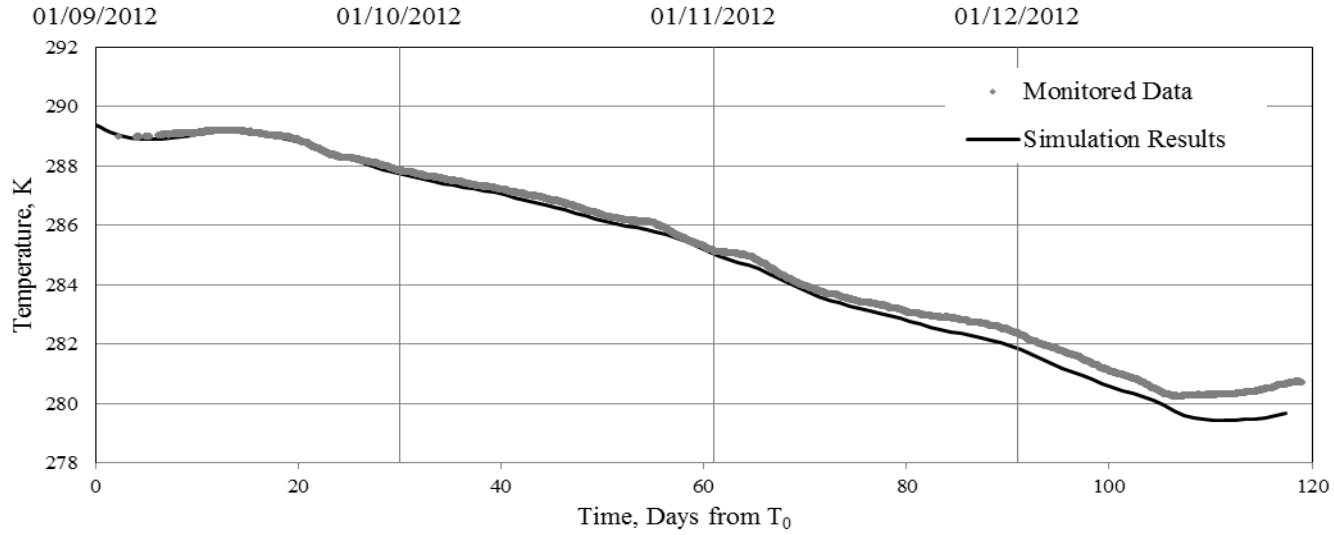

Figure G59 - Simulated and monitored ground temperatures at thermistor location BB8

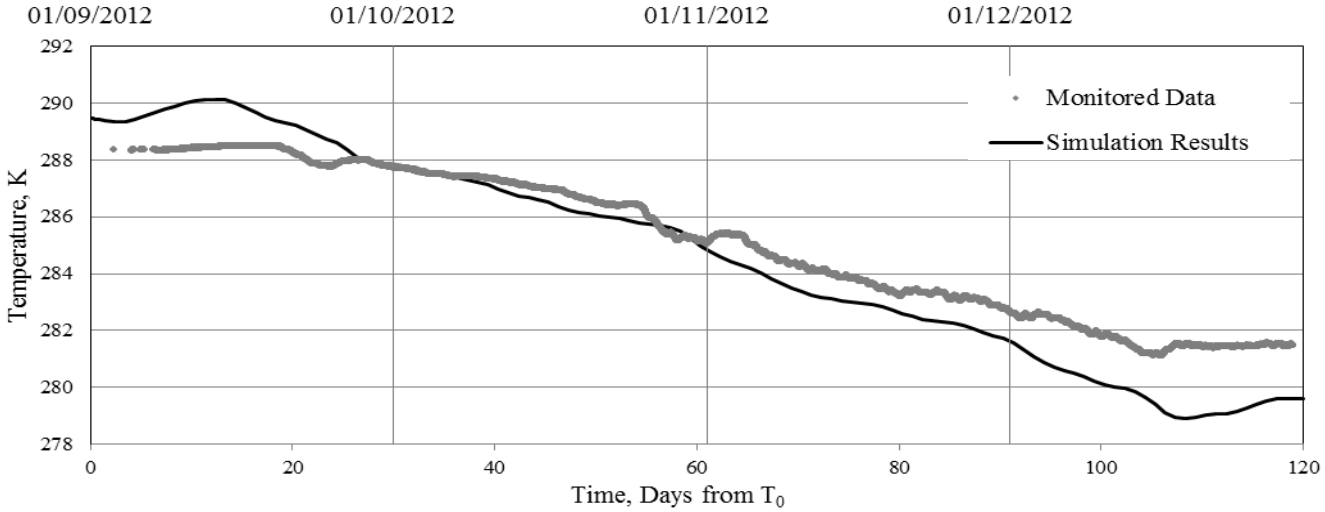

Figure G60 - Simulated and monitored ground temperatures at thermistor location BB9.

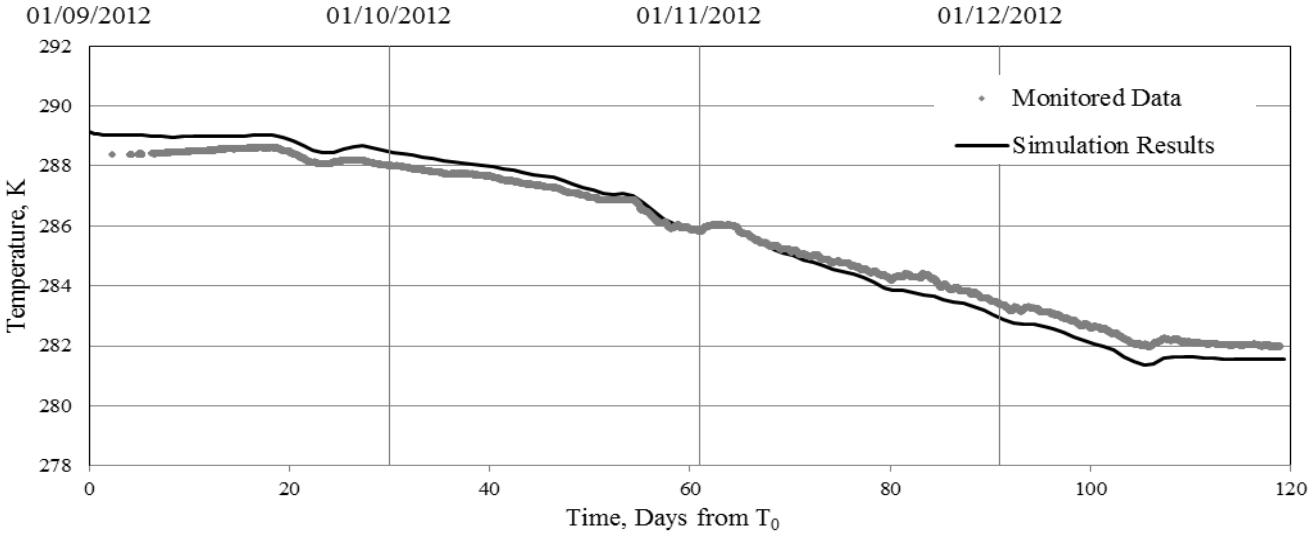

Figure G61 - Simulated and monitored ground temperatures at thermistor location BB10.

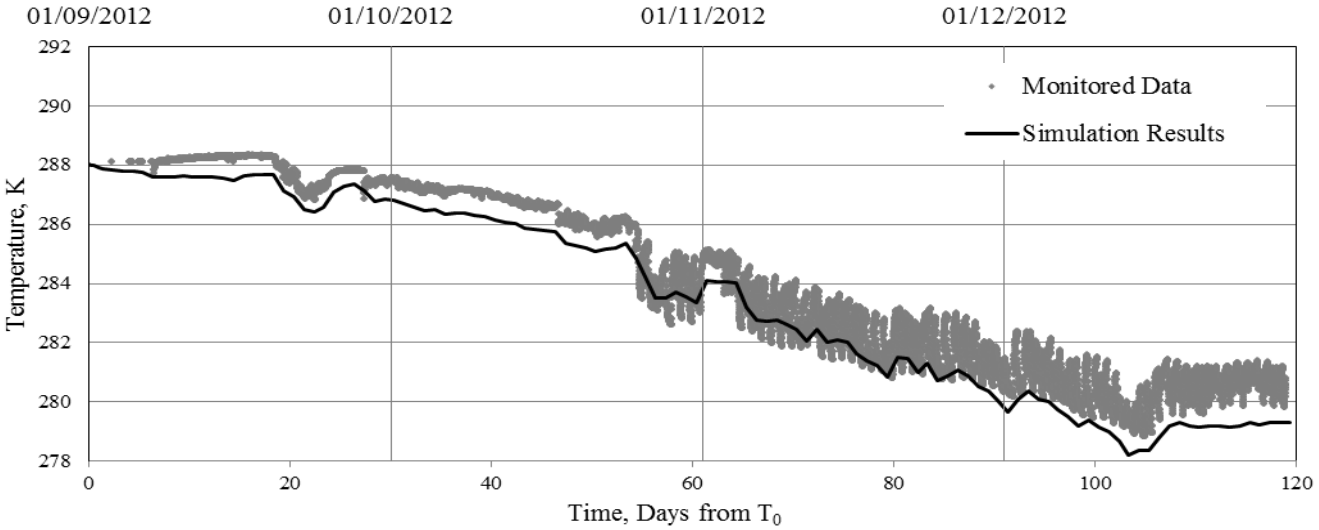

Figure G62 - Simulated and monitored ground temperatures at thermistor location BB11.

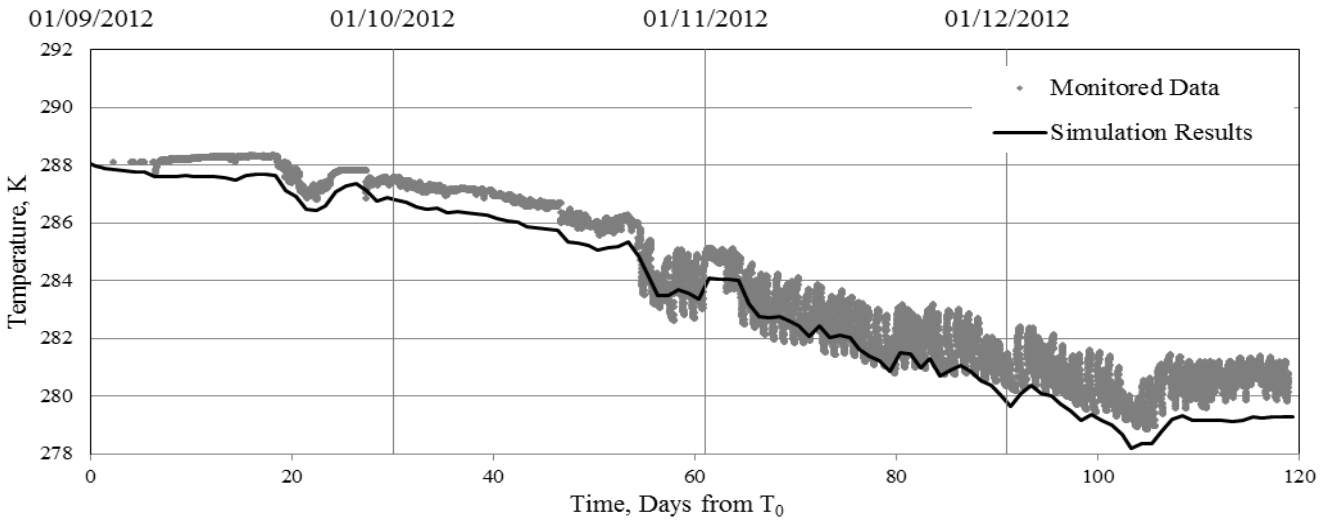

Figure G63 - Simulated and monitored ground temperatures at thermistor location BB12.

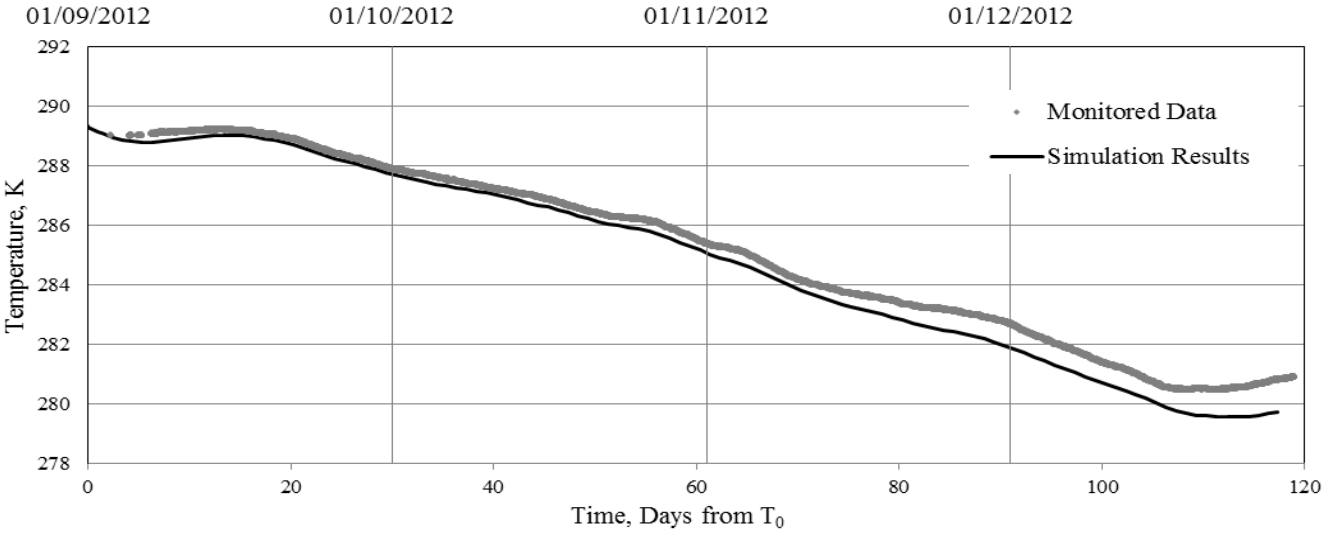

Figure G64 - Simulated and monitored ground temperatures at thermistor location BB13.

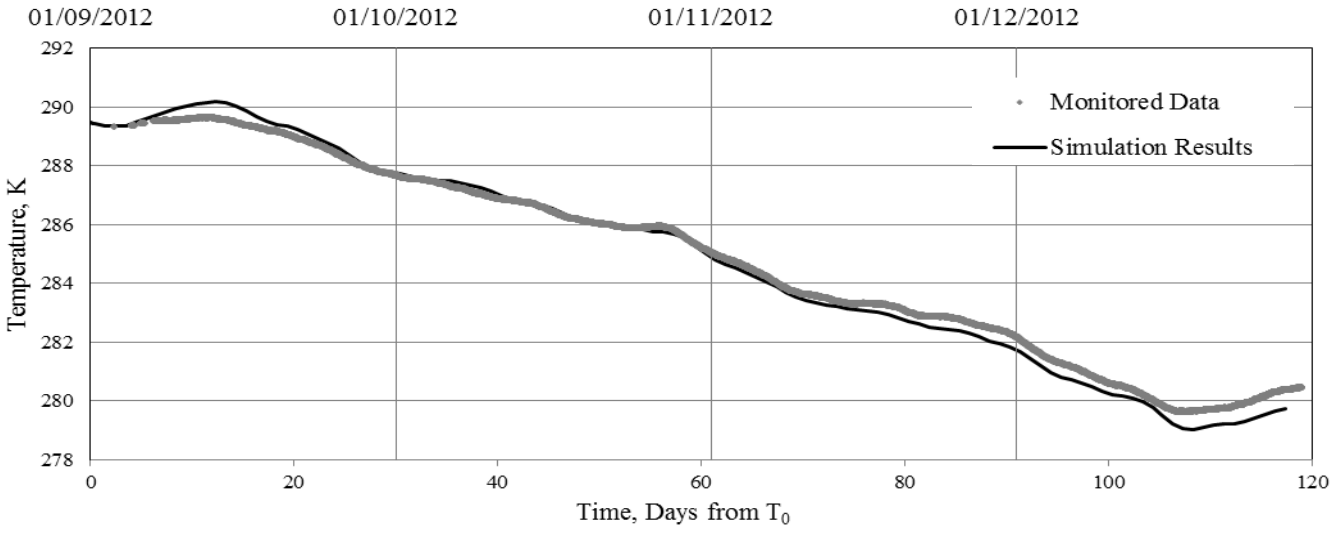

Figure G65 - Simulated and monitored ground temperatures at thermistor location BB14.

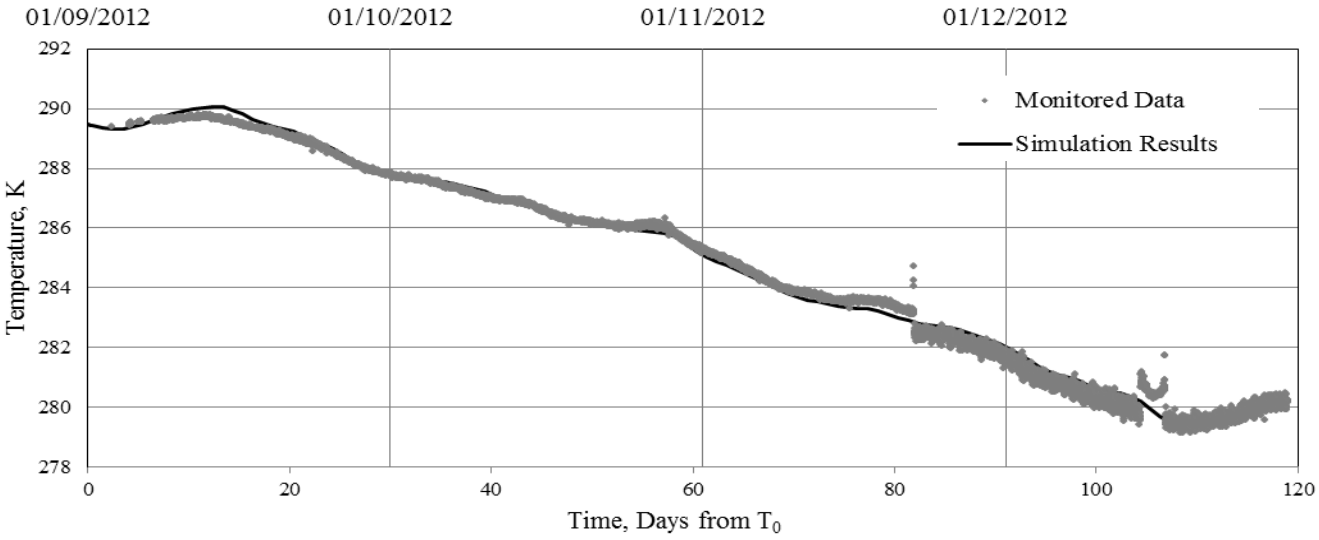

Figure G66 - Simulated and monitored ground temperatures at thermistor location BC1.

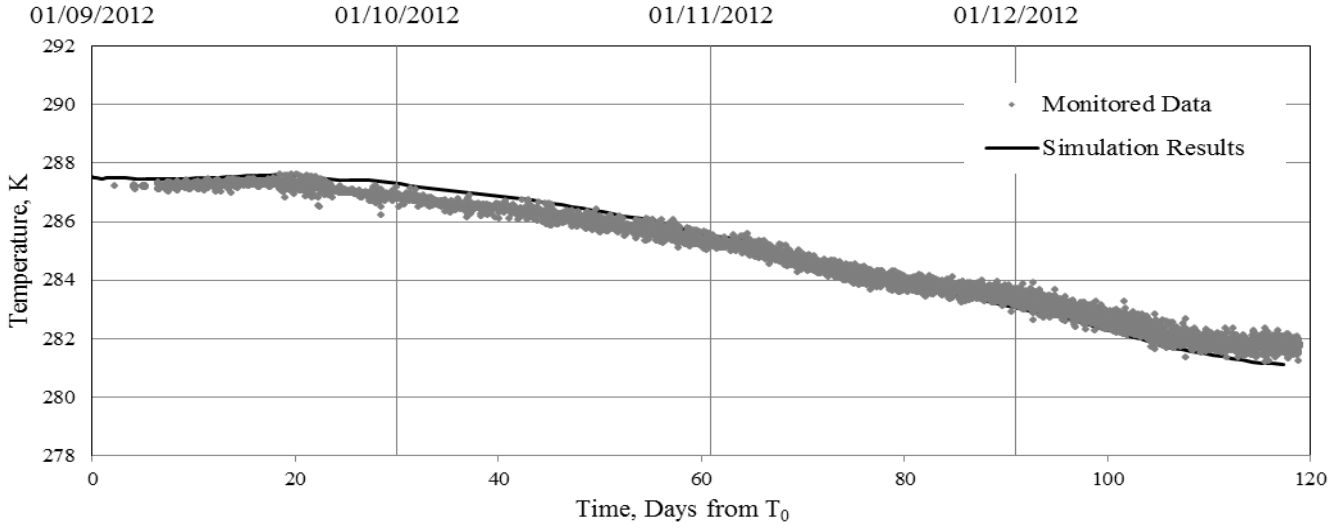

Figure G67 - Simulated and monitored ground temperatures at thermistor location BC3.

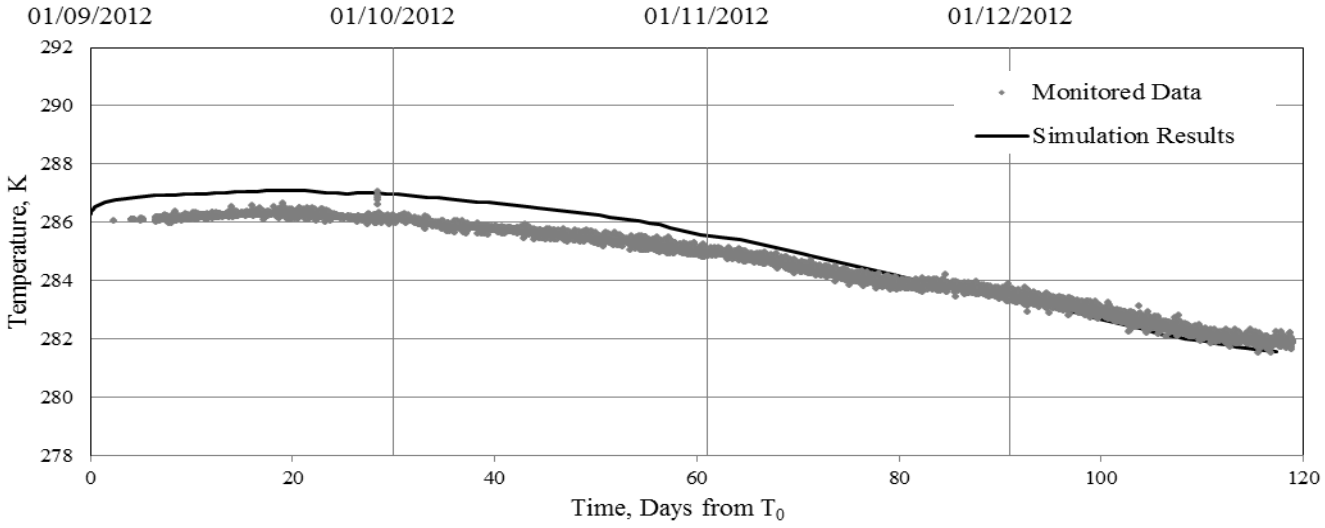

Figure G68 - Simulated and monitored ground temperatures at thermistor location BC4.

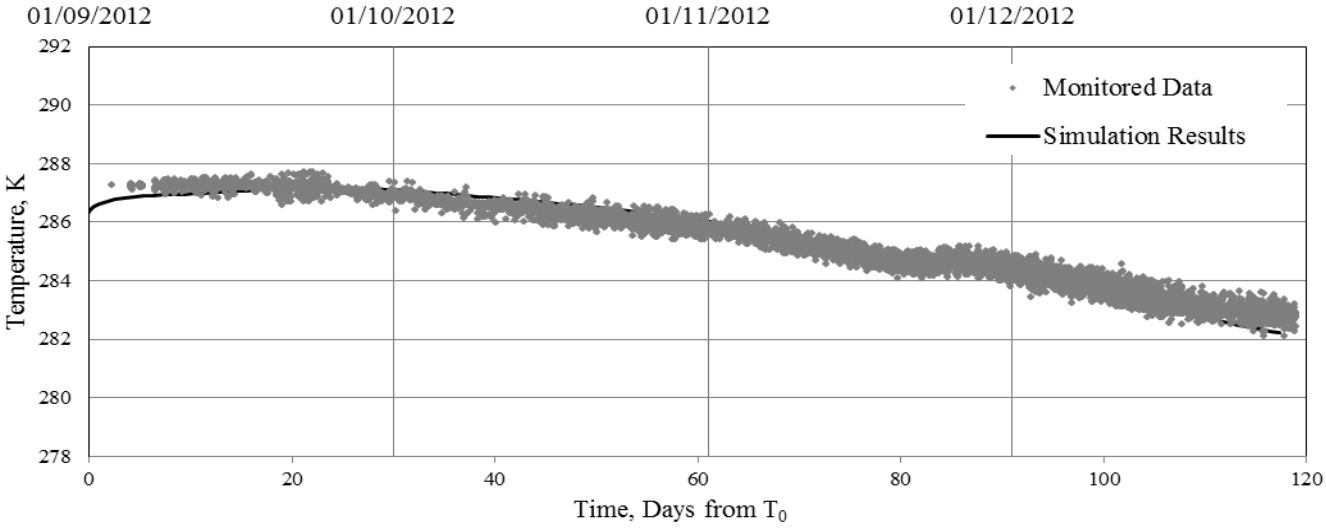

Figure G69 - Simulated and monitored ground temperatures at thermistor location BC5.

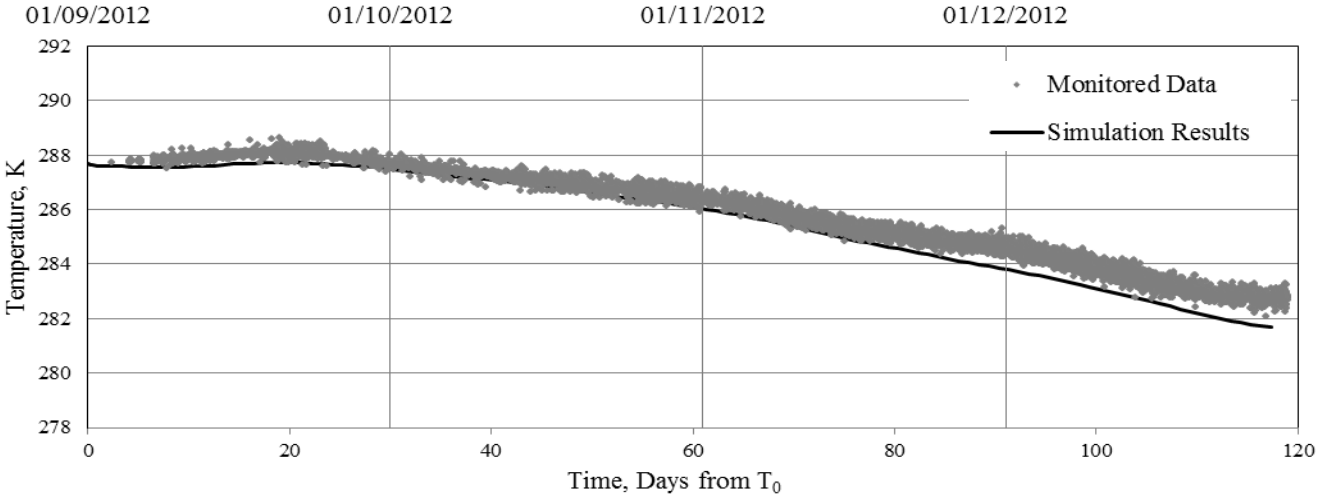

Figure G70 - Simulated and monitored ground temperatures at thermistor location BC6.

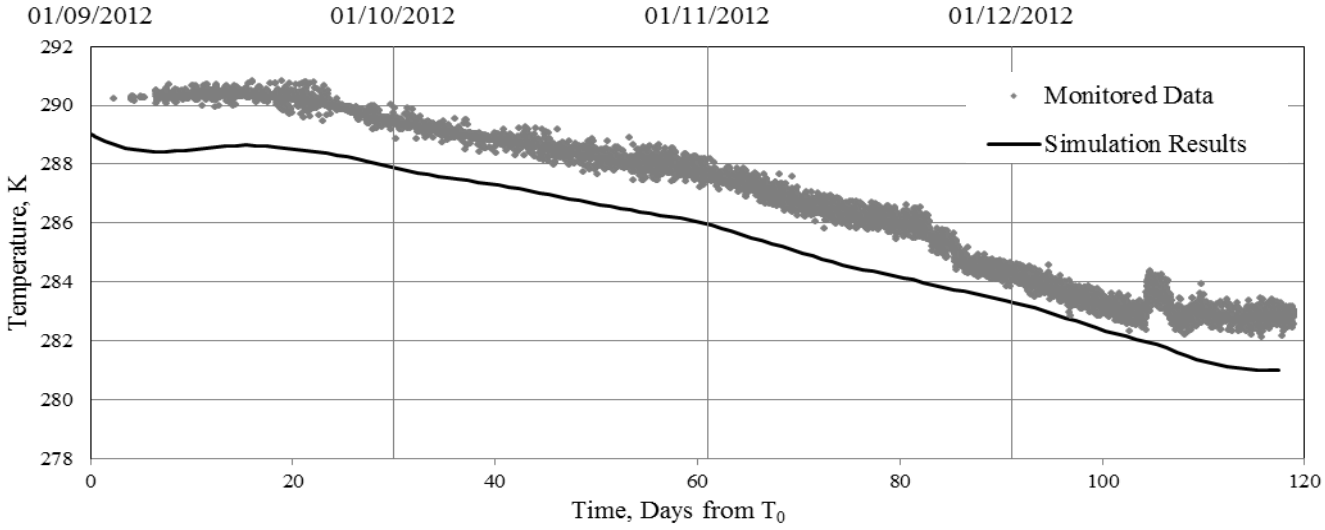

Figure G71 - Simulated and monitored ground temperatures at thermistor location BC7.

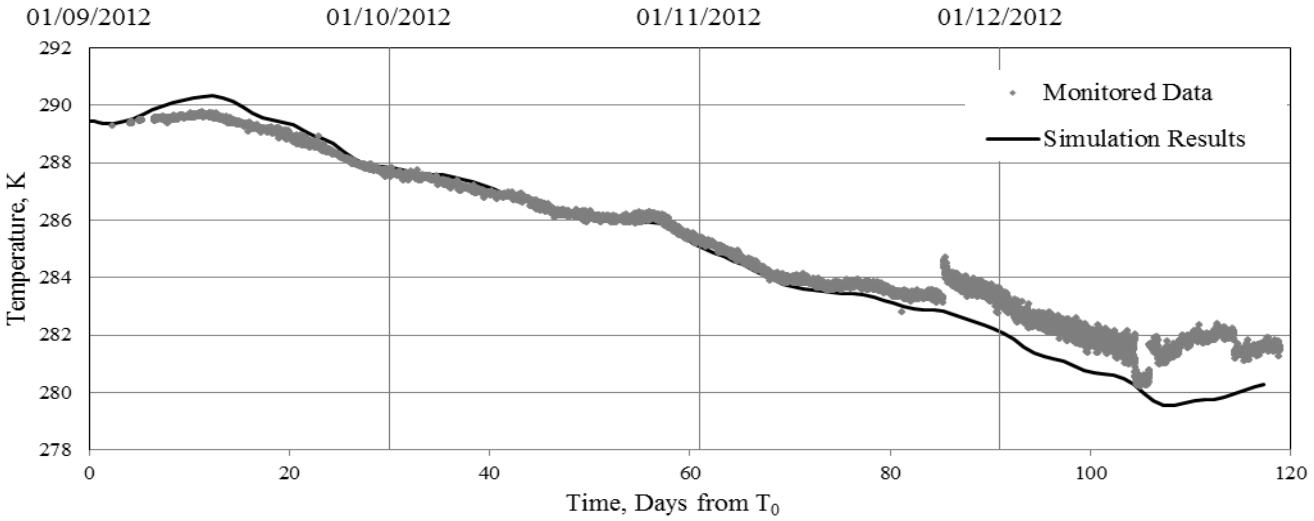

Figure G72 - Simulated and monitored ground temperatures at thermistor location BC8.

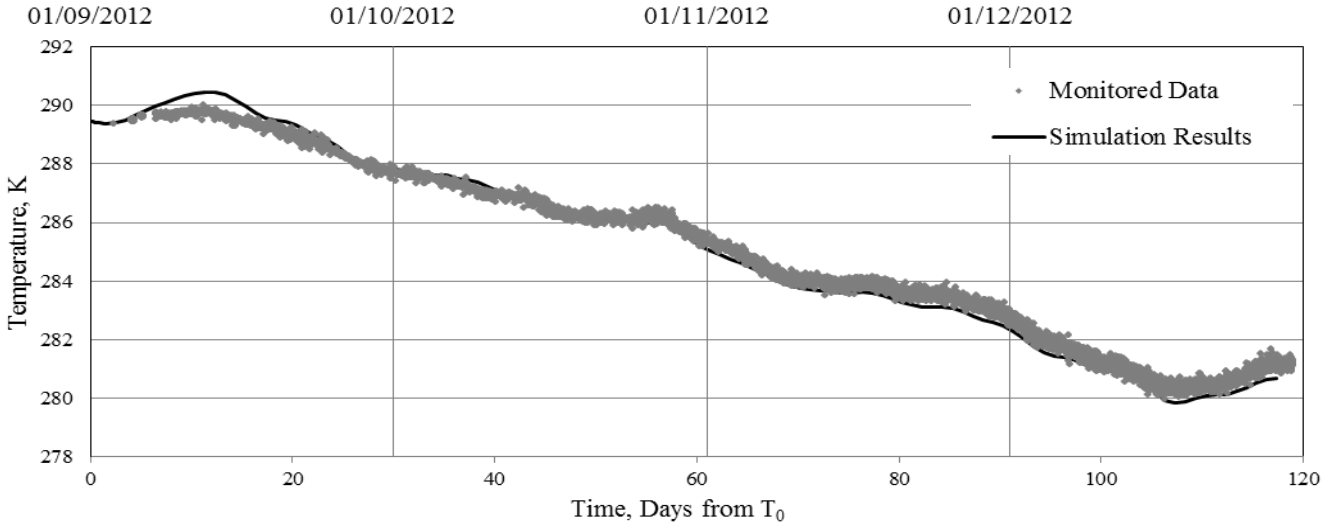

Figure G73 - Simulated and monitored ground temperatures at thermistor location BC9.

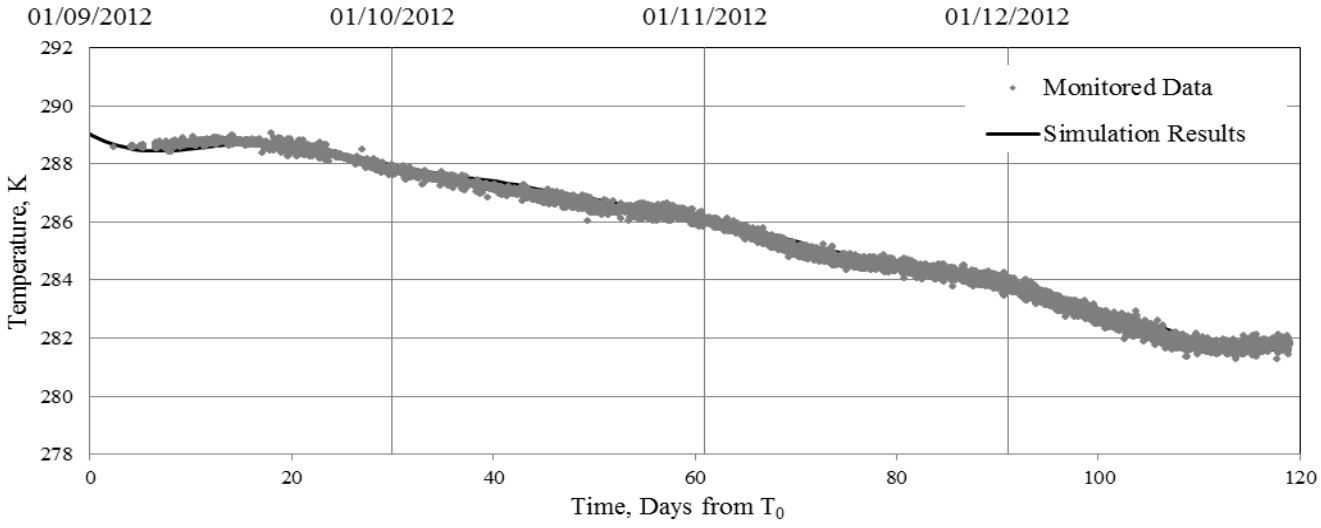

Figure G74 - Simulated and monitored ground temperatures at thermistor location BC10.

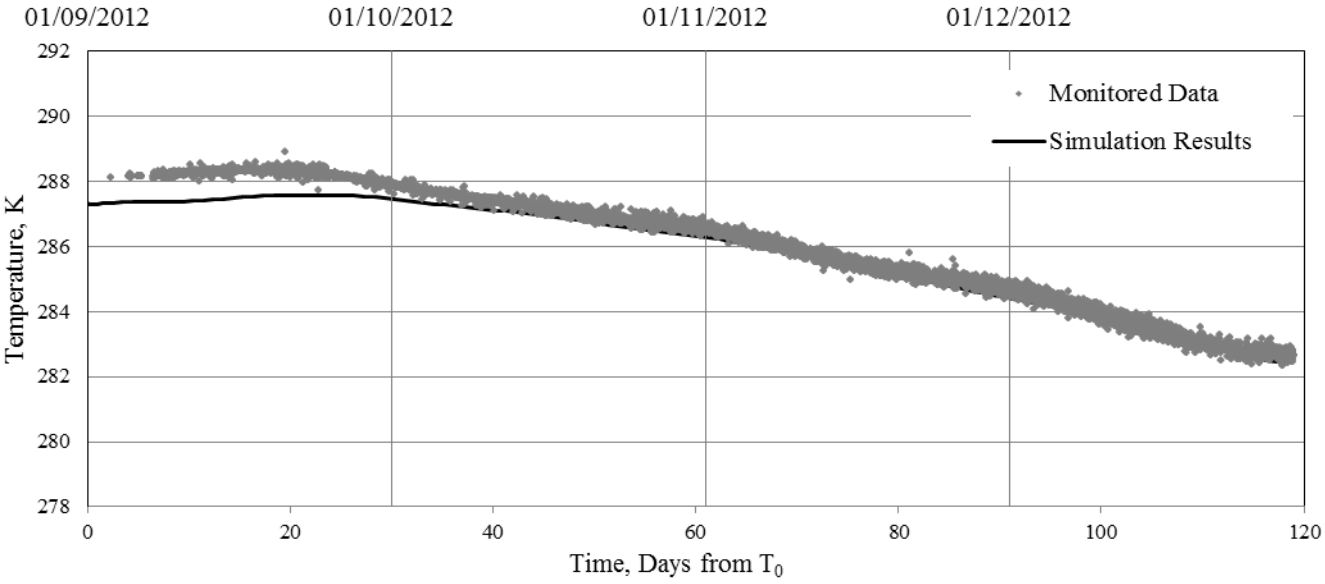

Figure G75 - Simulated and monitored ground temperatures at thermistor location BC11.

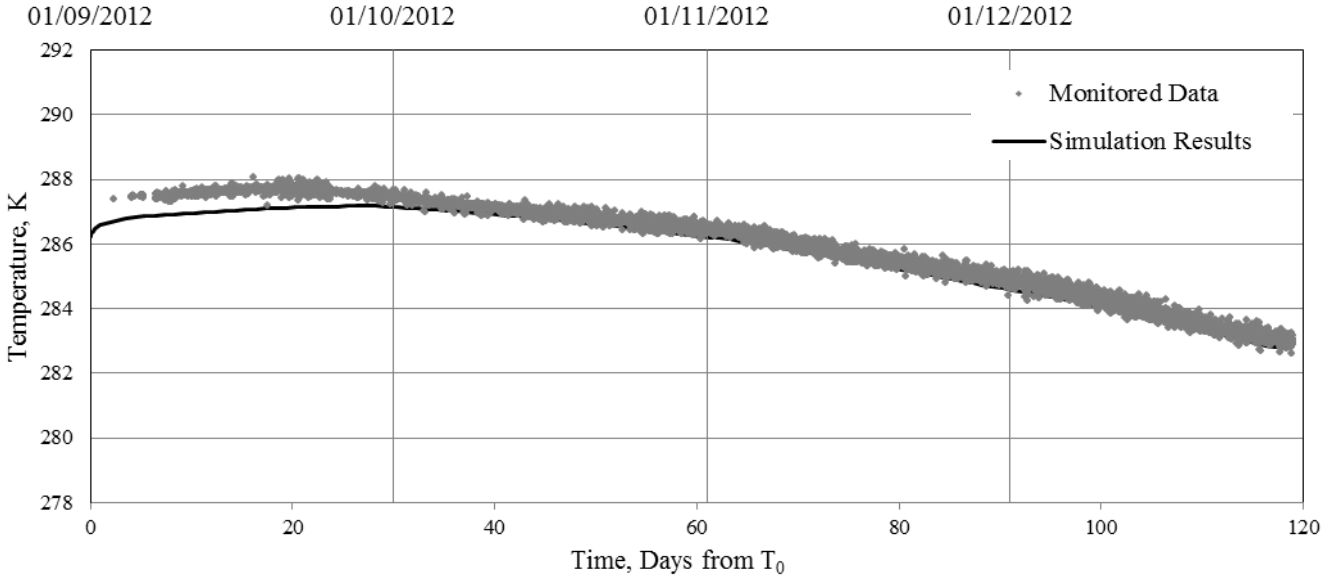

Figure G76 - Simulated and monitored ground temperatures at thermistor location BC12.

Appendix H

MIS 3005 Ground-loop calculations

Heat pump capacity/size (G) = 16 kW (as installed at monitoring site)

---

1. *Calculation of FLEQ (Full Load Equivalent) run hours:*

$$\text{FLEQ run hours} = \frac{\text{Total heating energy consumption (per year)}}{\text{Heat pump capcity}}$$

$$= \frac{92{,}159.86 \text{ kJ (as recorded)}}{3600} = 25,599.96 \text{ kWh/year}$$

$$= \frac{25{,}599.96}{16} = 1599.9 \text{ FLEQ run hours}$$

---

2. *Determination of maximum power per unit ground length (g):*

Interpolating between the MIS design tables for 1200 and 1800 FLEQ hours and applying a ground thermal conductivity of 2.3 W $m^{-1}K^{-1}$ gives a maximmum power extraction per meter length of 24 Wm^{-1}.

---

3. *Determination of ground-loop length:*

$$\text{Ground-loop length } (L_b) = \frac{G}{g}$$

$$= \frac{16{,}000}{24} = 666.67 \text{ m}$$